

# BOTTOM-UP APPROACH: A ROUTE FOR EFFECTIVE MULTI-MODAL IMAGING OF TUMORS

EDITED BY: Min Wu, Lu Yang, Dong-Hyun Kim, Changqiang Wu and Peng Mi  
PUBLISHED IN: Frontiers in Oncology





# frontiers

## Frontiers eBook Copyright Statement

The copyright in the text of individual articles in this eBook is the property of their respective authors or their respective institutions or funders. The copyright in graphics and images within each article may be subject to copyright of other parties. In both cases this is subject to a license granted to Frontiers.

The compilation of articles constituting this eBook is the property of Frontiers.

Each article within this eBook, and the eBook itself, are published under the most recent version of the Creative Commons CC-BY licence.

The version current at the date of publication of this eBook is CC-BY 4.0. If the CC-BY licence is updated, the licence granted by Frontiers is automatically updated to the new version.

When exercising any right under the CC-BY licence, Frontiers must be attributed as the original publisher of the article or eBook, as applicable.

Authors have the responsibility of ensuring that any graphics or other materials which are the property of others may be included in the CC-BY licence, but this should be checked before relying on the CC-BY licence to reproduce those materials. Any copyright notices relating to those materials must be complied with.

Copyright and source acknowledgement notices may not be removed and must be displayed in any copy, derivative work or partial copy which includes the elements in question.

All copyright, and all rights therein, are protected by national and international copyright laws. The above represents a summary only. For further information please read Frontiers' Conditions for Website Use and Copyright Statement, and the applicable CC-BY licence.

ISSN 1664-8714

ISBN 978-2-88974-453-4

DOI 10.3389/978-2-88974-453-4

## About Frontiers

Frontiers is more than just an open-access publisher of scholarly articles: it is a pioneering approach to the world of academia, radically improving the way scholarly research is managed. The grand vision of Frontiers is a world where all people have an equal opportunity to seek, share and generate knowledge. Frontiers provides immediate and permanent online open access to all its publications, but this alone is not enough to realize our grand goals.

## Frontiers Journal Series

The Frontiers Journal Series is a multi-tier and interdisciplinary set of open-access, online journals, promising a paradigm shift from the current review, selection and dissemination processes in academic publishing. All Frontiers journals are driven by researchers for researchers; therefore, they constitute a service to the scholarly community. At the same time, the Frontiers Journal Series operates on a revolutionary invention, the tiered publishing system, initially addressing specific communities of scholars, and gradually climbing up to broader public understanding, thus serving the interests of the lay society, too.

## Dedication to Quality

Each Frontiers article is a landmark of the highest quality, thanks to genuinely collaborative interactions between authors and review editors, who include some of the world's best academicians. Research must be certified by peers before entering a stream of knowledge that may eventually reach the public - and shape society; therefore, Frontiers only applies the most rigorous and unbiased reviews. Frontiers revolutionizes research publishing by freely delivering the most outstanding research, evaluated with no bias from both the academic and social point of view. By applying the most advanced information technologies, Frontiers is catapulting scholarly publishing into a new generation.

## What are Frontiers Research Topics?

Frontiers Research Topics are very popular trademarks of the Frontiers Journals Series: they are collections of at least ten articles, all centered on a particular subject. With their unique mix of varied contributions from Original Research to Review Articles, Frontiers Research Topics unify the most influential researchers, the latest key findings and historical advances in a hot research area! Find out more on how to host your own Frontiers Research Topic or contribute to one as an author by contacting the Frontiers Editorial Office: [frontiersin.org/about/contact](https://frontiersin.org/about/contact)



# BOTTOM-UP APPROACH: A ROUTE FOR EFFECTIVE MULTI-MODAL IMAGING OF TUMORS

Topic Editors:

**Min Wu**, Sichuan University, China

**Lu Yang**, Sichuan University, China

**Dong-Hyun Kim**, Northwestern University, United States

**Changqiang Wu**, North Sichuan Medical College, China

**Peng Mi**, Sichuan University, China

**Citation:** Wu, M., Yang, L., Kim, D.-H., Wu, C., Mi, P., eds. (2022). Bottom-Up Approach: A Route for Effective Multi-Modal Imaging of Tumors. Lausanne: Frontiers Media SA. doi: 10.3389/978-2-88974-453-4

# Table of Contents

- 06 Editorial: Bottom-Up Approach: A Route for Effective Multi-Modal Imaging of Tumors**  
Ruoxi Xie, Changqiang Wu, Lu Yang, Peng Mi, Dong-Hyun Kim and Min Wu
- 10 Diagnostic Imaging Methods and Comparative Analysis of Orbital Cavernous Hemangioma**  
Li Zhang, Xuying Li, Fei Tang, Lu Gan and Xin Wei
- 16 Quick Automatic Synthesis of Solvent-Free  $16\alpha$ - $[^{18}\text{F}]$  Fluoroestradiol: Comparison of Kryptofix 222 and Tetrabutylammonium Bicarbonate**  
Xiao Jiang, Yingchun Li, Xiaoxiong Wang, Taipeng Shen, Xiuli Li, Yutang Yao, Ge Zhang, Ying Kou, Jiaqi Shen, Zhifu Luo and Zhuzhong Cheng
- 25 A Novel Model Based on CXCL8-Derived Radiomics for Prognosis Prediction in Colorectal Cancer**  
Yanpeng Chu, Jie Li, Zhaoping Zeng, Bin Huang, Jiaojiao Zhao, Qin Liu, Huaping Wu, Jiangping Fu, Yin Zhang, Yefan Zhang, Jianqiang Cai and Fanxin Zeng
- 34 Deep Convolutional Neural Network Based on Computed Tomography Images for the Preoperative Diagnosis of Occult Peritoneal Metastasis in Advanced Gastric Cancer**  
Zixing Huang, Dan Liu, Xinzu Chen, Du He, Pengxin Yu, Baiyun Liu, Bing Wu, Jiankun Hu and Bin Song
- 44 Radiomic Feature-Based Predictive Model for Microvascular Invasion in Patients With Hepatocellular Carcinoma**  
Mu He, Peng Zhang, Xiao Ma, Baochun He, Chihua Fang and Fucang Jia
- 55 Combined T2 SPAIR, Dynamic Enhancement and DW Imaging Reliably Detect T Staging and Grading of Bladder Cancer With 3.0T MRI**  
Lihua Yuan, Danyan Li, Dan Mu, Xuebin Zhang, Weidong Kong, Le Cheng, Xin Shu, Bing Zhang and Zhishun Wang
- 64 Time Difference of Arrival on Contrast-Enhanced Ultrasound in Distinguishing Benign Inflammation From Malignant Peripheral Pulmonary Lesions**  
Min Tang, Qianrong Xie, Jiasi Wang, Xiaoyu Zhai, Hong Lin, Xiaoxue Zheng, Guoli Wei, Yan Tang, Fanwei Zeng, Yanpeng Chu, Jianqiong Song, Jianqiang Cai and Fanxin Zeng
- 72 Comparison of Diagnostic Performance of Five Different Ultrasound TI-RADS Classification Guidelines for Thyroid Nodules**  
Ruoning Yang, Xiuhe Zou, Hao Zeng, Yunuo Zhao and Xuelei Ma
- 79 Survival Prediction in Gallbladder Cancer Using CT Based Machine Learning**  
Zefan Liu, Guannan Zhu, Xian Jiang, Yunuo Zhao, Hao Zeng, Jing Jing and Xuelei Ma

- 87 ***Diagnostic Value of Telomerase Activity in Patients With Bladder Cancer: A Meta-Analysis of Diagnostic Test***  
Lei Peng, Jinze Li, Chunyang Meng, Jinming Li, Dandan Tang, Fangxue Guan, Peng Xu, Tangqiang Wei and Yunxiang Li
- 98 ***A Prediction Model for Optimal Primary Debulking Surgery Based on Preoperative Computed Tomography Scans and Clinical Factors in Patients With Advanced Ovarian Cancer: A Multicenter Retrospective Cohort Study***  
Yu Gu, Meng Qin, Ying Jin, Jing Zuo, Ning Li, Ce Bian, Yu Zhang, Rong Li, Yu-mei Wu, Chun-yan Wang, Ke-qiang Zhang, Ying Yue, Ling-ying Wu and Ling-ya Pan
- 108 ***A Correlative Study Between IVIM-DWI Parameters and the Expression Levels of Ang-2 and TKT in Hepatocellular Carcinoma***  
Jing Zheng, Xue Qin Gong, Yun Yun Tao, Ran Wang, Gang Yang, Jing Dong Li, Tian Ren, Zu Mao Li, Cui Yang, Wei Cheng Wang, Lin Yang and Xiao Ming Zhang
- 117 ***SurvNet: A Novel Deep Neural Network for Lung Cancer Survival Analysis With Missing Values***  
Jianyong Wang, Nan Chen, Jixiang Guo, Xiuyuan Xu, Lunxu Liu and Zhang Yi
- 126 ***Application of Multimodal and Molecular Imaging Techniques in the Detection of Choroidal Melanomas***  
Xuying Li, Lixiang Wang, Li Zhang, Fei Tang and Xin Wei
- 134 ***Intra-Individual Comparison of 18F-PSMA-1007 and 18F-FDG PET/CT in the Evaluation of Patients With Prostate Cancer***  
Xing Zhou, YingChun Li, Xiao Jiang, XiaoXiong Wang, ShiRong Chen, TaiPeng Shen, JinHui You, Hao Lu, Hong Liao, Zeng Li and ZhuZhong Cheng
- 142 ***Comparison of Radiomic Models Based on Low-Dose and Standard-Dose CT for Prediction of Adenocarcinomas and Benign Lesions in Solid Pulmonary Nodules***  
Jieke Liu, Hao Xu, Haomiao Qing, Yong Li, Xi Yang, Changjiu He, Jing Ren and Peng Zhou
- 153 ***The MRI-Visible Nanocomposite Facilitates the Delivery and Tracking of siRNA Loaded DC Vaccine in the Breast Cancer Model***  
Changqiang Wu, Wencheng Zhu, Rongrong Jin, Hua Ai and Ye Xu
- 165 ***Use of Radiomics to Improve Diagnostic Performance of PI-RADS v2.1 in Prostate Cancer***  
Mou Li, Ling Yang, Yufeng Yue, Jingxu Xu, Chencui Huang and Bin Song
- 174 ***Case Report: Extra-Articular Diffuse Tenosynovial Giant Cell Tumor of the Temporomandibular Joint***  
Xibiao Yang, Li Yao, Tianping Yu, Xiaoli Du and Qiang Yue
- 180 ***Is Additional Systematic Biopsy Necessary in All Initial Prostate Biopsy Patients With Abnormal MRI?***  
Xueqing Cheng, Jinshun Xu, Yuntian Chen, Zhenhua Liu, Guangxi Sun, Ling Yang, Jin Yao, Hao Zeng and Bin Song
- 188 ***Advances in Research on the Cardiovascular Complications of Acromegaly***  
Han Yang, Huiwen Tan, He Huang and Jianwei Li

- 201** *Intravoxel Incoherent Motion Model in Differentiating the Pathological Grades of Esophageal Carcinoma: Comparison of Mono-Exponential and Bi-Exponential Fit Model*  
Nian Liu, Xiongxiang Yang, Lixing Lei, Ke Pan, Qianqian Liu and Xiaohua Huang
- 210** *Preoperative Assessment for Event-Free Survival With Hepatoblastoma in Pediatric Patients by Developing a CT-Based Radiomics Model*  
Yi Jiang, Jingjing Sun, Yuwei Xia, Yan Cheng, Linjun Xie, Xia Guo and Yingkun Guo
- 222** *Cancer or Tuberculosis: A Comprehensive Review of the Clinical and Imaging Features in Diagnosis of the Confusing Mass*  
Yufan Xiang, Chen Huang, Yan He and Qin Zhang
- 230** *Individualized Prediction of Colorectal Cancer Metastasis Using a Radiogenomics Approach*  
Qin Liu, Jie Li, Lin Xu, Jiasi Wang, Zhaoping Zeng, Jiangping Fu, Xuan Huang, Yanpeng Chu, Jing Wang, Hong-Yu Zhang and Fanxin Zeng
- 240** *3D DenseNet Deep Learning Based Preoperative Computed Tomography for Detecting Myasthenia Gravis in Patients With Thymoma*  
Zhenguo Liu, Ying Zhu, Yujie Yuan, Lei Yang, Kefeng Wang, Minghui Wang, Xiaoyu Yang, Xi Wu, Xi Tian, Rongguo Zhang, Bingqi Shen, Honghe Luo, Huiyu Feng, Shiting Feng and Zunfu Ke
- 249** *Arterial Spin Labeling MRI for Predicting Microvascular Invasion of T1 Staging Renal Clear Cell Carcinoma Preoperatively*  
Han-Mei Zhang, Da-Guang Wen, Yi Wang, Yi-Ge Bao, Yuan Yuan, Yun-Tian Chen and Bin Song
- 256** *New TRUS Techniques and Imaging Features of PI-RADS 4 or 5: Influence on Tumor Targeting*  
Amy Inji Chang and Byung Kwan Park
- 263** *The Preoperative Diagnostic Value of MRI and Otoneural Tests in Acoustic Neuroma*  
Qingqing Dai, Meijun Zheng, Qiurong Chen, Hong Zheng and Bilan Li
- 269** *Artificial Intelligence in the Imaging of Gastric Cancer: Current Applications and Future Direction*  
Yun Qin, Yiqi Deng, Hanyu Jiang, Na Hu and Bin Song
- 280** *Role of MRI-Based Functional Imaging in Improving the Therapeutic Index of Radiotherapy in Cancer Treatment*  
Mei Li, Qin Zhang and Kaixuan Yang



# Editorial: Bottom-Up Approach: A Route for Effective Multi-Modal Imaging of Tumors

Ruoxi Xie<sup>1</sup>, Changqiang Wu<sup>2</sup>, Lu Yang<sup>3</sup>, Peng Mi<sup>4</sup>, Dong-Hyun Kim<sup>5</sup> and Min Wu<sup>1\*</sup>

<sup>1</sup> Huaxi Magnetic Resonance Research Center (HMRRRC), Department of Radiology, Functional and Molecular Imaging Key Laboratory of Sichuan Province, West China Hospital, Sichuan University, Chengdu, China, <sup>2</sup> Medical Imaging Key Laboratory of Sichuan Province and School of Medical Imaging, North Sichuan Medical College, Nanchong, China, <sup>3</sup> The Department of Urology, The Institute of Urology, West China Hospital, Sichuan University, Chengdu, China, <sup>4</sup> Department of Radiology, Center for Medical Imaging, and State Key Laboratory of Biotherapy, West China Hospital, Sichuan University, Chengdu, China, <sup>5</sup> Department of Radiology, Feinberg School of Medicine, Northwestern University, Chicago, IL, United States

**Keywords:** tumor, multi-modal probes, multi-parametric imaging, MRI, CT, fluorescence, PET-CT, PET-MRI

## Editorial on the Research Topic

### Bottom-Up Approach: a Route for Effective Multi-Modal Imaging of Tumors

## PREFACE

With the development of multidisciplinary integration, multi-modal imaging has become an important concept that is very popular in relevant research fields and has expanded to accommodate a wide range of advanced technologies. This change is something we are happy to see because it brings more possibilities, which further provide more perspectives and information for cancer research. This Research Topic gathers information about various technologies or methodologies, to consider the advantages of each and finally provide solutions for cancer diagnosis and treatment.

## CURRENT STATUS AND INNOVATION OF MULTIMODAL IMAGING

Imaging has become an indispensable means in the process of tumor diagnosis and clinically and the wide range of available imaging modalities, some of which are described herein, provide strong tools in discovering information about cancer. Among these available imaging modalities, magnetic resonance imaging (MRI), is a commonly used tool in clinical settings and is usually one of the first choices for tumor diagnosis. It has superior soft-tissue resolution to any other imaging modality, which makes it suitable for the diagnosis of most tumors. In addition, enhanced MRI detection can further strengthen its application. However, the relatively long scanning time and various types of artifacts sometimes limit its function. From the perspective of the articles in this Research Topic, exploiting advanced MRI sequences for better imaging effect is still necessary for tumor diagnosis.

Yuan et al. explore the diagnostic efficacy of the combination of different MRI sequences, including T<sub>2</sub>-weighted spectral attenuated inversion recovery (SPAIR) imaging, dynamic contrast-enhanced (DCE) imaging, and diffusion-weighted (DW) imaging. They found that T<sub>2</sub> SPAIR and DCE plus DW imaging provided useful information for evaluating T staging and grading in bladder cancer. As a

## OPEN ACCESS

### Edited and reviewed by:

Zaver Bhujwalla,  
Johns Hopkins University,  
United States

### \*Correspondence:

Min Wu  
wuminscu@scu.edu.cn

### Specialty section:

This article was submitted to  
Cancer Imaging and  
Image-directed Interventions,  
a section of the journal  
Frontiers in Oncology

**Received:** 10 November 2021

**Accepted:** 20 December 2021

**Published:** 14 January 2022

### Citation:

Xie R, Wu C, Yang L, Mi P, Kim D-H  
and Wu M (2022) Editorial: Bottom-Up  
Approach: A Route for Effective Multi-  
Modal Imaging of Tumors.  
Front. Oncol. 11:812472.  
doi: 10.3389/fonc.2021.812472

multi-parametric imaging modality, MRI can give far more information than we have ever thought. Zheng et al. found that the correlation between the parameters of intravoxel incoherent motion diffusion-weighted imaging (IVIM-DWI) and the expression of Ang-2 and TKT to be very useful for developing personalized treatment plans by non-invasive evaluation. Liu et al. examine the mono-exponential IVIM model. They outline that it is superior to the bi-exponential IVIM model in differentiating the pathological grades of esophageal squamous cell carcinoma (ESCC), proving it to be an ideal imaging modality for predicting pathological grades of ESCC.

Computed tomography (CT) is another commonly used imaging modality. Compared with MRI, it does not have an impressive soft tissue resolution, but the quicker scanning time for better temporal resolution and relatively low cost make it still a necessary inspection method for cancer diagnosis. Enhanced CT scanning is particularly sensitive to some tumors such as hepatoma and some abdominal tumors. Consequently, improving the performance of the CT devices and developing CT imaging agents with higher contrast and specificity are potential approaches to increasing the accuracy of CT in tumor diagnosis. Furthermore, similar to other imaging modalities, the radiomics model based on CT can excavate more information from a large number of images and effectively provide a prediction for the development of cancer.

Ultrasound (US) is an imaging modality with relatively high penetration that has the capability of real-time imaging. Based on contrast enhanced US, Tang et al. used a new index named time difference of arrival (TDOA), which uses the time difference between the contrast agent's arrival time of the lesion and adjacent lung tissue to discriminate the pathologic types of peripheral pulmonary lesions (PPLs). This retrospective study found that TDOA significantly distinguished benign inflammation and malignant PPLs, which increased the diagnostic accuracy of CEUS. However, the properties of sounds restrict its performance when meeting the tumors surrounded by air or bones. Fortunately, some advanced US contrast agents and invasive US scanning methods can help solve these problems (1). Nuclear imaging relies on radioactive rays emitted by radionuclides and sometimes shares some characteristics of molecular imaging like cellular or molecular level specificity. More advanced fusion technology in nuclear imaging such as positive electron emission CT (PET/CT) and PET/MRI can simultaneously obtain metabolism information and anatomical structure, providing the precise location and behaviors of tumor development. In this field of concern, the development of new tracers is still very popular. Zhou et al. performed an intra-individual comparison and found that 18F-PSMA-1007 showed superiority over 18F-FDG because of its high detecting rate of PC lesions and excellent tumor uptake. Generally speaking, from this brief review above, it is clear that the commonly used imaging methods have different advantages, but there is still a lot of room for improvement.

Molecular imaging is another important branch of multi-modal imaging, which relies on composite probes integrating different parts with multiple functions to realize precise tissue imaging. The tumor occurrence is a multi-factor process at the

cellular level, subcellular level, and molecular level, thus providing a huge stage for the application of molecular imaging. The recent innovation of molecular imaging generally includes aspects such as bimodal imaging, targeting, structure, synthesis, mechanism of drug release. Bimodal imaging requires the probe to be highly integrated and combines the advantages of different imaging modalities, thus we can dig out more information with higher efficiency. For instance, Xie et al. reported a bimodal MRI/near infrared fluorescence (NIRF) imaging nanoprobe, <sup>125</sup>I-ANG/Cy7-SPIONs (2) that used the retro-enantio isomer of angiopep-2 to mediate the nanoprobe targeting to glioma site. Due to the integration of Cy7 dye and SPIONs core, this nanoprobe finished the enhanced MR imaging and NIRF imaging of glioma with high specificity and sensitivity. The MRI/optical imaging bimodal imaging probe has been applied in many studies (3), because of its combination of high anatomical resolution from MRI, high sensitivity, and real-time imaging property from optical imaging (4).

In terms of the capability of targeting, finding new tumor targets with their corresponding ligands is an effective way to improve the targeting efficiency of the composite probes. Small molecules, like peptides, have become one of the most popular ligands for targeting, because they are small, easy to synthesize, and generally low immunogenic (5). Genomics research also helps in the discovery of more targets to develop new small molecule targeting ligands. Some research designed molecular probes with camouflage containing some intrinsic components in the body to deceive tumor cells. This biomimetic strategy has also achieved some impressive results. Deng et al. produced an aggregation-induced emission (AIE) probe coated with the NK cell membrane, NK@AIEdots, in which the NK cell membrane helped the probe cross the blood-brain barrier and target the glioma and finally realize through skull NIRF imaging and tumor treatment *via* photothermal effect (6). Then, the structure of the whole probe is strongly associated with its mechanism of drug release.

Recently, many composite probes with the activatable design have been developed, as they provide impressive lesion to normal tissue contrast, which is particularly valuable when we want to make a strict distinction between the two, for example during surgery. Zhan et al. designed an enzyme-activatable NIR-II nanoprobe unperturbed by tissue or background (A&MMP@Ag<sub>2</sub>S-AF7P) (7). In the normal state, the nanoprobe did not have effective imaging performance because of the quenching effects of its special structure. The structure of the nanoprobe would be destroyed by the MMP-14, which is an enzyme highly expressed on neuroblastoma, that can cleave to a part of the nanoprobe, resulting in the activation of the nanoprobe to emit significant NIRF imaging signals. As for the synthesis of the probes, a faster and simpler method is required. Therefore, the research seeking a product with faster and simpler synthesis while maintaining a similar efficacy is of particular concern.

In summary, as the potential innovations mentioned above indicate, there is still much room for the research and development of multi-modal imaging from a purely molecular imaging perspective. In the future, these composite probes will achieve incredible accuracy.



Many works in this Research Topic examine artificial intelligence (AI) methodologies such as radiomics, machine learning, and deep learning and apply them to the research of cancer imaging with impressive results, indicating the need to expand the concept of multi-modal imaging. Molecular imaging focuses on the characteristics of tumor changes at the cellular and molecular levels. AI methodology for imaging, a rapidly developing research field, can capture the feature and heterogeneity of the tumor across its whole volume. With certain processing, the extracted information from AI methodologies can be used as indicators for the diagnosis and prognosis of cancer. He et al. built a radiomics feature-based predictive model to predict the occurrence of microvascular invasion (MVI) in patients with hepatocellular carcinoma (HCC). They built the individual predictive nomogram including the Fradiomics score (Rad-score) and existing predictors (alpha fetoprotein, neutrophilic granulocyte, and preoperative hemoglobin) and found that its discrimination efficacy was higher than the existing predictors mentioned above, indicating that the radiomics feature-based predictive model could improve the preoperative prediction of MVI in HCC. Gu et al. developed a prediction model based on two clinical factors, namely the age and CA125 level and four radiological criteria by CT, which are abdominal bowel metastasis, spleen metastasis, diaphragmatic metastasis, and retroperitoneal lymph node enlargement (RLNE). Their results indicate that this model could predict unsatisfactory debulking surgery in patients with advanced ovarian cancer (AOC). Li et al. undertook a retrospective study to verify the efficacy of their radiomics model based on multi-parametric MRI on a diagnosis of prostate cancer (PCa). They found that when this model was added to PI-RADS, the performance of the PI-RADS was significantly improved for PCa diagnosis, suggesting the function of radiomics in improving the diagnostic performance of PI-RADS v2.1 in PCa. These studies prove that after the features in the images are extracted and processed by dimensionality reduction, the analyzed data can change the quality of the information provided by the traditional imaging modalities. Sometimes these features can be connected to other non-imaging features from laboratory indicators or genomics to improve the diagnosis and prognosis of cancer.

These imaging features can be associated with genomic, transcriptomic, and proteomic characteristics (8). From this point, we can build a bridge between molecular imaging and radiomics, because they can share and contribute critical information to each other. Chu et al. developed a model based on radiomics features to evaluate CXCL8 expression and found that the radiomics features reflected by tumor morphology could be influenced by gene expression, while CXCL8 is a gene that can regulate cytokine–cytokine receptor interaction and neutrophil migration pathway. Finally, they built a novel radiomics model that incorporated 12 radiomics features according to CXCL8 expression and tumor stage, which was a reliable approach to predict prognosis in colorectal cancer (CRC) patients. This type of study links the differences in genotypes with the heterogeneity in radiomics and found a correlation between them.

On the one hand, the findings in this Research Topic provide direct information for tumor imaging. On the other, the connection between differences in radiomics or other AI methodologies, as well as differences at the cellular and molecular levels, can also indirectly provide new targets for tumor molecular imaging. Moreover, given the rich information provided by AI methodologies, molecular imaging probes can also be more accurate in time and space, which not only identifies the location of the tumor but also specifically identifies the tumor staging and completes the time-specific imaging. At this level, multi-modal imaging is more like a new technology that integrates multiple imaging methodologies, where we can make full use of the information provided by images, computer science, materials, etc. to comprehensively re-consider the whole process of cancer development.

## EPILOGUE

We are grateful to the authors for contributing to this collection, providing new ideas and perspectives that have also inspired us deeply. This Research Topic will continue to welcome diverse tumor imaging studies and encourage the integration of different imaging methods. We believe that multi-modal imaging will become one of the ultimate solutions for tumor diagnosis and treatment.

## AUTHOR CONTRIBUTIONS

RX and MW wrote the paper text. All others were guest associate editor of the Research Topic and edited the text.

## FUNDING

This work was supported by the Chengdu International Science and Technology Cooperation Funding (Grant 2019-GH02-00074-HZ), the Chengdu Science and Technology Bureau (Grant 2021-YF05-00698-SN), the 1-3-5 Project for Disciplines of Excellence-Clinical Research Incubation Project, West China Hospital, Sichuan University (Grant 2021HXFH035), the Functional and Molecular Imaging Key Laboratory of Sichuan Province (Grant 2012JO0011), and the Scientific and Technological Achievements Transformation Fund of West China Hospital, Sichuan University (Grant CGZH21002).

## ACKNOWLEDGMENTS

We thank all authors who contributed their manuscripts to this Research Topic and the reviewers who provided rigorous reviews. We also thank the editorial board of the Cancer Imaging and Image-directed Interventions section for their support.

## REFERENCES

1. Rabut C, Yoo S, Hurt RC, Jin Z, Li H, Guo H, et al. Ultrasound Technologies for Imaging and Modulating Neural Activity. *Neuron* (2020) 108:93–110. doi: 10.1016/j.neuron.2020.09.003
2. Xie R, Wu Z, Zeng F, Cai H, Wang D, Gu L, et al. Retro-Enantio Isomer of Angiopep-2 Assists Nanoprobes Across the Blood-Brain Barrier for Targeted Magnetic Resonance/Fluorescence Imaging of Glioblastoma. *Signal Transduct Target Ther* (2021) 6:309. doi: 10.1038/s41392-021-00724-y
3. Yang CT, Hattiholi A, Selvan ST, Yan SX, Fang W, Chandrasekharan P, et al. Gadolinium-Based Bimodal Probes to Enhance T1-Weighted Magnetic Resonance/Optical Imaging. *Acta Biomater* (2020) 110:15–36. doi: 10.1016/j.actbio.2020.03.047
4. Albuquerque GM, Souza-Sobrinha I, Coiado SD, Santos BS, Fontes A, Pereira GAL, et al. Quantum Dots and Gd<sup>3+</sup> Chelates: Advances and Challenges Towards Bimodal Nanoprobes for Magnetic Resonance and Optical Imaging. *Top Curr Chem (Cham)* (2021) 379:12. doi: 10.1007/s41061-021-00325-x
5. Lu L, Zhang Q, Wang Z, Gao L, Shen J. Peptide-Modified Nanoparticles for Yumor Targeting and Molecular Imaging. *Curr Med Chem* (2021) 28:6411–36. doi: 10.2174/0929867327666201022122131
6. Deng G, Peng X, Sun Z, Zheng W, Yu J, Du L, et al. Natural-Killer-Cell-Inspired Nanorobots With Aggregation-Induced Emission Characteristics for Near-Infrared-II Fluorescence-Guided Glioma Theranostics. *ACS Nano* (2020) 14:11452–62. doi: 10.1021/acsnano.0c03824
7. Zhan Y, Ling S, Huang H, Zhang Y, Chen G, Huang S, et al. Rapid Unperturbed-Tissue Analysis for Intraoperative Cancer Diagnosis Using an Enzyme-Activated NIR-II Nanoprobe. *Angew Chem Int Ed Engl* (2021) 60:2637–42. doi: 10.1002/anie.202011903
8. Mayerhoefer ME, Materka A, Langs G, Häggström I, Szczypiński P, Gibbs P, et al. Introduction to Radiomics. *J Nucl Med* (2020) 61:488–95. doi: 10.2967/jnumed.118.222893

**Conflict of Interest:** The authors declare that the research was conducted in the absence of any commercial or financial relationships that could be construed as a potential conflict of interest.

**Publisher's Note:** All claims expressed in this article are solely those of the authors and do not necessarily represent those of their affiliated organizations, or those of the publisher, the editors and the reviewers. Any product that may be evaluated in this article, or claim that may be made by its manufacturer, is not guaranteed or endorsed by the publisher.

Copyright © 2022 Xie, Wu, Yang, Mi, Kim and Wu. This is an open-access article distributed under the terms of the Creative Commons Attribution License (CC BY). The use, distribution or reproduction in other forums is permitted, provided the original author(s) and the copyright owner(s) are credited and that the original publication in this journal is cited, in accordance with accepted academic practice. No use, distribution or reproduction is permitted which does not comply with these terms.





# Diagnostic Imaging Methods and Comparative Analysis of Orbital Cavernous Hemangioma

Li Zhang, Xuying Li, Fei Tang, Lu Gan and Xin Wei\*

West China Hospital, Sichuan University, Chengdu, China

Orbital cavernous hemangioma is the most common primary tumor in the orbit. With the development of histopathology, it has been confirmed that cavernous hemangioma is not a real tumor, but a special type of vascular malformation. Cavernous hemangioma malformation (CVM) is a more appropriate way to name it. At present, surgical resection is the main treatment for CVMs. The prognosis of the surgery mainly depends on the location and the size of the lesion as well as its relationship with the optic nerve. Therefore, effective imaging information is of great importance. This paper analyzes the radiological imaging characteristics and the advantages and disadvantages between them, including ultrasound, CT, MRI, and SPECT/CT imaging of CVMs, hoping to help improve our understanding of CVMs.

## OPEN ACCESS

### Edited by:

Changqiang Wu,  
North Sichuan Medical College, China

### Reviewed by:

Peng Lv,  
Lanzhou University Second  
Hospital, China  
Jing Han,  
Tangdu Hospital, China

### \*Correspondence:

Xin Wei  
weixin\_1982@163.com

### Specialty section:

This article was submitted to  
Cancer Imaging and Image-directed  
Interventions,  
a section of the journal  
Frontiers in Oncology

Received: 29 June 2020

Accepted: 18 August 2020

Published: 23 September 2020

### Citation:

Zhang L, Li X, Tang F, Gan L and  
Wei X (2020) Diagnostic Imaging  
Methods and Comparative Analysis of  
Orbital Cavernous Hemangioma.  
Front. Oncol. 10:577452.  
doi: 10.3389/fonc.2020.577452

**Keywords:** orbital cavernous hemangioma, radiography, computed tomography, magnetic resonance imaging, SPECT/CT, 99mTc-RBC

## INTRODUCTION

Cavernous hemangioma malformation (CHM) is the most common primary benign orbital tumor in adults, which constitutes 6–9% of orbital lesions. In a retrospective study of 1,264 patients with suspected orbital tumor during 1971–2002, Shields et al. (1) found that CHMs constituted 6.12% of all lesions. Furthermore, Bonavolont et al. (2) analyzed 2,480 patients with orbital lesions; they found that CHM constituted 9% of all lesions. Finally, in a pathological analysis of 455 patients with orbital soft tissue tumors, Liu et al. (3) revealed that 258 patients had CHMs, which constituted 75.9% of orbital vascular tumors and 56.7% of orbital soft tissue tumors. The locations and sizes of these lesions vary among patients; they can compress adjacent structures and cause corresponding symptoms (e.g., vision loss, visual field defect, and eye movement disorder). Currently, there is a consensus regarding treatment of CHMs; specifically, when lesions are found in eyes with other normal characteristics, follow-up observation should be performed. The risk of surgery was found to be greater than any theoretical benefit for patients without visual impairment, as well as for patients in whom it was unclear whether the lesion was stable or actively growing. In contrast, surgery should be considered if the patient has a serious visual field defect at the time of initial visit, or if the symptoms are mild with signs of active growth (e.g., new symptoms, changes, or aggravation of original symptoms) (4). The main approaches for surgical treatment of CHMs include: transconjunctival approach, lateral approach, skin approach, and lateral combined medial conjunctiva. The methods, efficacy, and safety differ among these approaches (5, 6). Accurate preoperative qualitative and localization diagnosis are important prerequisites for successful surgery. With the improvement of people's consciousness of health and the physical examinations become universal, much more ocular

diseases were detected in early stages. Accurately diagnosing CHM is of great significance for clinicians. Fully grasping the progression of the patients' conditions through images not only reduces the occurrence of serious complications such as vision loss, but help clinicians to deal with the lesions and surrounding tissues more confidently during the operation. Recently, studies regarding the histological and hemodynamic characteristics of CHMs have become increasingly in-depth, thus improving understanding regarding imaging manifestations of CHMs. Current diagnostic imaging methods for CHM mainly include ultrasound, computed tomography (CT), and magnetic resonance imaging (MRI). With the development of molecular imaging, radionuclide imaging technology has also been used for diagnosis of CHMs. The clinical characteristics, pathological characteristics, and imaging analysis are summarized in this review.

## CLINICAL CHARACTERISTICS

CHMs are more common among women (60–70%), potentially because of hormone level (7). The onset age ranges from 17 to 86 years (mean, 45 years). Most CHMs are unilateral single lesions, while unilateral multiple lesions and bilateral lesions are extremely rare; however, the incidence of bilateral lesions may higher than expected (8). The most probable location is the lateral region of the posteromedial orbital space. The main clinical manifestation is painless chronic progressive exophthalmos. Cytokine and hormonal stimulation during puberty or pregnancy may cause acute exophthalmos or orbital enlargement. If the lesion oppresses the optic nerve or affects blood supply to the optic nerve, visual field defects may appear. In a few patients, monocular vision loss has been caused by orbital apex involvement. Other uncommon symptoms include pain, eyelid swelling diplopia, and palpable mass (1).

## HISTOPATHOLOGICAL AND HEMODYNAMIC CHARACTERISTICS

Histopathology has revealed that orbital cavernous hemangioma is not a real tumor. Its occurrence does not involve the proliferation of vascular endothelial cells, which suggests that it should be regarded as a unique type of vascular malformation. The components of the lesion mainly comprise veins, with a small number of small arterial vessels. In terms of blood flow mechanics, this lesion comprises a non-dilated arteriovenous malformation with low blood flow (9, 10). CHM is a tumor essence wrapped by a complete capsule, which is formed by outwardly extended fibrous tissue between vascular sinuses. Microscopy analysis demonstrates that the cavernous malformation is an expanded cavernous space, lined with flat endothelial cells. It is separated by fibrous intervals and surrounded by collagen trabeculae and smooth muscle cells. Occasionally, thrombus or hyaline degeneration are present, and calcification is rare (11).

## RADIOLOGICAL IMAGING

### Conventional Ultrasound and Color Doppler Ultrasound (CDI)

Because of the complete capsule, the CHM boundary in ultrasound images has a clear margin and is slightly compressible. In addition, the CHM is composed of thin-walled enlarged blood sinuses with blood flow. Thus, we can see a large number of punctate echoes inside the tumors on B-scan. While on A-scan, it showed steep wave peak (indicating there is a capsule), regular medium high wave of internal reflection,  $45^\circ$  kappa angle (the imaginary angle between the internal reflection and the baseline reflection: the greater the angle, the more obvious the reduction), and moderate sound attenuation. Occasionally when it's difficult to distinguish CHM from schwannoma, the low reflection image of schwannoma on A-scan may help. Furthermore, blood in the blood sinuses is relatively static. Through CDI, no color blood flow signals or only a small number of punctate red and blue blood flow signals can be visualized (12–15). A study by Zhao et al. (16) revealed that slow compression of the eyeball during CDI causes most CHMs to exhibit rich red and blue blood flow signals; when partial pressure is maintained and no additional force is applied, the blood flow signals disappear. During slow relief of the pressure, the blood flow signals reappear; however, the color is distinct from that of pressurization (i.e., the original red signals become blue, while blue signals become red). This phenomenon is more obvious when the internal jugular vein is compressed. When the pressure is completely relieved, the blood flow signal disappears again. This process suggests that when the lesion is compressed, blood flow in the blood sinus is accelerated; this leads to the appearance of blood flow signals. In addition, when the pressure is maintained, either the blood sinus is blocked or blood flow recovers slowly, resulting in the disappearance of blood flow signals; when the pressure is relieved, blood rapidly fills the sinus cavity, which leads to reappearance of blood flow signals. The opposite blood flow signals during pressurization, compared with relief, indicate that revascularization of vascular sinuses is caused by venous return. This discovery provides novel clues for differential diagnosis of CHMs.

The advantages of ultrasound are its speed, non-invasive nature, and low cost; it is a very effective diagnostic method for CHMs. Nagaraju et al. (17) reported that the sensitivity, specificity, positive predictive value, negative predictive value, and accuracy of ultrasound in the diagnosis of ocular diseases were 94.2, 98.8, 99.1, 92.2, and 94.9%, respectively. However, there are notable limitations of this method. Ultrasound has limited value in detecting the size, location, and relationship of lesions, relative to surrounding structures. CDI imaging with compression is not obvious when lesions are deep or exhibit a complex location. Diagnosis may be difficult when lesions exhibit a complex internal composition, such as when they are accompanied by other vascular malformation components or inflammatory changes (e.g., when inflammatory cell infiltration occurs within the lesions). Furthermore, ultrasound is less useful for identification of lesions without extensive vasculature, such as schwannomas and pleomorphic adenomas (18).

## Ultrasonic Contrast

Also known as acoustic contrast, ultrasonic contrast is a technique that can enhance backscatter echo and improve the resolution, sensitivity, and specificity of ultrasound diagnosis using contrast agent. With the improvement of instrument performance and emergence of new acoustic contrast agents, ultrasonic contrast has increasing application in the diagnosis of ocular diseases, especially in retinochoroidal diseases. Because of the histological and hemodynamic characteristics of CHM, some clinicians have attempted to use contrast-enhanced ultrasound for its diagnosis. Ren et al. (19) reported that 49 of 52 patients (94.23%) diagnosed with CHMs showed typical enhancement patterns. Initial enhancement commonly appears at the periphery of the lesion, typically as small nodular protrusions. Occasionally, multiple nodular protrusions are fused; they slowly and gradually fill the lesion from the periphery to the center until reaching the peak of enhanced intensity, resulting in complete or incomplete filling of the whole lesion. After peak intensity is reached, it will be maintained for a short platform period, then gradually subside. This “snowball-like” dynamic enhancement pattern is the most characteristic manifestation of CHMs. Additionally, in ultrasonic contrast time-intensity curve, the enhancement pattern is slow onset and slow retreat (20). Contrast-enhanced ultrasound can directly reflect hemodynamic changes in the lesions; its advantages include absence of radiation, good repeatability, good patient tolerance, few adverse reactions, and usefulness for dynamic observation. However, thus far, ultrasonic contrast is more widely used in patients with chorioretinopathy, and there have been few studies regarding CHMs. Compared with traditional CT and MRI imaging, its advantages are unclear, and there remain inherent limitations of ultrasound imaging.

## CT

CT imaging has high-density resolution, which allows it to clearly show the size, position, and shape of the lesion, as well as its relationship with surrounding structures. Under conventional CT, most CHMs exhibit a similar appearance: predominantly located in the retrobulbar cone; oval or round shape; lobulated when enlarged; well-circumscribed; and homogeneous with smooth margins. In most patients, the transparent triangle area can be observed in the orbital apex. These features are not characteristic and have limited value in distinguishing CHM from neurofibroma, solitary fibroma, schwannoma, histiocytoma, and other tumors that may appear morphologically identical to CHMs. With the development of image technology, enhanced CT has enabled more detailed evaluation and identification of orbital lesions through different enhancement patterns, as well as better understanding of images with blood flow characteristics of the lesions. In contrast-enhanced CT images, CHMs exhibit poor and heterogeneous enhancement in early arterial and venous phases, due to their low arterial blood flow. Then, the contrast agent slowly accumulates and enhancement gradually increases, eventually resulting in persistent homogeneous enhancement in the late or delayed phase (21). This feature was confirmed in previous studies; Young et al. (22) also reported that most enhanced

CT images of CHMs showed heterogeneous enhancement or incomplete filling in the late or delayed phase (88.5%). This phenomenon may result from large blood sinuses in the lesion while the blood supply arteries are relatively small, which causes slow circulation in the lesion. Drainage veins are larger than the nutrient arteries; thus, when contrast agent from blood supply arteries initially enters the lesion, a portion of the contrast agent is already discharged. Therefore, it exhibits heterogeneous progressive enhancement. Dynamic contrast-enhanced CT is a very accurate and useful method for diagnosis of CHMs; generally, it is sufficiently effective to enable differential diagnosis relative to other lesions (e.g., schwannoma). Young et al. (22) have divided CHMs into three types (i.e., low speed, medium speed, and fast speed) according to the contrast agent filling speed; they found that the unique early spot or patchy enhancement on contrast-enhanced CT was more favorable for distinguishing lesions such as schwannoma, compared with contrast-enhanced MRI, which may demonstrate a confusing early diffuse enhancement pattern. However, contrast-enhanced CT increases the radiation dose to patients, which has partially limited its applications. Clinicians should consider the corresponding risks during selection of imaging methods.

## MRI

As a popular imaging diagnosis method, MRI can detect and diagnose lesions by comparing signal strengths of differently weighted images, and obtain multi-directional images to clearly show tissues and structures as well as the anatomical relationships among them. Compared with CT, MRI can better display the relationships of orbital lesions with the optic nerve. Non-contrast MRI images of CHM are mainly manifested as follows: the lesion on T1-weighted images exhibits a signal hypointense to fat and isointense to extraocular muscle, while on T2-weighted images it exhibits a signal hyperintense to fat. This manifestation is difficult to distinguish CHMs from schwannoma and other lesions; thus, enhanced MRI is needed. On enhanced MRI, the enhancement pattern of lesions is similar to that of dynamic enhanced CT, with nodular enhancement in the early phase and continuous and homogeneous enhancement in the late and delayed phases. This feature can be used to distinguish isolated neurofibromas and schwannomas, which are characterized by diffuse heterogeneous or homogeneous enhancement in the early phase (21). However, Young et al. (22) found that in the early stage of contrast-enhanced MRI, one-fifth of CHMs exhibited diffuse and homogeneous enhancement, which was identical to that of schwannomas and other lesions. This differed from the results reported by Xian et al. (23), who found that early phase enhancement of CHMs always began from a small spot or a specific area. Young et al. (22) also found that in 43.3% of lesions, the enhancement was heterogeneous in the late or delayed phase, similar to the findings on dynamic enhanced CT. This phenomenon may be related to the slow internal blood flow of CHMs, which causes contrast agent to be unable to completely fill the lesions (even in the late or delayed phase). Nevertheless, MRI is of great value in the diagnosis of CHMs. In particular,

using conventional MRI combined with enhanced MRI, the sensitivity was 79.4%; specificity was 100%; positive predictive value was 100%; negative predictive value was 83.7%; and accuracy was 90% (24). In quantitative dynamic magnetic resonance imaging, relevant parameters obtained based on the two-compartment dynamics model were further analyzed. With respect to the low internal blood flow characteristics of CHM and its abundant interstitium, as well as its relatively large extracellular space, the  $K_{trans}$  (rate of contrast agent distribution from plasma to extracellular space of blood vessels) and  $K_{ep}$  (rate at which contrast agents return from extracellular space to plasma) values were statistically significantly lower than those of schwannomas. Concurrently, resembling its enhancement pattern, the dynamic enhancement distribution pattern of the time intensity curve is mainly type I (i.e., continuously rising, such that signal strength increases slowly during observation; the curve exhibits a small ascending slope) (24–27). This feature aids in detection of the nature of the lesions and improves the reliability of diagnosis. However, the application of MRI also has limitations; in particular, patients with ferromagnetic implants or cardiac pacemakers, as well as patients with early pregnancy or claustrophobia, cannot undergo MRI. In addition, the gadolinium contrast agent used for contrast-enhanced MRI may cause renal systemic fibrosis in patients with renal insufficiency. Notably, accumulation of gadolinium contrast agent has been found during autopsies of individuals without renal dysfunction (28). In recent years, there has been increasing research regarding diffusion-weighted MRI, which is an important method for diagnosis of ischemic, infectious, and malignant diseases of the central nervous system. This non-invasive imaging method has a unique sensitivity for the free movement (diffusion) of water molecules in tissues. The apparent diffusion coefficient value of CHM is reportedly similar to that of solid tumors with medium density, which aids in differentiation from cystic lesions (28, 29). However, there have been few studies with relevant data and analysis regarding specific apparent diffusion coefficient thresholds for CHM, or regarding further differential diagnosis findings.

### 99mTc-RBC SPECT

Single-photon emission computed tomography (SPECT) is a modality used to achieve functional imaging of metabolic levels under pathological conditions, based on differences in blood circulation and tissue structure of lesions. It enables detection of cellular, molecular, and biochemical characteristics of lesions. Burrone et al. (30) reported that the characteristics of CHMs on SPECT imaging include the absence of intake during the early blood pool phase, followed by focal intake with persistent high consistency in the late phase. Additionally, false positive results were found within one hemangiopericytoma and one lymphangioma (both vascular diseases), which is consistent with the findings by Polite et al. (31); thus, more accurate CHM diagnosis is needed via combination with clinical manifestations, as well as CT and MRI manifestations. Nevertheless, the high sensitivity and specificity of SPECT imaging cannot be ignored. Dong et al. (32) performed further research regarding CHMs, using SPECT combined

with CT imaging. They reported two false positive results regarding a venous hemangioma and a leiomyosarcoma with contrast agent concentration in late delayed imaging; the venous hemangioma was confirmed by hemorrhage and the leiomyosarcoma was confirmed by local bone destruction through postoperative pathological examination. Surprisingly, the sensitivity, specificity, accuracy, positive predictive value, and negative predictive value of radionuclide  $^{99m}\text{Tc}$ -rbc SPECT plane imaging all reached 100% by further after-calibration analysis combined with visual analysis, semi-quantitative analysis, and receiver operating characteristic curve analysis (24). Although more large sample data are not available thus far,  $^{99m}\text{Tc}$ -RBC SPECT plane imaging is considered to have very high diagnostic efficiency for CHMs. By combination with CT to provide anatomical information, the imaging accuracy of SPECT has been further improved; it even has the potential for use as a preoperative diagnostic modality for CHMs. However, limitations remain, such as poor diagnostic efficiency for other orbital lesions, relatively time-consuming nature, high cost, considerable equipment requirements, and radiation effects.

### CONCLUSION

Applications of ultrasound, CT, MRI, and  $^{99m}\text{Tc}$ -RBC SPECT imaging in diagnosis for CHMs were discussed in this review. Ultrasonography is a non-invasive, rapid, and inexpensive diagnostic method; by combination with color Doppler ultrasound (based on internal lesion blood flow dynamics), ultrasonography can provide additional information regarding lesion characteristics, especially when using the method of eyeball compression. Although the diagnostic effectiveness is sufficient for CHMs, it may be difficult to make a fine diagnosis when the internal lesion structure is complex. In addition, the limited ability to supply information regarding anatomical structures is an inherent disadvantage of ultrasonography. To the best of our knowledge, there have been few studies regarding the application of contrast-enhanced ultrasound in CHM diagnosis, and we mainly cited from Chinese domestic literature. The characteristic “snowball-like” enhancement pattern for CHMs is an intuitive reflection of the internal hemodynamic properties of CHMs. CT and MRI are the most commonly used clinical imaging diagnostic techniques for orbital lesions. CT has better density resolution, while MRI has higher tissue resolution. However, both techniques have specific limitations in the differential diagnosis of CHMs. The imaging characteristics of lesions, such as schwannomas and pleomorphic adenomas, overlap with those of CHMs. Additional information regarding the internal nature of the lesion can be obtained through contrast-enhanced imaging. Furthermore, a more detailed comparison of enhancement patterns in the early phase and the late and delayed phases can facilitate accurate diagnosis. Additionally, the parameters of MRI dynamic enhancement and diffusion-weighted imaging provide further evidence for differential diagnosis. However, radiation, contrast agent allergy, and adverse reactions should be considered in the



application of CT and contrast methods. Notably,  $^{99m}\text{Tc}$ -RBC SPECT is considered molecular imaging; planar imaging reflects metabolism within the lesions. The different patterns and dosage of contrast agent intake are the basis of diagnosis. Based on combination with CT imaging, which provides anatomical information, the high diagnostic efficiency of  $^{99m}\text{Tc}$ -RBC SPECT has made it a reliable choice for diagnosis of CHMs. However, when it is applied for other orbital lesions, instead of CHMs alone, the diagnostic efficiency decreases markedly; thus, it is a good choice for analysis of patients with high suspicion of CHMs, or when other imaging modalities are unavailable. With the rapid development of imaging diagnosis methods, the concept of diagnosing only based on experience is no longer applicable. Through the storage and analysis of a large number of different medical records, we can speak with data, and conduct quantitative and semi quantitative analysis based on relevant parameters of image data, including blood flow rate and enhancement degree, so as to make best diagnosis. With further developments in imaging technology, more accurate data-based criteria may become a trend in preoperative diagnosis.

## REFERENCES

- Shields JA, Shields CL, Scartozzi R. Survey of 1264 patients with orbital tumors and simulating lesions: the 2002 Montgomery Lecture, part 1. *Ophthalmology*. (2004) 111:997–1008. doi: 10.1016/j.ophtha.2003.01.002
- Bonavolontà G, Strianese D, Grassi P, Comune C, Tranfa F, Uccello G, et al. An analysis of 2,480 space-occupying lesions of the orbit from 1976 to 2011. *Ophthal Plastic Reconstr Surgery*. (2013) 29:79–86. doi: 10.1097/IOP.0b013e31827a7622
- Liu H, Ren YJ, Cai FM, Yang JR, Li YP, Wang HF. Clinical and pathological observation of 455 cases of orbital soft tissue tumor. *Int J Ophthalmol*. (2019) 19:1795–9. doi: 10.3980/j.issn.1672-5123.2019.10.38
- Harris GJ. Cavernous hemangioma of the orbital apex: pathogenetic considerations in surgical management. *Am J Ophthalmol*. (2010) 150:764–73. doi: 10.1016/j.ajo.2010.07.027
- Liu QL, Wu BL, Ye XM. Effects of four surgical approaches on patients with deep cavernous hemangioma of the orbit. *Int J Ophthalmol*. (2019) 19:683–6. doi: 10.3980/j.issn.1672-5123.2019.4.36
- Liao HF, Wang YH, Huang Q, Gan PY, Wang AA. Analysis of the effect of different surgical methods on the cavernous hemangioma of the deep orbit. *Zhonghua Yan Ke Za Zhi*. (2017) 53:288–93. doi: 10.3760/cma.j.issn.0412-4081.2017.04.011
- Jayaram A, Lissner GS, Cohen LM, Karagianis AG. Potential correlation between menopausal status and the clinical course of orbital cavernous hemangiomas. *Ophthalmic Plastic Reconstr Surg*. (2015) 31:187–90. doi: 10.1097/IOP.0000000000000240
- Hentati A, Matar N, Dridi H, Bouali S, Jemel H. Bilateral orbital cavernous hemangioma. *Asian J Neurosurg*. (2018) 13:1222–4. doi: 10.4103/ajns.AJNS\_96\_17
- Nassiri N, Rootman J, Rootman DB, Goldberg RA. Orbital lymphaticovenous malformations: current and future treatments. *Surv Ophthalmol*. (2015) 60:383–405. doi: 10.1016/j.survophthal.2015.03.001
- Wassef M, Blei F, Adams D, Alomari A, Baselga E, Berenstein A, et al. Vascular anomalies classification: recommendations from the international society for the study of vascular anomalies. *Pediatrics*. (2015) 136:e203–14. doi: 10.1542/peds.2014-3673
- Taylor TD, Gupta D, Dalley RW, Keene CD, Anzai Y. Orbital neoplasms in adults: clinical, radiologic, and pathologic review. *Radiographics*. (2013) 33:1739–58. doi: 10.1148/rg.336135502

## AUTHOR CONTRIBUTIONS

XW brought up the idea and revised the manuscript. LZ collected information and wrote the manuscript. XL classified and sorted references for review. FT and LG helped with manuscript preparation and final version approval. All authors contributed to the article and approved the submitted version.

## FUNDING

This work was supported by grants from the Natural Science Foundation of China (No. 81200687), the Applied Basic Research Programs of Science and Technology Commission Foundation of Sichuan Province (No. 19YYJC0790), and the Innovative Spark Grant of Sichuan University (No. 2018SCUH0062).

## ACKNOWLEDGMENTS

We thank Ryan Chastain-Gross, Ph.D., from Liwen Bianji, Edanz Group China (www.liwenbianji.cn/ac), for editing the English text of a draft of this manuscript.

- Jiang HQ. The application of B-mode ultrasound and color Doppler ultrasound in the clinical diagnosis of orbital vascular diseases. *World Latest Med Information*. (2019) 19:44. doi: 10.19613/j.cnki.1671-3141.2019.44.141
- Zhu ZX. The applicational value of B-ultrasound and color Doppler ultrasound in orbital vascular diseases. *Yin Xiang Yan Jiu Yu Yi Xue Yin Yong*. (2019) 3:153–4.
- Zhang Y. To study the value of B ultrasound and color Doppler ultrasound in the clinical diagnosis of orbital vascular diseases. *Zhong Guo Ji Xu Yi Xue Jiao Yu*. (2018) 10:44–5. doi: 10.3969/j.issn.1674-9308.2018.06.024
- Karolczak-Kulesza M, Rudyk M, Niestrata-Ortiz M. Recommendations for ultrasound examination in ophthalmology. Part II: orbital ultrasound. *J Ultrasonography*. (2018) 18:349–54. doi: 10.15557/JoU.2018.0051
- Zhao H, Song GX, Gao JM, Sun FY, Tang DR, Xu Z. Significance of dynamic color Doppler flow imaging in orbital tumors. *Zhonghua Yi Xue Chao Sheng Za Zhi*. (2007) 4:273–5. doi: 10.3969/j.issn.1672-6448.2007.05.006
- Nagaraju RM, Gurushankar G, Bhimarao, Kadakola B. Efficacy of high frequency ultrasound in localization and characterization of orbital lesions. *J Clin Diagnostic Res*. (2015) 9:TC01–6. doi: 10.7860/JCDR/2015/13021.6428
- Yan J, Li Y. Unusual presentation of an orbital cavernous hemangioma. *J Craniofacial Surg*. (2014) 25:e348–9. doi: 10.1097/SCS.0000000000000774
- Ren XJ, Lu XZ, Niu H, Li XM, Wang Y, Xiao LH. Preliminary study on contrast-enhanced mode of orbital cavernous hemangioma. *Zhonghua Yi Xue Chao Sheng Za Zhi*. (2010) 7:603–8. doi: 10.3969/j.issn.1672-6448.2010.04.010
- Yao Z, Wenwei C. Application of contrast-enhanced ultrasound in diagnosis of orbital occupying lesions. *J Clin Ultrasound Med*. (2019) 21:2. doi: 10.3969/j.issn.1008-6978.2019.02.015
- Jayaram A, Cohen LM, Lissner GS, Karagianis AG. A retrospective review of cases preoperatively diagnosed by radiologic imaging as cavernous venous malformations. *Orbit*. (2017) 36:128–34. doi: 10.1080/01676830.2017.1279666
- Young SM, Kim YD, Lee JH, Woo KI. Radiological analysis of orbital cavernous hemangiomas: a review and comparison between computed tomography and magnetic resonance imaging. *J Craniofacial Surg*. (2018) 29:712–6. doi: 10.1097/SCS.0000000000004291
- Xian J, Zhang Z, Wang Z, Li J, Yang B, Chen Q, et al. Evaluation of MR imaging findings differentiating cavernous haemangiomas from schwannomas in the orbit. *Eur Radiol*. (2010) 20:2221–8. doi: 10.1007/s00330-010-1774-y
- Hua D. *The Study of SPECT/CT Dynamic/Static Combined Imaging in Differential Diagnosis of Orbital Tumors*. Tianjin Medical University. (2018).

25. Mei Y. *The Clinical Value of Quantitative Dynamic-Contrast Enhanced MR Imaging in the Diagnosis of Orbital Tumors*. TianJin Medical University. (2015).
26. Jittapiromsak N, Hou P, Liu HL, Sun J, Schiffman JS, Chi TL. Dynamic contrast-enhanced MRI of orbital and anterior visual pathway lesions. *Magn Reson Imaging*. (2018) 51:44–50. doi: 10.1016/j.mri.2018.04.016
27. Zhao L. *The Study of Magnetic Resonance Imaging Characteristics for the Diseases of Orbital Masses*. TianJin Medical University. (2018).
28. Hiwatashi A, Togao O, Yamashita K, Kikuchi K, Yoshikawa H, Obara M, et al. High resolution diffusion-weighted imaging for solitary orbital tumors: 3D turbo field echo with diffusion-sensitized driven-equilibrium (DSDE-TFE) preparation technique. *Clin Neuroradiol*. (2018) 28:261–6. doi: 10.1007/s00062-016-0556-6
29. Kalin-Hajdu E, Colby JB, Idowu O, Grumbine FL, Kang JM, Hirabayashi KS, et al. Diagnosing distensible venous malformations of the orbit with diffusion-weighted magnetic resonance imaging. *Am J Ophthalmol*. (2018) 189:146–54. doi: 10.1016/j.ajo.2018.02.005
30. Burrioni L, Borsari G, Pichierri P, Polito E, Toscano O, Grassetto G, et al. Preoperative diagnosis of orbital cavernous hemangioma: a <sup>99m</sup>Tc-RBC SPECT study. *Clin Nucl Med*. (2012) 37:1041–6. doi: 10.1097/RLU.0b013e318252d2ed
31. Polito E, Burrioni L, Pichierri P, Loffredo A, Vattimo AG. Technetium tc <sup>99m</sup>-labeled red blood cells in the preoperative diagnosis of cavernous hemangioma and other vascular orbital tumors. *Arch Ophthalmol*. (2005) 123:1678–83. doi: 10.1001/archophth.123.12.1678
32. Dong H, Zhang Z, Guo Y, Zhang H, Xu W. The application of technetium-99m-red blood cell scintigraphy in the diagnosis of orbital cavernous hemangioma. *Nucl Med Commun*. (2017) 38:744–7. doi: 10.1097/MNM.0000000000000711

**Conflict of Interest:** The authors declare that the research was conducted in the absence of any commercial or financial relationships that could be construed as a potential conflict of interest.

Copyright © 2020 Zhang, Li, Tang, Gan and Wei. This is an open-access article distributed under the terms of the Creative Commons Attribution License (CC BY). The use, distribution or reproduction in other forums is permitted, provided the original author(s) and the copyright owner(s) are credited and that the original publication in this journal is cited, in accordance with accepted academic practice. No use, distribution or reproduction is permitted which does not comply with these terms.



# Quick Automatic Synthesis of Solvent-Free $16\alpha$ -[ $^{18}\text{F}$ ] Fluoroestradiol: Comparison of Kryptofix 222 and Tetrabutylammonium Bicarbonate

Xiao Jiang<sup>1,2,3</sup>, Yingchun Li<sup>4</sup>, Xiaoxiong Wang<sup>1,2</sup>, Taipeng Shen<sup>1,2</sup>, Xiuli Li<sup>1,2</sup>, Yutang Yao<sup>1,2</sup>, Ge Zhang<sup>1,2</sup>, Ying Kou<sup>1,2</sup>, Jiaqi Shen<sup>1,2</sup>, Zhifu Luo<sup>3</sup> and Zhuzhong Cheng<sup>1,2\*</sup>

## OPEN ACCESS

### Edited by:

Changqiang Wu,  
North Sichuan Medical College, China

### Reviewed by:

Ji Hu,  
China Isotope & Radiation  
Corporation, China  
Yuchun Li,  
Sichuan University, China

### \*Correspondence:

Zhuzhong Cheng  
chengzhuzhong@163.com

### Specialty section:

This article was submitted to  
Cancer Imaging and Image-directed  
Interventions,  
a section of the journal  
Frontiers in Oncology

Received: 30 June 2020

Accepted: 17 August 2020

Published: 25 September 2020

### Citation:

Jiang X, Li Y, Wang X, Shen T, Li X,  
Yao Y, Zhang G, Kou Y, Shen J, Luo Z  
and Cheng Z (2020) Quick Automatic  
Synthesis of Solvent-Free  $16\alpha$ -[ $^{18}\text{F}$ ]  
Fluoroestradiol: Comparison of  
Kryptofix 222 and  
Tetrabutylammonium Bicarbonate.  
Front. Oncol. 10:577979.  
doi: 10.3389/fonc.2020.577979

<sup>1</sup> PET/CT Center, Sichuan Cancer Center, School of Medicine, Sichuan Cancer Hospital & Institute, University of Electronic Science and Technology of China, Chengdu, China, <sup>2</sup> Radiation Oncology Key Laboratory of Sichuan Province, Sichuan Cancer Center, School of Medicine, Sichuan Cancer Hospital & Institute, University of Electronic Science and Technology of China, Chengdu, China, <sup>3</sup> Institute of Isotope, China Institute of Atomic Energy, Beijing, China, <sup>4</sup> Department of Nuclear Medicine & Radiotherapy, Air Force Hospital of Western Theater Command, Chengdu, China

Estrogen receptor (ER) expression level of human breast cancer often reflects the stage of disease and is usually monitored by immunohistochemical staining *in vitro*. The preferable non-invasive and real-time diagnosis *in vivo* is more accessible by PET scan using  $16\alpha$ -[ $^{18}\text{F}$ ]FES. The objective of this study was to develop a quick automatic method for synthesis of solvent-free  $16\alpha$ -[ $^{18}\text{F}$ ]FES using a CFN-MPS-200 synthesis system and compare the catalytic efficiency of two phase transfer catalysts, Kryptofix 222/ $\text{K}_2\text{CO}_3$  ( $\text{K222}/\text{K}_2\text{CO}_3$ ) and tetrabutylammonium hydrogen carbonate ( $\text{TBA}\cdot\text{HCO}_3$ ). In this method, phase transfer catalysts  $\text{K222}/\text{K}_2\text{CO}_3$  and  $\text{TBA}\cdot\text{HCO}_3$  were used, respectively. The intermediate products were both hydrolyzed with hydrochloric acid and neutralized with sodium bicarbonate. The crude product was purified with semi-preparative HPLC, and the solvent was removed by rotary evaporation. The effects of radiofluorination temperature and time on the synthesis were also investigated. Radiochemical purity of solvent-free product was above 99% and the decay-corrected radiochemical yield of  $16\alpha$ -[ $^{18}\text{F}$ ]FES was obtained in  $48.7 \pm 0.95\%$  (catalyzed by  $\text{K222}/\text{K}_2\text{CO}_3$ ,  $n = 4$ ) and  $46.7 \pm 0.77\%$  (catalyzed by  $\text{TBA}\cdot\text{HCO}_3$ ,  $n = 4$ , respectively). The solvent-free  $16\alpha$ -[ $^{18}\text{F}$ ]FES was studied in clinically diagnosed breast cancer patients, and FES-PET results were compared with pathology diagnosis results to validate the diagnosis value of  $16\alpha$ -[ $^{18}\text{F}$ ]FES. The new method was more reliable, efficient, and time-saving. There was no significant difference in catalytic activity between  $\text{K222}/\text{K}_2\text{CO}_3$  and  $\text{TBA}\cdot\text{HCO}_3$ .

**Keywords:**  $16\alpha$ -[ $^{18}\text{F}$ ]fluoroestradiol, estrogen receptor, automatic synthesis, phase transfer catalyst, breast cancer

## INTRODUCTION

Estrogen receptor (ER) expression level in breast cancer is known as a meaningful prognostic indicator. ER-positive breast cancer is considered less aggressive and more sensitive to appropriate hormone therapies (1, 2). The traditional method for monitoring ER expression level is immunohistochemical staining with tumor biopsy samples *in vitro*, which is an invasive technique and cannot reflect the real-time ER expression level of primary and metastatic breast cancer or other tissues. An ideal non-invasive method monitoring real-time ER expression in the whole body is preferable in clinical practice.  $16\alpha$ - $[^{18}\text{F}]$ FES, an ER imaging biomarker, shows high binding affinity to ER. The utility of  $16\alpha$ - $[^{18}\text{F}]$ FES, especially in conjunction with  $[^{18}\text{F}]$ fluorodeoxyglucose, is considered of important diagnostic value.

It is a challenge for the routine synthesis of  $16\alpha$ - $[^{18}\text{F}]$ FES to meet clinical requirements. The first synthesis of  $16\alpha$ - $[^{18}\text{F}]$ FES was reported by Kiesewetter (3). In recent years, the synthesis of  $16\alpha$ - $[^{18}\text{F}]$ FES through different methods has been reported by several studies. However, most of these studies required more than 60 min with a low yield and mixed radiochemical impurities. Besides, whether  $\text{K}_2\text{CO}_3/\text{K}_2\text{CO}_3$  or  $\text{TBA}\cdot\text{HCO}_3$  was the appropriate phase transfer catalyst for automated synthesis of  $16\alpha$ - $[^{18}\text{F}]$ FES has not been investigated in these studies. Clinical applications of  $16\alpha$ - $[^{18}\text{F}]$ FES as an important tool to non-invasively measure ER expression will depend on its ideal radiochemical purity and steady routine production with a high yield.

In this study, we developed an automated, reliable, and time-saving method for the synthesis of solvent-free  $16\alpha$ - $[^{18}\text{F}]$ FES using a rotatory evaporator-equipped module with a commercially available precursor. We also investigated whether  $\text{K}_2\text{CO}_3/\text{K}_2\text{CO}_3$  or  $\text{TBA}\cdot\text{HCO}_3$  was the appropriate phase transfer catalyst and checked the quality of the radiopharmaceutical catalyzed by  $\text{K}_2\text{CO}_3/\text{K}_2\text{CO}_3$  or  $\text{TBA}\cdot\text{HCO}_3$  for potential clinical use. The solvent-free  $16\alpha$ - $[^{18}\text{F}]$ FES was studied in clinically diagnosed breast cancer patients, and FES-PET results were compared with pathology diagnosis results to validate the diagnosis value of  $16\alpha$ - $[^{18}\text{F}]$ FES.

## MATERIALS AND METHODS

### General

Reagents and solvents were purchased from Aldrich (Sigma-Aldrich, MO, USA) without further purification. The precursor, 3-methoxymethyl- $16\beta,17\beta$ -epiestriol-*O*-cyclic sulfone (MMSE), Kryptofix 222 (K222), and  $16\alpha$ - $[^{19}\text{F}]$ FES reference standard were obtained from ABX (ABX advanced biochemical compounds GmbH, Radeberg, Germany). Cartridges were purchased from Waters (Waters, MA, USA). Before use, QMA cartridge was flushed with 10 ml of potassium carbonate followed by 40 ml of water.

For automatic synthesis, CFN-MPS-200 module (Sumitomo Heavy Industries, Tokyo, Japan) was used and modified. Synthesis software was programmed in the Cupid system (Sumitomo Heavy Industries, Tokyo, Japan). Radioactivity

was counted in a dose calibrator (Capintec, NJ, USA). The semi-preparative HPLC (PU-2086 Plus, JASCO, Tokyo, Japan) equipped with a semi-preparative C18 column (YMC, YMC-Pack ODS-AM,  $10 \times 250$  mm,  $5 \mu\text{m}$ ), UV/Vis detector (fixed wavelength 280 nm, UV-2075 Plus, JASCO, Tokyo, Japan), and a radiation detector was used to purify the crude product at a flow rate of 4 ml/min, using 30% acetonitrile:30% ethanol:40% water (*v:v:v*) as the mobile phase. Analytical HPLC (Shimadzu LC-15, Suzhou, China) was used for the quality control of the final product, equipped with a UV/Vis detector preset to 280 nm, an analytical C18 column (Shimadzu WondaSil,  $4.6 \times 250$  mm,  $5 \mu\text{m}$ ), and a radioactive detector (Eckert & Ziegler, GA, USA). The column flow rate was 1 ml/min and was kept at approximately room temperature. The samples were eluted with a mobile phase of 30% acetonitrile:70% water (*v:v*).

### Automated Synthesis of $16\alpha$ - $[^{18}\text{F}]$ FES With Kryptofix 222

Based on  $^{18}\text{O}(\text{p}, \text{n})^{18}\text{F}$  nuclear reaction, 1.8 ml of target water containing  $[^{18}\text{O}]\text{H}_2\text{O}$  was irradiated with protons in a Sumitomo HM-10 cyclotron system (Sumitomo Heavy Industries, Tokyo, Japan) to produce  $[^{18}\text{F}]$ fluoride. The energy of incident protons was 10 MeV, and the beam current was about 60 mA. After the irradiation,  $[^{18}\text{F}]$ fluoride was transferred to the collection tube and then passed through a Sep-Pak light QMA cartridge. The trapped  $[^{18}\text{F}]$ fluoride was eluted with 0.9 ml of a mixed aqueous  $\text{K}_2\text{CO}_3/\text{K}_2\text{CO}_3$  (22 mg of K222 in 0.7 ml of acetonitrile and 5.8 mg of potassium carbonate in 0.2 ml of ultrapure water) and then the mixed solution was dried up. To make sure that the fluorination reaction was in an anhydrous condition, the residue was further dried by azeotropic distillation with another 0.5 ml of anhydrous acetonitrile. Two milligrams of MMSE in 1 ml of anhydrous acetonitrile was added to the completely dried reactor, and the mixture was heated at  $115^\circ\text{C}$  for 15 min. Then, the intermediate product was subsequently hydrolyzed by 1.5 ml of 2 M HCl at  $120^\circ\text{C}$  for 3.5 min. After cooling to room temperature, 1.5 ml of 5.6%  $\text{NaHCO}_3$  solution was added to neutralize the reaction mixture. For purification, the crude product was injected into semi-preparative HPLC, and the purification took about 9 min. The purified product was collected in the rotary evaporator to remove solvents and then passed through a sterile 0.22- $\mu\text{m}$  filter with 10 ml of saline containing 1 ml of ethanol.

The analytical HPLC system was adapted to measure the radiochemical and chemical purity of  $16\alpha$ - $[^{18}\text{F}]$ FES at a flow rate of 1 ml/min using 30% acetonitrile in water by comparing the HPLC spectrum of the  $16\alpha$ - $[^{19}\text{F}]$ FES reference standard in the same HPLC conditions. For stability test,  $16\alpha$ - $[^{18}\text{F}]$ FES in the final formula was tested 8 h after the synthesis using HPLC.

To discover how fluorination temperatures and times influence the yield,  $[^{18}\text{F}]$ fluorination was carried out for 5, 10, and 15 min at 105, 115, 125, and  $135^\circ\text{C}$ . The overall radiochemical yield was determined by purifying the product by semi-HPLC.



## Automated Synthesis of $16\alpha$ - $[^{18}\text{F}]$ FES With Tetrabutylammonium

To compare chemical purity and radiochemical yield,  $16\alpha$ - $[^{18}\text{F}]$ FES synthesis processes catalyzed by tetrabutylammonium bicarbonate ( $\text{TBA}\cdot\text{HCO}_3$ ) were the same compared with those catalyzed by K222 except that  $[^{18}\text{F}]$ fluoride trapped in the QMA cartridge was eluted by 500  $\mu\text{l}$  of 0.075 M  $\text{TBA}\cdot\text{HCO}_3$  dissolved in ethanol, and fluorination was achieved at  $135^\circ\text{C}$  for 10 min.

Residual TBA content in the final product was determined by TLC. Silica plates were spotted with 5  $\mu\text{l}$  of the final product, dried, and visualized with iodine. Brown spots will appear if TBA exists in the final product.

## Patients and PET/CT Procedure

Nine patients (mean age  $\pm$  SD,  $50.2 \pm 7.0$  years; age range, 41–63 years) with a clinical diagnosis of breast cancer were enrolled in the study between May 2017 and July 2017. All

patients underwent whole-body PET/CT scan with  $16\alpha$ - $[^{18}\text{F}]$ FES before surgery. Patients underwent the surgical operation within 1 month after the PET/CT scan, and definitive diagnosis was determined using postoperative pathohistology analysis. The study protocol was approved by the Sichuan Cancer Hospital Ethics Committee, and informed consent was obtained from all patients before the PET/CT scan.

All patients fasted 4 h before FES-PET. Approximately a dose of 148–222 MBq (4–6 mCi)  $16\alpha$ - $[^{18}\text{F}]$ FES was infused intravenously over 2 min. The whole-body scanning (2 min per table position) was performed 1 h after administration using a Siemens Biograph mCT-64 PET/CT scanner.

## Statistical Analysis

Means were compared using the two-tailed paired Student's *t* test. *P*-values  $<0.05$  were considered significant. Data analyses were carried out using GraphPad Prism Software Version 5.0 (GraphPad Software Inc., CA, USA).

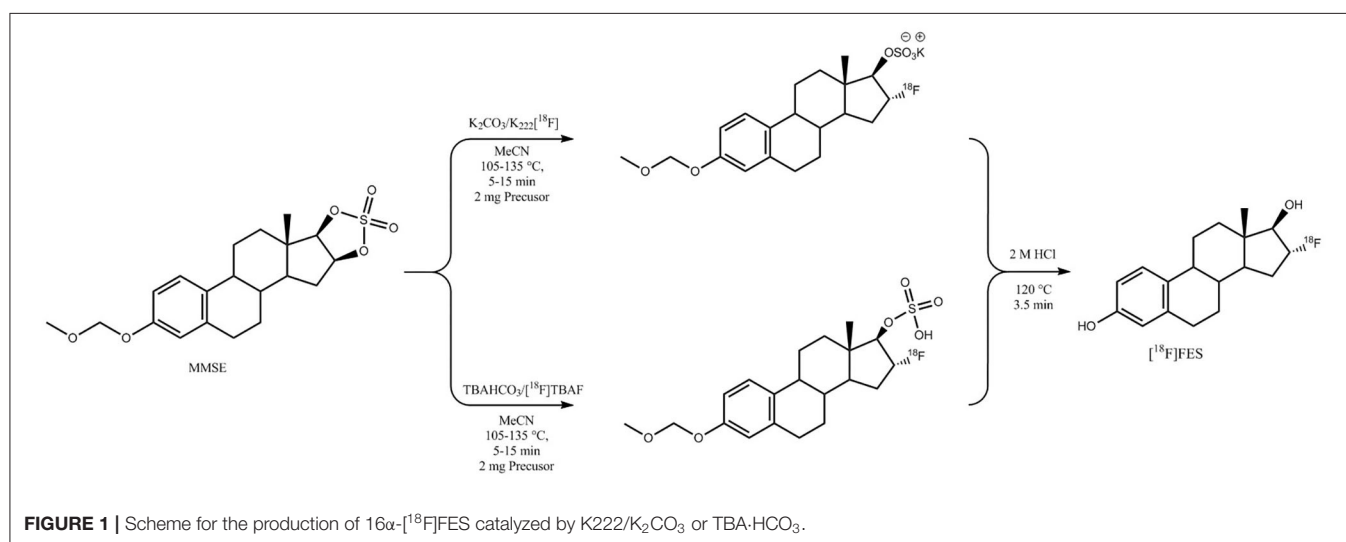


**TABLE 1 |** Investigation of synthesis conditions.

Entry	Precursor	Catalyst	Fluorination temperature ( $^\circ\text{C}$ )	Fluorination time (min)	Radiochemical yield (%)
1	2 mg MMSE/1 mL ACN	K222/ $\text{K}_2\text{CO}_3$	115	15	46.4
2	2 mg MMSE/1 mL ACN	K222/ $\text{K}_2\text{CO}_3$	115	15	47.8
3	2 mg MMSE/1 mL ACN	K222/ $\text{K}_2\text{CO}_3$	115	15	49.8
4	2 mg MMSE/1 mL ACN	K222/ $\text{K}_2\text{CO}_3$	115	15	50.6
5	2 mg MMSE/1 mL ACN	TBA- $\text{HCO}_3$	135	10	45.6
6	2 mg MMSE/1 mL ACN	TBA- $\text{HCO}_3$	135	10	47.0
7	2 mg MMSE/1 mL ACN	TBA- $\text{HCO}_3$	135	10	45.5
8	2 mg MMSE/1 mL ACN	TBA- $\text{HCO}_3$	135	10	48.8
9	2 mg MMSE/1 mL ACN	K222/ $\text{K}_2\text{CO}_3$	115	5	36.7
10	2 mg MMSE/1 mL ACN	K222/ $\text{K}_2\text{CO}_3$	115	10	41.3
11	2 mg MMSE/1 mL ACN	K222/ $\text{K}_2\text{CO}_3$	105	15	37.5
12	2 mg MMSE/1 mL ACN	K222/ $\text{K}_2\text{CO}_3$	125	15	50.4
13	2 mg MMSE/1 mL ACN	K222/ $\text{K}_2\text{CO}_3$	135	15	51.6

MMSE, 3-methoxymethyl- $16\beta$ ,  $17\beta$ -epi-estradiol-O-cyclic sulfone; ACN, acetonitrile; K222, Kryptofix 222; TBA, tetrabutylammonium.

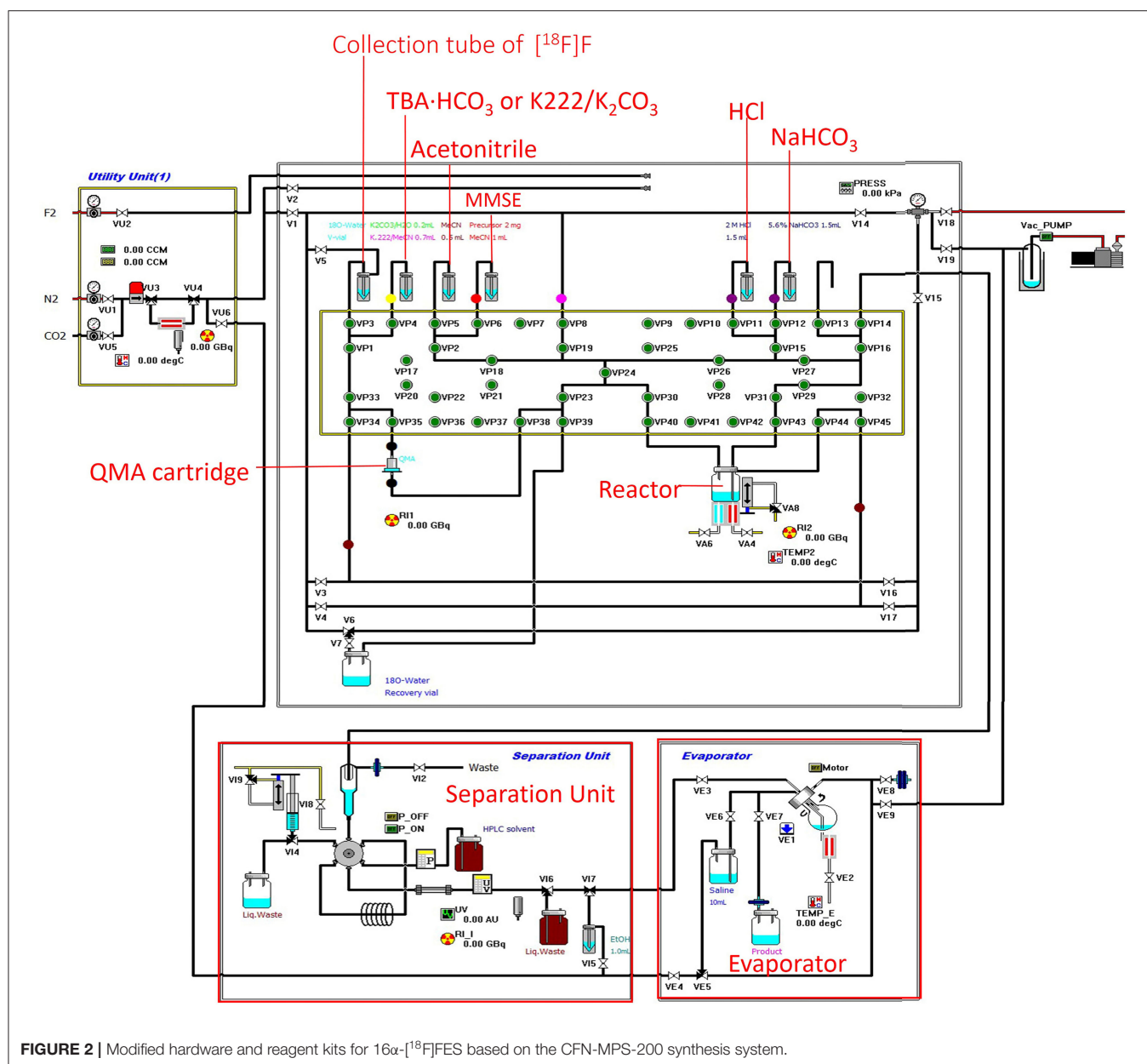


FIGURE 2 | Modified hardware and reagent kits for  $16\alpha$ - $[^{18}\text{F}]$ FES based on the CFN-MPS-200 synthesis system.

## RESULTS

### $[^{18}\text{F}]$ Fluorination and Hydrolysis: K222 Catalyzed vs. TBA Catalyzed

The procedures for the one-pot synthesis of  $16\alpha$ - $[^{18}\text{F}]$ FES were optimized and successfully performed (Figure 1). A total of 13 times synthesis were all successful, and the method was stable (Table 1). Hardware and reagent kits for  $16\alpha$ - $[^{18}\text{F}]$ FES using the CFN-MPS-200 synthesis system are shown in Figure 2. The commercially available precursor MMSE was used, and acetonitrile was chosen as the radiofluorination solvent instead of DMSO. Two different phase transfer catalysts ( $\text{K}_2\text{CO}_3/\text{K}_2\text{CO}_3$  and  $\text{TBA}\cdot\text{HCO}_3$ ) were used, respectively, while the purification methods were the same (by semi-preparative

HPLC purification). As purification results show in Figure 3A ( $\text{K}_2\text{CO}_3/\text{K}_2\text{CO}_3$  catalyzed) or Figure 3B ( $\text{TBA}\cdot\text{HCO}_3$  catalyzed), only one radioactive peak was detected and collected, with a retention time of 7.5 min (using  $\text{K}_2\text{CO}_3/\text{K}_2\text{CO}_3$ ) or 7.6 min (using  $\text{TBA}\cdot\text{HCO}_3$ ). After removing solvents by a rotary evaporator, the decay-corrected radiochemical yield of the final product  $16\alpha$ - $[^{18}\text{F}]$ FES was  $48.7 \pm 0.95\%$  (using  $\text{K}_2\text{CO}_3/\text{K}_2\text{CO}_3$ ,  $n = 4$ ) or  $46.7 \pm 0.77\%$  (using  $\text{TBA}\cdot\text{HCO}_3$ ,  $n = 4$ ).

### Quick Synthesis

$16\alpha$ - $[^{18}\text{F}]$ FES was synthesized rapidly in one pot with a high radiochemical yield and purity in this study. Overall, total  $\text{K}_2\text{CO}_3$ -catalyzed synthesis time was  $48 \pm 2$  min ( $n = 4$ ) and total  $\text{TBA}\cdot\text{HCO}_3$ -catalyzed synthesis time was  $48 \pm 3$  min ( $n = 4$ ); both included

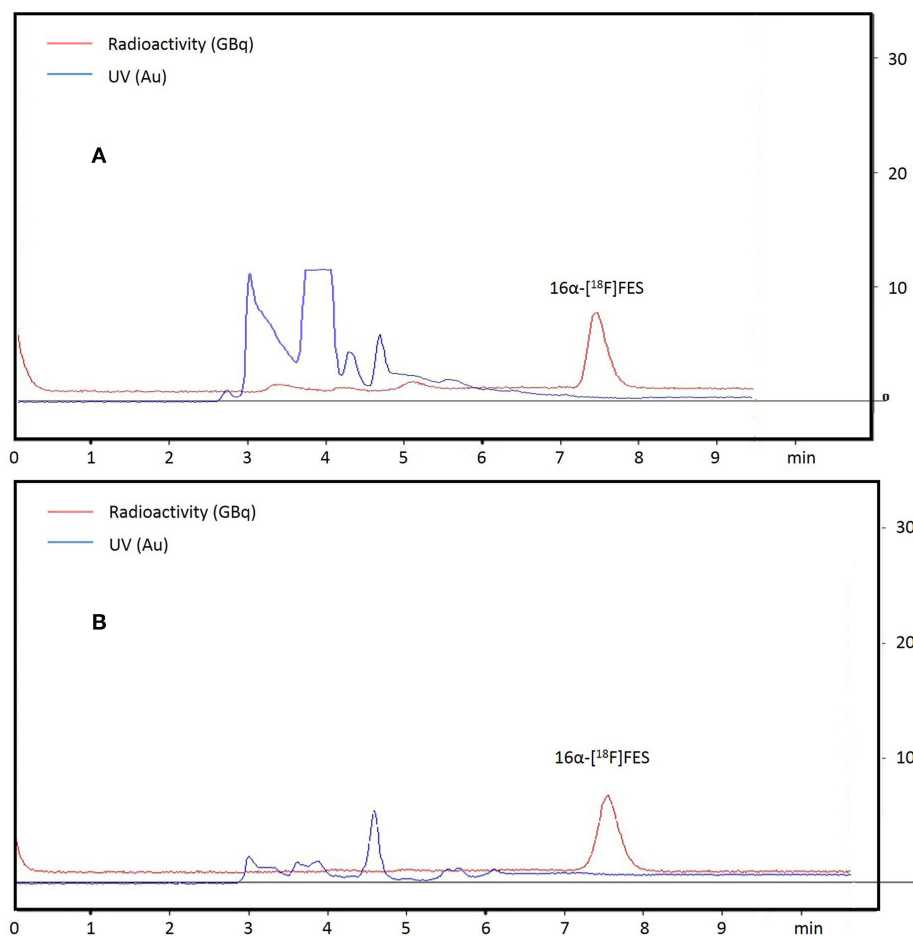


**FIGURE 3 |** The semi-preparative chromatogram of crude  $16\alpha$ - $[^{18}\text{F}]$ FES, UV absorbance at 280 nm. **(A)** The chromatogram of the crude product (using K222/ $\text{K}_2\text{CO}_3$ ). **(B)** The chromatogram of the crude product (using TBA- $\text{HCO}_3$ ).

two azeotropic distillations of  $[^{18}\text{F}]$ fluoride and acetonitrile, radiofluorination, hydrolysis, neutralization, HPLC purification, and desolventizing by rotary evaporator. In typical synthesis conditions, the six steps took the same time in both K222-catalyzed and TBA-catalyzed methods. Desolventizing by the rotary evaporator can reduce the solvent in the final formula to satisfy clinical use and takes about 10 min. If the synthesis of  $16\alpha$ - $[^{18}\text{F}]$ FES was aimed at research and development, omitting the desolventizing step could save 10 min and reduce product loss, which was stained with a rotary evaporator to obtain a high yield. Automated synthesis in commercially available synthesizer systems takes about 80 min, with a 10–20% uncorrected radiochemical yield (4–6).

### Rapid Quality Control of Radiochemical Purity and Chemical Purity

$16\alpha$ - $[^{18}\text{F}]$ FES is well known as an ideal PET tracer binding to ER. Radioactive impurities in  $16\alpha$ - $[^{18}\text{F}]$ FES product solution will influence the imaging for ER expression *in vivo*, and the high radiochemical purity of  $16\alpha$ - $[^{18}\text{F}]$ FES guarantees the accurate diagnosis. The final product was confirmed by comparing the

product with the authentic reference standard. The analytical HPLC chromatograms (**Figure 4**) showed that the retention time was 4.2 min and only one radioactive peak was detected, which suggested that the radiochemical purity of product was almost 100%. In this study,  $6\alpha$ - $[^{18}\text{F}]$ FES with ideal radiochemical purity was produced and the high radiochemical purity might be due to the semi-preparative HPLC purification system instead of SPE cartridges.

The content of residual TBA shown was below 50  $\mu\text{g}/\text{ml}$  according to the spot test. The value of the residual catalyst was below the limits stated in USP or Ph.Eur. (7, 8). Saline containing ethanol was used for the final product formula according to Mori (4). Analytical HPLC was used to determine the stability of the final product synthesized 8 h ago. The results showed that the long-term radiochemical purity of  $16\alpha$ - $[^{18}\text{F}]$ FES in saline containing ethanol at room temperature did not show any decomposition. There was no increase of chemical or radiochemical impurities. According to our study, purity, radiochemical yield, and stability between  $16\alpha$ - $[^{18}\text{F}]$ FES catalyzed by K222 and TBA showed no significant difference.

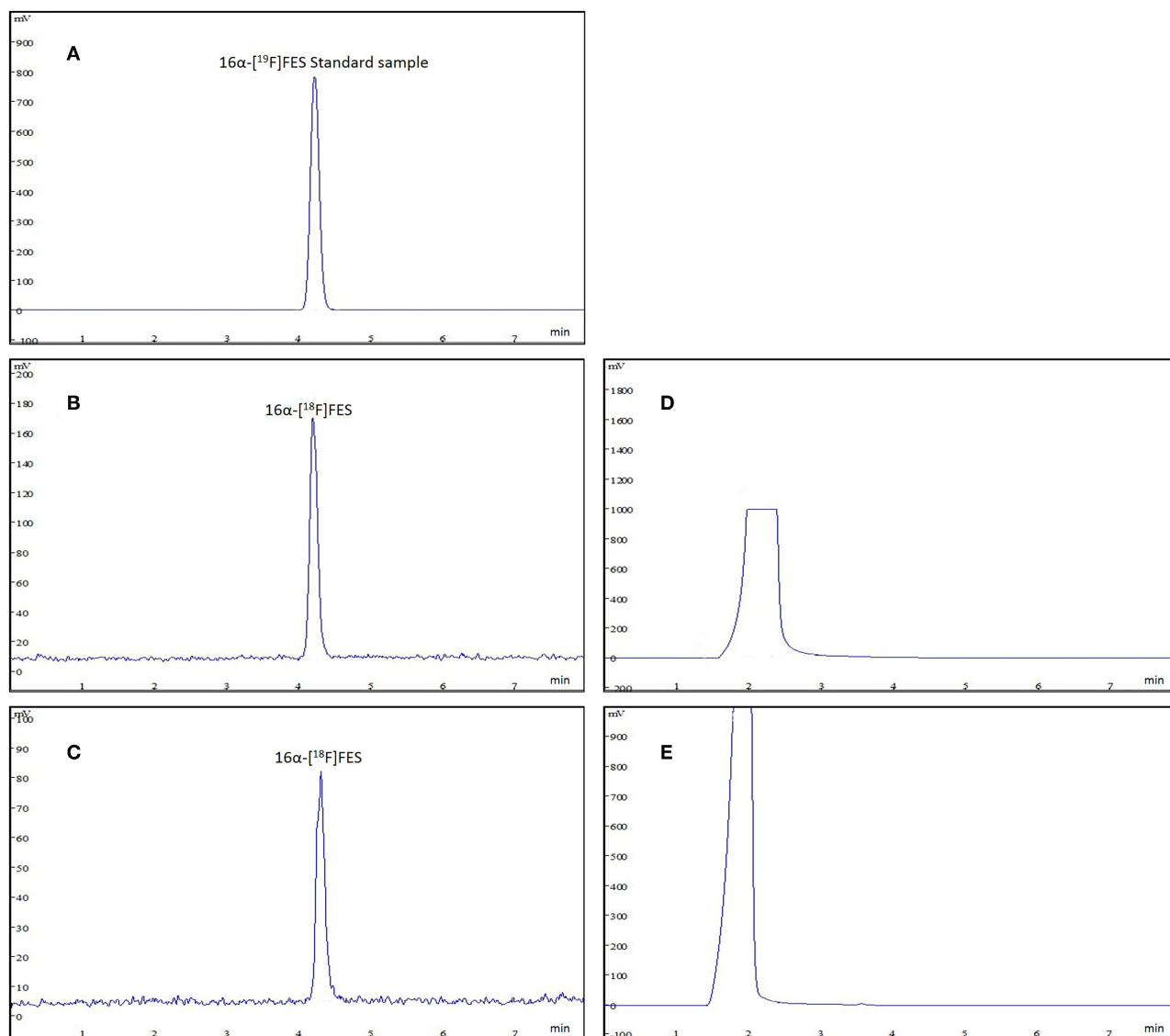


**FIGURE 4 |** The analytic HPLC chromatogram of purified  $16\alpha$ - $[^{18}\text{F}]$ FES, UV absorbance at 280 nm. The UV absorbance and radioactive signals were both transformed into electrical signals. **(A)** UV absorbance of  $16\alpha$ - $[^{19}\text{F}]$ FES reference standard. **(B)** The chromatogram of product (using  $\text{K}_2^{222}/\text{K}_2\text{CO}_3$ ) measured by radioactive detector. **(C)** The chromatogram of product (using  $\text{TBA}\cdot\text{HCO}_3$ ) measured by radioactive detector. **(D)** The chromatogram of product (using  $\text{K}_2^{222}/\text{K}_2\text{CO}_3$ ) measured by UV detector. **(E)** The chromatogram of product (using  $\text{TBA}\cdot\text{HCO}_3$ ) measured by UV detector.

## $16\alpha$ - $[^{18}\text{F}]$ FES PET/CT and ER Expressions

Representative cases of clinically diagnosed breast cancer FES-PET are given in **Figures 5, 6**. **Figure 5** shows a case with ER-positive breast cancer on the upper outer quadrant of the left breast. PET images showed high homogeneous  $16\alpha$ - $[^{18}\text{F}]$ FES accumulation, and immunohistochemical findings of this case are high expression of ER. The other case with ER-negative breast cancer on the right axillary lymph node (**Figure 6**) showed no uptake on PET images, and immunohistochemical findings of this case are no expression of ER.

## DISCUSSION

Because the synthesis of PET tracer is the key link of whole PET examination processes, the successful synthesis of  $16\alpha$ - $[^{18}\text{F}]$ FES needs to be guaranteed. In this study, the one-pot synthesis of  $16\alpha$ - $[^{18}\text{F}]$ FES including six steps, azeotropic distillation, fluorination, acidic hydrolysis,  $\text{NaHCO}_3$  neutralization, semi-preparative HPLC purification, and solvent removal, was successfully performed. The residual water in the reactor often causes failure of fluorination in routine synthesis of  $16\alpha$ - $[^{18}\text{F}]$ FES. Therefore, two improvements were developed: one

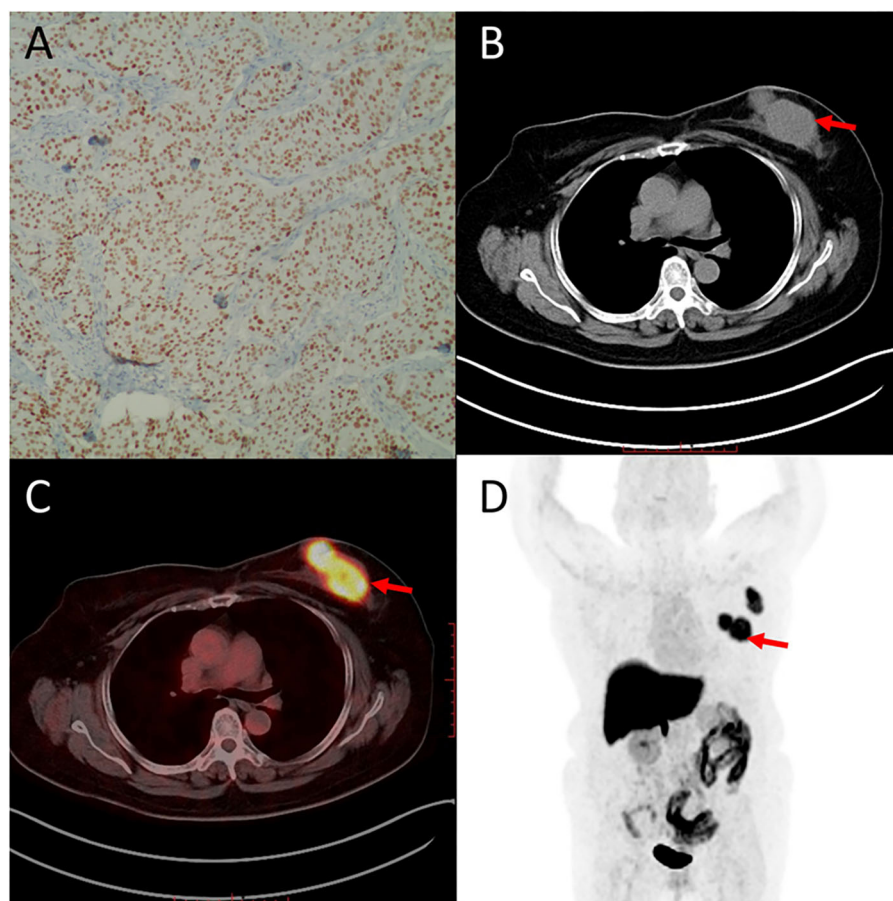


**FIGURE 5 |** Representative case of ER-positive breast cancer on the upper outer quadrant of the left breast (55 years). Immunohistochemistry staining images are shown for ER (A).  $16\alpha$ - $[^{18}\text{F}]$ FES PET/CT images (B–D) (red arrows) are shown. High accumulation of  $16\alpha$ - $[^{18}\text{F}]$ FES significantly corresponded with high expression of ER.

was that the reactor was dried up with an additional 0.5 ml of anhydrous acetonitrile before fluorination; the other was that the precursor MMSE would not be added in the reactor until it is confirmed, with the use of a camera, that the solution in the reactor was dried up and input into the computer. Because semi-preparative HPLC purified  $16\alpha$ - $[^{18}\text{F}]$ FES was stained with a rotary evaporator flask while removing the solvents, the radiochemical yield in this study was a little lower than that in previously reported studies (4, 9–11).

Water is not a suitable solvent for the synthesis of FES because fluorine has a high hydration energy. A polar aprotic solvent such as acetonitrile should be used in this  $\text{S}_{\text{N}}2$  nucleophilic substitution reaction.

The phase transfer catalyst plays an important role in the synthesis of various PET tracers. Many attempts have been made to develop nucleophilic substitution, which include  $^{18}\text{F}$ -CsF,  $^{18}\text{F}$ -Et<sub>4</sub>NF, and  $^{18}\text{F}$ -KHF. However, breakthrough of radiofluorination was not made until K222 was used as catalyst. Usually, the  $^{18}\text{F}^-$  washed out from the cyclotron target is accompanied by traces of metal ions from the surface of the target body. When passing through the light QMA anion exchange

ion, the  $^{18}\text{F}^-$  is retained and the metal ions will be lost in the  $^{18}\text{O}$ -water. Hence, it is necessary to introduce a positively charged counter ion to restore the  $^{18}\text{F}^-$  reactivity before evaporation of residual  $^{18}\text{O}$ -enriched water (12). Several types of positively charged counter ions have been used, including potassium ion complexed by a large ring structure such as K222 and tetrabutylammonium salts (13). As Knott et al. (5) reported, using TBA·HCO<sub>3</sub> in the synthesis of  $16\alpha$ - $[^{18}\text{F}]$ FES resulted in higher radioactive yield than using K222/K<sub>2</sub>CO<sub>3</sub> when the fluorination condition was 8 min in 130°C. In this study, we further investigated whether K222/K<sub>2</sub>CO<sub>3</sub> or TBA·HCO<sub>3</sub> is the appropriate phase transfer catalyst for the automated synthesis of  $16\alpha$ - $[^{18}\text{F}]$ FES. The results showed that there was no significant difference in catalytic activity between K222/K<sub>2</sub>CO<sub>3</sub> and TBA·HCO<sub>3</sub> when the fluorination condition was 15 min in 135°C. It was a significant information for the routine synthesis of  $16\alpha$ - $[^{18}\text{F}]$ FES.

ERs are known as essential sex hormone receptors and are the predominant receptor in breast tissue. It is reported that  $16\alpha$ - $[^{18}\text{F}]$ FES PET can measure the *in vivo* ER expression of breast cancer noninvasively (14). In our study,  $16\alpha$ - $[^{18}\text{F}]$ FES



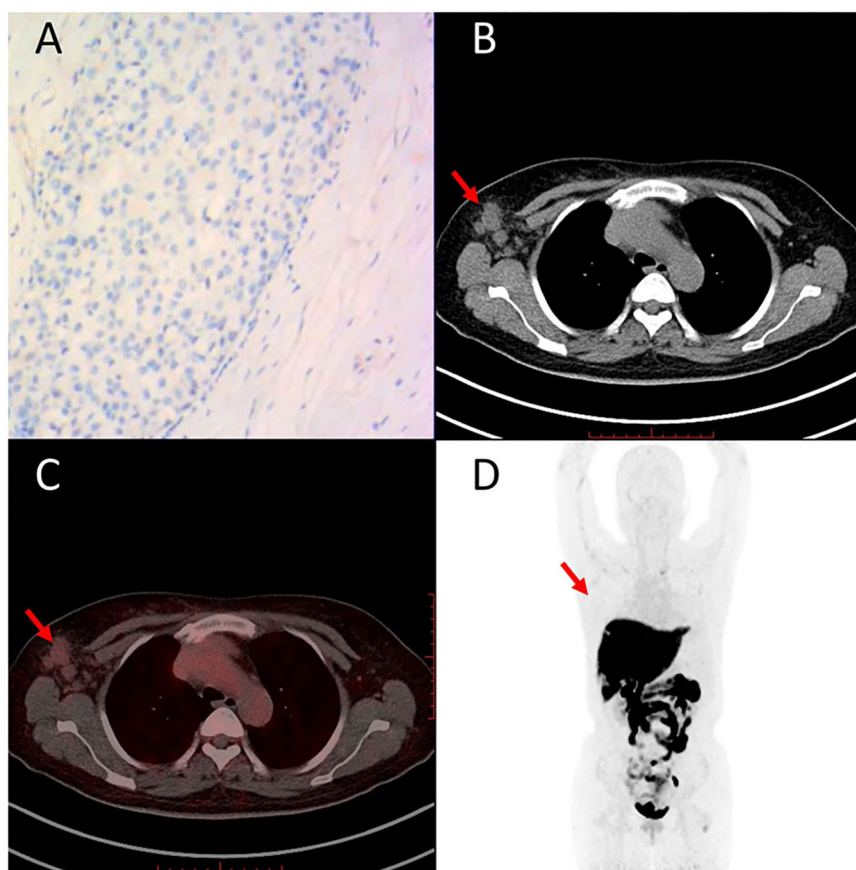


**FIGURE 6 |** Representative case of ER-negative breast cancer on right axillary lymph node (49 years). Immunohistochemistry staining images are shown for ER (A).  $16\alpha$ - $[^{18}\text{F}]$ FES PET/CT images (B–D) (red arrows) are shown. Low accumulation of  $16\alpha$ - $[^{18}\text{F}]$ FES significantly corresponded with low expression of ER.

uptake showed a significant correlation with ER expression in breast masses and axillary lymph node metastasis (Figures 5, 6). These results also reflect the successful synthesis of solvent-free  $16\alpha$ - $[^{18}\text{F}]$ FES in CFN-MPS-200 using module Kryptofix 222 or tetrabutylammonium bicarbonate.

## CONCLUSION

In this work, 13 times fully automatic synthesis of solvent-free  $16\alpha$ - $[^{18}\text{F}]$ FES had been successfully performed in the CFN-MPS-200 synthesis system through a six-step one-pot procedure with high radiochemical yield and radiochemical purity within a short time (<50 min). Solvent-free  $16\alpha$ - $[^{18}\text{F}]$ FES with high radiochemical purity was obtained with HPLC purification and desolventizing by a rotary evaporator and shows significant correlation with ER expression in patients. Moreover, two phase transfer catalysts, Kryptofix 222 and tetrabutylammonium bicarbonate, did not show significant difference in catalytic activity, radiochemical yield, radiochemical purity, and product stability in our study. In conclusion, we present a quick automatic method for synthesizing solvent-free  $16\alpha$ - $[^{18}\text{F}]$ FES that could be used in a commercial synthesis module with either Kryptofix 222 or tetrabutylammonium bicarbonate.

## DATA AVAILABILITY STATEMENT

The original contributions presented in the study are included in the article/supplementary material, further inquiries can be directed to the corresponding author/s.

## ETHICS STATEMENT

The studies involving human participants were reviewed and approved by Sichuan Cancer Hospital Ethic Committee. The patients/participants provided their written informed consent to participate in this study.

## AUTHOR CONTRIBUTIONS

XJ, YL, XW, TS, ZL, and ZC conceived and designed the study and helped to draft the manuscript. XL, YY, and GZ performed the data collection. YK and JS performed the statistical analysis. All authors read and critically revised the manuscript for intellectual content and approved the final manuscript.

## FUNDING

This work has been supported by the Sichuan Science and Technology Project (grant number 2019YJ0574).

## ACKNOWLEDGMENTS

We thank all members of the Radiation Oncology Key Laboratory of Sichuan Province for their support and Mr. Fuxin Cui for technical assistance.

## REFERENCES

1. Fisher B, Brown A, Mamounas E, Wieand S, Robidoux A, Margolese RG, et al. Effect of preoperative chemotherapy on local-regional disease in women with operable breast cancer: findings from national surgical adjuvant breast and bowel project B-18. *J Clin Oncol.* (1997) 16:2483–93. doi: 10.1200/JCO.1997.15.7.2483
2. Andrew ET, Ali N, Nuno LB, Sarah EP, Ian OE, Sam A, et al. A consensus prognostic gene expression classifier for Er positive breast cancer. *Genome Biol.* (2006) 7:R101. doi: 10.1186/gb-2006-7-10-r101
3. Kiesewetter DO, Katzenellenbogen JA, Kilbourn MR, Welch MJ. Synthesis of 16-fluoroestrogens by unusually facile fluoride ion displacement reactions: prospects for the preparation of fluorine-18 labeled estrogens. *Cheminform.* (1985) 16:136–9. doi: 10.1002/chin.198519315
4. Mori T, Kasamatsu S, Mosdzianowski C, Welch MJ, Yonekura Y, Fujibayashi Y. Automatic synthesis of 16  $\alpha$ -[(18)F]fluoro-17 $\beta$ -estradiol using a cassette-type [(18)F]fluorodeoxyglucose synthesizer. *Nucl Med Biol.* (2006) 33:281–6. doi: 10.1016/j.nucmedbio.2005.11.002
5. Knott KE, Grätz D, Hübner S, Jüttler S, Zankl C, Müller M. Simplified and automatic one-pot synthesis of 16 $\alpha$ -[18F]fluoroestradiol without high-performance liquid chromatography purification. *J Labelled Comp Rad.* (2011) 54:749–53. doi: 10.1002/jlcr.1916
6. Brodack JW, Kilbourn MR, Welch MJ, Katzenellenbogen JA. Application of robotics to radiopharmaceutical preparation: controlled synthesis of fluorine-18 16  $\alpha$ -fluoroestradiol-17  $\beta$ . *J Nucl Med.* (1986) 27:714–21.
7. Gaddum JH. *United States Pharmacopeia*. Hoboken, NJ: John Wiley & Sons, Inc. (2007).
8. *European Pharmacopoeia*. Strasbourg: European Pharmacopoeia (2013).
9. Liang S, Lan X, Zhang Y, Xu X, Li B. Fully automatic synthesis of [<sup>18</sup>F]Fes for reporter gene hERL expression imaging. *Nucl Med Commun.* (2012) 33:29–33. doi: 10.1097/MNM.0b013e32834d3b92
10. Lim JL, Zheng L, Berridge MS, Tewson TJ. The use of 3-methoxymethyl-16 $\beta$ , 17 $\beta$ -epiestriol-O-cyclic sulfone as the precursor in the synthesis of F-18 16 $\alpha$ -fluoroestradiol. *Nucl Med Biol.* (1996) 23:911–5. doi: 10.1016/S0969-8051(96)00126-6
11. Römer J, Füchtner F, Steinbach J, Johannsen B. Automated production of 16 $\alpha$ -[18F]fluoroestradiol for breast cancer imaging. *Nucl Med Biol.* (1999) 26:473–9. doi: 10.1016/S0969-8051(98)00098-5
12. Schlyer DJ. PET tracers and radiochemistry. *Ann Acad Med Singapore.* (2004) 33:146–54.
13. Yu S. Review of F-FDG synthesis and quality control. *Biomed Imaging Interv J.* (2006) 2:e57. doi: 10.2349/biij.2.4.e57
14. Tsujikawa T, Yoshida Y, Kiyono Y, et al. Functional oestrogen receptor  $\alpha$  imaging in endometrial carcinoma using 16 $\alpha$ -[18F]fluoro-17 $\beta$ -oestradiol PET. *Eur J Nucl Med Mol Imaging.* (2011) 38:37–45. doi: 10.1007/s00259-010-1589-8

**Conflict of Interest:** The authors declare that the research was conducted in the absence of any commercial or financial relationships that could be construed as a potential conflict of interest.

Copyright © 2020 Jiang, Li, Wang, Shen, Li, Yao, Zhang, Kou, Shen, Luo and Cheng. This is an open-access article distributed under the terms of the Creative Commons Attribution License (CC BY). The use, distribution or reproduction in other forums is permitted, provided the original author(s) and the copyright owner(s) are credited and that the original publication in this journal is cited, in accordance with accepted academic practice. No use, distribution or reproduction is permitted which does not comply with these terms.



# A Novel Model Based on CXCL8-Derived Radiomics for Prognosis Prediction in Colorectal Cancer

Yanpeng Chu<sup>1,2†</sup>, Jie Li<sup>1†</sup>, Zhaoping Zeng<sup>1†</sup>, Bin Huang<sup>3†</sup>, Jiaojiao Zhao<sup>1</sup>, Qin Liu<sup>1</sup>, Huaping Wu<sup>1</sup>, Jiangping Fu<sup>4</sup>, Yin Zhang<sup>4</sup>, Yefan Zhang<sup>5\*</sup>, Jianqiang Cai<sup>5\*</sup> and Fanxin Zeng<sup>1,6\*</sup>

<sup>1</sup> Department of Clinical Research Center, Dazhou Central Hospital, Dazhou, China, <sup>2</sup> Department of Cardiology, Peking University First Hospital, Beijing, China, <sup>3</sup> Department of Gastrointestinal Surgery, Nanchong Central Hospital, Nanchong, China, <sup>4</sup> Department of Oncology, Dazhou Central Hospital, Dazhou, China, <sup>5</sup> Department of Hepatobiliary Surgery, National Cancer Center/Cancer Hospital, Chinese Academy of Medical Sciences and Peking Union Medical College, Beijing, China, <sup>6</sup> School of Medicine, Sichuan University of Arts and Science, Dazhou, China

## OPEN ACCESS

### Edited by:

Peng Mi,  
Sichuan University, China

### Reviewed by:

Yanshan Wang,  
Mayo Clinic, United States  
Jianjun Sun,  
Inner Mongolia Medical  
University, China

### \*Correspondence:

Fanxin Zeng  
zengfx@pku.edu.cn  
Jianqiang Cai  
caijianqiang188@sina.com  
Yefan Zhang  
yefanzhang@126.com

<sup>†</sup>These authors have contributed  
equally to this work

### Specialty section:

This article was submitted to  
Cancer Imaging and Image-directed  
Interventions,  
a section of the journal  
Frontiers in Oncology

Received: 23 June 2020

Accepted: 14 August 2020

Published: 14 October 2020

### Citation:

Chu Y, Li J, Zeng Z, Huang B, Zhao J,  
Liu Q, Wu H, Fu J, Zhang Y, Zhang Y,  
Cai J and Zeng F (2020) A Novel  
Model Based on CXCL8-Derived  
Radiomics for Prognosis Prediction in  
Colorectal Cancer.  
Front. Oncol. 10:575422.  
doi: 10.3389/fonc.2020.575422

**Introduction:** Prognosis prediction is essential to improve therapeutic strategies and to achieve better clinical outcomes in colorectal cancer (CRC) patients. Radiomics based on high-throughput mining of quantitative medical imaging is an emerging field in recent years. However, the relationship among prognosis, radiomics features, and gene expression remains unknown.

**Methods:** We retrospectively analyzed 141 patients (from study 1) diagnosed with CRC from February 2018 to October 2019 and randomly divided them into training ( $N = 99$ ) and testing ( $N = 42$ ) cohorts. Radiomics features in venous phase image were extracted from preoperative computed tomography (CT) images. Gene expression was detected by RNA-sequencing on tumor tissues. The least absolute shrinkage and selection operator (LASSO) regression model was used for selecting imaging features and building the radiomics model. A total of 45 CRC patients (study 2) with immunohistochemical (IHC) staining of CXCL8 diagnosed with CRC from January 2014 to October 2018 were included in the independent testing cohort. A clinical model was validated for prognosis prediction in prognostic testing cohort (163 CRC patients from 2014 to 2018, study 3). We performed a combined radiomics model that was composed of radiomics score, tumor stage, and CXCL8-derived radiomics model to make comparison with the clinical model.

**Results:** In our study, we identified the CXCL8 as a hub gene in affecting prognosis, which is mainly through regulating cytokine–cytokine receptor interaction and neutrophil migration pathway. The radiomics model incorporated 12 radiomics features screened by LASSO according to CXCL8 expression in the training cohort and showed good performance in testing and IHC testing cohorts. Finally, the CXCL8-derived radiomics model combined with tumor stage performed high ability in predicting the prognosis of CRC patients in the prognostic testing cohort, with an area under the curve (AUC) of 0.774 [95% confidence interval (CI): 0.674–0.874]. Kaplan–Meier analysis of the overall



survival probability in CRC patients stratified by combined model revealed that high-risk patients have a poor prognosis compared with low-risk patients (Log-rank  $P < 0.0001$ ).

**Conclusion:** We demonstrated that the radiomics model reflected by *CXCL8* combined with tumor stage information is a reliable approach to predict the prognosis in CRC patients and has a potential ability in assisting clinical decision-making.

**Keywords:** colorectal cancer, *CXCL8*, transcriptomics, radiomics, prognosis

## INTRODUCTION

Colorectal cancer (CRC) is a common gastrointestinal tract malignancy. The incidence of CRC has a clear upward trend (1, 2) with the changes in human diet and lifestyle. In 2018, there were more than 1.8 million new cases of CRC worldwide, and accounting for about 850,000 deaths per year (3). Although great improvements have been achieved due to effective screening tools, refined surgical techniques, and molecular target drugs, the prognosis of CRC patients was not yet satisfactory. The 5-year survival rate of CRC patients with stage I or II cancer is  $>75\%$ . However, more than 20% of patients have already progressed to a distant stage at the first diagnosis, and the 5-year survival rate was only 14% (4). Therefore, early prognosis prediction and subsequent individual therapy strategies are greatly beneficial for CRC patients.

*CXCL8*, also known as interleukin-8, is a member of the chemokine family and is involved in inflammation and immune response (5). Previous studies have revealed an abnormal high expression of *CXCL8* in malignant tumors, which is mainly involved in tumor cell growth, apoptosis, invasion, and migration (6–12). Large-scale cohort studies have suggested that elevated plasma or serum *CXCL8* was associated with worse prognosis in melanoma, metastatic urothelial carcinoma, and renal cell carcinoma patients (13, 14). In terms of CRC, some studies have demonstrated that a high level of *CXCL8* could promote poor overall and disease-free survival. *In vitro* experiments implicated that *CXCL8* modulated CRC cells anoikis or induced the epithelial–mesenchymal transition to result in poor outcomes (8, 15). However, the underlying mechanistic connections among *CXCL8*, phenotypes, and CRC prognosis are extensively unknown.

Radiomics is an emerging and effective method for quantitative analysis based on high-throughput features of medical imaging, which mainly involves four steps: image acquisition, imaging segmentation, feature extraction and quantification, and feature selection and modeling (16). Increasing evidence presents the advantages of radiomics as a noninvasive approach in early diagnosis, prognosis prediction, and curative effect evaluation of tumors (17–19). In CRC patients, studies have demonstrated the successful application of radiomics in the prediction of lymph node metastasis and of outcomes and evaluation of sensitivity to drug therapy (19–21). Many studies focused on radiomics features or combined clinical factors and gene expression with radiomics in CRC; however, to our knowledge, the potential associations between radiomics, gene expression, and CRC remain to be fully elaborated.

Therefore, in our study, we aimed to explore the potential connections between *CXCL8* expression and imaging features and further develop and validate a radiomics model derived from *CXCL8* expression for individual preoperative prediction of prognosis in CRC patients.

## MATERIALS AND METHODS

### Patients

This study included three studies (cohorts) with a total of 355 patients who were pathologically diagnosed with CRC at Dazhou Central Hospital. Study 1 consisted of 147 patients (87 males and 60 females, mean age: 60.73 years), who underwent surgery from February 2018 to October 2019. CRC tissues and their adjacent normal tissues were collected and stored immediately in liquid nitrogen for RNA sequencing (RNA-seq) after radical resection. Among them, the RNA-seq data of 95 paired tissues from 1 year were used for bioinformatic analysis. Study 2 included 45 patients (27 males and 18 females, mean age: 63.28 years) with paraffin-embedded tumor tissues at the Department of Pathology from 2014 to 2018. Study 3 contained 163 patients (95 males and 68 females, mean age: 63.94 years) from 2014 to 2018. The clinical stage of tumors was classified according to tumor–node–metastasis (TNM) staging system [American Joint Committee on Cancer (AJCC) 8th edition staging system]. All patients' clinical information was obtained by electronic medical record. Detailed information of these patients is shown in **Table 1** and **Supplementary Table 1**. Patients in different studies have no significant difference in age, sex distribution, tumor stage, and tumor site proportion.

To explore the relationship between *CXCL8* levels and overall survival in patients with tumors, data from two phase 3 clinical studies (CheckMate 067 and CheckMate 025) were downloaded (14). CheckMate 067 included 887 patients with melanoma treated with nivolumab or ipilimumab or nivolumab plus ipilimumab. CheckMate 025 included 392 patients with renal cell carcinoma treated with nivolumab.

The study was approved by the medical ethics review committee of Dazhou Central Hospital (IRB00000003-17003). Written informed consent was obtained from patients in study 1 and study 2. The medical ethics review board waived the need for informed consent for study 3. The workflow of this study is presented in **Figure 1**.

### RNA-Sequencing

Total RNA of each sample was extracted by Trizol (TaKaRa Biomedical Technology, Beijing, China) according to the kit

**TABLE 1** | Characteristics of patients in three studies.

Characteristic	Study 1 (n = 147)	Study 2 (n = 45)	Study 3 (n = 163)	P
Age (mean ± SD)	60.73 ± 11.99	63.28 ± 10.38	63.94 ± 10.02	0.082
Sex, No. (%)				0.974
Male	87 (58.95)	27 (60.00)	95 (58.28)	
Female	60 (41.05)	18 (40.00)	68 (41.72)	
Tumor stage, No. (%)				0.202
0	4 (2.72)	0 (0.00)	0 (0.00)	
I	38 (25.85)	14 (31.11)	39 (23.93)	
II	40 (27.21)	10 (22.22)	59 (36.20)	
III	53 (36.05)	16 (35.56)	55 (33.74)	
IV	12 (8.16)	5 (11.11)	10 (6.14)	
Tumor sites, No. (%)				0.984
Rectum	100 (68.03)	31 (68.89)	109 (66.87)	
Right colon	24 (16.33)	7 (15.56)	23 (14.11)	
Left colon	21 (14.29)	6 (13.33)	28 (17.18)	
Multiple tumors	2 (1.36)	1 (2.22)	3 (1.84)	

The P-value of age: Kruskal-Wallis rank test. The P value of sex, tumor stage, tumor sites: chi-square test.

instructions. NanoPhotometer spectrophotometer and Agilent 2100 bioanalyzer were used to measure RNA purity and integrity, respectively. The mRNA was further enriched with Oligo (dT) magnetic beads and randomly interrupted with a bivalent cation in NEB Fragmentation Buffer. The library was constructed according to the NEB library construction method. After the library construction was completed, Qubit 2.0 Fluorometer was used for preliminary quantification. Subsequently, the insert size of the library was detected by Agilent 2100 bioanalyzer to ensure the quality of library. Qualified libraries were sequenced by Illumina with the sequencing strategy PE150. The original data file obtained by high-throughput sequencing was transformed into the raw data by CASAVA Base Calling analysis. Clean data for subsequent analysis were obtained by filtering the raw data, checking the sequencing error rate, and checking the GC content distribution. *CXCL8* expression levels in 147 patients of study 1 (141 had CT data, 6 had no CT data) were reflected by relative TPM value (TPM value in CRC tumors/TPM value in adjacent normal tissues) in transcriptome analysis. Patients with relative value above 10 were included in the high expression group and below 10 were included in the low expression group.

## Immunohistochemistry

Each paraffin-embedded tumor tissue was cut into 4-μm-thick sections by pathological sectioning machine (RM2245, Leica, Germany) and placed on a glass slide. The pathological sections were placed in a Water Bath-Slide Drier (PHY-III, China) and baked at 65°C for 2 h, and then after cooling, dewaxed twice with xylene for 20 min each time. The slices treated with different gradient concentrations of alcohol were repaired with EDTA repair solution. Then, 3% peroxidase blocker and blocking

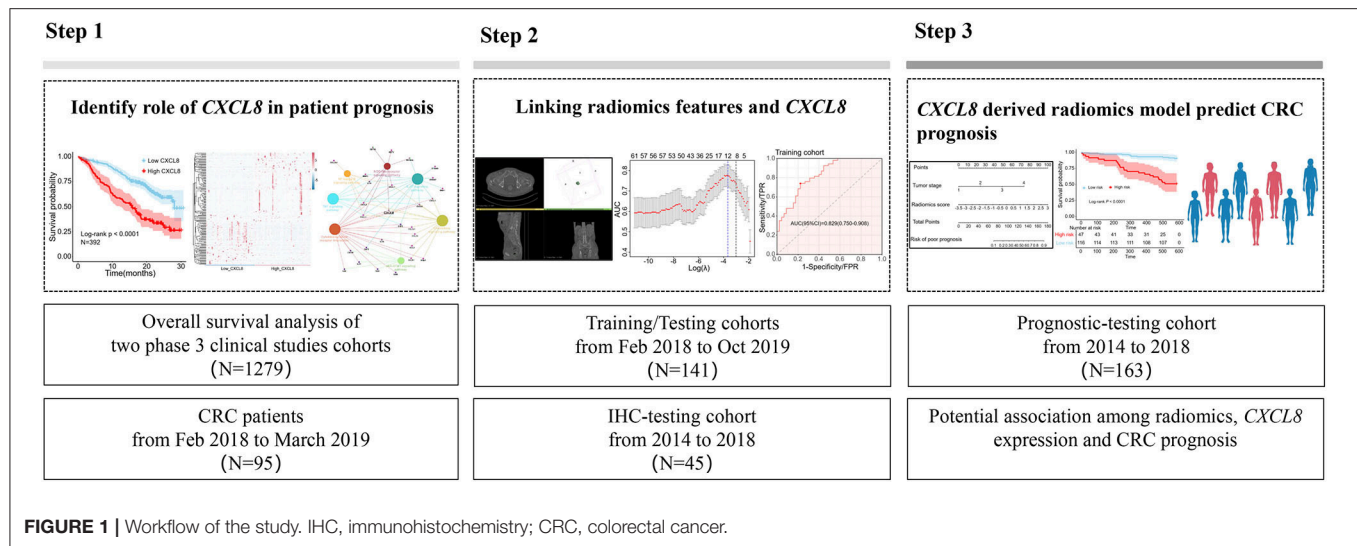
solution were added successively. *CXCL8* antibody (1:100, Affinity, USA) was used to analyze the sections. The results were collected by microscope (BA600-4, Motic, China) after sealing. The immunohistochemistry (IHC) score was calculated as follows: total score = intensity score × percentage score. Intensity score was based on staining intensities and mainly classified into four levels: negative (0), weak (1), moderate (2), and strong (3). Percentage score was based on the percentages of positive cells in staining and classified into five levels: <5% (0), 5–25% (1), 25–50% (2), 50–75% (3), and >75% (4). The IHC score ranging from 0 to 4 was defined as low *CXCL8* group and ranging from 5 to 12 was defined as high *CXCL8* group.

## CT Image Acquisition and Radiomics Signature Extraction

All patients underwent abdominal CT enhancement scan using SOMATOM Definition AS 64-slice CT (SIEMENS, Germany) before surgery. The parameters were as follows: 100 KV, CARE Dose4D, 0.5 s rotation time; detector collimation: 128 × 0.6 mm, field of view: 380 × 380 mm, matrix: 512 × 512. After the conventional CT scan, 60–80 ml of ioversol contrast agent (320 mgI/ml) was injected with a speed of 2–3 ml/s and a high-pressure syringe (Ulrich, Germany), and then injected normal saline (40 ml), arterial scan after 23 s, venous scan after 60 s, and delayed scan after 120 s. Prolong the delayed scan time appropriately according to the lesion. Contrast-enhanced CT reconstruction, the reconstruction thickness was 1 mm. DICOM data were retrieved from INFINTT Healthcare Co. Ltd. (Korea). The preoperative CT images of 349 patients enrolled in radiomics analysis from 2014 to 2019 were obtained and saved in DICOM format (**Supplementary Figure 1**). Among them, 141 patients with CT data were randomly divided into training cohort and testing cohort, 45 patients with IHC staining *CXCL8* were grouped as the IHC testing cohort, 163 patients with prognostic information were grouped as the prognostic testing cohort. Two professional observers used the 3D Slicer software to delineate the tumor tissue under the guidance of a clinical imaging specialist for building a 3D tumor tissue (22). Finally, a total of 854 radiomics eigenvalue results derived from each patient's CT images were collected for analysis.

## Statistical Analysis

Continuous data were presented as the mean ± standard deviation (SD), and Kruskal-Wallis rank test was performed to compare the difference among the three studies. Chi-square test was used to explore the difference in sex, tumor stage, and tumor site distribution. Differentially expressed genes (DEGs) were analyzed using the DESeq2 package in R software (Version: 3.6.3).  $|\log_2 \text{Fold change}| \geq 1$  and  $p\text{-adjust} < 0.05$  were chosen as the cutoff value for identifying DEGs. Gene Ontology (GO) and Kyoto Encyclopedia of Genes and Genomes (KEGG) pathway analysis were performed by Cytoscape (Version: 3.6.1) plug-in ClueGO and CluePedia, with  $\text{adj}_P\text{-value}$  (adjusted by Bonferroni)  $< 0.05$ . Mann-Whitney *U* test and Least absolute shrinkage and selection operator (LASSO) algorithm were performed for potential radiomics feature selection. The LASSO regression model was often adopted for feature selection in



high-dimensional data (23). An appropriate tuning parameter selection ( $\lambda$ ) with 8-fold cross validation was calculated in the LASSO, where radiomics features with LASSO coefficient unequal to zero were selected. Multivariable logistic regression analysis was used to establish the combined model. Kolmogorov–Smirnov (KS) curve and receiver operating characteristic (ROC) curve were conducted to evaluate the performance of the models. Figures were created using GraphPad Prism 8, Cytoscape, and R software. R packages “sampling” (version 2.8), “dplyr” (version 0.8.3), “pROC” (version 1.15.3), “purrr” (version 0.3.3), “tidyr” (version 1.0.0), “ggplot2” (version 3.2.1), “stringr” (version 1.4.0), “rmda” (version 1.6), “glmnet” (version 3.0-2), “survival” (version 3.1-8), “rms” (version 0.2.8.1), “givitir” (version 1.3), and “data.table” (version 1.12.8) were used.  $P$ -value  $< 0.05$  was considered statistically significant.

## RESULTS

### Identify the Role of CXCL8 in Colorectal Cancer

We analyzed the relationship between CXCL8 expression and the prognosis in two phase 3 clinical studies [CheckMate 067 (melanoma); CheckMate 025 (renal cell carcinoma)] (14). As shown in **Figures 2A,B**, patients with low CXCL8 levels had a better prognosis ( $N = 887$ , Log-rank  $p < 0.0001$ ;  $N = 392$ , Log-rank  $p < 0.0001$ ). In CRC patients, the study has reported that high CXCL8 levels in tumors were associated with poor prognosis (8). Furthermore, RNA-seq with 95 CRC tissues in our study was performed to explore the underlying mechanisms of different CXCL8 expressed levels in CRC. Compared with the low CXCL8 expressed group, 185 DEGs were identified in the high CXCL8 expressed group, with 112 genes upregulated and 73 genes downregulated (**Figures 2C,D**).

GO and KEGG pathway enrichment analyses were performed on 185 DEGs to illustrate their biological functions in CRC. The GO analysis totally revealed 55 significantly enriched GO terms, mainly including biological process, cellular component,

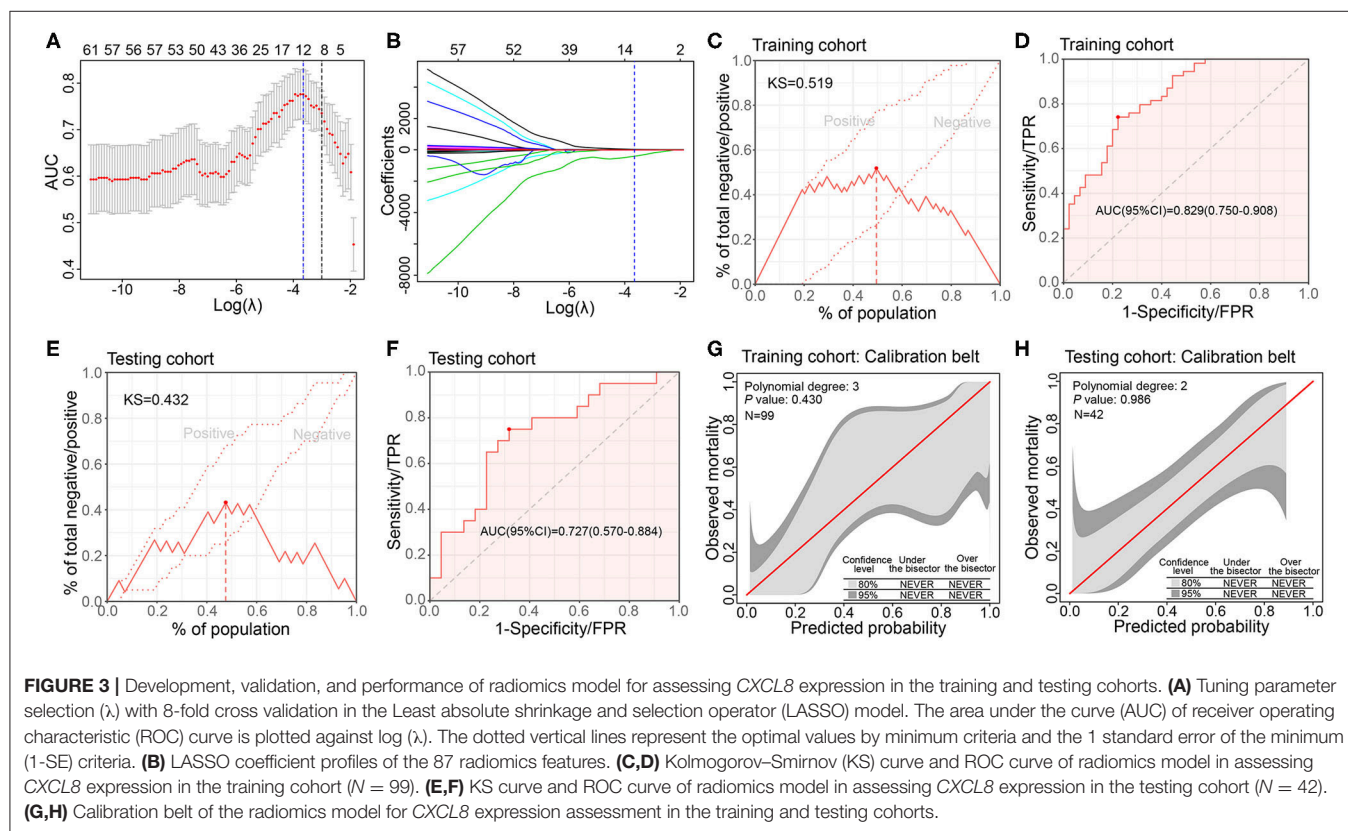
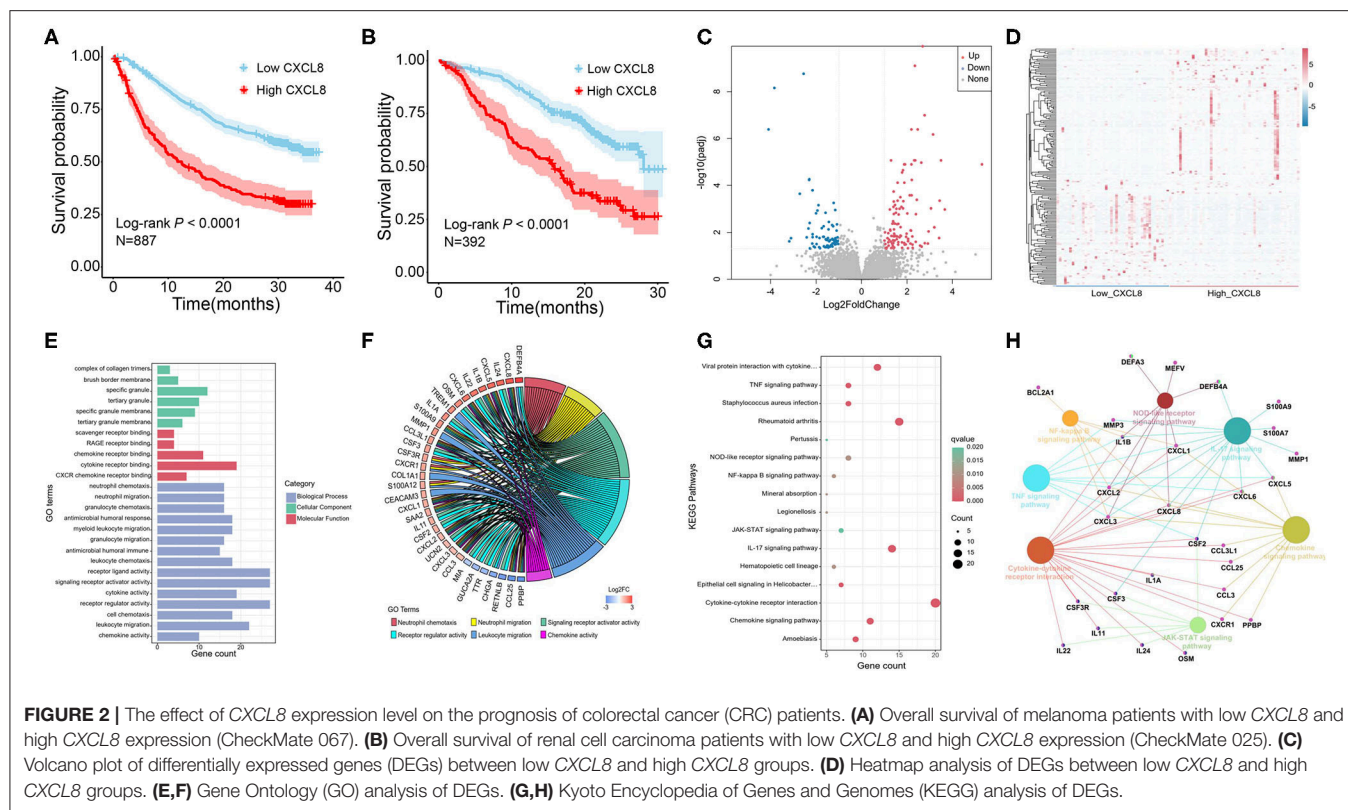
and molecular function analysis. The top 15 GO terms of biological process and all GO terms of both cellular component and molecular function are displayed in **Figure 2E**. In biological process analysis, neutrophil chemotaxis, neutrophil migration, signaling receptor activator activity, receptor regulator activity, leukocyte migration, and chemokine activity were the terms most related to CXCL8 (**Figure 2F**). There were 16 significant KEGG enrichment pathways, in which chemokine signaling pathway, cytokine–cytokine receptor interaction, nuclear factor (NF)- $\kappa$ B signaling pathway, NOD-like receptor signaling pathway, and IL-17 signaling pathway were highly associated with CXCL8 (**Figures 2G,H**). These results suggested that CXCL8 may affect CRC prognosis through regulating the above significant GO terms and KEGG pathways.

### Link of Radiomics Features and CXCL8 Expression

To link the CXCL8 expression and radiomics features, we developed and validated a model based on radiomics features to evaluate the CXCL8 expression (detected by RNA-seq) in 141 CRC patients. Of the extracted radiomics features firstly screened by Mann–Whitney  $U$  test ( $P < 0.01$ ), 12 of 87 features were finally selected as potential predictors by the LASSO regression model based on 99 patients in the training cohort, where the optimal  $\log(\lambda)$  value of  $-3.66$  was chosen according to 8-fold cross validation (**Figures 3A,B**). These features were displayed as an equation in **Supplementary Files**.

The radiomics model incorporated above 12 radiomics features, yielding a KS value of 0.519, AUC 0.829 (95% CI: 0.750–0.908), in the training cohort and KS value of 0.423, AUC 0.727 (95% CI: 0.570–0.884), in the testing cohort (**Figures 3C–F**). The sensitivity, specificity, positive predictive value (PPV), negative predictive value (NPV), and accuracy of the model in the two cohorts are presented in **Supplementary Table 2**. The GiViTi calibration belt revealed no significant deviations by the GiViTi calibration test in both cohorts ( $P = 0.430$ ,  $P = 0.986$ ) (**Figures 3G,H**).





We further verified the results in the IHC testing cohort with IHC staining of *CXCL8*. The radiomics model also showed a good performance in this cohort (KS value = 0.292, AUC = 0.682, 95% CI: 0.525–0.838) (**Figures 4A,B**). The sensitivity, specificity, PPV, NPV, and accuracy are shown in **Supplementary Table 2**. Two examples displayed that the model prediction results were in good agreement with the IHC results (**Figures 4C,D**). These results indicated that parts of the radiomics features indeed associated with *CXCL8* expression. The radiomics characteristics reflected by tumor morphology could be influenced by gene expression in the tumors.

## Prognosis Prediction With Combined Radiomics Model in Colorectal Cancer

To further investigate the possibility of radiomics features in clinical application, we performed above *CXCL8*-derived radiomics model for prognostic status prediction of CRC patients in a prognostic testing cohort with 163 patients. As demonstrated in **Supplementary Figure 2**, the radiomics model had certain ability in prognostic prediction (KS value = 0.308, AUC = 0.641, 95% CI: 0.527–0.756). Patients were predicted as low risk or high risk by the radiomics model. Kaplan–Meier survival analysis revealed a better prognosis in the low-risk group (Log-rank  $P < 0.0001$ ) (**Supplementary Figure 2**).

Furthermore, we analyzed the combination of clinical tumor stage data and radiomics model and observed that the combined radiomics model (combined tumor stage data and radiomics model) results in better performances in prognosis prediction (AUC = 0.774, 95% CI: 0.674–0.874) than the clinical model (AUC = 0.721, 95% CI: 0.625–0.818) and radiomics model (**Figure 5A** and **Supplementary Table 2**). The combined radiomics model that incorporated the clinical tumor stage data and radiomics score is presented as the nomogram (**Figure 5B**). The decision curve analyses based on the clinical model, radiomics model, and combined radiomics model are shown in **Figure 5C**. The analysis revealed that the combined radiomics model had a higher net benefit than other schemes. Hence, we tend to choose the combined radiomics model in clinical utility.

In the prognostic testing cohort, patients were stratified into high-risk and low-risk patients based on the cutoff value of combined radiomics model. As shown in **Figure 5D**, Kaplan–Meier survival analysis demonstrated a significant poor OS (Log-rank  $P < 0.0001$ ) in predicted high-risk patients, which suggested that the predictive value in prognosis of the *CXCL8*-derived combined radiomics model was reliable and practical.

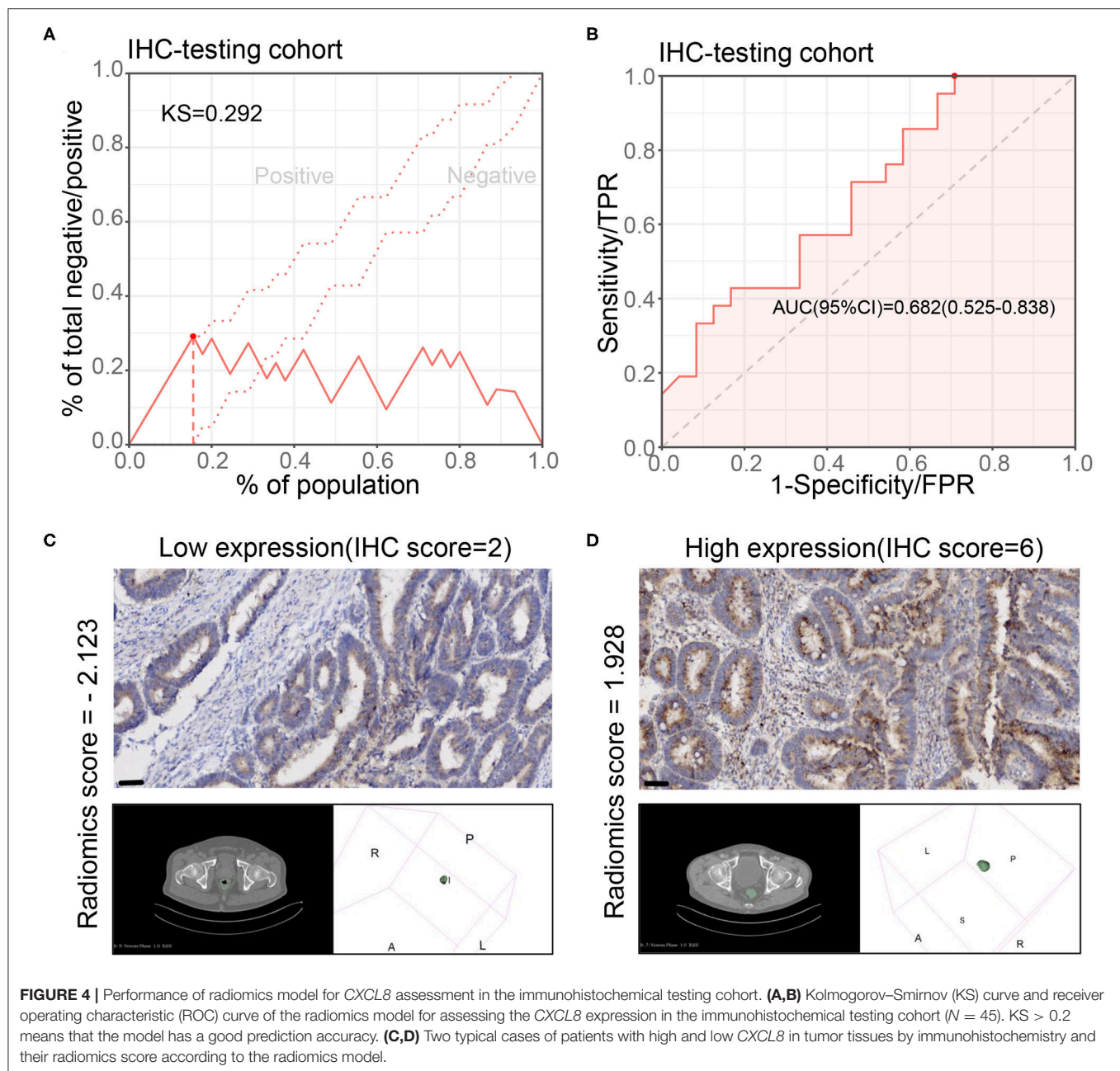
## DISCUSSION

Herein, we firstly identified *CXCL8* as a hub gene related to prognosis in cancers. In two clinical study cohorts, patients with high *CXCL8* levels showed poor prognosis. The underlying mechanisms of different *CXCL8* levels in CRC involved neutrophil chemotaxis and leukocyte migration regulation based on RNA-seq analysis in 95 CRC patients. Subsequently, 12

radiomics features were screened by LASSO method for *CXCL8* expression assessment in 99 CRC patients, and the novel model incorporating above 12 features showed good performance in training, testing, and IHC testing cohorts with AUC of 0.829, 0.727, and 0.682, respectively. We further evaluated whether the *CXCL8*-derived radiomics model had the ability of prognosis prediction in CRC patients. Our results found that the radiomics model could predict the prognosis of patients. Notably, the radiomics model with integrated tumor stage data has a better prognostic ability. Additionally, significant differences were found in survival probability between the high-risk and the low-risk patients based on the combined radiomics model.

*CXCL8* has been shown to promote tumor development in humans in a variety of ways. Recent studies have suggested that this cytokine can significantly affect the accumulation of immunosuppressive and tumor-promoting immune cells by interfering with the infiltration of leukocytes into tumors (24, 25). Tumor-derived *CXCL8* signaling can bias the tumor microenvironment toward immunosuppression through the transport of neutrophils and myeloid inhibitory cells [myeloid-derived suppressor cells (MDSCs)] with local resistance to antitumor immune responses (24, 26, 27). Large randomized studies revealed that elevated serum or plasma *CXCL8* was correlated with reduced clinical benefit of immune-checkpoint inhibitors (13, 14). Interestingly, we firstly used radiomics features to approach the evaluation of *CXCL8* expression levels, then applied the developed *CXCL8*-derived radiomics model to predict patients' prognoses in an independent testing cohort. The results demonstrated that high *CXCL8* in tumor tissues was positively associated with poor prognosis, which is in line with the above studies. Transcriptome sequencing suggested that the underlying mechanism was through regulating immune- and inflammatory-related pathways, while the basic and animal experiments are needed to verify results in the future.

Radiomics can perform quantitative analysis of lesions through a large number of radiological characteristics, which effectively solved the problem that tumor heterogeneity is difficult to be quantitatively evaluated. This has an important clinical application value and has been widely used to predict the prognosis of various cancer patients and improve the treatment strategies (19, 28, 29). Besides, previous studies have proposed that gene expression and pathway status could be evaluated by radiomics features in lung cancer and glioblastoma (30, 31). To our knowledge, no study has explored the underlying connections of imaging features and *CXCL8* expression in CRC. In this study, we identified and validated 12 imaging features with *CXCL8* levels. Due to the significant association between *CXCL8* and OS, we performed the *CXCL8*-derived radiomics model to predict the prognosis of CRC patients in a cohort with 163 patients. ROC analysis, decision curve, and Kaplan–Meier survival analysis demonstrated that the model had ability in poor prognosis prediction. Multiple perspectives data of tumors such as genomics, transcriptomics, metabonomics, clinical features, and radiomics have been combined to systematically describe the tumors. Clinically, the prognosis of cancers is closely related to the stage of tumors. Hence, in this study, we further compared the

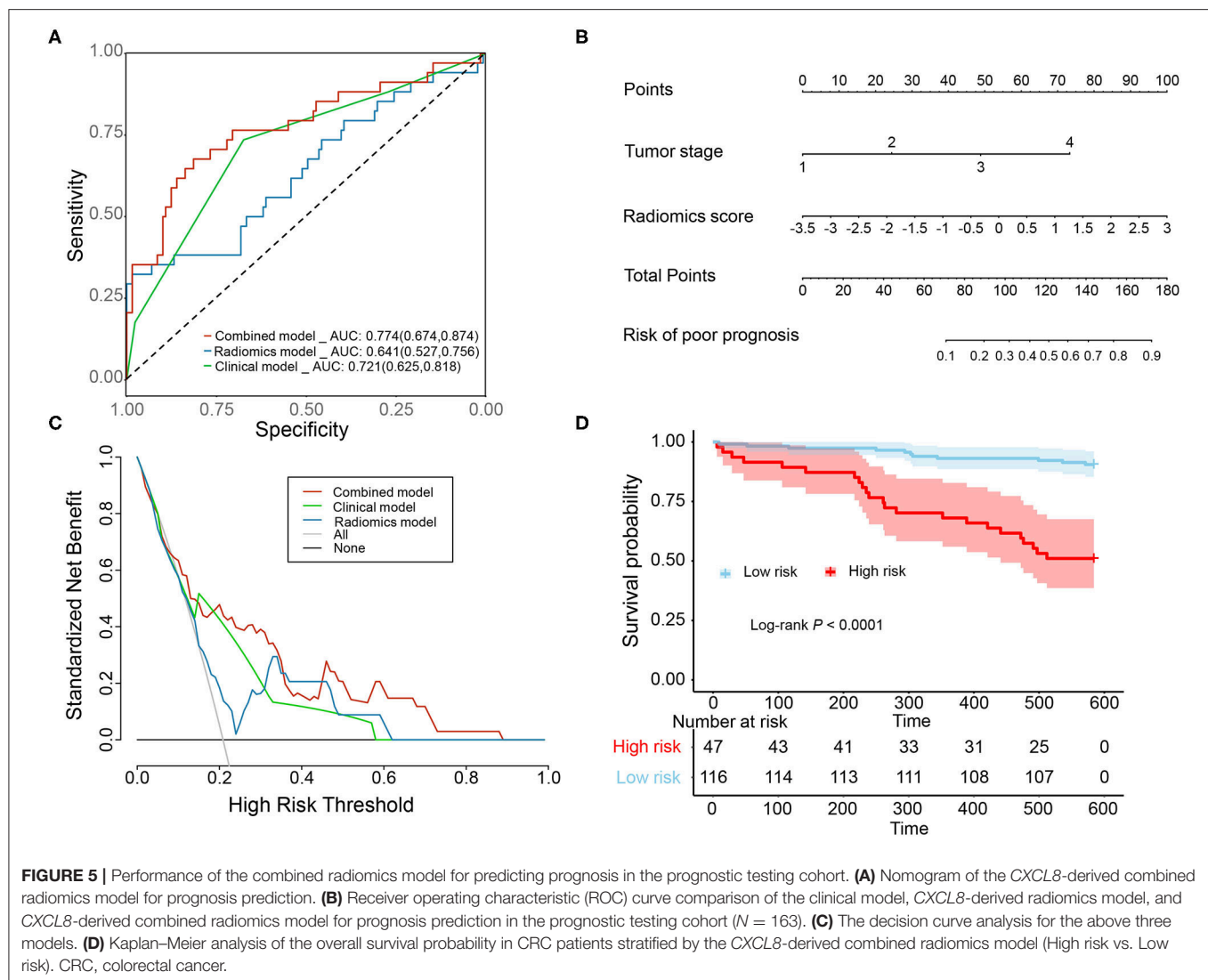


performance of clinical model, radiomics model, and combined radiomics model in prognosis prediction. The results revealed that the combined radiomics model had a higher AUC (0.774) compared with radiomics model (0.641) and clinical model (0.721). The decision curve demonstrated that the combined radiomics model achieved the best net benefit. Considering the effectiveness of clinical application, we finally recommend the combined radiomics model.

Although the *CXCL8*-derived combined model has been successfully applied in CRC prognosis prediction in our study, it had some limitations that need to be acknowledged. Firstly, this study is a hospital-based single-center retrospective

analysis, in which the genes and clinical characteristics of patients may not be representative of the population. Although we randomly divided the participants into independent training and testing cohort at a 7:3 ratio, there was still a lack of generalization and robust evaluation of the model. Secondly, some clinical studies have shown that *CXCL8* disorder is related to tumor prognosis. However, the specific mechanism of *CXCL8* affecting tumor prognosis needs further investigation in cells and animals. Thirdly, the region of interest of the tumor is drawn manually by experienced professionals, which is time-consuming and may increase the variability between observers. In the future, our results





should be verified in a prospective study of patients from multiple centers using more efficient and accurate lesion segmentation algorithms.

## CONCLUSIONS

Our study demonstrated that radiomics features could perform CXCL8 assessment and prognosis prediction in CRC patients, which has a positive application value for guiding clinical decision by analyzing preoperative CT images.

## DATA AVAILABILITY STATEMENT

The original contributions presented in the study are publicly available. This data can be found here: <https://bigd.big.ac.cn/gsa-human/browse/HRA000235>.

## ETHICS STATEMENT

The studies involving human participants were reviewed and approved by the medical ethics review committee of Dazhou Central Hospital. The patients/participants provided their written informed consent to participate in this study.

## AUTHOR CONTRIBUTIONS

FZ, JC, and YC participated in the study design and manuscript preparation. JL and JZ performed RNA-seq data analysis and prepared figures. ZZ and QL performed data analysis. BH enrolled the patients. YeZ revised the manuscript. All authors contributed to the article and approved the submitted version.

## FUNDING

This study was financially supported by the National Natural Science Foundation of China (81902861), Xinglin Scholars

Scientific Research Project Fund of Chengdu University of Traditional Chinese Medicine (YYZX2019012), the Scientific and Technology Fund of Sichuan Health Planning Committee (17PJ028 and 17ZD029), and the Scientific and Technology Fund of Sichuan Medical Association (S16029).

## REFERENCES

- Brody H. Colorectal cancer. *Nature*. (2015) 521:S1. doi: 10.1038/521S1a
- Arnold M, Sierra MS, Laversanne M, Soerjomataram I, Jemal A, Bray F. Global patterns and trends in colorectal cancer incidence and mortality. *Gut*. (2017) 66:683–91. doi: 10.1136/gutjnl-2015-310912
- Bray F, Ferlay J, Soerjomataram I, Siegel RL, Torre LA, Jemal A. Global cancer statistics 2018: GLOBOCAN estimates of incidence and mortality worldwide for 36 cancers in 185 countries. *CA Cancer J Clin*. (2018) 68:394–424. doi: 10.3322/caac.21492
- Siegel RL, Miller KD, Jemal A. Cancer statistics, 2019. *CA Cancer J Clin*. (2019) 69:7–34. doi: 10.3322/caac.21551
- Ha H, Debnath B, Neamati N. Role of the CXCL8-CXCR1/2 axis in cancer and inflammatory diseases. *Theranostics*. (2017) 7:1543–88. doi: 10.7150/thno.15625
- Li J, Liu Q, Huang X, Cai Y, Song L, Xie Q, et al. Transcriptional profiling reveals the regulatory role of CXCL8 in promoting colorectal cancer. *Front Genet*. (2019) 10:1360. doi: 10.3389/fgene.2019.01360
- Allegrini G, Coltelli L, Orlandi P, Fontana A, Camerini A, Ferro A, et al. Pharmacogenetic interaction analysis of VEGFR-2 and IL-8 polymorphisms in advanced breast cancer patients treated with paclitaxel and bevacizumab. *Pharmacogenomics*. (2014) 15:1985–99. doi: 10.2217/pgs.14.140
- Xiao YC, Yang ZB, Cheng XS, Fang XB, Shen T, Xia CF, et al. CXCL8, overexpressed in colorectal cancer, enhances the resistance of colorectal cancer cells to anoikis. *Cancer Lett*. (2015) 361:22–32. doi: 10.1016/j.canlet.2015.02.021
- Singh RK, Varney ML, Bucana CD, Johansson SL. Expression of interleukin-8 in primary and metastatic malignant melanoma of the skin. *Melanoma Res*. (1999) 9:383–7. doi: 10.1097/00008390-199908000-00007
- Fernando RI, Castillo MD, Litzinger M, Hamilton DH, Palena C. IL-8 signaling plays a critical role in the epithelial-mesenchymal transition of human carcinoma cells. *Cancer Res*. (2011) 71:5296–306. doi: 10.1158/0008-5472.CAN-11-0156
- Ning Y, Manegold PC, Hong YK, Zhang W, Pohl A, Lurje G, et al. Interleukin-8 is associated with proliferation, migration, angiogenesis and chemosensitivity in vitro and in vivo in colon cancer cell line models. *Int J Cancer*. (2011) 128:2038–49. doi: 10.1002/ijc.25562
- Chen L, Min L, Wang X, Zhao J, Chen H, Qin J, et al. Loss of RACK1 promotes metastasis of gastric cancer by inducing a miR-302c/IL8 signaling loop. *Cancer Res*. (2015) 75:3832–41. doi: 10.1158/0008-5472.CAN-14-3690
- Yuen KC, Liu LF, Gupta V, Madireddi S, Keerthivasan S, Li C, et al. High systemic and tumor-associated IL-8 correlates with reduced clinical benefit of PD-L1 blockade. *Nat Med*. (2020) 26:693–8. doi: 10.1038/s41591-020-0860-1
- Schalper KA, Carleton M, Zhou M, Chen T, Feng Y, Huang SP, et al. Elevated serum interleukin-8 is associated with enhanced intratumor neutrophils and reduced clinical benefit of immune-checkpoint inhibitors. *Nat Med*. (2020) 26:688–92. doi: 10.1038/s41591-020-0856-x
- Cheng XS, Li YF, Tan J, Sun B, Xiao YC, Fang XB, et al. CCL20 and CXCL8 synergize to promote progression and poor survival outcome in patients with colorectal cancer by collaborative induction of the epithelial-mesenchymal transition. *Cancer Lett*. (2014) 348:77–87. doi: 10.1016/j.canlet.2014.03.008
- Liu Z, Wang S, Dong D, Wei J, Fang C, Zhou X, et al. The applications of radiomics in precision diagnosis and treatment of oncology: opportunities and challenges. *Theranostics*. (2019) 9:1303–22. doi: 10.7150/thno.30309
- Thawani R, McLane M, Beig N, Ghose S, Prasanna P, Velcheti V, et al. Radiomics and radiogenomics in lung cancer: a review for the clinician. *Lung Cancer*. (2018) 115:34–41. doi: 10.1016/j.lungcan.2017.10.015
- Valdora F, Houssami N, Rossi F, Calabrese M, Tagliafico AS. Rapid review: radiomics and breast cancer. *Breast Cancer Res Treat*. (2018) 169:217–29. doi: 10.1007/s10549-018-4675-4
- Huang YQ, Liang CH, He L, Tian J, Liang CS, Chen X, et al. Development and validation of a radiomics nomogram for preoperative prediction of lymph node metastasis in colorectal cancer. *J Clin Oncol*. (2016) 34:2157–64. doi: 10.1200/JCO.2015.65.9128
- Dohan A, Gallix B, Guiu B, Le Malicot K, Reinhold C, Soyer P, et al. Early evaluation using a radiomic signature of unresectable hepatic metastases to predict outcome in patients with colorectal cancer treated with FOLFIRI and bevacizumab. *Gut*. (2020) 69:531–9. doi: 10.1136/gutjnl-2018-316407
- Dercle L, Lu L, Schwartz LH, Qian M, Tejpar S, Eggleton P, et al. Radiomics response signature for identification of metastatic colorectal cancer sensitive to therapies targeting EGFR pathway. *J Natl Cancer Inst*. (2020) 112:902–12. doi: 10.1093/jnci/djaa017
- Bruns N. [3D Slicer : Universal 3D visualization software]. *Unfallchirurg*. (2019) 122:662–3. doi: 10.1007/s00113-019-0654-4
- Gui J, Li H. Penalized Cox regression analysis in the high-dimensional and low-sample size settings, with applications to microarray gene expression data. *Bioinformatics*. (2005) 21:3001–8. doi: 10.1093/bioinformatics/bti422
- David JM, Dominguez C, Hamilton DH, Palena C. The IL-8/IL-8R axis: a double agent in tumor immune resistance. *Vaccines*. (2016) 4:22. doi: 10.3390/vaccines4030022
- Schinke C, Giricz O, Li W, Shastri A, Gordon S, Barreiro L, et al. IL8-CXCR2 pathway inhibition as a therapeutic strategy against MDS and AML stem cells. *Blood*. (2015) 125:3144–52. doi: 10.1182/blood-2015-01-621631
- Asfaha S, Dubeykovskiy AN, Tomita H, Yang X, Stokes S, Shibata W, et al. Mice that express human interleukin-8 have increased mobilization of immature myeloid cells, which exacerbates inflammation and accelerates colon carcinogenesis. *Gastroenterology*. (2013) 144:155–66. doi: 10.1053/j.gastro.2012.09.057
- Katoh H, Watanabe M. Myeloid-derived suppressor cells and therapeutic strategies in cancer. *Mediat Inflamm*. (2015) 2015:159269. doi: 10.1155/2015/159269
- Liu H, Zhang C, Wang L, Luo R, Li J, Zheng H, et al. MRI radiomics analysis for predicting preoperative synchronous distant metastasis in patients with rectal cancer. *Eur Radiol*. (2019) 29:4418–26. doi: 10.1007/s00330-018-5802-7
- Ou D, Blanchard P, Rosellini S, Levy A, Nguyen F, Leijenaar RTH, et al. Predictive and prognostic value of CT based radiomics signature in locally advanced head and neck cancers patients treated with concurrent chemoradiotherapy or bioradiotherapy and its added value to Human Papillomavirus status. *Oral Oncol*. (2017) 71:150–5. doi: 10.1016/j.oraloncology.2017.06.015
- Grossmann P, Stringfield O, El-Hachem N, Bui MM, Rios Velazquez E, Parmar C, et al. Defining the biological basis of radiomic phenotypes in lung cancer. *eLife*. (2017) 6:e23421. doi: 10.7554/eLife.23421
- Park JE, Kim HS, Park SY, Nam SJ, Chun SM, Jo Y, et al. Prediction of core signaling pathway by using diffusion- and perfusion-based MRI radiomics and next-generation sequencing in isocitrate dehydrogenase wild-type glioblastoma. *Radiology*. (2020) 294:388–97. doi: 10.1148/radiol.2019190913

## SUPPLEMENTARY MATERIAL

The Supplementary Material for this article can be found online at: <https://www.frontiersin.org/articles/10.3389/fonc.2020.575422/full#supplementary-material>

**Conflict of Interest:** The authors declare that the research was conducted in the absence of any commercial or financial relationships that could be construed as a potential conflict of interest.

Copyright © 2020 Chu, Li, Zeng, Huang, Zhao, Liu, Wu, Fu, Zhang, Zhang, Cai and Zeng. This is an open-access article distributed under the terms of the Creative Commons Attribution License (CC BY). The use, distribution or reproduction in other forums is permitted, provided the original author(s) and the copyright owner(s) are credited and that the original publication in this journal is cited, in accordance with accepted academic practice. No use, distribution or reproduction is permitted which does not comply with these terms.





# Deep Convolutional Neural Network Based on Computed Tomography Images for the Preoperative Diagnosis of Occult Peritoneal Metastasis in Advanced Gastric Cancer

## OPEN ACCESS

### Edited by:

Changqiang Wu,  
North Sichuan Medical College, China

### Reviewed by:

Zaiyi Liu,  
Guangdong Provincial People's  
Hospital, China  
Shenghong Ju,  
Southeast University, China

### \*Correspondence:

Jiankun Hu  
hujkwch@126.com  
Bin Song  
songlab\_radiology@163.com

<sup>†</sup>These authors have contributed  
equally to this work

### Specialty section:

This article was submitted to  
Cancer Imaging and  
Image-directed Interventions,  
a section of the journal  
Frontiers in Oncology

**Received:** 01 September 2020

**Accepted:** 12 October 2020

**Published:** 02 November 2020

### Citation:

Huang Z, Liu D, Chen X, He D, Yu P,  
Liu B, Wu B, Hu J and Song B (2020)  
Deep Convolutional Neural Network  
Based on Computed Tomography  
Images for the Preoperative Diagnosis  
of Occult Peritoneal Metastasis in  
Advanced Gastric Cancer.  
Front. Oncol. 10:601869.  
doi: 10.3389/fonc.2020.601869

Zixing Huang<sup>1†</sup>, Dan Liu<sup>1†</sup>, Xinzu Chen<sup>2</sup>, Du He<sup>3</sup>, Pengxin Yu<sup>4</sup>, Baiyun Liu<sup>4</sup>, Bing Wu<sup>1</sup>, Jiankun Hu<sup>2\*</sup> and Bin Song<sup>1\*</sup>

<sup>1</sup> Department of Radiology, West China Hospital, Sichuan University, Chengdu, China, <sup>2</sup> State Key Laboratory of Biotherapy, Department of Gastrointestinal Surgery and Laboratory of Gastric Cancer, Collaborative Innovation Center for Biotherapy, West China Hospital, Sichuan University, Chengdu, China, <sup>3</sup> Department of Pathology, West China Hospital, Sichuan University, Chengdu, China, <sup>4</sup> Institute of Advanced Research, Infervision, Beijing, China

We aimed to develop a deep convolutional neural network (DCNN) model based on computed tomography (CT) images for the preoperative diagnosis of occult peritoneal metastasis (OPM) in advanced gastric cancer (AGC). A total of 544 patients with AGC were retrospectively enrolled. Seventy-nine patients were confirmed with OPM during surgery or laparoscopy. CT images collected during the initial visit were randomly split into a training cohort and a testing cohort for DCNN model development and performance evaluation, respectively. A conventional clinical model using multivariable logistic regression was also developed to estimate the pretest probability of OPM in patients with gastric cancer. The DCNN model showed an AUC of 0.900 (95% CI: 0.851–0.953), outperforming the conventional clinical model (AUC = 0.670, 95% CI: 0.615–0.739;  $p < 0.001$ ). The proposed DCNN model demonstrated the diagnostic detection of occult PM, with a sensitivity of 81.0% and specificity of 87.5% using the cutoff value according to the Youden index. Our study shows that the proposed deep learning algorithm, developed with CT images, may be used as an effective tool to preoperatively diagnose OPM in AGC.

**Keywords:** stomach neoplasms, peritoneal neoplasms, deep learning, tomography, x-ray computed, neural networks, computer

## INTRODUCTION

According to the GLOBOCAN 2018 data, gastric cancer (GC) remains the fifth most common cancer and the third most deadly cancer worldwide (1). Peritoneal metastasis (PM) occurs in ~53–66% of patients diagnosed with metastatic GC (2), especially in younger patients with advanced gastric cancer (AGC) (3). Patients with PM thus may be subject to late detection or even improper

surgical treatment. Therefore, the early detection and diagnosis of PM in GC patients prior to surgery would be crucial for avoiding unnecessary resection and allow for optimal therapy selection in clinical practice (4–9).

Abdominal enhanced CT is considered the most common noninvasive modality of preoperative diagnosis in GC patients (5, 7, 9–11). Typical PM indications on CT images include omentum cake, extensive ascites, and parietal peritoneal thickening (12). Clinically, occult peritoneal metastasis (OPM) often refers to PM negativity on initial CT diagnosis that is revised to PM positivity following subsequent laparoscopy or surgery (12, 13). Due to the nature of OPM, it is often missed by radiologists when interpreting CT images alone, resulting in low detection sensitivity and diagnostic accuracy in AGC patients. It has been reported that approximately 16% of OPMs are missed on CT images (12, 14–16), even with multidisciplinary discussion (12, 13). MRI and PET/CT are considered second choices because they are less sensitive than abdominal enhanced CT in detecting peritoneal metastases (17–19). In addition, the costs of MRI and especially PET/CT are high. Recent advances in technology using laparoscopy have provided reliable preoperative methods to identify OPM in patients with AGC (5, 8–10, 20, 21). However, there are many medical concerns and adverse medical care issues due to its invasive and costly nature, and its application in appropriate patient selection remains controversial. Therefore, the development of a noninvasive method to facilitate the targeted diagnosis of OPM beyond conventional imaging is urgently needed.

Artificial intelligence (AI) technology, particularly deep learning, has shown remarkable progress in medical image interpretation (22–24). A typical deep learning approach, named convolutional neural network (CNN), is a novel and powerful tool for the image-based determination of complex relationships and has exhibited sophisticated performance for small feature detection and characterization (25–27). The literature has reported the use of CNNs in the detection and diagnosis of tumor diseases, such as prostate cancer, breast cancer, and lung cancer (28, 29), highlighting the value of deep learning in clinical practice.

We therefore aimed to develop a deep CNN (DCNN)-based model for the preoperative diagnosis of OPM in AGC patients and to compare its diagnostic performance with that of the conventional clinical model using logistic regression.

## MATERIALS AND METHODS

This retrospective study was approved by the Biomedical Research Ethics Committee of West China Hospital of Sichuan University, and the requirement for informed consent was waived.

### Patients

The study was carried out at Surgical Gastric Cancer Patient Registry of West China Hospital (id: WCH-SGCPR-2019-08). Patients were enrolled based on the following inclusion criteria:

(1) patients with AGC ( $cT \geq 2$ ) diagnosed by endoscopy–biopsy and CT; (2) patients who received whole abdominal enhanced CT scan preoperatively with a venous-image slice thickness of 2 mm; (3) patients without typical PM findings on CT, such as omental nodules or omental cake, extensive ascites, or irregular thickening with high peritoneal enhancement; and (4) patients with no other evidence of distant metastasis or other tumors. The exclusion criteria were as follows: (1) previous abdominal surgery; (2) previous abdominal malignancies or inflammatory diseases; (3) CT carried out more than 2 weeks before surgery; (4) poor stomach filling; (5) poor CT image quality due to artifacts; and (6) inability to visualize the primary lesion of gastric cancer on CT images. The selection process of patients included in this study is shown in **Figure 1**.

PM status confirmed: All patients were confirmed to have peritoneal metastasis by surgical or laparoscopic exploration. The laparoscopy procedure used here was a “Four-Step Procedure” of laparoscopic exploration for GC (30). During the procedure, the abdominal and peritoneal conditions were carefully examined. All suspicious peritoneal implants or ascites were sent for pathological biopsy or cytological examination. Existence of PM was determined using the American Joint Committee on Cancer guidelines in consensus between pathologists and surgeons.

### CT Image Acquisition

Prior to CT examination, patients were requested to fast for at least 6 h and orally ingested 600–1000 mL water. Patients were first trained to hold their breath during scanning with the scan range covering the entire abdomen and then scanned using a 128-slice scanner (SOMATOM Definition AS+, Siemens Healthcare, Forchheim, Germany) and a dual-source CT system (Somatom Definition Flash, Siemens Healthcare, Forchheim, Germany) with the following parameters: tube voltage, 120 kV; amperage, 210 mAs; slice thickness, 2 mm; slice interval, 2 mm; field of view, 35–50 cm; matrix,  $512 \times 512$ ; rotation time, 0.5 s; and pitch 1.0. With a trigger threshold of the aorta reaching 170 HU, a three-phase scan was obtained in the precontrast phase, the arterial phase at the trigger, and the portal vein phase 30 s after the trigger. Following an unenhanced scan, 1.2–1.5 mL/kg iodinated contrast agent [Iopamiro (370 mg I/mL), Shanghai Bracco Sine Pharmaceutical Corp Ltd, Shanghai, China] was injected intravenously at a flow rate of 2.5–3.0 mL/s using a high-pressure syringe (Medrad Stellant CT Injector System, Medrad Inc. Inianola, USA).

### Data Preparation

Portal vein-phase CT images were first exported to ITK-SNAP software (version 2.2.0; [www.itksnap.org](http://www.itksnap.org)) for manual segmentation. Gastric cancer lesions were then manually annotated by a radiologist (with 5 years of experience in gastroenterology imaging) and confirmed by another abdominal specialist (with 14 years of experience in gastroenterology imaging). Two radiologists reviewed all slices obtained from each patient, selected one slice with the largest tumor area and manually delineated the lesion to obtain the final regions of interest (ROIs) (**Figure 2**). The gastric lumen and artifacts were carefully avoided.

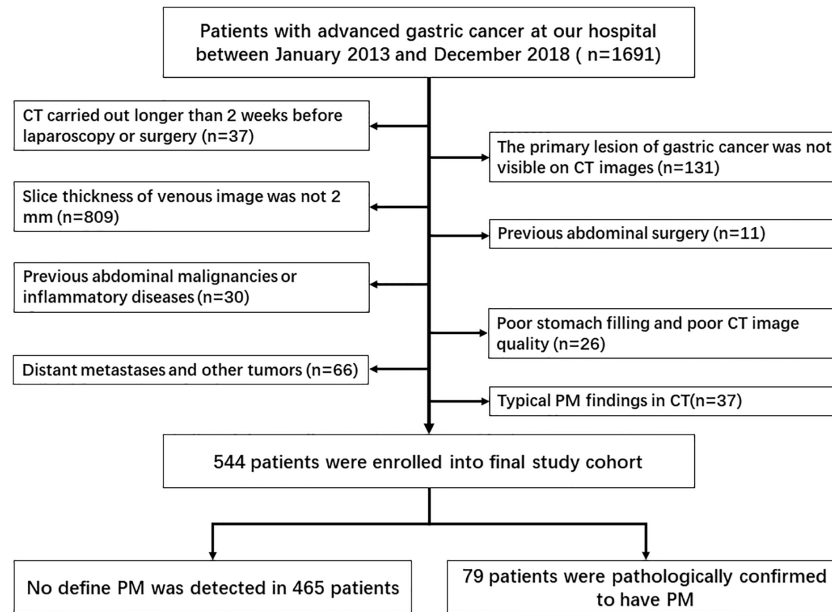


**FIGURE 1** | Flow chart of the selection process for the included studies.

## Image Preprocessing

We first converted the images into grayscale Joint Photographic Experts Group format based on each patient's CT images and the corresponding ROI masks. Before training the DCNN model, we applied data augmentation techniques to create new pseudoimages to expand the training sample size and enhance the model generalizability (31). Details of the data augmentation are explained in the **Supplementary Material**.

## DCNN Model

A simple workflow scheme for the development of the DCNN model is shown in **Figure 3**. The backbone of the DCNN model employs Xception (32), which had been pretrained on the ImageNet database (33, 34). The main structure contains a Depthwise Convolution block and a Depthwise Separable Convolution designed within the block. Considering the class imbalance among the number of PM-positive cases, we utilized a stacking

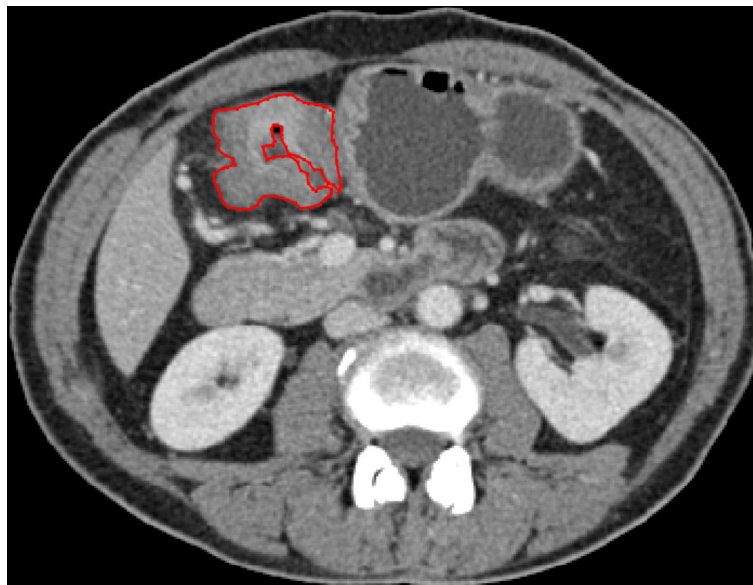


**FIGURE 2** | ROI annotation (red line) on a representative CT image, with the largest area of the primary lesion drawn on the axial plane.

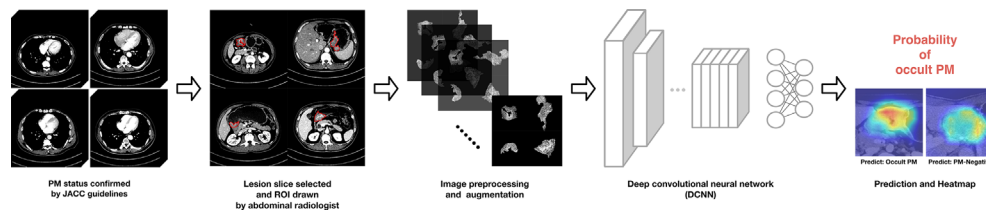


**FIGURE 3** | Proposed deep convolutional neural network (DCNN) workflow for OPM detection and prediction.

strategy to train the model (35). Model training details and the stacking strategy are presented in the **Supplementary Material**.

After the training was completed, the testing cohort was used as the input into the DCNN model, and the model performance was evaluated using receiver operating characteristic (ROC) analysis. Heatmaps generated by gradient-weighted class activation mapping (Grad-CAM) were applied to display activated areas of the presence of OPM predicted by the DCNN model.

## Clinical Model

The preoperative characteristic features were applied to a multivariable logistic regression analysis to determine independent predictors of OPM. Backward stepwise selection was utilized based on the Akaike information criterion (AIC) (36). The clinical model was then developed based on the independent characteristic features and applied to the testing cohort. The diagnostic performance of the clinical model was assessed using ROC analysis. The cutoff for the ROC curve was determined by the Youden index.

## Statistical Analysis

Considering the class imbalance in the testing cohort, we used bootstrapping ( $n = 1000$ ) to calculate the 95% confidence intervals (CIs). A decision curve was plotted to evaluate model efficacy by quantifying the net benefits at different probability thresholds. Differences in continuous variables were analyzed with the independent t-test, and differences in categorical variables were analyzed with the chi-squared test. DeLong's test was used to compare the ROC curves of models. The generalizability of the DCNN model was evaluated in subgroups of age and sex using ROC curves. All statistical analyses were performed with R software (version 3.5.0; <http://www.Rproject.org>) and SPSS 22.0 (IBM, Armonk, NY, USA). A two-tailed  $p$  value lower than 0.05 was considered statistically significant.

## RESULTS

Finally, a total of 544 patients (age, 17–87 years; median age, 60 years), including 359 men and 185 women, were enrolled in this study. All patients were confirmed with advanced GC based on end-point diagnoses, among who 79 patients were confirmed as OPM-positive using laparoscopy, while the rest ( $n = 465$ ) were defined as PM-negative. **Table 1** shows the enrolled patients'

demographic information. The determination of OPM presence is described in detail in the **Supplementary Material**. None of the patients were treated with neoadjuvant chemotherapy.

The entire cohort of 544 patients was randomly divided into a training set comprising 395 patients (58 OPM-positive and 337 PM-negative) and a testing set comprising 149 patients (21 OPM-positive and 128 PM-negative).

## Clinical Characteristics in the Training and Testing Cohorts

As shown in **Table 1**, there were significant differences between lesion location and Borrmann type for the OPM-positive and PM-negative groups in the training cohort ( $p < 0.001$ ). There was no significant difference in age, sex, carcinoembryonic antigen (CEA), or carbohydrate antigen 19-9 (CA19-9) between the OPM-positive and PM-negative groups in the entire cohort.

## Diagnostic Performance Measurements Clinical Model

As shown in **Table 2**, multivariable logistic regression analysis identified the Location-L/L+D and Borrmann type as independent predictors ( $p < 0.05$ ) for OPM positivity and PM negativity. A clinical model that incorporated the independent predictors was developed, and a ROC curve was created. The area under the ROC curve (AUC) was 0.670 (95% CI: 0.615–0.739). The sensitivity of the clinical model for the testing cohort was 85.7%, with a specificity of 44.5% (**Table 3**).

## DCNN Model

Along with the performance generated in the clinical model, **Table 3** also shows the diagnostic performance of the DCNN model using the same testing cohort. In the bootstrapping validation, the DCNN model yielded an AUC of 0.900 (95% CI: 0.851–0.953), a sensitivity of 81.0% and a specificity of 87.5%. Comparison of the ROC curves of the models suggested that the DCNN model significantly outperformed the clinical model ( $p < 0.001$ ). The ROC curves of the DCNN model and clinical model are shown in **Figure 4**.

## Stratified Analysis of Sex and Age

Deep learning algorithms frequently suffer from issues of generalizability. To test the generalization ability of the proposed DCNN model, we performed stratification analysis

**TABLE 1 |** Characteristics of patients in the training and testing cohorts.

Characteristic	Training cohort (N = 395)				p	Validation cohort (N = 149)				p
	OPM Pos(N = 58)		OPM Neg(N = 337)			OPM Pos(N = 21)		OPM Neg(N = 128)		
	Mean	Std	Mean	Std		Mean	Std	Mean	Std	
Age (years)	58.17	13.24	57.99	11.74	0.451	55.86	16.33	60.41	10.76	0.121
	N	%	N	%		N	%	N	%	
Gender					0.270					0.469
Male	34	58.6	226	67.1		12	57.1	87	68.0	
Female	24	41.4	111	32.9		9	42.9	41	32.0	
Location					0.002					0.116
U/U+M	12	20.7	68	20.2		3	14.3	36	28.1	
M/M+L	20	34.5	63	18.7		6	28.6	18	14.1	
L/L+D	18	31.0	181	53.7		9	42.9	63	49.2	
U+E	1	1.7	11	3.3		0	0.0	5	3.9	
Whole stomach	7	12.1	14	4.2		3	14.3	6	4.7	
Borrmann type					0.000					0.009
Type 1, 2	48	82.8	194	57.6		18	85.7	71	55.5	
Type 3, 4	10	17.2	143	42.4		3	14.3	57	44.5	
CEA					0.313					0.128
normal	36	62.1	235	69.7		18	85.7	88	68.8	
elevated	22	37.9	102	30.3		3	14.3	40	31.2	
CA19-9					0.091					0.221
normal	37	63.8	254	75.4		11	52.4	88	68.8	
elevated	21	36.2	83	24.6		10	47.6	40	31.2	

p was derived from the univariable association analyses between each characteristic and PM status. PM; Positive, POS; Negative, Neg; Standard deviation, Std; number, N; Upper stomach, U; Middle stomach, M; Lower stomach, L; Duodenum, D; Esophagus, E; carcinoembryonic antigen, CEA; carbohydrate antigen 19-9, CA19-9.

**TABLE 2 |** Variables and coefficients of the clinical model.

Variable	Clinic model		
	$\beta$	OR (95% CI)	p
Intercept	-2.2351	—	—
L/L+D	-0.7910	0.453(0.247–0.832)	0.010
Borrmann type	1.1324	3.103(1.504–6.401)	0.002

OR, Odds Ratio; CI, Confidence interval.

**TABLE 3 |** Model performance and DeLong's test.

Performance	Testing cohort	
	DCNN model	Clinical model
TP	17	18
TN	112	57
FN	4	3
FP	16	71
Sensitivity	0.810	0.857
Specificity	0.875	0.445
AUC	0.900	0.670
	(0.851–0.953)	(0.615–0.739)
p	\	< 0.001

DCNN, deep convolutional neural network; TP, True Positive; TN, True Negative; FN, False Negative; FP, False Positive; AUC, area under curve.

on the testing set subgrouped by sex and age. As shown in **Table 4**, the DCNN model presented good accuracy in the discrimination of OPM positivity and PM negativity among the different subgroups.

## Heatmap Analysis

**Figure 5** shows two representative cases with a cropped Grad-CAM view superimposed heatmaps on the original CT images. The OPM-positive case 24 was diagnosed by the DCNN model with a prediction score of 0.768, exhibiting activated status in the highlighting subregions. Furthermore, PM-negative case 88 was diagnosed by the DCNN model with a prediction score of 0.015, exhibiting inactivated status in all subregions.

## Clinical Use

The decision curve shown in **Figure 6** was used to compare the benefit of the DCNN model, all-laparoscopy and no-laparoscopy schemes. We found that if the threshold probability for the clinical decision was less than 80% (i.e., if the improper surgical procedure for OPM-positive patients was considered more harmful than laparoscopic exploration), the patient would benefit more from the findings of the DCNN model than either the all-laparoscopy or no-laparoscopy schemes.

## DISCUSSION

In this study, we developed a DCNN model to identify OPM in AGC patients prior to surgical treatment. The DCNN model yielded an AUC of 0.900 and sensitivity of 81.0%, which was significantly greater than that of the clinical model (AUC of 0.532,  $p < 0.001$ ). The proposed DCNN model was based on 2D images, focusing on the clinical characteristics of the primary AGC patients identified with OPM. To our knowledge, this is the first deep learning study for OPM detection and diagnosis in AGC patients.



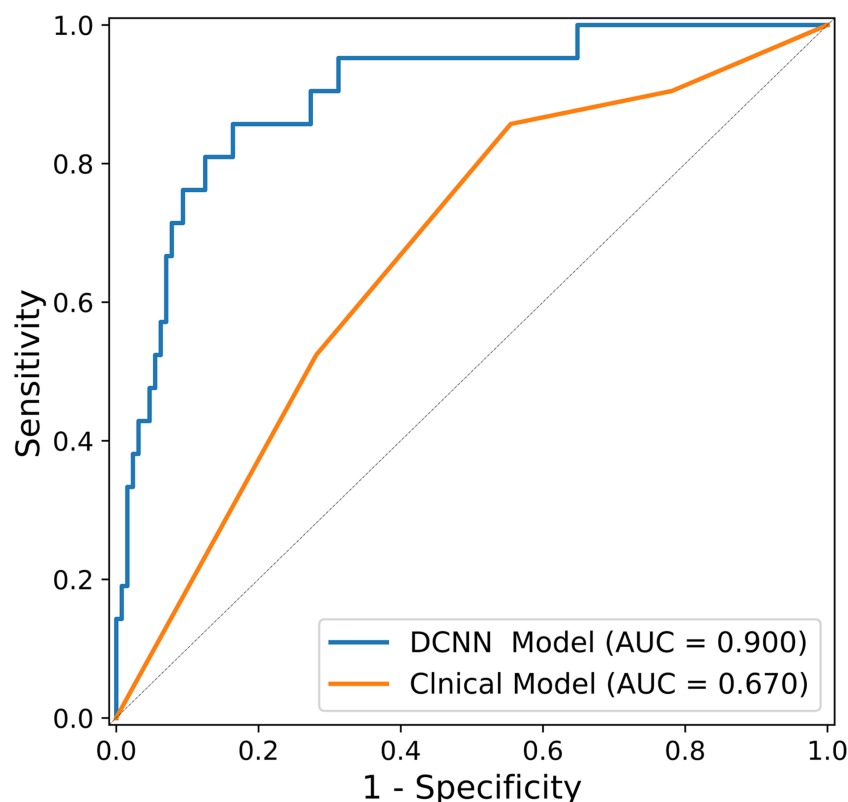


**FIGURE 4** | ROC curves of the DCNN model and the clinical model on the testing dataset (n = 149).

**TABLE 4** | Stratified analysis for DCNN model in the testing cohort.

Performance	Age		Gender	
	< 60	≥60	Female	Male
Sensitivity	0.800	1.000	0.889	0.833
Specificity	0.980	0.718	0.902	0.862
AUC	0.896	0.904	0.924	0.888
95% CI	0.811–1.000	0.845–0.955	0.851–0.989	0.825–0.956

DCNN, convolutional neural network, AUC, area under curve, CI, Confidence interval.

Few published papers have focused on the preoperative assessment of PM status in GC patients (12, 14–16, 37). Previously, CT examination was chosen as the preferable diagnostic imaging modality for PM detection, while MRI and PET/CT were considered secondary choices (38). However, the reported detectability of PM on CT images varied substantially, with an average poor sensitivity of ~ 50% (13, 19). More recently, Dong et al. reported a radiomics study using CT phenotypes of primary tumors and nearby peritoneum to accurately predict OPM in AGC patients (39). While the concept of “seed and soil”, a classic theory of tumor metastasis (40), was applied in Dong’s study, the delineated ROI of the peritoneum may not have been representative of the entire “soil” condition. In our study, we focused on the characteristic features of primary tumors and their correlation with a high possibility of OPM to develop a predictive model powered by a DCNN.

Previous studies have shown that clinical factors, including Lauren type, Borrmann type, tumor location and differentiation degree, could be important predictors for PM (39, 41). However, preoperative biopsy findings do not typically include the Lauren type and the differentiation degree of GC; these are more often identified in postoperative pathological diagnosis. Therefore, Lauren type and differentiation degree were not included in our study. By incorporating the tumor location and Borrmann type (the independent predictors) in our clinical model, we found that the model had decreased diagnostic accuracy and an AUC of 0.670, suggesting that the involvement of only preoperative clinical features may not be effective for PM prediction in AGC patients. Compared to the clinical model, the proposed DCNN model yielded satisfactory performance and exhibited good generalization ability among patients of different ages and sexes (Table 4). Furthermore, the



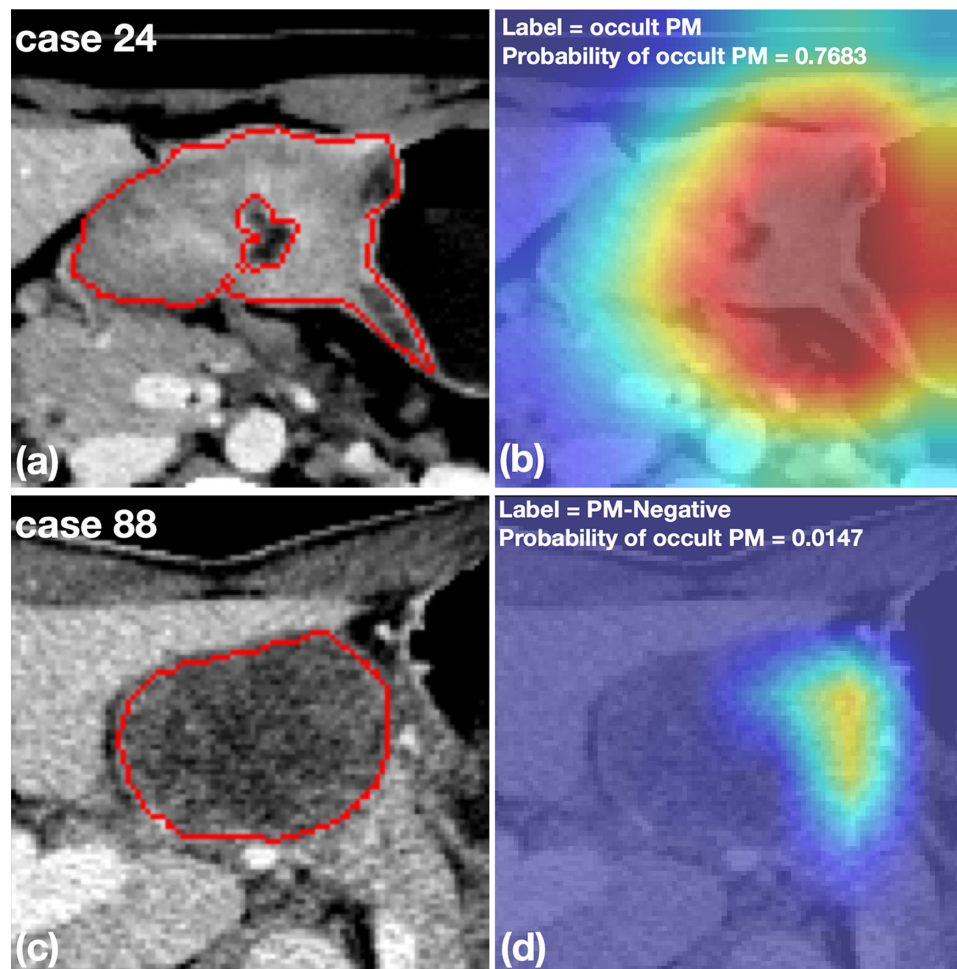


**FIGURE 5** | Representative cases with cropped CT images and heatmaps generated by Grad-CAM. **(A, B)** An OPM-positive patient with pathologically confirmed peritoneal tumor implants during surgery. The DCNN model correctly diagnosed the OPM region with the highest probability of 0.7683. **(C, D)** A PM-negative patient who was misclassified by the DCNN model with a probability of OPM of 0.0147. The subsequent surgery confirmed the patient to have no PM in the peritoneum.

availability of heatmaps (**Figure 5**) provided a visual display of the PM detection estimated by the DCNN model, which could make it easier for surgeons and oncologists to make clinical assessments accordingly.

The decision of whether to begin surgical treatment in patients with gastric cancer is often a dilemma because of the ambiguity of the PM condition (4). Patients without PM on preoperative CT (but PM positivity at surgery) may undergo an unnecessary surgical procedure due to inadequate preoperative imaging and interpretation. The decision curve analysis (**Figure 6**) in our study provided an assessment of the value of the DCNN model. For patients with OPM (PM-negative) on conventional CT images, the proposed DCNN model is more suitable than the all-laparoscopy scheme or no-laparoscopy scheme based on the risk of PM. Similarly, if the DCNN model suggested a high possibility of OPM, it would be relatively beneficial to perform diagnostic laparoscopy for confirmation.

Our study indeed has several limitations. First, the delineated ROIs obtained from a single slice (2D) might not be representative of the entire tumor. ROIs extracted from 2D or 3D images may have an impact on model development and optimization. 3D analysis of the entire tumor is one of our further study interests. Second, we used retrospective datasets to develop the DCNN model and examined a relatively small number of clinical factors. Other factors, such as serological tumor markers, are not initially available on CT scans and may account for any incomplete data. Third, OPM samples were enrolled in the study cohort based on the combined results from initial CT examination (negative) and laparoscopy (positive), which limited the sample size. Finally, external validation is needed to assess the model's diagnostic performance and generalizability across different medical institutions.

In conclusion, compared to a conventional clinical model built using logistic regression, the proposed DCNN model achieved superior diagnostic accuracy for OPM detection and

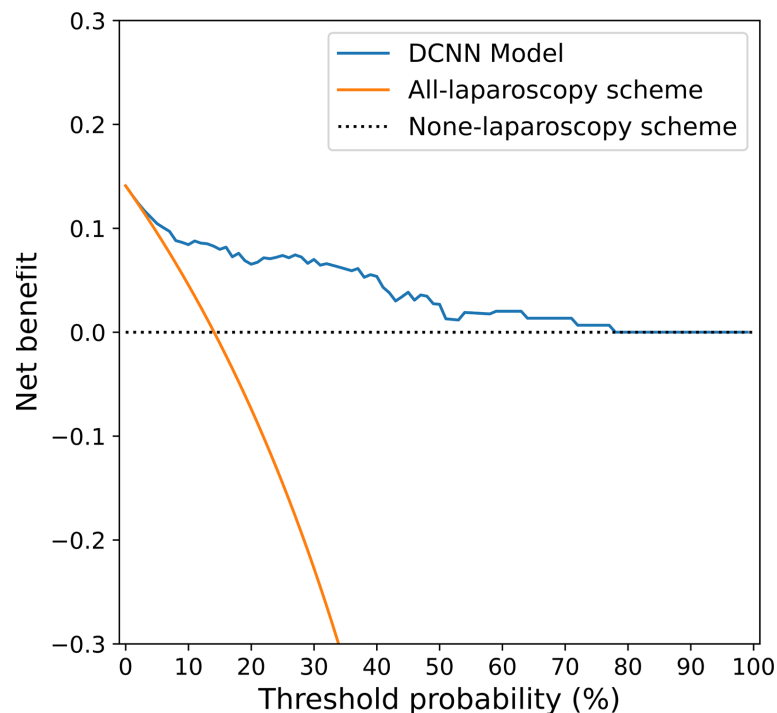


**FIGURE 6** | Decision curve analysis for the DCNN model and the all-laparoscopy and no-laparoscopy schemes. Blue line: DCNN prediction model, where the probability of predicting OPM ranges from a minimum of 0 to a maximum of 80%; orange line: all-laparoscopy scheme, assuming all patients should undergo laparoscopy to confirm the presence of OPM; dotted line: no-laparoscopy scheme, assuming no possibility of PM in patients (i.e., the presence of OPM).

diagnoses in AGC patients. The DCNN model may have significant clinical implications for early detection and proper surgical treatment for patients with AGC.

## DATA AVAILABILITY STATEMENT

The original contributions presented in the study are included in the article/**Supplementary Material**. Further inquiries can be directed to the corresponding authors.

## ETHICS STATEMENT

The studies involving human participants were reviewed and approved by Biomedical Research Ethics Committee of West China Hospital of Sichuan University. Written informed consent for participation was not required for this study in accordance with the national legislation and the institutional requirements.

## AUTHOR CONTRIBUTIONS

ZH, JH, and BS conceived and designed the study. ZH drafted the original paper. DL, XC, and DH extracted all data and performed the analyses. PY and BL conducted deep learning

modeling and statistical analysis based on data. BW, JH, and BS supervised the project and provided direction and guidance throughout the preparation of this manuscript. BS revised the final manuscript. JH provided funding for the study. All authors contributed to the article and approved the submitted version.

## FUNDING

This work was supported by the 1\*3\*5 Project for Disciplines of Excellence, West China Hospital, Sichuan University (no. ZY2017304).

## ACKNOWLEDGMENTS

The authors acknowledge the other members for their contributions to the research, including Jiangfen Wu, Xinyi Fan, Fan Xiang, and Dan Bai.

## SUPPLEMENTARY MATERIAL

The Supplementary Material for this article can be found online at: <https://www.frontiersin.org/articles/10.3389/fonc.2020.601869/full#supplementary-material>

## REFERENCES

- Bray F, Ferlay J, Soerjomataram I, Siegel RL, Torre LA, Jemal A. Global cancer statistics 2018: GLOBOCAN estimates of incidence and mortality worldwide for 36 cancers in 185 countries. *CA Cancer J Clin* (2018) 68:394–424. doi: 10.3322/caac.21492
- Coccolini F, Cotte E, Glehen O, Lotti M, Poiasina E, Catena F, et al. Intraperitoneal chemotherapy in advanced gastric cancer. Meta-analysis of randomized trials. *Eur J Surg Oncol* (2014) 40:12–26. doi: 10.1016/j.ejso.2013.10.019
- Thomassen I, van Gestel YR, van Ramshorst B, Luyer MD, Bosscha K, Nienhuijs SW, et al. Peritoneal carcinomatosis of gastric origin: a population-based study on incidence, survival and risk factors. *Int J Cancer* (2014) 134:622–8. doi: 10.1002/ijc.28373
- Kitayama J, Ishigami H, Yamaguchi H, Sakuma Y, Horie H, Hosoya Y, et al. Treatment of patients with peritoneal metastases from gastric cancer. *Ann Gastroenterol Surg* (2018) 2:116–23. doi: 10.1002/ags3.12060
- Wang FH, Shen L, Li J, Zhou ZW, Liang H, Zhang XT, et al. The Chinese Society of Clinical Oncology (CSCO): clinical guidelines for the diagnosis and treatment of gastric cancer. *Cancer Commun (Lond)* (2019) 39:10. doi: 10.1186/s40880-019-0349-9
- Guner A, Yildirim R. Surgical management of metastatic gastric cancer: moving beyond the guidelines. *Transl Gastroenterol Hepatol* (2019) 4:58. doi: 10.21037/tgh.2019.08.03
- Coburn N, Cosby R, Klein L, Knight G, Malthaner R, Mamazza J, et al. Staging and surgical approaches in gastric cancer: a clinical practice guideline. *Curr Oncol* (2017) 24:324–31. doi: 10.3747/co.24.3736
- Coburn N, Cosby R, Klein L, Knight G, Malthaner R, Mamazza J, et al. Staging and surgical approaches in gastric cancer: A systematic review. *Cancer Treat Rev* (2018) 63:104–15. doi: 10.1016/j.ctrv.2017.12.006
- Muro K, Van Cutsem E, Narita Y, Pentheroudakis G, Baba E, Li J, et al. Pan-Asian adapted ESMO Clinical Practice Guidelines for the management of patients with metastatic gastric cancer: a JSMO-ESMO initiative endorsed by CSCO, KSMO, MOS, SSO and TOS. *Ann Oncol* (2019) 30:19–33. doi: 10.1093/annonc/mdy502
- Guideline Committee of the Korean Gastric Cancer Association (KGCA). Development Working Group & Review Panel. Korean Practice Guideline for Gastric Cancer 2018: an Evidence-based, Multi-disciplinary Approach. *J Gastric Cancer* (2019) 19:1–48. doi: 10.5230/jgc.2019.19.e8
- Smyth EC, Verheij M, Allum W, Cunningham D, Cervantes A, Arnold D, et al. Gastric cancer: ESMO Clinical Practice Guidelines for diagnosis, treatment and follow-up. *Ann Oncol* (2016) 27:v38–38v49. doi: 10.1093/annonc/mdw350
- Kim SJ, Kim HH, Kim YH, Hwang SH, Lee HS, Park DJ, et al. Peritoneal metastasis: detection with 16- or 64-detector row CT in patients undergoing surgery for gastric cancer. *Radiology* (2009) 253:407–15. doi: 10.1148/radiol.2532082272
- Burbidge S, Mahady K, Naik K. The role of CT and staging laparoscopy in the staging of gastric cancer. *Clin Radiol* (2013) 68:251–5. doi: 10.1016/j.crad.2012.07.015
- Chang DK, Kim JW, Kim BK, Lee KL, Song CS, Han JK, et al. Clinical significance of CT-defined minimal ascites in patients with gastric cancer. *World J Gastroenterol* (2005) 11:6587–92. doi: 10.3748/wjg.v11.i42.6587
- Yan TD, Yonemura Y, Morris DL. Surgical strategies for gastric cancer with synchronous peritoneal carcinomatosis. *Br J Surg* (2007) 94:642; author reply 642–3. doi: 10.1002/bjs.5867. (Br J Surg 2006; 93: 1530–1535).
- Yajima K, Kanda T, Ohashi M, Wakai T, Nakagawa S, Sasamoto R, et al. Clinical and diagnostic significance of preoperative computed tomography findings of ascites in patients with advanced gastric cancer. *Am J Surg* (2006) 192:185–90. doi: 10.1016/j.amjsurg.2006.05.007
- Marcus C, Subramaniam RM. PET/Computed Tomography and Precision Medicine: Gastric Cancer. *PET Clin* (2017) 12:437–47. doi: 10.1016/j.cpet.2017.05.004
- Lim JS, Yun MJ, Kim MJ, Hyung WJ, Park MS, Choi JY, et al. CT and PET in stomach cancer: preoperative staging and monitoring of response to therapy. *Radiographics* (2006) 26:143–56. doi: 10.1148/rg.261055078
- Wang Z, Chen JQ. Imaging in assessing hepatic and peritoneal metastases of gastric cancer: a systematic review. *BMC Gastroenterol* (2011) 11:19. doi: 10.1186/1471-230X-11-19
- Ramos RF, Scalón FM, Scalón MM, Dias DI. Staging laparoscopy in gastric cancer to detect peritoneal metastases: A systematic review and meta-analysis. *Eur J Surg Oncol* (2016) 42:1315–21. doi: 10.1016/j.ejso.2016.06.401
- Sugarbaker PH. Preoperative Assessment of Cancer Patients with Peritoneal Metastases for Complete Cytoreduction. *Indian J Surg Oncol* (2016) 7:295–302. doi: 10.1007/s13193-016-0518-0
- Hamet P, Tremblay J. Artificial intelligence in medicine. *Metabolism* (2017) 69S:S36–S64. doi: 10.1016/j.metabol.2017.01.011
- Huang S, Yang J, Fong S, Zhao Q. Artificial intelligence in cancer diagnosis and prognosis: Opportunities and challenges. *Cancer Lett* (2020) 471:61–71. doi: 10.1016/j.canlet.2019.12.007
- Cuocolo R, Caruso M, Perillo T, Ugga L, Petretta M. Machine Learning in oncology: A clinical appraisal. *Cancer Lett* (2020) 481:55–62. doi: 10.1016/j.canlet.2020.03.032
- Hosny A, Parmar C, Quackenbush J, Schwartz LH, Aerts H. Artificial intelligence in radiology. *Nat Rev Cancer* (2018) 18:500–10. doi: 10.1038/s41568-018-0016-5
- Mayer RC, Leung J. Artificial intelligence and deep learning - Radiology's next frontier. *Clin Imaging* (2018) 49:87–8. doi: 10.1016/j.clinimag.2017.11.007
- Deig CR, Kanwar A, Thompson RF. Artificial Intelligence in Radiation Oncology. *Hematol Oncol Clin North Am* (2019) 33:1095–104. doi: 10.1016/j.hoc.2019.08.003
- Wang H, Zhou Z, Li Y, Chen Z, Lu P, Wang W, et al. Comparison of machine learning methods for classifying mediastinal lymph node metastasis of non-small cell lung cancer from 18F-FDG PET/CT images. *EJNMMI Res* (2017) 7:11. doi: 10.1186/s13550-017-0260-9
- Ehteshami Bejnordi B, Veta M, Johannes van Diest P, van Ginneken B, Karssemeijer N, Litjens G, et al. Diagnostic Assessment of Deep Learning Algorithms for Detection of Lymph Node Metastases in Women With Breast Cancer. *JAMA* (2017) 318:2199–210. doi: 10.1001/jama.2017.14585
- Liu K, Chen XZ, Zhang WH, Zhang DY, Luo Y, Yu Y, et al. “Four-Step Procedure” of laparoscopic exploration for gastric cancer in West China Hospital: a retrospective observational analysis from a high-volume institution in China. *Surg Endosc* (2019) 33:1674–82. doi: 10.1007/s00464-018-6605-2
- Wong SC, Gatt A, Stamatescu V, McDonnell MD. Understanding data augmentation for classification: when to warp. In: *2016 International Conference on Digital Image Computing: Techniques and Applications*. Institute of Electrical and Electronics Engineers (2016). p. 59–64.
- Chollet F. Xception: Deep Learning with Depthwise Separable Convolutions [arXiv]. *arXiv* (2016) 14:pp–14. doi: 10.1109/CVPR.2017.195
- Russakovsky O, Deng J, Su H, Krause J, Satheesh S, Ma S, et al. ImageNet Large Scale Visual Recognition Challenge. *Int J Comput Vision* (2015) 115:211–52. doi: 10.1007/s11263-015-0816-y
- Kim DH, MacKinnon T. Artificial intelligence in fracture detection: transfer learning from deep convolutional neural networks. *Clin Radiol* (2018) 73:439–45. doi: 10.1016/j.crad.2017.11.015
- Wolpert DH. STACKED GENERALIZATION. *Neural Netw* (1992) 5:241–59. doi: 10.1016/S0893-6080(05)80023-1
- Sakamoto Y, Kitagawa G. *Akaike information criterion statistics*. Dordrecht, The Netherlands: Kluwer Academic Publishers (1987).
- Kim SH, Choi YH, Kim JW, Oh S, Lee S, Kim BG, et al. Clinical significance of computed tomography-detected ascites in gastric cancer patients with peritoneal metastases. *Med (Baltimore)* (2018) 97:e9343. doi: 10.1097/MD.00000000000009343
- Laghi A, Bellini D, Rengo M, Accarpio F, Caruso D, Biacchi D, et al. Diagnostic performance of computed tomography and magnetic resonance imaging for detecting peritoneal metastases: systematic review and meta-analysis. *Radiol Med* (2017) 122:1–15. doi: 10.1007/s11547-016-0682-x
- Dong D, Tang L, Li ZY, Fang MJ, Gao JB, Shan XH, et al. Development and validation of an individualized nomogram to identify occult peritoneal metastasis in patients with advanced gastric cancer. *Ann Oncol* (2019) 30:431–8. doi: 10.1093/annonc/mdz001
- Akhtar M, Haider A, Rashid S, Al-Nabet A. Paget’s “Seed and Soil” Theory of Cancer Metastasis: An Idea Whose Time has Come. *Adv Anat Pathol* (2019) 26:69–74. doi: 10.1097/PAP.0000000000000219

41. Kim M, Jeong WK, Lim S, Sohn TS, Bae JM, Sohn IS. Gastric cancer: development and validation of a CT-based model to predict peritoneal metastasis. *Acta Radiol* (2020) 61(6):732–42. doi: 10.1177/0284185119882662. 284185119882662

**Conflict of Interest:** The authors declare that the research was conducted in the absence of any commercial or financial relationships that could be construed as a potential conflict of interest.

Copyright © 2020 Huang, Liu, Chen, He, Yu, Liu, Wu, Hu and Song. This is an open-access article distributed under the terms of the Creative Commons Attribution License (CC BY). The use, distribution or reproduction in other forums is permitted, provided the original author(s) and the copyright owner(s) are credited and that the original publication in this journal is cited, in accordance with accepted academic practice. No use, distribution or reproduction is permitted which does not comply with these terms.



# Radiomic Feature-Based Predictive Model for Microvascular Invasion in Patients With Hepatocellular Carcinoma

Mu He<sup>1</sup>, Peng Zhang<sup>1</sup>, Xiao Ma<sup>2</sup>, Baochun He<sup>2</sup>, Chihua Fang<sup>1\*</sup> and Fucang Jia<sup>2\*</sup>

<sup>1</sup> The First Department of Hepatobiliary Surgery, Zhujiang Hospital, Southern Medical University, Guangdong Provincial Clinical and Engineering Center of Digital Medicine, Guangzhou, China, <sup>2</sup> Research Laboratory for Medical Imaging and Digital Surgery, Shenzhen Institutes of Advanced Technology, Chinese Academy of Sciences, Shenzhen, China

## OPEN ACCESS

### Edited by:

Dong-Hyun Kim,  
Northwestern University,  
United States

### Reviewed by:

Huijie Jiang,  
Second Affiliated Hospital of Harbin  
Medical University, China  
Ren Xuequn,  
Huaihe Hospital of Henan University,  
China

### \*Correspondence:

Chihua Fang  
fangch\_dr@163.com  
Fucang Jia  
fc.jia@siaat.ac.cn

### Specialty section:

This article was submitted to  
Cancer Imaging and  
Image-directed Interventions,  
a section of the journal  
Frontiers in Oncology

**Received:** 19 June 2020

**Accepted:** 14 October 2020

**Published:** 05 November 2020

### Citation:

He M, Zhang P, Ma X, He B, Fang C  
and Jia F (2020) Radiomic Feature-  
Based Predictive Model for  
Microvascular Invasion in Patients  
With Hepatocellular Carcinoma.  
Front. Oncol. 10:574228.  
doi: 10.3389/fonc.2020.574228

**Objective:** This study aimed to build and evaluate a radiomics feature-based model for the preoperative prediction of microvascular invasion (MVI) in patients with hepatocellular carcinoma.

**Methods:** A total of 145 patients were retrospectively included in the study pool, and the patients were divided randomly into two independent cohorts with a ratio of 7:3 (training cohort:  $n = 101$ , validation cohort:  $n = 44$ ). For a pilot study of this predictive model another 18 patients were recruited into this study. A total of 1,231 computed tomography (CT) image features of the liver parenchyma without tumors were extracted from portal-phase CT images. A least absolute shrinkage and selection operator (LASSO) logistic regression was applied to build a radiomics score (Rad-score) model. Afterwards, a nomogram, including Rad-score as well as other clinicopathological risk factors, was established with a multivariate logistic regression model. The discrimination efficacy, calibration efficacy, and clinical utility value of the nomogram were evaluated.

**Results:** The Rad-score scoring model could predict MVI with the area under the curve (AUC) of 0.637 (95% CI, 0.516–0.758) in the training cohort as well as of 0.583 (95% CI, 0.395–0.770) in the validation cohort; however, the aforementioned discriminative approach could not completely outperform those existing predictors (alpha fetoprotein, neutrophilic granulocyte, and preoperative hemoglobin). The individual predictive nomogram which included the Rad-score, alpha fetoprotein, neutrophilic granulocyte, and preoperative hemoglobin showed a better discrimination efficacy with AUC of 0.865 (95% CI, 0.786–0.944), which was higher than the conventional methods' AUCs (nomogram vs Rad-score, alpha fetoprotein, neutrophilic granulocyte, and preoperative hemoglobin at  $P < 0.001$ ,  $P = 0.025$ ,  $P < 0.001$ , and  $P = 0.001$ , respectively). When applied to the validation cohort, the nomogram discrimination efficacy was still outbalanced those above mentioned three remaining methods (AUC: 0.705; 95% CI, 0.537–0.874). The calibration curves of this proposed method showed a satisfying



consistency in both cohorts. A prospective pilot analysis showed that the nomogram could predict MVI with an AUC of 0.844 (95% CI, 0.628–1.000).

**Conclusions:** The radiomics feature-based predictive model improved the preoperative prediction of MVI in HCC patients significantly. It could be a potentially valuable clinical utility.

**Keywords:** hepatocellular carcinoma, microvascular invasion, radiomics, nomogram, computed tomography

## INTRODUCTION

Hepatocellular carcinoma (HCC) is considered as the sixth most high incidence cancer and HCC is also as the world's third leading cause of cancer deaths. Among the primary cancer of the liver, HCC is the predominant pathological type and has become a significant public health-care concern (1, 2). Among the current treatment strategies for HCC, the optimal and most efficient treatment is radical surgical resection. In the past several decades, along with the development of modern medical imaging technology and improved surgical skills, the success ratio of hepatectomy for HCC has increased continuously (3). In spite of this, the postoperative five-year recurrence ratio of HCC is approximately 70%, which is unsatisfactory and indicates a significant influence on overall survival for HCC patients (4). Microvascular invasion (MVI) is a crucial predictive factor for recurrence among HCC patients who underwent hepatectomy for tumor resection or received liver transplant surgery, and most patients with early recurrence were pathologically verified as MVI positive (5, 6). Therefore, prediction for MVI before surgery has significant clinical value for decision making, postoperative adjuvant therapy and comprehensive prognostic evaluation of patients with HCC.

Tumor macrovascular invasion of hepatic vein and/or portal vein in HCC patients can be identified through contrast-enhanced computed tomography (CECT) or magnetic resonance imaging (MRI) examination before surgery (7). Conversely, microvascular invasion (MVI) cannot be detected directly by means of preoperative radiologic examination. In addition, the effectiveness of preoperative pathological biopsy for MVI is unsatisfactory to some extent. Hence, the gold standard to verify the occurrence of MVI is to evaluate the surgical specimen slices through preoperative pathological examination (i.e., H&E staining, etc.) which limits its application as a predictive factor for comprehensive prognosis assessment (8). Imaging markers are emerging as preoperative predictive factors for tumor heterogeneity that have the potential to predict MVI in a high-throughput, high-precision, and noninvasive manner. Current published studies have indicated that the correlation between the MVI and imaging features could be quantitatively analyzed for further research on the occurrence and progression of MVI. Imaging features could be extracted from the following medical imaging modalities: contrast-enhanced CT, gadolinium-ethoxybenzyl-diethylenetriamine penta-acetic acid (Gd-EOB-DTPA; EOB Primovist®)-enhanced magnetic resonance imaging (MRI) and <sup>18</sup>F-fluorodeoxyglucose positron emission tomography (PET).

In addition, those imaging features incorporated laborator testing, quantitative or qualitative results to establish predictive models to classify whether patients with HCC are MVI positive or negative, which is of great value for surgeons to evaluate liver transplant recipients or HCC therapy scheme decision making (9–11). In addition, radiomics is an emerging methodology for medical imaging analysis that applies machine learning algorithms and statistical analysis software to obtain high-throughput radiological features for prognosis prediction or tumor-related overall survival analysis. In the past, our research group's study results indicated that radiomics-based predictive models have the potential to predict the occurrence of posthepatectomy liver failure and the occurrence of postpancreaticoduodenectomy pancreatic fistula among a study cohort with satisfactory predictive performance (12, 13). Recent studies showing predictive radiomics models based on contrast-enhanced CT (CECT) as an easy-to-use, efficient, and noninvasive prediction method for MVI have provided reliable instruction for the definite diagnosis of whether HCC patients had MVI preoperatively (14, 15). Precise prediction of MVI before surgery has significant clinical implications for issues such as efficient stratification of treatment strategies, optimization of treatment schemes, and establishment of comprehensive surgery planning for HCC patients with MVI positivity or negativity. Due to the specific biological characteristics of MVI, the contrast agent in CECT likely enters the vessels of tumors and then diffuses into the microvessels over the range of one centimeter around the primary lesion. An enlarged surgical margin (usually over one centimeter) was verified to decrease the postoperative tumor recurrence ratio, indicating the presence of MVI, among patients with HCC (16, 17). For patients who have a tumor diameter less than three centimeters and are highly suspected to be MVI positive, anatomical hepatectomy is necessary. For non-anatomical hepatectomy, the surgical margin should be over one centimeter from the primary lesion (18, 19). Compared with surgical resection, radiofrequency ablation is not a rational option for small (diameter under three centimeters) HCC patients combined with MVI because of high postoperative recurrence ratio (20).

The radiomic predictive model incorporates clinical predicative factors and imaging characteristic features into a reliable and efficient MVI risk-stratification scoring system, which helps clinical practitioners provide optimal treatment schemes for HCC patients.

In the present study, we aimed at build as well as evaluate a radiomics nomogram based on CT imaging textural features

incorporated with clinically related risk factors for MVI occurrence prediction among HCC patients before surgery.

## MATERIALS AND METHODS

### Patients

The data originated from 146 patients who received liver resection at Zhujiang Hospital, Southern Medical University, between January 2012 and December 2018, were retrospectively collected and analyzed. The patients with HCC were carefully selected, and the inclusion standards as indicated below: (1) Be at least 18 years old, both male and female were included; (2) contrast-enhanced CT scans were performed within one week before surgery; and (3) all surgical specimens were confirmed to be HCC by MVI evaluation and histopathological examination. The exclusion standards were as follows: (1) previous hepatectomy; (2) HCC lesion boundaries not clearly visible on CT images; (3) preoperative treatment, including transhepatic arterial chemotherapy and embolization, portal vein embolization, radiofrequency ablation therapy, targeted cancer therapy, etc.; and (4) incomplete clinical data or pathology data. Patients were randomly allocated into two independent cohorts as training cohort and validation cohort according to a ratio of 7:3. An additional 18 patients between January and December 2019 were enrolled in a prospective pilot analysis, and all patients signed the informed consent. The Ethics Review Board of Zhujiang Hospital, Southern Medical University, approved this study and supervised the procedures.

### Histopathological Analysis

The final diagnostic results, including MVI grade, were based on pathologic reports of surgical specimens. On the basis of the Clinical Practice Guidelines of Chinese Society of Pathology (21), the definite diagnosis of MVI was based on the pathological standard as follows: MVI was graded according to the number of cells seen in the endothelial vascular lumen by microscopic examination, and then MVI was categorized as three additional subgrades, M0 indicating no MVI; M1 for fewer than five MVI occurrence in adjoining liver parenchyma and the distance from tumors was under one centimeter (which is also regarded as the low-risk group); and M2 for more than five MVI in adjoining liver parenchyma and the distance from tumors was greater than one centimeter (regarded as the high-risk group). All specimen slices were reviewed and analyzed by two pathologists who had at least 10 to 15 years of hepatic pathology experience. Aforementioned two specialists were blinded to the related clinicopathological as well medical imaging examination information of the patients who were included in the study cohort. When there was a disagreement, a consistency review was performed.

### CT Data Collection

All CT examinations were finished in our hospital spiral CT (128-slice, Siemens Medical system, Erlangen, Germany). To ensure

the consistency of the image data, all the scanning parameters were set as follows: 120 kV, 250–300 mAs, and a matrix of  $512 \times 512$ . The slice thickness and interval were set as one mm and zero mm, respectively, and image reconstruction was set to 1 mm. To obtain contrast-enhanced image data, 90 ml iodine contrast agent (iodine concentration: 350 mg/ml) was administered *via* a vein by a contrast injector at a speed of 3 milliliter per second, and dynamic contrast-enhanced imaging data acquisition was performed at fixed time points: for the arterial phase, acquisition occurred at approximately 30–33 s after administration; for the portal vein phase, it was 67–70 s, and for the equilibrium phase, 177–180 s. After the entire acquisition procedure was completed, we selected the portal venous phase raw data for texture analysis. All the medical images in this study were collected from the Pictures Archiving and Communication System at our hospital radiology department.

### Radiomics Feature Extraction

The holistic radiomics modeling procedure was shown in **Figure 1**. We extracted a total of 1,231 CT image features from the liver parenchyma without tumors. The extracted image features were categorized into four types as follows: diagnostic intensity for liver parenchyma (N=13), original hepatic textural feature (N=100), tumor size and shape-based feature (N=430), and wavelet (N=688). The mathematical descriptions of each corresponding feature above can be found in the website of the open-source application PyRadiomics (<https://pyradiomics.readthedocs.io/en/latest/>).

### Data Analysis

One hundred forty-five patients were included in the study pool, therefore, those patients were randomly allocated into two independent cohorts according to a ratio of 7:3 (training cohort:  $n = 101$ , validation cohort:  $n = 44$ ). An additional 18 patients were also enrolled into this study for a prospective pilot analysis which was aimed to evaluate its underlying clinical practice potency.

A histologic diagnosis of tumor with microvascular invasion or tumor without microvascular invasion was entered as a dependent variable in a least absolute shrinkage and selection operator (LASSO) logistic regression algorithm. As to the LASSO logistic regression, we applied 10-fold cross validation method to identified the optimal regularization parameter lambda, which reduces the mean cross-validation error at maximum extent. those image features who were considered as non-zero coefficients within the LASSO regression model were regarded as most predictive radiomics features and were chosen for calculating the radiomics score. The radiomics score was calculated through a formula which in brief was a semple linear combination of the selected radiomics based features multiplied by their corresponding coefficients.

The radiomics score as well as other clinicopathological risk variables, including age, sex, tumor sizes, viral hepatitis etiology, drinking history, alpha fetoprotein content, tumor numbers, neutrophil counts, lymphocyte counts, neutrophil-lymphocyte ratio, preoperative alanine transaminase, preoperative aspartate

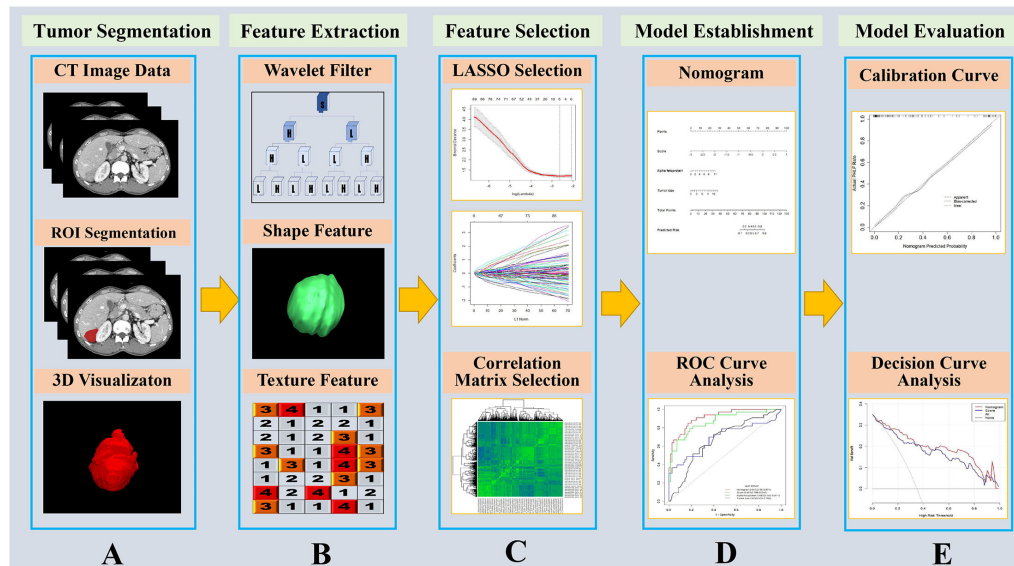


**FIGURE 1 |** Flow chart of the study. **(A)** The portal vein contrast-enhanced computed tomography (CECT) image was used as input, and the liver was segmented by homemade segmentation software (22) and manually corrected. The tumor ROI was contoured by a radiologist with more than 10 years of experience. **(B)** The liver parenchyma without tumor was set as the ROI image, and features containing as shape related features, texture related features and wavelet filtered features which were extracted by PyRadiomics software (23). **(C)** The extracted features were reduced via least absolute shrinkage and selection operator (LASSO) and correlation matrix selection. **(D)** The radiomics features and other clinicopathological variables were applied to establish a nomogram for predict microvascular invasion, and ROI curve analysis was conducted. **(E)** The nomogram model was evaluated with calibration curve and decision curve analysis.

aminotransferase, preoperative total bilirubin, preoperative hemoglobin, preoperative albumin, preoperative blood platelet counts, preoperative prothrombin time, and histopathological differentiation degree, were used in a multivariate logistic regression model as predictive factors for tumors with microvascular invasion or tumors without microvascular invasion among training cohort. The optimal model selection was performed applying a backward stepwise selection procedure through utilizing likelihood ratio testing with Akaike information criterion (AIC). Nomogram was constructed based on those significant features in the multivariate logistic regression model among which radiomics score as well as clinicopathological risk factors were included.

The nomogram's predictive accuracy was evaluated by three methods. First, discrimination efficacy was assessed through the result of the area under the area under curve (AUC) with values ranging from 0.5 (which means mentioned model possess no discrimination potent) to 1 (which means mentioned model possess a perfect discrimination potent). Second, by plotting the predicted probability of the nomogram relative to the ratio of the observed events on a series of equidistant values within the range of predicted probabilities, the power of calibration can be evaluated visually. In addition, decision curve analysis (DCA) was carried out to tell physicians the interval of threshold probabilities to judge whether the prediction model would be of clinical benefit or not. If the typical threshold probabilities of tumors with microvascular invasion or tumors without microvascular invasion at which surgeons would opt for comprehensive treatment lie within a certain benefit range, the model is of clinical value.

## Statistical Analysis

For statistical analysis in this study an open source software R (version 3.6.1) was applied. (<https://www.r-project.org>). consider the various type of data, we employed different statistical test as below: for continuous variables, the Mann-Whitney U test were used for the comparison. Correspondingly, as for categorical variables, the Chi-square test was used for the comparison. in order to conduct LASSO logistic regression analysis we used “glmnet” package, “pROC” package was applied for calculation and comparisons of AUC and ROC plotting of each model as well as for nomogram training and calibration “rms” package was employed, in addition for decision curve analysis we chosen “rmda” package to conduct it. A two-sided  $P$  value  $< 0.05$  was considered as indicative of statistical significance. For the final independent predictors included in this prediction model selection, we applied both univariant logistic regression and multivariant logistic regression and the factors whose  $P$  value  $< 0.05$  were considered as indicative of final independent predictors.H

## RESULTS

### Patient Demographics and Clinicopathological Characteristics

The demographics and clinicopathological characteristics of the study participants are displayed in **Table 1**. It is clearly that there were no differences between the training cohort and the

**TABLE 1 |** Demographic and clinicopathologic characteristics of the study participants.

Characteristic	Training cohort (N=101)	Validation cohort (N=44)	P value
Age, median (IQR), years	50.00 (41.00–58.00)	47.50(43.00–59.50)	0.957
Sex, N (%)			
Female	19 (18.8)	7 (15.9)	0.854
Male	82 (81.2)	37 (84.1)	
Etiology of viral hepatitis, N (%)			
None	22 (21.8)	9 (20.5)	0.291
Hepatitis B	73 (72.3)	31 (70.5)	
Hepatitis C	3 (3.0)	2 (4.5)	
Hepatitis E	2 (2.0)	0 (0.0)	
Hepatitis B + C	0 (0.0)	2 (4.5)	
Hepatitis B + E	1 (1.0)	0 (0.0)	
Drinking history, N (%)			
No	87 (86.1)	38 (86.4)	1.000
Yes	14 (13.9)	6 (13.6)	
Alpha fetoprotein content, median (IQR)	3.16 (1.46–6.36)	2.15 (0.82–4.94)	0.067
Number of tumors, median (IQR)	1.00 (1.00–1.00)	1.00 (1.00–1.00)	0.469
Neutrophil counts, median (IQR)	3.84 (3.19–4.90)	3.93 (2.96–4.95)	0.877
Lymphocyte counts, median (IQR)	1.74 (1.30–2.20)	1.69 (1.33–2.15)	0.877
Neutrophil-lymphocyte ratio, median (IQR)	2.26 (1.65–2.97)	2.41 (1.62–3.33)	0.752
Preoperative alanine transaminase, median (IQR)	35.00 (20.00–51.00)	31.50(20.50–47.25)	0.380
Preoperative aspartate aminotransferase, median (IQR)	35.00 (23.00–45.00)	31.00(23.50–44.00)	0.523
Preoperative total bilirubin, median (IQR)	11.50 (8.00–16.40)	10.30 (8.75–14.60)	0.940
Preoperative hemoglobin, median (IQR)	135.00(120.00–149.00)	134.50(120.75–151.00)	0.908
Preoperative albumin, median (IQR)	39.00 (36.00–41.60)	40.70(35.95–42.73)	0.541
Preoperative blood platelet counts, median (IQR)	172.00(143.00–246.00)	195.00(141.25–256.00)	0.563
Preoperative prothrombin time, median (IQR)	13.70 (13.00–14.20)	13.45(12.67–14.20)	0.242
Histopathological differentiation degree, N (%)			
Poor	64 (63.4)	27 (61.4)	0.438
Moderate	22 (21.8)	7 (15.9)	
Well	15 (14.9)	10 (22.7)	
Tumor with or without microvascular invasion (%)			
With	71 (70.3)	28 (63.6)	0.550
Without	30 (29.7)	16 (36.4)	

validation cohort. The median ages of these two cohorts were 50.0 and 47.5 years, respectively. As for patient gender in both cohort male was ponderance proportion (81.2% and 84.1%, respectively). In addition, for positive occurrence ratio there were 30 (29.7%) and 16 (36.4%) patients who experienced tumors with microvascular invasion among training cohort as well validation cohort, respectively. For patients among pilot study, those data are displayed in **Table 2**.

## Development of the Rad-Score

A total of 1,231 features were extracted from the image data for each patient. These 1,231 features were reduced to 2 possible indicators based on the 101 patients among training cohort. The Rad-score formula constructed through a simple linear combination of aforementioned 2 indicators multiplied by LASSO coefficients as follows: Rad-score=55186.42 + 37645.32\*log-sigma-3-0-mm-3D\_gldm\_SmallDependence LowGrayLevelEmphasis - 46900.48 \* log-sigma-5-0-mm-3D\_gldm\_Idmn (**Figure 2**). Patients who had tumors without MVI obtained relatively lower Rad-scores generally than patients who suffered from tumors combined with microvascular invasion. This discrepancy was detected between on Rad-scores (median (interquartile range)) among training cohort (–2.567 (–6.731~1.592) vs 0.164 (–5.160~4.068), respectively,  $P=0.013$ )

also among the validation cohort (–2.477 (–7.465~0.864) vs 0.123 (–6.434~3.899), respectively,  $P=0.369$ ).

## Development, Validation, and Assessment of the Nomogram

Both univariate and multivariate logistic regression analysis were conducted combining the Rad-score as well as clinical stage among training cohort. The backward stepwise selection process selected Rad-score, alpha fetoprotein content, neutrophil counts, and preoperative hemoglobin as the final independent predictors. A prediction model was constructed and is shown as a nomogram in **Figure 3**. The odds ratios of the prediction model are presented in **Table 3**. Among the training cohort, the AUC of the nomogram was 0.865 (95% CI 0.786–0.944). among validation cohort, the AUC was 0.705 (95% CI: 0.537–0.874). The AUC value of the ROC curve of the nomogram was significantly higher than that of each independent predictor (nomogram vs Rad-score, alpha fetoprotein, neutrophilic granulocyte, and preoperative hemoglobin at  $P < 0.001$ ,  $P = 0.025$ ,  $P < 0.001$ , and  $P = 0.001$ , respectively). The particular results of the discriminatory efficiency are shown in **Figures 3C, D**. This indicates that the Rad-score incorporated with another three clinicopathological factors possessed a greater diagnostic efficiency than any single independent predictors. The calibration curve analysis of this purposed predictive model presents good



**TABLE 2 |** Demographic and clinicopathologic characteristics of the pilot participants.

Characteristic	Pilot (N=18)
Age, median (IQR), years	52.00 (48.25–57.25)
Sex, N (%)	
Female	3 (16.7)
Male	15 (83.3)
Etiology of viral hepatitis, N (%)	
Hepatitis B	10 (55.6)
None	8 (44.4)
Drinking history, N (%)	
No	18 (100.0)
Alpha fetoprotein content, median (IQR)	7.70 (4.42–23.05)
Number of tumors, median (IQR)	1.00 (1.00–1.00)
Neutrophil counts, median (IQR)	3.54 (3.07–4.67)
Lymphocyte counts, median (IQR)	2.02 (1.51–2.68)
Neutrophil-lymphocyte ratio, median (IQR)	1.89 (1.15–2.38)
Preoperative alanine transaminase, median (IQR)	32.00 (21.00–57.75)
Preoperative aspartate aminotransferase, median (IQR)	28.00 (24.25–39.25)
Preoperative total bilirubin, median (IQR)	14.25 (10.92–15.20)
Preoperative hemoglobin, median (IQR)	143.50 (124.50–148.25)
Preoperative albumin, median (IQR)	36.80 (34.55–40.28)
Preoperative blood platelet counts, median (IQR)	195.00 (172.50–250.75)
Preoperative prothrombin time, median (IQR)	13.35 (12.70–13.85)
Histopathological differentiation degree, N (%)	
Poor	13 (72.2)
Moderate	1 (5.6)
Well	4 (22.2)
Tumor with or without microvascular invasion, N (%)	
With	11 (61.1)
Without	7 (38.9)

agreement among our research for either the training cohort or validation cohort (Figures 4 and 5).

The DCA curve showed that as threshold probability was within a range from 0.1 to 1.0, this nomogram could obtain a

greater net benefit than either “treat none” or “treat all” scheme. The nomogram also received higher net benefit than the Rad-score alone across the reasonable threshold probabilities range.

## DISCUSSION

In this study, we established as well assessed radiomics model based on CT imaging textural features and clinically related risk factors for accurate prediction of MVI of HCC before surgical resection. The efficacy of this predictive model was average-to-good but did not totally outperform other current predictive models or scoring systems. Therefore, we developed and evaluated a predictive nomogram based on radiological characteristics to predict the incidence of MVI. Our predictive nomogram included factors such as AFP, NLR, routine blood tests, liver function, and pathological examination results and a combination of potential MVI predictive imaging features. Our results were consistent with previous studies; higher serum AFP level, NLR or poorly differential tumor cell type had a positive correlation with the incidence of MVI among patients with HCC. Through the results of decision curve analysis, independent predictive risk factors such as AFP, NLR, or radiomics features had beneficial effects on improving the predictive power of MVI, which was consistent with current studies; however, the diagnostic efficacy of the model did not outperform other existing predictive models or scoring systems. When we combined the above independent predictive risk factors into a comprehensive diagnostic nomogram, the diagnostic efficacy exceeded the predictive power of any single predictive factor or a combination of predictive factors, and its performance showed satisfactory consistency in both the training cohort and validation cohort. The aforementioned nomogram could improve the

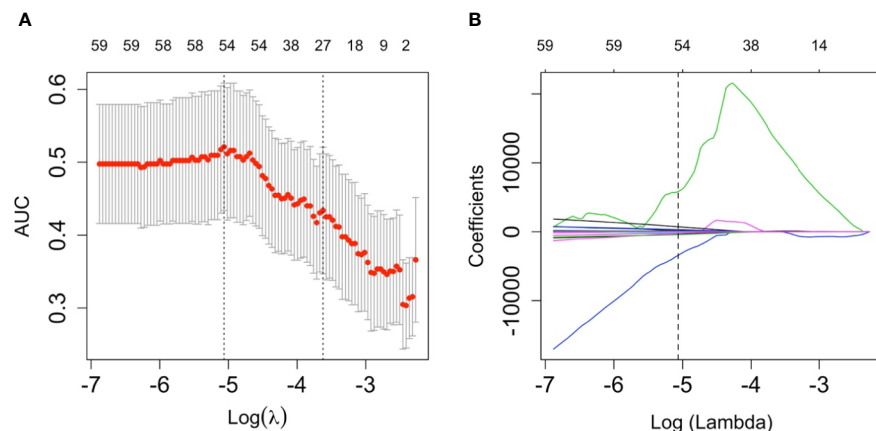


**FIGURE 2 |** The least absolute shrinkage and selection operator (LASSO) logistic regression algorithm was employed to determine the most significant radiomics features in terms of microvascular invasion (MVI) prediction as well calculated for the Rad-score. (A) a ten-fold cross validation method was employed to select the optimal lambda parameter contained in the LASSO algorithm that minimized the mean squared error. The mean-squared errors between upper bound and lower bound standard deviations were plotted according to the lambda changing sequence. The vertical dotted lines in the graph stands for the two selected lambdas. The lambda on the left corner of graph provided the minimum mean cross-validation error, meanwhile, the lambda on the right corner of graph provided the most optimal regularized model which the error within one minimal standard error, therefore, the optimal lambda value 0.0063, whose  $\log(\lambda) = -5.0637$ , was employed to feature selection. (B) A coefficient profile plot of the LASSO model was produced. Every single curve represents the trajectory changing of each independent predictor. The greater lambda is, the more the coefficients are reduced. The vertical dotted line indicates the optimal lambda, which results in two coefficients.



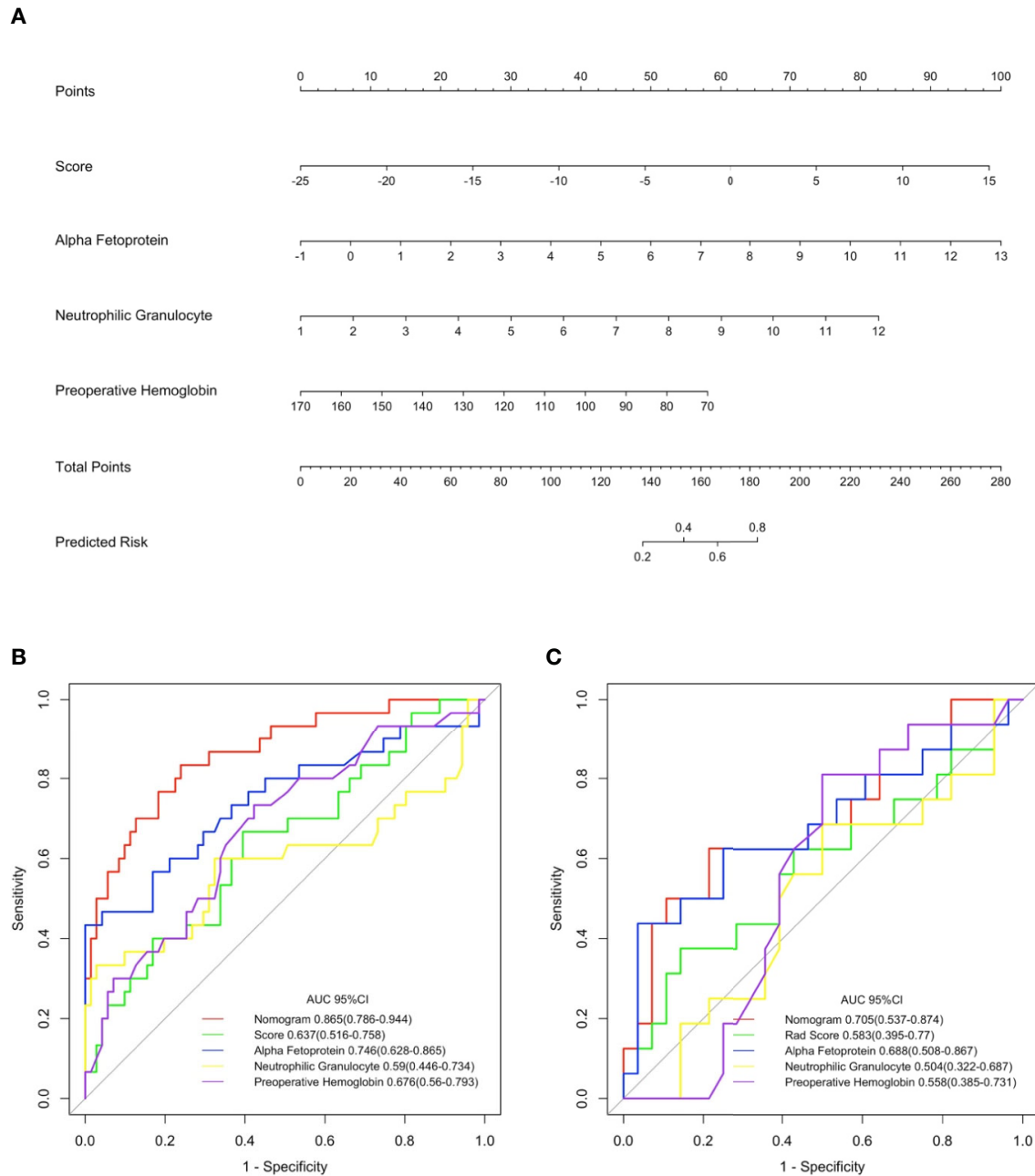


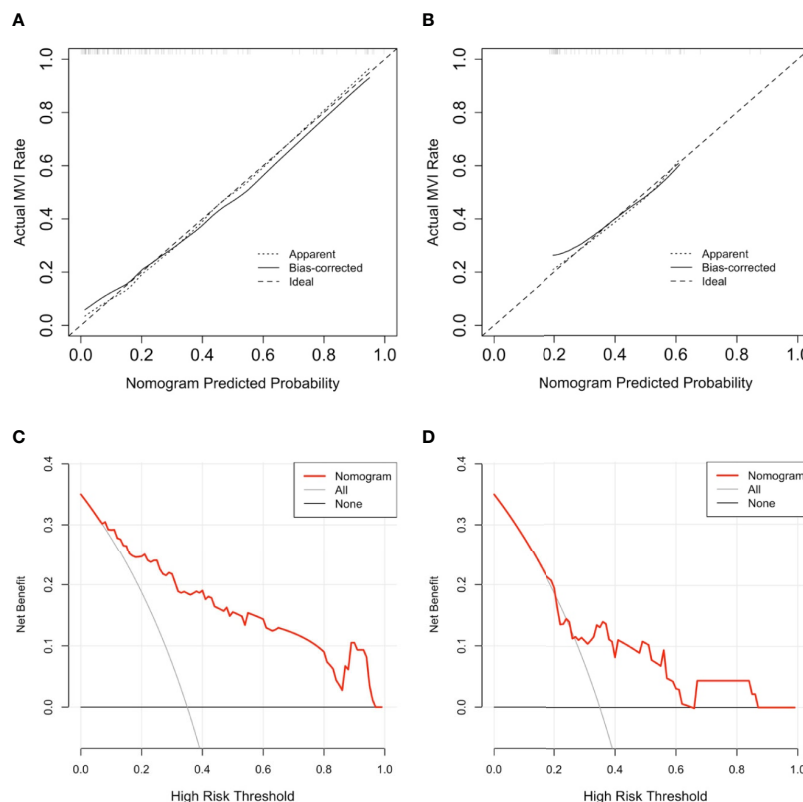
**FIGURE 3 |** Nomogram for the prediction of the tumor with microvascular invasion occurring or not and its discrimination performance. **(A)** data among the training cohort were employed to establish the purposed monogram which the Rad-score, alpha fetoprotein, neutrophilic granulocyte and preoperative hemoglobin were incorporated. Instructions for reading the nomogram: Find the Rad-score in the Rad-score axis; a straight line was drew to the point axis and the intersection point stands for actual points of the predicted probability which a patient with microvascular invasion (MVI) occurrence or not according to the own Rad-score; repeat above mentioned procedures for another predictors each straight line was drew to the points axis; calculated the total points obtained from each predictor and located it on the total points axis; draw a line perpendicular to the predict risk axis to determine the patient's risk (24). **(B, C)** display the result of ROC curves analysis for the nomogram and each individual predictor in predicting whether tumors with microvascular invasion occurred among the training and validation cohorts, respectively.

individual predictive accuracy of MVI for patients with HCC preoperatively, and the results of decision curve analysis showed that this practical nomogram had the potential to be applied in daily clinical practice.

The diagnosis of HCC depends on radiological examination, such as CT imaging or MRI, to a large extent, which makes it preferable to perform quantitative or qualitative imaging analysis based on the radiomics method. The radiomics method can

**TABLE 3 |** Risk factors for the diagnosis of tumors with microvascular invasion.

Characteristic	Univariate logistic regression		Multivariate logistic regression	
	OR (95% CI)	P value	OR (95% CI)	P value
Score	1.093(1.017-1.176)	0.016*	1.158(1.041-1.29)	0.007*
Age	0.991(0.958-1.025)	0.596	NA	NA
Sex	0.897(0.305-2.635)	0.843	NA	NA
Size of tumors	0.974(0.849-1.117)	0.705	NA	NA
Etiology of viral hepatitis	1.077(0.371-3.128)	0.892	NA	NA
Drinking history	1.969(0.618-6.269)	0.252	NA	NA
Alpha fetoprotein content	1.447(1.216-1.721)	<0.001*	1.533(1.22-1.927)	<0.001*
Number of tumors	0.623(0.111-3.507)	0.592	NA	NA
Neutrophil counts	1.379(1.09-1.745)	0.007*	1.567(1.138-2.158)	0.006*
Lymphocyte counts	0.849(0.441-1.634)	0.624	NA	NA
Neutrophil-lymphocyte ratio	1.212(0.956-1.536)	0.113	NA	NA
Preoperative alanine transaminase	1.004(0.995-1.013)	0.416	NA	NA
Preoperative aspartate aminotransferase	1.007(0.999-1.015)	0.081	NA	NA
Preoperative total bilirubin	0.995(0.967-1.024)	0.747	NA	NA
Preoperative hemoglobin	0.966(0.944-0.989)	0.004*	0.966(0.938-0.995)	0.022*
Preoperative albumin	0.961(0.883-1.046)	0.355	NA	NA
Preoperative blood platelet counts	1.007(1.003-1.012)	0.003*	NA	NA
Preoperative prothrombin time	1.035(0.75-1.427)	0.835	NA	NA
Histopathological differentiation degree	2.765(1.014-7.538)	0.047*	NA	NA

\* $P < 0.05$ .

**FIGURE 4 |** The result of calibration curve analysis as well decision curve analysis for the purposed nomogram. **(A, B)** show the calibration curves analysis for the nomogram in predicting whether tumors with microvascular invasion occurrence among training cohort as well as validation cohort, respectively. the dashed line stands for perfect prediction, the dotted line represents apparent estimates of predicted vs. observed values, meanwhile the solid line on behalf of bias correcting estimates employing 1,000 bootstrap sampling. **(C, D)** show the result of decision curve analysis for the nomogram in predicting whether tumors with microvascular invasion occurrence among training cohort as well as validation cohort, respectively. The result of decision curve analysis indicated that assume the threshold probability that is located in an interval of 0.2 to 0.86, microvascular invasion (MVI) prediction using the nomogram can give more net benefit than by treating either no or all patients in all cohorts.

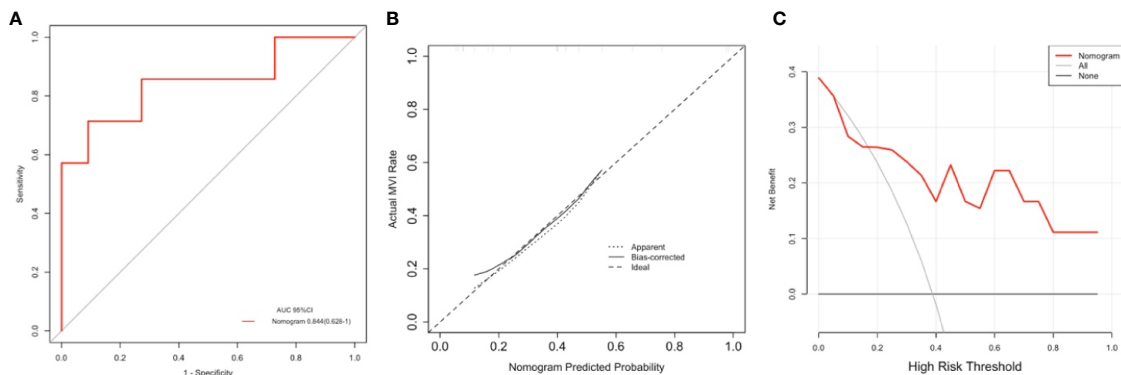


**FIGURE 5 |** The area under the curve (AUC) **(A)**, calibration curve **(B)**, and decision curve analysis (DCA) **(C)** of the nomogram to prospectively analyze the pilot cohort. This purposed radiomics feature-based nomogram was able to predict tumors combined microvascular invasion (MVI) occurrence with an AUC of 0.844 (95% confidence interval:0.628–1.000) **(A)** the result calibration curve showed that the radiomics nomogram was with the ideal line **(B)** and as to result of the DCA represented that at the situation where the threshold probability was within a range from 0.2 to 1.0 **(C)**, this purposed nomogram obtained greater net benefit than either “treat none” or “treat all” scheme, suggesting that this purposed nomogram is still a good clinical utility.

extract a large number of specific imaging features from radiological images, such as CT images, magnetic resonance images or PET-CT images, in a high-throughput and automatic manner and then utilize those radiomics imaging features with clinicopathological data to establish statistical models for judgment of tumor characteristics or optimal treatment choice and prognosis for individual patients (25). Therefore, radiomics can connect medical imaging and personalized medicine. However, due to the lack of a comprehensive standardized assessment of clinical significance and scientific integrity in previously radiomics studies, it is difficult to promote the application of radiomics image analysis methods among different institutions (26). In current clinical practice, for the reason that there are no known single and highly reliable predictive factors for the incidence of MVI, combining multiple MVI status-related factors with radiomics signatures to build multivariate radiomic models is a feasible option. Previous published studies have utilized multiple imaging modal images (e.g., CT, MR, ultrasound) with radiomics algorithms to predict the incidence of MVI preoperatively and then achieve the ultimate goal of assisting in choosing an optimal surgical treatment or predicting the early recurrence of HCC to provide a reasonable treatment scheme for those patients (27–29). With the rapid development and improvement of radiomics technology, we are able to identify high risky HCC patients with MVI with higher accuracy and better efficacy before surgery which have great significance in terms such as select appropriate surgical therapy strategy, give assistance to confirm rational resection scope to achieve radical hepatectomy for HCC patients rather than barely refer to tumor location, size or two-dimensional spatial relationship between intrahepatic vasculatures as conventional method did consider of the high postoperative recurrence ratio, for patients whose tumor size lower than three millimeters also susceptible to MVI positive anatomical hepatectomy are recommended as first choice than radiofrequency ablation, for patients susceptible to MVI positive

when select to perform non-anatomical hepatectomy, the distance from resection margin tumor should beyond one millimeter to decrease the risk of postoperative recurrence (20). Accurately prediction of MVI occurrence has contributed to achieve radical tumor resection for patients with HCC in addition prolong the disease-free survival to the maximum extent. MVI as a significant factor which influence long term survival rate, radiomics features based prediction model applied to this crucial issue will provide more effective guidance for subsequent clinical researches and therapy scheme making.

Related studies have shown that approximately 85% of MVI is located within one millimeter (which is called the peritumoral area) of the margin of tumors (30). In this research, we extracted both peritumoral and intratumoral CT radiomics features to establish a nomogram model. Zhao et al. (31) established a scoring system using predictive factors such as intratumoral arteries, nonnodular HCC type also the absence of a tumor vessel based on CECT images to predict MVI preoperatively, take no account of tumor size or diameter. The AUCs of aforementioned scoring system were 0.872 and 0.856 among training cohort as well validation cohort, respectively. Lei et al. (32) built a nomogram scoring model with risk factors such as tumor diameter, number, vessel condition, serum AFP content, platelet level, HBV-DNA loading in addition with representative dynamical magnetic resonance imaging features for predicting MVI occurrence among patients suffered from HBV-related HCC under the Milan criteria, which shows satisfactory predictive efficiency whose AUC was 0.81 among training cohort also 0.80 among validation cohort. Similarly, Renzulli et al. (9) applied integration of three imaging features of predictive significance, gaining an AUC of 0.90. In terms of clinicopathological risk factors among our study, AFP, neutrophilic granulocyte, and preoperative hemoglobin content were of greater importance than the Rad-score in the regression model. When applied in the validation cohort, the discernibility ability of proposed model outperformed three conventional method mentioned in this article. For calibration

curve analysis, the result in both cohorts are satisfying, furthermore, the result of decision curve analysis showed this proposed model possessed clinical application potential. The result of pilot study demonstrated that the accuracy of this model is preferably among study data set (whose AUC was 0.844, 95% confidential interval was 0.628–1.000).

## Limitations

There are certainly some underlying limitations to this study. First, the analysis results suffer from inherent selection biases without a large enough number of included patients. Second, due to the study cohort selection from a single center, which could not offer sufficient diversity of characteristics to be representative of the general population, the lack of external validation from other centers was a shortcoming of this study. Moreover, heterogeneity of CT images will give rise to bias during the procedures as image features extraction and segmentation for region of interest. In the follow-up study, a larger study cohort and external validation will test and improve the efficacy and feasibility of this model for patient management and clinical decision-making for MVI prediction in HCC. Therefore, unified standards in addition with elaborated and rigorous assessment for quality of study images should be established in order to acquire more reliable study data.

## CONCLUSIONS

We have built and evaluated a novel radiomics feature-based nomogram to predict the incidence of MVI among patients suffered from HCC. the purposed nomogram has provided one novel method for risk identification of MVI incidence and of radiomics features as a supplementary resource to clinicopathological data and conventional CT images that could lower the medical costs and improve the availability of clinical decision-making and treatment scheme guidance.

## REFERENCES

- Forner A, Reig M, Bruix J. Hepatocellular carcinoma. *Lancet* (2018) 391 (10127):1301–14. doi: 10.1016/S0140-6736(18)30010-2
- Miller KD, Nogueira L, Mariotto AB, Rowland JH, Yabroff KR, Alfano CM, et al. Cancer treatment and survivorship statistics, 2019. *CA Cancer J Clin* (2019) 69(5):363–85. doi: 10.3322/caac.21565
- Fang C, Zhang P, Qi X. Digital and intelligent liver surgery in the new era: Prospects and dilemmas. *Ebiomedicine* (2019) 41:693–701. doi: 10.1016/j.ebiom.2019.02.017
- Vilarinho S, Calvisi DF. New advances in precision medicine for hepatocellular carcinoma recurrence prediction and treatment. *Hepatology* (2014) 60(6):1812–4. doi: 10.1002/hep.27311
- Lim KC, Chow PK, Allen JC, Chia GS, Lim M, Cheow PC, et al. Microvascular invasion is a better predictor of tumor recurrence and overall survival following surgical resection for hepatocellular carcinoma compared to the Milan criteria. *Ann Surg* (2011) 254(1):108–13. doi: 10.1097/SLA.0b013e31821ad884
- Iguchi T, Shirabe K, Aishima S, Wang H, Fujita N, Ninomiya M, et al. New pathologic stratification of microvascular invasion in hepatocellular carcinoma: Predicting prognosis after living-donor liver transplantation. *Transplantation* (2015) 99(6):1236–42. doi: 10.1097/TP.0000000000000489

## DATA AVAILABILITY STATEMENT

The raw data supporting the conclusions of this article will be made available by the authors, without undue reservation.

## ETHICS STATEMENT

The studies involving human participants were reviewed and approved by The Ethics Review Board of Zhujiang Hospital, Southern Medical University. The patients/participants provided their written informed consent to participate in this study.

## AUTHOR CONTRIBUTIONS

CF and FJ conceived of the presented idea. PZ collected the data. MH, XM, BH, and FJ analyzed the data. MH drafted the manuscript. All authors reviewed the manuscript and FJ made corrections to the manuscript. All authors contributed to the article and approved the submitted version.

## FUNDING

This work was supported by grants from the National Key R&D Program, China (Nos. 2019YFC0118100 and 2016YFC0106500), the Major Instrument Project of National Natural Science Fund of China (No. 81627805), the Shenzhen Key Basic Science Program (JCYJ20170413162213765 and JCYJ20180507182437217), the NSFC-Shenzhen Union Program (U1613221), the Youth Program of Natural Science Foundation of Anhui Province (2008085QH418), the Key-Area Research and Development Program of Guangdong Province (2020B010165004), and the National Key Research and Development Program (2017YFC0110903).

- Costentin CE, Ferrone CR, Arellano RS, Ganguli S, Hong TS, Zhu AX. Hepatocellular carcinoma with macrovascular invasion: Defining the optimal treatment strategy. *Liver Cancer* (2017) 6(4):360–74. doi: 10.1159/000481315
- Sumie S, Nakashima O, Okuda K, Kuromatsu R, Kawaguchi A, Nakano M, et al. The significance of classifying microvascular invasion in patients with hepatocellular carcinoma. *Ann Surg Oncol* (2014) 21(3):1002–9. doi: 10.1245/s10434-013-3376-9
- Renzulli M, Brocchi S, Cucchetti A, Mazzotti F, Golfieri R. Can current preoperative imaging be used to detect microvascular invasion of hepatocellular carcinoma? *Radiology* (2015) 279(2):150998. doi: 10.1148/radiol.2015150998
- Lee S, Kim SH, Ji EL, Dong HS, Park CK. Preoperative Gadoxetic acid-enhanced MRI for predicting microvascular invasion in patients with single hepatocellular carcinoma. *J Hepatol* (2017) 67(3):526–34. doi: 10.1016/j.jhep.2017.04.024
- Kornberg A, Freesmeyer M, Rthel EB, Jandt K, Katenkamp K, Steenbeck J, et al. 18F-FDG-Uptake of hepatocellular carcinoma on PET predicts microvascular tumor invasion in liver transplant patients. *Am J Transplant* (2009) 9(3):592–600. doi: 10.1111/j.1600-6143.2008.02516.x
- Cai W, He B, Hu M, Zhang W, Xiao D, Yu H, et al. A radiomics-based nomogram for the preoperative prediction of posthepatectomy liver failure in patients with hepatocellular carcinoma. *Surg Oncol* (2019) 28:78–85. doi: 10.1016/j.suronc.2018.11.013

13. Zhang W, Cai W, He B, Xiang N, Fang C, Jia F. A radiomics-based formula for the preoperative prediction of postoperative pancreatic fistula in patients with pancreaticoduodenectomy. *Cancer Manag Res* (2018) 10:6469–78. doi: 10.2147/CMAR.S185865
14. Jie P, Jing Z, Qifan Z, Yikai X, Jie Z, Li L. A radiomics nomogram for preoperative prediction of microvascular invasion risk in hepatitis B virus-related hepatocellular carcinoma. *Diagn Intervent Radiol* (2018), 121–7. doi: 10.5152/dir.2018.17467
15. Xu X, Zhang HL, Liu QP, Sun SW, Zhang J, Zhu FP, et al. Radiomic analysis of contrast-enhanced CT predicts microvascular invasion and outcome in hepatocellular carcinoma. *J Hepatol* (2019) 70(6):1133–44. doi: 10.1016/j.jhep.2019.02.023
16. Orcutt ST, Anaya DA. Liver resection and surgical strategies for management of primary liver cancer. *Cancer Control J Moffitt Cancer Center* (2018) 25 (1):544014718. doi: 10.1177/1073274817744621
17. Nakashima Y, Nakashima O, Tanaka M, Okuda K, Nakashima M, Kojiro M. Portal vein invasion and intrahepatic micrometastasis in small hepatocellular carcinoma by gross type. *Hepatol Res* (2003) 26(2):142–7. doi: 10.1016/s1386-6346(03)00007-x
18. Lafaro K, Grandhi MS, Herman JM, Pawlik TM. The importance of surgical margins in primary malignancies of the liver. *J Surg Oncol* (2016) 113(3):296–303. doi: 10.1002/jso.24123
19. Du M, Chen L, Zhao J, Tian F, Zeng H, Tan Y, et al. Microvascular invasion (MVI) is a poorer prognostic predictor for small hepatocellular carcinoma. *BMC Cancer* (2014) 14(1):38. doi: 10.1186/1471-2407-14-38
20. Lee S, Kang TW, Song KD, Lee MW, Rhim H, Lim HK, et al. Effect of microvascular invasion risk on early recurrence of hepatocellular carcinoma after surgery and radiofrequency ablation. *Ann Surg* (2019). doi: 10.1097/SLA.0000000000003268
21. Wen-Ming CHBJ, Guideline C. Practice guidelines for the pathological diagnosis of primary liver cancer: 2015 update. *World J Gastroentero* (2016) 22(42):9279–87. doi: 10.3748/wjg.v22.i42.9279
22. He B, Huang C, Sharp G, Zhou S, Hu Q, Fang C, et al. Fast Automatic 3D liver segmentation based on a three-level AdaBoost-guided active shape model. *Med Phys* (2016) 43(5):2421–34. doi: 10.1118/1.4946817
23. Griethuysen JJM, Fedorov A, Parmar C, Hosny A, Aucoin N, Narayan V, et al. Computational radiomics system to decode the radiographic phenotype. *Cancer Res* (2017) 77(21):e104–7. doi: 10.1158/0008-5472.CAN-17-0339
24. Motzer RJ, Bukowski RM, Figlin RA, Hutson TE, Dror Michaelson M, Kim ST, et al. Prognostic nomogram for Sunitinib in patients with metastatic renal cell carcinoma. *Cancer* (2008) 113(7):1552–8. doi: 10.1002/cncr.23776
25. Lewis S, Hectors S, Taouli B. Radiomics of hepatocellular carcinoma. *Abdom Radiol* (2020). doi: 10.1007/s00261-019-02378-5
26. Lambin P, Leijenaar RTH, Deist TM, Peerlings J, de Jong EEC, van Timmeren J, et al. Radiomics: the bridge between medical imaging and personalized medicine. *Nat Rev Clin Oncol* (2017) 14(12):749–62. doi: 10.1038/nrclinonc.2017.141
27. Feng ST, Jia Y, Liao B, Huang B, Zhou Q, Li X, et al. Preoperative prediction of microvascular invasion in hepatocellular cancer: a radiomics model using Gd-EOB-DTPA-enhanced MRI. *Eur Radiol* (2019) 29(9):4648–59. doi: 10.1007/s00330-018-5935-8
28. Chen L, Li W, Xian M, Zheng X, Lin Y, Liu B, et al. Preoperative prediction of tumour deposits in rectal cancer by an artificial neural network-based US radiomics model. *Eur Radiol* (2020) 30(4):1969–79. doi: 10.1007/s00330-019-06558-1
29. Ji G, Zhu F, Xu Q, Wang K, Wu M, Tang W, et al. Radiomic features at contrast-enhanced CT predict recurrence in early stage hepatocellular carcinoma: A multi-institutional study. *Radiology* (2020) 294(3):568–79. doi: 10.1148/radiol.2020191470
30. Roayaie S, Blume IN, Thung SN, Guido M, Fiel MI, Hiotis S, et al. A system of classifying microvascular invasion to predict outcome after resection in patients with hepatocellular carcinoma. *Gastroenterology* (2009) 137(3):850–5. doi: 10.1053/j.gastro.2009.06.003
31. Zhao H, Hua Y, Dai T, He J, Tang M, Fu X, et al. Development and validation of a novel predictive scoring model for microvascular invasion in patients with hepatocellular carcinoma. *Eur J Radiol* (2017) 88(Complete):32–40. doi: 10.1016/j.ejrad.2016.12.030
32. Lei Z, Li J, Dong W, Yong X, Wang Q, Si A, et al. Nomogram for preoperative estimation of microvascular invasion risk in Hepatitis B virus-related hepatocellular carcinoma within the Milan Criteria. *JAMA Surg* (2016) 151 (4):356–63. doi: 10.1001/jamasurg.2015.4257

**Conflict of Interest:** The authors declare that the research was conducted in the absence of any commercial or financial relationships that could be construed as a potential conflict of interest.

Copyright © 2020 He, Zhang, Ma, He, Fang and Jia. This is an open-access article distributed under the terms of the Creative Commons Attribution License (CC BY). The use, distribution or reproduction in other forums is permitted, provided the original author(s) and the copyright owner(s) are credited and that the original publication in this journal is cited, in accordance with accepted academic practice. No use, distribution or reproduction is permitted which does not comply with these terms.





# Combined T2 SPAIR, Dynamic Enhancement and DW Imaging Reliably Detect T Staging and Grading of Bladder Cancer With 3.0T MRI

Lihua Yuan<sup>1,2†</sup>, Danyan Li<sup>1†</sup>, Dan Mu<sup>1</sup>, Xuebin Zhang<sup>1</sup>, Weidong Kong<sup>1</sup>, Le Cheng<sup>1</sup>, Xin Shu<sup>1</sup>, Bing Zhang<sup>1\*</sup> and Zhishun Wang<sup>2\*</sup>

## OPEN ACCESS

### Edited by:

Min Wu,  
Sichuan University, China

### Reviewed by:

Yuntian Chen,  
Sichuan University, China  
Qijun Shen,  
Zhejiang University, China  
Zhongxiang Ding,  
Zhejiang University, China

### \*Correspondence:

Bing Zhang  
zhangbing\_nanjing@vip.163.com  
Zhishun Wang  
zw2105@cumc.columbia.edu

<sup>†</sup>These authors have contributed  
equally to this work and share  
first authorship

### Specialty section:

This article was submitted to  
Cancer Imaging and  
Image-directed Interventions,  
a section of the journal  
Frontiers in Oncology

Received: 12 July 2020

Accepted: 12 October 2020

Published: 10 November 2020

### Citation:

Yuan L, Li D, Mu D, Zhang X, Kong W,  
Cheng L, Shu X, Zhang B and Wang Z  
(2020) Combined T2 SPAIR, Dynamic  
Enhancement and DW Imaging  
Reliably Detect T Staging and Grading  
of Bladder Cancer With 3.0T MRI.  
Front. Oncol. 10:582532.  
doi: 10.3389/fonc.2020.582532

<sup>1</sup> Department of Radiology, Gulou Clinical College of Nanjing Medical University, Nanjing, China, <sup>2</sup> Department of Psychiatry, Vagelos College of Physicians and Surgeons, Columbia University, New York, NY, United States

**Objectives:** To evaluate bladder cancer by integrating multiple imaging features acquired using multimodal 3.0T magnetic resonance imaging (MRI).

**Methods:** We prospectively enrolled 163 consecutive patients including 142 men (mean age, 65.2 years) and 21 women (mean age, 65.8 years). We evaluated the efficiency and reliability of the multiple imaging modalities including T2-weighted spectral attenuated inversion recovery (SPAIR) imaging, dynamic contrast-enhanced (DCE) imaging and diffusion-weighted (DW) imaging, and the imaging feature, apparent diffusion coefficient (ADC) in the identification of the T staging and grading. We compared our imaging findings with the results of histological examination using McNemar's test. We reported the results under the significance of  $p < 0.05$ . Approval for the study was obtained from the local institutional review board.

**Results:** The sensitivity and specificity using T2 SPAIR plus DW imaging (sensitivity: 85.2%; specificity: 93.2%), DCE plus DW imaging (sensitivity: 92.4%; specificity: 96.8%), and all the three imaging modalities combined, i.e., T2 SPAIR plus DCE plus DW imaging (sensitivity: 92.5%; specificity: 97.4%), were significantly greater than using T2 SPAIR imaging alone (sensitivity: 74.1%; specificity: 72.2%). One hundred six (93.0%) lesions showed a thin, pedicle arch-like shape and thus primarily demonstrated to be in Ta stage; by contrast, a large number of lesions (137 [85.6%]) were sessile and were found to be in T1 stage. The differences in the ADC were significant between low-grade ( $877.57 \pm 24.15$ ) and high-grade ( $699.54 \pm 23.82$ ) lesions ( $P < .01$ ).

**Conclusions:** T2 SPAIR and DCE plus DW imaging provided useful information for evaluating T staging and grading in bladder cancer. Those imaging features to distinguish Ta stage from T1 stage were presented.

**Keywords:** T2 SPAIR, dynamic contrast-enhanced, diffusion-weighted imaging, bladder cancer, multimodal magnetic resonance imaging

## INTRODUCTION

Bladder cancer is the most common cancer of the urinary system (1). Globally, it is the ninth most common cause of cancer-related death in humans. The prevalence of bladder cancer in males is three to four times greater than in females. In females, however, bladder cancer is often confirmed with more advanced disease at presentation and less favorable outcomes after treatment (2). Currently, the definitive diagnosis of bladder cancer depends on histological confirmation by cystoscopy or surgery. The contribution of magnetic resonance imaging (MRI) to the diagnosis of bladder cancer has been reported (3). However, conventional images with an echo-planar MR sequence cannot identify primary tumor and can be inaccurate in identifying local staging (4). Based on the opinion of the updated guidelines on bladder cancer, it is necessary to distinguish T1 from Ta cancer then to distinguish the low grade bladder cancer from the high grade one by which it is an important indicator of whether cystectomy is required. MRI with 3.0T may be useful for accurate pretreatment staging, predicting the early response to treatment and providing non-invasive alternatives to cystoscopy for those requiring long-term surveillance, including some advanced scanning modes such as dynamic contrast-enhanced (DCE) and diffusion-weighted imaging (DWI) (5). Because of the fact that different scanning sequences focus on different aspects of imaging features, combination of different sequences can provide more comprehensive and detailed imaging diagnosis of bladder cancer. In addition, based on the opinion of the updated guidelines on bladder cancer (1), more accurate imaging information could be contributed to bladder cancer staging with 3.0T MRI. In this study, we aimed to investigate bladder cancer using the integration of multiple imaging modalities with 3.0T MR; to compare imaging features with pathological results regarding cancer staging; and to evaluate the correlation between apparent diffusion coefficient (ADC) values and histological grade.

## MATERIALS AND METHODS

### Patients

Between January 2016 and March 2017, 163 patients who presented with gross (macroscopic) hematuria with normal findings from upper urinary tract ultrasonographic evaluation were prospectively enrolled. They were evaluated initially by ultrasonography (US) or cystoscopy. The population included 142 (87.1%) men ( $65.2 \pm 10.6$  years old; range, 42–87 years) and 21 (12.9%) women ( $65.8 \pm 10.5$  years old; range 57–81 years). For the whole group, the mean age was  $65.3 \pm 10.2$  years old (range, 42–87 years). Single lesions were found in 58 cases (35.6%), and multiple lesions were found in 105 cases (64.4%) (Table 1). Patients with cystoscopically proven bladder cancer were subjected to dual-source parallel RF excitation technology MRI and subsequently underwent TUR-BT (transurethral resection of bladder cancer) or radical resection. None of the patients had received TURBT before MRI scanning. Exclusion criteria included upper urinary tract cancer or stones, a history of

**TABLE 1 |** Demographic and Clinical Characteristics.

Characteristic	No. (%) of patients (n = 163)
<b>Age</b>	
Age of All Subjects	$65.3 \pm 10.2$ (42–87)
Age of Males	$65.2 \pm 10.6$ (42–87)
Age of Females	$65.8 \pm 10.5$ (57–81)
<b>Sex</b>	
Male	142 (87.1%)
Female	21 (12.9%)
<b>Lesions</b>	
Single lesions	58 cases (35.6%)
Multiple lesions	105 cases (64.4%)
<b>Operative technique</b>	
Transurethral resection of tumor	92 (56%)
Radical/Partial cystectomy	71 (44%)

urinary tract trauma, contraindications to MR imaging (e.g., pacemaker or metallic prostheses) or cystoscopy (e.g., unfit for anesthesia or urethral stricture), and refusal to consent to the study. Approval for the study was obtained from the local institutional review board. Written informed consent was obtained from all of the patients.

### MRI Acquisition

Before MRI scanning, proper bladder distension was necessary. Patients were asked to start drinking water half an hour before the MRI and to keep their bladder full at the time of the examination. Checked the bladder filling degree on the image of the localizer, and delayed the examination if the bladder was not full.

All of the measurements on patients were carried out using a 3.0-Tesla imager (Intera Achieva; 3.0T TX, Philips, Best, Netherlands) with respiratory triggering. Axial, orthogonal, high-resolution T2-weighted spectral attenuated inversion recovery (SPAIR), DCE and DW images were acquired sequentially on the same axial orientation using a 16-channel SENSE (Sensitivity-Encoding) abdominal coil. The following parameters were used for T2 SPAIR high-resolution MR of the urinary bladder: TR = 5,000 ms, TE = 110 ms, band width = 50 kHz,  $320 \times 256$  matrix, slice thickness of 3 mm, intersection gap of 1 mm, and field of view (FOV) = 40 cm. DW images were obtained using a single-shot fast spin-echo sequence with chemical shift-selective fat-suppression techniques ( $b = 0$  and  $800 \text{ s/mm}^2$  [DW gradients applied in three orthogonal directions]; matrix,  $128 \times 128$ ; section thickness, 3 mm; gap, 1 mm; field of view, 30 cm; number of sections, 19–24; number of signals acquired, 14; sensitivity encoding factor, 2; acquisition time, 7 min). Sequentially, T1-weighted DCE imaging was performed to use full time points, including precontrast scanning (with a flip angle of  $10^\circ$ ) and dynamic scanning (with a flip angle of  $10^\circ$ ) after a single-dose injection of gadopentetate dimeglumine (Omniscan, GE Healthcare, Waukesha, WI, USA) at a dose of  $0.1 \text{ mmol/kg}$ . The final total scan time was maintained within 4 min. The field of view (AP/RL/FH) was  $300/300/200 \text{ mm}$ ; the voxel size was  $8 \text{ mm}^3$ ; TR and TE were the limit set by the machine; and the average acquisition times averaged 80 s (range, 0–80 s, 20 time-points and 2 s time interval).

## MR Image Analysis

All MR images were independently examined by two radiologists (DM and XZ, with 10 and 30 years of experience, respectively). The observers knew where the cancer was and ignored all other information. A bi-exponential model was used to describe the behavior of the diffusion-weighted signal in the lesions considered in this study. Seven image sets were reviewed as follows: T2 SPAIR images alone, DCE images alone, DW images alone, T2 SPAIR plus DCE images, T2 SPAIR plus DW images, DCE plus DW images, and all three image types combined. First, the T2 SPAIR alone, DCE alone, DW alone, and T2 SPAIR plus DCE images were interpreted, and then the remaining sets (T2 SPAIR plus DW images, DCE plus DW images, and all three image types combined) were evaluated after 2 weeks. When these three types of images were interpreted together, T2 SPAIR and DCE images were mainly used to identify anatomical structures, and DW images were used to assess the extent of the cancer. The apparent diffusion coefficient (ADC) values of the bladder masses, urine and normal bladder wall were measured.

## Cancer Staging

Differentiation between noninvasive and invasive urothelial cancer is critical to the treatment planning. The non-muscle-invasive urothelial cancer of the bladder ( $\leq T1$ ) requires greatly varying but the unified requirement for risk adaptive treatment and monitoring was to provide thorough care while minimizing the burden associated with treatment. However, the high-stage ( $\geq T2$ ) tumors with high recurrence rate and low progression rate demand intensive care and timely consideration of radical cystectomy (1, 6).

To evaluate the performance and agreement of the two reviewers at identifying bladder tumors the reviewers were requested to classify the cancer into the following two categories (invasive or non-invasive cancer) and subcategories in accordance with the 2009 TNM system of the International Union Against Cancer (7): non-invasive cancer (Tis; Ta; T1) and invasive cancer (T2; T3; T4) (Table 2). The staging standard used was similar to the T2 weighted images (9, 10) and contrast-enhanced images (11), and we defined a new standard for DW images, two image types or three image types combined in this study. Because of the difference in the recurrence and progression rates regarding Ta- and T1-stage cancer (6), the cancer size and cancer histological grade were also evaluated.

**TABLE 2 |** T Staging for Bladder Cancer.

Categories	Stage	Description
Non-invasive Bladder Cancer	Tis	Carcinoma <i>in situ</i>
	Ta	Papillary non-invasive tumor
	T1	Tumor invades subepithelial connective tissue
Invasive Bladder Cancer	T2a	Tumor invades superficial muscle
	T2b	Tumor invades deep muscle
	T3a	Tumor invades perivesical tissue microscopically
	T3b	Tumor invades perivesical tissue macroscopically
	T4a	Tumor invades prostate, uterus, or vagina
	T4b	Tumor invades pelvic or abdominal wall

Source—Reference (8).

## Definition of Non-Invasive and Invasive Cancer on T2 SPAIR Imaging

Since a low signal intensity (SI) line could be observed on the T2 SPAIR image of the normal bladder wall, when the low signal intensity line was obvious (Figure 1A), the bladder wall was considered to be intact ( $\leq T1$ ). The bladder was considered to be infiltrated by the cancer ( $\geq T2$ ) (Figure 3A) when the low SI line was destroyed focally in the region underlying the cancer (12).

## Definition of Non-Invasive and Invasive Cancer on DCE Imaging

On contrast-enhanced images, submucosal linear enhancement (SLE) is shown immediately after the injection of contrast agent, while SI in muscle layer was still low. Therefore, an integral SLE adjacent to a cancer is indicative of stage Ta (Figure 1B). When SLE is disrupted by a cancer, this situation was considered stage T1 or higher disease. On both T2 SPAIR and contrast-enhanced images, cancer extending into an adjacent organ or the abdominal wall was classified as T4 (13).

## Definition of Non-Invasive and Invasive Cancer on DW Imaging

On DW images, bladder cancer shows high SI (14). We assumed that an intermediate SI line delineated the low SI region between the cancer and muscle, which could reflect a muscle layer and a submucosal stalk, respectively (Figure 1C). We propose a new DW staging standard: a thin, flat, high SI area corresponding to the cancer or a high SI cancer with a low SI submucosal stalk or a thickened submucosa indicates stage T1 or lower; stage T2 of high SI cancer with smooth margin and no submucous stalk; extension into the perivesical fat with an irregular margin indicates stage T3; and extension into adjacent organs indicates stage T4 (15).

## Histopathologic Analysis

The histopathologic findings of bladder cancer specimens were compared with the preoperative MRI findings for each patient by using the McNemar test. With the difference in cancer biology, growth pattern, and recurrence between low-grade and high-grade bladder cancer, cancer was classified into two grades: low-grade anaplasia and high-grade anaplasia (7).

## ADC Value Measurement

The index of cancer was selected based on the pathological findings in patients with multiple bladder cancers. ADC values, which were used to quantitatively analyze the degree of diffusion for the index cancer, were calculated at a workstation (Philips View Forum R4.1; Philips, Best, Netherlands) using the following formula (16):

$$ADC = \frac{\ln\left(\frac{S(b_1)}{S(b_0)}\right)}{b_1} \quad (1)$$

where  $b$  is the attenuation coefficient (depending only on gradient pulses parameters: (i) gradient intensity and (ii) gradient duration;  $S(b_0)$  is the MRI signal when  $b = b_0 = 0$  s/mm<sup>2</sup>;  $S(b_1)$  is the MRI signal when  $b = b_1 > 0$ , where we used



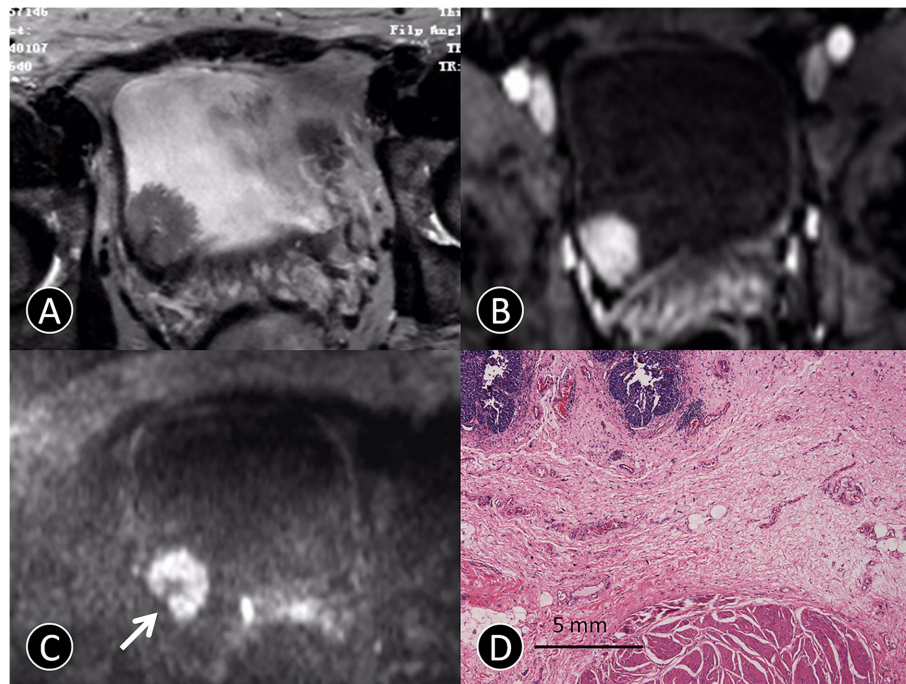


**FIGURE 1** | MR images of a 72-year-old man with pTa urothelial carcinoma. **(A)** The transverse T2 SPAIR image shows an oval mass on the right bladder wall without obvious a C-shaped high SI area (arrow). **(B)** The transverse DCE image shows an oval mass that is significantly enhanced, and the submucosa is slightly enhanced without obvious a C-shaped high SI area (arrow). **(C)** The transverse DW MR image shows a C-shaped high SI area with a low SI stalk connecting to the right side of bladder wall with a thin pedicle and small contact area (arrow). **(D)** The photomicrograph of a specimen obtained at TUR shows papillary cancer (blue) with a submucosal stalk (red line) consisting of markedly edematous submucosa, fibrous tissue, capillaries, and mild inflammatory cell infiltration (Hematoxylin-eosin staining; original magnification,  $\times 40$ ).

$b_1 = 800 \text{ s/mm}^2$ . A trained image analyst and radiologist manually plotted a contour within a region of interest (ROI) to maximize coverage of index cancer on a transverse ADC map on a slice showing the maximal cancer diameter. The ROI was carefully drawn to exclude the surrounding urine. For cancer with a cancer stalk that showed low signal intensity on DW imaging, the ROI was drawn excluding the stalk. The ADC value of each pixel in the ROI was quantified, and the mean and standard deviation (SD) of the ADC values were calculated. ADC values were measured to estimate the degree of diffusion.

## Statistical Analysis

The data were processed using statistical software (SPSS, version 15; SPSS, Chicago, IL, USA), with conventional cystoscopy or the final histopathologic report as the reference standard. We evaluated the sensitivity, specificity, accuracy, positive predictive value (PPV), negative predictive value (NPV), and Cohen's kappa coefficient ( $\kappa$ ) (to measure inter-rater reliability) of T2 SPAIR, DCE and DW images to identify bladder cancer and the cause of the hematuria. A comparison of imaging findings with cystoscopy and histology was subsequently performed using the McNemar test. The ADC values of histological low-grade and high-grade urothelial cancer were compared using t test. A p value less than 0.05 was considered to indicate statistical significance.

## RESULTS

### Optimization of Imaging Protocols

The sensitivity, specificity, and overall accuracy of the consensus of the two observers for differentiating cancer ( $\leq T1$ ) from cancer ( $\geq T2$ ) are summarized in **Table 3**. The sensitivities and specificities using T2 SPAIR plus DW imaging (sensitivity: 85.2%; specificity: 93.2%), DCE plus DW imaging (sensitivity: 92.4%; specificity: 96.8%), and all the three imaging modalities combined, i.e., T2 SPAIR plus DCE plus DW imaging (sensitivity: 92.5%; specificity: 97.4%), were significantly greater than using T2 SPAIR imaging alone (sensitivity: 74.1%; specificity: 72.2%). The accuracies achieved using T2 SPAIR plus DW images (90.1%), DCE plus DW images (93.6%), or all the three image types combined (95.2%) were also greater than the accuracy achieved using T2 SPAIR images alone (73.0%).

Interobserver agreement of each interpretation is summarized in **Table 3**. Interobserver agreement of all the three imaging modalities (T2 SPAIR plus DCE plus DW imaging) combined was the highest ( $\kappa = 0.91$ ,  $p < 0.01$ ) compared to T2 SPAIR plus DW images ( $\kappa = 0.76$ ,  $p < 0.05$ ) and DCE plus DW images ( $\kappa = 0.88$ ,  $p < 0.01$ ).

### Cancer Characteristics

The 163 patients with 375 tumors were used to evaluate the ability to differentiate T1 and lower cancers from T2 and higher

**TABLE 3** | Diagnostic Accuracy for Differentiating Cancer Stage ( $\leq T1$ ) from Cancer stage ( $\geq T2$ ).

Imaging Set	Sensitivity	Specificity	Accuracy	PPV	NPV	$\kappa$ Value	P Value
T2 SPAIR	74.1%	72.2%	73.0%	0.50	0.92	0.70	<0.05
DCE	80.2%	85.7%	84.3%	0.56	0.90	0.88	<0.05
DW	83.7%	90.3%	90.0%	0.67	0.93	0.63	<0.05
T2 SPAIR +DCE	84.1%	86.3%	83.5%	0.71	0.91	0.55	<0.05
T2 SPAIR +DW	85.2%	93.2%	90.1%	0.54	0.86	0.76	<0.05
DCE+DW	92.4%	96.8%	93.6%	0.67	0.93	0.88	<0.05
T2 SPAIR +DCE+DW	92.5%	97.4%	95.2%	0.80	0.93	0.91	<0.01

PPV, positive predictive value; NPV, negative predictive value.

cancers. The pathologic stage was between Ta and T1 in 73% (274 of 375) of tumors, and T2 or higher stage cancers occurred in 27.0% (101 of 375) of tumors. T2 or higher stage tumors were divided into T2 (17% [64 of 375]), T3 (6% [22 of 375]), and T4 (4% [15 of 375]) regarding pathology. The cancers measured 0.61–88.5 mm in maximum diameter (mean, 24.6 mm). Histological diagnoses were all urothelial carcinoma ( $n = 363$ ) and urothelial carcinoma with adenocarcinoma ( $n = 12$ ). The histological grade was low grade in 120 (31.9%) of the 98 tumors and high grade in 255 (68.1%) of the tumors.

## Differentiation of Ta Cancer From T1 Cancer

Specific features of non-invasive cancer (Ta and T1) are summarized in **Table 4**. Because of the difference in cancer biology, growth pattern, and recurrence between low-grade bladder cancer with T1 stage and high-grade bladder cancer with T1 stage, it is necessary to distinguish T1 from Ta cancer before to distinguish low-grade bladder cancer from high-grade.

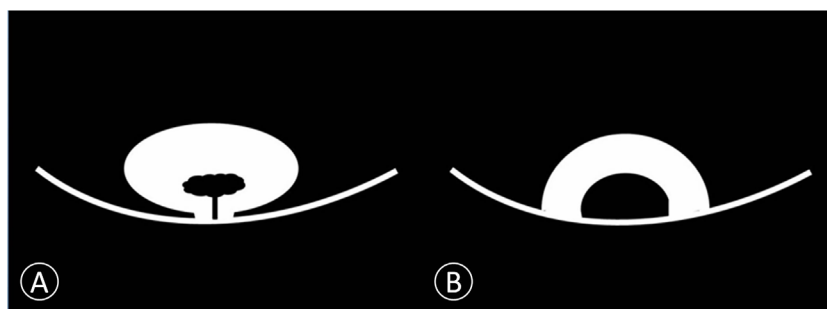
**TABLE 4** | Related Indicators in Non-invasive Bladder Cancer (Ta and T1).

		Ta	T1	P Value
No. of tumors in each patient		2.1	1.9	0.12
Cancer size		35 mm	37 mm	0.09
No. of arch-like shapes on DWI	Papillary	106	8	<0.05
	Sessile	23	137	<0.05
No. of tumors according to histological grade	Low-grade	62	31	<0.05
	High-grade	73	108	<0.05

It is not necessary to distinguish Ta with low-grade from Ta with high-grade bladder cancer. No significant difference was found in the number and size of cancer between the Ta and T1 groups in each patient (**Table 4**). However, papillary cancer accounted for most of stage Ta bladder cancer, and the main feature of T1 stage cancer was an arch-like shaped sessile tumor with a wide base (**Figure 2** and **Table 4**). Most of the Ta cancers were low grade, whereas most of the T1 cancers were high grade (**Table 4**).

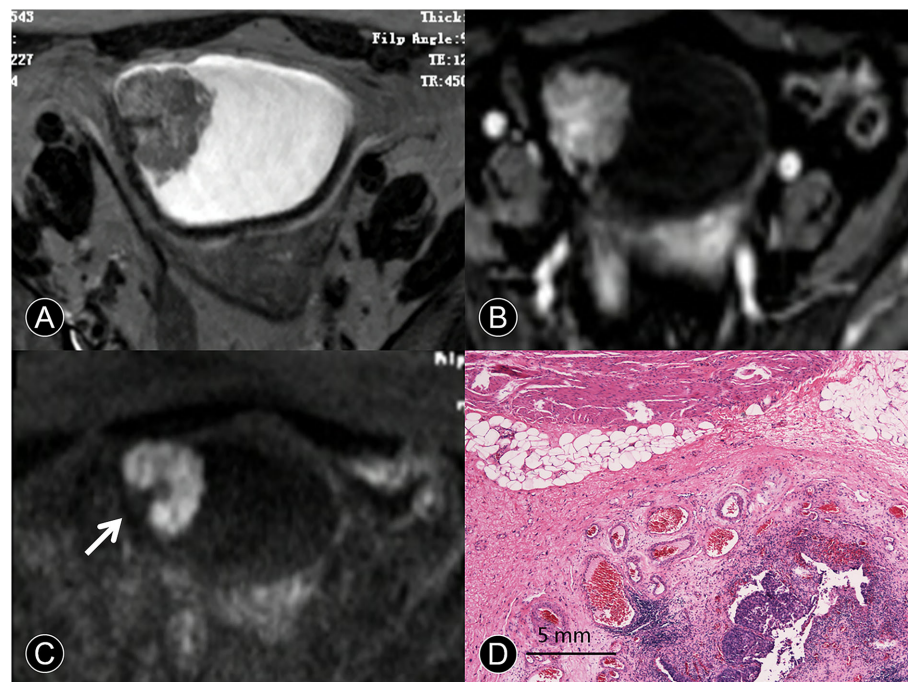
## Comparison of Imaging Findings and Histopathology as the Gold Standard

Image quality, despite some distortions commonly observed on DW-MRI, was sufficient in all 163 patients to allow for interpretation. The three hundred seventy-five tumors obtained using radical cystectomy ( $n = 85$ ) or TUR ( $n = 290$ ) were available for histopathologic correlation. The phase of enhancement of the submucosal tissue was earlier than that of the cancer component in Ta cancer at dynamic phases (98/129 [76%]; **Figure 1B**). However, the cancer component enhanced as strongly as the submucosal tissue at all dynamic phases in T1 cancer (131/145 [90.3%]; **Figure 3B**). In terms of histopathology, the high, intermediate, and low SI areas on DW images corresponded well to cancer, smooth muscle, and submucosal connective tissue, respectively (**Figures 1A, D**). The DW imaging finding of high SI bladder cancer together with a low SI submucosal stalk resembled an arch-like inchworm shape and was found in 268/274 (97.8%) patients with  $\leq T1$  disease (**Figure 3C**). All of the invasive urothelial cancers showed a smooth or slightly irregular contour or irregular margins toward the



**FIGURE 2** | Schematic diagram of non-invasive bladder cancer. **(A)** Cancer is connected to the bladder wall by a thin pedicle with a small contact area. We proposed this model as papillary cancer that could be observed on DWI. **(B)** Cancer is connected to the bladder wall with a wide base contact area. We proposed this model as sessile cancer that could be observed on DWI.





**FIGURE 3** | MR images of a 65-year-old man with pT1 urothelial carcinoma. **(A)** The transverse T2 SPAIR image shows an oval mass on the right discontinuous bladder wall without obvious a C-shaped high SI area (arrow). **(B)** The transverse DCE image shows an oval mass that is enhanced, the central part of the mass is significantly enhanced, and the submucosa is slightly enhanced without obvious a C-shaped high SI area (arrow). **(C)** The transverse DW MR image shows a C-shaped high SI area with a low SI stalk connecting to the right side of the bladder wall with a wide base contact area (arrow). **(D)** The photomicrograph of a specimen shows papillary cancer invading the submucosa (Hematoxylin-eosin staining; original magnification,  $\times 40$ ).

perivesical fat, a finding that correlated with pathologic findings (Figure 4).

### ADC and Histological Grade

The correlation between ADC and histological grade is summarized in Figure 5. The mean ADC of the 375 bladder tumors was  $788.56 \pm 21.27 \times 10^{-3} \text{ mm}^2/\text{s}$ . The differences in ADC values were significant between low-grade with  $877.57 \pm 24.15 \times 10^{-3} \text{ mm}^2/\text{s}$  and high-grade tumors with  $699.54 \pm 23.82 \times 10^{-3} \text{ mm}^2/\text{s}$  ( $P < 0.01$ ).

## DISCUSSION

We have systematically evaluated multiple MRI modalities including T2 SPAIR, DCE, and DW imaging and their combination in the diagnosis of bladder cancer, specifically in staging and grading of cancers at stages  $\leq T1$  (tumor invades subepithelial connective tissue) and at stages  $\geq T2$  (tumor invades superficial and deep muscles), which is of great significance in clinical applications. We have found that the integration of T2 SPAIR imaging, DCE imaging, and DW imaging yields the highest sensitivity, specificity, accuracy, observer-agreement among single one or any two combinations of them. We also found that the apparent diffusion coefficient (ADC) data extracted from DW images are significantly different between

low- and high-grade cancers that are determined by using histological data, indicating that the ADC data have a unique potential in objectively identifying the grade of bladder cancer without using invasive histological diagnosis.

The preoperative evaluation of different stages of bladder cancer with MRI is a viable and secure tool for surgical patients. The accuracy of the distinction between stage T1 or lower and stage T2 or higher has been reported to be approximately 75% to 95% (8, 17). The overall accuracy for diagnosing cancer stage is approximately 52% to 93% (8, 17, 18). Hayashi et al. showed the accuracy of 52–93%, and the overall diagnostic accuracy of 83% using an endorectal coil (8). Takeuchi et al. showed the accuracy of 92%, and the overall staging accuracy of 98% using a cardiac coil (17). In our study, the accuracy was 95% when a body coil was used (Table 3). This value was higher than that in Hayashi's report (8) but slightly lower than Takeuchi's report (17). The causes might be the different employment of the coils and different size of samples. Additional causes could be related to the different sizes of the field of view (FOV) or other differences in the scanning parameters. It was found out that DCE images combined with DWI could contribute to improving the accuracy significantly. A possible cause is that the DCE images might show the cancer margin, component, bladder muscle layer and submucosa in different forms of enhancement throughout the different phases. The DCE images acting in a complementary way and a potential benefit of the combined use of DWI that

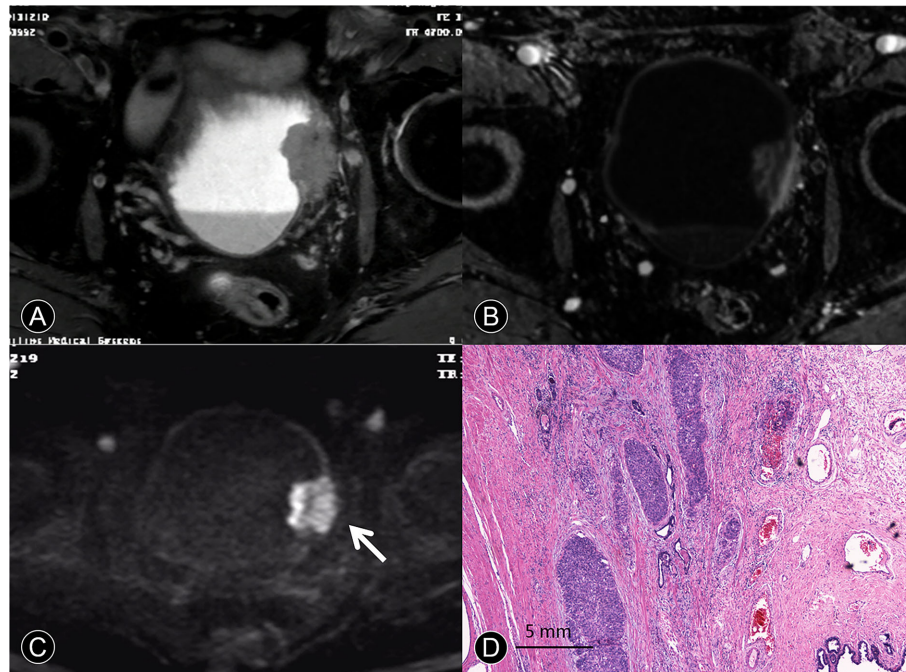


**FIGURE 4** | MR images of a 63-year-old man with pT4a urothelial carcinoma. **(A)** The transverse T2 SPAIR image shows large nonpapillary cancer on the deformed muscle layer. The SI of the muscle layer at base of the cancer is elevated, and there is clear evidence of perivesical invasion. **(B)** The DCE image of the axial section leftward to the wall of the bladder does not depict cancer contour because microvessels surrounding the cancer are also enhanced. **(C)** The transverse DW image shows a large cancer with an irregular margin spreading toward the surrounding fat tissue (arrow). **(D)** A photomicrograph of the specimen shows papillary cancer invading the muscular layer and prostate (Hematoxylin-eosin staining; original magnification,  $\times 40$ ).

detected the phenomenon of water molecule movement were further explored. It was reported that DW images are useful not only in cancer staging but also in being a reference model for other sequences (19). Bladder is a hollow muscular structure that

pumps fluids using peristaltic motion. MRI is not good enough at staging each detail of the hollow organ. For example, it is not easy to distinguish T2 from T3, as well as T3a from T3b, well and accurately. Additionally, with the thin bladder wall and even thinner muscular structure, the low resolution of DWI is not good at observing the cancer margin and normal muscular structure. Fortunately, according to histology, genetics research and new guidelines (1, 6, 7, 20), radical cystectomy was suggested to treat patients with higher stages of bladder cancer from T2 to T4a. It was reported that T2-weighted imaging was not sufficient to distinguish cancer from the muscle layer of bladder. Cancer and the muscle layer have similar SI in 81% of T2-weighted images (18). However, T2 SPAIR techniques provided improved the insensitivity to field heterogeneity (21). The diagnostic evaluation of combined T2 SPAIR, DWI and DCE images in bladder cancer T stage would be advocated for better assay results (Table 3).

The judgment of the cancer margin or depth invaded in the bladder wall is helpful for the recruitment and selection for surgery (22). The width of the inflammation zone and width of the submucosa were detected between normal tissues and cancer of the bladder (Figure 1D). These facts suggest that the border between normal tissues and cancer of the bladder could be determined by the structural difference between the tissue components using MRI. The high-quality images of MRI could

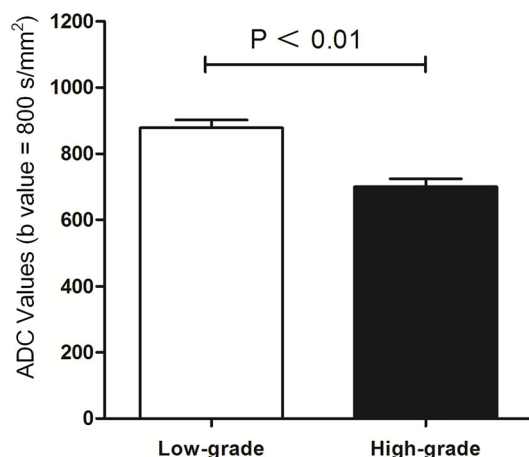


**FIGURE 5** | Comparison between histological low-grade and high-grade urothelial cancer according to ADC value (mm<sup>2</sup>/s).

help to detect the localization of the bladder cancer cell boundary (9).

The typical crab-like appearance of cancer was not noted in bladder cancer from Ta to T1 stage. The results showed that the total detection of cancer with integration of multiple imaging modalities was better than any imaging alone ( $P < 0.05$ ; **Table 3**). The possible reasons for the difference might be that the basic principle of T2 SPAIR and dynamic contrast-enhanced MRI provides evidence of anatomy and contrast enhancement. DWI is extremely sensitive to any net translational movement of water molecules, and its signal intensity is influenced by many factors (23). Therefore, the integration of all of the modalities is better than any used alone.

MR Imaging features of bladder cancer are essential for cancer staging (18, 24). Saito et al. (25) reported that the stalk extending from the bladder wall to the center of the cancer consisted of capillaries, inflammatory cells, fibrous tissues, and edema. Our results showed that pathological tissue related to the enhancing region in the early phase of dynamic contrast agent-enhanced images and the low SI area found on DW images in the center of the cancer primarily consisted of edematous submucosa, fibrous tissue, capillaries, and mild inflammatory cell infiltration (**Figures 1D, 2D, and 3D**). These features were frequent on dynamic contrast agent-enhanced and DW images for all T1 or lower cancers confirmed by pathology, findings that were similar to those in a previous report (17). The imaging feature of the stalk might correspond to the low-stage bladder cancer with microvessels and reactive tissue by long-term inflammatory. Additionally, the difference in imaging stage from Ta to T1 would be related to the size of the tumor in contact with the bladder wall (**Figure 2 and Table 4**).

In the treatment of localized, invasive bladder cancer, the standard treatment remains radical surgical removal of the bladder within standard limits (1). For patients with inoperable locally advanced tumors (T4b), primary radical cystectomy is a palliative option and is not recommended as a curative treatment (1). Therefore, it is important to perform a preliminary assessment of cancer boundaries and determine whether the pelvic or abdominal wall is invaded on MRI. In our study, the sensitivity, specificity, and accuracy achieved using T2 SPAIR, DCE plus DW imaging for diagnosing T4 tumors were all high and are summarized in **Table 3**. DCE plus DW images appear to provide useful information for evaluating cancer contours and size. To our knowledge, no detailed reports have been published concerning T4 bladder cancer with DCE plus DW images. Thus, it would be beneficial to comprehensively evaluate the scope of T4 invasion.

The choice of surgical approach is based not only on the clinical staging of bladder cancer but also on the combination of a comprehensive cancer grade assessment (1, 6). Bladder cancer grades are based on the blood supply and morphologic features of cancer cells as reported previously (26). ADCs representing the degree of restriction of water molecules or diffusivity are inversely correlated with the tissue cellularity and integrity of the cell membranes (27). ADCs have been successfully applied to other parts of the human body in cancer grading (28, 29).

Matsuki et al. reported that ADCs of bladder cancer were lower than those of the surrounding structures (14). In our study, the mean ADC of high-grade cancer was significantly lower than that of low-grade cancer ( $P < 0.05$ ), and all high-grade cancer had an ADC less than  $699.54 \pm 23.82 \text{ mm}^2/\text{s}$  ( $b = 800$ ). There was a high correlation between ADCs and histological grade ( $Z > 0.8$ ) that was different from that in previous reports, in which cancer was divided into G1 to G3. Our research combined ADCs with the latest bladder cancer grading. Although the evaluation of cancer grading from ADCs is influenced by several factors (29), the ADCs might still partly predict the histological grade of bladder cancer.

Our study had a number of limitations. First, tumors were divided into noninvasive and invasive urothelial tumors from T1 to T4. There were no accurate methods of differentiating sub-staging, for example, as well as no emphasis on Tis and discrimination between T3a and T3b. These differences in classification might have led to a higher accuracy. The division method is closely related to the development level of MRI and surgical treatment. In addition, the distribution of T stage was uneven with a large number of T1 or lower cancers and a small number of pT2 or higher cancers. The cause may be that patients with stage T1 or lower cancers constitute the main segment of the bladder cancer population. Additionally, our primary objectives were to discriminate between stage T1 or lower cancer and stage T2 or greater cancer, a factor that was crucial for the appropriate treatment of patients with bladder cancer.

In conclusion, the method of T2 SPAIR, DCE plus DW images provided useful information for the more accurate evaluation of T stage in bladder cancer, particularly for differentiating Ta from T1 or lower cancer from T2 or higher cancer. The 3.0T MR imaging features between Ta and T<sub>1</sub> of bladder cancer were presented. The combination of T2 SPAIR, DCE plus DW images plays a crucial role in the staging and grading of bladder cancer.

## DATA AVAILABILITY STATEMENT

The raw data supporting the conclusions of this article will be made available by the authors, without undue reservation.

## ETHICS STATEMENT

The studies involving human participants were reviewed and approved by the Ethics Committee of Nanjing Drum Tower Hospital. Written informed consent was obtained from all of the patients.

## AUTHOR CONTRIBUTIONS

LY designed the study and contributed to its conception. LY, DL and ZW were major contributors in the writing of the manuscript. Acquisition of data was by DM. Analysis and



interpretation of data were by XZ and WK. LC and XS checked the experimental data and provided advice. BZ and ZW revised the manuscript for important intellectual content. All authors contributed to the article and approved the submitted version.

## REFERENCES

- Witjes JA, Comperat E, Cowan NC, De Santis M, Gakis G, Lebreton T, et al. EAU guidelines on muscle-invasive and metastatic bladder cancer: summary of the 2013 guidelines. *Eur Urol* (2014) 65(4):778–92. doi: 10.1016/j.eururo.2013.11.046
- Dobrich J, Daneshmand S, Fisch M, Lotan Y, Noon AP, Resnick MJ, et al. Gender and Bladder Cancer: A Collaborative Review of Etiology, Biology, and Outcomes. *Eur Urol* (2016) 69(2):300–10. doi: 10.1016/j.eururo.2015.08.037
- Panebianco V, De Berardinis E, Barchetti G, Simone G, Leonardo C, Grompone MD, et al. An evaluation of morphological and functional multi-parametric MRI sequences in classifying non-muscle and muscle invasive bladder cancer. *Eur Radiol* (2017) 27(9):3759–66. doi: 10.1007/s00330-017-4758-3
- van der Pol CB, Chung A, Lim C, Gandhi N, Tu W, McInnes MDF, et al. Update on multiparametric MRI of urinary bladder cancer. *J Magn Reson Imaging* (2018) 48(4):882–96. doi: 10.1002/jmri.26294
- Wu X, Pertovaara H, Dastidar P, Vornanen M, Paavola L, Marjomaki V, et al. ADC measurements in diffuse large B-cell lymphoma and follicular lymphoma: a DWI and cellularity study. *Eur J Radiol* (2013) 82(4):e158–64. doi: 10.1016/j.ejrad.2012.11.021
- Babjuk M, Bohle A, Burger M, Capoun O, Cohen D, Comperat EM, et al. EAU Guidelines on Non-Muscle-invasive Urothelial Carcinoma of the Bladder: Update 2016. *Eur Urol* (2017) 71(3):447–61. doi: 10.1016/j.eururo.2016.05.041
- Delahunt B, Egevad L, Samarasinghe H, Varma M, Verrill C, Chevillet J, et al. UICC drops the ball in the 8th edition TNM staging of urological cancers. *Histopathology* (2017) 71(1):5–11. doi: 10.1111/his.13200
- Hayashi N, Tochigi H, Shiraiishi T, Takeda K, Kawamura J. A new staging criterion for bladder carcinoma using gadolinium-enhanced magnetic resonance imaging with an endorectal surface coil: a comparison with ultrasonography. *BJU Int* (2000) 85(1):32–6. doi: 10.1046/j.1464-410x.2000.00358.x
- Verma S, Rajesh A, Prasad SR, Gaitonde K, Lall CG, Mouraviev V, et al. Urinary bladder cancer: role of MR imaging. *Radiographics* (2012) 32(2):371–87. doi: 10.1148/rg.322115125
- Chhabra S, Hegde P, Singhal P. Primary small cell carcinoma of the urinary bladder—mini-review of the literature. *Asian Pac J Cancer Prev* (2012) 13(8):3549–53. doi: 10.7314/apjcp.2012.13.8.3549
- Panebianco V, Narumi Y, Altun E, Bochner BH, Efsthathiou JA, Hafeez S, et al. Multiparametric Magnetic Resonance Imaging for Bladder Cancer: Development of VI-RADS (Vesical Imaging-Reporting And Data System). *Eur Urol* (2018) 74(3):294–306. doi: 10.1016/j.eururo.2018.04.029
- Narumi Y, Kadota T, Inoue E, Kuriyama K, Horinouchi T, Kasai K, et al. Bladder wall morphology: in vitro MR imaging-histopathologic correlation. *Radiology* (1993) 187(1):151–5. doi: 10.1148/radiology.187.1.8451403
- Barentsz JO, Jager GJ, van Vierzen PB, Witjes JA, Strijk SP, Peters H, et al. Staging urinary bladder cancer after transurethral biopsy: value of fast dynamic contrast-enhanced MR imaging. *Radiology* (1996) 201(1):185–93. doi: 10.1148/radiology.201.1.8816542
- Matsuki M, Inada Y, Tatsugami F, Tanikake M, Narabayashi I, Katsuo Y. Diffusion-weighted MR imaging for urinary bladder carcinoma: initial results. *Eur Radiol* (2007) 17(1):201–4. doi: 10.1007/s00330-006-0281-7
- Lee M, Shin SJ, Oh YT, Jung DC, Cho NH, Choi YD, et al. Non-contrast magnetic resonance imaging for bladder cancer: fused high b value diffusion-weighted imaging and T2-weighted imaging helps evaluate depth of invasion. *Eur Radiol* (2017) 27(9):3752–8. doi: 10.1007/s00330-017-4759-2
- Le Bihan D, Breton E, Lallemand D, Grenier P, Cabanis E, Laval-Jeantet M. MR imaging of intravoxel incoherent motions: application to diffusion and perfusion in neurologic disorders. *Radiology* (1986) 161(2):401–7. doi: 10.1148/radiology.161.2.3763909
- Takeuchi M, Sasaki S, Ito M, Okada S, Takahashi S, Kawai T, et al. Urinary bladder cancer: diffusion-weighted MR imaging—accuracy for diagnosing T stage and estimating histologic grade. *Radiology* (2009) 251(1):112–21. doi: 10.1148/radiol.2511080873
- Tekes A, Kamel I, Imam K, Szarf G, Schoenberg M, Nasir K, et al. Dynamic MRI of bladder cancer: evaluation of staging accuracy. *AJR Am J Roentgenol* (2005) 184(1):121–7. doi: 10.2214/ajr.184.1.01840121
- Oki H, Hayashida Y, Oki H, Kakeda S, Aoki T, Taguchi M, et al. DWI findings of autoimmune pancreatitis: comparison between symptomatic and asymptomatic patients. *J Magn Reson Imaging* (2015) 41(1):125–31. doi: 10.1002/jmri.24508
- Dancik GM, Owens CR, Iczkowski KA, Theodorescu D. A cell of origin gene signature indicates human bladder cancer has distinct cellular progenitors. *Stem Cells* (2014) 32(4):974–82. doi: 10.1002/stem.1625
- Lauenstein TC, Sharma P, Hughes T, Heberlein K, Tudorascu D, Martin DR. Evaluation of optimized inversion-recovery fat-suppression techniques for T2-weighted abdominal MR imaging. *J Magn Reson Imaging* (2008) 27(6):1448–54. doi: 10.1002/jmri.21350
- Kirkali Z, Chan T, Manoharan M, Algaba F, Busch C, Cheng L, et al. Bladder cancer: epidemiology, staging and grading, and diagnosis. *Urology* (2005) 66(6 Suppl 1):4–34. doi: 10.1016/j.urol.2005.07.062
- Kang DH, Kim BM, Kim DJ, Suh SH, Kim DII, Kim YS, et al. MR-DWI-positive lesions and symptomatic ischemic complications after coiling of unruptured intracranial aneurysms. *Stroke* (2013) 44(3):789–91. doi: 10.1161/STROKEAHA.112.669853
- Rajesh A, Sokhi HK, Fung R, Mulcahy KA, Bankart MJ. Bladder cancer: evaluation of staging accuracy using dynamic MRI. *Clin Radiol* (2011) 66(12):1140–5. doi: 10.1016/j.crad.2011.05.019
- Saito W, Amanuma M, Tanaka J, Heshiki A. Histopathological analysis of a bladder cancer stalk observed on MRI. *Magn Reson Imaging* (2000) 18(4):411–5. doi: 10.1016/s0730-725x(00)00124-7
- Solomon JP, Hansel DE. Morphologic and Molecular Characteristics of Bladder Cancer. *Surg Pathol Clin* (2015) 8(4):663–76. doi: 10.1016/j.path.2015.07.003
- Kamel IR, Liapi E, Reyes DK, Zahurak M, Bluemke DA, Geschwind JF. Unresectable hepatocellular carcinoma: serial early vascular and cellular changes after transarterial chemoembolization as detected with MR imaging. *Radiology* (2009) 250(2):466–73. doi: 10.1148/radiol.2502072222
- Cipolla V, Santucci D, Guerrieri D, Drudi FM, Meggiorini ML, de Felice C. Correlation between 3T apparent diffusion coefficient values and grading of invasive breast carcinoma. *Eur J Radiol* (2014) 83(12):2144–50. doi: 10.1016/j.ejrad.2014.09.015
- Thust SC, Hassanein S, Bisdas S, Rees JH, Hyare H, Maynard JA, et al. Apparent diffusion coefficient for molecular subtyping of non-gadolinium-enhancing WHO grade II/III glioma: volumetric segmentation versus two-dimensional region of interest analysis. *Eur Radiol* (2018) 28(9):3779–88. doi: 10.1007/s00330-018-5351-0

## FUNDING

This work was supported by the Project of Nanjing health and Family Planning Commission (YKK17089).

**Conflict of Interest:** The authors declare that the research was conducted in the absence of any commercial or financial relationships that could be construed as a potential conflict of interest.

Copyright © 2020 Yuan, Li, Mu, Zhang, Kong, Cheng, Shu, Zhang and Wang. This is an open-access article distributed under the terms of the Creative Commons Attribution License (CC BY). The use, distribution or reproduction in other forums is permitted, provided the original author(s) and the copyright owner(s) are credited and that the original publication in this journal is cited, in accordance with accepted academic practice. No use, distribution or reproduction is permitted which does not comply with these terms.



# Time Difference of Arrival on Contrast-Enhanced Ultrasound in Distinguishing Benign Inflammation From Malignant Peripheral Pulmonary Lesions

Min Tang<sup>1†</sup>, Qianrong Xie<sup>2†</sup>, Jiasi Wang<sup>2†</sup>, Xiaoyu Zhai<sup>3†</sup>, Hong Lin<sup>4</sup>, Xiaoxue Zheng<sup>1</sup>, Guoli Wei<sup>1</sup>, Yan Tang<sup>1</sup>, Fanwei Zeng<sup>1</sup>, Yanpeng Chu<sup>2</sup>, Jianqiong Song<sup>1\*</sup>, Jianqiang Cai<sup>5\*</sup> and Fanxin Zeng<sup>2\*</sup>

## OPEN ACCESS

### Edited by:

Lu Yang,  
Sichuan University, China

### Reviewed by:

Shandong Yu,  
Capital Medical University, China  
Hanxue Zhao,  
Capital Medical University, China

### \*Correspondence:

Jianqiong Song  
2695521198@qq.com  
Jianqiang Cai  
caijianqiang188@sina.com  
Fanxin Zeng  
zengfx@pku.edu.cn

<sup>†</sup>These authors have contributed  
equally to this work

### Specialty section:

This article was submitted to  
Cancer Imaging and  
Image-directed Interventions,  
a section of the journal  
Frontiers in Oncology

Received: 01 July 2020

Accepted: 15 October 2020

Published: 12 November 2020

### Citation:

Tang M, Xie Q, Wang J, Zhai X, Lin H,  
Zheng X, Wei G, Tang Y, Zeng F,  
Chu Y, Song J, Cai J and Zeng F  
(2020) Time Difference of Arrival on  
Contrast-Enhanced Ultrasound  
in Distinguishing Benign  
Inflammation From Malignant  
Peripheral Pulmonary Lesions.  
Front. Oncol. 10:578884.  
doi: 10.3389/fonc.2020.578884

<sup>1</sup> Department of Ultrasound Imaging, Dazhou Central Hospital, Dazhou, China, <sup>2</sup> Department of Clinical Research Center, Dazhou Central Hospital, Dazhou, China, <sup>3</sup> Key Laboratory of Carcinogenesis and Translational Research (Ministry of Education/Beijing), Department of Thoracic Medical Oncology, Peking University Cancer Hospital and Institute, Beijing, China, <sup>4</sup> Department of Public Health Information, Sichuan Center for Disease Control and Prevention, Chengdu, China, <sup>5</sup> Department of Hepatobiliary Surgery, National Cancer Center/Cancer Hospital, Chinese Academy of Medical Sciences and Peking Union Medical College, Beijing, China

**Introduction:** Worldwide, the incidence and mortality of lung cancer are at the highest levels, and the most lesions are located in the lung periphery. Despite extensive screening and diagnosis, the pathologic types of peripheral pulmonary lesions (PPLs) are difficult to diagnose by noninvasive examination. This study aimed to identify a novel index—time difference of arrival (TDOA)—to discriminate between benign inflammation and malignant PPLs.

**Methods:** Using contrast-enhanced ultrasound (CEUS), we retrospectively analyzed 96 patients with PPLs who had undergone biopsy to confirm the pathologic types. All data were collected from Dazhou Central Hospital between December 2012 and July 2019. The parameters of CEUS were analyzed by two assistant chief physicians of ultrasound diagnosis. Area under the receiver operating characteristic curve analysis, sensitivity, specificity, positive predictive value, and negative predictive value were calculated to assess the diagnostic ability of different indices.

**Results:** We found that the TDOA significantly distinguished benign inflammation from malignant lesions. The TDOA was markedly increased in patients with malignant lesions than benign inflammation lesions ( $P < 0.001$ ). Compared with conventional time-intensity curve (TIC) indices, TDOA showed high diagnostic accuracy (area under the curve = 0.894). Moreover, conventional diagnostic indices did not affect the diagnostic performance of TDOA by adjusting the receiver operating characteristic curve.

**Conclusion:** TDOA is feasible for the diagnosis of benign inflammation and malignant PPLs.

**Keywords:** contrast-enhanced ultrasound, peripheral pulmonary lesions, time difference of arrival, benign inflammation lesions, malignant lesions



## INTRODUCTION

Lung cancer is one of the most common malignant tumors in the world with the highest incidence and mortality (1). According to the location of the tumor, lung cancer is divided into central type and peripheral type. Peripheral lung cancer accounts for about 70% of all lung cancer types and is difficult to be diagnosed with no obvious symptoms (2). The 5-year survival rate of lung cancer is about 70%–90% in the early stage (3–5), but approximately 75% patients are first diagnosed only in an advanced stage (6).

Common clinical methods such as dynamic contrast-enhanced magnetic resonance imaging (7), contrast-enhanced computed tomography (8, 9), low-dose computed tomography (10), and bronchoscopy (11) are used to diagnose the lung lesions. However, these methods have obvious diagnostic shortcomings, such as exposure to heavy dose of radiation (12), high cost (13, 14), and high false positive rates (15, 16). Some studies also have shown that the diagnostic capability of bronchoscopy is significantly reduced because of the increase in distance from the hilum and the small volume of tumor (17–19). Therefore, it is essential to improve the current screening and diagnostic ability.

Peripheral pulmonary lesions (PPLs) are close to the pleura, which can be easily detected by ultrasound. Contrast-enhanced ultrasound (CEUS) is a novel technique for real-time observation of disease states by using microbubble-based contrast agents (20, 21). CEUS has found application in many conditions such as myocardial inflammation (22), type I diabetes (23), carotid plaque (24), chronic kidney disease (25), and metastatic liver disease (9). A previous study has showed that the wash-in slope, time to peak intensity (TTP) and mean

transit time (MTT) analyzed by CEUS can be used to distinguish the difference between malignant thoracic injuries and benign lesions (26). However, the low sensitivity and specificity of these conventional parameters for diagnosing PPLs by time intensity curves (TICs) analysis limits the application of CEUS.

In this study, we aimed to identify a novel index to diagnose the PPLs. For this purpose, we systematically analyzed the clinical data of 96 patients with PPLs and evaluated the efficacy of using time difference of arrival (TDOA) to distinguish between benign inflammation and malignant lesions.

## MATERIALS AND METHODS

### Patients

We retrospectively analyzed 324 patients with PPLs who had undergone CEUS and biopsy or histopathologic examination in our hospital between December 2012 and July 2019. The inclusion criteria were as follows: i) Age from 18 to 85 years old; ii) With contrast ultrasound and biopsy or histopathologic examination; iii) Under contrast conditions, all patients with peripulmonary lesions significantly enhanced after contrast-enhanced ultrasound compared with those without contrast medium injection were hypervascular lesions. The exclusion criteria were as follows: i) Patients with bleeding tendency, severe cardiac insufficiency, pulmonary hypertension, aortic aneurysm, mental disorders, and other causes of pulmonary insufficiency; ii) Patients allergic to contrast media, with poor physical condition and not cooperating with researchers. All patients were diagnosed by biopsy. 96 patients of them were

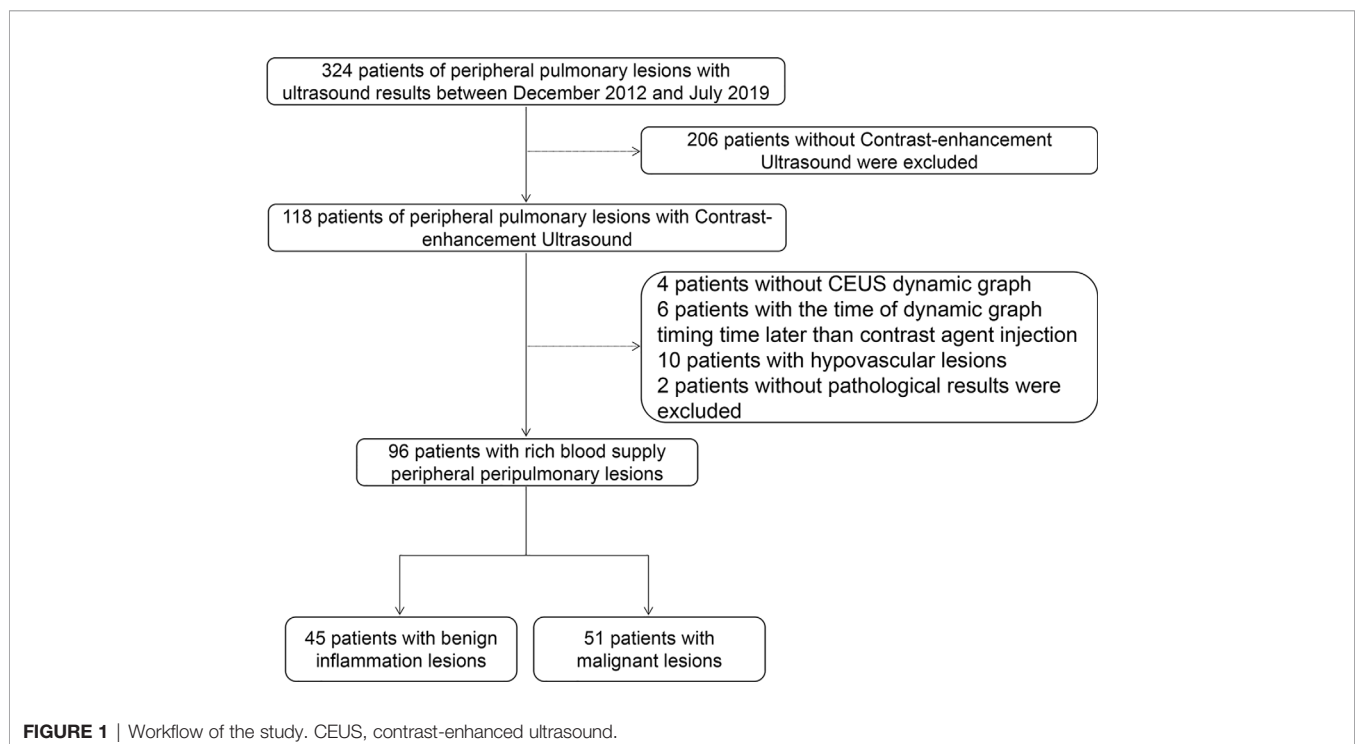


**TABLE 1 |** Characteristics of 96 patients with peripheral pulmonary lesions.

	Benign inflammation lesions (N = 45)	Malignant lesions (N = 51)
Male gender, n (%)	32 (71.1)	39 (76.5)
Age, year, mean (SE)	59.5 (2.18)	63.9 (1.01)
Left lung, n (%)	22 (48.9)	31 (60.8)
Smoking, n (%)		
Current/Former	26 (57.8)	33 (64.7)
Never	18 (40.0)	17 (33.3)
Unclearly	1 (2.22)	1 (1.96)
Alcohol consumption, n (%)		
Never	21 (46.7)	25 (49.0)
Frequently/Occasionally	22 (48.9)	25 (49.0)
Unclearly	2 (4.4)	1 (1.96)
Medical history, n (%)		
Hypertension	7 (15.6)	7 (13.7)
Diabetes	4 (8.89)	4 (7.84)
Pulmonary diseases	4 (8.89)	4 (7.84)
Malignant tumors	1 (2.22)	3 (5.88)
Pathologic types, n (%)		
Nonspecific inflammation	37 (82.2)	—
Specific inflammation	8 (17.8)	—
Squamous cell carcinoma	—	23 (45.1)
Adenocarcinoma	—	21 (41.2)
Other	0	7 (13.7)

SE, standard error. There was no significant difference among the groups ( $P > 0.05$ ).

included in this study and their ages ranged from 20 to 85 years (**Figure 1, Table 1**). Of the 96 patients, 45 had benign inflammation lesions: 37 (82.2%) and eight (17.8%) cases of nonspecific and specific inflammation, respectively. The remaining 51 patients had malignant lesions: 23 (45.1%) cases of squamous cell carcinoma and 21 (41.2%) of adenocarcinoma; the remaining seven (13.7%) patients had other malignancies. Patients were predominantly male (71.1% in the benign inflammation lesions group and 76.5% in the malignant lesions group). Left lung lesions accounted for 48.9% and 60.8% lesions in the benign inflammation and malignant lesions groups, respectively. There were no significant differences in demographic characteristics between the benign inflammation and malignant lesions groups (**Table 1**). The study was approved by the ethics committee of Dazhou Central Hospital (IRB00000003-19008).

## Analysis of CEUS Parameters

A LOGIQ-E9 color Doppler ultrasonic diagnostic apparatus equipped with CEUS software, TIC analysis software, and a 3.5–5 MHz probe (GE Healthcare, Milwaukee, WI) were used in this study. The contrast agent for injection was white powder sulfur hexafluoride microbubble (SonoVue) for injection (Bracco SpA, Milan, Italy). Five milliliters physiological saline (0.9% NaCl) was added and agitated to form a microbubble suspension. We used conventional ultrasound to observe the size of the lesion, internal echo, and blood flow. Then, we placed the largest section of the lesion in the center of the display to initiate a double-contrast CEUS mode. Briefly,

2.4 mL sulfur hexafluoride microbubble suspensions were rapidly injected *via* the elbow vein, followed by a rapid bolus injection of 5 mL normal saline. The built-in timer of the ultrasound instrument was activated and observed for 3 min. All images were stored and analyzed.

Two assistant chief physicians with 5 years' experience in ultrasound diagnosis who were blinded to the pathological diagnosis of the patient, observed the filling characteristics of the contrast agent in the lesion and performed the CEUS analysis together and reached an agreement. First, we observed the blood supply in the mass and the area where the large vessels were located, distinguished the active area from the necrotic area, traced the real part of the lesion and the adjacent lung tissue as the regions of interest (ROI), and ensured the same ROI in each depiction. Then, the TIC software that comes with the LOGIQ-E9 color Doppler ultrasound was used to quantitatively analyze the arrival time (AT) of the lesion and adjacent lung tissues. Next, we obtained the values TDOA (in triplicate) of time difference between the AT of the lesion and adjacent lung tissue (=lesion contrast agent AT-adjacent lung tissue contrast agent AT), TTP, initial intensity (II), peak intensity (PI), area under the curve (AUC), rake ratio (K), mean square error (MSE), and curve gradient and calculated the average. After the analysis, the receiver operating characteristic (ROC) curve of adjacent lung tissue, lesion contrast agent AT and TDOA were drawn. The Youden's index was calculated to determine the best cut-off point of lesion AT and adjacent lung tissue time difference. If the arrival time was greater than the best cut-off point, the lesion was considered malignant; otherwise, it was considered benign inflammation.

## Puncture Biopsy

A physician with > 5 years' experience performed the ultrasound biopsy of all patients. Infection markers, bleeding, and coagulation time of patients were required to be normal. The blood supply and large vessels in the mass were observed, and the puncture point was located in the area with blood supply but not large vessels. During the operation, the puncture point was fixed, the distance from the sampling point in the mass was measured, the puncture area was disinfected with iodine tincture, and the puncture point was anesthetized with 2% lidocaine for local infiltration. Next, under the guidance of contrast-enhanced ultrasound, an 18G automatic biopsy gun was used for subcutaneous penetration. The obtained specimens were fixed in 10% formaldehyde solution and sent for pathological examination.

## Statistical Analysis

Quantitative data were expressed as mean (standard error [SE]), and the difference between groups was analyzed by student's *t*-test. The categorical data were expressed as numerical percentages. When theoretical frequency  $1 \leq N < 5$ , continuous correction chi-square test was used, and Pearson chi-square test was used for all theoretical frequencies  $n > 5$ . The sensitivity and specificity of the optimal cut-off point were calculated from the area under the

ROC curve. The ROC curve constructed from logistic regression and the ROC-AUC difference was analyzed by the DeLong's test.  $P < 0.05$  was considered statistically significant. All the statistical methods were two tailed. The free degree of  $t$ -test for age, long diameter, and arrival time was 94, while the free degree of  $t$ -test for other parameters produced by the TIC analysis was 80.

## RESULTS

### Ultrasound Characteristics

The mean long diameter was 5.54 cm for the benign inflammation lesions group and 7.71 cm for the malignant lesions group ( $P < 0.001$ ). Benign inflammation lesions were mainly wedge shaped, while malignant lesions were mainly spherical ( $P < 0.001$ ). However, the conventional two-dimensional ultrasound indicators were not specific enough for the differential diagnosis of benign inflammation and malignant lesions. In this study, the PI, II, TTP, AUC, K, MSE, and gradient values could only be obtained from 34 and 48 patients with benign inflammation and malignant lesions, respectively. Furthermore, we found that the perfusion method, TTP, and PI produced by CEUS also showed no difference between the benign inflammation and malignant lesions groups ( $P > 0.05$ ) (Table 2).

**TABLE 2 |** CEUS parameters of 96 patients with peripheral pulmonary lesions.

	Benign inflammation lesions (N = 45)	Malignant lesions (N = 51)	P-value
Two-dimensional ultrasound			
Long diameter (cm), mean (SE)	5.54 (0.26)	7.71 (0.40)	< 0.001
Lesion shape, n (%)			< 0.001
Wedge	26 (57.8)	4 (7.84)	
Irregular	14 (31.1)	20 (39.2)	
Spherical	5 (11.1)	27 (52.9)	
Bronchial tree sign, n (%)	7 (15.6)	6 (11.8)	0.59
CEUS			
Perfusion method, n (%)			0.22
Even perfusion	26 (57.8)	23 (45.1)	
Perfusion defect	19 (42.2)	28 (54.9)	
TIC analysis, mean (SE)			
Lesion AT (s)	5.54 (0.44)	8.69 (0.51)	< 0.001
Adjacent lung tissue AT (s)	4.45 (0.38)	4.65 (0.38)	0.71
Time difference of arrival (s)	1.09 (0.20)	4.03 (0.29)	< 0.001
Peak intensity (dB) <sup>a</sup>	23.8 (1.29)	22.3 (1.03)	0.34
Initial intensity (dB) <sup>a</sup>	-66.9 (4.30)	-66.8 (2.99)	0.99
Time to peak (s) <sup>a</sup>	17.5 (2.14)	14.5 (1.49)	0.24
Area under the curve <sup>a</sup>	1895 (88.9)	1802 (74.6)	0.42
Rake ratio <sup>a</sup>	4.50 (0.47)	4.59 (0.42)	0.88
Mean-square error <sup>a</sup>	9.41 (1.22)	7.81 (0.75)	0.24
Gradient <sup>a</sup>	1.89 (0.19)	2.05 (0.16)	0.52

<sup>a</sup>Only 34 benign inflammation lesion patients and 48 malignant lesion patients had the peak intensity, initial intensity, time to peak, area under the curve, rake ratio, mean-square error and gradient value.

CEUS, contrast-enhanced ultrasound; TIC, time-intensity curve; AT, arrival time.

### Diagnostic Performance Comparison of Arrival Time

Based on TIC analysis, we generated the lesion AT, adjacent lung tissue AT, and a novel method of TDOA. The lesion AT and TDOA in the benign inflammation lesions group was shorter than those of the malignant lesions group ( $P < 0.001$ ), but there was no difference in the adjacent lung tissue AT between both groups (Figure 2 and Figure S1). TDOA had the largest area under the curve (AUC, 0.894), compared with the lesion arrival time (AUC, 0.785) and adjacent lung tissue arrival time (AUC, 0.495) (Figure 3). The optimal cut-off value of TDOA was 2.42 s. The sensitivity and specificity of TDOA were 86.3% (95% CI: 76.5–94.1) and 88.9% (95% CI: 80.0–97.8), respectively. Positive predictive value (PPV) and negative predictive value (NPV) were 85.1% (95% CI: 71.7–93.8) and 89.8% (95% CI: 77.8–96.6), respectively (Table 3). The PPV and NPV of TDOA were higher than the lesion AT and adjacent lung tissue AT.

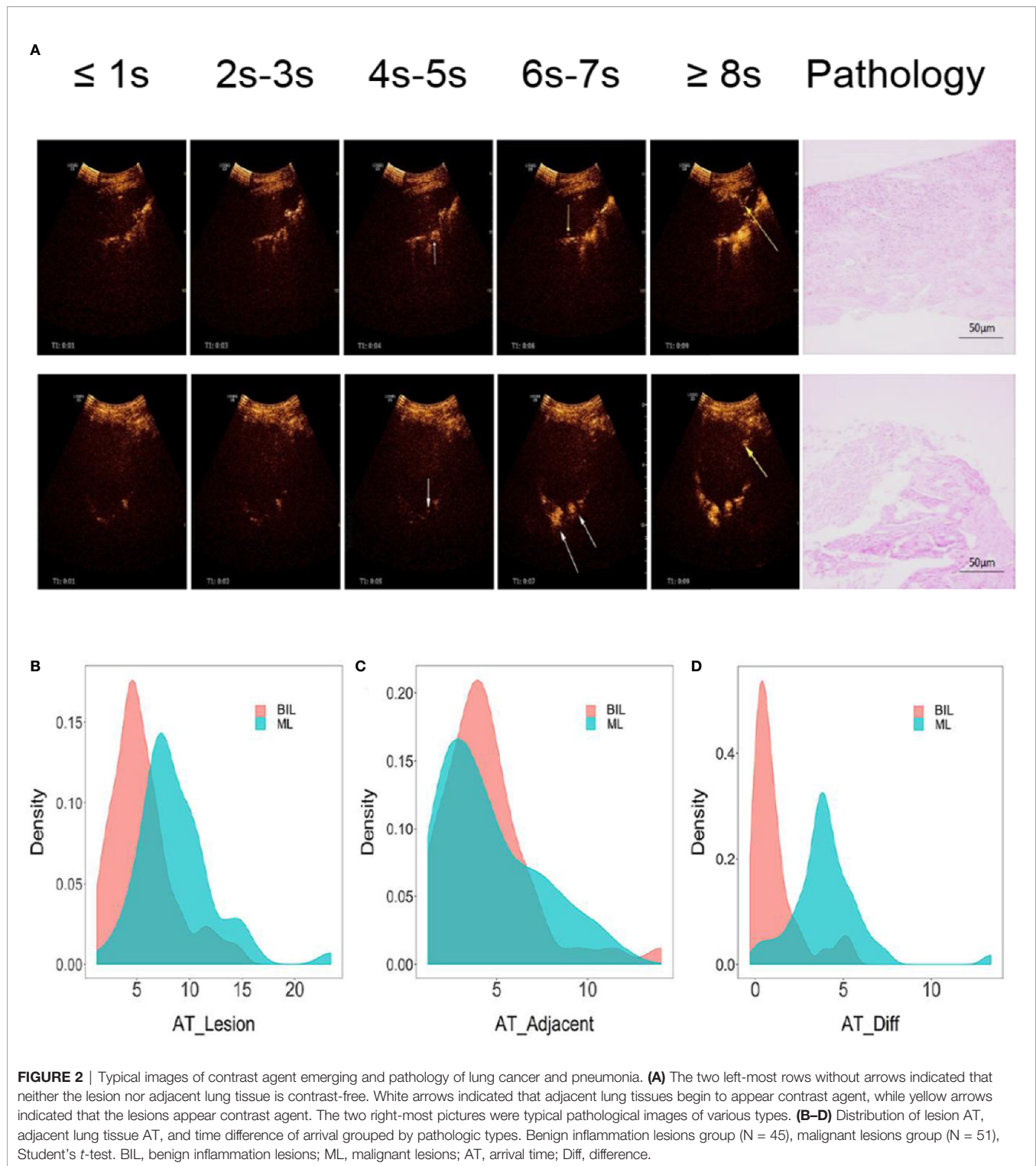
### ROC Curve of TDOA Adjusted by the Index of Patients

To evaluate whether other CEUS parameters or clinical information affected the prediction performance of TDOA, we used different indicators to adjust the ROC curve. The adjusted ROC curve showed that other indicators such as age or TTP did not affect the diagnostic performance of TDOA (Figure 4 and Figure S2). Next, we investigated the role of AT in the subgroup analysis. The results showed that the lesion AT and adjacent lung tissue AT could not distinguish between non-specific and specific inflammation. Significantly, TDOA could differentiate between the two groups well (Figure S3). However, all AT parameters did not distinguish between squamous cell carcinoma and adenocarcinoma (Figure S4).

## DISCUSSION

Although many imaging technologies have been used to diagnose the PPLs, there are considerable limitations, especially in terms of diagnostic capability (17), cost (13), and radiation exposure (12), which pose challenges to PPLs diagnosis. In this study, we identified a novel method for the differential diagnosis of benign inflammation and malignant PPLs using TDOA produced by CEUS. Our results showed that the TDOA was significantly increased in the malignant lesions group than the benign inflammation lesions group. Notably, conventional diagnostic parameters did not affect the diagnostic performance of TDOA.

Previous study has indicated that CEUS divides the arterial phases into pulmonary and bronchial in the PPLs, and the pulmonary artery phase is slightly earlier than the bronchial artery phase (27). In this study, we found that the TDOA of the malignant lesions group (4.03 s) was significantly longer than the benign inflammation lesions group (1.09 s). This finding is



supported by previous studies that showed that the blood supply of malignant tumors mainly originates from the bronchial artery, while the blood supply of non-neoplastic pulmonary lesions comes from the pulmonary and bronchial arteries (28).

A large body of evidence has debated the value of CEUS in diagnosing lung diseases (29, 30). We found that TDOA produced by CEUS could well distinguish between benign inflammation and malignant lesions (AUC: 0.894). In addition,



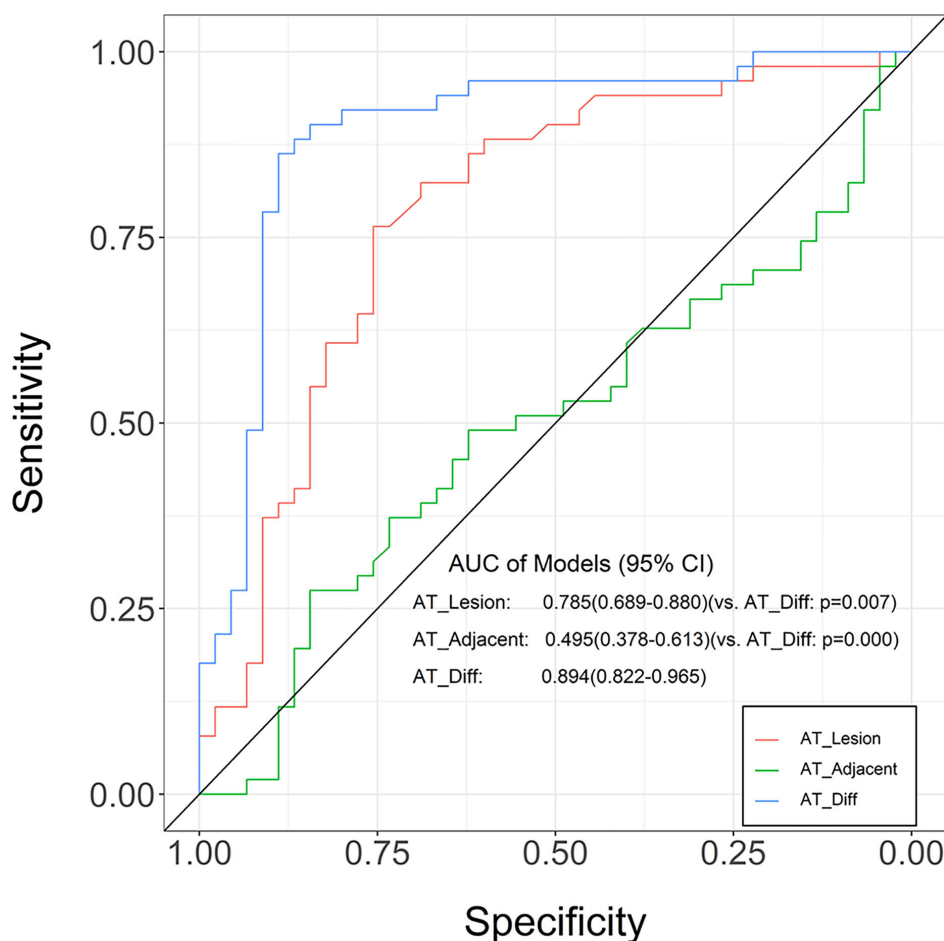


**FIGURE 3 |** Receiver operating characteristic (ROC) curves for the lung tissue AT, lesion AT, and time difference of arrival in distinguishing between benign inflammation and malignant lesions. Compared with adjacent lung tissue AT and lesion AT, the time difference of arrival was greater in AUC. The ROC curve is expressed by diagnostic sensitivity and specificity. AT, arrival time; Diff, difference.

**TABLE 3 |** Diagnostic performance of lesion AT, adjacent lung tissue AT, and time difference of arrival in benign inflammation lesions and malignant lesions group.

Items	AT_Lesion	AT_Adjacent	AT_Diff
AUC	0.785 (0.689–0.880)	0.495 (0.378–0.613)	0.894 (0.822–0.965)
Cut-off (s)	6.55	2.48	2.42
Sensitivity (%) (95% CI)	76.5 (64.7–86.3)	27.5 (15.7–39.2)	86.3 (76.5–94.1)
Specificity (%) (95% CI)	75.6 (64.4–88.9)	84.4 (73.3–95.6)	88.9 (80.0–97.8)
PPV (%) (95% CI)	73.9 (58.9–85.7)	33.3 (14.6–57.0)	85.1 (71.7–93.8)
NPV (%) (95% CI)	78.0 (64.0–88.5)	49.3 (37.6–61.1)	89.8 (77.8–96.6)

AUC, area under the curve; PPV, positive predictive value; NPV, negative predictive value; CI, confidence interval; AT, arrival time; Diff, difference.

compared to the lesion AT, the TDOA excluded the influence of the patient's heart function (31), blood supply status of the lesion area, and injection rate of the contrast agent (26). In our study, the TDOA had a higher sensitivity and specificity than the lesion AT and the adjacent lung tissue AT. Based on TIC analysis, we generated many parameters such as TTP. No significant

differences were found between the benign inflammation and malignant lesions group (**Table 2**). Our findings are distinct from previously reported data on the role of TTP (26). These results suggested that the diagnostic performance of TDOA was better than the conventional parameters. Furthermore, our results showed that there was no significant difference between the



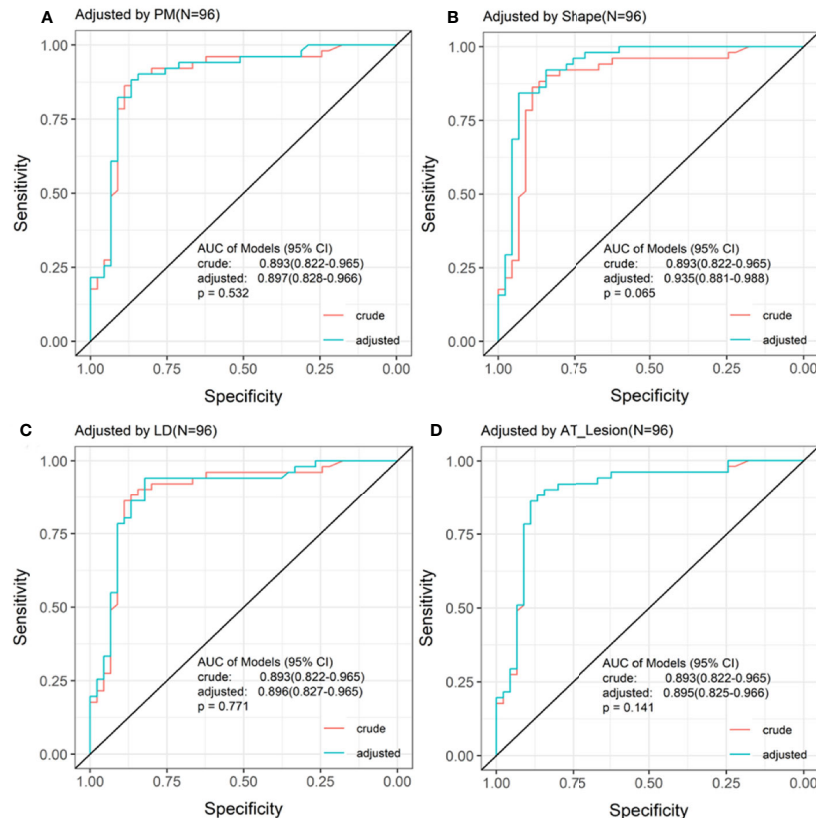


**FIGURE 4 |** Receiving operating characteristic (ROC) curve adjusted by the indices of patients. The ROC curve adjusted by the top four different indices for patients. There was no significant difference between crude ROC and adjusted ROC curve. AT, arrival time; PM, perfusion method.

crude and adjusted ROC curve, indicating that other indicators did not affect the diagnostic performance of TDOA.

Our study has some limitations. First, it was a single-center study and the number of patients was relatively small. Second, the major type of benign lesions were inflammation. More pathologic types of benign lesions are required to validate the applicability of TDOA. Last, it was a retrospective study.

## CONCLUSIONS

We systemically analyzed and validated TDOA produced by CEUS to distinguish between benign inflammation and malignant PPLs with high diagnostic accuracy. These findings showed that the TDOA could be a feasible, sensitive, and specific method to diagnose PPLs.

## DATA AVAILABILITY STATEMENT

The raw data supporting the conclusions of this article will be made available by the authors, without undue reservation.

## ETHICS STATEMENT

The study was approved by the Ethics Committee of Dazhou Central Hospital (IRB00000003-19008). The Ethics Committee waived the need for patients to sign informed consent.

## AUTHOR CONTRIBUTIONS

FXZ designed the study, revised the manuscript, and the figure. MT analyzed the CEUS parameters. QX drafted the manuscript and analyzed the data. JW analyzed the data. XYZ and JC revised the manuscript. HL collected the clinical characteristics and information. XXZ collected the clinical characteristics and information. GW analyzed the TICs. YT analyzed the TICs. FWZ organized the basic data. YC revised the manuscript and organized the basic data. JS recruited patients with PPLs and collected the clinical characteristics and information. All authors contributed to the article and approved the submitted version.

## FUNDING

This study was funded by the National Natural Science Foundation of China (81902861), “Xinglin Scholars” Scientific Research Project

Fund of Chengdu university of traditional Chinese medicine (YYZX2019012), the Scientific Research Fund of Technology Bureau in Dazhou (17YYJC0004, 17YYJC0001), Key Research and Development Project Fund of Science and Technology Bureau in Dazhou, Sichuan Province (20ZDYF0001).

## REFERENCES

- Bray F, Ferlay J, Soerjomataram I, Siegel RL, Torre LA, Jemal A. Global cancer statistics 2018: GLOBOCAN estimates of incidence and mortality worldwide for 36 cancers in 185 countries. *CA Cancer J Clin* (2018) 68:394–424. doi: 10.3322/caac.21492
- Akata S, Yoshimura M, Nishio R, Park J, Saito K, Uchida O, et al. High-resolution computed tomographic findings of small peripherally located squamous cell carcinoma. *Clin Imaging* (2008) 32:259–63. doi: 10.1016/j.clinimag.2007.10.002
- Shah R, Sabanathan S, Richardson J, Mearns AJ, Goulden C. Results of surgical treatment of stage I and II lung cancer. *J Cardiovasc Surg (Torino)* (1996) 37:169–72.
- Nesbitt JC, PJ Jr., Walsh GL, Roth JA, Mountain CF. Survival in early-stage non-small cell lung cancer. *Ann Thorac Surg* (1995) 60:466–72. doi: 10.1016/0003-4975(95)00169-L
- Goldstraw P, Rami-Porta R, Asamura H, Ball D, Beer DG, Beyruti R, et al. The IASLC Lung Cancer Staging Project: Methodology and Validation Used in the Development of Proposals for Revision of the Stage Classification of NSCLC in the Forthcoming (Eighth) Edition of the TNM Classification of Lung Cancer. *J Thorac Oncol* (2016) 11:1433–46.
- Mountain CF. Revisions in the International System for Staging Lung Cancer. *Chest* (1997) 111:1710–7. doi: 10.1378/chest.111.6.1710
- Kono R, Fujimoto K, Terasaki H, Muller NL, Kato S, Sadohara J, et al. Dynamic MRI of solitary pulmonary nodules: comparison of enhancement patterns of malignant and benign small peripheral lung lesions. *AJR Am J Roentgenol* (2007) 188:26–36. doi: 10.2214/AJR.05.1446
- Chu ZG, Sheng B, Liu MQ, Lv FJ, Li Q, Ouyang Y. Differential Diagnosis of Solitary Pulmonary Inflammatory Lesions and Peripheral Lung Cancers with Contrast-enhanced Computed Tomography. *Clinics (Sao Paulo)* (2016) 71:555–61. doi: 10.6061/clinics/2016/10/01
- Dietrich CF, Kratzer W, Strobe D, Danse E, Fessl R, Bunk A, et al. Assessment of metastatic liver disease in patients with primary extrahepatic tumors by contrast-enhanced sonography versus CT and MRI. *World J Gastroenterol* (2006) 12:1699–705. doi: 10.3748/wjg.v12.i11.1699
- National Lung Screening Trial Research T, Aberle DR, Adams AM, Berg CD, Black WC, Clapp JD, et al. Reduced lung-cancer mortality with low-dose computed tomographic screening. *N Engl J Med* (2011) 365:395–409. doi: 10.1056/NEJMoa102873
- Greenhill SR, Kovitz KL. *Flexible Bronchoscopy*. 3rd ed. The United States of America: Wiley-Blackwell (2012).
- Salminen E, Niiniviita H, Järvinen H, Heinävaara SJAR. Cancer Death Risk Related to Radiation Exposure from Computed Tomography Scanning Among Testicular Cancer Patients. *Anticancer Res* (2017) 37:831–4. doi: 10.21873/anticancer.11385
- Nordin AB, Sales S, Nielsen JW, Adler B, Bates DG, Kenney B. Standardized ultrasound templates for diagnosing appendicitis reduce annual imaging costs. *J Surg Res* (2018) 221:77–83. doi: 10.1016/j.jss.2017.07.002
- Meier-Schroers M, Homs R, Gieseke J, Schild HH, Thomas D. Lung cancer screening with MRI: Evaluation of MRI for lung cancer screening by comparison of LDCT- and MRI-derived Lung-RADS categories in the first two screening rounds. *Eur Radiol* (2019) 29:898–905. doi: 10.1007/s00330-018-5607-8
- Pinsky PF, Bellinger CR, Miller DP. False-positive screens and lung cancer risk in the National Lung Screening Trial: Implications for shared decision-making. *J Med Screen* (2017) 25:110–2. doi: 10.1177/0969141317727771
- Shen H. Low-dose CT for lung cancer screening: opportunities and challenges. *Front Med* (2017) 12:116–21. doi: 10.1007/s11684-017-0600-1
- Baaklini WA, Reinoso MA, Gorin AB, Sharafkaneh A, Manian P. Diagnostic yield of fiberoptic bronchoscopy in evaluating solitary pulmonary nodules. *Chest* (2000) 117:1049–54. doi: 10.1378/chest.117.4.1049
- Schreiber G, McCrory DC. Performance characteristics of different modalities for diagnosis of suspected lung cancer: summary of published evidence. *Chest* (2003) 123:115S–28S. doi: 10.1378/chest.123.1\_suppl.115S
- Dhillon SS, Harris K. Bronchoscopy for the diagnosis of peripheral lung lesions. *J Thorac Dis* (2017) 9:S1047–58. doi: 10.21037/jtd.2017.05.48
- Schneider A, Johnson L, Goodwin M, Schelleman A, Bellomo R. Bench-to bedside review: contrast enhanced ultrasonography—a promising technique to assess renal perfusion in the ICU. *Crit Care* (2011) 15:157. doi: 10.1186/cc10058
- Correas JM, Bridal L, Lesavre A, Mejean A, Claudon M, Helenon O. Ultrasound contrast agents: properties, principles of action, tolerance, and artifacts. *Eur Radiol* (2001) 11:1316–28. doi: 10.1007/s003300100940
- Stein DC, Xu L, Khanicheh E, Ellersdottir E, Ochoa-Espinosa A, Mitterhuber M, et al. Noninvasive Contrast-Enhanced Ultrasound Molecular Imaging Detects Myocardial Inflammatory Response in Autoimmune Myocarditis. *Circ Cardiovasc Imaging* (2016) 9:e004720. doi: 10.1161/CIRCIMAGING.116.004720
- St Clair JR, Ramirez D, Passman S, Benninger RKP. Contrast-enhanced ultrasound measurement of pancreatic blood flow dynamics predicts type 1 diabetes progression in preclinical models. *Nat Commun* (2018) 9:1742. doi: 10.1038/s41467-018-03953-y
- Nakamura J, Nakamura T, Deyama J, Fujioka D, Kawabata K, Obata JE, et al. Assessment of carotid plaque neovascularization using quantitative analysis of contrast-enhanced ultrasound imaging is useful for risk stratification in patients with coronary artery disease. *Int J Cardiol* (2015) 195:113–9. doi: 10.1016/j.ijcard.2015.05.107
- Cao W, Cui S, Yang L, Wu C, Liu J, Yang F, et al. Contrast-Enhanced Ultrasound for Assessing Renal Perfusion Impairment and Predicting Acute Kidney Injury to Chronic Kidney Disease Progression. *Antioxid Redox Signal* (2017) 27:1397–411. doi: 10.1089/ars.2017.7006
- Qureshi NR, Hintze C, Risse F, Kopp-Schneider A, Eberhardt R, Kauczor HU, et al. The feasibility of low mechanical index contrast enhanced ultrasound (CEUS) in distinguishing malignant from benign thoracic lesions. *Ultrasound Med Biol* (2011) 37:1747–54. doi: 10.1016/j.ultrasmedbio.2011.08.003
- Hong-Xia Z, Wen H, Ling-Gang C, Wen-Jia C, Shuo L, Li-Juan D, et al. New Method for Discriminating between Bronchial and Pulmonary Arterial Phases using Contrast-Enhanced Ultrasound. *Ultrasound Med Biol* (2016) 42:1441–9. doi: 10.1016/j.ultrasmedbio.2016.01.029
- Eldridge L, Moldobaeva A, Zhong Q, Jenkins J, Snyder M, Brown RH, et al. Bronchial Artery Angiogenesis Drives Lung Tumor Growth. *Cancer Res* (2016) 76:5962–9. doi: 10.1158/0008-5472.CAN-16-1131
- Yin S, Cui Q, Wang S, Fan Z, Yan K. Analysis of Contrast-Enhanced Ultrasound Perfusion Patterns and Time-Intensity Curves for Metastatic Lymph Nodes From Lung Cancer: Preliminary Results. *J Ultrasound Med* (2018) 37:385–95. doi: 10.1002/jum.14345
- Sperandeo M, Rea G, Grimaldi MA, Trovato F, Dimitri LM, Carnevale V. Contrast-enhanced ultrasound does not discriminate between community acquired pneumonia and lung cancer. *Thorax* (2017) 72:178–80. doi: 10.1136/thoraxjnl-2016-208913
- Dietrich CF, Averkiou MA, Correas JM, Lassau N, Leen E, Piscaglia F. An EFSUMB introduction into Dynamic Contrast-Enhanced Ultrasound (DCE-US) for quantification of tumour perfusion. *Ultraschall Med* (2012) 33:344–51. doi: 10.1055/s-0032-1313026

## SUPPLEMENTARY MATERIAL

The Supplementary Material for this article can be found online at: <https://www.frontiersin.org/articles/10.3389/fonc.2020.578884/full#supplementary-material>

**Conflict of Interest:** The authors declare that the research was conducted in the absence of any commercial or financial relationships that could be construed as a potential conflict of interest.

Copyright © 2020 Tang, Xie, Wang, Zhai, Lin, Zheng, Wei, Tang, Zeng, Chu, Song, Cai and Zeng. This is an open-access article distributed under the terms of the Creative Commons Attribution License (CC BY). The use, distribution or reproduction in other forums is permitted, provided the original author(s) and the copyright owner(s) are credited and that the original publication in this journal is cited, in accordance with accepted academic practice. No use, distribution or reproduction is permitted which does not comply with these terms.



# Comparison of Diagnostic Performance of Five Different Ultrasound TI-RADS Classification Guidelines for Thyroid Nodules

Ruoning Yang<sup>1,2†</sup>, Xiuhe Zou<sup>3†</sup>, Hao Zeng<sup>1</sup>, Yunuo Zhao<sup>1</sup> and Xuelei Ma<sup>1\*</sup>

<sup>1</sup> Department of Biotherapy, State Key Laboratory of Biotherapy, West China Hospital, Cancer Center, Sichuan University, Chengdu, China, <sup>2</sup> West China Hospital, West China School of Medicine, Sichuan University, Chengdu, China, <sup>3</sup> Department of Thyroid Surgery, West China Hospital of Sichuan University, Chengdu, China

## OPEN ACCESS

### Edited by:

Changqiang Wu,  
North Sichuan Medical College, China

### Reviewed by:

Nan Song,  
Capital Medical University, China  
Wuteng Cao,  
The Sixth Affiliated Hospital of Sun  
Yat-sen University, China

### \*Correspondence:

Xuelei Ma  
drmaxuelei@gmail.com

<sup>†</sup>These authors have contributed  
equally to this work

### Specialty section:

This article was submitted to  
Cancer Imaging and  
Image-directed Interventions,  
a section of the journal  
Frontiers in Oncology

**Received:** 24 August 2020

**Accepted:** 15 October 2020

**Published:** 16 November 2020

### Citation:

Yang R, Zou X, Zeng H, Zhao Y and  
Ma X (2020) Comparison of Diagnostic  
Performance of Five Different  
Ultrasound TI-RADS Classification  
Guidelines for Thyroid Nodules.  
Front. Oncol. 10:598225.  
doi: 10.3389/fonc.2020.598225

**Objectives:** We aimed to evaluate and compare the diagnostic performance of five ultrasound thyroid imaging reporting and data system (TI-RADS) classification guidelines for thyroid nodules through a review and meta-analysis.

**Methods:** We searched for relevant studies before February 2020 in PubMed. Then we pooled the sensitivity, specificity, likelihood ratios, diagnostic odds ratios, and area under the summary receiver operating characteristic curves. And the diagnostic odds ratios were used to compare the performance.

**Results:** We totally included 19 studies with 4,696 lesions in this research. The pooled sensitivity of American College of Radiology (ACR) guidelines, American Thyroid Association (ATA) guidelines, TI-RADS proposed by Kwak (Kwak TI-RADS), Korean Thyroid Association/Korean Society of Thyroid Radiology (KTA/KSThR) guidelines for malignancy risk and European Thyroid Association (ETA) guidelines is between 0.84 and 0.94. The pooled specificity is 0.68, 0.44, 0.62, 0.47, and 0.61, respectively. And the RDOR is 1.57 (ACR vs ATA), 1.37 (ACR vs ETA), 1.80 (ACR vs Kwak), 1.74 (ARC vs KTA).

**Conclusions:** The results suggest that five classification guidelines are all effective methods for differential diagnosis of benign and malignant thyroid nodules and ACR guideline is a better choice.

**Keywords:** thyroid nodule, meta-analysis, TI-RADS, ultrasound, malignancy, diagnostic performance

## INTRODUCTION

Thyroid nodules are easily found in the general population, especially in women (1), and about 10% of patients with thyroid nodules are at risk of malignancy, and the percentage keeps going up (2, 3). Malignant nodules and benign nodules are treated in completely different ways. It's still a big challenge for clinicians to rule out malignancy of the thyroid nodules. At present, ultrasound is a primary, cheap, noninvasive, fast, and valuable tool to identify the thyroid nodules. For suspected thyroid nodules, a surgery or fine-needle aspiration cytology (FNAC) is recommended (4). Benign and malignant nodules have some similar ultrasound features from modulation to size. The ultrasound diagnosis varies with the

experience of radiologists, and operators, image acquisition and interpretation are subjective which can easily lead to misdiagnosis or overtreatment (5).

To conduct an objective detection, the thyroid imaging reporting and data system (TI-RADS) was proposed, which is used to classify thyroid nodules and recommend further treatment (6). Nowadays, there are five common classification systems used in clinic. Among the guidelines, the American College of Radiology (ACR) guidelines, the Korean Thyroid Association/Korean Society of Thyroid Radiology (KTA/KSThR) guidelines, and the European Thyroid Association (ETA) guidelines are recommended by the radiological association, and the American Thyroid Association (ATA) guidelines are in clinical guidelines (1, 7–9).

Although these five guidelines prove to be effective in managing thyroid nodules, there are no guidelines based on a lot of reliable data to prove which is the best (10). And many clinical trials in progress are used to compare their effectiveness, but these results are biased. The primary purpose of this research is to compare the diagnostic effectivity of the five guidelines for thyroid nodules to address the lack of consistency and avoid wasting of medical resources.

## METHOD

### Literature Search Strategy

We followed the guidelines for the systematic review and meta-analysis of diagnostic studies. Then we too retrieved PubMed for related studies with English language only before February 2020, using the terms as follows: “sensitivity”, “specificity”, “TI-RADS (or thyroid imaging reporting and data system)”, “ACR (or The American Thyroid Association)”, “ATA (or American Thyroid Association)”, “Kwak (or TI-RADS proposed by Kwak)”, “ETA (or EU TI-RADS)”, “KTA (or Korean Thyroid Association/Korean Society of Thyroid Radiology)”. Two reviewers (RN Yang and YN Zhao) independently reviewed the articles in accordance with the inclusion and exclusion criteria. Disagreements were adjusted by consensus (XL Ma).

### Inclusion and Exclusion Criteria

Studies with following inclusion criteria were included: (a) There is enough general information in the article. (b) One or more guidelines are used to evaluate the ultrasound features of thyroid nodules. (c) The study has definite diagnostic criteria. (d) There is sufficient data in the article, whether it is data that can be found directly in the article (sensitivity, specificity, and PPV) or data that can be calculated based on the article [positives (TP), true negatives (TN), false positives (FP), and false negatives (FN)] to fill the diagnostic  $2 \times 2$  table (FN, FP, TP, and TN). And the exclusion criterion is that data in the article is not enough or the grading system is not designed to evaluate ultrasound features. Finally, a total of 19 articles are included.

### Data Extraction

Two reviewers (RN Yang and YN Zhao) picked up some main characters from the studies as following: author, year, country,

number of patients, number of nodules, mean age, involved guideline, gold standard, malignant lesions, and benign lesions. And we obtained the four numbers of TP, TN, FP, and FN for each guideline in different studies by two ways: (1) We got the data from the article directly. (2) Based on the data (sensitivity, specificity, PPV, and NPV) obtained from the articles, we finished the diagnostic  $2 \times 2$  table. CAL software was used here (11).

### Statistical Analysis

On the bases of TP, TN, FP, and FN, we computed the pooled sensitivity, specificity, positive and negative likelihood ratios (PLR and NLR), and diagnostic odds ratio (AUC), with 95% confidence intervals (CI), using the Meta-Disc version 1.4 statistical software (12).

Additionally, using the Meta-Disc version 1.4 statistical software (12), we examined the relationship between sensitivity and specificity by constructing the summary receiver operator characteristic (SROC) curves (13).

At last, we made a head-to-head comparison using R 3.5.1 to calculate the relative diagnostic odds ratio (RDOR) with 95% CI. According to the RDOR, we compared the diagnostic performance among the five guidelines. At comparison, classified into A and B, two guidelines were involved. In A vs B, when the value is greater than 1, A has higher performance. If the value is smaller than 1, B has greater performance. When the value is greater, the performance is better. For all studies, the inconsistency index ( $I^2$ ) and  $\chi^2$  test were used to assess heterogeneity, and it was considered high heterogeneity if the  $I^2$  value was higher than 50% (14). A random-effect model was chosen in this research (15).

### Quality of Studies and Publication Bias

We used Quality Assessment of Diagnostic Accuracy Studies version 2 (QUADAS-2) performed in Review Manager 5.2 to assess the quality of the studies included in this analysis. The method mainly evaluated the articles from four domains: (a) patient selection, (b) index test, (c) reference standard, and (d) flow and timing (16). Each domain is rated as three risks (low, high, and unclear). Publication bias was evaluated by the funnel plot asymmetry test using Stata version 11.0 software.

## RESULTS

### Literature Research and Study Characteristics

At first, we searched 200 articles by reading their abstract, and 166 articles didn't agree with the inclusion criterion. Then we reviewed the rest of the articles further, and 11 articles didn't have enough data to finish the  $2 \times 2$  table. Another five articles were not related to ultrasound features. Therefore, 19 articles (17–35) were included in this study. The process of including articles is in **Figure 1**.

The studies were published from 2015 to 2020. The number of patients is from 92 to 4,585, and the number of nodules in the



included articles varies from 100 to 4,696, which means some patients have more than one nodule. All data were calculated based on the number of nodules. All thyroid nodules were diagnosed of malignancy through postoperative pathological results or the pathology results of FNAC. We totally included 19 articles, 12 of which involved ACR TI-RADS. 10 articles involved ACR guidelines, and Kwak TI-RADS was mentioned in six articles. The data of the KTA guideline and EU TI-RADS were obtained from four articles respectively.

The above characteristics were shown in **Table 1**.

## Diagnostic Accuracy

After pooling all the data of the 19 studies together, we got the final data. The pooled sensitivity of ACR guidelines, ATA guidelines, Kwak TI-RADS, KTA guidelines for malignancy risk, and ETA guidelines is between 0.84 and 0.94. The pooled specificity is 0.68, 0.44, 0.62, 0.47, and 0.61, respectively. We also build SROC curves showing the area under the curve (AUC) with 0.8553, 0.9101, 0.8976, 0.9022, and 0.8810, respectively, for ACR, Kwak TI-RADS, ATA, KTA, and EU TI-RADS guideline groups, on behalf of the accuracy. All pooled sensitivity, specificity, PLR, NLR, DOR, and the AUC values for all the reference standards are shown in detail in **Table 2**. As for RDOR, we found a high result when ACR was compared with other guidelines. The specific results are listed in **Table 3**.

## Quality Assessment

The results of the quality assessment are outlined in **Figure 2**. In conclusion, the quality of the studies was satisfactory.

## Assessment of Publication Bias

There is no clear publication bias for DOR of the five guidelines.

## DISCUSSION

TI-RADS classification guidelines classify the thyroid nodules according to the imaging characteristics under ultrasound, including the size, number, calcification, boundary, echoic pattern, aspect ratio, and internal structure. The guidelines are aimed to help determine which thyroid nodules require FNAC to reduce overdiagnosis or missed-diagnosis. The reduction of unnecessary FNAC can prevent the waste of economy and the physical pain of patients. It can also guide further treatment and estimate the risk of recurrence. However, the recommended size thresholds for FNAC are different in different guidelines. At present, there are many studies about the diagnostic efficacy of the five guidelines, but the results vary. These differences between studies may be due in part to differences among observers and study populations, especially in retrospective studies. In this research, we included 19 studies to analyze the diagnostic efficacy of the five diagnostic criteria.

Our meta-analysis systematically estimated the diagnostic efficacy of five different ultrasound classification guidelines in detecting malignancy risk. The pooled sensitivity of the ACR TI-RADS, ATA guidelines, Kwak TI-RADS, KTA guidelines, and ETA is between 0.84 and 0.94. The pooled specificity is 0.68, 0.44, 0.62, 0.47, and 0.61, respectively. The AUC which can represent the diagnostic performance of the ACR TI-RADS, ATA guidelines, Kwak TI-RADS KTA guideline, and ETA is 0.8553, 0.8976, 0.9101, 0.9022, and 0.8810. In theory, AUC above 0.8 is diagnostic (36). The results of our research suggested that all the five guidelines have property. Besides, ACR guidelines showed the best diagnostic performance in the head to head comparison.

Our results were similar with a previous meta-analysis published in 2019 (37). But that article just included 12 studies with 18,750 thyroid nodules, and the data it included was used to

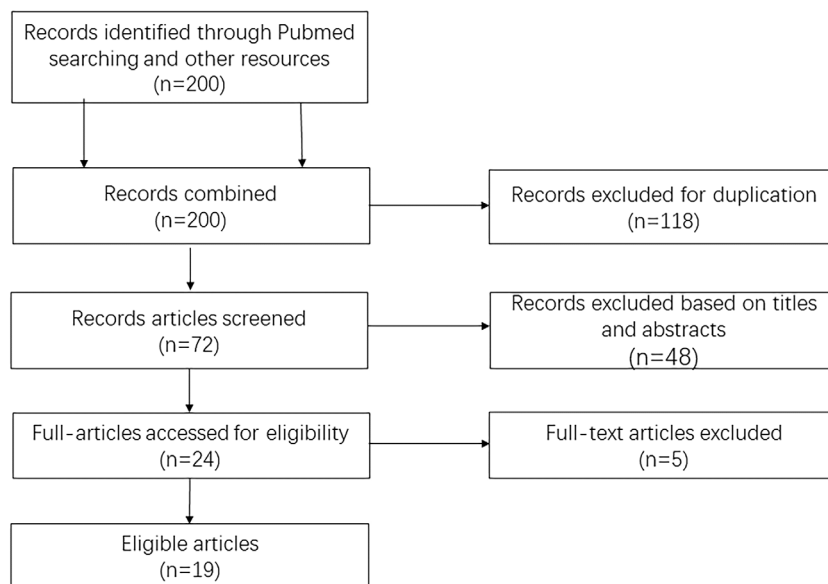


**FIGURE 1** | Flowchart of the literature search and selection schema.



**TABLE 1 |** Baseline characteristics of included studies.

Author	Year	Country	Patients, n	Nodules, n	MeanAge	Guidelines	Standard	Malignant lesions	Benign lesions
Zhang (18)	2020	China	1,271	1,271	48	ACR/ATA/Kwak/KTA	Needle biopsy, surgical resection	736	535
Gao (19)	2019	China	1,764	2,544	—	ACR/ATA/Kwak	Surgical resection	1,681	863
Barbosa (20)	2019	Brazil	139	140	49	ACR/ATA	Needle biopsy, surgical resection	66	74
Jabar (21)	2019	India	127	127	—	ACR/Kwak	Needle biopsy, surgical resection	23	104
Xv (24)	2019	China	370	432	43	ACR	Needle biopsy, surgical resection	258	174
Yoon (25)	2019	Korea	1,836	2,274	55	ACR/KTA	Needle biopsy, surgical resection	300	1,974
Huang (26)	2019	USA	137	250	58	ACR/ATA	Surgical resection	65	185
Ruan (27)	2019	China	918	1,001	46	ATA	Needle biopsy, surgical resection	392	609
Wang (22)	2017	China	1,011	1,011	51	Kwak	Surgical resection	464	547
Liu (23)	2015	China	2,921	3,980	52	Kwak	Needle biopsy	228	3,752
Ha (17)	2018	Korea	1,802	2,000	51	KTA, ATA, ACR	Needle biopsy, surgical resection	1,546	454
Mohammadi (28)	2019	Canada	—	425	—	ATA	Needle biopsy	31	394
Wu (29)	2019	China	894	1,000	—	ATA, ACR	Needle biopsy, surgical resection	530	470
Xu (30)	2019	China	2,031	2,465	48	KTA, ACR, ETA	Surgical resection	885	1,146
Yoon.J (31)	2017	Korea	4,585	4,696	51	ATA, Kwak	Needle biopsy, surgical resection	1,044	3,652
Hoang (32)	2018	USA	92	100	52	ACR	Needle biopsy, surgical resection	15	85
Li (33)	2019	China	128	130	48	ACR	Needle biopsy, surgical resection	73	57
Trimboli (34)	2019	Switzerland	475	1,058	53	ETA	Needle biopsy, surgical resection	—	—
Maino (35)	2018	Italy	340	432	57	ATA, ETA	Needle biopsy	—	—

**TABLE 2 |** Pooled estimates of the sensitivity, specificity, PLR, NLR, DOR, AUC, and SE (AUC).

Reference guideline	N <sup>a</sup>	Pooled sensitivity (95% CI)	Pooled specificity (95% CI)	Pooled PLR (95% CI)	Pooled NLR (95% CI)	Pooled DOR (95% CI)	AUC	SE (AUC)
ACR	13	0.85(0.84–0.86)	0.68(0.6–0.69)	2.98(2.37–3.75)	0.22(0.16–0.29)	15.23(9.23–25.11)	0.8553	0.0311
Kawk	6	0.94(0.94–0.95)	0.62(0.6–0.63)	3.23(0.90–11.61)	0.08(0.04–0.16)	43.15(19.09–97.53)	0.9101	0.0621
ATA	10	0.94(0.94–0.95)	0.44(0.43–0.45)	2.06(1.54–2.75)	0.16(0.10–0.28)	13.33(5.90–30.14)	0.8976	0.0414
KTA	4	0.85(0.83–0.86)	0.47(0.46–0.48)	2.60(1.2–5.57)	0.18(0.08–0.39)	14.57(5.77–36.84)	0.9022	0.0430
ETA	4	0.85(0.83–0.87)	0.61(0.59–0.62)	2.84(1.43–5.64)	0.21(0.13–0.34)	13.18(4.89–35.5)	0.8810	0.0561

na, number of studies; PLR, positive likelihood ratios; NLR, negative likelihood ratios; DOR, diagnostic odds ratio; AUC, area under the curve.

**TABLE 3 |** Relative diagnostic odds ratio (RDOR) with 95% confidence limit.

B A	ACR	ATA	ETA	Kawk	KTA
ACR	—	0.6387(0.3678–1.1090)	0.7308(0.3000–1.7803)	0.5564(0.2552–1.2131)	0.5734(0.2759–1.1919)
ATA	1.5658(0.9017–2.7189)	—	1.1443(0.4532–2.8897)	0.8713(0.3995–1.8999)	0.8979(0.4072–1.9802)
ETA	1.3683(0.5617–3.3332)	0.8739(0.3461–2.2067)	—	0.7614(0.2498–2.3208)	0.7846(0.3075–2.0020)
Kawk	1.7972(0.8243–3.9183)	1.3134(0.5264–2.5028)	1.3138(0.4309–4.0035)	—	1.0306(0.3927–2.7048)
KTA	1.7439(0.8390–3.6247)	1.1137(0.5050–2.4561)	1.2745(0.4995–3.2518)	0.9703(0.3697–2.5466)	—

SROC, summary receiver operator characteristics.

describe the unnecessary FNA rates. There are 19 articles of 24,325 thyroid nodules in our research. Compared with the published article, we can include the articles with indirect data and finish the diagnostic  $2 \times 2$  table using Cal software. Besides, in an article we both included, our article included the data of

diagnostic performance for malignant thyroid nodules which better describes the diagnostic efficiency. It can influence the pooled results.

The TI-RADS guidelines based on ultrasound have been widely used in clinics, providing recommendation for further

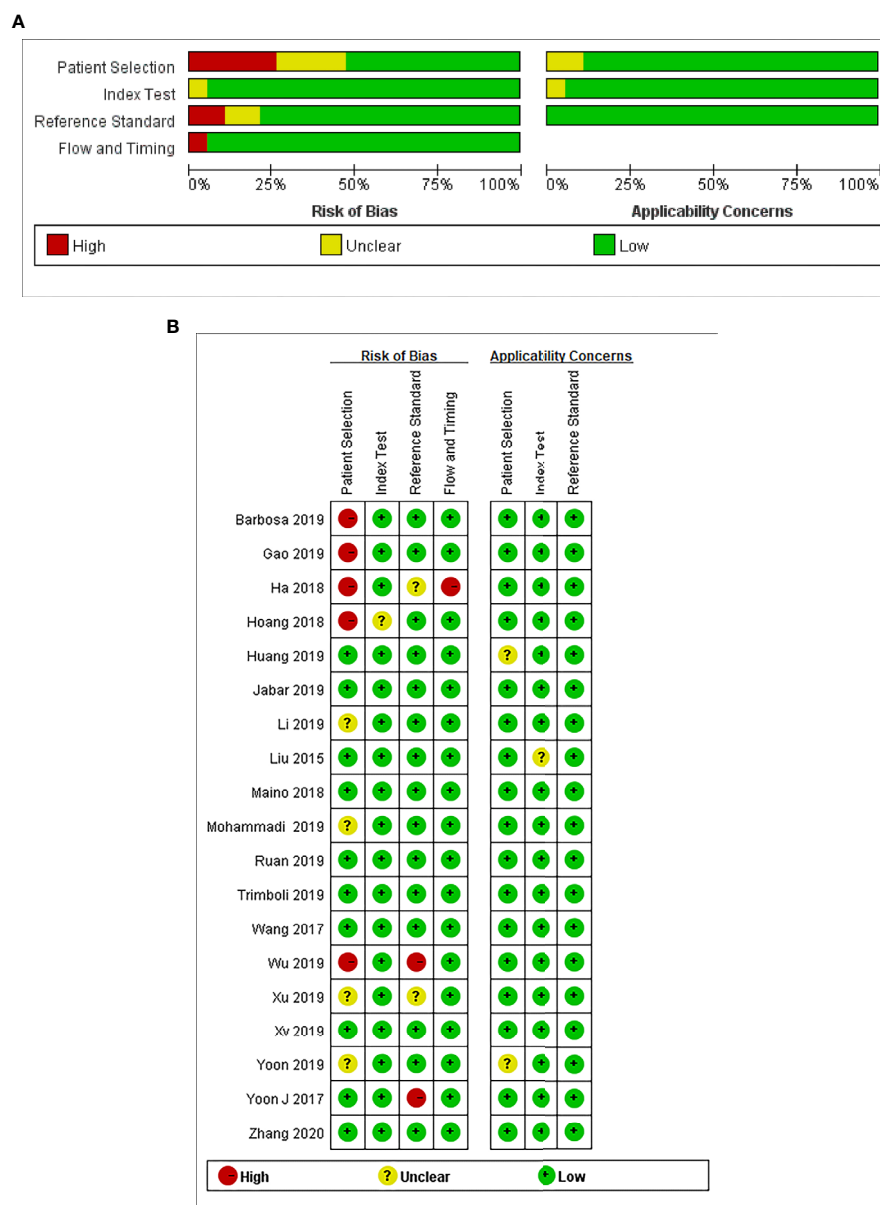


**FIGURE 2 | (A)** Risk of bias and applicability concerns graph: review authors' judgments about each domain presented as percentages across the included studies. **(B)** Risk of bias and applicability concerns summary: review authors' judgments about each domain for each included study.

diagnosis and treatment while reducing the influence of subjective factors in diagnosing. In our study, we can see the five guidelines all have great diagnostic performance with high AUC above 0.8. However, there are similarities and differences among the five guidelines in structure, risk stratification, size thresholds, and diagnostic performance. More studies need to be done. The structure of the five classification guidelines is internally different. The ACR guidelines and Kwak TI-RADS are point-based systems, and the other three guidelines are based on the pattern. Compared with point-based guidelines, the

simplified pattern-based guidelines are more intuitive and feasible clinically but with decreased accuracy. Although the point-based guidelines are cumbersome, they're easy to control by clinical doctors, especially estimating individual nodules, which are with great accuracy. However, in clinical application, complex analyses and calculations always require the help of computers (10, 38). Every guideline has been divided into several categories to evaluate the thyroid nodules. As the risk stratification categories rise, the risk of the malignancy is increased, but the five guidelines have differences in the

classification. For example, a category five or four thyroid nodule in ETA may be classified as ACR T4/3 or KTA T4/3, and a nodule of KTA T3 (low suspicion) and ETA category 3 (low risk) may be classified as ACR T2, which means not suspicious. Different classification criteria like the above may lead to different specificities, and as the results in our research, the ACR guidelines surely had the highest specificity. It also means less recommendation for FNAC, but the rate of misdiagnosis increases. We need more studies to discuss. As for the performance of recommendation for FNAC, the five guidelines have different size thresholds, and the thresholds also change with categories in different guidelines. For example, for ACR TI-RADS, the threshold of categories three, four, and five is 2.5, 1.5, and 1cm, respectively (39). Some studies (17) have shown ACR TI-RADS have the most effective criteria which can avoid the unnecessary biopsies effectively. Our results also confirmed this, with the highest RDOR for ACR TI-RADS. Nodule size is an important standard for guidelines and further treatment. The too large thyroid nodules with low malignancy risk will suggest surgery or FNAC.

In addition, there are several limitations in this research. Firstly, the final diagnosis was determined by cytology or pathology. It may be influenced by the operators or observers, with possible bias. Especially in retrospective studies, we are not sure whether subjective factors affect the diagnosis. This influence can't be avoided. The second limitation is caused by the patient selection of included studies. Some studies have

included more patients with malignant nodules which could influence the sensitivity and specificity. Thirdly, we didn't have enough data for KTA guidelines and ETA to analyze. Lastly, all analyses are based on the ultrasound; the intra-observer and inter-observer variability still exists.

In conclusion, our research indicates that the five classification guidelines are all effective methods for differential diagnosis of benign and malignant thyroid nodules. They can be used before further diagnosis or treatment as an effective recommendation. In head to head comparison, the result suggests ACR guideline is a better choice in the benign and malignant diagnosis with high diagnostic accuracy. However, we still need more studies to prove our findings.

## AUTHOR CONTRIBUTIONS

All authors directly participated in the planning, execution, or analysis of the study and wrote the manuscript. RY conducted the literature review, planned and performed all statistical analyses. HZ and XZ provided input and direction for the analytic strategy and editing of the manuscript. YZ reviewed the included articles and provided editing of the manuscript. XM provided technical quality control to ensure accuracy of reported results. All authors contributed to the article and approved the submitted version.

## REFERENCES

- Haugen BR, Alexander EK, Bible KC, Doherty GM, Mandel SJ, Nikiforov YE, et al. 2015 American Thyroid Association Management Guidelines for Adult Patients with Thyroid Nodules and Differentiated Thyroid Cancer: The American Thyroid Association Guidelines Task Force on Thyroid Nodules and Differentiated Thyroid Cancer. *Thyroid* (2016) 26(1):1–133. doi: 10.1089/thy.2015.0020
- Brito JP, Morris JC, Montori VM. Thyroid cancer: zealous imaging has increased detection and treatment of low risk tumours. *Bmj* (2013) 347:f4706. doi: 10.1136/bmj.f4706
- Miller KD, Siegel RL, Lin CC, Mariotto AB, Kramer JL, Rowland JH, et al. Cancer treatment and survivorship statistics, 2016. *CA Cancer J Clin* (2016) 66(4):271–89. doi: 10.3322/caac.21349
- Ozdemir D, Bestepe N, Faki S, Kilicarslan A, Parlak O, Ersoy R, et al. Comparison of thyroid fine needle aspiration biopsy results before and after implementation of Bethesda classification. *Cytopathology* (2017) 28(5):400–6. doi: 10.1111/cyt.12437
- Kwak JY, Han KH, Yoon JH, Moon HJ, Son EJ, Park SH, et al. Thyroid imaging reporting and data system for US features of nodules: a step in establishing better stratification of cancer risk. *Radiology* (2011) 260(3):892–9. doi: 10.1148/radiol.11110206
- An JY, Unsdrofer KML, Weinreb JC. BI-RADS, C-RADS, CAD-RADS, LI-RADS, Lung-RADS, NI-RADS, O-RADS, PI-RADS, TI-RADS: Reporting and Data Systems. *Radiographics* (2019) 39:1435–6. doi: 10.1148/rg.2019190087
- Shin JH, Baek JH, Chung J, Ha EJ, Kim JH, Lee YH, et al. Ultrasonography Diagnosis and Imaging-Based Management of Thyroid Nodules: Revised Korean Society of Thyroid Radiology Consensus Statement and Recommendations. *Korean J Radiol* (2016) 17:370–95. doi: 10.3348/kjr.2016.17.3.370
- Russ G, Bonnema SJ, Erdogan MF, Durante C, Ngu R, Leenhardt L. European Thyroid Association Guidelines for Ultrasound Malignancy Risk Stratification of Thyroid Nodules in Adults: The EU-TIRADS. *Eur Thyroid J* (2017) 6(5):225–37. doi: 10.1159/000478927
- Tessler FN, Middleton WD, Grant EG, Hoang JK, Berland LL, Teeffey S, et al. ACR Thyroid Imaging, Reporting and Data System (TI-RADS): White Paper of the ACR TI-RADS Committee. *J Am Coll Radiol* (2017) 14(5):587–95. doi: 10.1016/j.jacr.2017.01.046
- Ha SM, Ahn HS, Baek JH, Ahn HY, Chung YJ, Cho BY, et al. Validation of Three Scoring Risk-Stratification Models for Thyroid Nodules. *Thyroid* (2017) 27(12):1550–7. doi: 10.1089/thy.2017.0363
- Ma X, Zeng H, Zhang J, Chen L, Jia H. New practical methods to obtain crucial data in performing diagnostic meta-analysis of the published literature. *J Evid Based Med* (2018) 11:56–63. doi: 10.1111/jebm.12281
- Zamora J, Abraira V, Muriel A, Khan K, Coomarasamy A. Meta-DiSc: a software for meta-analysis of test accuracy data. *BMC Med Res Methodol* (2006) 6:31. doi: 10.1186/1471-2288-6-31
- Moses LE, Shapiro D, Littenberg B. Combining independent studies of a diagnostic test into a summary ROC curve: data-analytic approaches and some additional considerations. *Stat Med* (1993) 12:1293–316. doi: 10.1002/sim.4780121403
- Higgins JP, Thompson SG, Deeks JJ, Altman DG. Measuring inconsistency in meta-analyses. *Bmj* (2003) 327:557–60. doi: 10.1136/bmj.327.7414.557
- Dimnes J, Deeks J, Kirby J, Roderick P. A methodological review of how heterogeneity has been examined in systematic reviews of diagnostic test accuracy. *Health Technol Assess* (2005) 9:1–113, iii. doi: 10.3310/hta9120
- Whiting PF, Rutjes AW, Westwood ME, Mallett S, Deeks JJ, Reitsma J, et al. QUADAS-2: a revised tool for the quality assessment of diagnostic accuracy studies. *Ann Intern Med* (2011) 155(8):529–36. doi: 10.7326/0003-4819-155-8-201110180-00009
- Ha EJ, Na DG, Baek JH, Sung JY, Kim JH, Kang SY. US Fine-Needle Aspiration Biopsy for Thyroid Malignancy: Diagnostic Performance of Seven Society Guidelines Applied to 2000 Thyroid Nodules. *Radiology* (2018) 287(3):893–900. doi: 10.1148/radiol.2018171074

18. Zhang WB, et al. Comparisons of ACR TI-RADS, ATA guidelines, Kwak TI-RADS, and KTA/KSThR guidelines in malignancy risk stratification of thyroid nodules. *Clin Hemorheol Microcirc* (2020). doi: 10.3233/ch-190778
19. Gao L, Xi X, Jiang Y, Yang X, Wang Y, Zhu S, et al. Comparison among TIRADS (ACR TI-RADS and KWAK- TI-RADS) and 2015 ATA Guidelines in the diagnostic efficiency of thyroid nodules. *Endocrine* (2019) 64(1):90–6. doi: 10.1007/s12020-019-01843-x
20. Barbosa TLM, Junior COM, Graf H, Cavalvanti T, Trippia MA, da Silveira Ugino RT, et al. ACR TI-RADS and ATA US scores are helpful for the management of thyroid nodules with indeterminate cytology. *BMC Endocr Disord* (2019) 19(1):112. doi: 10.1186/s12902-019-0429-5
21. Jabar ASS, Koteswara P, Andrade J. Diagnostic reliability of the Thyroid Imaging Reporting and Data System (TI-RADS) in routine practice. *Pol J Radiol* (2019) 84:e274–80. doi: 10.5114/pjr.2019.86823
22. Wang Y, Lei KR, He YP, Li XL, Ren WW, Zhao CK, et al. Malignancy risk stratification of thyroid nodules: comparisons of four ultrasound Thyroid Imaging Reporting and Data Systems in surgically resected nodules. *Sci Rep* (2017) 7(1):11560. doi: 10.1038/s41598-017-11863-0
23. Zhang J, Liu BJ, Xu HX, Xu JM, Zhang YF, Liu C, et al. Prospective validation of an ultrasound-based thyroid imaging reporting and data system (TI-RADS) on 3980 thyroid nodules. *Int J Clin Exp Med* (2015) 8(4):5911–7.
24. Xu Y, Qi X, Zhao X, Ren W, Ding W. Clinical diagnostic value of contrast-enhanced ultrasound and TI-RADS classification for benign and malignant thyroid tumors: One comparative cohort study. *Med (Baltimore)* (2019) 98:e14051. doi: 10.1097/md.00000000000014051
25. Yoon SJ, Na DG, Gwon HY, Paik W, Kim WJ, Song JS, et al. Similarities and Differences Between Thyroid Imaging Reporting and Data Systems. *AJR Am J Roentgenol* (2019) 213(2):W76–84. doi: 10.2214/AJR.18.20510
26. Huang BL, Ebner SA, Makkar JS, Bentley-Hibbert S, McConnell RJ, Lee JA, et al. A Multidisciplinary Head-to-Head Comparison of American College of Radiology Thyroid Imaging and Reporting Data System and American Thyroid Association Ultrasound Risk Stratification Systems. *Oncologist* (2020) 25(5):398–403. doi: 10.1634/theoncologist.2019-0362
27. Ruan JL, Yang HY, Liu RB, Liang M, Han P, Xu XL, et al. Fine needle aspiration biopsy indications for thyroid nodules: compare a point-based risk stratification system with a pattern-based risk stratification system. *Eur Radiol* (2019) 29(9):4871–8. doi: 10.1007/s00330-018-5992-z
28. Mohammadi M, Betel C, Burton KR, Higgins KM, Ghorab Z, Halperin IJ. Retrospective Application of the 2015 American Thyroid Association Guidelines for Ultrasound Classification, Biopsy Indications, and Follow-up Imaging of Thyroid Nodules: Can Improved Reporting Decrease Testing? *Can Assoc Radiol J* (2019) 70(1):68–73. doi: 10.1016/j.carj.2018.09.001
29. Wu XL, Du JR, Wang W, Jin CX, Sui GQ, Yang DY, et al. Comparison and preliminary discussion of the reasons for the differences in diagnostic performance and unnecessary FNA biopsies between the ACR TIRADS and 2015 ATA guidelines. *Endocrine* (2019) 65(1):121–31. doi: 10.1007/s12020-019-01886-0
30. Xu T, Wu Y, Wu RX, Zhang YZ, Gu JY, Ye XH, et al. Validation and comparison of three newly-released Thyroid Imaging Reporting and Data Systems for cancer risk determination. *Endocrine* (2019) 64(2):299–307. doi: 10.1007/s12020-018-1817-8
31. Yoon JH, Han K, Kim EK, Moon HJ, Kwak JY. Diagnosis and Management of Small Thyroid Nodules: A Comparative Study with Six Guidelines for Thyroid Nodules. *Radiology* (2017) 283:560–9. doi: 10.1148/radiol.2016160641
32. Hoang JK, Middleton WD, Farjat AE, Langer JE, Reading CC, Teefey S, et al. Reduction in Thyroid Nodule Biopsies and Improved Accuracy with American College of Radiology Thyroid Imaging Reporting and Data System. *Radiology* (2018) 287(1):185–93. doi: 10.1148/radiol.2018.172572
33. Li X, Hou XJ, Du LY, Wu JQ, Wang L, Wang H, et al. Virtual Touch Tissue Imaging and Quantification (VTIQ) combined with the American College of Radiology Thyroid Imaging Reporting and Data System (ACR TI-RADS) for malignancy risk stratification of thyroid nodules. *Clin Hemorheol Microcirc* (2019) 72(3):279–91. doi: 10.3233/ch-180477
34. Trimboli P, Ngu R, Royer B, Giovannella L, Bigorgne C, Simo R, et al. A multicentre validation study for the EU-TIRADS using histological diagnosis as a gold standard. *Clin Endocrinol (Oxf)* (2019) 91(2):340–7. doi: 10.1111/cen.13997
35. Maino F, Forleo R, Martinelli M, Fralassi N, Barbato F, Pilli T, et al. Prospective Validation of ATA and ETA Sonographic Pattern Risk of Thyroid Nodules Selected for FNAC. *J Clin Endocrinol Metab* (2018) 103(6):2362–8. doi: 10.1210/jc.2018-00274
36. Metz CE. Basic principles of ROC analysis. *Semin Nucl Med* (1978) 8:283–98. doi: 10.1016/s0001-2998(78)80014-2
37. Castellana M, Castellana C, Treglia G, Giorgino F, Giovannella L, Russ G, et al. Performance of Five Ultrasound Risk Stratification Systems in Selecting Thyroid Nodules for FNA. *J Clin Endocrinol Metab* (2020) 105(5):dgz170. doi: 10.1210/clinem/dgz170
38. Choi YJ, Baek JH, Baek SH, Shim WH, Lee KD, Lee HS, et al. Web-Based Malignancy Risk Estimation for Thyroid Nodules Using Ultrasonography Characteristics: Development and Validation of a Predictive Model. *Thyroid* (2015) 25(12):1306–12. doi: 10.1089/thy.2015.0188
39. Tessler FN, Middleton WD, Grant EG. Thyroid Imaging Reporting and Data System (TI-RADS): A User's Guide. *Radiology* (2018) 287:29–36. doi: 10.1148/radiol.2017171240

**Conflict of Interest:** The authors declare that the research was conducted in the absence of any commercial or financial relationships that could be construed as a potential conflict of interest.

Copyright © 2020 Yang, Zou, Zeng, Zhao and Ma. This is an open-access article distributed under the terms of the Creative Commons Attribution License (CC BY). The use, distribution or reproduction in other forums is permitted, provided the original author(s) and the copyright owner(s) are credited and that the original publication in this journal is cited, in accordance with accepted academic practice. No use, distribution or reproduction is permitted which does not comply with these terms.



# Survival Prediction in Gallbladder Cancer Using CT Based Machine Learning

Zefan Liu<sup>1†</sup>, Guannan Zhu<sup>1†</sup>, Xian Jiang<sup>1</sup>, Yunuo Zhao<sup>1</sup>, Hao Zeng<sup>1</sup>, Jing Jing<sup>1\*</sup> and Xuelei Ma<sup>1,2\*</sup>

<sup>1</sup> Laboratory of Tumor Targeted and Immune Therapy, Clinical Research Center for Breast, West China Hospital, Sichuan University, Chengdu, China, <sup>2</sup> State Key Laboratory of Biotherapy, Department of Biotherapy, Cancer Center, West China Hospital, Sichuan University, Chengdu, China

## OPEN ACCESS

### Edited by:

Changqiang Wu,  
North Sichuan Medical College, China

### Reviewed by:

Nan Song,  
Capital Medical University, China  
Mian Guo,  
Second Affiliated Hospital of Harbin  
Medical University, China

### \*Correspondence:

Jing Jing  
jj\_zcy@vip.163.com  
Xuelei Ma  
drmaxuelei@gmail.com

<sup>†</sup>These authors have contributed  
equally to this work

### Specialty section:

This article was submitted to  
Cancer Imaging and  
Image-directed Interventions,  
a section of the journal  
Frontiers in Oncology

**Received:** 09 September 2020

**Accepted:** 02 November 2020

**Published:** 27 November 2020

### Citation:

Liu Z, Zhu G, Jiang X, Zhao Y, Zeng H,  
Jing J and Ma X (2020) Survival  
Prediction in Gallbladder Cancer Using  
CT Based Machine Learning.  
Front. Oncol. 10:604288.  
doi: 10.3389/fonc.2020.604288

**Objective:** To establish a classifier for accurately predicting the overall survival of gallbladder cancer (GBC) patients by analyzing pre-treatment CT images using machine learning technology.

**Methods:** This retrospective study included 141 patients with pathologically confirmed GBC. After obtaining the pre-treatment CT images, manual segmentation of the tumor lesion was performed and LIFEx package was used to extract the tumor signature. Next, LASSO and Random Forest methods were used to optimize and model. Finally, the clinical information was combined to accurately predict the survival outcomes of GBC patients.

**Results:** Fifteen CT features were selected through LASSO and random forest. On the basis of relative importance GLZLM-HGZE, GLCM-homogeneity and NGLDM-coarseness were included in the final model. The hazard ratio of the CT-based model was 1.462(95% CI: 1.014–2.107). According to the median of risk score, all patients were divided into high and low risk groups, and survival analysis showed that high-risk groups had a poor survival outcome ( $P = 0.012$ ). After inclusion of clinical factors, we used multivariate COX to classify patients with GBC. The AUC values in the test set and validation set for 3 years reached 0.79 and 0.73, respectively.

**Conclusion:** GBC survival outcomes could be predicted by radiomics based on LASSO and Random Forest.

**Keywords:** radiomics, machine learning, gallbladder cancer, prognosis, random forest

## INTRODUCTION

Gallbladder cancer (GBC) is the fifth most common tumor of the digestive system and accounts for 95% of malignant tumors in the biliary system (1). The lack of specific clinical manifestations in the early stage, coupled with high invasive biological features and abnormal anatomic location of the gallbladder, results in poor survival outcomes (2, 3). In addition, due to the low sensitivity to



chemotherapy and radiotherapy, and the lack of effective therapeutic targets, surgical resection is still the main treatment option (4). At present, widespread concern about the survival outcomes of GBC has been aroused. Researchers hope to distinguish patients with higher prognostic risk, so as to implement personalized medical treatment. So far, prognostic analyses of GBC have depended on laboratory-tested indicators such as tumor markers, nutritional indicators, and gene expression signatures, but these indicators lack an intuitive analysis of the whole tumor lesion (5–7).

Lesions can be directly observed by radiological images in clinic and lesion information not visible to the naked eye can be provided by radiomics. In recent years, radiomics has been developed to focus on the extraction and mining massive medical imaging data. It is hypothesized that these selected imaging features reflect specific tumor phenotypes (8, 9). Because these image signatures provide a comprehensive picture of the entire tumor entity, the heterogeneity of these signatures may have implications for clinical events such as treatment response, survival outcomes and disease progression. Some studies have focused on the appearance of imaging features at different cancer stages (10, 11). In addition many other studies have reported the effect of imaging features on survival outcomes, but no studies have been reported on GBC.

GBC survival prediction model is of great significance for patients' prognosis assessment, treatment mode selection, surgical patient selection, postoperative adjuvant treatment plan determination, high-risk recurrence patient identification, follow-up frequency formulation, and rational use of medical resources. In this study, we assessed a number of CT-based radiomics parameters to predict patient's overall survival (OS). Patient cohort with a total of 141 patients was used to analyze image data, extract features, and perform model tests. All the selected parameters were evaluated for their predictive power and stability. Finally, we combined clinical information for a cost-effective prediction.

## METHODS

### Patient Selection

The flow of data analysis and processing is shown in **Figure 1**. The records of patients from 2010 to 2017 were selected from the Department of Hepatobiliary surgery through an electronic medical review. Inclusion criteria for patients: 1) Pathological examination Confirmed GBC; 2) Perform CT scan before tumor biopsy or surgery. Some patients were excluded because of the history of liver surgery or other liver lesions leading to gallbladder lesions that could not be identified (**Table 1**). Considering that conventional CT, including CT and Contrast-enhanced CT, is commonly used tests in clinical practice and have good cost-effectiveness, it was selected as the study object. Finally, a total of 141 patients were included in this study, and CT images were collected from Radiology Department.

All procedures involving human participants comply with ethical standards bodies and/or national research councils. Ethics

Committee of Sichuan University approved this retrospective study. Written informed consent (written informed consent for patients under 16 years of age must be signed by a parent or guardian) is required before radiological examination for all patients.

### Image Recognition and Feature Extraction

CT scanning was performed using 64-MDCT Scanner (Brilliance64, Philips Medical Systems, Eindhoven, The Netherlands) or 128-MDCT scanner (Somatom Definition AS+, Siemens Healthcare Sector, Forchheim, Germany) before going through any treatment.

All CT examinations were performed under the following conditions: 120 kVp; 199 mAs; 12.9 ctdIVOL (mGy); 460.7 DLP (mGy\*cm); pitch, 0.75–1.0; rotation time, 0.5–0.75 s; collimation, 0.625 mm; section thickness, 2.0 or 5.0 mm.

The ROI area was sketched by two experienced radiologists. Due to the limited recognition ability of ordinary CT for GBC and the boundary of cancer is usually fuzzy, we followed the following principle when making segmentation: 1) delineate solid lesions with high density of GBC and avoid low-density areas such as bile, 2) delineate the definite tumor part when it is difficult to recognize the blurring around the lesion, and 3) excluded samples with disagreement among radiologists.

We used the image feature extraction software LIFEx to obtain the texture signatures of CT images (12). Based on each layer of CT image, we depicted the boundary of the lesion in the two-dimensional region of interest (ROI) and finally obtained a three-dimensional ROI. ROI is described by independent radiologists who do not know the patient's diagnosis (**Supplement Figure 1**). The maximum, minimum, mean, and standard deviation of the density values in the ROI region were calculated. From the obtained data, Gray-level co-occurrence matrix (GLCM), Neighborhood gray-level different matrix (NGLDM), Gray level run length matrix (GLRLM), and the Gray level zone length matrix (GLZLM) were calculated. We obtained a total of 54 radiomics parameters (**Supplementary Table 3**).

### Statistic Analysis Workflow

First, all the collected samples were randomly divided into test set and validation set according to a ratio of 7:3. We used the sample function of R software to make randomization, and conducted a hypothesis test on the age of the randomized patients between the two groups (**Supplementary Table 4**). The results showed that the average age difference between the two groups was not statistically significant ( $P > 0.05$ ). Therefore, we selected the group accounting for 70% as the training set for the follow-up analysis of the model. Then, the signatures from image texture were filtered by least absolute and Selection Operator (LASSO) (13). After 100 repeated simulations, signatures with the best robustness were selected. In order to optimize the model, we use the random forest to further screen the selected signatures and obtain the final machine learning model. We performed a multivariate Cox regression analysis of radiological parameters and clinical characteristics and drew a nomogram. The survival curve was plotted by Kaplan-Meier analysis and tested by log-rank test.

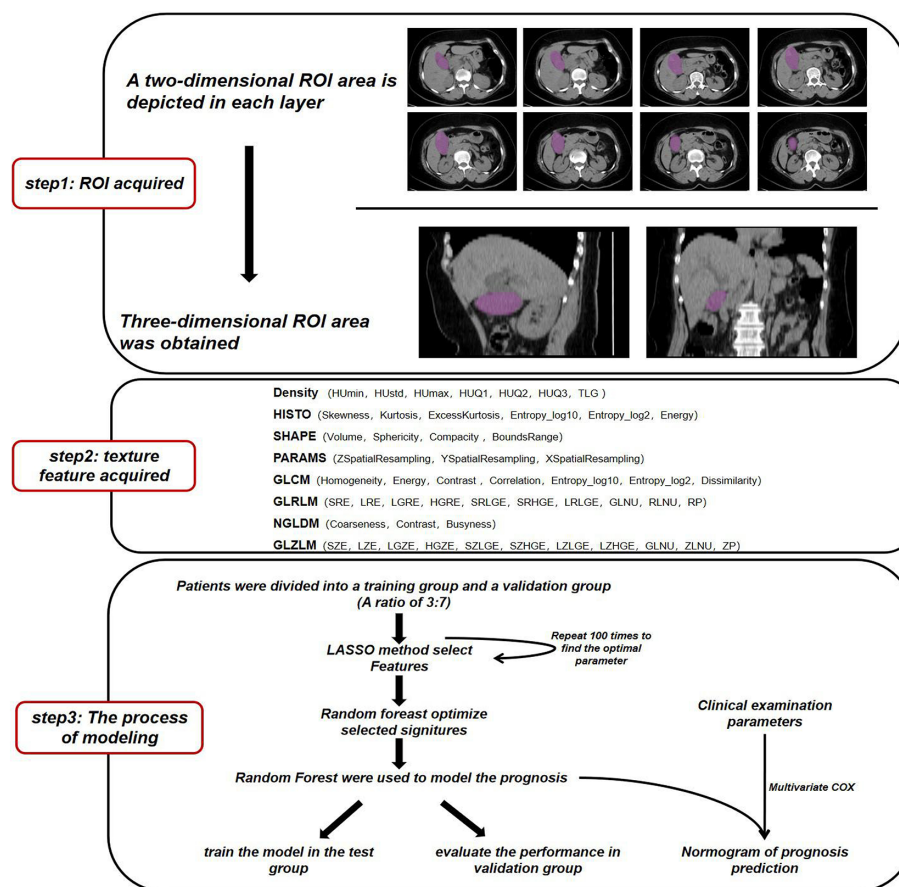


FIGURE 1 | Workflow for image processing and machine learning.

## RESULTS

### Establishment of a Model Using Radiomics Signatures

First, we randomly divided the patients into a training group and a test group, with a split ratio of 7:3. Then, LASSO method was used to make simulation in the training group for up to 100 times and 15 signatures were selected. The results are shown in **Figure 2**. Next, the random forest was used to further optimize. According to the relative importance, three most important parameters were screened out (**Supplementary Table 2**). Then, we built a model based on random forest algorithm. The risk score for each patient is calculated and the risk score distribution for each patient is shown in **Figure 3**. By comparing the high with low risk groups, we found that the high risk group had a worse overall survival. And GLZLM-HGZE, and GLCM-homogeneity increased risk, but the increase of NGLDM-coarseness reduces the risk, so we think GLZLM-HGZE and GLCM-homogeneity may be a risk factor of GBC, and NGLDM-coarseness is more likely to be a protective factor.

Correlation analysis shows that the correlation degree of these three factors is low (**Supplementary Table 5**). The Univariate COX shows the risk score had a hazard ratio of 1.534 (95% CI: 1.078–2.183). Finally, we validated this model in the verification group (**Supplementary Table 1**). The model had a good performance, with high-risk individuals had poorer survival outcomes than low-risk individuals. In addition, the survival rate of high-risk patients was significantly lower than that of low-risk patients ( $P = 0.012$ ).

### Prognostic Model Performed Based on Clinical Data and Radiomics

In order to achieve better performance, we analyzed a variety of clinical indicators of patients, including age, gender, and tumor stage. Through multivariate COX analysis, we screened out the prognostic indicators affecting the survival of patients with GBC, including surgery or not, liver metastasis and lymph node metastasis grade (**Table 2**). Next, we randomly divided the patients into two groups to conduct model training and testing. We used multivariate COX to predict the overall

**TABLE 1 |** The general condition of the patients in this study.

Patient (Total=141)	Patient characteristics		
	Male	Female	
Gender	56(39.7%)	85(60.3%)	
Age	<30 23(16.3%)	30-50 84(59.5%)	>50 34(24.1%)
T stage	I-II 49(32.8%)	III-IV 92(65.2%)	
N stage	NO 67(47.5%)	N1 56(39.7%)	N2 18(12.7%)
M stage	MO 82(58.1%)	M1 56(39.7%)	
Liver metastasis	Yes 78(55.3%)	No 63(44.6%)	
Jaundice	<40 u/ml 33(23.4%)	>=40 u/ml 108(76.5%)	NA
CA199	<35 u/ml 59(41.8%)	>=35 u/ml 79(56.0%)	3(2.12%)
CA125	<5 µg/L 85(60.2%)	>=5 µg/L 53(37.5%)	3(2.12%)
CEA	<20 µg/L 90(63.8%)	>=20 µg/L 48(34.0%)	3(2.12%)
AFP	Yes 130(92.1%)	No 8(5.67%)	3(2.12%)
Surgical treatment	114(80.8%)	27(19.1%)	

survival of the patients by combining three selected clinical indicators (Liver metastasis, surgery, and lymph node metastasis grade) and radiomics risk score (**Table 3**). Finally, we use a nomogram to visualize the performance of the model (**Figure 4**) and evaluated the prediction accuracy through ROC curve. The results of nomograms showed that the 1- and 3-year prediction reached 0.7465 and 0.7974 in the training group and 0.7271 and 0.7314 in the validation group, respectively. **Figure 5** also shows the comparison between the ideal model and the actual nomogram prediction. The calibration chart shows that the actual model is basically consistent with the ideal model, indicating that our model has a high accuracy.

## DISCUSSION

In this study, CT scan data combined with machine learning methods was used to predict overall survival outcomes in GBC patients. Firstly, we use LASSO to filtered raw data and acquire a robust parameter set. Then we use the random forest to making further optimization. Finally, three parameters including GLZLM-HGZE, GLCM-homogeneity, and NGLDM-coarseness were obtained. The three parameters were correlated with the prognostic risk of the patients, and the prognostic model got a hazard ratio of 1.549. The clinical parameters analysis results showed that lymph node metastasis grade, surgery or not and liver metastasis situation are prognostic factors. In combination with these indicators and CT risk score, we get a model for prognosis of GBC. Moreover, the 3-year AUC value of the predictive model in the random validation group reached 0.797.

It is of great guiding significance for the selection of treatment options and clinical decision support of patients with GBC to find the key prognostic factors related to the survival time and establish an individual and accurate survival prediction model. At present, the prognosis studies of GBC mainly focus on the clinical and pathological examination (6, 14, 15). There are many factors affecting postoperative survival of GBC patients, including TNM stage of tumor, degree of tumor differentiation, liver infiltration, jaundice, and lymph node dissection. The TNM staging is widely used in clinical, but only includes tumor infiltration depth (T stage), lymph node metastasis (N stage), and distant metastases (M stage), with limited survival prediction value. It only for a class of patients, cannot achieve individualized accurate prediction to adjust subsequent treatment. Many studies have focused on the effect of clinical examination on the prognosis of GBC, including inflammatory factors and nutritional indicators (16, 17). However, the original data of those researches almost come from one laboratory examination, and there may be fluctuations in the same individual during different times. Meanwhile, these markers lack specificity, and the mechanism

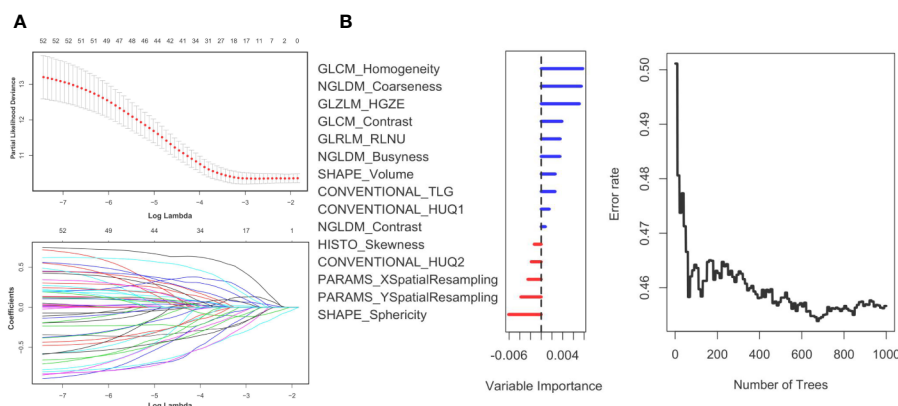


**FIGURE 2 |** Panel (A) shows the Lasso result. Panel (B) shows the random forest result. The left (B) shows the order of the out-of-bag importance of the selected parameters. The right picture shows relationship between the error rate and the number of classification trees.

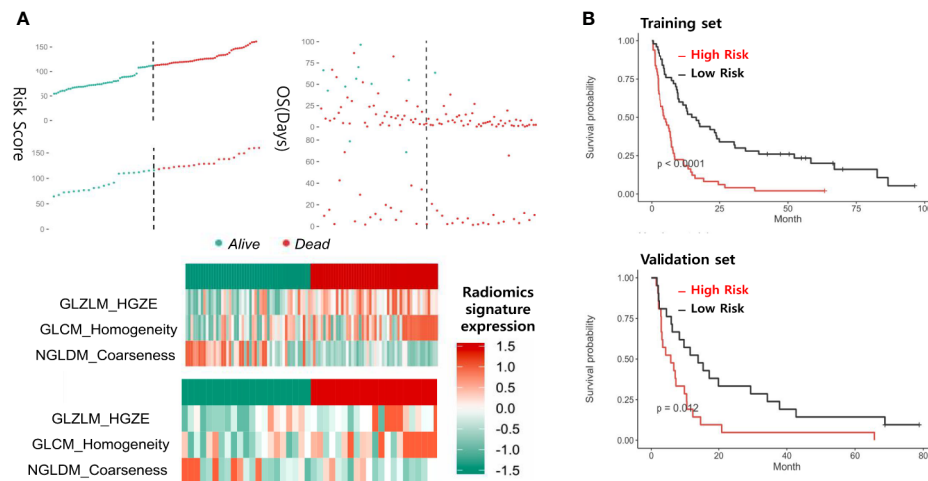


**FIGURE 3 |** Panel (A) shows the distribution of risk scores and the values of the three CT parameters in the training and test groups. Panel (B) shows the survival of patients at high or low risk after being grouped by median.

**TABLE 2 |** The results of a multivariate COX analysis.

	P value	HR	Low 95% CI	High 95% CI
Radiomics Risk Score	0.040	1.495	1.019	2.194
Surgery	0.087	0.672	0.426	1.059
Liver metastasis	0.026	1.615	1.060	2.459
N Stage	0.037	1.797	1.035	3.122
Jaundice	0.834	0.953	0.606	1.498
T stage	0.696	1.223	0.447	3.343
Sex	0.456	0.862	0.582	1.275
Age	0.942	1.02	0.602	1.727

**TABLE 3 |** The results of a multivariate analysis combined with clinical examination and radiologic parameters.

	P value	HR	Low 95.0%CI	High 95.0%CI
Liver metastasis	0.009	1.620	1.126	2.322
Surgery	0.077	0.668	0.427	1.044
Radiomics Risk Score	0.042	1.462	1.014	2.107
N Stage	0.042	1.730	1.020	2.935

of the correlation between these indicators and tumor outcome is still to be studied. Moreover, clinical data can only reflect the partial biological manifestations of tumor and lack a comprehensive description of entire tumor lesions.

Radiomics is a promising approach to acquire a large amount of intuitive data through the analysis of entire tumor lesion and metastasis. Compared with the molecular features detected by popular omics techniques such as genomics and proteomics, radiomics can better overcome the temporal and spatial specificity of the whole course of cancer. Meanwhile, texture analysis can provide quantitative and semi-quantitative parameters to reflect tumor heterogeneity, which is of great

significance in tumor research (18, 19). However, there are few studies of this type conducted in GBC, ascribed to the uniformed data is acquired in clinical experiment. A variety of medical images are applied in clinical decision-making, mainly including CT scan, contrast-enhanced CT, multi-parameter MRI, and PET-CT. CT is the most common and cost-effective data acquisition of original lesions before treatment among them. Although reconstructed MRI sequences and contrast-enhanced CT have advantages in the identification and differentiation of tumors, these detection methods are still not widely used in most areas of China. In terms of applying machine learning, the heterogeneity of tumor tissues is included in multiple texture parameters, thus, the analysis of texture parameters alone cannot fully reflect the overall characteristics of the tumor. Considering this problem, we believe that a complex model integrating different texture signatures is needed to fully identify the total tumor lesion. Also, the random forest is a powerful machine learning method, which has been proved to be able to implement the correct classification work successfully (20, 21). Adopting the concept of integrated learning, random forest has a good accuracy in current machine learning algorithms by combining multiple decision tree models. Moreover, it can process high-dimensional data and be applied in big data effectively. In particular, it can evaluate the importance of each feature in classification. Therefore, in this study, the random forest can better identify parameters and establish classifiers.

However, our study still has three main limitations. Firstly, analyzing CT scan data alone cannot replace other image acquisition methods (such as enhanced CT, mpMRI, reconstructed multiple sequences ADC, and DTI) in real clinical work. Secondly, limited by the size of the sample, there are not enough enhanced CT data and MRI data, thus,



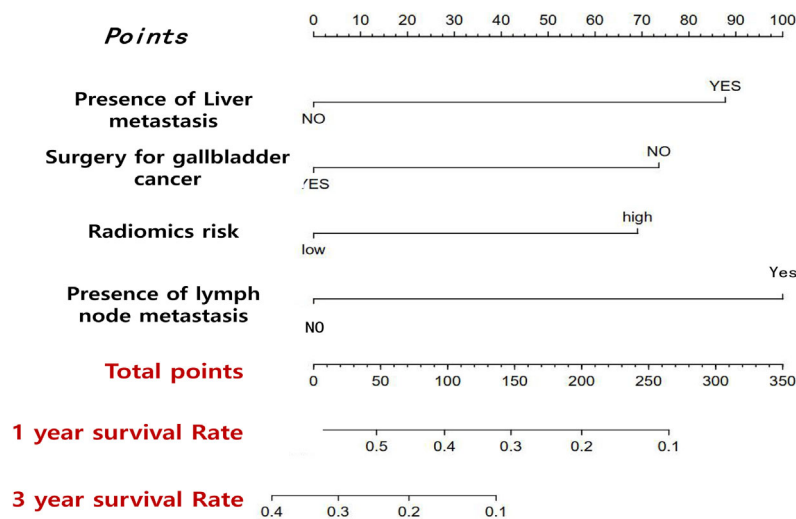


**FIGURE 4** | Nomogram that predicts the overall prognosis survival of gallbladder cancer patients after multiple factors are included.

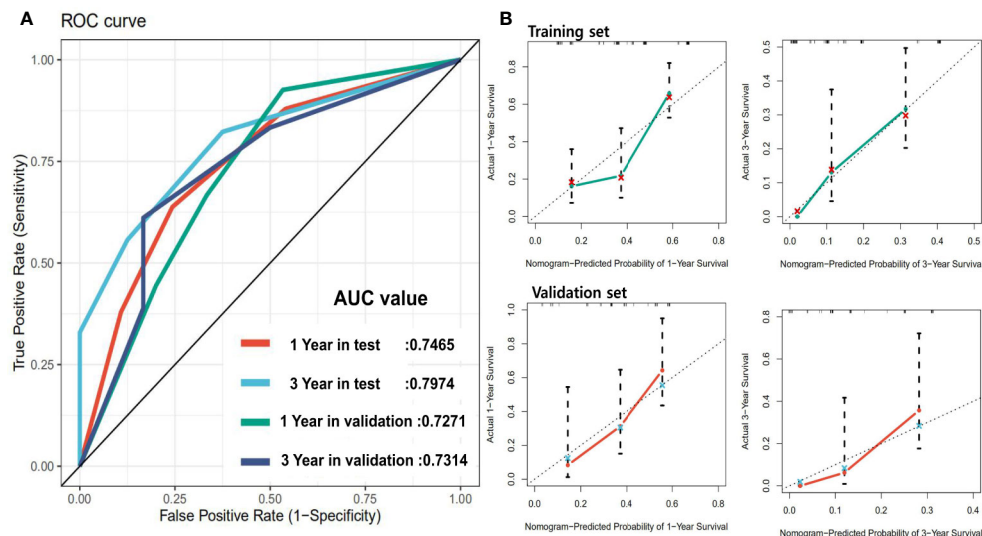


**FIGURE 5** | Panel (A) shows the ROC of the prognostic survival model incorporating with clinical parameters. Panel (B) is the calibration curve of the model.

this study was not compared with a variety of advanced scanning techniques. Third, our research was limited by its retrospective data. These findings might have better clinical implications, if confirmed in prospective studies. Fourth, the patients included in the study were all from a single center, which may result in the lack of sufficient extensibility of the classifier. Considering the differences of medical institutions in obtaining original images and the differences in manual segmentation of lesions, we cannot guarantee that this machine learning classifier performs well on external data sources. But all of the research methods and analysis

used in the study come from open-source data packets, which mean that the analysis process needs to be repeated on other data.

## CONCLUSION

We found associations between established CT imaging parameters and overall survival. Radiomics-based non-invasive technology represented promising ability in predicting the overall survival of gallbladder carcinoma, although more

extensive testing are necessary to perfect this technology in real clinical use.

## DATA AVAILABILITY STATEMENT

The original contributions presented in the study are included in the article/**Supplementary Material**. Further inquiries can be directed to the corresponding authors.

## ETHICS STATEMENT

The studies involving human participants were reviewed and approved by Ethics Committee of Sichuan University. The patients/participants provided their written informed consent to participate in this study. Written informed consent was obtained from the individual(s) for the publication of any potentially identifiable images or data included in this article.

## AUTHOR CONTRIBUTIONS

ZL, XM, and JJ are responsible for conceiving and designing the subject. ZL, GZ, XJ and HZ conduct data analysis

and article writing. YZ and HZ are responsible for data processing. ZL and GZ make the same contribution to this paper. All authors contributed to the article and approved the submitted version.

## SUPPLEMENTARY MATERIAL

The Supplementary Material for this article can be found online at: <https://www.frontiersin.org/articles/10.3389/fonc.2020.604288/full#supplementary-material>

**SUPPLEMENTARY FIGURE 1** | Shows an example of ROI segmentation.

**SUPPLEMENTARY TABLE 1** | Shows radiomics parameters and prognostic risk scores for all patients.

**SUPPLEMENTARY TABLE 2** | Shows the importance of the 15 parameters analyzed by LASSO in the random forest.

**SUPPLEMENTARY TABLE 3** | Shows the values of all radiomics parameters for all patients.

**SUPPLEMENTARY TABLE 4** | Shows the demographic parameters, some laboratory test parameters and median survival time for all patients.

**SUPPLEMENTARY TABLE 5** | Shows the correlation between all image parameters in the model.

## REFERENCES

- Hundal R, Shaffer EA. Gallbladder cancer: epidemiology and outcome. *Clin Epidemiol* (2014) 6:99–109. doi: 10.2147/CLEP.S37357
- Cronin KA, Ries LA, Edwards BK. The Surveillance, Epidemiology, and End Results (SEER) Program of the National Cancer Institute. *Cancer* (2014) 120 Suppl 23:3755–7. doi: 10.1002/cncr.29049
- Henley SJ, Weir HK, Jim MA, Watson M, Richardson LC. Gallbladder Cancer Incidence and Mortality, United States 1999–2011. *Cancer Epidemiol Biomarkers* (2015) 24:1319–26. doi: 10.1158/1055-9965.EPI-15-0199
- Kakaei F, Beheshtirouy S, Nejatollahi SM, Zarrintan S, Mafi MR. Surgical treatment of gallbladder carcinoma: a critical review. *Updates Surg* (2015) 67:339–51. doi: 10.1007/s13304-015-0328-x
- Eil R, Hansen PD, Cassera M, Orloff SL, Sheppard BC, Diggs B, et al. Bile duct involvement portends poor prognosis in resected gallbladder carcinoma. *Gastrointest Cancer Res* (2013) 6:101–5.
- Sicklick JK, Fanta PT, Shimabukuro K, Kurzrock R. Genomics of gallbladder cancer: the case for biomarker-driven clinical trial design. *Cancer Metastasis Rev* (2016) 35:263–75. doi: 10.1007/s10555-016-9602-8
- Wang YF, Feng FL, Zhao XH, Ye ZX, Zeng HP, Li Z, et al. Combined detection tumor markers for diagnosis and prognosis of gallbladder cancer. *World J Gastroenterol* (2014) 20:4085–92. doi: 10.3748/wjg.v20.i14.4085
- Lambin P, Rios-Velazquez E, Leijenaar R, Carvalho S, van Stiphout RG, Granton P, et al. Radiomics: extracting more information from medical images using advanced feature analysis. *Eur J Cancer* (2012) 48:441–6. doi: 10.1016/j.ejca.2011.11.036
- Aerts HJ, Velazquez ER, Leijenaar RT, Parmar C, Grossmann P, Carvalho S, et al. Decoding tumour phenotype by noninvasive imaging using a quantitative radiomics approach. *Nat Commun* (2014) 5:4006. doi: 10.1038/ncomms5644
- Hunter LA, Krafft S, Stingo F, Choi H, Martel MK, Kry SF, et al. High quality machine-robust image features: identification in nonsmall cell lung cancer computed tomography images. *Med Phys* (2013) 40:121916. doi: 10.1118/1.4829514
- Chen C, Guo X, Wang J, Guo W, Ma X, Xu J. The Diagnostic Value of Radiomics-Based Machine Learning in Predicting the Grade of Meningiomas Using Conventional Magnetic Resonance Imaging: A Preliminary Study. *Front Oncol* (2019) 9:1338. doi: 10.3389/fonc.2019.01338
- Nioche C, Orlhac F, Boughdad S, Reuze S, Goya-Outi J, Robert C, et al. LIFEX: A Freeware for Radiomic Feature Calculation in Multimodality Imaging to Accelerate Advances in the Characterization of Tumor Heterogeneity. *Cancer Res* (2018) 78:4786–9. doi: 10.1158/0008-5472.CAN-18-0125
- Friedman J, Hastie T, Tibshirani R. Regularization Paths for Generalized Linear Models via Coordinate Descent. *J Stat Softw* (2010) 33:1–22. doi: 10.18637/jss.v033.i01
- Sasaki E, Nagino M, Ebata T, Oda K, Arai T, Nishio H, et al. Immunohistochemically demonstrated lymph node micrometastasis and prognosis in patients with gallbladder carcinoma. *Ann Surg* (2006) 244:99–105. doi: 10.1097/01.sla.0000217675.22495.6f
- He C, Cai Z, Zhang Y, Lin X. Prognostic Model to Predict Cancer-Specific Survival for Patients With Gallbladder Carcinoma After Surgery: A Population-Based Analysis. *Front Oncol* (2019) 9:1329. doi: 10.3389/fonc.2019.01329
- Zheng P, Wang X, Hong Z, Shen F, Zhang Q. Preoperative fasting hyperglycemia is an independent prognostic factor for postoperative survival after gallbladder carcinoma radical surgery. *Cancer Manag Res* (2019) 11:1425–32. doi: 10.2147/CMAR.S192273
- Deng Y, Zhang F, Yu X, Huo C-L, Sun Z-G, Wang S. Prognostic Value Of Preoperative Systemic Inflammatory Biomarkers In Patients With Gallbladder Cancer And The Establishment Of A Nomogram. *Cancer Manage Res Volume* (2019) 11:9025–35. doi: 10.2147/CMAR.S218119
- Huang YQ, Liang CH, He L, Tian J, Liang CS, Chen X, et al. Development and Validation of a Radiomics Nomogram for Preoperative Prediction of Lymph Node Metastasis in Colorectal Cancer. *J Clin Oncol* (2016) 34:2157–64. doi: 10.1200/JCO.2015.65.9128
- Delzell DAP, Magnuson S, Peter T, Smith M, Smith BJ. Machine Learning and Feature Selection Methods for Disease Classification With Application to

- Lung Cancer Screening Image Data. *Front Oncol* (2019) 9:1393. doi: 10.3389/fonc.2019.01393
20. Lebedev AV, Westman E, Van Westen GJ, Kramberger MG, Lundervold A, Aarsland D, et al. I. Alzheimer's Disease Neuroimaging, and c. the AddNeuroMed, Random Forest ensembles for detection and prediction of Alzheimer's disease with a good between-cohort robustness. *NeuroImage Clin* (2014) 6:115–25. doi: 10.1016/j.nicl.2014.08.023
  21. Ueno Y, Forghani B, Forghani R, Dohan A, Zeng XZ, Chamming's F, et al. Endometrial Carcinoma: MR Imaging-based Texture Model for Preoperative Risk Stratification-A Preliminary Analysis. *Radiology* (2017) 284:748–57. doi: 10.1148/radiol.2017161950

**Conflict of Interest:** The authors declare that the research was conducted in the absence of any commercial or financial relationships that could be construed as a potential conflict of interest.

Copyright © 2020 Liu, Zhu, Jiang, Zhao, Zeng, Jing and Ma. This is an open-access article distributed under the terms of the Creative Commons Attribution License (CC BY). The use, distribution or reproduction in other forums is permitted, provided the original author(s) and the copyright owner(s) are credited and that the original publication in this journal is cited, in accordance with accepted academic practice. No use, distribution or reproduction is permitted which does not comply with these terms.



# Diagnostic Value of Telomerase Activity in Patients With Bladder Cancer: A Meta-Analysis of Diagnostic Test

Lei Peng<sup>1†</sup>, Jinze Li<sup>1†</sup>, Chunyang Meng<sup>1†</sup>, Jinming Li<sup>2</sup>, Dandan Tang<sup>3</sup>, Fangxue Guan<sup>4</sup>, Peng Xu<sup>5</sup>, Tangqiang Wei<sup>1</sup> and Yunxiang Li<sup>1\*</sup>

## OPEN ACCESS

### Edited by:

Lu Yang,  
Sichuan University, China

### Reviewed by:

Bangshun He,  
Nanjing Medical University, China  
Cao Dehong,  
Sichuan University, China

### \*Correspondence:

Yunxiang Li  
liyunxiang369@126.com

<sup>†</sup>These authors have contributed  
equally to this work

### Specialty section:

This article was submitted to  
Cancer Imaging and  
Image-directed Interventions,  
a section of the journal  
Frontiers in Oncology

**Received:** 06 June 2020

**Accepted:** 04 November 2020

**Published:** 03 December 2020

### Citation:

Peng L, Li J, Meng C, Li J,  
Tang D, Guan F, Xu P, Wei T and  
Li Y (2020) Diagnostic Value of  
Telomerase Activity in Patients  
With Bladder Cancer: A Meta-  
Analysis of Diagnostic Test.  
Front. Oncol. 10:570127.  
doi: 10.3389/fonc.2020.570127

<sup>1</sup> Department of Urology, Nanchong Central Hospital, The Second Clinical College, North Sichuan Medical College (University), Nanchong, China, <sup>2</sup> Department of Urology, The Affiliated Hospital of Medical College, North Sichuan Medical College (University), Nanchong, China, <sup>3</sup> Department of Cardiothoracic Surgery, Shenzhen People's Hospital, Affiliated Hospital of Jinan University, Shenzhen, China, <sup>4</sup> Internal Medicine, People's Hospital of Yanyuan, Xichang City, China, <sup>5</sup> Department of Cardiology, The Affiliated Hospital of Medical University, Guizhou Medical University, Guizhou, China

**Background:** This study aimed to evaluate the diagnostic value of telomerase activity (TA) for bladder cancer (BC) by meta-analysis.

**Methods:** We conducted a systematic search of studies published on PubMed, Embase, and Web of Science up to June 1, 2019. We used Stata 15 and Review Manager 5.3 for calculations and statistical analysis.

**Results:** To evaluate the diagnostic value of TA for BC, we performed a meta-analysis on 22 studies, with a total of 2,867 individuals, including sensitivity, specificity, positive and negative likelihood ratio (PLR, NLR), diagnostic odds ratio (DOR), and 95% confidence intervals (CIs). The pooled parameters were calculated from all studies, and we found a sensitivity of 0.79 (95% CI: 0.72–0.84), a specificity of 0.91 (95% CI: 0.87–0.94), a PLR of 8.91 (95% CI: 5.91–13.43), an NLR of 0.24 (95% CI: 0.15–0.37), a DOR of 37.90 (95% CI: 23.32–61.59), and an AUC of 0.92 (95% CI: 0.90–0.94). We also conducted a subgroup analysis based on the different stages and grades of BC. Results from the subgroup analysis showed that there was no significant difference in TA in either high and low stages of BC, but that low-grade tumors had a lower TA than high-grade tumors.

**Conclusions:** TA can be used as a potential biomarker for the diagnosis of bladder cancer with its high specificity. Rigorous and high-quality prospective studies are required to verify our conclusion.

**Keywords:** bladder cancer, telomerase activity, meta-analysis, diagnosis, biomarker



## BACKGROUND

Bladder cancer (BC) is a malignant tumor with very high invasiveness and is one of the ten most common cancer types occurring in both males and females (1, 2). BC can generally be identified using pain-free methods such as macroscopic hematuria or microscopic hematuria, but these methods usually lead to a poor prognosis (3).

Due to the lack of specific clinical symptoms in BC patients, early diagnosis has a great impact on treatment and prognosis (4). Generally, urine cytology, histology, and cystoscopy are the most common methods for diagnosis of BC (5). Biopsy *via* cystoscope for pathological diagnosis is the gold standard for the diagnosis of bladder cancer. Its intuitive characteristics are quite reliable for the diagnosis of BC, but this invasive operation will bring great pain to patients, and its expensive charges also affect its clinical frequency of use and late follow-up (6). The search for a better, lower-risk, accurate, and easy-to-manage methodology for the diagnosis of BC has been ongoing (7).

Detection of telomerase activity (TA) is a non-invasive and effective auxiliary test for the diagnosis of BC (8). Telomerase is correlated to the maintenance of the telomere length in tumor cells and the infinite division of cells. Telomerase activity is present in tumor cells, but it is not typically detected in the normal tissues surrounding the tumor (9). Compared with cystoscopy, the detection of TA can be usually performed using a urine or bladder irrigation solution, which greatly reduces the patient's fear of medical examination and also facilitates follow-up (10).

Non-invasive diagnostic methods have become a popular and emerging field. There are many studies reporting the accuracy of TA in the diagnosis of BC. However, these diagnostic capabilities are reported by different research groups and thus have significant differences between them. The limitations of these studies are sampling errors and confounding factors within the experiment. Taking into account the limitations of single studies, we performed a meta-analysis based on several research samples and used statistical calculations to better understand the diagnostic efficiency of TA in patients with BC. Some studies have previously revealed the relationship between telomere length and various cancers (11). Based on these studies, we further explored the relationship between TA and BC, with the objective of determining the status of telomeres and telomerase activity and their role in BC.

## METHODS

### Literature Search and Eligibility Criteria

We systematically retrieved relevant literature from the PubMed, Embase, and Web of Science databases from inception to June 1,

2019. We used TA, BC, and urine as the search terms, and the search language was limited to English. We also searched the relevant references' directories to avoid missing other relevant documents.

Studies that meet the following requirements were included in our research: patients diagnosed with BC using the gold standard cystoscopy, studies with the diagnostic value of TA reflected in the research article, and studies with sufficient data on true positive (TP), false positive (FP), false negative (FN), and true negative (TN). Duplicate articles, insufficient quality, studies focusing on other diseases, letters, comments, case reports, and editorials were excluded from our analysis. The review process was assessed by two authors, independently.

### Data Extraction

Studies that meet the following requirements can be included in our research: (1) A patient must be pathologically confirmed and diagnosed as bladder cancer. (2) The patient does not have other malignant tumors of the urinary system. (3) The patient did not perform any invasive transurethral procedures before taking the patient's urine sample or bladder wash. (4) The telomerase activity in urine or washing fluid samples of all patients has been verified by scientific reagents. (5) The original study provided the number of samples that scientifically proved the telomerase activity in urine or bladder irrigation fluid samples: the number of patients or healthy people whose telomerase activity was positive/negative. Duplicate studies, low-quality studies, studies that cannot extract complete trial data, focus on other diseases, letters, comments, editorials, and case reports are excluded. This process was independently retrieved by two authors (LP and JZL).

### Quality Evaluation

We used the Quality Assessment of Diagnostic Accuracy Studies 2 (QUADAS-2) to assess the quality of the included studies. We also used a quantitative method to assess the selected studies. The QUADAS-2 included 14 items (12). Key domains are assessed to determine the risk of bias and applicability. Signaling questions are included to facilitate judgments, with the risk being low if all signaling answer for a domain is 'yes', and if the answer to any question is 'no' suggesting potential bias exists. Concerns about applicability are determined as 'low', 'high', or 'unclear'.

### Statistical Analysis

We used Stata 15 (StataCorp LP, University City, Texas, USA) and Review Manager 5.3 for the statistical analysis. Using a Q test and  $I^2$  to evaluate the heterogeneity of the study,  $I^2 > 50\%$  improvement was considered as significantly heterogeneous (13). We used a bivariate model to calculate the pooled sensitivity, specificity, positive and negative likelihood ratios (PLRs and NLRs), diagnostic odds ratio (DOR), and the 95% confidence interval (CI) (14). We calculated the area under the receiver operator characteristic curve (SROC, AUC). AUC

**Abbreviations:** BC, Bladder Cancer; TA, Telomerase Activity; QUADAS-2, Quality Assessment of Diagnostic Accuracy Studies 2; TP, True Positives; FP, False Positives; FN, False Negatives; TN, True Negatives; ROC, Receiver Operating Characteristic; SROC, Summary Receiver Operator Characteristic; PLRs, Positive Likelihood Ratios; NLRs, Negative Likelihood Ratios; DORs, Diagnostic Odds Ratios; CI, Confidence Intervals.

varied from 0.5 to 1. If the area was equal to 1, then diagnosis had perfect discrimination. If the area was 0.5, then diagnostic ability was considered as poor (15). Deeks funnel plot was used to assess the publication bias, and Fagan plots showed the relationship between the prior probability, the likelihood ratio, and posterior test probability (16).  $P < 0.05$  was considered to be statistically significant.

## RESULTS

### Study Selection and Study Characteristics

**Figure 1** presents the literature search selection process. Initially, we identified a total of 515 studies through the selected databases and manually retrieve. Of these, 195 duplicate records were excluded. After analysis of the title, abstract, and topic, 260 other articles were excluded. 60 articles remained, which were subjected to full text analysis and assessment of eligibility, following which another 38 articles, 14 reviews, six case reports, four Letters, five articles for which data could not be extracted, and nine irrelevant articles were excluded. Finally, we included 22 studies in our qualitative and quantitative analysis (7, 9, 10, 17–35).

In **Table 1**, the characteristics of 22 articles were included in this meta-analysis of TA for BC. The years of these articles are from 1997 to 2010. 2,867 sample individuals from all over the world were included in the study. Most of them were multicenter studies. Sample sizes range from 42 to 185; among 22 studies, five were conducted in Asia (Japan and Israel), six from the United States, 10 from Europe (UK, Germany, Italy and Poland), and an African (Egypt) study. The fourfold table data was presented in **Table 1**.

### Quality Assessment

**Table 1** lists the quality scores for each study. Each article scored 11 points or higher. According to the QUADAS-2 scoring standard, 18 studies were classified with a middle to high score.

### Pooled Diagnostic Values

Since the value of  $I^2$  was greater than 50%, the random effects model was used to combine sensitivity and specificity. The diagnostic value of TA for the detection of BC is shown in **Table 2**. The overall sensitivity and specificity were recorded as 0.79 (95% CI: 0.72–0.84) and 0.91 (95% CI: 0.87–0.94, **Figure 2**), respectively. The Youden Index was 0.7. The pooled PLR was 8.91 (95% CI: 5.91–13.43), NLR was 0.24 (95% CI: 0.15–0.37), and DOR was 37.90 (95% CI: 23.32–61.59). The overall SROC curve is shown in **Figure 3**, with an AUC of 0.92 (95% CI: 0.90–0.94). The Fagan plot is shown in **Figure 4**. The prior probability was 20%, and the post-test probability was 69% for LR-positive and 6% for LR-negative. The diagnostic accuracy for detecting TA in BC was found to be satisfied.

### Subgroup Analyses

We performed a subgroup analysis of TA based on different stages and grades of the tumors. We specified Tis, Ta, or T1 for a low stage tumor, and T2 and above for a high stage tumor. Similarly, we specified that grade 1 is a low-grade tumor and grades 2–3 is a high-grade tumor. According to the results of the heterogeneity test, we used a fixed model for meta-analysis for both grade and stage, and the results and forest map are shown in **Figure 5**. In our comparison of the different subgroups, the  $P$  value was  $>0.05$ , suggesting that there was no significant difference in TA in either the high or low stages of a tumor (**Figure 5**). When comparing the different grades, we observed a  $P=0.001$ , suggesting that low-grade tumors have lower TA than high-grade tumors.

### Publication Bias

The Deeks plot showed there was no publication bias ( $P = 0.83$ , **Figure 6**).

### Heterogeneity and Sensitivity Analysis

According to the results of the forest plot, the heterogeneity of TA was high in both sensitivity ( $I^2 = 89.04\%$ ) and specificity ( $I^2 = 83.86\%$ ). Due to the obvious heterogeneity among the studies, the random effects model was implemented in the calculation and statistics of the combined results to obtain a relatively conservative confidence interval.

### Meta-Regression Analysis

Meta-regression analyses were performed on study design (predesign), gold standard selection, and description (samemth and retest), diagnostic test to be evaluated (index), and patient characteristics (subject). It can be seen from the forest plot that in the 22 studies we included, gold standard selection, diagnostic test evaluation, and patient characteristics have statistically significant effects on the heterogeneity of sensitivity and specificity ( $P < 0.05$ , **Figure 7**).

## DISCUSSION

To our knowledge, this is the first meta-analysis of the diagnostic efficacy for TA in BC. We found that TA is optimal among various other indicators and proved to be an excellent diagnostic.

BC, as a malignant tumor with high morbidity and mortality, has received wide attention, both for its diagnosis and treatment (36). As accepted, cystoscopy has been the gold standard for the diagnosis of BC. Despite its reliability, as an invasive examination, it is performed under local anesthesia, causing strong discomfort to patients (7). A simpler diagnostic would be preferable and would also minimize the damage caused by the examination. There is a shift in the continuous detection and

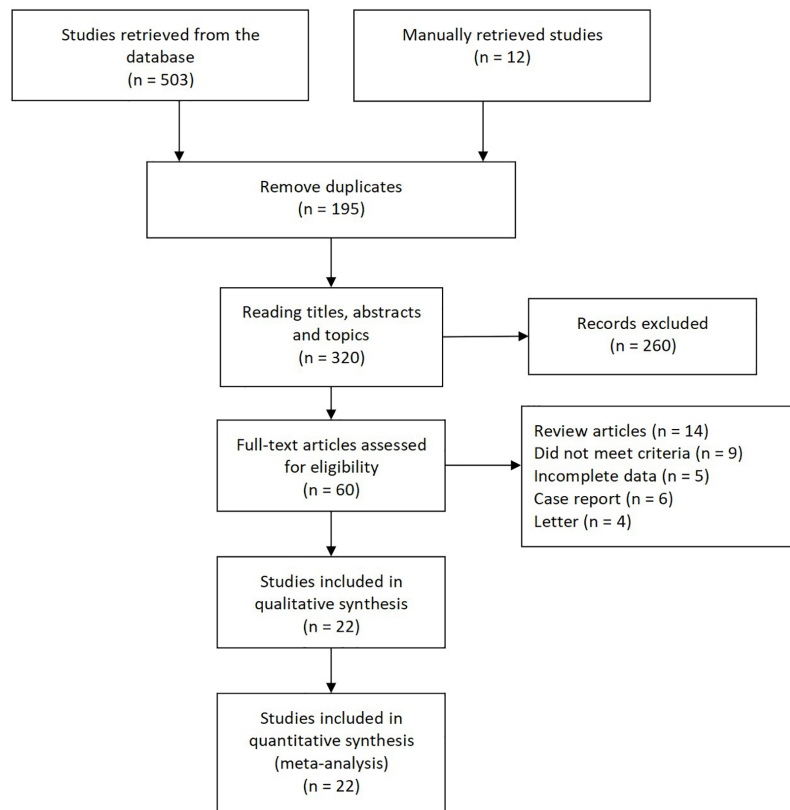


**FIGURE 1** | Flow diagram depicting the selection process for all articles found in literature.

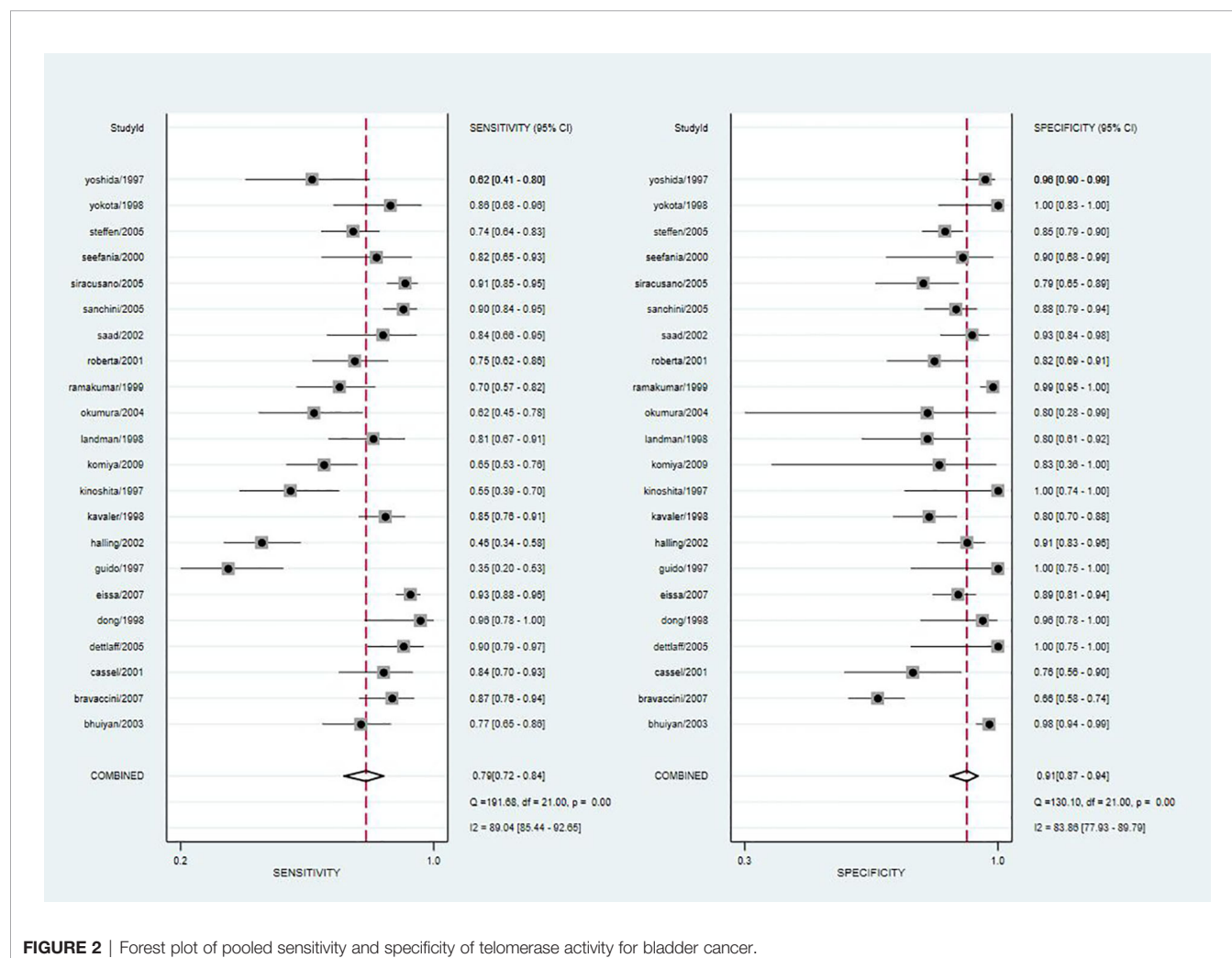
**TABLE 1** | Characteristics of the included studies in the meta-analysis.

NO.	Author	Year	Region	Experiment	Control	Study design	Study population	TP	FP	FN	TN	Score of quality
1	Bhuiyan et al. (10)	2003	USA	65	162	Prospective	Multicenter	50	4	15	158	11
2	Bravaccini et al. (7)	2007	Italy	68	144	Prospective	Multicenter	59	49	9	95	10
3	Cassel et al. (9)	2001	Israel	44	29	Retrospective	Single center	37	7	7	22	11
4	Dettlaff et al. (18)	2005	Poland	52	13	Prospective	Single center	47	0	5	13	11
5	Dong et al. (26)	1998	Korea	23	23	Prospective	Single center	22	1	1	22	9
6	Eissa et al. (19)	2007	Egypt	200	115	Prospective	Single center	185	13	15	102	10
7	Guido et al. (17)	1997	USA	37	13	Prospective	Multicenter	13	0	24	13	11
8	Halling et al. (22)	2002	USA	70	80	Prospective	Single center	32	7	38	73	10
9	Kavaler et al. (23)	1998	USA	104	82	Prospective	Single center	88	16	16	66	10
10	Kinoshita et al. (24)	1997	Japan	42	12	Prospective	Single center	23	0	19	12	9
11	Komiya et al. (27)	2009	Japan	75	6	Prospective	Single center	49	1	26	5	10
12	Landman et al. (25)	1998	USA	47	30	Prospective	Single center	38	6	9	24	11
13	Okumura et al. (28)	2004	Japan	37	5	Prospective	Multicenter	23	1	14	4	10
14	Ramakuma et al. (29)	1999	UK	57	139	Prospective	Single center	40	2	17	137	12
15	Roberta et al. (20)	2001	Italy	56	50	Retrospective	Single center	42	9	14	41	10
16	Saad et al. (30)	2002	UK	37	68	Prospective	Single center	26	5	5	63	10
17	Sanchini et al. (31)	2005	Italy	134	84	Prospective	Multicenter	121	10	13	74	11
18	Siracusano et al. (32)	2005	Italy	153	52	Retrospective	Single center	139	11	14	41	9
19	Stefania et al. (21)	2000	Italy	33	20	Prospective	Single center	27	2	6	18	10
20	Steffen et al. (33)	2005	Germany	94	160	Prospective	Single center	70	24	24	136	10
21	Yokota et al. (34)	1998	Japan	29	20	Prospective	Multicenter	25	0	4	20	11
22	Yoshida et al. (35)	1997	UK	26	83	Prospective	Single center	16	3	10	80	12

**TABLE 2** | Summary estimated of diagnostic performance of telomerase activity for bladder cancer.

Category	SEN <sup>1</sup> (95%CI)	SPE <sup>2</sup> (95%CI)	PLR <sup>3</sup> (95%CI)	NLR <sup>4</sup> (95%CI)	DOR <sup>5</sup> (95%CI)	AUC <sup>6</sup> (95%CI)
Overall	0.79(0.65–0.86)	0.98(0.94–0.99)	8.91(5.91–13.43)	0.24(0.15–0.37)	37.90(23.32–61.59)	0.92(0.90–0.94)

<sup>1</sup>SEN, Sensitivity; <sup>2</sup>SPE, Specificity; <sup>3</sup>PLR, Positive Likelihood Ratios; <sup>4</sup>NLR, Negative Likelihood Ratios; <sup>5</sup>DOR, Diagnostic Odds Ratios; <sup>6</sup>AUC, Area under the curve.



development of BC test methods from macro to micro, and role of markers in urine is being explored for the detection and diagnosis of BC (18, 19).

Telomeres are composed of repeated gene sequences and related proteins. Their main role is to avoid end-to-end fusion and nuclear cleavage during chromosome division (18). Telomerase reverse telomeres shortening during cell division. This is one of the essential processes for the permanent life of tumor cells (9). We hypothesized that in tumor cells, telomerase activity would be higher than in normal cells. Many scholars have studied the relationship between TA and BC, but due to limitations in detection technology and in sample size, the

conclusions were so far inconsistent. We integrated and analyzed research done by other authors and included a sample group large enough for performance of meta-analysis, aiming at comprehensive evaluation of the diagnostic validity for looking into TA in BC, with a goal of providing better guidance for clinical practice.

A number of studies have shown that the sensitivity of the telomerase assay for urothelial carcinoma is lower in voided urine specimens than in bladder washings (17, 22, 24). However, urine is easier to obtain than bladder washings and also easier to collect from the patient's perspective. In our meta-analysis, the overall sensitivity was 0.79 (95% CI: 0.72–



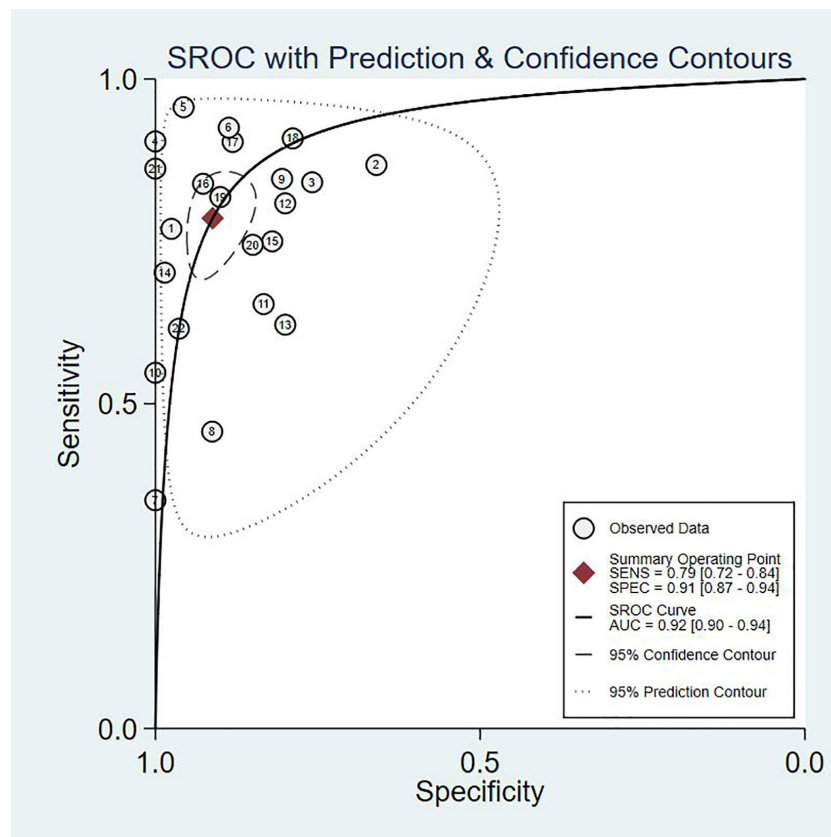


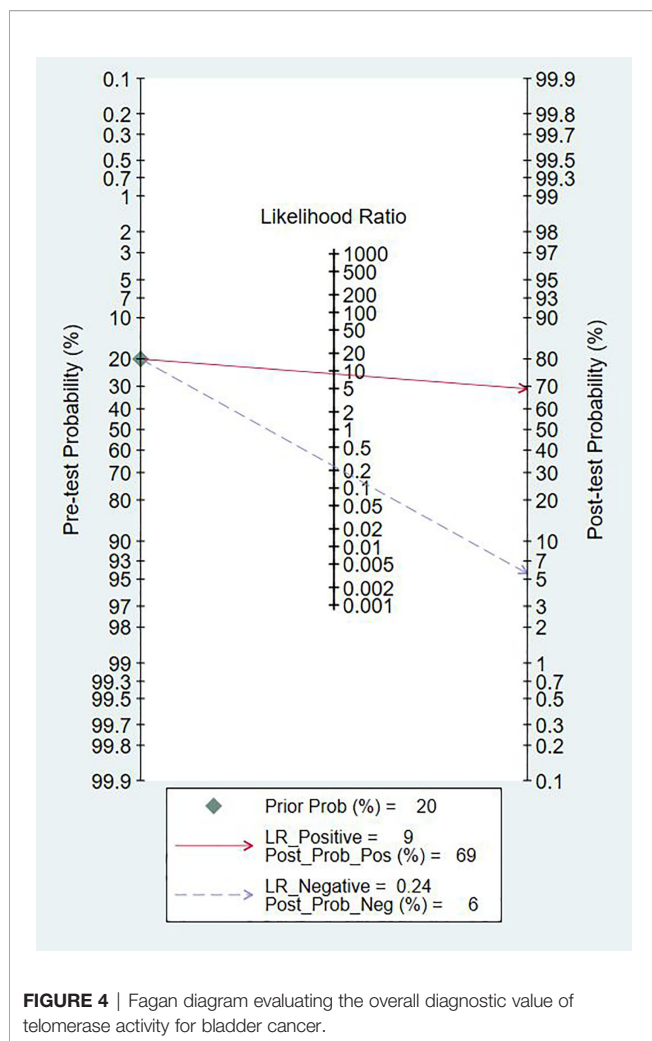
**FIGURE 3** | The SROC curve of telomerase activity for bladder cancer.

0.84), the specificity was 0.91 (95% CI: 0.87–0.94), and the Youden index was 0.7. AUC was 0.92 (95% CI: 0.90–0.94), which was in line with our initial predictions. Using these composite indicators, we showed that TA could be a good and accurate indicator for the diagnosis of BC. A diagnostic test can typically be considered to have a high value when both sensitivity and specificity are  $>0.7$ . In this study, consistently with our predictions, the sensitivity results reached this value for 16 articles, again indicating the superiority of TA in the diagnosis of BC. However, the sensitivity values provided in the other two studies were significantly lower (17, 22). The reason for this analysis was that, due to the technical level of the test, the sample size and bias between the samples might have led to different final results. In relation to the specificity results, 21 of the included studies reached 0.7 or higher, showing that the results were not significantly different between the studies and confirming our hypothesis and indicating the excellent specificity of TA for the diagnosis of BC. The higher the value of DOR, the better the diagnostic ability for the selected method. In our study, the DOR value was 37.90 (95% CI: 23.32–61.59), suggesting that the overall accuracy was high. The overall PLR value was 8.91 (95% CI: 5.91–13.43), suggesting that patients with BC have a TA 8.91 times higher than normal, and a total NLR of 0.24

(95% CI: 0.15–0.37), meaning that normal individuals suffering from BC was of 25%. In the judging criteria,  $PLR > 10$ ,  $NLR < 0.1$ , the diagnostic efficiency for this method was higher. Taking this aspect into account, we can conclude that the diagnostic efficiency of TA for BC is suboptimal. At the same time, we also noticed that the publication bias shown by Deek's funnel plot (**Figure 6**) has a P-value of 0.83. This shows that there is no significant publication bias among the studies. However, according to the results of Meta regression analysis, the included studies are not consistent due to gold standard selection, diagnostic test evaluation, and patient characteristics, which may be the direct cause of significant heterogeneity (**Figure 7**).

To investigate the TA relationship between different staging and grading, we performed a subgroup analysis. In terms of staging, we considered Tis, Ta, and T0 as low-stage tumors, while T2–T4 as high stage. When grading, grade 1 was considered a low-grade tumor, and grades 2 and 3 were considered high-grade tumors. Thus, through meta-analysis, the association between them was evaluated. We found there was no absolute difference in TA between high-stage and low-stage tumors ( $P > 0.05$ ) or between different grades, using meta-analysis. Our results showed that the TA in low-grade tumors was significantly lower than in high-grade tumors ( $P = 0.001$ ). We





believe that this is because the higher the grade, the lower the degree of differentiation, the stronger the invasive ability, and the higher the TA, consistent with results reported by Bravaccini et al (7). Detecting TA is not the only non-invasive method used in the diagnosis of BC, and other markers such as nuclear matrix protein (NMP)-22, bladder tumor antigen (BTA), cytokeratin 20 could also be evaluated. Studies have reported that BTA and cytokeratin 20 are not sensitive markers for low-grade tumors. For grade 1 tumors, the sensitivity of BTA and cytokeratin was 13 and 6%, respectively and NMP-22 had a specificity of 70% in the diagnosis of BC (9, 22, 25). NMP-22 is a quick, point of care test having higher sensitivity. In a diagnostic test that included 380 samples, the sensitivity of NMP-22 was 81.9% but at the cost of specificity of 76.97% (37). According to a meta-analysis that included 22 studies, the diagnostic accuracy of urine cytokeratin 20 for bladder cancer is improved with the progression of tumor stage and grade (38). A high-quality meta-analysis including 57 papers showed that across biomarkers, sensitivities ranged from 0.57 to 0.82 and specificities ranged from 0.74 to 0.88. Urine biomarkers plus cytological assessment are more sensitive, but no more specific. It is easy to cause missed diagnosis. For patients

with low-stage and low-grade tumors, the accuracy of urine biomarkers is poor (39). Therefore, as individual indicators, these markers may work better than invasive methods, but the diagnostic performance should take into consideration composite indicators.

Cystoscopy biopsy, as an invasive examination method, brings pain to patients to a certain extent. For elderly men with enlarged prostate, cystoscopy is more likely to cause prostate bleeding, pain, infection, and other related complications. Anatomically shorter urethra of female patients solves some obstacles for cystoscope access. If the patient has bladder inflammation or tuberculosis infection, the biopsy forceps for the removal of bladder mucosa tissue will make the incidence of bleeding, infection, severe pain, and other complications higher. Whether the clinician's judgment on the location of the lesion is accurate also affects whether the patient needs to undergo a second cystoscopy to determine the lesion. At present, the diagnosis of malignant tumors is transitioning from invasive to non-invasive. Finding suitable body fluid/blood biomarkers to improve tumor diagnosis is the current research direction. The continuous improvement of the detection technology of telomerase activity in the urine of patients with bladder cancer also indicates that the research of telomerase is becoming more precise and is expected to be widely used in clinical applications in the future (10, 40).

We followed the PRISM guidelines for our meta-analysis (41). However, at present, our meta-analysis still has some limitations. Firstly, of all the studies included here, most of the research samples were from Europe and the United States, which may skew our research due to racial differences. Secondly, in each group of controlled studies, the patients studied may have presented with other diseases. Since the mechanisms are unknown for these, the interactions between the different diseases may have led to changes in the accuracy of our results. Finally, in the subgroup analysis, we combined the different stages and grades of tumours into a single control. Due to the influence of the original data, it was not able to be detailed enough in different stages and grades. Compared with cystoscopy, although not further clinically applied, TA does have a higher advantage in diagnosing BC with its relatively high sensitivity and non-invasive mode of operation. A larger sample size, tighter design, and longer follow-up randomized controlled trials are also needed to validate.

## CONCLUSIONS

Based on current evidence, TA can be used as a potential biomarker for the diagnosis of bladder cancer with its high specificity. However, TA performance is not always satisfactory in terms of sensitivity, which may require repeated testing. The maturity of the testing technology will also affect the false negative rate. Further studies in TA is needed, which is more in line with the concept of non-invasive diagnosis of diseases. Rigorous and high-quality prospective studies are required to verify our conclusion.

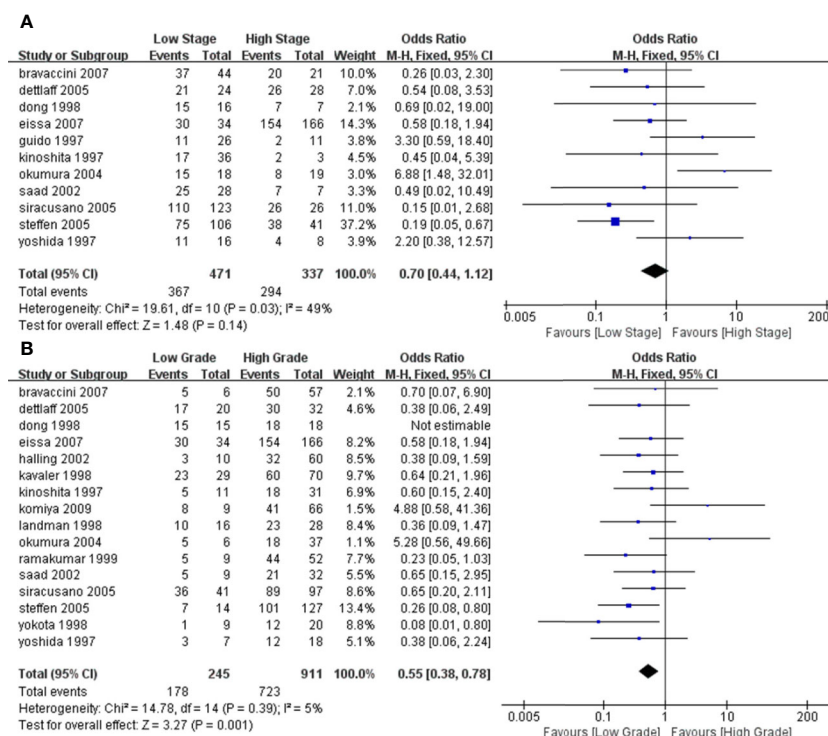


**FIGURE 5** | Forest plot depicting the pooled stages and grades for telomerase activity for bladder cancer (A). Forest plot for different stages (B); Forest plot for different grades.

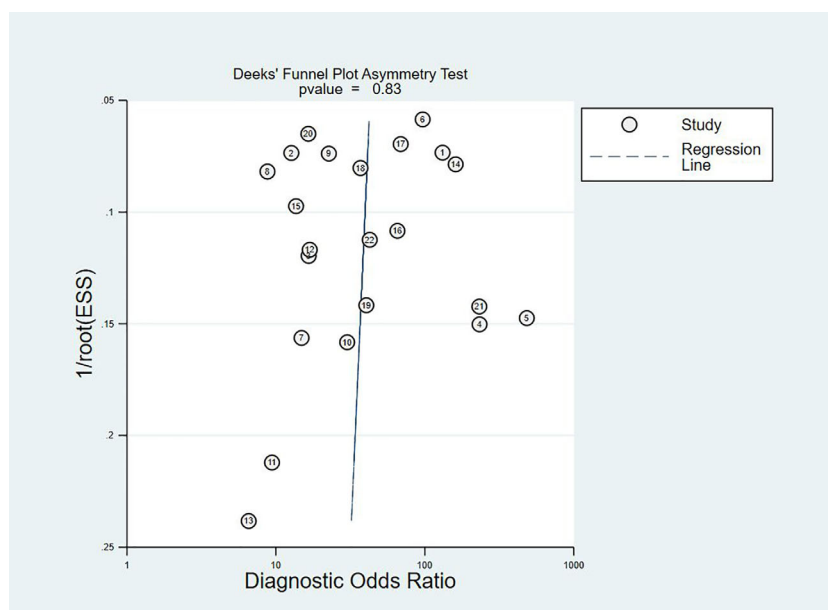


**FIGURE 6** | Deek's funnel plot to evaluate the publication bias.

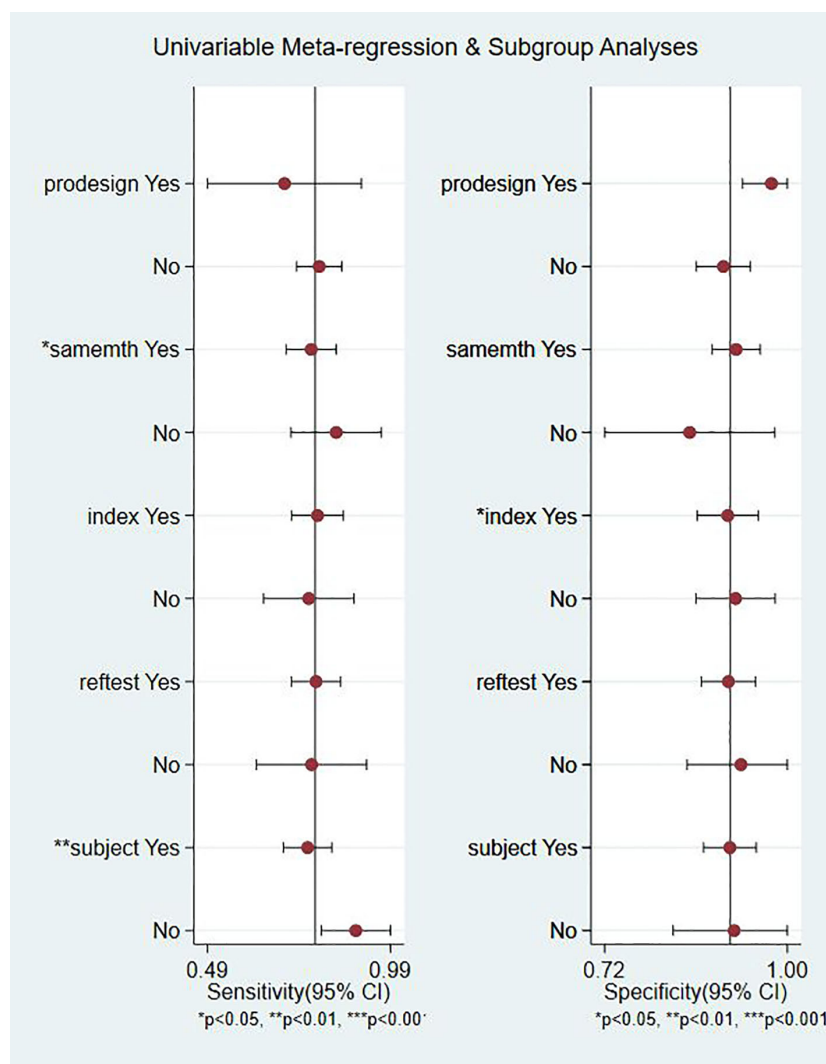


**FIGURE 7 |** Meta regression and subgroup analysis.

## DATA AVAILABILITY STATEMENT

The datasets presented in this study can be found in online repositories. The names of the repository/repository and accession number(s) can be found in the article/supplementary material.

## AUTHOR CONTRIBUTIONS

Conceived and designed the experiments: YL. Analyzed the data: LP, JZL, CM. Contributed reagents/materials/analysis: JML, DT, TW, PX, and FG. Wrote the manuscript: LP and JZL. All authors contributed to the article and approved the submitted version.

## FUNDING

This study was supported by Sichuan Science and Technology Program under Grant number 2020YFS0320; National Natural Science Foundation of China, grant number: 81900617, application code: H0503, relying unit code: 63700708A0140-0268; Sichuan Provincial Health Committee Program of China, grant Number: 20PJ305.

## ACKNOWLEDGMENTS

The authors thank Ms Xinnan Gou for providing continuous encouragement to LP to pursue his career in medicine. This manuscript has been released as a pre-print at Research Square (42).

## REFERENCES

- Li T, Zou L, Zhang J, Li G, Ling L. Non-invasive diagnosis of bladder cancer by detecting telomerase activity in human urine using hybridization chain reaction and dynamic light scattering. *Anal Chim Acta* (2019) 1065:90–7. doi: 10.1016/j.aca.2019.03.039
- Smith AB, Jaeger B, Pinheiro LC, Edwards LJ, Tan HJ, Nielsen ME, et al. Impact of bladder cancer on health-related quality of life. *BJU Int* (2018) 121(4):549–57. doi: 10.1111/bju.14047
- DeGeorge KC HH, Hodges SC. Bladder Cancer: Diagnosis and Treatment. *Am Fam Physician* (2017) 8(96):507–14.
- Schmitz-Drager BJ, Droller M, Lokeshwar VB, Lotan Y, Hudson MA, van Rhijn BW, et al. Molecular markers for bladder cancer screening, early diagnosis, and surveillance: the WHO/ICUD consensus. *Urol Int* (2015) 94(1):1–24. doi: 10.1159/000369357
- Cavallo D, Casadio V, Bravaccini S, Iavicoli S, Pira E, Romano C, et al. Assessment of DNA damage and telomerase activity in exfoliated urinary cells as sensitive and noninvasive biomarkers for early diagnosis of bladder cancer in ex-workers of a rubber tyres industry. *BioMed Res Int* (2014) 2014:370907. doi: 10.1155/2014/370907
- Sun M, Trinh QD. Diagnosis and staging of bladder cancer. *Hematol Oncol Clin North Am* (2015) 29(2):205–18, vii. doi: 10.1016/j.hoc.2014.10.013
- Bravaccini S, Sanchini MA, Granato AM, Gunelli R, Nanni O, Amadori D, et al. Urine telomerase activity for the detection of bladder cancer in females. *J Urol* (2007) 178(1):57–61. doi: 10.1016/j.juro.2007.03.025
- Bladder cancer: diagnosis and management of bladder cancer (c): NICE. Bladder cancer: diagnosis and management of bladder cancer (2017). *BJU Int* (2015) 120(6):755–65. doi: 10.1111/bju.14045
- Cassel A, Rahat MA, Lahat N, Lindenfeld N, Mecz Y, A. S. Telomerase activity and cytokeratin 20 as markers for the detection and followup of transitional cell carcinoma: an unfulfilled promise. *J Urol* (2001) 3(166):841–4. doi: 10.1016/s0022-5347(05)65848-x
- Bhuiyan J, Akhter J, O'Kane DJ. Performance characteristics of multiple urinary tumor markers and sample collection techniques in the detection of transitional cell carcinoma of the bladder. *Clinica Chimica Acta* (2003) 331(1-2):69–77. doi: 10.1016/s0009-8981(03)00074-3
- Wentzensen IM, Mirabello L, Pfeiffer RM, Savage SA. The association of telomere length and cancer: a meta-analysis. *Cancer Epidemiol Biomarkers Prev* (2011) 20(6):1238–50. doi: 10.1158/1055-9965.EPI-11-0005
- Whiting PF RA, Westwood ME, Mallett S, Deeks JJ, Reitsma JB, Leeflang MM, et al. QUADAS-2: a revised tool for the quality assessment of diagnostic accuracy studies. *Ann Intern Med* (2011) 8(155):529–36. doi: 10.7326/0003-4819-155-8-201110180-00009
- Higgins JP TS, Deeks JJ, Altman DG. Measuring inconsistency in meta-analyses. *BMJ* (2003) 7414(327):557–60. doi: 10.1136/bmj.327.7414.557
- Reitsma JB, Glas AS, Rutjes AW, Scholten RJ, Bossuyt PM, Zwinderman AH. Bivariate analysis of sensitivity and specificity produces informative summary measures in diagnostic reviews. *J Clin Epidemiol* (2005) 58(10):982–90. doi: 10.1016/j.jclinepi.2005.02.022
- Hamza TH, Arends LR, van Houwelingen HC, Stijnen T. Multivariate random effects meta-analysis of diagnostic tests with multiple thresholds. *BMC Med Res Methodol* (2009) 9:73. doi: 10.1186/1471-2288-9-73
- Song F KK, Dinnes J, Sutton AJ. Asymmetric funnel plots and publication bias in meta-analyses of diagnostic accuracy. *Int J Epidemiol* (2002) 1(31):88–95. doi: 10.1093/ije/31.1.88
- Dalbagni G HW, Zhang ZF, Cordon-Cardo C, Saigo P, Fair WR, Herr H, et al. Evaluation of the telomeric repeat amplification protocol (TRAP) assay for telomerase as a diagnostic modality in recurrent bladder cancer. *Clin Cancer Res* (1997) 9(3):1593–8.
- Dettlaff-Pokora A, Matuszewski M, Schlichtholz B. Telomerase activity in urine sediments as a tool for noninvasive detection of bladder cancer. *Cancer Lett* (2005) 222(1):83–8. doi: 10.1016/j.canlet.2004.09.004
- Eissa S, Swellam M, Ali-Labib R, Mansour A, El-Malt O, Tash FM. Detection of telomerase in urine by 3 methods: evaluation of diagnostic accuracy for bladder cancer. *J Urol* (2007) 178(3 Pt 1):1068–72. doi: 10.1016/j.juro.2007.05.006
- Fedriga R GR, Nanni O, Bacci F, Amadori D, Calistri D. Telomerase activity detected by quantitative assay in bladder carcinoma and exfoliated cells in urine. *Neoplasia* (2001) 5(3):446–50. doi: 10.1038/sj.neo.7900191
- Gelmini S CA, Salvadori B, Pazzagli M, Selli C, Orlando C. Comparison of telomerase activity in bladder carcinoma and exfoliated cells collected in urine and bladder washings, using a quantitative assay. *Clin Cancer Res* (2000) 7(6):2771–6.
- Halling KC KW, Sokolova IA, Karnes RJ, Meyer RG, Powell EL, Sebo TJ, et al. A comparison of BTA stat, hemoglobin dipstick, telomerase and Vysis UroVysion assays for the detection of urothelial carcinoma in urine. *J Urol* (2002) 5(167):2001–6. doi: 10.1016/s0022-5347(05)65072-0
- Kavaler E LJ, Chang Y, Droller MJ, Liu BC. Detecting human bladder carcinoma cells in voided urine samples by assaying for the presence of telomerase activity. *Cancer* (1998) 4(82):708–14. doi: 10.1002/(sici)1097-0142(19980215)82:4<708::aid-cncr14>3.0.co;2-1
- Kinoshita H OO, Kakehi Y, Mishina M, Mitsumori K, Itoh N, Yamada H, et al. Detection of telomerase activity in exfoliated cells in urine from patients with bladder cancer. *J Natl Cancer Inst* (1997) 4(82):724–30. doi: 10.1093/jnci/89.10.724
- Landman J CY, Kavaler E, Droller MJ, Liu BC. Sensitivity and specificity of NMP-22, telomerase, and BTA in the detection of human bladder cancer. *Urology* (1998) 3(52):398–402. doi: 10.1016/s0090-4295(98)00219-2
- Lee DH YS, Hong SJ, Chung BH, Kim IY. Telomerase: a potential marker of bladder transitional cell carcinoma in bladder washes. *Clin Cancer Res* (1998) 3(4):535–8.
- Morii A, Komiya A, Okumura A, Fuse H. Telomerase activity in bladder cancer tissue. *Exp Ther Med* (2010) 1(1):85–8. doi: 10.3892/etm\_00000015
- Okumura A MI, Nagakawa O, Fuse H. Telomerase activity is correlated with lower grade and lower stage bladder carcinomas. *Int J Urol* (2004) 12(11):1082–6. doi: 10.1111/j.1442-2042.2004.00960.x
- Ramakumar JB S, Besse JA, Roberts SG, Wollan PC, Blute ML, O'Kane DJ. Comparison of screening methods in the detection of bladder cancer. *J Urol* (1999) 161:388–94.
- Saad A HD, McNicholas TA, Boustead GB, Morgan S, Woodman AC. A study comparing various noninvasive methods of detecting bladder cancer in urine. *BJU Int* (2002) 4(89):369–73. doi: 10.1046/j.1464-4096.2001.01699.x
- Sanchini MA GR, Nanni O, Bravaccini S, Fabbri C, Sermasi A, Bercovich E, et al. Relevance of urine telomerase in the diagnosis of bladder cancer. *JAMA* (2005) 16(294):2052–6. doi: 10.1001/jama.294.16.2052
- Siracusano S, Niccolini B, Knez R, Tiberio A, Benedetti E, Bonin S, et al. The simultaneous use of telomerase, cytokeratin 20 and CD4 for bladder cancer detection in urine. *Eur Urol* (2005) 47(3):327–33. doi: 10.1016/j.eururo.2004.10.007
- Weikert S, Krause H, Wolff I, Christoph F, Schrader M, Emrich T, et al. Quantitative evaluation of telomerase subunits in urine as biomarkers for noninvasive detection of bladder cancer. *Int J Cancer* (2005) 117(2):274–80. doi: 10.1002/ijc.21168
- Yokota K KK, Inoue Y, Kanayama H, Kagawa S. Semi-quantitative analysis of telomerase activity in exfoliated human urothelial cells and bladder transitional cell carcinoma. *Br J Urol* (1998) 5(82):727–32. doi: 10.1046/j.1464-410x.1998.00827.x
- Yoshida K ST, Tahara H, Woodman A, Bolodeoku J, Nargund V, Fellows G, et al. Telomerase activity in bladder carcinoma and its implication for noninvasive diagnosis by detection of exfoliated cancer cells in urine. *Cancer* (1997) 2(79):362–9. doi: 10.1002/(sici)1097-0142(19970115)79:2<362::aid-cncr20>3.0.co;2-y
- Martinez Rodriguez RH, Buisan Rueda O, Ibarz L. Bladder cancer: Present and future. *Med Clin (Barc)* (2017) 149(10):449–55. doi: 10.1016/j.medcli.2017.06.009
- Sajid MT, Zafar MR, Ahmad H, Ullah S, Mirza ZI, Shahzad K. Diagnostic accuracy of NMP 22 and urine cytology for detection of transitional cell

- carcinoma urinary bladder taking cystoscopy as gold standard. *Pakistan J Med Sci* (2020) 36(4):705–10. doi: 10.12669/pjms.36.4.1638
38. Mi Y, Zhao Y, Shi F, Zhang M, Wang C, Liu X. Diagnostic accuracy of urine cytokeratin 20 for bladder cancer: A meta-analysis. *Asia-Pacific J Clin Oncol* (2019) 15(2):e11–9. doi: 10.1111/ajco.13024
  39. Chou R, Gore JL, Buckley D, Fu R, Gustafson K, Griffin JC, et al. Urinary Biomarkers for Diagnosis of Bladder Cancer: A Systematic Review and Meta-analysis. *Ann Intern Med* (2015) 163(12):922–31. doi: 10.7326/m15-0997
  40. Wang J, Zhang J, Li T, Shen R, Li G, L L. Strand displacement amplification-coupled dynamic light scattering method to detect urinary telomerase for non-invasive detection of bladder cancer. *Biosens Bioelectron* (2019) 131:143–8. doi: 10.1016/j.bios.2019.02.014
  41. Moher D, Liberati A, Tetzlaff J, Altman DG, Group P. Preferred reporting items for systematic reviews and meta-analyses: the PRISMA statement. *BMJ* (2009) 339:b2535. doi: 10.1136/bmj.b2535
  42. Lei Peng JL, Zhengju R, et al. Diagnostic value of Telomerase Activity in patients with Bladder cancer: a meta-analysis of diagnostic test, 11 October 2019. PREPRINT (Version 2) available at Research Square (<https://doi.org/10.21203/rs.2.11915/v2>).

**Conflict of Interest:** The authors declare that the research was conducted in the absence of any commercial or financial relationships that could be construed as a potential conflict of interest.

Copyright © 2020 Peng, Li, Meng, Li, Tang, Guan, Xu, Wei and Li. This is an open-access article distributed under the terms of the Creative Commons Attribution License (CC BY). The use, distribution or reproduction in other forums is permitted, provided the original author(s) and the copyright owner(s) are credited and that the original publication in this journal is cited, in accordance with accepted academic practice. No use, distribution or reproduction is permitted which does not comply with these terms.





## OPEN ACCESS

## Edited by:

Min Wu,  
Sichuan University, China

## Reviewed by:

Antoni Lluca Abella,  
University Jaume I (UJI), Spain  
Valerio Gallotta,  
Catholic University of the Sacred  
Heart, Italy  
Giuseppe Vizzielli,  
Catholic University of the Sacred  
Heart, Italy

## \*Correspondence:

Ling-ya Pan  
panyl@pumch.cn  
Ling-ying Wu  
wulingying@cscoc.org.cn

<sup>†</sup>These authors have  
contributed equally to this work

## Specialty section:

This article was submitted to  
Cancer Imaging and  
Image-directed Interventions,  
a section of the journal  
Frontiers in Oncology

Received: 29 September 2020

Accepted: 18 November 2020

Published: 07 January 2021

## Citation:

Gu Y, Qin M, Jin Y, Zuo J, Li N, Bian C,  
Zhang Y, Li R, Wu Y-m, Wang C-y,  
Zhang K-q, Yue Y, Wu L-y and Pan L-y  
(2021) A Prediction Model  
for Optimal Primary Debulking  
Surgery Based on Preoperative  
Computed Tomography Scans  
and Clinical Factors in Patients  
With Advanced Ovarian Cancer:  
A Multicenter Retrospective  
Cohort Study.  
Front. Oncol. 10:611617.  
doi: 10.3389/fonc.2020.611617

# A Prediction Model for Optimal Primary Debulking Surgery Based on Preoperative Computed Tomography Scans and Clinical Factors in Patients With Advanced Ovarian Cancer: A Multicenter Retrospective Cohort Study

Yu Gu<sup>1†</sup>, Meng Qin<sup>1†</sup>, Ying Jin<sup>1</sup>, Jing Zuo<sup>2</sup>, Ning Li<sup>2</sup>, Ce Bian<sup>3</sup>, Yu Zhang<sup>4</sup>, Rong Li<sup>5</sup>, Yu-mei Wu<sup>6</sup>, Chun-yan Wang<sup>7</sup>, Ke-qiang Zhang<sup>8</sup>, Ying Yue<sup>9</sup>, Ling-ying Wu<sup>2\*</sup> and Ling-ya Pan<sup>1\*</sup>

<sup>1</sup> Department of Obstetrics and Gynecology, Peking Union Medical College Hospital, Chinese Academy of Medical Sciences and Peking Union Medical College, Beijing, China, <sup>2</sup> Department of Obstetrics and Gynecology, National Cancer Center/Cancer Hospital, Chinese Academy of Medical Sciences and Peking Union Medical College, Beijing, China, <sup>3</sup> Department of Obstetrics and Gynecology, The West China Second University Hospital of Sichuan University, Chengdu, China, <sup>4</sup> Department of Obstetrics and Gynecology, Xiangya Hospital of Central South University, Changsha, China, <sup>5</sup> Department of Obstetrics and Gynecology, Chongqing University Cancer Hospital, Chongqing, China, <sup>6</sup> Department of Obstetrics and Gynecology, Beijing Obstetrics and Gynecology Hospital, Capital Medical University, Beijing, China, <sup>7</sup> Department of Obstetrics and Gynecology, Liaoning Cancer Hospital & Institute, Cancer Hospital of China Medical University, Shenyang, China, <sup>8</sup> Department of Obstetrics and Gynecology, Hunan Cancer Hospital, The Affiliated Cancer Hospital of Xiangya School of Medicine, Central South University, Changsha, China, <sup>9</sup> Department of Obstetrics and Gynecology, The First Hospital of Jilin University, Jilin, China

**Objective:** This study assessed the predictive value of preoperative computed tomography (CT) scans and clinical factors for optimal debulking surgery (ODS) in patients with advanced ovarian cancer (AOC).

**Methods:** Patients with AOC in International Federation of Gynecology and Obstetrics (FIGO) stage III-IV who underwent primary debulking surgery (PDS) between 2016 and 2019 from nine tertiary Chinese hospitals were included. Large-volume ascites, diffuse peritoneal thickening, omental cake, retroperitoneal lymph node enlargement (RLNE) below and above the inferior mesenteric artery (IMA), and suspected pelvic bowel, abdominal bowel, liver surface, liver parenchyma and portal, spleen, diaphragm and pleural lesions were evaluated on CT. Preoperative factors included age, platelet count, and albumin and CA125 levels.

**Results:** Overall, 296 patients were included, and 250 (84.5%) underwent ODS. The prediction model included age >60 years ( $P=0.016$ ; prediction index value, PIV=1), a CA125 level >800 U/ml ( $P=0.033$ , PIV=1), abdominal bowel metastasis ( $P=0.034$ , PIV=1), spleen metastasis ( $P<0.001$ , PIV=2), diaphragmatic metastasis ( $P=0.014$ , PIV=2), and an

RLNE above the IMA ( $P < 0.001$ ,  $PIV = 2$ ). This model had superior discrimination ( $AUC = 0.788 > 0.750$ ), and the Hosmer-Lemeshow test indicated its stable calibration ( $P = 0.600 > 0.050$ ). With the aim of maximizing the accuracy of prediction and minimizing the rate of inappropriate explorations, a total  $PIV \geq 5$  achieved the highest accuracy of 85.47% and identified patients who underwent suboptimal PDS with a specificity of 100%.

**Conclusions:** We developed a prediction model based on two preoperative clinical factors and four radiological criteria to predict unsatisfactory debulking surgery in patients with AOC. The accuracy of this prediction model needs to be validated and adjusted in further multicenter prospective studies.

**Keywords:** ovarian cancer, computed tomography scans, prediction model, primary debulking surgery, neoadjuvant chemotherapy, multicenter study

## INTRODUCTION

Epithelial ovarian cancer is currently the most malignant carcinoma of the female reproductive system with the highest mortality rate (1). Approximately two-thirds of ovarian cancer patients are initially diagnosed with advanced ovarian cancer (AOC) mainly due to the lack of early detection methods and specific symptoms for ovarian cancer (2). Primary debulking surgery (PDS) followed by platinum-based chemotherapy has been the standard treatment for patients with International Federation of Gynecology and Obstetrics (FIGO) stage IIIC or IV (3, 4) for many years. However, the traditional management of ovarian cancer has changed since two multicenter randomized phase III trials [EORTC 55971 (5) and CHORUS (6)] reported that neoadjuvant chemotherapy (NACT) followed by interval debulking surgery (IDS) was not inferior to PDS. NACT refers to chemotherapy as the primary treatment, which is administered to reduce the tumor burden before debulking surgery is performed (7, 8). The SCORPION (9) and JCOG0602 (10) clinical trials commonly considered that NACT-IDS was not inferior to PDS-CT due to less surgical aggressiveness and postoperative morbidity rates as well as better quality of life scores.

RD after debulking surgery is one of the most important independent risk factors for survival in AOC patients (11), regardless of surgery complexity or the administration of NACT (12, 13). Optimal debulking surgery (ODS) is considered optimal if the residual tumor (RD) is less than 1 cm in maximum diameter or thickness, which is associated with better survival outcomes than those achieved with suboptimal debulking surgery (SDS) (14, 15). Thus, improving the satisfactory cytoreduction rate and prolonging the overall survival of ovarian cancer patients are long-term goals for gynecological oncologists. The main value of NACT is reducing the tumor load and improving the feasibility of surgery and rate of ODS (16). However, many scholars have suggested that this benefit of surgery after NACT does not translate to a corresponding survival advantage and even increases the resistance of ovarian cancer patients to adjuvant

chemotherapy (17–19). Two RCTs (5, 6) and some retrospective studies (20, 21) have shown no significant differences in survival outcomes between patients who receive NACT-IDS and those who receive PDS. Therefore, we explored a preoperative method of selecting the appropriate initial treatment option for AOC patients with the aim of achieving a high rate of ODS while avoiding excessive NACT (22).

Several researchers have explored specific preoperative detection methods for predicting ODS rates, including clinical factors, laboratory test results, radiological examination, laparoscopy evaluation and molecular features (23–28). Computed tomography (CT), as the most important and widely accepted imaging examination, is used to identify tumor distribution and a high tumor burden before performing cytoreduction (24). Recent studies have reported that the combination of clinical factors and CT could have a high accuracy of predicting ODS rates (29–32). The synthesized prediction system evaluates the correlation between clinical factors and CT findings to predict ODS rates and shows better sensitivity and specificity than clinical experience or limited screening methods. Several Western scholars have reported imaging-based models for predicting SDS rates in ovarian cancer patients (24, 29–36). However, it is difficult to apply and promote these models in various Chinese hospitals, especially in hospitals with doctors who have less experience in gynecological oncology. Although debulking surgery to reduce the sizes of residual tumors to the greatest extent possible should be the focus of cytoreductive efforts, complete resection is not feasible for all these hospitals due to the different levels of experience of gynecological teams. Therefore, it is necessary to develop an evidenced-based model to predict ODS for application in Chinese centers with multiple levels of experience.

We wanted to initially perform a retrospective study on a model development cohort and then perform a prospective study on a model validation cohort to make adjustments. We herein aimed to perform a multicenter retrospective cohort study to assess the values of preoperative CT and clinical factors and develop a scoring system for predicting the absence of ODS in patients with AOC undergoing primary surgery.

## MATERIALS AND METHODS

### Study Population

Nine Chinese tertiary hospitals participated in this retrospective cohort study: Peking Union Medical College Hospital (PUMCH) as the main research center and eight other centers. Patients with FIGO stage III or IV ovarian, fallopian tube, or primary peritoneal cancer who underwent PDS between 09/01/2016 and 09/01/2019 were included. Patients with any of the following characteristics were excluded: 1) received neoadjuvant chemotherapy; 2) lacked critical clinical or operation data; and 3) underwent repeated collections. All patients provided written informed consent under approval by the ethics committee of their hospital. Patients who met the inclusion criteria were divided into two groups: 1) the ODS group: no gross RD and RD < 1 cm in maximum tumor diameter and 2) the SDS group: RD ≥ 1 cm in maximum tumor diameter.

### Data Collection

Key clinical data and CT image locations were recorded into unified electronic case report forms (CRFs) under an institutional review board-approved protocol and were obtained within 4 weeks before primary surgery. All contrast-enhanced CT scans were performed on modern technology conventional and spiral CT scanners, and were reviewed by the digital picture archiving system and at least two experienced radiologists. The preoperative clinical factors included the patient's age, platelet count, albumin level, and CA125 level. The effect of age was shown to be independent of other variables, including the stage and grade (37). Compared to older patients, younger women with AOC have a survival advantage (38). In addition, increasing evidence indicates that the platelet count is a useful biomarker of long-term outcomes in patients with OC (39). The median OS was significantly decreased in patients with thrombocytosis or elevated CA125 levels (40). The following CT image locations were evaluated: 1) medium/large-volume ascites (defined as the presence of ascites on at least 2/3 of CT slices); 2) diffuse peritoneal thickening (defined as the presence of at least 2 separate peritoneal implants each > 4 mm in size); 3) omental cake; 4) pelvic bowel metastasis ≥ 1 cm (including the rectum and sigmoid colon); 5) abdominal bowel metastasis ≥ 1 cm (including the small intestine as well as the ascending, transverse, and descending colon); 6) liver surface lesion (including the hepatorenal space); 7) liver parenchyma and portal lesion; 8) spleen metastasis (including the spleen surface and parenchyma); 9) diaphragmatic metastasis ≥ 1 cm; 10) pleural metastasis ≥ 1 cm; 11) retroperitoneal lymph node enlargement (RLNE) below the level of the inferior mesenteric artery (IMA) ≥ 1 cm (including pelvic lymph nodes); 12) and RLNE above the level of the IMA ≥ 1 cm (including the superior phrenic lymph node). The data used to support the findings of this study are available from the corresponding author upon request.

### Statistical Analysis

All statistical analyses were performed using SPSS software (version 23.0; SPSS Inc., Chicago, IL, USA). Student's t-tests and Mann-Whitney U tests were used to compare continuous

variables. Pearson's chi-squared tests and Fisher's exact tests were used to compare categorical variables. Continuous variables with a normal distribution are presented as the means ± standard deviations (SDs), and nonnormally distributed variables are reported as the medians ± interquartile ranges (IQRs) (41). Each of the clinical factors and radiological criteria were individually evaluated by using logistic regression for the univariate analysis. Then, all the variables with significant differences based on the univariate analysis were calculated by binary logistic regression with stepwise forward selection. The associations were evaluated by odds ratios (ORs) and corresponding 95% confidence intervals (CIs). Then, a prediction model was constructed using the variables with significant differences based on the multivariate analysis, and the prediction index value (PIV) was systematically calculated by the weight of each variable and corresponding functions. Statistical significance was set at  $P < 0.050$ .

The receiver operating characteristic (ROC) curve was drawn to evaluate the discrimination performance of the prediction model. The area under the curve (AUC) and 95% CI were determined to assess its prediction ability. The Hosmer-Lemeshow (H-L) goodness of fit test was used to evaluate the calibration performance of the prediction model (41). The sensitivity, specificity, positive predictive value (PPV), negative predictive value (NPV), and accuracy of each PIV were calculated according to different cut-off values. Sensitivity was defined as the number of patients receiving SDS and were correctly identified (true positives) divided by the total number of patients receiving SDS (true positives + false negatives). Specificity was defined as the number of patients receiving ODS who were correctly identified (true negatives) divided by the total number of patients receiving ODS (true negatives + false positives). The PPV was calculated as the number of true positives divided by the total number of positive results (true positives + false positives), and the NPV was defined as the number of true negatives divided by the total number of negative results (true negatives + false negatives). Accuracy was calculated as the number of true positives plus true negatives (total number correct) divided by the total number of patients studied (42). Youden's index (or the C-index), which indicates the maximum potential effectiveness of a biomarker, is a common summary measure of the ROC curve (43). We used Youden's index to determine the cut-off PIV point that yielded the maximum sensitivity and specificity for predicting suboptimal cytoreduction.

## RESULTS

### Flow Diagram and Characteristics of Included Patients

**Figure S1** shows the flow chart of this study population. A total of 303 patients from nine centers were enrolled. After excluding five patients without critical information and two duplicate patients, a total of 296 AOC patients who met the inclusion criteria were ultimately included. A total of 250 patients were in the ODS group (including 163 patients with no RD and 87 patients with an RD of 0–1 cm), and 46 patients were in the SDS group. We kept the

power of the study maximum. **Table 1** shows the preoperative clinical factors and radiological criteria of the included ovarian cancer patients. The mean patient age was 53.5 ( $\pm$  10.5) years in the ODS group and 55.7 ( $\pm$  12.8) years in the SDS group. There was no significant difference in the perioperative platelet count ( $P=0.781$ ) or perioperative albumin level ( $P=0.869$ ) between the two groups. The most common abnormalities observed on CT images were omental cake (53.4%), diffuse peritoneal thickening (38.9%), and pelvic bowel metastasis (34.5%). For most of the radiological criteria, there were significant differences between the two groups, thus indicating that the comparison of these variables was meaningful.

## Assessment of the Prediction Model

**Table 2** shows the univariate analysis of the included ovarian cancer patients. In the univariate analysis, two clinical factors were associated with suboptimal cytoreduction: age $>60$  years ( $P=0.019$ ) and perioperative CA125 level $>800$  U/ml ( $P=0.023$ ). Nine radiological criteria were related to suboptimal cytoreduction: diffuse peritoneal thickening ( $P=0.046$ ), omental cake ( $P=0.008$ ), pelvic bowel metastasis ( $P=0.007$ ), abdominal bowel metastasis ( $P=0.012$ ), liver surface lesion ( $P<0.001$ ), liver parenchyma and portal lesion ( $P=0.005$ ), spleen metastasis ( $P<0.001$ ), diaphragmatic metastasis ( $P=0.008$ ), and RLNE above the level of the IMA ( $P<0.001$ ). Then, we performed a

**TABLE 1** | The preoperative clinical factors and radiological criteria and of included ovarian cancer patients.

Variables	ODS group (N = 250)	SDS group (N = 46)	P
<b>Preoperative clinical factor</b>			
<b>Age</b>	53.5 $\pm$ 10.5	55.7 $\pm$ 12.8	0.017
$\leq 60$ years	180 (72.0)	25 (54.3)	
$> 60$ years	70 (28.0)	21 (45.7)	
<b>Perioperative CA125</b>	472.8 $\pm$ 650.6	573.2 $\pm$ 1052.6	0.021
$\leq 800$ U/ml	188 (75.2)	27 (58.7)	
$> 800$ U/ml	62 (24.8)	19 (41.3)	
<b>Perioperative platelet</b>	255.9 $\pm$ 0	255.9 $\pm$ 1.5	0.781
$\leq 350$ ( $10^9$ /L)	221 (88.4)	40 (87.0)	
$> 350$ ( $10^9$ /L)	29 (11.6)	6 (13.0)	
<b>Perioperative albumin</b>	44.2 $\pm$ 3.8	44.0 $\pm$ 2.7	0.869
$\leq 35$ g/L	18 (7.2)	3 (6.5)	
$> 35$ g/L	232 (92.8)	43 (93.5)	
<b>Radiological criterion</b>			
<b>Median-Large volume ascites</b>	64 (25.6)	18 (39.1)	0.059
<b>Diffuse peritoneal thickening</b>	91 (36.4)	24 (52.2)	0.044
<b>Omental cake</b>	125 (50.0)	33 (71.7)	0.007
<b>Pelvic bowel metastasis</b>	78 (31.2)	24 (52.2)	0.006
<b>Abdominal bowel metastasis</b>	33 (13.2)	13 (28.3)	0.010
<b>Liver surface lesion</b>	39 (15.6)	20 (43.5)	$<0.001$
<b>Liver parenchyma and portal lesion</b>	13 (5.2)	8 (17.4)	0.003
<b>Spleen metastasis</b>	19 (7.6)	14 (30.4)	$<0.001$
<b>Diaphragmatic metastasis</b>	3 (1.2)	4 (8.7)	0.002
<b>Pleural metastasis</b>	4 (1.6)	2 (4.3)	0.224
<b>RLNE below the level of IMA</b>	65 (26.0)	18 (39.1)	0.068
<b>RLNE above the level of IMA</b>	32 (12.8)	16 (34.8)	$<0.001$

Data are presented as number (%) or mean ( $\pm$  SD) or median ( $\pm$  IQR). ODS, Optimal debulking surgery; SDS, Suboptimal debulking surgery; RLNE, Retroperitoneal lymph nodes enlargement; IMA, Inferior mesenteric artery.

**TABLE 2** | The univariate analysis of included ovarian cancer patients.

Variables	N	OR	95%CI	P
<b>Age</b>				0.019
$\leq 60$ years	205	1		
$> 60$ years	91	2.160	1.136–4.107	
<b>Perioperative CA125</b>				0.023
$\leq 800$ U/ml	215	1		
$> 800$ U/ml	81	2.134	1.110–4.101	
<b>Perioperative platelet</b>				0.781
$\leq 350$ ( $10^9$ /L)	261	1		
$> 350$ ( $10^9$ /L)	35	1.143	0.446–2.930	
<b>Perioperative albumin</b>				0.869
$> 35$ g/L	275	1		
$\leq 35$ g/L	21	0.899	0.254–3.185	
<b>Median-Large volume ascites</b>				0.062
No	214	1		
Yes	82	0.535	0.278–1.032	
<b>Diffuse peritoneal thickening</b>				0.046
No	181	1		
Yes	115	1.906	1.012–3.591	
<b>Omental cake</b>				0.008
No	138	1		
Yes	158	2.538	1.276–5.051	
<b>Pelvic bowel metastasis</b>				0.007
No	194	1		
Yes	102	2.406	1.272–4.550	
<b>Abdominal bowel metastasis</b>				0.012
No	250	1		
Yes	46	2.590	1.237–5.424	
<b>Liver surface lesion</b>				$<0.001$
No	237	1		
Yes	59	4.162	2.118–8.179	
<b>Liver parenchyma and portal lesion</b>				0.005
No	275	1		
Yes	21	3.838	1.492–9.874	
<b>Spleen metastasis</b>				$<0.001$
No	263	1		
Yes	33	5.319	2.431–11.639	
<b>Diaphragmatic metastasis</b>				0.008
No	289	1		
Yes	7	7.841	1.694–36.295	
<b>Pleural metastasis</b>				0.243
No	290	1		
Yes	6	2.795	0.497–15.728	
<b>RLNE below the level of IMA</b>				0.071
No	213	1		
Yes	83	1.830	0.949–3.526	
<b>RLNE above the level of IMA</b>				$<0.001$
No	248	1		
Yes	48	3.633	1.784–7.399	

N, number; OR, Odds ratio; RLNE, Retroperitoneal lymph nodes enlargement; IMA, Inferior mesenteric artery.

multivariate analysis based on the significant factors from the univariate analysis. We further calculated the PIV, which was assigned based on the multivariate regression coefficient and OR. **Table 3** shows the prediction model of all significant clinical and radiological criteria based on the multivariate analysis for ODS. The predictive index parameters related to a high risk of successful SDS included age $>60$  years ( $P=0.016$ , PIV=1), CA125 level $>800$  U/ml ( $P=0.033$ , PIV=1), abdominal bowel metastasis ( $P=0.034$ , PIV=1), spleen metastasis ( $P<0.001$ , PIV=2), diaphragmatic metastasis ( $P=0.014$ , PIV=2), and RLNE above the level of the IMA ( $P<0.001$ , PIV=2).



**TABLE 3** | The model of significant clinical and radiological criteria based on multivariate analysis for predicting suboptimal debulking surgery.

Predictive index parameter	N	RC	OR	95%CI	P	PIV
<b>Preoperative clinical factor</b>						
<b>Age</b>		0.875			0.016	
≤60 years	205		1			0
>60 years	91		2.399	1.179–4.883		1
<b>Perioperative CA125</b>		0.799			0.033	
≤800 U/ml	215		1			0
>800 U/ml	81		2.223	1.067–4.631		1
<b>Radiological criterion</b>						
<b>Abdominal bowel metastasis</b>		0.888			0.034	
No	250		1			0
Yes	46		2.430	1.070–5.516		1
<b>Spleen metastasis</b>		1.546			<0.001	
No	263		1			0
Yes	33		4.692	1.987–11.077		2
<b>Diaphragmatic metastasis</b>		2.116			0.014	
No	289		1			0
Yes	7		8.300	1.537–44.818		2
<b>RLNE above the level of IMA</b>		1.570			<0.001	
No	248		1			0
Yes	48		4.808	2.176–10.623		2

N, number; RC, Regression coefficient; OR, Odds ratio; PIV, Prediction index value; RLNE, Retroperitoneal lymph nodes enlargement; IMA, Inferior mesenteric artery.

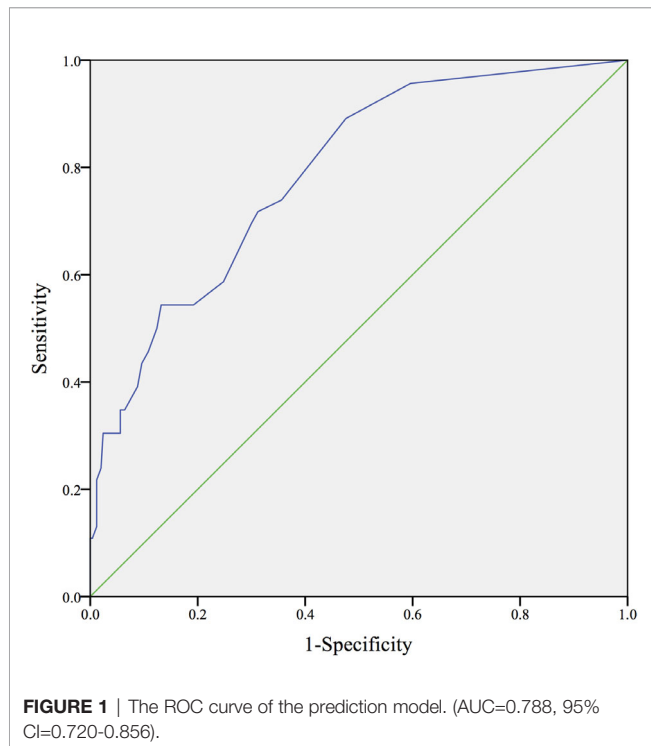
## Evaluation of the Prediction Model

**Figure 1** shows the ROC curve of the prediction model. The AUC was 0.788 (greater than 0.750), showing that this prediction model has superior discrimination. In addition, there was no significant difference between the predictive value and real value in the Hosmer-Lemeshow test ( $X^2 = 2.752$ ,  $P=0.600>0.050$ ), which indicated the stable calibration of the prediction model. **Table 4** shows the overall prediction model according to different cut-off values. The PIV ranged from 0 to nine points. The sensitivity,

specificity, PPV, NPV, and overall accuracy of each PIV were determined. Youden's index of the ROC curve was 41.5%, which corresponded to a sensitivity of 89.1% and a specificity of 52.4%. Consequently, with the aim of maximizing the accuracy of prediction and minimizing the rate of inappropriate explorations, a PIV of  $\geq 5$  achieved the highest accuracy of 85.47% and identified patients who underwent SDS with a specificity of 100%.

## DISCUSSION

At present, NACT-IDS is an alternative treatment option for AOC patients who may initially have a low incidence of ODS (7, 8). However, there is no unified standard method of selecting appropriate patients or determining the best time to perform PDS. Some gynecologists reported that the following clinical factors were associated with a high rate of unsatisfactory cytoreduction: 1) extensive implant metastasis in the upper abdomen or thorax and a large tumor burden throughout

**TABLE 4** | The overall prediction model according to different cut-off values.

PIV	Sensitivity (%)	Specificity (%)	PPV (%)	NPV (%)	Accuracy (%)
≥0	100.00	0.00	15.54	N/A	15.54
≥1	95.65	40.40	22.80	98.06	48.99
≥2	71.74	68.80	29.73	92.97	69.26
≥3	54.35	86.80	43.10	91.18	81.76
≥4	30.43	94.80	51.85	88.10	84.80
≥5	6.52	100.00	100.00	85.32	85.47
≥6	2.17	100.00	100.00	84.75	84.80
≥7	2.17	100.00	100.00	84.75	84.80
≥8	0.00	100.00	100.00	84.46	84.80
≥9	0.00	100.00	100.00	84.46	84.80

PIV, prediction index value; PPV, positive predictive value; NPV, negative predictive value; N/A, not applicable.



the whole body and 2) a poor performance status that could not tolerate cytoreduction (e.g., advanced age, high-risk complications, or the combination of a large amount of ascites and hydrothorax) (16, 44). However, this type of clinical report lacks scientific evidence and cannot be widely accepted and applied by different gynecologists in various hospitals. Therefore, the selection of appropriate AOC patients for undergoing primary surgery to obtain the highest success rate of ODS has been a focus in the past few decades.

Laparoscopy can be used to assess the probability of having no residual tumor before PDS and to evaluate tumor size, the degree of tumor spread, and tumor infiltration in surrounding tissues (26, 27, 45). Fagotti et al. developed a widely accepted staging laparoscopy scoring system for determining candidates for primary surgery (46) that includes omental cake (PIV=1), extensive peritoneal (PIV=1) and diaphragmatic (PIV=1) carcinosis, mesenteric retraction (PIV=2), bowel (PIV=2) and stomach (PIV=2) infiltration, and superficial spleen and/or liver metastasis (PIV=2). At a PIV $\geq$ 8, the probability of ODS during laparotomy is equal to 0; thus, NACT is initially recommended. This laparoscopy model can avoid an unnecessary exploratory laparotomy and improve individualized treatment for AOC patients. However, as an invasive manipulation procedure, laparoscopy has the risks of anesthesia and surgical complications (11). In addition, the evaluation of lesions under retroperitoneal and retrohepatic areas is limited (47). Furthermore, we must consider the cost-effectiveness benefit: laparoscopy is more time consuming and expensive than other preoperative examinations (47). Due to the above limitations, it is difficult to perform a staging laparoscopy before PDS in most Chinese hospitals. In addition, the molecular features played important roles in patients with OC, affecting the status of the BRCA gene and homologous recombination deficiency (HRD) (28, 48). However, primary targeted therapy for OC lacks sufficient evidence, and most patients cannot afford the high cost of gene detection. Therefore, we aimed to develop a preoperative evaluation model that combines clinical features with imaging examination features to allow patients to obtain the greatest benefit.

The model used to predict the rate of unsatisfactory debulking surgery in our study ultimately included two preoperative clinical factors and four radiological criteria based on the multivariate analysis of all enrolled patients. The two clinical factors, age $>$ 60 years and CA125 level $>$ 800 U/ml, indicated that elderly patients who have a high tumor burden and a poor general condition are not suitable for PDS. The four radiological criteria showed that tumors located in the upper abdomen or thorax, such as the diaphragm, spleen, and upper retroperitoneal lymph nodes, greatly influence the cytoreduction rate, as they are truly difficult to remove in debulking surgery. The evaluation of retroperitoneal disease extension plays a very important prognostic role for patients with OC (49, 50). Our prediction model is a scoring system; therefore, the difficulty of PDS and the rate of having no RD are not determined by a single high-risk factor but rather by the accumulation degree of high-risk factors. This may be attributed to poor surgical tolerance, a long surgical

time, and surgical complications during PDS if an AOC patient has a high score in our prediction model. Therefore, our model is basically consistent with the experience of gynecological oncologists (44, 51) but has more scientific- and evidence-based support.

Several scholars have published imaging-based models for predicting SDS rates in ovarian cancer patients (24, 29–31, 33–36, 52); these are summarized in **Table 5**. Among them, the model from Suidan et al. at Memorial Sloan-Kettering Cancer Center (MSKCC) is one of the most common and high evidence-based imaging models (29). However, in our practical application, it was found that the imaging classification of this model is excessively detailed and complex and often requires professional senior imaging doctors to read CT scans. It is difficult for gynecologists at different levels to apply this model, and there is also great difficulty in promoting this model in Chinese hospitals. Therefore, we initially roughly divided the body into several large areas based on our previous surgical experience (e.g., the pelvic and abdominal bowels, spleen, liver, and RLN). Our model may be more operable and applicable than the MSKCC model for gynecologic oncologists in various Chinese hospitals. In addition, our prediction model has a specificity of 100% and an accuracy of 85.47%, which shows superior discrimination and stable calibration.

On the other hand, Lluca et al. proposed a predictive model with the peritoneal cancer index (PCI), which can provide more detailed information about peritoneal spread. The PCI is used to quantitatively assess cancer distribution in the peritoneum based on the sizes of lesions in 13 abdominopelvic regions, and patients were classified into three categories with scores of 1–10, 11–20, and  $>$ 20 (53). In the pilot study, their models predicted suboptimal or complete and optimal cytoreductive surgery with sensitivities of 83% (R4 model) and 69% (R3 model). A PCI $>$ 20 was a major risk factor for unresectability in patients with AOC (52). In our study, peritoneal metastasis was evaluated in the variable statistics but was not included in the final multivariate model. PCI is a preferable supplement to our model, which could be improved by including this assessment of the PCI. In addition, several studies reported that minimally invasive interval debulking surgery (MI-IDS) played a positive role in the quality of life and surgery complications (27, 54). However, the range of surgical resection in MI-IDS is limited, and a thorough peritoneal evaluation is not possible. It is difficult to reach ODS, resulting in residual tumors and worsened oncologic outcomes. MI-IDS may be considered limited to low-complexity standard debulking surgery (55, 56).

Moreover, the greatest advantage of this study is that it was a multicenter study that collected patient data from nine large tertiary hospitals in China. The large-scale study, wide area coverage, and high quantity of enrolled patients ensured the diversity and credibility of this report. This retrospective study is not only the basis for creating a predictive model but can also be further verified in subsequent multicenter prospective studies. After modification and identification, it may ultimately be promoted in most hospitals in China, thus achieving the purpose of this whole study.

**TABLE 5 |** The model comparison of predicting suboptimal debulking surgery based on radiological criteria in ovarian cancer from published reports.

Study	Types	Clinical factors	CT factors	Model ability
<b>Axtell et al. (33)</b>	Multi-Institutional Reciprocal Validation Study (UCLA, et al.)	–	①Diaphragm disease ②large bowel mesentery implants	A sensitivity of 79%, a specificity of 75%, and an accuracy of 77%.
<b>Ferrandina et al. (31)</b>	Retrospective, single center (Italy)	①Age ②CA-125 ③ECOG-PS	①DPT ②Peritoneal implants>2 cm ③Bowel mesentery involvement ④Omental cake ⑤Pelvic sidewall involvement and/or hydroureter ⑥Suprarenal aortic lymph nodes>1cm ⑦ Infrarenal aortic lymph nodes>2 cm ⑧Superficial liver metastases>2 cm and/or intraparenchymal liver metastases any size ⑨Large volume ascites	Specificity>75%, PPV and NPV>50%, Accuracy>60%
<b>Stashwick et al. (29)</b>	Retrospective, single center (Denver)	①Albumin<2.7 (PIV=1) ②CA-125≥500 (PIV=1)	①Bowel mesentery involvement>2 cm (PIV=1) ②Diffuse peritoneal studding (PIV=2) ③Para-aortic lymphadenopathy>2 cm(PIV=1) ④Splenic disease>1 cm (PIV=1)	The sensitivity, specificity, PPV, and NPV were 94%, 75%, 80%, and 93%.
<b>Fujwara et al. (35)</b>	Retrospective, single center (Osaka)	–	Both: ①DPT ②Infrarenal para-aortic or pelvic lymph node ③Bowel encasement tumor≥2 cm ④Any tumor implants in the cul-de-sac Model 1: Adds consideration to any tumors in the pelvic or retroperitoneum Model 2: ①Bowel mesenteries≥2 cm ②Omental caking≥2 cm) ③Ascites fluid	Model 1: accuracy of 90.8%Model 2: accuracy of 93.9%
<b>Kim et al. (34)</b>	Retrospective, single center (Iksan)	–	①Omental extension to the stomach or spleen ②Inguinal or pelvic lymph nodes	A PPV of 100%, a specificity of 100%, and an accuracy of 45.8%.
<b>Shim et al. (30)</b>	Retrospective, single center (Seoul)	Surgical aggressive index	①Diaphragm disease ②Ascites ③Peritoneal carcinomatosis ④Small bowel mesentery implant ⑤Tumoral uptake ratio	A predictive accuracy of 88.1%.
<b>Janco et al. (36)</b>	Retrospective, single center (Mayo Clinic)	①ECOG performance status ≥2 (OR=5.13)	①DPT (OR=3.94) ②Lymphadenopathy (OR=3.00)	A sensitivity of 23.1% and specificity of 94.1%.
<b>Nasser et al. (24)</b>	Retrospective, single center (London)	–	①Diaphragmatic ②Spleen ③Large bowel ④Small bowel ⑤Rectum ⑥Porta hepatis ⑦Mesenteric disease ⑧Lymph node	A high specificity of 65% but low sensitivity.
<b>Suidan et al. (28)</b>	Prospective, non-randomized, multicenter (MSKCC, et al.)	①Age ≥ 60 years (OR= 1.5) ②CA-125≥600 U/mL (OR = 1.3) ③ASA 3–4 (OR= 1.6);	①SMA (OR=4.1) ②Splenic hilum/ligaments (OR= 1.4) ③Lesser sac>1cm (OR=2.2) ④Gastrohepatic ligament/porta hepatis (OR=1.4) ⑤Gallbladder fossa/intersegmental fissure (OR=2) ⑥Suprarenal RLN (OR=1.3) ⑦Small bowel (OR=1.1) ⑧Moderate-severe ascites (OR=2.2).	When a predictive score was 0–2, 3–5, 6–8, and ≥9, the predictive SDS rate was 45%, 68%, 87%, and 96%.
<b>Llueca et al. (52)</b>	Retrospective, single center	–	①Lung metastasis ②Hepatic metastasis in 3 or more segments ③Hepatic segments ④Severe hepatic pedicle involvement ⑤Progression after NACT ⑥Diffuse serous small bowel disease	A sensitivity of 83% (R4 model) and 69% (R3 model).

CT, Computed tomography scan; PIV, prediction index value; PPV, positive predictive value; NPV, negative predictive value; DPT, Diffuse peritoneal thickening; OR, Odds ratio; PIV, Prediction index value; MSKCC, Memorial Sloan-Kettering Cancer Center; SMA, Superior mesenteric artery; RLN, Retroperitoneal lymph nodes; SDS, Suboptimal debulking surgery.

There are several limitations to this study. First, due to the natural limitations of retrospective research, unknown potential confounders and selection biases may be present (57). However, we attempted to make a unified standard for collecting patients and evaluating CT sites to ensure that all data were collected in a similar manner. Moreover, we balanced the confounding factors between the two groups by Cox multivariate regression analysis when there were a few heterogeneities in baseline factors between the ODS and SDS groups. Second, the horizontal differentiation among multiple centers may lead to data deviations. The centers participating in this study were all high-quality large-scale hospitals in China, and gynecologists had sufficient experience in the diagnosis and treatment of ovarian cancer. The inclusion criteria for our study population and data collection were unified standards. The capabilities of performing debulking surgery and reading CT scans were similar among the various centers. Currently, a multicenter, nonrandom prospective study is

ongoing. We expect this prediction model to be verified and adjusted by collecting additional data.

## CONCLUSION

In conclusion, we developed a prediction model based on two preoperative clinical factors and four radiological criteria for predicting unsatisfactory debulking surgery in AOC patients: included age>60 years (PIV=1), CA125 level>800 U/ml (PIV=1), abdominal bowel metastasis (PIV=1), spleen metastasis (PIV=2), diaphragmatic metastasis (PIV=2), and RLNE above the level of the IMA (PIV=2). A total PIV of ≥5 in this model may indicate a high risk associated with undergoing SDS, with an accuracy of 85.47% and a specificity of 100%. The accuracy of this prediction model needs to be validated and adjusted in further multicenter prospective studies. We look forward to collecting additional

information from ovarian cancer patients and learning from research experience at other centers.

## DATA AVAILABILITY STATEMENT

The raw data supporting the conclusions of this article will be made available by the authors, without undue reservation.

## ETHICS STATEMENT

The studies involving human participants were reviewed and approved by the ethics committee of each hospital. In the main center, all patients provided written informed consent under approval by the ethics committee of Peking Union Medical College Hospital.

## AUTHOR CONTRIBUTIONS

L-YW and L-YP conceptualized the study. YG, MQ, and YJ contributed to the methodology. YJ, JZ, and NL validated the

study. YG, MQ, and YJ contributed to the formal analysis and investigation. YG and MQ wrote and prepared the original draft. All authors wrote and prepared the original draft. L-YW and L-YP acquired the funding. All authors provided the resources. L-YW and L-YP supervised the study. All authors contributed to the article and approved the submitted version.

## FUNDING

This project was supported by The Fund of The National Key R&D Program of China 2016YFC1303700 (Affiliated project 2016YFC1303701, 2016.9-2020.12). Furthermore, this project was also supported by CAMS Innovation Fund for Medical Sciences (CIFMS-2017-I2M-1-002, 2017.01-2020.12).

## SUPPLEMENTARY MATERIAL

The Supplementary Material for this article can be found online at: <https://www.frontiersin.org/articles/10.3389/fonc.2020.611617/full#supplementary-material>

## REFERENCES

- Jemal A, Siegel R, Ward E, Murray T, Xu J, Thun MJ. Cancer statistics, 2007. *CA Cancer J Clin* (2007) 57(1):43–66. doi: 10.3322/canjclin.57.1.43
- van Altena AM, Karim-Kos HE, de Vries E, Kruitwagen RF, Massuger LF, Kiemeny LA. Trends in therapy and survival of advanced stage epithelial ovarian cancer patients in the Netherlands. *Gynecol Oncol* (2012) 125(3):649–54. doi: 10.1016/j.ygyno.2012.02.033
- Fago-Olsen CL, Ottesen B, Kehlet H, Markauskas A, Mosgaard BJ, Ottosen C, et al. Neoadjuvant chemotherapy as ovarian cancer treatment: ever more used with major regional differences. *Danish Med J* (2012) 59(8):A4477.
- Zivanovic O, Aldini A, Carlson JW, Chi DS. Advanced cytoreductive surgery: American perspective. *Gynecol Oncol* (2009) 114(2 SUPPL.):S3–9. doi: 10.1016/j.ygyno.2008.11.033
- Vergote I, Tropé CG, Amant F, Kristensen GB, Ehlen T, Johnson N, et al. Neoadjuvant chemotherapy or primary surgery in stage IIIC or IV ovarian cancer. *New Engl J Med* (2010) 363(10):943–53. doi: 10.1016/S0140-6736(14)62223-6
- Kehoe S, Hook J, Nankivell M, Jayson GC, Kitchener H, Lopes T, et al. Primary chemotherapy versus primary surgery for newly diagnosed advanced ovarian cancer (CHORUS): an open-label, randomised, controlled, non-inferiority trial. *Lancet* (2015) 386(9990):249–57. doi: 10.1016/S0140-6736(14)62223-6
- Morgan RJ Jr., Alvarez RD, Armstrong DK, Burger RA, Castells M, Chen LM, et al. Ovarian cancer, version 3.2012: Featured updates to the NCCN guidelines. *JNCCN J Natl Compr Cancer Netw* (2012) 10(11):1339–49. doi: 10.6004/jnccn.2012.0140
- Wright AA, Bohlke K, Armstrong DK, Bookman MA, Cliby WA, Coleman RL, et al. Neoadjuvant chemotherapy for newly diagnosed, advanced ovarian cancer: Society of Gynecologic Oncology and American Society of Clinical Oncology Clinical Practice Guideline. *Gynecol Oncol* (2016) 143(1):3–15. doi: 10.1016/j.ygyno.2016.05.022
- Fagotti A, Ferrandina MG, Vizzielli G, Pasciuto T, Fanfani F, Gallotta V, et al. Randomized trial of primary debulking surgery versus neoadjuvant chemotherapy for advanced epithelial ovarian cancer (SCORPION-NCT01461850). *Int J Gynecol Cancer* (2020) 30(11):1657–64. doi: 10.1136/ijgc-2020-001640
- Onda T, Satoh T, Saito T, Kasamatsu T, Nakanishi T, Nakamura K, et al. Comparison of treatment invasiveness between upfront debulking surgery versus interval debulking surgery following neoadjuvant chemotherapy for stage III/IV ovarian, tubal, and peritoneal cancers in a phase III randomised trial: Japan Clinical Oncology Group Study JCOG0602. *Eur J Cancer* (2016) 64:22–31. doi: 10.1016/j.ejca.2016.05.017
- Gomez-Hidalgo NR, Martinez-Cannon BA, Nick AM, Lu KH, Sood AK, Coleman RL, et al. Predictors of optimal cytoreduction in patients with newly diagnosed advanced-stage epithelial ovarian cancer: Time to incorporate laparoscopic assessment into the standard of care. *Gynecol Oncol* (2015) 137(3):553–8. doi: 10.1016/j.ygyno.2015.03.049
- Aletti GD, Dowdy SC, Gostout BS, Jones MB, Stanhope CR, Wilson TO, et al. Aggressive surgical effort and improved survival in advanced-stage ovarian cancer. *Obstet Gynecol* (2006) 107(1):77–85. doi: 10.1097/01.AOG.0000192407.04428.bb
- Rutten MJ, Sonke GS, Westermann AM, van Driel WJ, Trum JW, Kenter GG, et al. Prognostic Value of Residual Disease after Interval Debulking Surgery for FIGO Stage IIIC and IV Epithelial Ovarian Cancer. *Obstet Gynecol Int* (2015) 2015:464123. doi: 10.1155/2015/464123
- Pineda M, Plaxe SC, Powell MA, Ratner E. Ovarian Cancer, Version 1.2016. *J Natl Compr Cancer Netw JNCCN* (2016) 14(9):1134–63. doi: 10.6004/jnccn.2016.0122
- Chi D, Eisenhauer E, Lang J, Huh J, Haddad L, Abu-Rustum N, et al. What is the optimal goal of primary cytoreductive surgery for bulky stage IIIC epithelial ovarian carcinoma (EOC)? *Gynecol Oncol* (2006) 103(2):559–64. doi: 10.1016/j.ygyno.2006.03.051
- Qin M, Jin Y, Ma L, Zhang YY, Pan LY. The role of neoadjuvant chemotherapy followed by interval debulking surgery in advanced ovarian cancer: a systematic review and meta-analysis of randomized controlled trials and observational studies. *Oncotarget* (2018) 9(9):8614–28. doi: 10.18632/oncotarget.23808
- Fagö-Olsen CL, Ottesen B, Kehlet H, Antonsen SL, Christensen IJ, Markauskas A, et al. Does neoadjuvant chemotherapy impair long-term survival for ovarian cancer patients? A nationwide Danish study. *Gynecol Oncol* (2014) 132(2):292–8. doi: 10.1016/j.ygyno.2013.11.035

18. Bristow RE, Chi DS. Platinum-based neoadjuvant chemotherapy and interval surgical cytoreduction for advanced ovarian cancer: a meta-analysis. *Gynecol Oncol* (2006) 103(3):1070–6. doi: 10.1016/j.ygyno.2006.06.025
19. Rauh-Hain JA, Melamed A, Wright A, Gockley A, Clemmer JT, Schorge JO, et al. Overall Survival Following Neoadjuvant Chemotherapy vs Primary Cytoreductive Surgery in Women With Epithelial Ovarian Cancer: Analysis of the National Cancer Database. *JAMA Oncol* (2016) 145(1):68–9. doi: 10.1001/jamaoncol.2016.4411
20. Milam MR, Tao X, Coleman RL, Harrell R, Bassett R, Dos Reis R, et al. Neoadjuvant chemotherapy is associated with prolonged primary treatment intervals in patients with advanced epithelial ovarian cancer. *Int J Gynecol Cancer* (2011) 21(1):66–71. doi: 10.1097/IGC.0b013e3182013e2f
21. Inciura A, Simavicius A, Juozaityte E, Kurtinaitis J, Nadisauskiene R, Svedas E, et al. Comparison of adjuvant and neoadjuvant chemotherapy in the management of advanced ovarian cancer: a retrospective study of 574 patients. *BMC Cancer* (2006) 6:153. doi: 10.1186/1471-2407-6-153
22. Kang S, Park SY. To predict or not to predict? The dilemma of predicting the risk of suboptimal cytoreduction in ovarian cancer. *Ann Oncol* (2011) 22 (SUPPL.8):23–8. doi: 10.1093/annonc/mdr530
23. Zeng J, Yin J, Song X, Jin Y, Li Y, Pan L. Reduction of CA125 Levels During Neoadjuvant Chemotherapy Can Predict Cytoreduction to No Visible Residual Disease in Patients with Advanced Epithelial Ovarian Cancer, Primary Carcinoma of Fallopian tube and Peritoneal Carcinoma. *J Cancer* (2016) 7(15):2327–32. doi: 10.7150/jca.16761
24. Nasser S, Lazaridis A, Evangelou M, Jones B, Nixon K, Kyrgiou M, et al. Correlation of pre-operative CT findings with surgical & histological tumor dissemination patterns at cytoreduction for primary advanced and relapsed epithelial ovarian cancer: A retrospective evaluation. *Gynecol Oncol* (2016) 143(2):264–9. doi: 10.1016/j.ygyno.2016.08.322
25. Brun JL, Rouzier R, Selle F, Houry S, Uzan S, Darai E. Neoadjuvant chemotherapy or primary surgery for stage III/IV ovarian cancer: contribution of diagnostic laparoscopy. *BMC Cancer* (2009) 9:171. doi: 10.1186/1471-2407-9-171
26. Vizzielli G, Costantini B, Tortorella L, Petrillo M, Fanfani F, Chiantera V, et al. Influence of intraperitoneal dissemination assessed by laparoscopy on prognosis of advanced ovarian cancer: an exploratory analysis of a single-institution experience. *Ann Surg Oncol* (2014) 21(12):3970–7. doi: 10.1245/s10434-014-3783-6
27. Vizzielli G, Costantini B, Tortorella L, Pitruzzella I, Gallotta V, Fanfani F, et al. A laparoscopic risk-adjusted model to predict major complications after primary debulking surgery in ovarian cancer: A single-institution assessment. *Gynecol Oncol* (2016) 142(1):19–24. doi: 10.1016/j.ygyno.2016.04.020
28. Gallotta V, Conte C, D'Indinosante M, Capoluongo E, Minucci A, De Rose AM, et al. Prognostic factors value of germline and somatic brca in patients undergoing surgery for recurrent ovarian cancer with liver metastases. *Eur J Surg Oncol J Eur Soc Surg Oncol Br Assoc Surg Oncol* (2019) 45(11):2096–102. doi: 10.1016/j.ejso.2019.06.023
29. Suidan RS, Ramirez PT, Sarasoehn DM, Teitcher JB, Iyer RB, Zhou Q, et al. A multicenter assessment of the ability of preoperative computed tomography scan and CA-125 to predict gross residual disease at primary debulking for advanced epithelial ovarian cancer. *Gynecol Oncol* (2017) 145(1):27–31. doi: 10.1016/j.ygyno.2017.02.020
30. Stashwick C, Post MD, Arruda JS, Spillman MA, Behbakht K, Davidson SA, et al. Surgical risk score predicts suboptimal debulking or a major perioperative complication in patients with advanced epithelial ovarian, fallopian tube, or primary peritoneal cancer. *Int J Gynecol Cancer* (2011) 21 (8):1422–7. doi: 10.1097/IGC.0b013e31822c7704
31. Shim SH, Lee SJ, Kim SO, Kim SN, Kim DY, Lee JJ, et al. Nomogram for predicting incomplete cytoreduction in advanced ovarian cancer patients. *Gynecol Oncol* (2015) 136(1):30–6. doi: 10.1016/j.ygyno.2014.11.004
32. Ferrandina G, Sallustio G, Fagotti A, Vizzielli G, Paglia A, Cucci E, et al. Role of CT scan-based and clinical evaluation in the preoperative prediction of optimal cytoreduction in advanced ovarian cancer: a prospective trial. *Br J Cancer* (2009) 101(7):1066–73. doi: 10.1038/sj.bjc.6605292
33. Axtell AE, Lee MH, Bristow RE, Dowdy SC, Cliby WA, Raman S, et al. Multi-institutional reciprocal validation study of computed tomography predictors of suboptimal primary cytoreduction in patients with advanced ovarian cancer. *J Clin Oncol* (2007) 25(4):384–9. doi: 10.1200/jco.2006.07.7800
34. Kim HJ, Choi CH, Lee YY, Kim TJ, Lee JW, Bae DS, et al. Surgical outcome prediction in patients with advanced ovarian cancer using computed tomography scans and intraoperative findings. *Taiwanese J Obstetr Gynecol* (2014) 53(3):343–7. doi: 10.1016/j.tjog.2013.10.041
35. Fujwara K, Yoshino K, Enomoto T, Fujita M, Ueda Y, Miyatake T, et al. Usefulness of computed tomography in predicting cytoreductive surgical outcomes for ovarian cancer. *Arch Gynecol Obstetr* (2011) 284(6):1501–7. doi: 10.1007/s00404-011-1864-3
36. Janco JMT, Glaser G, Kim B, McGree ME, Weaver AL, Cliby WA, et al. Development of a prediction model for residual disease in newly diagnosed advanced ovarian cancer. *Gynecol Oncol* (2015) 138(1):70–7. doi: 10.1016/j.ygyno.2015.04.013
37. Fourcadier E, Trétarre B, Gras-Aygon C, Ecarnot F, Daurès J-P, Bessaoud F. Under-treatment of elderly patients with ovarian cancer: a population based study. *BMC Cancer* (2015) 15:937–. doi: 10.1186/s12885-015-1947-9
38. Chan JK, Urban R, Cheung MK, Osann K, Shin JY, Husain A, et al. Ovarian cancer in younger vs older women: a population-based analysis. *Br J Cancer* (2006) 95(10):1314–20. doi: 10.1038/sj.bjc.6603457
39. Zhou Q, Huang F, He Z, Zuo MZ. Clinicopathological and prognostic significance of platelet count in patients with ovarian cancer. *Climacteric J Int Menopause Soc* (2018) 21(1):60–8. doi: 10.1080/13697137.2017.1406911
40. Chen JP, Huang QD, Wan T, Tu H, Gu HF, Cao JY, et al. Combined score of pretreatment platelet count and CA125 level (PLT-CA125) stratified prognosis in patients with FIGO stage IV epithelial ovarian cancer. *J Ovarian Res* (2019) 12 (1):72. doi: 10.1186/s13048-019-0544-y
41. du Prel J-B, Röhrig B, Hommel G, Blettner M. Choosing statistical tests: part 12 of a series on evaluation of scientific publications. *Dtsch Arztebl Int* (2010) 107(19):343–8. doi: 10.3238/arztebl.2010.0343
42. Parikh R, Mathai A, Parikh S, Chandra Sekhar G, Thomas R. Understanding and using sensitivity, specificity and predictive values. *Indian J Ophthalmol* (2008) 56(1):45–50. doi: 10.4103/0301-4738.37595
43. Ruopp MD, Perkins NJ, Whitcomb BW, Schisterman EF. Youden Index and optimal cut-point estimated from observations affected by a lower limit of detection. *Biom J* (2008) 50(3):419–30. doi: 10.1002/bimj.200710415
44. Vergote IB, Van Nieuwenhuysen E, Vanderstichele A. How to Select Neoadjuvant Chemotherapy or Primary Debulking Surgery in Patients With Stage IIIC or IV Ovarian Carcinoma. *J Clin Oncol* (2016) 34 (32):3827–8. doi: 10.1200/jco.2016.69.7458
45. Rutten MJ, Gaarenstroom KN, Van Gorp T, van Meurs HS, Arts HJ, Bossuyt PM, et al. Laparoscopy to predict the result of primary cytoreductive surgery in advanced ovarian cancer patients (LapOvCa-trial): a multicentre randomized controlled study. *BMC Cancer* (2012) 12:31. doi: 10.1186/1471-2407-12-31
46. Fagotti A, Ferrandina G, Fanfani F, Garganese G, Vizzielli G, Carone V, et al. Prospective validation of a laparoscopic predictive model for optimal cytoreduction in advanced ovarian carcinoma. *Am J Obstet Gynecol* (2008) 199(6):642 e1–6. doi: 10.1016/j.ajog.2008.06.052
47. Rutten MJ, Leeflang MM, Kenter GG, Mol BWJ, Buist M. Laparoscopy for diagnosing resectability of disease in patients with advanced ovarian cancer. *Cochrane Database Systemat Rev* (2014) (2). doi: 10.1002/14651858.CD009786.pub2/abstract
48. Gallotta V, Bruno M, Conte C, Giudice MT, Davià F, Moro F, et al. Salvage lymphadenectomy in recurrent ovarian cancer patients: Analysis of clinical outcome and BRCA1/2 gene mutational status. *Eur J Surg Oncol J Eur Soc Surg Oncol Br Assoc Surg Oncol* (2020) 46(7):1327–33. doi: 10.1016/j.ejso.2020.01.035
49. Gallotta V, Ferrandina G, Vizzielli G, Conte C, Lucidi A, Costantini B, et al. Hepatoceliac Lymph Node Involvement in Advanced Ovarian Cancer Patients: Prognostic Role and Clinical Considerations. *Ann Surg Oncol* (2017) 24(11):3413–21. doi: 10.1245/s10434-017-6005-1
50. Gallotta V, Fanfani F, Fagotti A, Chiantera V, Legge F, Gueli Alletti S, et al. Mesenteric lymph node involvement in advanced ovarian cancer patients undergoing rectosigmoid resection: prognostic role and clinical considerations. *Ann Surg Oncol* (2014) 21(7):2369–75. doi: 10.1245/s10434-014-3558-0
51. Schorge JO, Clark RM, Lee SI, Penson RT. Primary debulking surgery for advanced ovarian cancer: Are you a believer or a dissenter? *Gynecol Oncol* (2014) 135(3):595–605. doi: 10.1016/j.ygyno.2014.10.007
52. Lluca A, Serra A, Delgado K, Maiocchi K, Jativa R, Gomez L, et al. A radiologic-laparoscopic model to predict suboptimal (or complete and optimal) debulking surgery in advanced ovarian cancer: a pilot study. *Int J Womens Health* (2019) 11:333–42. doi: 10.2147/ijwh.s198355



53. Lluca A, Escrig J, Serra-Rubert A, Gomez-Quiles L, Rivadulla I, Jativa-Porcar R, et al. Prognostic value of peritoneal cancer index in primary advanced ovarian cancer. *Eur J Surg Oncol* (2018) 44(1):163–9. doi: 10.1016/j.ejso.2017.11.003
54. Gueli Alletti S, Vizzielli G, Lafuenti L, Costantini B, Fagotti A, Fedele C, et al. Single-Institution Propensity-Matched Study to Evaluate the Psychological Effect of Minimally Invasive Interval Debulking Surgery Versus Standard Laparotomic Treatment: From Body to Mind and Back. *J Minim Invasive Gynecol* (2018) 25(5):816–22. doi: 10.1016/j.jmig.2017.12.007
55. Gueli Alletti S, Bottoni C, Fanfani F, Gallotta V, Chiantera V, Costantini B, et al. Minimally invasive interval debulking surgery in ovarian neoplasm (MISSION trial-NCT02324595): a feasibility study. *Am J Obstet Gynecol* (2016) 214(4):503.e1–e6. doi: 10.1016/j.ajog.2015.10.922
56. Fagotti A, Gueli Alletti S, Corrado G, Cola E, Vizza E, Vieira M, et al. The INTERNATIONAL MISSION study: minimally invasive surgery in ovarian neoplasms after neoadjuvant chemotherapy. *Int J Gynecol Cancer* (2019) 29(1):5–9. doi: 10.1136/ijgc-2018-000012
57. Vizzielli G, Fanfani F, Chiantera V, Tortorella L, Lucidi A, Petrillo M, et al. Does the diagnosis center influence the prognosis of ovarian cancer patients submitted to neoadjuvant chemotherapy? *Anticancer Res* (2015) 35(5):3027–32.

**Conflict of Interest:** The authors declare that the research was conducted in the absence of any commercial or financial relationships that could be construed as a potential conflict of interest.

Copyright © 2021 Gu, Qin, Jin, Zuo, Li, Bian, Zhang, Li, Wu, Wang, Zhang, Yue, Wu and Pan. This is an open-access article distributed under the terms of the Creative Commons Attribution License (CC BY). The use, distribution or reproduction in other forums is permitted, provided the original author(s) and the copyright owner(s) are credited and that the original publication in this journal is cited, in accordance with accepted academic practice. No use, distribution or reproduction is permitted which does not comply with these terms.





# A Correlative Study Between IVIM-DWI Parameters and the Expression Levels of Ang-2 and TKT in Hepatocellular Carcinoma

Jing Zheng<sup>1</sup>, Xue Qin Gong<sup>1</sup>, Yun Yun Tao<sup>1</sup>, Ran Wang<sup>1</sup>, Gang Yang<sup>2</sup>, Jing Dong Li<sup>2</sup>, Tian Ren<sup>3</sup>, Zu Mao Li<sup>4</sup>, Cui Yang<sup>1</sup>, Wei Cheng Wang<sup>1</sup>, Lin Yang<sup>1\*</sup> and Xiao Ming Zhang<sup>1</sup>

<sup>1</sup> Medical Imaging Key Laboratory of Sichuan Province, Department of Radiology, Affiliated Hospital of North Sichuan Medical College, Nanchong, China, <sup>2</sup> Institute of Hepato-Biliary-Intestinal Disease, Department of Hepatobiliary Surgery, Affiliated Hospital of North Sichuan Medical College, Nanchong, China, <sup>3</sup> Department of Medical Record Statistics, Affiliated Hospital of North Sichuan Medical College, Nanchong, China, <sup>4</sup> Department of Pathology, Affiliated Hospital of North Sichuan Medical College, Nanchong, China

## OPEN ACCESS

### Edited by:

Min Wu,  
Sichuan University, China

### Reviewed by:

Bin Song,  
Sichuan University, China  
Guolin Ma,  
China-Japan Friendship Hospital,  
China

### \*Correspondence:

Lin Yang  
linyngmd@163.com

### Specialty section:

This article was submitted to  
Cancer Imaging and  
Image-directed Interventions,  
a section of the journal  
Frontiers in Oncology

**Received:** 13 August 2020

**Accepted:** 23 November 2020

**Published:** 15 January 2021

### Citation:

Zheng J, Gong XQ, Tao YY, Wang R, Yang G, Li JD, Ren T, Li ZM, Yang C, Wang WC, Yang L and Zhang XM (2021) A Correlative Study Between IVIM-DWI Parameters and the Expression Levels of Ang-2 and TKT in Hepatocellular Carcinoma. *Front. Oncol.* 10:594366. doi: 10.3389/fonc.2020.594366

**Background:** Noninvasive evaluation of the expression of angiopoietin-2 (Ang-2) and transketolase (TKT) in hepatocellular carcinoma (HCC) is of great significance for the clinical development of individualized treatment plans. However, the correlation between intravoxel incoherent motion diffusion weighted imaging (IVIM-DWI) and the expression of Ang-2 and TKT has not been reported. We sought to investigate the correlations between IVIM-DWI parameters and Ang-2 and TKT expression levels in HCCs.

**Methods:** Conventional non-enhanced magnetic resonance imaging (MRI) and IVIM-DWI and dynamic contrast MRI were performed for 61 patients with HCC before surgical treatment. Various IVIM-DWI parameters, such as apparent diffusion coefficient (ADC), slow apparent diffusion coefficient (D), fast apparent diffusion coefficient (D\*) and fraction of fast apparent diffusion coefficient (f), were calculated using Function-MADC software. Expression levels of Ang-2 and TKT in HCC were detected *via* immunohistochemical staining and classified into two grades. Independent sample *t* tests were used to compare differences in parameters between the two groups. The Spearman rank correlation test was used to analyze the correlations between IVIM-DWI parameters and Ang-2 and TKT expression levels in HCCs.

**Results:** The D\* and f values were significantly higher in the high Ang-2 group than in the low Ang-2 group; there were no obvious between-group differences in ADC and D. Ang-2 expression was positively correlated with D\* and f but not with ADC and D. The ADC and D values were significantly lower in the high TKT group than in the low TKT group, whereas the between-group differences for D\* and f were not significant. TKT expression was negatively correlated with ADC and D but not with D\* and f.

**Conclusions:** IVIM-DWI can be used to evaluate Ang-2 and TKT expression in HCC.

**Keywords:** hepatocellular carcinoma, intravoxel incoherent motion, diffusion-weighted imaging, angiopoietin-2, transketolase

## INTRODUCTION

Hepatocellular carcinoma (HCC) is one of the most common malignant tumors of the digestive system, and it has severe disease burden (1). Traditional imaging methods only show the size and scope of the tumor from the morphological perspective, and they do not reflect water molecule diffusion in tumor tissues. Continuous development of magnetic resonance technology has promoted the use of diffusion-weighted imaging (DWI)-based functional magnetic resonance imaging (MRI) in tumor diagnosis and treatment. However, the apparent diffusion coefficient (ADC) measured using DWI reflects water molecule diffusion and capillary perfusion but not the diffusion of pure water molecules in tissues. Intravoxel incoherent motion (IVIM)-DWI proposed by Le Bihan et al. (2, 3) uses a bi-exponential model to obtain multiple parameters, including  $D$ ,  $D^*$ , and  $f$ , which distinguish the diffusion of water molecules from the perfusion of capillaries. In recent years, studies have shown the application value of IVIM-DWI in the differential diagnosis of liver cancer (4, 5), histological grading (6–8), and evaluating topical treatment response (9, 10).

Antiangiogenesis therapy for tumors is currently a research hotspot. Angiopoietin (Ang) is an important angiogenic factor. The Ang family members mainly include Ang-1, Ang-2, Ang-3, Ang-4 and angiopoietin-like proteins, among which Ang-2 is strongly expressed and localized predominantly in cancer cells (11). Transketolase (TKT) (12) is one of the key enzymes in the nonoxidative part of the pentose phosphate pathway (PPP), and PPP provides approximately 85% of the pentose sugar required for DNA synthesis in tumor cells (13). Studies have shown that TKT promotes tumor cell proliferation and invasion, which are related to tumor prognosis and recurrence (14–17).

Noninvasive evaluation of the expression of Ang-2 and TKT in HCC is of great significance for clinical development of individualized treatment plans. However, the correlation between IVIM-DWI and the expression of Ang-2 and TKT has not been reported. Therefore, the present study investigated the correlation between IVIM-DWI parameters and the expression of Ang-2 and TKT in HCC tissues to noninvasively evaluate the expression of HCC Ang-2 and TKT, as well as to provide reference information for HCC antiangiogenesis targeted therapy.

## MATERIALS AND METHODS

### Study Population

We enrolled 61 cases of HCC that received surgical resection in our hospital from January 2018 to September 2019. Inclusion criteria: (1) did not receive surgery, topical therapy, radiotherapy, chemotherapy or targeted therapy; (2) lesion diameter was greater than 1 cm; and (3) postoperative pathology confirmed HCC. Exclusion criteria: (1) MRI contraindications; (2) poor image quality; and (3) incomplete data. All patients underwent upper abdominal plain MRI scan, IVIM-DWI and enhanced MRI scan before surgery.

### MRI Scan

The Discovery 750 3.0T superconducting magnetic resonance scanner (GE, USA) was used with a 32-channel phased array surface coil. All study subjects fasted for more than 4 h and received breathing exercises before the MR scan.

Scanning sequence: Breath-hold transverse-plane fat-suppressed T1WI, respiratory-triggered transverse-plane fat-suppressed T2WI and IVIM-DWI scans were conducted (Table 1). Nine b-values were selected from the IVIM-DWI sequence ( $b=0, 20, 50, 100, 150, 200, 400, 800$ , and  $1000$ ). A high-pressure syringe was used to inject the gadolinium-diethylenetriamine penta-acetic acid (Gd-DTPA) contrast agent (15–20 ml) through the vein on the back of the hand at an injection speed of 2–2.5 ml/s, and images of the hepatic artery phase, portal phase and equilibrium phase were collected.

### Data Measurement

Function-MADC software on a GE AW 4.4 Workstation was used to select the slice with the largest solid tumor area on the IVIM-DWI sequence, and a region of interest (ROI) with an area of 70–80 mm<sup>2</sup> was manually selected, avoiding areas with tumor necrosis, hemorrhage or cystic degeneration. The ADC,  $D$ ,  $D^*$  and  $f$  pseudocolor maps were generated, and the ADC value,  $D$  value,  $D^*$  value and  $f$  value were measured. Each parameter value was measured three times, and the average was calculated.

### Immunohistochemical Detection

The Ang-2 antibody was purchased from Abcam (UK, catalog number ab153934) and was diluted 1:250. The TKT antibody was purchased from Santa Cruz (USA, catalog number SC-390179) and was diluted 1:100. HCC specimens were embedded in paraffin and sectioned continuously at a thickness of 5  $\mu$ m for Hematoxylin-Eosin (HE) and immunohistochemical staining. Two physicians separately evaluated the same section. Disagreements were resolved after discussion. For each section, the staining intensities in six high-power fields were recorded. The scoring standards for Ang-2 and TKT protein expression intensity were as described in the literature (11, 12) as follows: 0 points (no staining), one point (weak staining), two points (moderate staining), and three points (strong staining). According to the scoring results, subjects were divided into the following two groups: low expression group with scores of one point and below and high expression group with scores of two points and above (18, 19).

**TABLE 1 |** Magnetic resonance (MR) imaging scanning sequences and parameters.

Sequence	TR/TE (ms)	FA(°)	Matrix (mm <sup>2</sup> )	FOV(mm <sup>2</sup> )	ST(mm)
T1WI	4/2	12	260×192	320×320–360×360	2.6
T2WI	2,609/97	110	384×384	320×320–380×380	5
DCE MRI	4/2	12	224×192	320×320–360×360	5
IVIM-DWI	3,529/60.8	90	128×160	340×340–360×360	5

TR, repetition time; TE, echo time; FA, flip angle; FOV, field of view; ST, section thickness; DCE, dynamic contrast-enhanced.

## Statistical Analysis

SPSS22.0 software was used for data analysis. Testing for normality indicated that the parameter values for IVIM-DWI conformed with normal distributions. The independent sample *t* test was used to compare the differences in parameters between two groups with different expression levels of Ang-2 and TKT. Spearman's correlation analysis was used to analyze the correlation between IVIM-DWI parameters and the expression of Ang-2 and TKT.  $P < 0.05$  was considered significantly different.

## RESULTS

There were 61 cases enrolled in this study, including 55 males and six females aged 29–70 years old with an average age of  $50.3 \pm 10.4$  years. Lesion size ranged from 1.2 to 16.1 cm with an average size of  $5.1 \pm 3.3$  cm.

Among the 61 cases of HCC, 35 cases had high expression of Ang-2, and 26 cases had low expression of Ang-2. Moreover, 30 cases had high expression of TKT, and 31 cases had low expression of TKT. The  $D^*$  and  $f$  values were significantly higher for the high Ang-2 expression group ( $55.71 \pm 19.21 \times 10^{-3} \text{ mm}^2/\text{s}$  and  $27.58 \pm 8.09\%$ , respectively) than for the low Ang-2 expression group ( $32.25 \pm 19.22 \times 10^{-3} \text{ mm}^2/\text{s}$  and  $17.29 \pm 5.66\%$ , respectively), whereas the ADC and  $D$  values did not significantly differ between the two groups ( $1.20 \pm 0.22 \times 10^{-3} \text{ mm}^2/\text{s}$  and  $0.92 \pm 0.20 \times 10^{-3} \text{ mm}^2/\text{s}$ , respectively, for the high expression group and  $1.14 \pm 0.24 \times 10^{-3} \text{ mm}^2/\text{s}$  and  $0.87 \pm 0.17 \times 10^{-3} \text{ mm}^2/\text{s}$ , respectively, for the low expression group). The  $D^*$  and  $f$  values were positively correlated with Ang-2 expression ( $r = 0.578$ ,  $p < 0.05$  and  $r = 0.645$ ,  $p < 0.05$ , respectively). In contrast, the ADC and  $D$  values were not significantly correlated with Ang-2 expression ( $r = 0.132$ ,  $p > 0.05$  and  $r = 0.106$ ,  $p > 0.05$ , respectively). The ADC and  $D$  values were significantly lower for the high TKT expression group ( $1.09 \pm 0.21 \times 10^{-3} \text{ mm}^2/\text{s}$  and  $0.83 \pm 0.19 \times 10^{-3} \text{ mm}^2/\text{s}$ , respectively) than for the low TKT expression group ( $1.25 \pm 0.21 \times 10^{-3} \text{ mm}^2/\text{s}$  and  $0.95 \pm 0.17 \times 10^{-3} \text{ mm}^2/\text{s}$ , respectively), whereas the  $D^*$  and  $f$  values did not significantly differ between the two groups ( $45.32 \pm 23.95 \times 10^{-3} \text{ mm}^2/\text{s}$  and  $22.22 \pm 9.24\%$ , respectively, for the high expression group and  $46.09 \pm 23.65 \times 10^{-3} \text{ mm}^2/\text{s}$  and  $24.13 \pm 8.31\%$ , respectively, for the low expression group). The ADC and  $D$  values were negatively correlated with TKT expression ( $r = -0.376$ ,  $p < 0.05$  and  $r = -0.386$ ,  $p < 0.05$ , respectively). In contrast, the  $D^*$  and  $f$  values were not correlated with TKT expression ( $r = 0.040$ ,  $p > 0.05$  and  $r = -0.136$ ,  $p > 0.05$ , respectively) (Tables 2–4; Figures 1–4).

## DISCUSSION

Angiogenesis is closely related to the occurrence and development of tumors (20–23). Ang-2 is highly expressed in HCC tissues (18, 20, 24, 25), and Ang-2 is positively correlated with tumor microvessel density (MVD) (26). The following mechanisms are potential ways in which Ang-2 promotes

**TABLE 2 |** Comparison of intravoxel incoherent motion diffusion weighted imaging (IVIM-DWI) parameters between groups with different Ang-2 expression.

	Low expression group (n=26)	High expression group (n=35)	<i>t</i>	<i>p</i>
ADC	$1.14 \pm 0.24$	$1.20 \pm 0.22$	0.968	0.337
<i>D</i>	$0.87 \pm 0.17$	$0.92 \pm 0.20$	0.995	0.324
$D^*$	$32.25 \pm 19.22$	$55.71 \pm 19.21$	4.381	0.000
<i>f</i>	$17.29 \pm 5.66$	$27.58 \pm 8.09$	5.549	0.000

The units for apparent diffusion coefficient (ADC), *D*, and  $D^*$  values are  $\times 10^{-3} \text{ mm}^2/\text{s}$ , and the unit for *f* is %.

**TABLE 3 |** Comparison of intravoxel incoherent motion diffusion weighted imaging (IVIM-DWI) parameters between high and low transketolase (TKT) expression groups.

	Low expression group (n=31)	High expression group (n=30)	<i>t</i>	<i>p</i>
ADC	$1.25 \pm 0.21$	$1.09 \pm 0.21$	3.023	0.004
<i>D</i>	$0.95 \pm 0.17$	$0.83 \pm 0.19$	2.539	0.014
$D^*$	$46.09 \pm 23.65$	$45.32 \pm 23.95$	0.126	0.900
<i>f</i>	$24.13 \pm 8.31$	$22.22 \pm 9.24$	0.852	0.398

The units for apparent diffusion coefficient (ADC), *D*, and  $D^*$  values are  $\times 10^{-3} \text{ mm}^2/\text{s}$ , and the unit for *f* is %.

**TABLE 4 |** Correlations between intravoxel incoherent motion diffusion weighted imaging (IVIM-DWI) parameters and the expression of Ang-2 and transketolase (TKT).

Spearman correlation	Ang-2		TKT	
	<i>r</i>	<i>p</i>	<i>r</i>	<i>p</i>
ADC	0.132	0.312	-0.376	0.003
<i>D</i>	0.106	0.417	-0.386	0.002
$D^*$	0.578	0.000	0.040	0.757
<i>f</i>	0.645	0.000	-0.136	0.296

angiogenesis (27–29): (1) Ang-2 antagonizes the effect of Ang-1 on Tie-2, which inhibits Tie-2 signaling and disrupts signals mediating stable endothelial cell interaction in the Tie-2 signaling pathway, leading to the instability for existing blood vessels; and (2) Ang-2 and VEGF synergistically promote the formation of tumor blood vessels.

Ang-2 is used to monitor tumor response to antiangiogenesis targeted therapy (30). A prior study has shown (31) that a prepared single-chain variable fragment (scFv) Ang-2 single-chain antibody has a significant inhibitory effects on the angiogenesis and tumor growth of HCC *in vivo* and *in vitro*. In addition, specific Ang-2 targeted intervention may act by reshaping the neovascular network and changing the tumor microenvironment. Mueller et al. (32) showed that combined therapy with dual-targeting of Ang-2 and VEGF significantly inhibits tumor activity and that compared to single-targeted therapy of Ang-2 or VEGF, combined therapy has obvious advantages. Moreover, Mueller et al. suggested that antiangiogenesis therapy is helpful for fighting chemotherapy resistance. Previous research on plumbagin inhibition of angiogenesis-mediated tumor growth in HCC has shown (33)

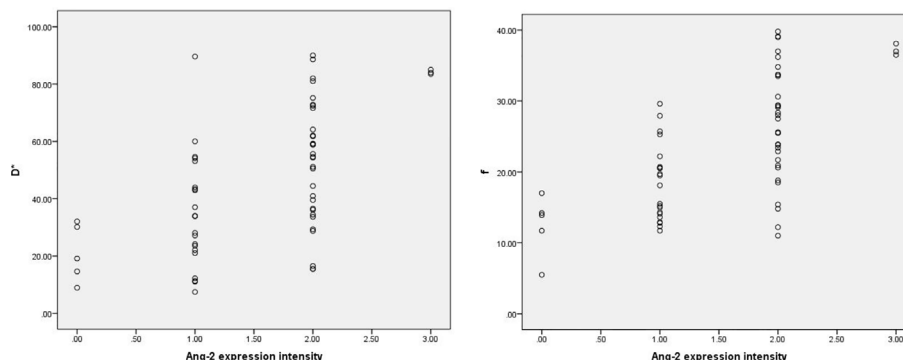


**FIGURE 1** | Scatter plots showing that  $D^*$  and  $f$  values were significantly correlated with intensity of Ang-2 expression.. The units for  $D^*$  values are  $\times 10^{-3} \text{mm}^2/\text{s}$ , and the unit for  $f$  is %.

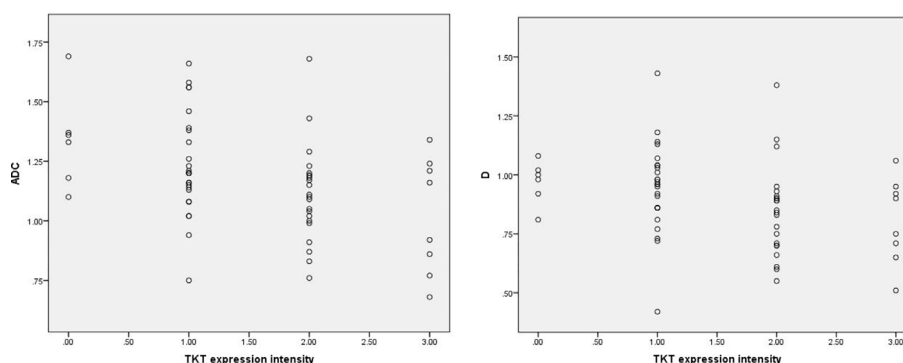


**FIGURE 2** | Scatter plots showing that ADC and  $D$  values were significantly correlated with intensity of TKT expression. The units for apparent diffusion coefficient (ADC) and  $D$  values are  $\times 10^{-3} \text{mm}^2/\text{s}$ .

that plumbagin inhibits the expression of Ang/Tie2 and has significant antitumor activity, suggesting that plumbagin may be a promising antiangiogenesis drug.

TKT has a high positive expression rate in HCC tissues (16), and TKT enhances the proliferation, migration, invasion and colony formation ability of liver cancer cells (17). Yang et al. (34) showed that TKT protects cervical cancer cells from cisplatin treatment and that targeting TKT may have a therapeutic effect on cervical cancer. Studies on metastatic ovarian cancer have shown (19) that inhibiting TKT expression blocks the proliferation of the SKOV-3 cell line, which is an ovarian cancer cell line, and that oxythiamine, an inhibitor of TKT activity, significantly inhibits the proliferation of four ovarian cancer cell lines and primary serous ovarian cancer cells isolated from the patient's ascites. Li et al. (35) studied the relationship between TKT expression and bile acid levels in mouse liver cancer tissues. The results showed that TKT is transported to the nuclei of liver cancer cells by interacting with the signal transducer and activator of transcription-1 (STAT-1). TKT then inhibits the expression of the farnesoid receptor (FXR) (a tumor suppressor gene) by promoting the binding of histone

deacetylase-3 (HDAC-3) to the FXR promoter, causing increases in intrahepatic bile acid (related to the occurrence of liver cancer). The lack of hepatocyte TKT reduces the level of intrahepatic bile acid, which provides an opportunity for liver cancer treatment. The results of the above studies suggest that TKT may be a novel target for tumor treatment.

Studies have shown that IVIM-DWI noninvasively evaluates tumor angiogenesis (3). Lee et al. (36) studied the relationship between IVIM-DWI parameters of mouse colorectal cancer tissue and MVD, and they reported that the  $D^*$  and  $f$  values are significantly correlated with MVD but that there is no correlation between the MVD and either ADC or  $D$ . Lee et al. showed (37) that the value of the IVIM-DWI parameter  $f$  is significantly correlated with MVD for HCC and may be used to evaluate the antiangiogenic effect of sorafenib. Wang et al. (38–40) also obtained similar results.

Song et al. (40) divided 25 human gastric cancer-bearing nude mice into a control group and a treatment group, and they performed IVIM-DWI scans. The results showed that the tumor tissue MVD is significantly reduced after chemotherapy and that



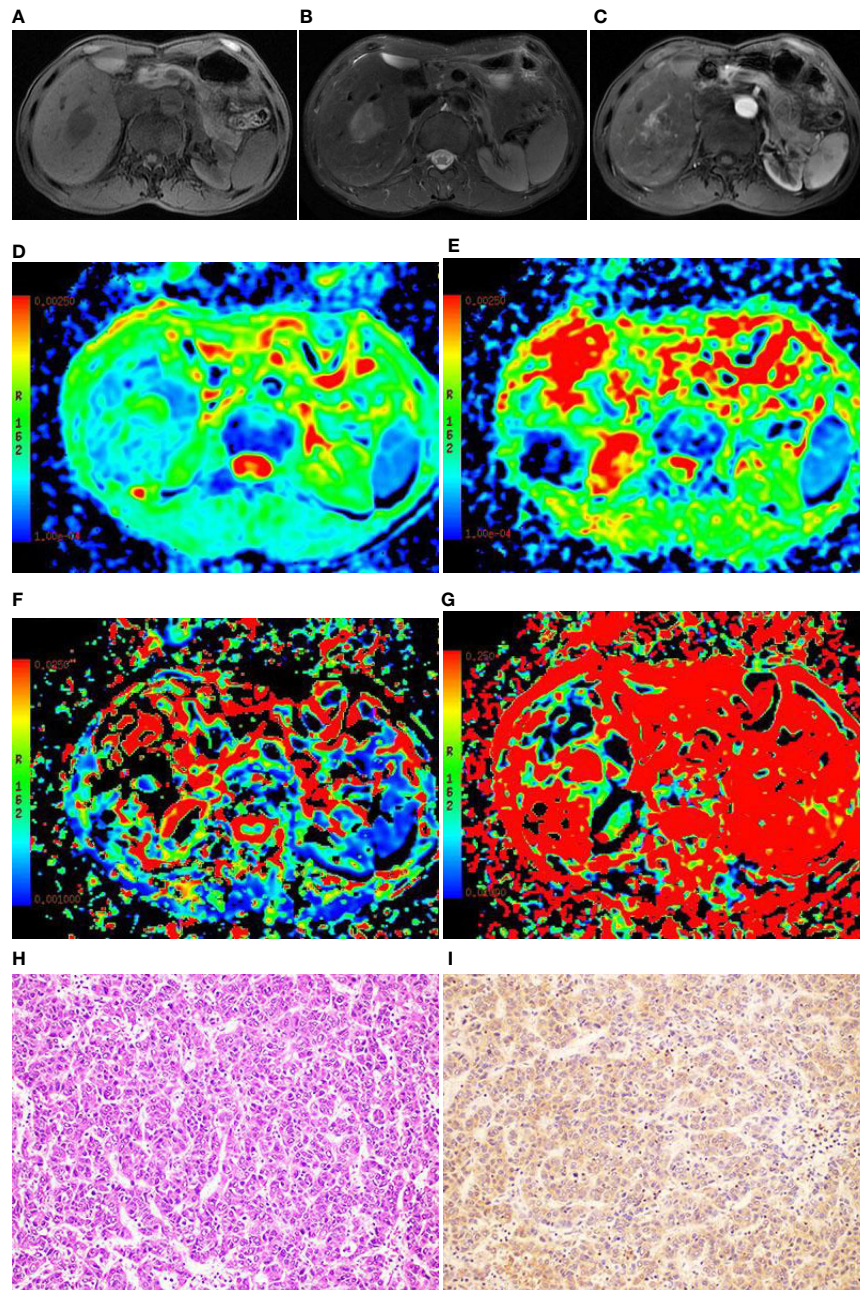


**FIGURE 3** | Images of a 49-year-old male with hepatocellular carcinoma (HCC) in the right lobe of the liver. **(A)** T1WI image showing the lesion with slight hyposignal; **(B)** T2WI image showing the lesion with heterogeneous hypersignal; **(C)** magnetic resonance (MR) enhanced scan showing the lesion with obvious heterogeneous enhancement; **(D)** On the apparent diffusion coefficient (ADC) map, the ADC value was  $1.21 \times 10^{-3} \text{ mm}^2/\text{s}$ ; **(E)** On the D map, the D value was  $1.03 \times 10^{-3} \text{ mm}^2/\text{s}$ ; **(F)** On the D\* map, the D\* value was  $71.6 \times 10^{-3} \text{ mm}^2/\text{s}$ ; **(G)** On the f map, the f value was 33.5%; **(H)** The HE staining (x200) showing that the cancer cells were arranged in a beam-like structure; **(I)** Ang-2 immunohistochemical staining image (x200) showing that Ang-2 was highly expressed.

MVD is positively correlated with the D\* and f values of the perfusion-related parameters. Joo et al. used IVIM-DWI imaging technology to quantitatively evaluate the therapeutic effect of vascular disrupting agents on rabbit VX2 liver tumors (41). The results showed that the D\* and f values in the treatment group are significantly reduced 4 h after treatment but then recover to

baseline at 24 h. In addition, the results demonstrated that the D value significantly increases at 24 h and that the extent of decrease in the f and D\* values within 4 h is correlated with the extent of increase in tumor volume measured during the 7-day follow-up after treatment. The above results suggest that the D\* and f values may be early predictors for evaluating tumor



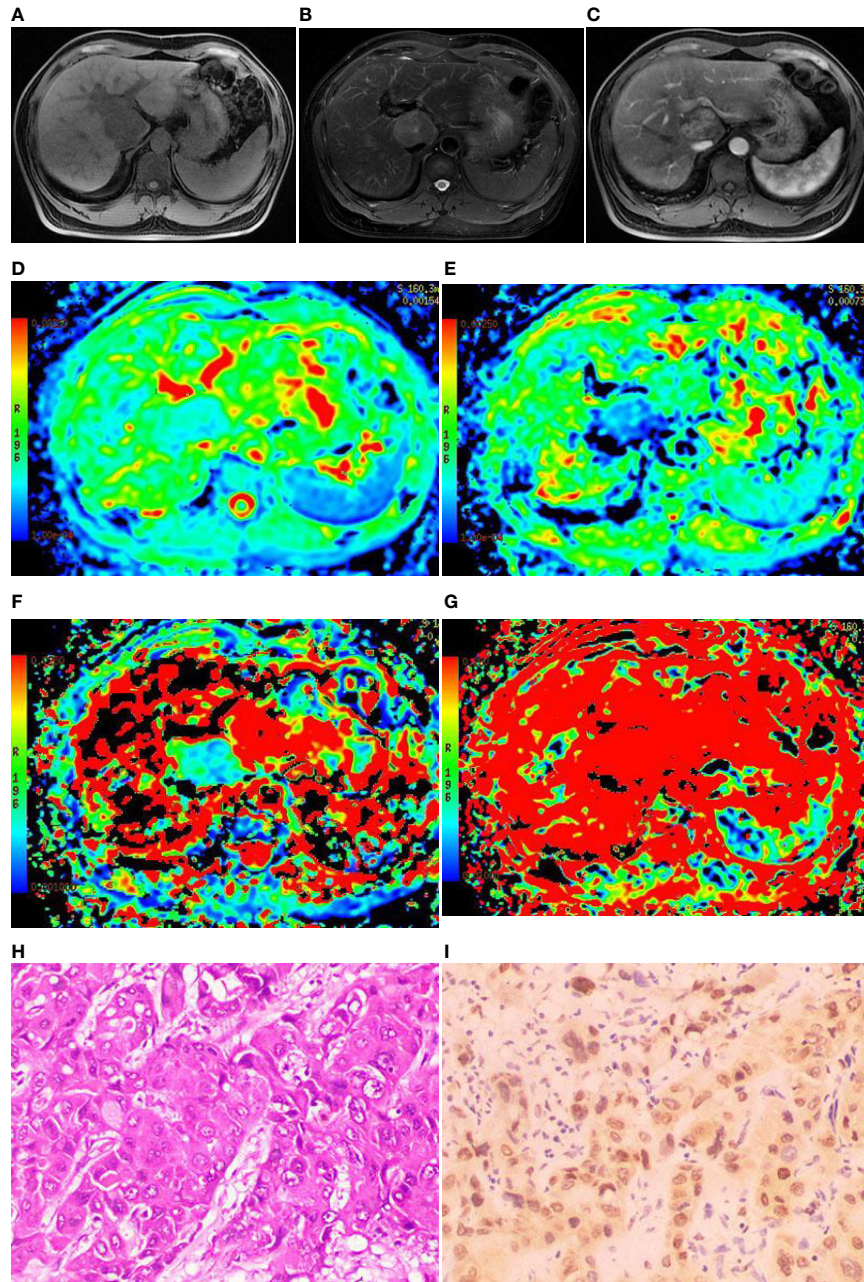


**FIGURE 4** | Images of a 44-year-old male with hepatocellular carcinoma (HCC) in hepatic caudal lobe. **(A)** The T1WI image showing the lesion with slight hyposignal; **(B)** The T2WI image showing the lesion with heterogeneous hypersignal; **(C)** The magnetic resonance (MR) enhanced showing the lesion with obvious heterogeneous enhancement; **(D)** On the apparent diffusion coefficient (ADC) map, the ADC value was  $1.08 \times 10^{-3} \text{ mm}^2/\text{s}$ ; **(E)** On the D map, the D value was  $0.81 \times 10^{-3} \text{ mm}^2/\text{s}$ ; **(F)** On the D\* map, the D\* value was  $24.1 \times 10^{-3} \text{ mm}^2/\text{s}$ ; **(G)** On the f map, the f value was 15.5%; **(H)** Hematoxylin-Eosin (HE) staining (×200) showed that the cancer cells were arranged in a beam-like structure; **(I)** Immunohistochemistry (×200) showed that transketolase (TKT) was highly expressed.

treatment response. The present study showed that the D\* and f values of HCC tissue were significantly correlated with the expression of Ang-2. Higher Ang-2 expression resulted in greater D\* and f values and more abundant microcirculation perfusion of HCC tissue, which was consistent with the above results.

Ki-67 promotes the proliferation of cancer cells (42). Surov et al. (43) showed that Ki-67 is negatively correlated with the values of the IVIM-DWI parameters, ADC and D. Wang et al. (44) and Xiao et al. (45) also obtained similar results. The present study demonstrated that the ADC and D values were lower for the high TKT expression group than for the low TKT expression

group and indicated that TKT expression was negatively correlated with the ADC and D values. These results may be due to TKT promoting cancer cell proliferation, resulting in limited diffusion of free water molecules, thereby reducing the ADC and D values, which reflect the diffusion of water molecules in the tissue (17, 19).

In recent years, several studies have suggested that TKT has a certain role in promoting angiogenesis, but its specific mechanism is still unclear (16). In our study, there were no differences in the values of the  $D^*$  and  $f$  blood perfusion parameters between the different expression groups of TKT. In future studies, it is necessary to verify the angiogenesis effect of TKT and to explore the correlation between the values of the  $D^*$  and  $f$  blood perfusion parameters of HCC IVIM-DWI and the expression of TKT.

The present study had the following limitations: (1) the sample size was relatively small, and larger sample sizes are needed for subsequent studies; (2) solid tumor regions were selected, and the ROIs were manually delineated, which may have introduced measurement errors (46); and (3) the current selection of  $b$ -values was not standardized, which may have impacted the results. For the IVIM-DWI model, at least four different  $b$ -values (including  $b=0$ ) are required to perform double exponential fitting to the signal. Studies (47) have shown that as the value of  $b$  gradually decreases, the deviation between the measured parameter value and the reference parameter value continues to increase. At present, most studies use approximately 10  $b$ -values (47–50). Therefore, 9  $b$ -values were used in this study based on referring to the literature. In the future, the standardization of the  $b$  number and distribution of  $b$ -values should be investigated (4, 47, 48).

## REFERENCES

1. Fitzmaurice C, Allen C, Barber RM, Barregard L, Bhutta ZA, Brenner H, et al. Global, Regional, and National Cancer Incidence, Mortality, Years of Life Lost, Years Lived With Disability, and Disability-Adjusted Life-years for 32 Cancer Groups, 1990 to 2015: A Systematic Analysis for the Global Burden of Disease Study. *JAMA Oncol* (2017) 3:524–48. doi: 10.1001/jamaoncol.2016.5688
2. Le Bihan D, Breton E, Lallemand D, Grenier P, Cabanis E, Laval-Jeantet M. MR imaging of intravoxel incoherent motions: application to diffusion and perfusion in neurologic disorders[J]. *Radiology* (1986) 161:401–7. doi: 10.1148/radiology.161.2.3763909
3. Le Bihan D, Breton E, Lallemand D, Aubin ML, Vignaud J, Laval-Jeantet M. Separation of diffusion and perfusion in intravoxel incoherent motion MR imaging. *Radiology* (1988) 168:497–505. doi: 10.1148/radiology.168.2.3393671
4. Peng J, Zheng J, Yang C, Wang R, Zhou Y, Tao YY, et al. Intravoxel incoherent motion diffusion-weighted imaging to differentiate hepatocellular carcinoma from intrahepatic cholangiocarcinoma. *Sci Rep* (2020) 10:7717. doi: 10.1038/s41598-020-64804-9
5. Luo M, Zhang L, Jiang XH, Zhang WD. Intravoxel incoherent motion: application in differentiation of hepatocellular carcinoma and focal nodular hyperplasia. *Diagn Interv Radiol* (2017) 23:263–71. doi: 10.5152/dir.2017.16595
6. Zhu SC, Liu YH, Wei Y, Li LL, Dou SW, Sun TY, et al. Intravoxel incoherent motion diffusion-weighted magnetic resonance imaging for predicting histological grade of hepatocellular carcinoma: Comparison with

## CONCLUSIONS

The results of the present study suggested that IVIM-DWI can be used to noninvasively evaluate the expression of Ang-2 and TKT in HCC.

## DATA AVAILABILITY STATEMENT

The original contributions presented in the study are included in the article/supplementary material. Further inquiries can be directed to the corresponding author.

## AUTHOR CONTRIBUTIONS

JZ and LY wrote the paper. JZ, RW, YYT, XQG, CY, ZML, and WCW collected the data and performed immunohistochemical staining. TR performed statistical analysis. GY and JDL performed surgical resection. XMZ designed the research. All authors contributed to the article and approved the submitted version.

## FUNDING

This work was supported by Projects of the Department of Science and Technology of Sichuan Province (No. 2016JY0105) and the Department of Education of Sichuan Province (No. 18ZB0222).

- conventional diffusion-weighted imaging. *World J Gastroenterol* (2018) 24:929–40. doi: 10.3748/wjg.v24.i8.929
7. Sokmen BK, Sabet S, Oz A, Server S, Namal E, Dayangac M, et al. Value of Intravoxel Incoherent Motion for Hepatocellular Carcinoma Grading. *Transplant Proc* (2019) 51:1861–6. doi: 10.1016/j.transproceed.2019.02.027
8. Wei Y, Gao F, Wang M, Huang Z, Tang H, Li J, et al. Intravoxel incoherent motion diffusion-weighted imaging for assessment of histologic grade of hepatocellular carcinoma: comparison of three methods for positioning region of interest. *Eur Radiol* (2019) 29:535–44. doi: 10.1007/s00330-018-5638-1
9. Peng J, Yang C, Zheng J, Wang R, Zhou Y, Wang WC, et al. Intravoxel Incoherent Motion Diffusion Weighted Imaging for the Therapeutic Response of Transarterial Chemoembolization for Hepatocellular Carcinoma. *J Cancer Ther* (2019) 10:591–601. doi: 10.4236/jct.2019.107048
10. Zhang Y, Kuang S, Shan Q, Rong D, Zhang Z, Yang H, et al. Can IVIM help predict HCC recurrence after hepatectomy? *Eur Radiol* (2019) 29:5791–803. doi: 10.1007/s00330-019-06180-1
11. Moon WS, Rhyu KH, Kang MJ, Lee DG, Yu HC, Yeum JH, et al. Overexpression of VEGF and angiopoietin 2: a key to high vascularity of hepatocellular carcinoma? *Mod Pathol* (2003) 16:552–7. doi: 10.1097/01.MP.0000071841.17900.69
12. Kochetov GA. Functional flexibility of the transketolase molecule. *Biochem (Mosc)* (2001) 66:1077–85. doi: 10.1023/a:1012424711871
13. Wood T. Physiological functions of the pentose phosphate pathway. *Cell Biochem Funct* (1986) 4:241–7. doi: 10.1002/cbf.290040403
14. Hu J, Ni S, Cao Y, Zhang T, Wu T, Yin X, et al. The Angiogenic Effect of microRNA-21 Targeting TIMP3 through the Regulation of MMP2

- and MMP9. *PLoS One* (2016) 11:e149537. doi: 10.1371/journal.pone.0149537
15. Sitohy B, Nagy JA, Dvorak HF. Anti-VEGF/VEGFR therapy for cancer: reassessing the target. *Cancer Res* (2012) 72:1909–14. doi: 10.1158/0008-5472.CAN-11-3406
  16. Li Y, Tan G, Xiong QS, Bing Z, Wei C, Jian YY, et al. Transketolase contributes to hepatocellular carcinoma migration, invasion, angiogenesis, and tumorigenesis. *Trans Cancer Res* (2018) 7:1–9. doi: 10.21037/tcr.2017.10.26
  17. Qin Z, Xiang C, Zhong F, Liu Y, Dong Q, Li K, et al. Transketolase (TKT) activity and nuclear localization promote hepatocellular carcinoma in a metabolic and a non-metabolic manner. *J Exp Clin Cancer Res* (2019) 38:154. doi: 10.1186/s13046-019-1131-1
  18. Chen ZB, Shen SQ, Ding YM, Wang WX, Tao JP, Liang LJ, et al. The angiogenic and prognostic implications of VEGF, Ang-1, Ang-2, and MMP-9 for hepatocellular carcinoma with background of hepatitis B virus. *Med Oncol* (2009) 26:365–71. doi: 10.1007/s12032-008-9130-7
  19. Ricciardelli C, Lokman NA, Cheruvu S, Tan IA, Ween MP, Pyragius CE, et al. Transketolase is upregulated in metastatic peritoneal implants and promotes ovarian cancer cell proliferation. *Clin Exp Metastasis* (2015) 32:441–55. doi: 10.1007/s10585-015-9718-1
  20. Wada H, Nagano H, Yamamoto H, Yang Y, Kondo M, Ota H, et al. Expression pattern of angiogenic factors and prognosis after hepatic resection in hepatocellular carcinoma: importance of angiopoietin-2 and hypoxia-induced factor-1 alpha. *Liver Int* (2006) 26:414–23. doi: 10.1111/j.1478-3231.2006.01243.x
  21. Folkman J. Angiogenesis in cancer, vascular, rheumatoid and other disease. *Nat Med* (1995) 1:27–31. doi: 10.1038/nm0195-27
  22. Wang FT, Sun W, Zhang JT, Fan YZ. Cancer-associated fibroblast regulation of tumor neo-angiogenesis as a therapeutic target in cancer. *Oncol Lett* (2019) 17:3055–65. doi: 10.3892/ol.2019.9973
  23. Hanahan D, Weinberg RA. Hallmarks of cancer: the next generation. *Cell* (2011) 144:646–74. doi: 10.1016/j.cell.2011.02.013
  24. Sugimachi K, Tanaka S, Taguchi K, Aishima S, Shimada M, Tsuneyoshi M. Angiopoietin switching regulates angiogenesis and progression of human hepatocellular carcinoma. *J Clin Pathol* (2003) 56:854–60. doi: 10.1136/jcp.56.11.854
  25. Mitsuhashi N, Shimizu H, Ohtsuka M, Wakabayashi Y, Ito H, Kimura F, et al. Angiopoietins and Tie-2 expression in angiogenesis and proliferation of human hepatocellular carcinoma. *Hepatology* (2003) 37:1105–13. doi: 10.1053/jhep.2003.50204
  26. Zhang ZL, Liu ZS, Sun Q. Expression of angiopoietins, Tie2 and vascular endothelial growth factor in angiogenesis and progression of hepatocellular carcinoma. *World J Gastroenterol* (2006) 12:4241–5. doi: 10.3748/wjg.v12.i26.4241
  27. Maisonnier PC, Suri C, Jones PF, Bartunkova S, Wiegand SJ, Radziejewski C, et al. Angiopoietin-2, a natural antagonist for Tie2 that disrupts in vivo angiogenesis. *Science* (1997) 277:55–60. doi: 10.1126/science.277.5322.55
  28. Etoh T, Inoue H, Tanaka S, Barnard GF, Kitano S, Mori M. Angiopoietin-2 is related to tumor angiogenesis in gastric carcinoma: possible in vivo regulation via induction of proteases. *Cancer Res* (2001) 61:2145–53. doi: 10.1046/j.1523-5394.2001.009002104.x
  29. Kunz P, Hoffend J, Altmann A, Dimitrakopoulou-Strauss A, Koczan D, Eisenhut M, et al. Angiopoietin-2 overexpression in morris hepatoma results in increased tumor perfusion and induction of critical angiogenesis-promoting genes. *J Nucl Med* (2006) 47:1515–24. doi: 10.1016/j.jnucmed.2008.09.016
  30. Folkman J. Role of angiogenesis in tumor growth and metastasis. *Semin Oncol* (2002) 29:15–18. doi: 10.1053/sonc.2002.37263
  31. Zhang ZL, Zhang JF, Yuan YF, He YM, Liu QY, Mao XW, et al. Suppression of angiogenesis and tumor growth in vitro and in vivo using an anti-angiopoietin-2 single-chain antibody. *Eep Ther Med* (2014) 7:543–52. doi: 10.3892/etm.2014.1476
  32. Mueller T, Freystein J, Lucas H, Schmoll HJ. Efficacy of a Bispecific Antibody Co-Targeting VEGFA and Ang-2 in Combination with Chemotherapy in a Chemoresistant Colorectal Carcinoma Xenograft Model. *Molecules* (2019) 24:2685. doi: 10.3390/molecules24162865
  33. Wei Y, Yang Q, Zhang Y, Zhao T, Liu X, Zhong J, et al. Plumbagin restrains hepatocellular carcinoma angiogenesis by suppressing the migration and invasion of tumor-derived vascular endothelial cells. *Oncotarget* (2017) 8:15230–41. doi: 10.18632/oncotarget.14774
  34. Yang H, Wu XL, Wu KH, Zhang R, Ju LL, Ji Y, et al. MicroRNA-497 regulates cisplatin chemosensitivity of cervical cancer by targeting transketolase. *Am J Cancer Res* (2016) 6:2690–9.
  35. Li M, Zhang X, Lu Y, Meng S, Quan H, Hou P, et al. The nuclear translocation of transketolase inhibits the farnesoid receptor expression by promoting the binding of HDAC3 to FXR promoter in hepatocellular carcinoma cell lines. *Cell Death Dis* (2020) 11:31. doi: 10.1038/s41419-020-2225-6
  36. Lee HJ, Rha SY, Chung YE, Shim HS, Kim YJ, Hur J, et al. Tumor perfusion-related parameter of diffusion-weighted magnetic resonance imaging: correlation with histological microvessel density. *Magn Reson Med* (2014) 71:1554–8. doi: 10.1002/mrm.24810
  37. Lee Y, Lee SS, Cheong H, Lee CK, Kim N, Son WC, et al. Intravoxel incoherent motion MRI for monitoring the therapeutic response of hepatocellular carcinoma to sorafenib treatment in mouse xenograft tumor models. *Acta Radiol* (2017) 58:1045–53. doi: 10.1177/0284185116683576
  38. Wang Z, Su MY, Najafi A, Nalcioğlu O. Effect of vasodilator hydralazine on tumor microvascular random flow and blood volume as measured by intravoxel incoherent motion (IVIM) weighted MRI in conjunction with Gd-DTPA-Albumin enhanced MRI. *Magn Reson Imag* (2001) 19:1063–72. doi: 10.1016/s0730-725x(01)00431-3
  39. Klau M, Mayer P, Bergmann F, Maier-Hein K, Hase J, Hackert T, et al. Correlation of Histological Vessel Characteristics and Diffusion-Weighted Imaging Intravoxel Incoherent Motion-Derived Parameters in Pancreatic Ductal Adenocarcinomas and Pancreatic Neuroendocrine Tumors. *Invest Radiol* (2015) 50:792–7. doi: 10.1097/RLI.0000000000000187
  40. Song XL, Kang HK, Jeong GW, Ahn KY, Jeong YY, Kang YJ, et al. Intravoxel incoherent motion diffusion-weighted imaging for monitoring chemotherapeutic efficacy in gastric cancer. *World J Gastroenterol* (2016) 22:5520–31. doi: 10.3748/wjg.v22.i24.5520
  41. Joo I, Lee JM, Han JK, Choi BI. Intravoxel incoherent motion diffusion-weighted MR imaging for monitoring the therapeutic efficacy of the vascular disrupting agent CKD-516 in rabbit VX2 liver tumors. *Radiology* (2014) 272:417–26. doi: 10.1148/radiol.14131165
  42. Cui X, Chen H, Cai S, Tang Q, Fang X. Correlation of apparent diffusion coefficient and intravoxel incoherent motion imaging parameters with Ki-67 expression in extrahepatic cholangiocarcinoma. *Magn Reson Imag* (2019) 63:80–4. doi: 10.1016/j.mri.2019.08.018
  43. Surov A, Meyer HJ, Höhn AK, Behrmann C, Wienke A, Spielmann RP, et al. Correlations between intravoxel incoherent motion (IVIM) parameters and histological findings in rectal cancer: preliminary results. *Oncotarget* (2017) 8:21974–83. doi: 10.18632/oncotarget.15753
  44. Wang F, Wu LM, Hua XL, Zhao ZZ, Chen XX, Xu JR. Intravoxel incoherent motion diffusion-weighted imaging in assessing bladder cancer invasiveness and cell proliferation. *J Magn Reson Imag* (2018) 47:1054–60. doi: 10.1002/jmri.25839
  45. Xiao Z, Zhong Y, Tang Z, Qiang J, Qian W, Wang R, et al. Standard diffusion-weighted, diffusion kurtosis and intravoxel incoherent motion MR imaging of sinonasal malignancies: correlations with Ki-67 proliferation status. *Eur Radiol* (2018) 28:2923–33. doi: 10.1007/s00330-017-5286-x
  46. Ahlawat S, Khandheria P, Del GF, Morelli J, Subhawong TK, Demehri S, et al. Interobserver variability of selective region-of-interest measurement protocols for quantitative diffusion weighted imaging in soft tissue masses: Comparison with whole tumor volume measurements. *J Magn Reson Imag* (2016) 43:446–54. doi: 10.1002/jmri.24994
  47. Dyvorne H, Jajamovich G, Kakite S, Kuehn B, Taouli B. Intravoxel incoherent motion diffusion imaging of the liver: optimal b-value subsampling and impact on parameter precision and reproducibility. *Eur J Radiol* (2014) 83:2109–13. doi: 10.1016/j.ejrad.2014.09.003
  48. Yamada I, Aung W, Himeno Y, Nakagawa T, Shibuya H. Diffusion coefficients in abdominal organs and hepatic lesions: evaluation with intravoxel incoherent motion echo-planar MR imaging. *Radiology* (1999) 210:617–23. doi: 10.1148/radiology.210.3.r99fe17617
  49. Luciani A, Vignaud A, Cavet M, Nhieu JTV, Mallat A, Ruel L, et al. Liver cirrhosis: intravoxel incoherent motion MR imaging-pilot study. *Radiology* (2008) 249:891–9. doi: 10.1148/radiol.2493080080



50. Patel J, Sigmund EE, Rusinek H, Oei M, Babb JS, Taouli B. Diagnosis of cirrhosis with intravoxel incoherent motion diffusion MRI and dynamic contrast-enhanced MRI alone and in combination: preliminary experience. *J Magn Reson Imaging* (2010) 31:589–600. doi: 10.1002/jmri.22081

**Conflict of Interest:** The authors declare that the research was conducted in the absence of any commercial or financial relationships that could be construed as a potential conflict of interest.

Copyright © 2021 Zheng, Gong, Tao, Wang, Yang, Li, Ren, Li, Yang, Wang, Yang and Zhang. This is an open-access article distributed under the terms of the Creative Commons Attribution License (CC BY). The use, distribution or reproduction in other forums is permitted, provided the original author(s) and the copyright owner(s) are credited and that the original publication in this journal is cited, in accordance with accepted academic practice. No use, distribution or reproduction is permitted which does not comply with these terms.





# SurvNet: A Novel Deep Neural Network for Lung Cancer Survival Analysis With Missing Values

Jianyong Wang<sup>1</sup>, Nan Chen<sup>2</sup>, Jixiang Guo<sup>1</sup>, Xiuyuan Xu<sup>1</sup>, Lunxu Liu<sup>2\*</sup> and Zhang Yi<sup>1\*</sup>

<sup>1</sup> Machine Intelligence Laboratory, College of Computer Science, Sichuan University, Chengdu, China, <sup>2</sup> Department of Thoracic Surgery, West China Hospital and West China School of Medicine, Sichuan University, Chengdu, China

## OPEN ACCESS

### Edited by:

Changqiang Wu,  
North Sichuan Medical College,  
China

### Reviewed by:

Quan Guo,  
Michigan State University,  
United States  
Xi Wang,  
The Chinese University of  
Hong Kong, China

### \*Correspondence:

Lunxu Liu  
lunxu\_liu@aliyun.com  
Zhang Yi  
zhangyi@scu.edu.cn

### Specialty section:

This article was submitted to  
Cancer Imaging and  
Image-directed Interventions,  
a section of the journal  
Frontiers in Oncology

**Received:** 30 July 2020

**Accepted:** 04 December 2020

**Published:** 20 January 2021

### Citation:

Wang J, Chen N, Guo J, Xu X, Liu L  
and Yi Z (2021) SurvNet: A Novel Deep  
Neural Network for Lung Cancer  
Survival Analysis With Missing Values.  
Front. Oncol. 10:588990.  
doi: 10.3389/fonc.2020.588990

Survival analysis is important for guiding further treatment and improving lung cancer prognosis. It is a challenging task because of the poor distinguishability of features and the missing values in practice. A novel multi-task based neural network, SurvNet, is proposed in this paper. The proposed SurvNet model is trained in a multi-task learning framework to jointly learn across three related tasks: input reconstruction, survival classification, and Cox regression. It uses an input reconstruction mechanism cooperating with incomplete-aware reconstruction loss for latent feature learning of incomplete data with missing values. Besides, the SurvNet model introduces a context gating mechanism to bridge the gap between survival classification and Cox regression. A new real-world dataset of 1,137 patients with IB-IIA stage non-small cell lung cancer is collected to evaluate the performance of the SurvNet model. The proposed SurvNet achieves a higher concordance index than the traditional Cox model and Cox-Net. The difference between high-risk and low-risk groups obtained by SurvNet is more significant than that of high-risk and low-risk groups obtained by the other models. Moreover, the SurvNet outperforms the other models even though the input data is randomly cropped and it achieves better generalization performance on the Surveillance, Epidemiology, and End Results Program (SEER) dataset.

**Keywords:** survival analysis, prognosis prediction, deep neural networks, multi-task learning, missing value

## INTRODUCTION

In clinical research, the development of effective survival analysis methods for censored data is always required to evaluate the relationship between the risk factors and event of interest (1, 2). It has been widely applied to modeling the prognosis of cancers to help to optimize and improve cancer treatment (3–6).

Lung cancer is one of the most heterogeneous cancers and has distinct prognoses. A great deal of work has been conducted on lung cancer prognostic prediction in recent decades, among which the series of tumor node metastasis classification (TNM classification) for lung cancer is the most famous one (4, 7, 8). It has been the guideline for clinical treatment. In the eighth edition of TNM classification for lung cancer, the five-year survival rate of the IB-IIA stage ranged from 65 to 73%, which is relatively high. However, in the practice, many IB-IIA stage patients present with a recurrence and die within five years after treatment. Distinguishing the IB-IIA stage patients with a

high risk of recurrence and death from low-risk patients is worthwhile for guiding further treatment and may improve the lung cancer prognosis. Additionally, the clinicopathologic variable used in TNM classification is limited for personalized prediction for different patients and it is limited to integrate new variables into the existing prognosis models (9). There is a great need for a new survival analysis method to establish fine-grained prognoses for individual patients with IB-IIA stage lung cancer for more accurate individual prediction by integrating an expanding number of prognostic factors.

Cox (2, 10, 11) proportional hazards regression is one of the most well-known survival analysis methods. It has been implemented in many famous software toolboxes and been widely used in many prognosis prediction tasks (8), such as TNM classification for lung cancer (4, 7, 8). The Cox proportional hazards model is semi-parametric and is subject to a linear model (12). It makes an important assumption about the hazard function, which is that covariances that affect the hazard rate are independent. However, in practice, the relationship between variables and the outcome is complex and unknown and there may be interactions among variables (13). Deep neural networks (DNNs) is apparent to be a promising method to solve these problems.

The DNN is a class of biologically inspired computational models towards artificial intelligence. It has been proven that DNNs can approximate any non-linear function when provided with sufficient neurons. Generally, a DNN can be a very complex non-linear model and learn latent features from data directly (14). It has achieved many impressive results in various applications, such as image classification (15, 16), natural language processing (17–20), and biomedical analysis (14, 21–23) in addition to survival analysis (1, 2, 7, 11, 24–26).

Generally, most of DNN based methods for survival analysis could be divided into two paradigms. The first is to formulate the survival analysis as a classification problem to evaluate survival probability at different fixed time points (9, 27, 28). In (27), neural networks were used to improve the prediction accuracy of the five-year survival of patients with breast cancer. Lundina et al. demonstrated that a neural network model trained on some prognostic factors can accurately predict specific 5-, 10-, and 15-year breast cancer survival (9).

The other paradigm is to extend Cox regression with DNNs, in which DNNs are used to extract the features of the patient and trained using Cox-like cost function with the gradient-based method. In (12), the authors proposed the Cox-Net model for prognosis prediction on high-throughput omics data and implemented it with the Theano math library in Python to achieve an efficient computational time using GPUs. Huang et al. modified the Cox-Net method to use multi-omics survival analysis learning on breast cancer (26). Moreover, (16), DNN was applied to cardiac motion analysis for human survival prediction and outperformed the traditional Cox models. However, Cox-Net inherited the limitation of Cox models, which is that it was not designed to estimate the probability of survival at a fixed time. Therefore, it is necessary to study how to design a unified model that integrates the good

properties of the aforementioned two paradigms to improve the performance.

Moreover, the dataset used in survival analysis commonly contains incomplete data with missing values in practice. In many cases, most of the patients with missing values are excluded (2, 29). Omitting patients with missing values limits the number of patients to train the prognosis model and may introduce substantial biases in the study, whereas using patients with missing values may harm the performance. The learning of the latent feature of incomplete data with missing values in survival analysis by using DNNs should be evaluated further.

To address the aforementioned problems, in this study, we propose a multi-task based neural network model, SurvNet, for survival analysis of real-world datasets of patients with IB-IIA stage lung cancer. The main contributions are as follows:

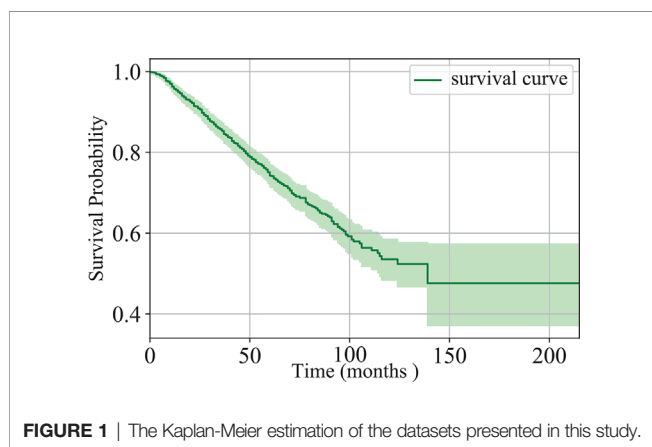
- An input reconstruction mechanism cooperating with incomplete-aware reconstruction loss is proposed in the SurvNet for latent feature learning of incomplete data with missing values.
- A context gating mechanism is proposed in the SurvNet to bridge the gap between survival classification and Cox regression for prognosis prediction.
- The proposed SurvNet model is trained in a multi-task learning framework to jointly learn across three related tasks: input reconstruction, survival classification, and Cox regression.
- A new real-world dataset is collected to evaluate the performance of the prognosis prediction models for IB-IIA stage non-small lung cancer.

The proposed method is compared with the traditional Cox model and Cox-Net in the experiments. The experiment results demonstrate that the proposed SurvNet outperforms the other models with a much higher concordance index ( $C_{index}$ ). The difference between high and low risk groups obtained by SurvNet is more significant than that of high and low risk groups obtained by the other models. Furthermore, it achieves better performance on incomplete data with missing values and better generalization performance on Surveillance, Epidemiology, and End Results Program (SEER) dataset.

## MATERIALS AND METHODS

### Datasets

In this study, we collected the data of 1,280 patients with IB-IIA stage non-small cell lung cancer at West China Hospital, from 2005 to 2018. There are 1,137 patients remaining after the exclusion of patients with unknown survival time. Of the 1,137 patients, 346 died and the others are missing follow-up or still alive. The survival time of the patients is in the range of (1,215) months. **Figure 1** shows the Kaplan-Meier estimation of the dataset. Clearly, the five-year survival probability of the patients at the IB-IIA stage is relatively high. However, 42, 97, 160, 219, and 263 patients died in 1-, 2-, 3-, 4-, and 5-year respectively. Distinguishing the IB-IIA stage patients with a high risk of



recurrence or death from low-risk patients is worthwhile for guiding further treatment and improving the non-small lung cancer prognosis.

In this study, nine clinicopathologic variables are taken into account for prognosis prediction. The distribution of the variables in the final patient series used in the study is shown in **Table 1**. In practice, it is difficult to ensure all of the variables were recorded for each patient. As illustrated in **Table 1**, there are lots of missing values (denoted as “unknown”). Of 1,137 patients, 961 contains missing values (at least one of the clinicopathologic variables is missing). It brings a great challenge for prognosis prediction models.

Of nine clinicopathologic variables, age and tumor size are continuous variables, whereas the others are encoded using

**TABLE 1** | Distribution of clinicopathologic variables in our datasets of patients with IB-IIA stage lung cancer. Missing values are denoted as “unknown”.

Clinicopathologic variables	Value	Num of patients
Age	Range (18–86)	1,137
Tumor Size	Range (0.3–5)	778
	<b>Unknown</b>	359
Sex	Female	670
	Male	467
Tumor Location	Left Upper	287
	Left Lower	186
	Right Upper	367
	Right Middle	87
	Right Lower	210
Differentiation	Lower	501
	Middle or High	542
	<b>Unknown</b>	94
Cancer Type	Adenocarcinoma	843
	Squamous carcinoma	294
Lymph node management	Dissection	1,015
	Biopsy or No Management	97
	<b>Unknown</b>	25
Pleura Immersion	Yes	656
	No	87
	<b>Unknown</b>	394
Operation	Lobectomy	53
	Sub Lobectomy	1,084

discrete values, for example, –1 for females and 1 for males. The missing values are filled with zeros. Thus, the clinicopathologic variables of each patient are represented by a 9 dimension vector. Formally, the proposed dataset can be formulated into a set of triplets  $\{(x_i, s_i, t_i) \mid i = 1, 2, \dots, n\}$ , where  $n$  is the number of the patients,  $x_i \in R^9$  is a vector of 9 clinicopathologic variables that describes the  $i$ -th patient,  $s_i$  is the patient's end state, that is, 1 for dead or 0 for alive, and  $t_i$  is the patient's survival time.

## Problem Definition

In this study, the aim is to dichotomize the patients in the dataset into high and low risk groups according to their prognosis index. This can be formulated as:

$$d_x = \begin{cases} 1, & \text{if } p_x > PI \\ 0, & \text{if } p_x \leq PI \end{cases} \quad (1)$$

where  $PI$  is a constant and the prognosis index  $p_x$  is calculated by

$$p_x = F(x) \quad (2)$$

where  $F$  is generally a complex non-linear function. Thus, the core task of the prognosis prediction task is to determine a suitable function  $F$ .

However, it is difficult to estimate the prognosis index function  $F$  for fine-grained prognosis prediction of IB-IIA stage lung cancer. There are three challenges:

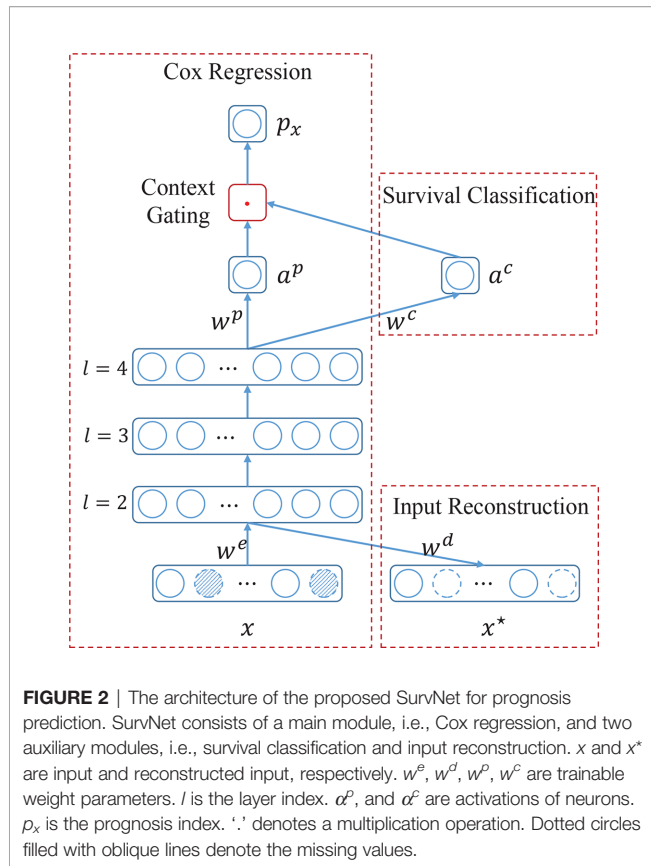
- For most patients, the end event (death) has not yet happened. It is known as censoring. In other words, we could not get actual survival times for these patients.
- Most of the patients contain at least one missing value. Omitting patients with missing values may bias the result, whereas using patients with missing values may harm the performance. It is a great obstacle for machine learning methods (30, 31).
- The distinguishing feature is difficult to learn for patients with IB-IIA stage lung cancer.

## Multi-Task Based SurvNet for Prognosis Prediction

To overcome the aforementioned difficulties, in this study, a novel multi-task based neural network namely SurvNet is proposed for the prognosis prediction of IB-IIA stage lung cancer. As **Figure 2** illustrated, the proposed SurvNet consists of three modules: Cox regression module, survival classification module, and input reconstruction module. Cox regression module is the main backbone of SurvNet and is used to represent the Function  $F$  for prognosis prediction. Survival classification module and input reconstruction module are auxiliary modules that aim to improve the performance of SurvNet for fine-grained prognosis prediction on incomplete data with missing values.

### Input Reconstruction Module

The missing value is a common phenomenon in survival analysis. The suitable method to deal with the missing values is always desired to improve the performance of prognosis prediction models. In the proposed SurvNet, we use zeros to



fill the missing values and then learn the latent feature of incomplete data by input reconstruction.

Given an input  $x$ , it is first encoded into latent feature vector  $a^2$  (the output of layer 2). Then  $a^2$  would be fed into input reconstruction module to be decoded into  $x^*$ , a reconstruction of input  $x$ . Formally, it can be formulated as:

$$\begin{cases} a^2 = f(w^e x) \\ x^* = w^d a^2, \end{cases} \quad (3)$$

where  $w^e$  and  $w^d$  are encoder and decoder weights,  $x$  and  $x^*$  are input and reconstruction respectively.  $f$  denotes the non-linear activation function. Actually, the input layer, 2<sup>nd</sup> layer, and the input reconstruction layer composes an autoencoder network (See Figure 2).

Generally, mean square error (MSE) is used to make  $x^*$  approximate  $x$  as accurately as possible. However, it is not suitable for input with missing values since we do not know the true values at such locations and do not want to reconstruct a new vector with missing values too. To address this problem, an incomplete-aware cost function is proposed to learn the latent feature of incomplete data with missing values.

Let the binary vector  $r$  denote the locations of missing values in input  $x$ :

$$r(j) = \begin{cases} 0, & \text{the } j\text{-th element of } x \text{ is missing} \\ 1, & \text{otherwise} \end{cases} \quad (4)$$

The proposed incomplete-aware cost function is formulated as:

$$J_{re} = \frac{1}{2n} \sum_{i=1}^n \|r_i \cdot (x_i^* - x_i)\|_2 \quad (5)$$

where  $i$  is the sample index and “.” denotes the elementwise product.

### Survival Classification Module

To fully  $x_p$ , utilize the relationship among the input variables  $x_i$ , end state  $s_i$  and survival time  $t_i$ , we introduce an auxiliary survival classification module to the SurvNet. The output of this module  $a^c$  denotes the probability of the patient living over  $T$  years or not. In other words, it learns a patient's survival probability at some fixed time point  $T$ . Formally,  $a^4$  could be calculated as:

$$a^c = \sigma(w^c a^4) \quad (6)$$

where  $w^c$  and  $a^4$  are weight connection and output of layer 4, and  $\sigma(z) = 1/(1 + \exp(-z))$ . In this study, layer 3 is a batch norm layer.  $a^4$  could be calculated as:

$$\begin{cases} a^4 = \tanh(w^3 a^3) \\ a^3 = \frac{a^2 - E[a^2]}{\sqrt{\text{Var}[a^2] + \epsilon}}, \end{cases} \quad (7)$$

where  $w^3$  is weight connection and  $\tanh(z) = (\exp(-z) - \exp(z))/(\exp(-z) + \exp(z))$ .  $E$  and  $\text{Var}$  denote the expectation and variance, respectively.  $\epsilon$  is a small constant.

In this manuscript, the learning of survival classification module could be formulated as a binary classification task, which aims to minimize the following cost function:

$$J_c = \sum_i \delta_i (d_i \cdot \log(a^c) + (1 - d_i) \cdot (\log(1 - a^c))). \quad (8)$$

where  $d_i$  is the survival state of the patient  $i$ , which is defined as

$$d_i = \begin{cases} 1, & \text{if } t_i > T \\ 0, & \text{if } t_i < T \text{ and } s_i == 1, \end{cases} \quad (9)$$

and  $\delta_i$  denotes whether a patient is a valid sample classification task and it is defined as

$$\delta_i = \begin{cases} 1, & \text{if } t_i < T \text{ and } s_i == 0 \\ 0, & \text{otherwise.} \end{cases} \quad (10)$$

It means that patients censored before  $T$  are ignored.

### Cox Regression Module

This is the main backbone of the proposed SurvNet. As Figure 2 illustrated, it consists of several successive feedforward layers, such as fully connected layer, batch normalization (32), and dropout layer, and a new context gating submodule that does not exist in the traditional Cox-Net (12).

Given an input  $x$ , the high-level representation  $a^L$  could be calculated layer by layer. Specifically, the activation  $a^p$  is computed as

$$a^p = w^p a^L. \quad (11)$$



In the traditional Cox-Net (12),  $\alpha^p$  would be expressed as log hazard ratio in Cox regression. However, in the proposed SurvNet, the distribution of log hazard ratio  $\alpha^p$  is adjusted by survival probability  $\alpha^c$  by using context gating mechanism:

$$p_x = \alpha^p \cdot \alpha^c. \quad (12)$$

Then, we take  $p_x$  as log hazard ratio in Cox regression and use the following log partial likelihood for Cox regression:

$$J_{cox} = \sum_{i: s_i=1}^n \left( p_{x_i} - \log \left( \sum_{j: t_j \leq t_i} p_{x_j} \right) \right), \quad (13)$$

where  $i$  and  $j$  are sample indexes.

The context gating mechanism is inspired by the attention mechanism where the input is adjusted by the attention coefficient. It is notable that the proposed context gating mechanism bridges the gap between Cox regression and survival classification to improve the performance. On the one hand, in the Cox regression, it is supposed that the larger the survival time, the larger the prognosis index. It reveals that the prognosis indexes of patients that are alive at some fixed time point  $T$  should be larger than the patients that died at that time point. On the other hand, the survival classification aims to predict the survival state of a given patient at a fixed time point  $T$ . As Equation (12) illustrates, the survival prediction  $\alpha^c$  serves as a context coefficient that adjusts the hazard ratio  $\alpha^p$  automatically thus to produce a better prognosis index that has good distribution at time point  $T$ .

### Multi-Task Learning

To train the proposed SurvNet, three learning tasks are optimized synchronously. The final cost function could be formulated as:

$$J = \alpha J_{cox} + \beta J_C + \gamma J_{re}, \quad (14)$$

where  $\alpha$ ,  $\beta$ , and  $\gamma$  are the coefficients that balance the Cox regression, survival classification, and input reconstruction tasks. By using gradient-based algorithms, the (local) minimal of cost function  $J$  could be found iteratively.

## EXPERIMENTS

### Evaluation Metrics

To evaluate the performance of the proposed model, two metrics were used. One is the Harrell's concordance index ( $C_{index}$ ), which is valued from 0 to 1. It is an extension of the area under the receiver operating characteristic curve to censored time-to-event data (16, 26).

Generally, it is defined as

$$C_{index} = \frac{\sum_{i,j} s_i \cdot I(p_i, p_j) \cdot I(t_i, t_j)}{\sum_{i,j} s_i \cdot I(t_i, t_j)} \quad (15)$$

Where  $i$  and  $j$  are sample indexes.  $s$ ,  $t$ , and  $p$  are end state, survival time and hazard ratio of a given sample, respectively.  $I(z_1, z_2)$  is defined as:

$$I(z_1, z_2) = \begin{cases} 1, & \text{if } z_1 < z_2 \\ 0, & \text{otherwise.} \end{cases} \quad (16)$$

The other metric is the survival analysis with the log-rank test. Kaplan-Meier survival curves are generated by dichotomizing all patients in the testing dataset into low-risk and high-risk groups *via* the median hazard ratio. The corresponding log-rank p-value indicates the ability of the model to differentiate two risk groups. The lower the p-values, the better the model performance.

## Running Configuration

### Datasets

To train the prognosis models, the presented dataset was randomly split into train set (682 patients), validation set (227 patients), and test set (228 patients). Furthermore, we also obtained a SEER dataset (9,534 patients) by selecting the IB-IIA stage lung cancer patients from SEER to test the generalization performance of the models.

### Models

The proposed SurvNet was compared with the traditional Cox proportional hazards model and neural network extended Cox model (Cox-Net). For a fair comparison, the Cox-Net shared the same architecture with the Cox regression module in SurvNet except for the context gating module. The network settings is presented in **Table 2**. Besides, we set  $T = 36$  for SurvNet and the coefficients  $\alpha$ ,  $\beta$ , and  $\gamma$  were set to 0.2, 1, 3, respectively. The RMSProp (33) with default learning parameters in Pytorch was used as the optimizer and the weight decay was set to 0.00001. All of the networks run 100 epochs with batch size 64. For each run, the weight parameters that achieved the best  $C_{index}$  on the validation dataset were used to evaluate the performance of the model on the test dataset.

### Performance on Our Dataset

To eliminate the influence of initial values of neural networks, we run Cox-Net, SurvNet, and SurvNet-ae (SurvNet without survival classification module) five times. For each running, the model with the highest  $C_{index}$  on the validation dataset is selected to evaluate the performance on the test dataset. The boxplot of the  $C_{index}$  is presented in **Figure 3**. It demonstrates that the proposed SurvNet with and without survival classification module outperformed the Cox-Net significantly by the using input reconstruction module to learning the latent feature of incomplete data with missing values. And the proposed survival classification module further improves the network's performance. Besides, the best  $C_{index}$  of traditional Cox model, Cox-Net, and the proposed SurvNet are 0.5612, 0.5627, 0.6367,

**TABLE 2** | Network settings for Cox-Net and SurvNet.

Layer	Neurons
1	9 (input)
2	64 (tanh)
3	Batch normalization
4	32 (tanh)

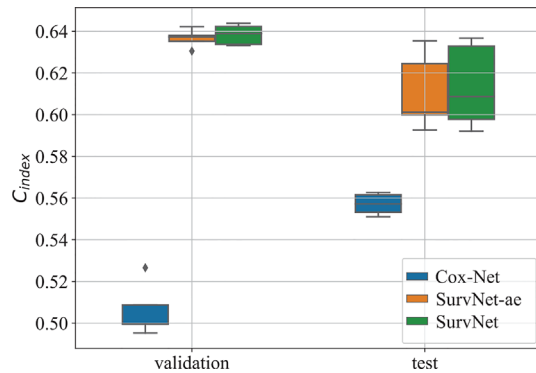


**FIGURE 3** | The boxplot of the  $C_{index}$  on the validation dataset and test dataset. “SurvNet-ae” denotes the SurvNet without survival classification module.

respectively. The proposed SurvNet outperforms the other models significantly.

Furthermore, by interpreting the outputs of the models as the log hazard ratio, two groups (high risk and low risk) are obtained by using Eq. (1) where  $PI$  was set to the median of log hazard ratios. The Kaplan-Meier estimation of the Cox model, Cox-Net and the proposed SurvNet on the test dataset are presented in **Figure 4**. The log-rank  $p$ -values (the lower the better) of the three methods are 0.293, 0.072, 0.002. It is obvious that the difference between high and low risk groups obtained by neural network based models is more significant than that of high and low risk groups obtained by the Cox model. Moreover, the difference between high and low risk groups obtained by SurvNet is most significant. It demonstrates that the proposed SurvNet achieves the best performance.

In addition, the distribution of survival times of patients in each group is presented in **Figure 5**. The proposed SurvNet achieves the largest median survival time for low risk group and the lowest median survival time for high risk group. It demonstrates that the proposed method improves the performance of fine-grained prognosis prediction for IB-IIA stage non-small cell lung cancer.

## Robustness on Missing Values

To further evaluate the robustness of prognosis models on incomplete data with missing values, we randomly zeroed the values of the input vector in the test dataset with drop probability  $dp$  and then evaluated the performance of the trained models. For each drop probability  $dp$ , we run each model 100 times.

The boxplot of  $C_{index}$  is illustrated in **Figure 6**. As drop probability gets large, the performance of the three models gets worse. Notably, the proposed SurvNet performed more stable and the  $C_{index}$  of the SurvNet is always larger than that of the Cox model and Cox-Net significantly.

## Generalization Performance on SEER Dataset

The generalization performance is an important measurement of prognosis models. SEER dataset has been widely used in the

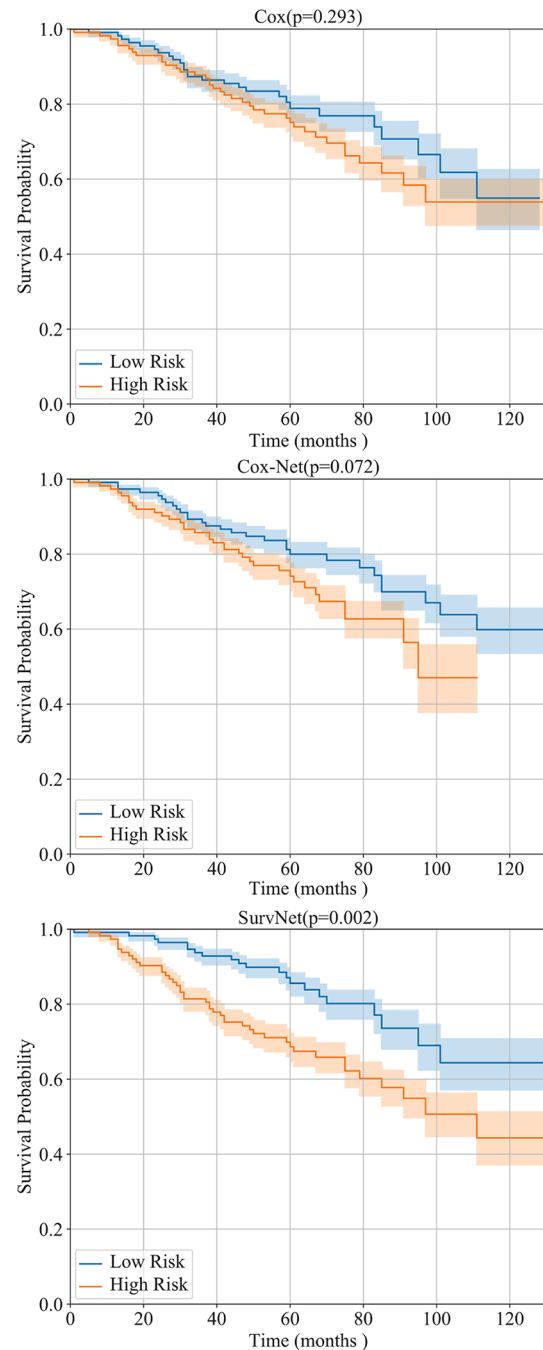
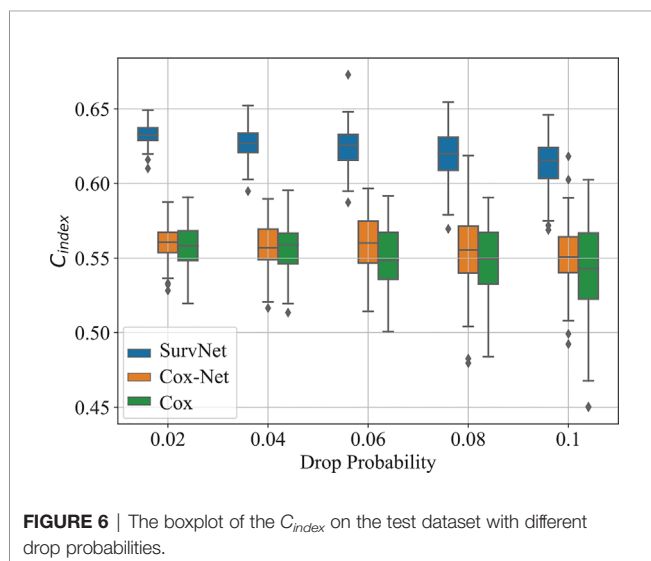
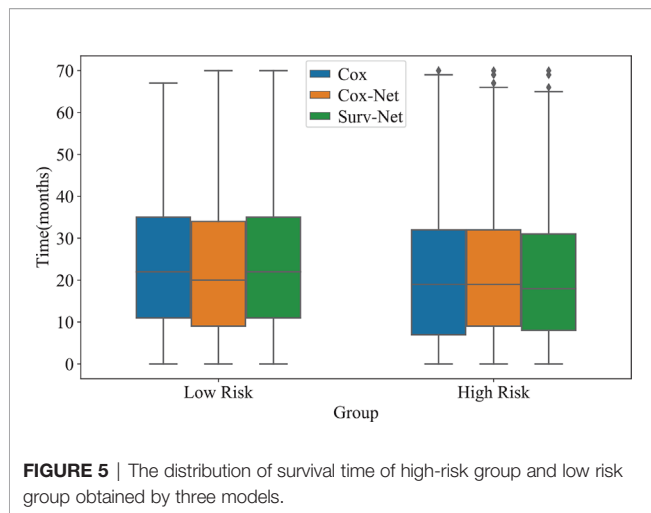


**FIGURE 4** | Performance of the Cox model, Cox-Net, and the proposed SurvNet on our test dataset. The Kaplan-Meier estimation (with 95% confidence intervals) of high risk and low risk groups are shown and the log-rank test was performed to compare survival curves between two groups.

literature. In this study, we focused on the IB-IIA stage non-small lung cancer and obtained a dataset of 9,534 patients.

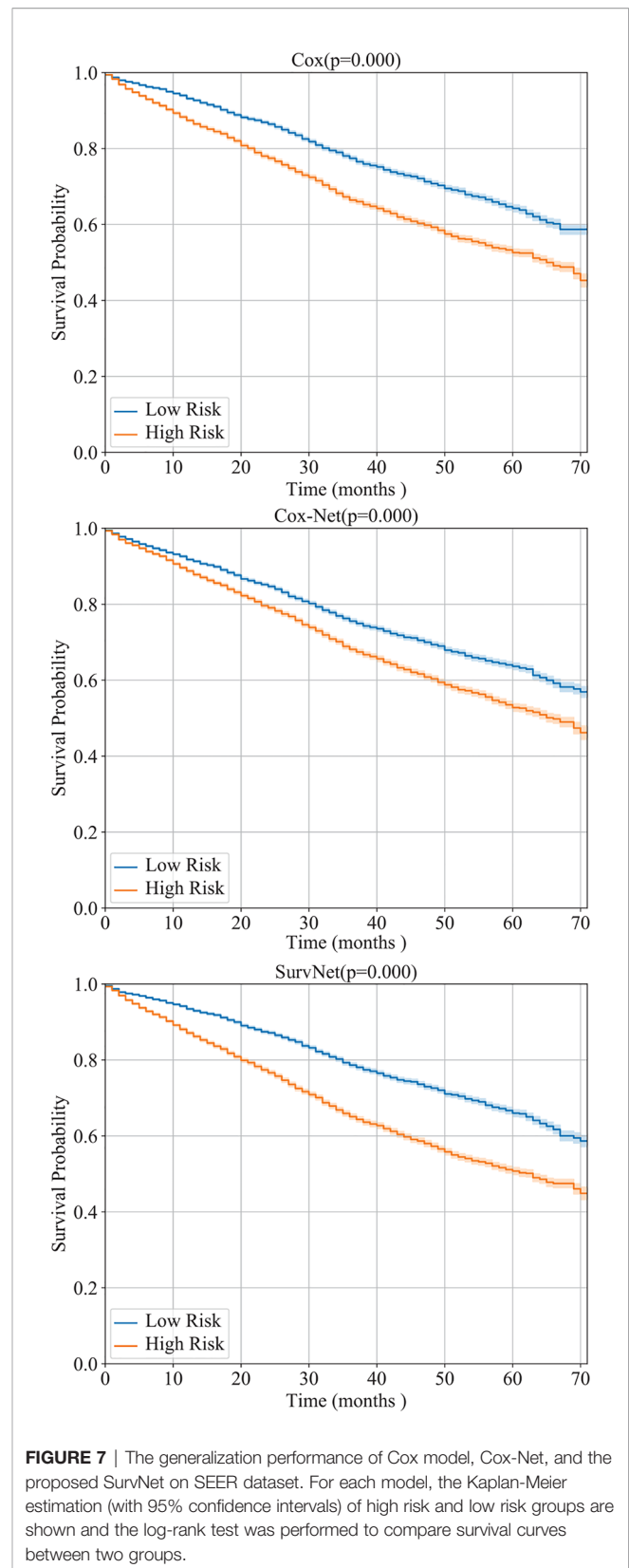
We evaluated the models, which have been trained using our dataset, on the obtained SEER dataset. The  $C_{index}$  of Cox model, Cox-Net, and SurvNet are 0.5955, 0.5617, and 0.6003,



respectively. Besides, as the Kaplan-Meier estimation presented in **Figure 7** shows, the difference between high and low risk groups obtained SurvNet is more significant than that of high and low risk groups obtained by other two models. The proposed SurvNet achieves better generalization performance than the Cox model and Cox-Net.

## CONCLUSION

Prognosis prediction for IB-IIA stage lung cancer is important for improving the accuracy of the management of lung cancer. In this study, a new real-world dataset is collected and a novel multi-task based neural network, SurvNet, is proposed to further improve the prognosis prediction for IB-IIA stage lung cancer. In the proposed SurvNet, the input reconstruction module overcomes the problems by missing values and the proposed context gating mechanism



could bridge the gap between Cox regression and survival classification. By training in a multi-task framework, the proposed SurvNet outperforms the traditional Cox model and Cox-Net significantly. It achieved higher  $C_{index}$ s and lower  $p$ -values on the proposed dataset and better generalization performance on the SEER dataset. It is apparent to be a promising method for survival analysis tasks. A limitation of the proposed SurvNet may lie on the survival classification module which just considers survivals on some fixed time point rather than a set of non-overlap time intervals. Future work will be focused on how to integrate survival classification module that classifies the survivals into a set of time intervals with the Cox regression module to further improve the performance on prognosis prediction.

## DATA AVAILABILITY STATEMENT

The raw data supporting the conclusions of this article will be made available by the authors, without undue reservation.

## REFERENCES

- Pölsterl S, Conjeti S, Navab N, Katouzian A. Survival analysis for high-dimensional, heterogeneous medical data: Exploring feature extraction as an alternative to feature selection. *Artif Intell Med* (2016) 72:1–11. doi: 10.1016/j.artmed.2016.07.004
- Jing B, Zhang T, Wang Z, Jin Y, Liu K, Qiu W, et al. A deep survival analysis method based on ranking. *Artif Intell Med* (2019) 98:1–9. doi: 10.1016/j.artmed.2019.06.001
- Wang Y, Wang D, Ye X, Wang Y, Yin Y, Jin Y. A tree ensemble-based two-stage model for advanced-stage colorectal cancer survival prediction. *Inf Sci* (2019) 474:106–24. doi: 10.1016/j.ins.2018.09.046
- Rami-Porta R, Bolejack V, Crowley J, Ball D, Kim J, Lyons G, et al. The iaslc lung cancer staging project: proposals for the revisions of the t descriptors in the forthcoming eighth edition of the tnm classification for lung cancer. *J Thoracic Oncol* (2015) 10:990–1003. doi: 10.1097/JTO.0000000000000559
- Kim S, Park T, Kon M. Cancer survival classification using integrated data sets and intermediate information. *Artif Intell Med* (2014) 62:23–31. doi: 10.1016/j.artmed.2014.06.003
- Zupan B, Demšar J, Kattan MW, Beck J, Bratko I. Machine learning for survival analysis: a case study on recurrence of prostate cancer. *Artif Intell Med* (2000) 20:59–75. doi: 10.1016/S0933-3657(00)00053-1
- Goldstraw P, Chansky K, Crowley J, Rami-Porta R, Asamura H, Eberhardt WE, et al. The iaslc lung cancer staging project: proposals for revision of the tnm stage groupings in the forthcoming (eighth) edition of the tnm classification for lung cancer. *J Thoracic Oncol* (2016) 11:39–51. doi: 10.1016/j.jtho.2015.09.009
- Detterbeck FC, Boffa DJ, Kim AW, Tanoue LT. The eighth edition lung cancer stage classification. *Chest* (2017) 151:193–203. doi: 10.1016/j.chest.2016.10.010
- Lundin M, Lundin J, Burke HB, Toikkanen S, Pylkkanen L, Joensuu H. Artificial neural networks applied to survival prediction in breast cancer. *Oncology* (1999) 57:281–6. doi: 10.1159/000012061
- Cox DR. Regression models and life-tables. *J R Stat Society: Ser B (Methodological)* (1972) 34:187–202. doi: 10.1111/j.2517-6161.1972.tb00899.x
- Lin H, Zelterman D. *Modeling survival data: extending the Cox model*. Taylor & Francis (2002). doi: 10.1198/tech.2002.s656
- Ching T, Zhu X, Garmire LX. Cox-nnet: An artificial neural network method for prognosis prediction of high-throughput omics data. *PLoS Comput Biol* (2018) 14:e1006076. doi: 10.1371/journal.pcbi.1006076
- Chi C-L, Street WN, Wolberg WH. Application of artificial neural network-based survival analysis on two breast cancer datasets. In: *AMIA Annual Symposium Proceedings*, vol. 2007. American Medical Informatics Association (2007). p. 130.
- Wang J, Ju R, Chen Y, Zhang L, Hu J, Wu Y, et al. Automated retinopathy of prematurity screening using deep neural networks. *EBioMedicine* (2018a) 35:361–8. doi: 10.1016/j.ebiom.2018.08.033
- Silver D, Schrittwieser J, Simonyan K, Antonoglou I, Huang A, Guez A, et al. Mastering the game of go without human knowledge. *Nature* (2017) 550:354. doi: 10.1038/nature24270
- Raghavendra U, Fujita H, Bhandary SV, Gudigar A, Tan JH, Acharya UR. Deep convolution neural network for accurate diagnosis of glaucoma using digital fundus images. *Inf Sci* (2018) 441:41–9. doi: 10.1016/j.ins.2018.01.051
- Cho K, van Merriënboer B, Gulcehre C, Bahdanau D, Bougares F, Schwenk H, et al. Learning Phrase Representations using RNN Encoder Decoder for Statistical Machine Translation. In: *Proceedings of the 2014 Conference on Empirical Methods in Natural Language Processing*. In: *EMNLP*. Stroudsburg, PA, USA: Association for Computational Linguistics (2014). p. 1724–34. doi: 10.3115/v1/D14-1179
- Vinyals O, Toshev A, Bengio S, Erhan D. Show and tell: A neural image caption generator. In: *Proceedings of the IEEE conference on computer vision and pattern recognition* (2015). p. 3156–64. doi: 10.1109/CVPR.2015.7298935
- Wang J, Zhang L, Guo Q, Yi Z. Recurrent Neural Networks With Auxiliary Memory Units. *IEEE Trans Neural Networks Learn Syst* (2018c) 29:1652–61. doi: 10.1109/TNNLS.2017.2677968
- Wang J, Zhang L, Chen Y, Yi Z. A new delay connection for long short-term memory networks. *Int J Neural Syst* (2018b) 28:1750061. doi: 10.1142/S0129065717500617
- Acharya UR, Fujita H, Oh SL, Hagiwara Y, Tan JH, Adam M. Application of deep convolutional neural network for automated detection of myocardial infarction using ecg signals. *Inf Sci* (2017) 415:190–8. doi: 10.1016/j.ins.2017.06.027
- Ng E, Acharya UR, Keith LG, Lockwood S. Detection and differentiation of breast cancer using neural classifiers with first warning thermal sensors. *Inf Sci* (2007) 177:4526–38. doi: 10.1016/j.ins.2007.03.027
- Daoud H, Bayoumi M. Efficient Epileptic Seizure Prediction based on Deep Learning. *IEEE Trans Biomed Circuits Syst* (2019) 13(5):804–13. doi: 10.1109/TBCAS.2019.2929053
- Bello GA, Dawes TJ, Duan J, Biffi C, de Marvao A, Howard LS, et al. Deep-learning cardiac motion analysis for human survival prediction. *Nat Mach Intell* (2019) 1:95. doi: 10.1038/s42256-019-0019-2
- Ching T, Zhu X, Garmire L. Cox-nnet: an artificial neural network cox regression for prognosis prediction. *BioRxiv* (2016) 093021. doi: 10.1101/093021

## AUTHOR CONTRIBUTIONS

ZY and LL designed the research. ZY, JW, JG, and XX implemented the proposed method and analyzed the data. LL and NC were responsible for the dataset. JW wrote the manuscript. All authors discussed the results and commented on the manuscript. All authors contributed to the article and approved the submitted version.

## FUNDING

This work was supported by the National Natural Science Foundation of China (grant no. 61906127), the National Major Science and Technology Projects (grant no. 2018AAA0100201), and the Major Scientific and Technological Projects of the New Generation of Artificial Intelligence in Sichuan Province in 2018 (grant no. 2018GZDZX0035).



26. Huang Z, Zhan X, Xiang S, Johnson TS, Helm B, Yu CY, et al. Salmon: Survival analysis learning with multi-omics neural networks on breast cancer. *Front Genet* (2019) 10:166. doi: 10.3389/fgene.2019.00166
27. Burke HB, D. B. R, Goodman PH. Artificial neural networks improve the accuracy of cancer survival prediction. *Cancer* (1997) 79:857–62. doi: 10.1002/(SICI)1097-0142(19970215)79:4<857::AID-CNCR24>3.0.CO;2-Y
28. Park K, Ali A, Kim D, An Y, Kim M, Shin H. Robust predictive model for evaluating breast cancer survivability. *Eng Appl Artif Intell* (2013) 26:2194–205. doi: 10.1016/j.engappai.2013.06.013
29. Kalderstam J, Edén P, Bendahl P-O, Strand C, Fernö M, Ohlsson M. Training artificial neural networks directly on the concordance index for censored data using genetic algorithms. *Artif Intell Med* (2013) 58:125–32. doi: 10.1016/j.artmed.2013.03.001
30. Deb R, Liew AW-C. Missing value imputation for the analysis of incomplete traffic accident data. *Inf Sci* (2016) 339:274–89. doi: 10.1016/j.ins.2016.01.018
31. Aydilek IB, Arslan A. A hybrid method for imputation of missing values using optimized fuzzy c-means with support vector regression and a genetic algorithm. *Inf Sci* (2013) 233:25–35. doi: 10.1016/j.ins.2013.01.021
32. Ioffe S, Szegedy C. Batch normalization: Accelerating deep network training by reducing internal covariate shift. In: *Int Conf Mach Learning* (2015) 448–56.
33. Zou F, Shen L, Jie Z, Zhang W, Liu W. A sufficient condition for convergences of adam and rmsprop. In: *Proceedings of the IEEE Conference on Computer Vision and Pattern Recognition* (2019). p. 11127–35. doi: 10.1109/CVPR.2019.01138

**Conflict of Interest:** The authors declare that the research was conducted in the absence of any commercial or financial relationships that could be construed as a potential conflict of interest.

Copyright © 2021 Wang, Chen, Guo, Xu, Liu and Yi. This is an open-access article distributed under the terms of the Creative Commons Attribution License (CC BY). The use, distribution or reproduction in other forums is permitted, provided the original author(s) and the copyright owner(s) are credited and that the original publication in this journal is cited, in accordance with accepted academic practice. No use, distribution or reproduction is permitted which does not comply with these terms.



# Application of Multimodal and Molecular Imaging Techniques in the Detection of Choroidal Melanomas

Xuying Li<sup>1†</sup>, Lixiang Wang<sup>1†</sup>, Li Zhang<sup>1</sup>, Fei Tang<sup>2</sup> and Xin Wei<sup>1,2†\*</sup>

<sup>1</sup> Department of Ophthalmology, West China Hospital, Sichuan University, Chengdu, China, <sup>2</sup> Department of Ophthalmology, ShangjinNanfu Hospital, Chengdu, China

## OPEN ACCESS

### Edited by:

Changqiang Wu,  
North Sichuan Medical College, China

### Reviewed by:

Peng Li,  
Lanzhou University Second Hospital,  
China  
Rong Li,  
The First Affiliated Hospital of Xi'an  
Medical University, China

### \*Correspondence:

Xin Wei  
weixin\_1982@163.com

<sup>†</sup>These authors have contributed  
equally to this work

### Specialty section:

This article was submitted to  
Cancer Imaging and  
Image-directed Interventions,  
a section of the journal  
Frontiers in Oncology

**Received:** 15 October 2020

**Accepted:** 16 December 2020

**Published:** 01 February 2021

### Citation:

Li X, Wang L, Zhang L, Tang F and  
Wei X (2021) Application of Multimodal  
and Molecular Imaging Techniques in  
the Detection of Choroidal  
Melanomas.  
Front. Oncol. 10:617868.  
doi: 10.3389/fonc.2020.617868

Choroidal melanomas are the most common ocular malignant tumors worldwide. The onset of such tumors is insidious, such that affected patients often have no pain or obvious discomfort during early stages. Notably, enucleation is required for patients with a severe choroidal melanoma, which can seriously impact their quality of life. Moreover, choroidal melanomas metastasize early, often to the liver; this eventually causes affected patients to die of liver failure. Therefore, early diagnosis of choroidal melanomas is extremely important. Unfortunately, an early choroidal melanoma is easily confused with a choroidal nevus, which is the most common benign tumor of the eye and does not often require surgical treatment. This review discusses recent advances in the use of multimodal and molecular imaging to identify choroidal melanomas and choroidal nevi, detect early metastasis, and diagnose patients with choroidal melanomas.

**Keywords:** choroidal melanoma, multimodal imaging, diagnosis, staging, positron-emission tomography/computed tomography scan

## INTRODUCTION

Choroidal melanomas are the most common intraocular malignant tumors worldwide, as well as the second most common type of malignant melanoma. However, the current consensus is that choroidal melanomas and cutaneous melanomas are different types of tumors (1). Thus, their causes, pathogenesis, diagnosis, treatment, and prognosis are quite different (2). Choroidal melanomas can originate from choroidal nevi, which are the most common benign ocular tumors and typically do not require surgical treatment. Notably, 6–10% of patients with a choroidal melanoma have a second primary tumor (3). Furthermore, patients with an advanced unilateral retinoblastoma may have isolated choroidal melanocytosis in the contralateral eye, which can progress to a choroidal melanoma (4, 5).

Choroidal melanomas have an insidious onset and often do not result in pain or obvious discomfort, until they cause inflammation, neovascular glaucoma, or ocular extension (3). Nevertheless, patients with a severe choroidal melanoma require enucleation, which can seriously impact their quality of life. In the past decade, radiotherapy has gradually become the first-line treatment for such patients (6); this treatment modality includes proton beam and plaque

brachytherapy (7). However, compared with enucleation, the 5-year survival rate of radiotherapy has not significantly improved (8).

The prognosis of a choroidal melanoma is closely linked with its cytogenetic type and histological grade, which is a distinguishing feature from other cancers (9). The haplotype of chromosome 3 and amplification of chromosome 8 are significantly associated with tumor metastasis, consistent with the American Joint Committee on Cancer (AJCC) staging of the tumor. In addition, a combination of AJCC staging and cytogenetic status can provide greater accuracy than separate assessment methods in predicting patient prognosis (10). At the genetic level, mutations in *BAP1*, *EIF1AX*, *SF3B1* and other genes have been shown to affect patient prognosis; specifically, patients with *EIF1AX* mutations have relatively more positive prognoses, while patients with *SF3B1* mutations are more prone to have advanced metastasis. Furthermore, absence of the tumor suppressor gene *BAP1* will lead to tumor metastasis, thus significantly reducing the survival rate among affected patients (11–13). Choroidal melanomas have been classified into two types on the basis of the gene expression profile: I (low-risk) and II (high-risk) (14). For patients with type II uveal melanoma, the prognosis is not influenced by interventions, but has a strong relationship with the largest basal diameter (LBD); LBD < 12 mm is associated with better prognosis (14, 15). Many prognostic prediction models have been developed, including the Liverpool Uveal Melanoma Prognosticator Online; this model combines tumor histology (e.g., LBD), genetic status (e.g., chromosome 3 monosomy), and other factors to predict all-cause mortality and support personalized treatment (16–18).

Metastasis reportedly affects 50% of patients with uveal melanomas (1). The most common route of choroidal melanoma metastasis is through blood to the liver (19); this event occurs early in the progression of disease. Some results have implied that early metastasis occurs 5 years before the diagnosis and treatment of a choroidal melanoma (3). Other studies have suggested that metastasis is inevitable for patients with choroidal melanomas (20); there remains no optimal scheme or evidence for the treatment of metastatic uveal melanomas (1).

Because of the insidious onset and poor prognosis of choroidal melanomas, early diagnosis of affected patients is extremely important (14). The gold standard for tumor diagnosis is a biopsy and subsequent pathological examination. However, fine-needle aspiration biopsy of the vitreous body in an eye with a choroidal melanoma can lead to seeding of the ciliary body and sclera (21). Therefore, fine needle aspiration biopsy is not an ideal diagnostic method for patients with a suspected choroidal melanoma. Furthermore, early non-invasive diagnosis is important for timely detection of choroidal melanomas and prediction of patient prognosis.

This review focuses on the important roles of multimodal and molecular imaging (e.g., positron emission tomography/computed tomography [PET/CT]) in the identification and monitoring of choroidal nevi, early detection of choroidal melanomas, and recognition of metastasis.

## IDENTIFICATION AND MONITORING OF CHOROID NEVUS

According to the Collaborative Ocular Melanoma Study classification, a choroidal nevus constitutes a choroidal melanocytic lesion with LBD  $\leq 5$  mm and thickness  $\leq 1$  mm (22). Most instances of choroidal nevus (91%) occur in the posterior portion of the eye (22). Histologically, a nevus is composed of benign cells (i.e., atypical melanocytes). A choroidal nevus is not a congenital condition and most often is acquired (23). Some studies indicate that a high estrogen level and high body mass index are important risk factors for choroidal nevi (24). Furthermore, Singh et al. suggested that systematic resistance to estrogen leads to obesity and increased body mass index; they presumed that this mechanism contributes to choroidal nevus onset. Studies of postmenopausal women also revealed that the incidence of choroidal nevi was twofold greater in overweight women than in normal-weight women. Vitamin C has been reported to reduce the incidence of choroidal nevi (22).

However, when the mass thickness is > 2 mm, as measured by ultrasound, the hazard ratio significantly increases for transformation from a choroidal nevus to a choroidal melanoma (25). Additional risk factors include worse Snellen visual acuity, empty echo findings on ultrasound, LBD > 5 mm on fundus examination, subretinal fluid on optical coherence tomography (OCT) examination, and orange pigment deposition (i.e., lipochrome) on autofluorescence examination (26–29). Traditional angiography methods (e.g., fluorescein angiography) are important for differentiating a choroidal nevus from a choroidal melanoma on the basis of subretinal vessel morphology. Current OCT technology is suitable for observation of vascular morphology information. When a choroidal nevus exhibits long-term exudative subretinal fluid and multiple punctures, OCT angiography (OCTA) shows choroidal neovascularization, consistent with fluorescein angiography findings (24, 30). Swept-source OCT can show narrow border vessels significantly related to the subretinal fluid (31); enhanced depth imaging (EDI)-OCT has demonstrated thin blood vessels covering 94% of choroidal nevi (32). Francis et al. (31) proposed that the tumor diameter is closely related to secondary retinopathy, while OCT can distinguish a choroidal nevus by identifying fine retinal structure. OCTA can reveal that the Bruch's membrane–retinal pigment epithelium–Bruch's membrane complex is complete and regular in a choroidal nevus, while the Bruch's membrane–retinal pigment epithelium–Bruch's membrane complex and the shape of the outer retinal layer are fuzzy in a choroidal melanoma (33). Notably, EDI-OCT has shown that photoreceptor cells exposed to subretinal fluid in a choroidal nevus exhibit atrophy (i.e., “stalactites” or “cracks”), while photoreceptor cells in a small melanoma became loose and exhibit “furry” morphology, with more irregular retinal layers accompanied by considerable structural damage (22, 26, 32). OCTA can distinguish the macular characteristics of choroidal

nevi and choroidal melanomas; Valverde et al. suggested that the mass thickness is closely related to the difference of macular characteristics. The superimposed macular microvascular changes are smaller in choroidal nevi (34); the central macular thickness, fovea avascular area, and choroidal capillary thickness are similar to those parameters in healthy fellow eyes. In choroidal melanomas, central macular thickness increases, fovea avascular area increases, and choroidal capillary thickness decreases; moreover, the blood flow rate is considerably lower than normal (11.2%) (33).

## DIAGNOSIS OF CHOROID MELANOMA

For large choroidal melanomas, the diagnosis is mainly performed by slit lamp examination, indirect ophthalmoscopy, fluorescein angiography, and ultrasound (35). For early small choroidal melanomas, there is controversy regarding the most suitable diagnostic approach. Kivela et al. reported that biopsy should be performed to distinguish this type of tumor from a choroidal nevus (35), whereas Singh et al. stated that fine needle aspiration cytology should not be used due to the risk of tumor spread (3). Therefore, imaging is particularly important for the diagnosis of choroidal melanomas. Currently available imaging methods for choroidal melanomas include ultrasound (A-mode, B-mode, and color Doppler), magnetic resonance imaging (MRI), and OCT (i.e., swept-source OCT, spectral domain OCT, EDI-OCT, and OCTA). Each approach has unique advantages and disadvantages in various situations.

Since choroidal melanomas usually appear as low reflectivity, A-mode ultrasound can provide the best imaging effect (26). In A-mode ultrasound, choroidal melanomas exhibit low echo, smooth attenuation, and vascular pulsation (3). In B-mode ultrasound, choroidal melanomas can appear to be bulging. If the tumor penetrates Bruch's membrane, it will assume a collar button or mushroom-like appearance; such tumors have no echo and contain a cavity in the posterior wall. These tumors also contain a choroid gap and orbital shadow (3, 36). Real-time high-resolution ultrasound (i.e., fusion ultrasound) can demonstrate choroidal melanoma and optic nerve structures in real time. Additionally, MRI combined with real-time color Doppler ultrasound can observe the tumor structure and evaluate the retrobulbar vascular system (37). Ultrasound is considered the most important method for evaluation of choroidal melanoma progression; ultrasound is superior to MRI in the detection of extrascleral extension (38, 39). When a choroidal melanoma involves the optic nerve, the fundus may have a similar manifestation of optic neuritis; MRI may show the tumor as a mass adjacent to the optic nerve. However, ultrasound evaluation can show the absence of an echo and reveal intraocular components, thus aiding in diagnosis of the mass (40). Nevertheless, for small choroidal melanomas, the specificity of ultrasound involving subretinal fluid is low, because such tumors cannot be distinguished from retinal thickening, cystic changes, and pigment epithelial detachment (41). EDI-OCT can partially compensate for this deficiency (36, 42).

MRI has limited diagnostic value for choroidal melanomas (3). For large tumors or those with poorly reflective structures in ultrasound examination, MRI can be used to detect whether the mass has penetrated through the sclera (36). However, the presence of nonspecific inflammation, angiogenesis, and motion artifacts can lead to false positive results (38).

OCT can reveal extensive details of choroidal melanomas. In particular, this method can show whether the choroidal melanoma surface is regular and lobular (43), whether it exhibits normal retinal thickness and a complete photoreceptor cell layer, and whether extensive retinal detachment and "debris" are present in the dorsal retina (19). Swept-source OCT can show fine details of the choroid near the fovea and posterior pole (44). Furthermore spectral domain OCT can help to observe lesions in the pigment epithelium (45). The combined use of OCT and fundus fluorescein angiography can help to identify subretinal fluid and orange pigment (35). Previous studies have shown that 60% of the subretinal fluid in a choroidal melanoma is patchy, while 40% is diffuse (46). EDI-OCT is an effective tool to identify structural changes in the retina in patients with small choroidal melanomas (47). This method can show retinal edema, "fluffy" or lost photoreceptor cells, an irregular ganglion cell layer, broken connections between internal and external segments, an irregular inner plexus layer, the loss of external membrane, and other structural damage (26). It is also more accurate for measurement of tumor thickness, compared with ultrasound. Specifically, the tumor thickness is 55% greater when measured by ultrasound than when measured by EDI-OCT, which reveals the most actual thickness. Additionally, EDI-OCT can identify a subclinical level of peripheral subretinal fluid that is not yet visible *via* ophthalmoscopy (36). Therefore, EDI-OCT is important in the early diagnosis and evaluation of choroidal melanomas.

In addition to the retinal structure, advancements in OCT technology have improved the visibility of the tumor vasculature. Large choroidal melanomas have a double cycle; extensive and progressive fluorescence are evident under fundus fluorescein angiography (3). Furthermore, swept-source OCT can clearly display the intrinsic tumor vasculature, with an effect similar to that of indocyanine green angiography (48). With the exception of hemangiomas, most choroidal tumors show internal compression of the vasculature (45). Therefore, OCTA shows that choroidal melanomas have a dense and irregular vascular network in the outer retinal layer and choroidal layer, while choroidal nevi show reduced blood flow in the corresponding area (49).

## PET/CT TO PREDICT RECURRENCE OR METASTASIS OF CHOROIDAL MELANOMA

As mentioned above, early melanocyte aggressiveness is closely related to tumor prognosis. Therefore, evaluation of the risks of choroidal melanoma recurrence and metastasis on the basis of early cytological behavior can provide timely prognostic information; this can be combined with histological evaluation



of the tumor to provide more guidance for medical decision-making. PET/CT is appropriate for this application; it can aid in early intervention before morphological recurrence and tumor metastasis, thus greatly improving patient survival.

PET/CT is typically used to evaluate tumor activity and the risks of recurrence or metastasis by means of cell metabolism assessment. Metabolic activity is negatively correlated with metastasis duration (50). Parameters related to cell metabolism include maximum standardized uptake value (SUVmax) and metabolic rate of glucose. SUVmax is defined as the ratio between the radiation concentration and the injection dose in the region with the highest uptake signals of  $^{18}\text{F}$ -fluorodeoxyglucose ( $^{18}\text{F}$ -FDG, the analog of glucose) and other tracers; this parameter can be used to semi-quantitatively evaluate cellular metabolic rates (51). The metabolic rate of glucose is the product of  $^{18}\text{F}$ -FDG clearance rate and blood glucose concentration (i.e., glucose uptake rate per unit of tracer distribution) (52). This parameter can accurately quantify the degree of metabolic activity; it also helps to distinguish among tumor cell types, thereby indirectly evaluating the risks of recurrence and metastasis. Notably, epithelioid cell melanomas have worse prognoses than spindle cell melanomas (53). Similarly, SUVmax and LBD are significantly associated with metastatic death. Higher SUVmax is reportedly indicative of greater tumor diameter or thickness (54). Among patients with choroidal melanoma who underwent 6 months of treatment, choroidal thickness was significantly reduced, compared with baseline (55). Therefore, the magnitude of SUVmax may influence the therapeutic effect. Furthermore, the magnitude of SUVmax is reportedly related to the pathological classification of melanoma. Higher SUVmax often indicated a nodular tumor, while lower SUVmax implied diffuse infiltration (54). Chromosome 3 monosomy and chromosome 8 amplification are strongly correlated with choroidal melanoma metastasis. The metastasis and prognosis of choroidal melanoma are mainly related to the above cytogenetic changes, rather than the AJCC stage. Notably, some studies have suggested that SUVmax is related to chromosome 3 monosomy in choroidal melanomas. Among those tumors, 92% have SUVmax > 2.5, while 67% have SUVmax > 4. Therefore, SUVmax > 4 may be an indirect indicator of chromosome 3 monosomy in choroidal melanomas (56).

PET can qualitatively assess tumor development by monitoring variations in cell metabolism. Surveillance with  $^{18}\text{F}$ -FDG PET/CT may exclude metastasis or suggest necrotic choroidal melanoma if cell metabolism is obviously low. Clinically significant changes in the metabolic activity of a lesion may indicate local recurrence (57, 58).

## COMBINED MULTIMODAL AND MOLECULAR IMAGING TO ASSESS METASTASIS OF CHOROIDAL MELANOMA

### Routine Detection of Liver Metastasis

The liver is the most common metastatic site of choroidal melanomas (59), such that approximately half of affected patients have liver metastasis (60). Moreover, liver metastases

are often the first non-ocular locations affected (61). The median disease-free survival time of patients with choroidal melanoma is 26 months, while the median survival time is only 8 months after initial metastasis detection (62). Patients often die of liver failure, manifested by ascites and hepatomegaly. Biopsy of metastases revealed a maximum size of 100 cm<sup>2</sup> (63). Presumably, the most important factors influencing survival rate are the levels of liver enzymes, especially lactate dehydrogenase and alkaline phosphatase (64). Mariani et al. have found that if LDH is 1.5 times higher than normal, it indicates poor prognosis of the patient (65). If these levels have been normal and the disease-free interval is > 36 months, the overall survival period is expected to be considerably longer (62). Therefore, early treatment of metastasis and management of liver enzyme levels are important considerations for patient survival.

Serial hepatic ultrasound and confirmatory scans (e.g., CT) can reveal asymptomatic metastasis (66). However, Mariani et al. have suggested that USG can only detect lesions on the liver surface, which indicated the limited effect (65). For newly diagnosed uveal melanoma, MRI staging can accurately recognize early liver metastasis (61, 67). Mariani et al. believe that the number and maximum surface area (>800mm<sup>2</sup>) of metastasis under MRI can be used as important indicators to predict the survival rate of patients (65). Because of the vascular richness in uveal melanoma, a metastasis on MRI appears as multiple enhanced solid liver lesions with the high T1 signal characteristic of melanomas (68). Diffuse-weighted images (DWI) can be used to detect more metastasis, which appearances as the high signal, and the lesion can still exist when the dispersion sensitivity coefficient is adjusted to the highest, thus more metastasis < 5mm can be detected, regardless of the location of the metastasis in the liver (65). Regarding the frequency of MRI detection, intervals of 3 months (60) and 6 months (69) have been suggested.

In CT scans, liver metastases often constitute multiple, heterogeneous, hypodense, and enhanced lesions, with an average size of 46.8 cm<sup>2</sup> (63). The detection efficiency of dual-energy CT with low kVp is superior to that of virtual 120 kVp CT with digital subtraction angiography images (70). Positive CT or MRI findings were compared with positive ultrasound findings; the results showed that 53% of the CT/MRI findings were completely consistent with ultrasound findings, 11% were completely inconsistent, 29% were negative findings on ultrasound, and 7% could not detect the positive findings on ultrasound. It has been suggested that CT scans of the chest, abdomen, and pelvis should be performed before the assessment of the patient's prognosis (71). Thus, CT/MRI is presumed to constitute a more efficient approach than ultrasound; in particular, confirmatory MRI scanning may be useful in patients with abnormal liver enzyme levels (72).

### Usefulness of PET Staging for Choroidal Melanomas

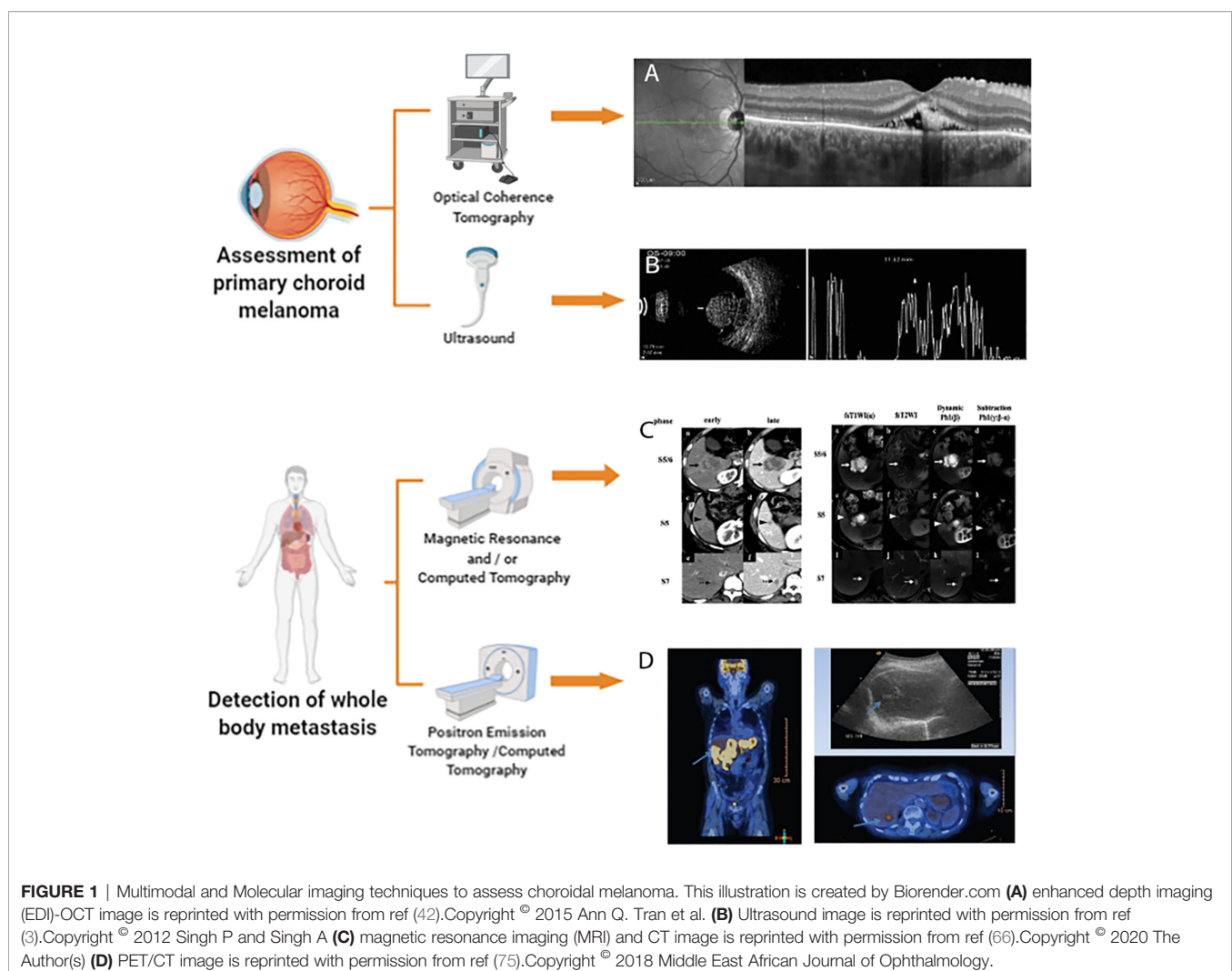
According to the AJCC, choroidal melanomas are divided into the following four stages: T1, LBD < 10 mm and thickness <

2.5 mm; T2, LBD 10–16 mm and thickness 2.5–10 mm; T3, LBD > 16 mm and thickness > 10 mm, without extraocular invasion; T4, LBD > 16 mm and thickness > 10 mm, with extraocular invasion. T1 and T2 stages are each divided into three clinical sub-stages on the basis of the external invasion status: none, microscopically visible, and visible with the unaided eye. Thus, extraocular invasion status (i.e., extraocular extension and metastasis) is important for the staging of choroidal melanomas.

Although PET/CT is not currently used as a routine method for detection of metastasis, it can be used to detect metastasis in patients with normal CT findings and normal liver enzyme levels (73, 74). Thus, this approach is helpful for metastasis screening and tumor staging; it can also be used as a supplementary alternative for patients with contraindications to MRI (75). Most liver metastases can be qualitatively detected through PET/CT, in combination with  $^{18}\text{F}$ -FDG to detect local uptake and MRI for confirmatory diagnosis (76, 77). Furthermore, PET/CT is suitable for detecting extrahepatic metastases of T4 stage tumors (78). Second primary cancers in 10% of patients with choroidal melanomas can be detected by PET/CT (77). However,

the initial staging value of PET/CT for choroidal melanoma is not superior to MRI (76, 79), because PET/CT can only detect 33% of T2 stage tumors and 75% of T3 stage tumors (80). Small liver lesions cannot be detected by PET/CT (59, 79), while MRI of the abdomen and chest can detect nearly all metastases of uveal melanomas (81). In addition to lung and liver metastases, PET/CT can detect suspected local uptake of  $^{18}\text{F}$ -FDG in lymph nodes, which can then be confirmed by ultrasound and fine needle aspiration cytology (58). Therefore, ultrasound combined with PET/CT has been proposed for the initial staging of choroidal melanomas; chest radiography combined with analysis of liver enzyme levels may be appropriate for long-term staging (77).

Because PET/CT can assess cell metabolism and anatomical changes throughout the body, it is applicable for use in all patients with choroidal melanoma who require evaluation and/or restaging of extrahepatic metastases (82). **Figure 1** accounts for the current multimodal and molecular imaging techniques assessing the primary tumor and metastasis of choroidal melanomas.



## DISCUSSION

Choroidal melanomas are insidious tumors prone to extraocular extension and metastasis. Therefore, early diagnosis of choroidal melanomas and timely detection of metastases are particularly important. Early choroidal melanomas can easily be confused with choroidal nevi, so accurate identification of choroidal nevi is needed. Pathological examination is considered the gold standard for cancer diagnosis; thus far, invasive examination is not recommended for early choroidal melanomas. Therefore, non-invasive imaging methods are critical for the assessment of patients with suspected choroidal melanoma. Ultrasound is an important method for the diagnosis and monitoring of choroidal melanomas; in combination with other imaging techniques, ultrasound enables real-time observation of tumors and their posterior structures. Compared with ultrasound, OCT methods (especially EDI-OCT) provide more accurate and detailed observations of the morphology and blood supply of choroidal melanomas, offering valuable information for the diagnosis and monitoring of these tumors. MRI and CT are of limited value during diagnosis of the primary tumor, but are indispensable for tumor staging and metastasis detection. PET/CT is a powerful supplement to the above imaging methods for the staging of choroidal melanomas; it can identify metastases that not detected in a timely manner by conventional imaging methods.

Current technology allows the use of PET/CT to assess the risks of tumor recurrence and metastasis at the cytological level, prior to histological changes, by monitoring the metabolic behavior of melanoma cells. This information provides a reference for medical decisions and has the potential to greatly improve the survival and quality of life for affected patients. At the same time, there is an unavoidable challenge that the use of

SPECT (such as  $^{123}\text{I}$ IMP-SPECT) has the higher detection rate than  $^{18}\text{F}$ FDG-PET/CT (83). Therefore, more effective radioactive tracer should be actively sought for PET/CT imaging of choroidal melanoma, so as to improve the sensitivity of PET/CT to the detection of micro-liver metastasis.

## AUTHOR CONTRIBUTIONS

The co-first authors of this article, XL and LW, were responsible for the conception and design of the manuscript, and conducted data collection and analysis, made valuable and constructive changes to the content of the manuscript, confirmed the final version of this article, and agreed responsible for all matters related to the publication of this manuscript. The corresponding author, XW, who is in charge of the publishing process and established the core idea of this manuscript. Two co-authors, LZ and FT, provided many valuable suggestions and sources and made some crucial amendments to the manuscript. All authors contributed to the article and approved the submitted version.

## FUNDING

This work was supported by grants from the Natural Science Foundation of China (No.82070954), The Applied Basic Research Programs of Science and Technology Commission Foundation of Sichuan Province (No.19YYJC0790), and The Innovative Spark Grant of Sichuan University (No.2018SCUH0062).

## REFERENCES

- Carvajal RD, Schwartz GK, Tezel T, Marr B, Francis JH, Nathan PD. Metastatic disease from uveal melanoma: treatment options and future prospects. *Br J Ophthalmol* (2017) 101:38–44. doi: 10.1136/bjophthalmol-2016-309034
- Chattopadhyay C, Kim DW, Gombos DS, Oba J, Qin Y, Williams MD, et al. Uveal melanoma: From diagnosis to treatment and the science in between. *Cancer* (2016) 122:2299–312. doi: 10.1002/cncr.29727
- Singh P, Singh A. Choroidal melanoma. *Oman J Ophthalmol* (2012) 5:3–9. doi: 10.4103/0974-620X.94718
- Augsburger JJ, Brooks CC, Correa ZM. Isolated choroidal melanocytosis: clinical update on 37 cases. *Graefes Arch Clin Exp Ophthalmol* (2020) 258:2819–29. doi: 10.1007/s00417-020-04919-x
- Brooks CC, Augsburger JJ, Correa ZM. Unilateral retinoblastoma with contralateral isolated choroidal Melanocytosis: case report of an unexpected presentation. *BMC Ophthalmol* (2018) 18:251. doi: 10.1186/s12886-018-0916-x
- Messineo D, Barile D, Morrone S. Meta-analysis on the utility of radiotherapy for the treatment of Ocular Melanoma. *Clin Ter* (2020) 170:89–98. doi: 10.7417/CT.2020.2195
- Thornton S, Coupland SE, Heimann H, Hussain R, Groenewald C, Kacperek A, et al. Effects of plaque brachytherapy and proton beam radiotherapy on prognostic testing: a comparison of uveal melanoma genotyped by microsatellite analysis. *Br J Ophthalmol* (2020) 104:1462–6. doi: 10.1136/bjophthalmol-2019-315363
- Afshar AR, Damato BE, Stewart JM, Zablotzka LB, Roy R, Olshen AB, et al. Next-Generation Sequencing of Uveal Melanoma for Detection of Genetic Alterations Predicting Metastasis. *Transl Vis Sci Technol* (2019) 8:18. doi: 10.1167/tvst.8.2.18
- Damato B, Eleuteri A, Taktak AFG, Coupland SE. Estimating prognosis for survival after treatment of choroidal melanoma. *Prog Retin Eye Res* (2011) 30:285–95. doi: 10.1016/j.preteyeres.2011.05.003
- Bagger M, Andersen MT, Andersen KK, Heegaard S, Andersen MK, Kiilgaard JF. The Prognostic Effect of American Joint Committee on Cancer Staging and Genetic Status in Patients With Choroidal and Ciliary Body Melanoma. *Invest Ophthalmol Vis Sci* (2015) 56:438–44. doi: 10.1167/iiov.14-15571
- Dogrusöz M, Jager MJ. Genetic prognostication in uveal melanoma. *Acta Ophthalmol (Copenh)* (2018) 96:331–47. doi: 10.1111/aos.13580
- Yavuziyigitoglu S, Koopmans AE, Verdijk RM, Vaarwater J, Eussen B, van Bodegom A, et al. Uveal Melanomas with SF3B1 Mutations. *Ophthalmology* (2016) 123:1118–28. doi: 10.1016/j.opththa.2016.01.023
- Field MG, Decatur CL, Kurtenbach S, Gezgin G, van der Velden PA, Jager MJ, et al. PRAME as an Independent Biomarker for Metastasis in Uveal Melanoma. *Clin Cancer Res* (2016) 22:1234–42. doi: 10.1158/1078-0432.CCR-15-2071
- Walter SD, Chao DL, Feuer W, Schiffman J, Char DH, Harbour JW. Prognostic Implications of Tumor Diameter in Association With Gene Expression Profile for Uveal Melanoma. *JAMA Ophthalmol* (2016) 134:734–40. doi: 10.1001/jamaophthalmol.2016.0913
- Binkley E, Triozzi PL, Rybicki L, Achberger S, Aldrich W, Singh A. A prospective trial of adjuvant therapy for high-risk uveal melanoma: assessing 5-year survival outcomes. *Br J Ophthalmol* (2020) 104:524–8. doi: 10.1136/bjophthalmol-2019-314461
- Cunha Rola A, Taktak A, Eleuteri A, Kalirai H, Heimann H, Hussain R, et al. Multicenter External Validation of the Liverpool Uveal Melanoma Prognosticator Online: An OOG Collaborative Study. *Cancers* (2020) 12:477. doi: 10.3390/cancers12020477



17. Damato B, Eleuteri A, Hussain R, Kalirai H, Thornton S, Taktak A, et al. Parsimonious Models for Predicting Mortality from Choroidal Melanoma. *Invest Ophthalmol Vis Sci* (2020) 61:35. doi: 10.1167/iov.61.4.35
18. Eleuteri A, Taktak AFG, Coupland SE, Heimann H, Kalirai H, Damato B. Prognostication of metastatic death in uveal melanoma patients: A Markov multi-state model. *Comput Biol Med* (2018) 102:151–6. doi: 10.1016/j.combiomed.2018.09.024
19. Yan B, Fu T, Liu Y, Wei W, Dai H, Fang W, et al. Tc-99m-3PRGD2 single-photon emission computed tomography/computed tomography for the diagnosis of choroidal melanoma A preliminary STROBE-compliant observational study. *Med (Baltimore)* (2018) 97:e12441. doi: 10.1097/MD.00000000000012441
20. Damato B. Ocular treatment of choroidal melanoma in relation to the prevention of metastatic death - A personal view. *Prog Retin Eye Res* (2018) 66:187–99. doi: 10.1016/j.preteyeres.2018.03.004
21. Ndulue J K, Mashayekhi AL, Shields C. Ciliary Body Seeding after Pars Plana Transvitreal Fine-Needle Aspiration Biopsy of Choroidal Melanoma. *J Ophthalmic Vis Res* (2020) 15:252–5. doi: 10.18502/jovr.v15i2.6744
22. Singh AD, Kalyani P, Topham A. Estimating the Risk of Malignant Transformation of a Choroidal Nevus. *Ophthalmology* (2005) 112:1784–9. doi: 10.1016/j.ophtha.2005.06.011
23. Lücke J, Grisanti S, Tura A. Aktuelle Diagnostik bei choroidalen Nävi. *Klin Monatsblätter Für Augenheilkd* (2018) 235:730–9. doi: 10.1055/s-0043-102592
24. Chien JL, Sioufi K, Surakiatchanakul T, Shields JA, Shields CL. Choroidal nevus: a review of prevalence, features, genetics, risks, and outcomes. *Curr Opin Ophthalmol* (2017) 28:228–37. doi: 10.1097/ICU.0000000000000361
25. Shields CL, Dalvin LA, Yu MD, Ancona-Lezama D, Di Nicola M, Williams BK, et al. CHOROIDAL NEVUS TRANSFORMATION INTO MELANOMA PER MILLIMETER INCREMENT IN THICKNESS USING MULTIMODAL IMAGING IN 2355 CASES: The 2019 Wendell L. Hughes Lecture. *Retina* (2019) 39:1852–60. doi: 10.1097/IAE.00000000000002508
26. Shields CL, Kaliki S, Rojanaporn D, Ferenczy SR, Shields JA. Enhanced Depth Imaging Optical Coherence Tomography of Small Choroidal Melanoma: Comparison With Choroidal Nevus. *Arch Ophthalmol* (2012) 130:850. doi: 10.1001/archophthol.2012.1135
27. Dalvin LA, Shields CL, Ancona-Lezama DA, Yu MD, Di Nicola M, Williams BK Jr., et al. Combination of multimodal imaging features predictive of choroidal nevus transformation into melanoma. *Br J Ophthalmol* (2019) 103:1441–7. doi: 10.1136/bjophthalmol-2018-312967
28. Shields CL, Lim L-AS, Dalvin LA, Shields JA. Small choroidal melanoma: detection with multimodal imaging and management with plaque radiotherapy or AU-011 nanoparticle therapy. *Curr Opin Ophthalmol* (2019) 30:206–14. doi: 10.1097/ICU.0000000000000560
29. Shields CL, Dalvin LA, Ancona-Lezama D, Yu MD, Di Nicola M, Williams BK, et al. CHOROIDAL NEVUS IMAGING FEATURES IN 3,806 CASES AND RISK FACTORS FOR TRANSFORMATION INTO MELANOMA IN 2,355 CASES: The 2020 Taylor R. Smith and Victor T. Curtin Lecture. *Retina* (2019) 39:1840–51. doi: 10.1097/IAE.00000000000002440
30. Pellegrini M, Corvi F, Say EAT, Shields CL, Staurengi G. OPTICAL COHERENCE TOMOGRAPHY ANGIOGRAPHY FEATURES OF CHOROIDAL NEOVASCULARIZATION ASSOCIATED WITH CHOROIDAL NEVUS. *Retina* (2018) 38:1338–46. doi: 10.1097/IAE.0000000000001730
31. Francis JH, Pang CE, Abramson DH, Milman T, Folberg R, Mrejen S, et al. Swept-Source Optical Coherence Tomography Features of Choroidal Nevi. *Am J Ophthalmol* (2015) 159:169–76.e1. doi: 10.1016/j.ajo.2014.10.011
32. Shah SU, Kaliki S, Shields CL, Ferenczy SR, Harmon SA, Shields JA. Enhanced Depth Imaging Optical Coherence Tomography of Choroidal Nevus in 104 Cases. *Ophthalmology* (2012) 119:1066–72. doi: 10.1016/j.ophtha.2011.11.001
33. Ghassemi F, Mirshahi R, Fadakar K, Sabour S. Optical coherence tomography angiography in choroidal melanoma and nevus. *Clin Ophthalmol* (2018) 12:207–14. doi: 10.2147/OPHTH.S148897
34. Valverde-Megias A, Say EAT, Ferenczy SR, Shields CL. DIFFERENTIAL MACULAR FEATURES ON OPTICAL COHERENCE TOMOGRAPHY ANGIOGRAPHY IN EYES WITH CHOROIDAL NEVUS AND MELANOMA. *Retina* (2017) 37:731–40. doi: 10.1097/IAE.0000000000001233
35. Kivelä T, Jager MJ, Desjardins L, Kivelä T, Damato B. Diagnosis of Uveal Melanoma. In: *Developments in Ophthalmology*. Basel: KARGER. Available at: <https://www.karger.com/Article/FullText/330613> (Accessed September 12, 2020).
36. Girbardt C, Rehak M, Wiedemann P. Diagnostisches Vorgehen bei Verdacht auf Aderhautmelanom. *Klin Monatsblätter Für Augenheilkd* (2018) 235:1393–7. doi: 10.1055/s-0042-123827
37. Walter U, Niendorf T, Graessl A, Rieger J, Krüger P-C, Langner S, et al. Ultrahigh field magnetic resonance and colour Doppler real-time fusion imaging of the orbit – a hybrid tool for assessment of choroidal melanoma. *Eur Radiol* (2014) 24:1112–7. doi: 10.1007/s00330-014-3101-5
38. Jacobsen BH, Ricks C, Harrie RP. Ocular ultrasound versus MRI in the detection of extrascleral extension in a patient with choroidal melanoma. *BMC Ophthalmol* (2018) 18:320. doi: 10.1186/s12886-018-0990-0
39. Thakkar H, Tyagi M, Bharwada R, Billore P, Mithal K. Role of echography in diagnostic dilemma in choroidal masses. *Indian J Ophthalmol* (2014) 62:167. doi: 10.4103/0301-4738.128626
40. Lemaître S, Zmuda M, Jacomet PV, Lévy-Gabriel C, Dendale R, Berges O, et al. Small Choroidal Melanoma Revealed by a Large Extrascleral Extension. *Ocul Oncol Pathol* (2017) 3:240–6. doi: 10.1159/000455870
41. Krema H, Habal S, Gonzalez JE, Pavlin CJ. ROLE OF OPTICAL COHERENCE TOMOGRAPHY IN VERIFYING THE SPECIFICITY OF ULTRASONOGRAPHY IN DETECTING SUBTLE SUBRETINAL FLUID ASSOCIATED WITH SMALL CHOROIDAL MELANOCYTIC TUMORS. *Retina* (2014) 34:360–5. doi: 10.1097/IAE.0b013e3182993dd9
42. Tran AQ, Eadie JA, Altaweel MM. Shaggy photoreceptors with subfoveal fluid associated with a distant choroidal melanoma. *Case Rep Ophthalmol Med* (2015) 2015:187542. doi: 10.1155/2015/187542
43. Vishnevskia-Dai V, Zur D, Yaacobi S, Moroz I, Newman H, Neudorfer M. Optical Coherence Tomography: An Adjunctive Tool for Differentiating between Choroidal Melanoma and Metastasis. *J Ophthalmol* (2016) 2016:1–7. doi: 10.1155/2016/9803547
44. Ung C, Láins I, Silverman RF, Woods R, Lane AM, Papakostas TD, et al. Evaluation of choroidal lesions with swept-source optical coherence tomography. *Br J Ophthalmol* (2019) 103:88–93. doi: 10.1136/bjophthalmol-2017-311586
45. Sayanagi K, Pelayes DE, Kaiser PK, Singh AD. 3D Spectral Domain Optical Coherence Tomography Findings in Choroidal Tumors. *Eur J Ophthalmol* (2011) 21:271–5. doi: 10.5301/EJO.2010.5848
46. Samuelsson D, Sznage M, Engelsberg K, Wittström E. Clinical, optical coherence tomography, and fundus autofluorescence findings in patients with intraocular tumors. *Clin Ophthalmol* (2016) 10:1953–64. doi: 10.2147/OPHTH.S109222
47. Myakoshina EB, Saakyan SV. Optical coherence tomography in diagnostics of small choroidal melanoma. *Vestn Oftalmol* (2020) 136:56. doi: 10.17116/oftalma202013601156
48. Pellegrini M, Staurengi G. Swept-source Optical Coherence Tomography Angiography Imaging in a Case of Uveal Melanoma. *Ophthalmology* (2017) 124:729. doi: 10.1016/j.ophtha.2016.11.017
49. Cennamo G, Romano MR, Breve MA, Velotti N, Reibaldi M, de Crecchio G, et al. Evaluation of choroidal tumors with optical coherence tomography: enhanced depth imaging and OCT-angiography features. *Eye* (2017) 31:906–15. doi: 10.1038/eye.2017.14
50. Lee CS, Cho A, Lee KS, Lee SC. Association of high metabolic activity measured by positron emission tomography imaging with poor prognosis of choroidal melanoma. *Br J Ophthalmol* (2011) 95:1588–91. doi: 10.1136/bjo.2010.198085
51. Soret M, Bacharach SL, Buvat I. Partial-Volume Effect in PET Tumor Imaging. *J Nucl Med* (2007) 48:932–45. doi: 10.2967/jnumed.106.035774
52. Keramida G, Peters AM. Fasting hepatic glucose uptake is higher in men than women. *Physiol Rep* (2017) 5:e13174. doi: 10.14814/phy2.13174
53. Calcagni ML, Mattoli MV, Blasi MA, Petrone G, Sammarco MG, Indovina L, et al. A prospective analysis of 18F-FDG PET/CT in patients with uveal melanoma: comparison between metabolic rate of glucose (MRglu) and standardized uptake value (SUV) and correlations with histopathological features. *Eur J Nucl Med Mol Imaging* (2013) 40:1682–91. doi: 10.1007/s00259-013-2488-6
54. Matsuo T, Ogino Y, Ichimura K, Tanaka T, Kaji M. Clinicopathological correlation for the role of fluorodeoxyglucose positron emission tomography computed tomography in detection of choroidal malignant melanoma. *Int J Clin Oncol* (2014) 19:230–9. doi: 10.1007/s10147-013-0538-5



55. Lee JH, Lee SC, Cho A, Keum KC, Suh Y-G, Lee CS. Association Between Choroidal Thickness and Metabolic Activity on Positron Emission Tomography in Eyes With Choroidal Melanoma. *Am J Ophthalmol* (2015) 160:1111–5.e2. doi: 10.1016/j.ajo.2015.08.031
56. Papastefanou VP, Islam S, Szyzsko T, Grantham M, Sagoo MS, Cohen VML. Metabolic activity of primary uveal melanoma on PET/CT scan and its relationship with monosomy 3 and other prognostic factors. *Br J Ophthalmol* (2014) 98:1659–65. doi: 10.1136/bjophthalmol-2014-305304
57. Romero-Aroca P, Montero-Jaime M, Intriago B, Riu F, Peña-Gonzalez KB, Almena-García M. <sup>18</sup> FDG-PET/CT Assessing the Absence of Cell Viability and Excluding Metastatic Disease in a Case of Necrotic Choroidal Melanoma. *Eur J Ophthalmol* (2012) 22:288–92. doi: 10.5301/ejo.5000016
58. Sabate M, García JR, Valls E, Moragas M, Soler M, Riera E, et al. Utilidad de la PET-TC con 18F-FDG en un caso de recidiva del melanoma de coroides. *Rev Esp Med Nucl E Imagen Mol* (2012) 31:167–8. doi: 10.1016/j.rem.2011.10.009
59. Balasubramanya R, Selvarajan SK, Cox M, Joshi G, Deshmukh S, Mitchell DG, et al. Imaging of ocular melanoma metastasis. *Br J Radiol* (2016) 89:20160092. doi: 10.1259/bjr.20160092
60. Piperno-Neumann S, Servois V, Mariani P, Plancher C, Lévy-Gabriel C, Lumbroso-Le Rouic L, et al. Prospective study of surveillance testing for metastasis in 100 high-risk uveal melanoma patients. *J Fr Ophthalmol* (2015) 38:526–34. doi: 10.1016/j.jfo.2015.04.005
61. Francis JH, Catalanotti F, Landa J, Barker CA, Shoushtari AN, Abramson DH. Hepatic abnormalities identified by staging MRI and accuracy of MRI of patients with uveal melanoma. *Br J Ophthalmol* (2019) 103:1266–71. doi: 10.1136/bjophthalmol-2018-312612
62. Lorenzo D, Piulats JM, Ochoa M, Arias L, Gutiérrez C, Català J, et al. Clinical predictors of survival in metastatic uveal melanoma. *Jpn J Ophthalmol* (2019) 63:197–209. doi: 10.1007/s10384-019-00656-9
63. Patel M. Characterization of Computed Tomography Scan Abnormalities in Patients With Biopsy-Proven Hepatic Metastases From Uveal Melanoma. *Arch Ophthalmol* (2011) 129:1576. doi: 10.1001/archophthalmol.2011.263
64. Khoja L, Atenafu EG, Suci S, Leyvraz S, Sato T, Marshall E, et al. Meta-analysis in metastatic uveal melanoma to determine progression free and overall survival benchmarks: an international rare cancers initiative (IRCI) ocular melanoma study. *Ann Oncol* (2019) 30:1370–80. doi: 10.1093/annonc/mdz176
65. Mariani P, Dureau S, Savignoni A, Rouic LL-L, Levy-Gabriel C, Piperno-Neumann S, et al. Development of a Prognostic Nomogram for Liver Metastasis of Uveal Melanoma Patients Selected by Liver MRI. *Cancers* (2019) 11:863. doi: 10.3390/cancers11060863
66. Choudhary MM, Gupta A, Bena J, Emch T, Singh AD. Hepatic Ultrasonography for Surveillance in Patients With Uveal Melanoma. *JAMA Ophthalmol* (2016) 134:174. doi: 10.1001/jamaophthalmol.2015.4810
67. Muraki R, Morita Y, Ida S, Kitajima R, Furuhashi S, Kiuchi R, et al. Multimodal therapy with surgery and adjuvant nivolumab for late-onset multiple liver metastases of choroidal malignant melanoma: a case report. *Surg Case Rep* (2020) 6:187. doi: 10.1186/s40792-020-00948-0
68. Bellerive C, Ouellet E, Kamaya A, Singh AD. Liver Imaging Techniques: Recognition of Uveal Melanoma Metastases. *Ocul Oncol Pathol* (2018) 4:254–60. doi: 10.1159/000485424
69. Marshall E, Romaniuk C, Ghaneh P, Wong H, McKay M, Chopra M, et al. MRI in the detection of hepatic metastases from high-risk uveal melanoma: a prospective study in 188 patients. *Br J Ophthalmol* (2013) 97:159–63. doi: 10.1136/bjophthalmol-2012-302323
70. Altenbernd J, Wetter A, Forsting M, Umutlu L. Dual-energy CT of liver metastases in patients with uveal melanoma. *Eur J Radiol Open* (2016) 3:254–8. doi: 10.1016/j.ejro.2016.10.003
71. Davanzo JM, Binkley EM, Bena JF, Singh AD. Risk-stratified systemic surveillance in uveal melanoma. *Br J Ophthalmol* (2019) 103:1868–71. doi: 10.1136/bjophthalmol-2018-313569
72. Rantala ES, Peltola E, Helminen H, Hernberg M, Kivelä TT. Hepatic Ultrasonography Compared With Computed Tomography and Magnetic Resonance Imaging at Diagnosis of Metastatic Uveal Melanoma. *Am J Ophthalmol* (2020) 216:156–64. doi: 10.1016/j.ajo.2020.03.049
73. Rodríguez-Marco NA, Caicedo-Zamudio C, Solanas-Álava S, Gil-Arnaiz I, Córdoba-Iturriagaioitia A, Andonegui-Navarro J. PET/TC de cuerpo completo para la detección de metástasis de melanoma corioideo. *Sist Sanit Navar* (2014) 37:293–8. doi: 10.4321/S1137-66272014000200013
74. Finger PT. Whole body PET/CT for initial staging of choroidal melanoma. *Br J Ophthalmol* (2005) 89:1270–4. doi: 10.1136/bjo.2005.069823
75. Donaldson MJ, Pulido JS, Mullan BP, Inwards DJ, Cantrill H, Johnson MR, et al. Combined positron emission tomography/computed tomography for evaluation of presumed choroidal metastases. *Clin Experiment Ophthalmol* (2006) 34:846–51. doi: 10.1111/j.1442-9071.2006.01364.x
76. Orcurto V, Denys A, Voelter V, Schalenbourg A, Schnyder P, Zografos L, et al. 18F-fluorodeoxyglucose positron emission tomography/computed tomography and magnetic resonance imaging in patients with liver metastases from uveal melanoma: results from a pilot study. *Melanoma Res* (2012) 22:63–9. doi: 10.1097/CMR.0b013e32834d3dcb
77. Cohen VL, Pavlidou E, Costa J, Arora A, Szyzsko T, Sagoo M, et al. Staging uveal melanoma with whole-body positron-emission tomography/computed tomography and abdominal ultrasound: Low incidence of metastatic disease, high incidence of second primary cancers. *Middle East Afr J Ophthalmol* (2018) 25:91. doi: 10.4103/meajo.MEAJO\_96\_18
78. Fretton A, Chin KJ, Raut R, Tena LB, Kivelä T, Finger PT. Initial PET/CT Staging for Choroidal Melanoma: AJCC Correlation and Second Nonocular Primaries in 333 Patients. *Eur J Ophthalmol* (2012) 22:236–43. doi: 10.5301/ejo.5000049
79. Servois V, Mariani P, Malhaire C, Petras S, Piperno-Neumann S, Plancher C, et al. Preoperative staging of liver metastases from uveal melanoma by magnetic resonance imaging (MRI) and fluorodeoxyglucose-positron emission tomography (FDG-PET). *Eur J Surg Oncol EJSO* (2010) 36:189–94. doi: 10.1016/j.ejso.2009.08.010
80. Murphy G, Hussey D, Metser U. Non-cutaneous melanoma: is there a role for <sup>18</sup>F-FDG PET-CT? *Br J Radiol* (2014) 87:20140324. doi: 10.1259/bjr.20140324
81. Breazzano MP, Daniels AB. Initial staging imaging for uveal melanoma: what's necessary and what's extraneous? *Invest Ophthalmol Vis Sci* (2017) 58:4412.
82. Klingenstein A, Haug AR, Nentwich MM, Tiling R, Schaller UC. Whole-body F-18-fluoro-2-deoxyglucose positron emission tomography/computed tomography imaging in the follow-up of metastatic uveal melanoma. *Melanoma Res* (2010) 20:511–6. doi: 10.1097/CMR.0b013e3283403d6c
83. Kato K, Kubota T, Ikeda M, Tadokoro M, Abe S, Nakano S, et al. Low efficacy of 18F-FDG PET for detection of uveal malignant melanoma compared with 123I-IMP SPECT. *J Nucl Med* (2006) 47:404–9.

**Conflict of Interest:** The authors declare that the research was conducted in the absence of any commercial or financial relationships that could be construed as a potential conflict of interest.

Copyright © 2021 Li, Wang, Zhang, Tang and Wei. This is an open-access article distributed under the terms of the Creative Commons Attribution License (CC BY). The use, distribution or reproduction in other forums is permitted, provided the original author(s) and the copyright owner(s) are credited and that the original publication in this journal is cited, in accordance with accepted academic practice. No use, distribution or reproduction is permitted which does not comply with these terms.



# Intra-Individual Comparison of 18F-PSMA-1007 and 18F-FDG PET/CT in the Evaluation of Patients With Prostate Cancer

Xing Zhou<sup>1,2†</sup>, YingChun Li<sup>3†</sup>, Xiao Jiang<sup>1</sup>, XiaoXiong Wang<sup>1</sup>, ShiRong Chen<sup>1</sup>, TaiPeng Shen<sup>1</sup>, JinHui You<sup>2</sup>, Hao Lu<sup>1</sup>, Hong Liao<sup>4</sup>, Zeng Li<sup>4</sup> and ZhuZhong Cheng<sup>1,2\*</sup>

<sup>1</sup> Radiation Oncology Key Laboratory of Sichuan Province, PET/CT Centre, Sichuan Cancer Hospital, Chengdu, China,

<sup>2</sup> Department of Nuclear Medicine, Affiliated Hospital of North Sichuan Medical College, Nanchong, China, <sup>3</sup> Department of Nuclear Medicine & Radiotherapy, Air Force Hospital of Western Theater Command, Chengdu, China, <sup>4</sup> Radiation Oncology Key Laboratory of Sichuan Province, Department of Urology, Sichuan Cancer Hospital, Chengdu, China

## OPEN ACCESS

### Edited by:

Peng Mi,  
Sichuan University, China

### Reviewed by:

Sean Yan,  
Singapore General Hospital,  
Singapore  
Feng Wang,  
Nanjing Hospital affiliated to Nanjing  
Medical University, China

### \*Correspondence:

ZhuZhong Cheng  
chengzhzhong@163.com

<sup>†</sup>These authors share first authorship

### Specialty section:

This article was submitted to  
Cancer Imaging and  
Image-directed Interventions,  
a section of the journal  
Frontiers in Oncology

**Received:** 20 July 2020

**Accepted:** 23 November 2020

**Published:** 01 February 2021

### Citation:

Zhou X, Li Y, Jiang X, Wang X, Chen S,  
Shen T, You J, Lu H, Liao H, Li Z and  
Cheng Z (2021) Intra-Individual  
Comparison of 18F-PSMA-1007 and  
18F-FDG PET/CT in the Evaluation of  
Patients With Prostate Cancer.  
Front. Oncol. 10:585213.  
doi: 10.3389/fonc.2020.585213

**Purpose:** 18F labelled PSMA-1007 presents promising results in detecting prostate cancer (PC), while some pitfalls exist meanwhile. An intra-individual comparison of 18F-FDG and 18F-PSMA-1007 in patients with prostate cancer were aimed to be performed in the present study. Then, the pitfalls of 18F-PSMA-1007 PET/CT in imaging of patients with prostate cancer were analyzed.

**Methods and Material:** 21 prostate cancer patients underwent 18F-PSMA-1007 PET/CT as well as 18F-FDG PET/CT before treatment. All positive lesions were noticed in both 18F-PSMA-1007 PET/CT and 18F-FDG PET/CT, then differentiated PC metastasis from benign lesions. The SUVmax, SUVmean and TBR of lesions, up to 10 metastases and 10 benign lesions per patients were recorded (5 for bone, 5 for soft tissue metastasis). The distribution of positive lesions were analyzed for two imaging. Detection rates, SUVmax, SUVmean and TBR in 18F-PSMA-1007 PET/CT and 18F-FDG PET/CT were compared, respectively. The optimal cut-off values of SUVmax, SUVmean for metastases vs. benign lesions was found through areas under ROC in 18F-PSMA-1007.

**Results:** The detection rates of primary lesions in 18F-PSMA-1007 PET/CT was higher than that of 18F-FDG PET/CT (100% (21/21) vs. 67% (14/21)). For extra-prostatic lesions, 18F-PSMA-1007 PET/CT revealed 124 positive lesions, 49 (49/124, 40%) attributed to a benign origin; 18F-FDG PET/CT revealed 68 positive lesions, 14 (14/68, 21%) attributed to a benign origin. The SUVmax, SUVmean, TBR of primary tumor in 18F-PSMA-1007 PET/CT was higher than that in 18F-FDG PET/CT (15.20 vs. 4.20 for SUVmax; 8.70 vs. 2.80 for SUVmean; 24.92 vs. 4.82 for TBR, respectively); The SUVmax, SUVmean, TBR of metastases in 18F-PSMA-1007 PET/CT was higher than that in 18F-FDG PET/CT (10.72 vs. 4.42 for SUVmax; 6.67 vs. 2.59 for SUVmean; The TBR of metastases was 13.3 vs. 7.91). For 18F-FDG PET/CT, the SUVmax, SUVmean in metastases was higher than that in benign lesions (4.42 vs. 3.04 for SUVmax, 2.59 vs. 1.75 for SUVmean, respectively). Similarly, for 18F-PSMA-1007 PET/CT, the SUVmax, SUVmean in

metastases was significantly higher than that in benign lesions (10.72 vs. 3.14 for SUVmax, 6.67 vs. 1.91 for SUVmean, respectively), ROC suggested that SUVmax=7.71, SUVmean=5.35 might be the optimal cut-off values for metastases vs. benign lesions.

**Conclusion:** The pilot study suggested that 18F-PSMA-1007 showed superiority over 18F-FDG because its high detecting rate of PC lesions and excellent tumor uptake. While non-tumor uptake in 18F-PSMA-1007 may lead to misdiagnosis, recognizing these pitfalls and careful analysis can improve the accuracy of diagnosis.

**Keywords:** 18F-PSMA-1007, 18F-FDG, PET/CT, prostate cancer, pitfalls

## INTRODUCTION

Prostate cancer is the second most common cancer in men (1). Early detection and accurate staging leads to improved clinical decision making. Different from traditional imaging (e.g., computed tomography (CT), magnetic resonance imaging (MRI)), whole-body imaging seems to be an advantage for PET/CT. Recently, the study of prostate-specific membrane antigen (PSMA) is growing and suggesting impressive results in the diagnosis and staging of prostate cancer (2–4).

18F labelled prostate-specific membrane antigen (PSMA)-1007 is a novel PSMA-based radiopharmaceutical, it was introduced into clinical practice because its excellent tumor uptake and high sensitivity for detecting lesions (5–7). Furthermore, 18F-PSMA-1007 is mainly cleared by hepatobiliary system, providing clinical practice benefits (8–10). 18F-FDG is the most widely used radiotracer, which is effective for diagnosis and staging of prostate cancer (11). So far, 18F-PSMA-1007 has not been compared with 18F-FDG yet.

Recently, with the extensive application of PSMA-target tracer, the pitfalls of PSMA-target PET has been found increasingly (12–15). The uptake of PSMA-ligand in other malignant and benign pathologies (e.g., celiac and other ganglia, fracture, degenerative changes) causes challenge to clinical diagnosis. Recognizing these limitations can be essential.

The aim of present study was to perform an intra-individual comparison of 18F-FDG and 18F-PSMA-1007 in the evaluation of patients with prostate cancer. Then analyzed the pitfalls that may appear when conducting 18F-PSMA-1007 PET/CT in order to reduce the probability of misdiagnosis.

## MATERIALS AND METHODS

### Patients

A total of 21 patients (median age, 66 y; range, 50–82 y) with pathologically diagnosed as prostate cancer underwent 18F-PSMA-1007 PET/CT and 18F-FDG PET/CT before treatment. 18 (86%) of these patients were diagnosed as prostate cancer with perineal prostate biopsy; two (9%) patients were confirmed by biopsy of pelvic lymph node, ala of ilium, respectively; one (5%) patient was diagnosed by biopsy with cystoscope. The Gleason score was available for 16 patients, the median Gleason score was 9 (range 7–10). The treatment of patients was as follows, eight

(38%) of the patients received exclusively androgen deprivation therapy (ADT), two (10%) patients was received ADT after docetaxel chemotherapy. Four (19%) patients was treated with only radical prostatectomy. Seven (33%) was treated with ADT after radical prostatectomy.

The study was ethically approved by the Institutional Ethics Committee (Ethics Committee of Sichuan Cancer Hospital, JS-2017-01-02) and in accordance to the local regulations of China. All patients signed a written informed consent form. The patients characteristics were listed in **Table 1**.

### Radiosynthesis and Quality Control

18F-PSMA-1007 was synthesized by a one-step method using an automated radiosynthesizer (Sumitomo, Japan) as was described (16). 18F<sup>+</sup> was acquired by (18F)/H<sub>2</sub>18O nuclear reaction, and then loaded onto quarternary methylamine column (Waters, America), After eluted by 0.75 ml tetrabutylammonium hydrogen carbonate (TBAHCO<sub>3</sub>) solution (ABX, Radeberg, Germany), it was transferred into reactor and followed by the addition of 0.4 ml anhydrous acetonitrile (Sigma, America), then removal of water with the temperature of 95°C. 1.2 ml dimethyl sulfoxide (ABX, Radeberg, Germany) which dissolved with PSMA-1007 precursor (ABX, Radeberg, Germany) was added into reactor and performed fluorination reaction at 85°C for 10 min. Then diluted with 6 ml of 5% ethano and loaded onto PS-H+ and C18ec (ABX, Radeberg, Germany) followed by 4 ml of 30% ethanol. Final product was eluted with 4 ml of 30% ethanol and was added into 0.1 ml of 100 mg/L Vitamin C solution, 36 mL of 0.9% NaCl, then was sterilized by 0.22 μm filter (Millipore, America). High-performance liquid chromatography (HPLC, Shimadzu, Japan) was performed to test chemical purity, Further quality control (appearance, color, clarity, PH, and adionuclidic purity) was done and in compliance with current pharmacopoeias. The synthesis of 18F-FDG was performed as reported by Gallagher et al. (17).

### Imaging Procedures

To reduce the mutual interference of the two radiotracers, imaging was carried out at different days. The median 6.5 (range 1.0–34.0) days passed from 18F-PSMA-1007 to 18F-FDG. Patients fasted for at least 6 h prior to injection of the 18F-FDG and blood sugar level is lower than 15 mg/L. The injected activity of 18F-FDG were mean 388 ± 55 MBq (range 281–503 MBq) and scanning was performed 60 min after

**TABLE 1 |** Patient characteristics.

PatientNo.	Age(y)	Gleason score	Days from PSMA PET/CT To FDG PET/CT	initial PSA (ng/mL)	Local tumor growth (n)		Lymph node metastases (n)		bone metastases (n)	
					FDG	PSMA	FDG	PSMA	FDG	PSMA
1	73		4	183.00	1	1	>10	>10	>10	>10
2	63	4+3	9	5.00	1	1	0	1	0	3
3	71	4+5	1		1	2	0	0	0	0
4	74	3+4	4	10.65	0	1	0	1	0	0
5	72	4+4	7	30.14	1	1	1	5	0	2
6	82		3	100.00	1	1	2	3	>10	>10
7	64	5+4	3	153.00	0	2	>10	>10	>10	>10
8	80		1	70.50	0	>2	1	5	2	6
9	63	4+3	5	147.00	1	1	0	5	1	1
10	68	5+5	34	16.22	1	2	0	0	0	1
11	68	4+3		9.90	1	>2	0	7	0	3
12	74	4+4	18	25.63	1	>2	0	0	0	1
13	50		7	15.50	1	1	0	3	1	2
14	65	4+5	9		0	1	0	4	0	0
15	66	4+4	6	184.00	1	1	1	5	0	0
16	66	5+4	5	50.80	0	1	4	7	0	0
17	56	3+4	9	31.60	0	1	0	2	2	4
18	65	4+5	7	91.30	1	2	5	6	>10	>10
19	75		7		1	1	0	0	0	2
20	56	5+5	11	200.00	1	>2	0	2	0	0
21	64	4+4	3	20.01	0	1	0	0	6	6

injection, while the injected activity of 18F-PSMA-1007 were  $348 \pm 52$  MBq (range 266–458 MBq), and according to Giesel et al. (5) imaging began 180 min after injection. All scans were obtained on a Biograph mCT-64 PET/CT scanner (Siemens). Non-enhanced low-dose (1.3–1.5 mSv) CT scan was performed with CT parameters (140 keV, 42 mA) section width of 8 mm, pitch of 0.8, and CT datas were used for attenuation correction. The PET-scan, PET was acquired in 3-D FlowMotion with an acquisition time of 2 min per bed position. Both scans was performed from vertex to the mid-thigh. Images were reconstructed with an ordered-subset expectation-maximization iterative reconstruction algorithm (three iterations, 21 subsets).

## Image Analysis and Quantification

All images were evaluated by two double board-certified nuclear medicine physician. Volumes of interest (VOI) were drawn around lesions using an maximum standardized uptake value (SUVmax) threshold of isocontour of 42% (18). Intra-prostatic lesions were defined as positive if the tracer-uptake was focal and higher than surrounding prostate tissue (19). Other soft tissue and bone metastases were judged as positive when there were obvious morphological changes meanwhile corresponding lesions showed increased radiotracer-uptake above normal surroundings (20). Benign lesions were recognised based on typical pitfalls (e.g., ganglia, fracture, degenerative changes, and unspecific lymph nodes) in PSMA ligand PET imaging and information from CT (14). All PET positive lesions were counted and lesions grouped into: (a) local tumor growth, (b) soft tissue metastases [including lymph node (LN) metastases, other soft tissue metastases (e.g., lung, liver)] (c) bone metastases, (d) benign lesions. In accordance with previous studies, obturator muscle was chosen as background and VOI was drawn around it (19, 21). Tumor-to-background ratio

(TBR) were defined as SUVmax of lesions/SUVmax of obturator muscle. for the SUVs (SUVmax and SUVmean), TBR of primary tumor, up to 10 metastases per patients were recorded (five for bone, five for soft tissue metastasis); the SUVs (SUVmax and SUVmean) of up to 10 benign lesions per patients were recorded.

## Statistical Analysis

Statistical analysis was performed using SPSS software, version 24.0 (IBM Corp.). The nonparametric Mann-Whitney U test for two independent samples was used to compare the SUVs, TBR of all lesions. When performed 18F-PSMA-1007 PET/CT, Areas under receiver operating characteristic curves (ROC) were calculated and optimal cut-off values of SUV in metastases vs. benign lesions were calculated using the Youden's index.  $P < 0.05$  were considered significant.

## RESULTS

The median initial PSA was 41.20 ng/ml (range, 5.00–200.00 ng/ml). The median of 6.5 d (range, 1.0–34.0 d) passed from 18F-PSMA-1007 PET/CT to 18F-FDG PET/CT. The SUVmax of urinary bladder was significantly lower in 18F-PSMA-1007 PET/CT than in 18F-FDG PET/CT (median SUVmax of 2.40 (range 0.60–11.00) vs. 15.64 (range 6.19–35.47),  $P < 0.001$ ). No statistically significant difference was found when evaluating the SUVmax of 18F-FDG PET/CT and 18F-PSMA-1007 PET/CT for obturator muscle (median SUVmax of 0.75 vs. 0.70,  $P = 0.061$ ) (Table 2).

## Local Lesion Finding and Uptake

Among these 21 prostate cancer patients, 18F-PSMA-1007 PET/CT detected all patients (100%), eight (38%) cases of them had



**TABLE 2 |** Comparison of mean SUV and TBR of lesions in 18F-PSMA-1007 PET and 18F-FDG PET.

	18F-PSMA-1007				18F-FDG			
	n	SUVmax	SUVmean	TBR	n	SUVmax	SUVmean	TBR
urinary bladder	21	2.40 (0.60–11.00)			21	15.64(6.19–35.47)		
obturator muscle	21	0.70(0.35–0.92)			21	0.75(0.57–1.64)		
local lesion	21	15.20 (6.20–75.00)	8.70(3.80–43.00)	24.92(8.41–117.06)	14	4.20(2.80–10.50)	2.80(1.60–6.30)	4.82(1.00–14.00)
metastase	75	10.72 (1.42–79.70)	6.67(0.89–50.16)	13.3(1.61–96.02)	54	4.42(1.05–12.41)	2.59(0.86–7.81)	7.91(1.28–96.02)
benign lesions	49	3.14(1.26–12.98)	1.91(0.89–8.30)		14	3.04(1.71–5.60)	1.75(0.86–3.38)	

TBR, tumor-to-background ratio.

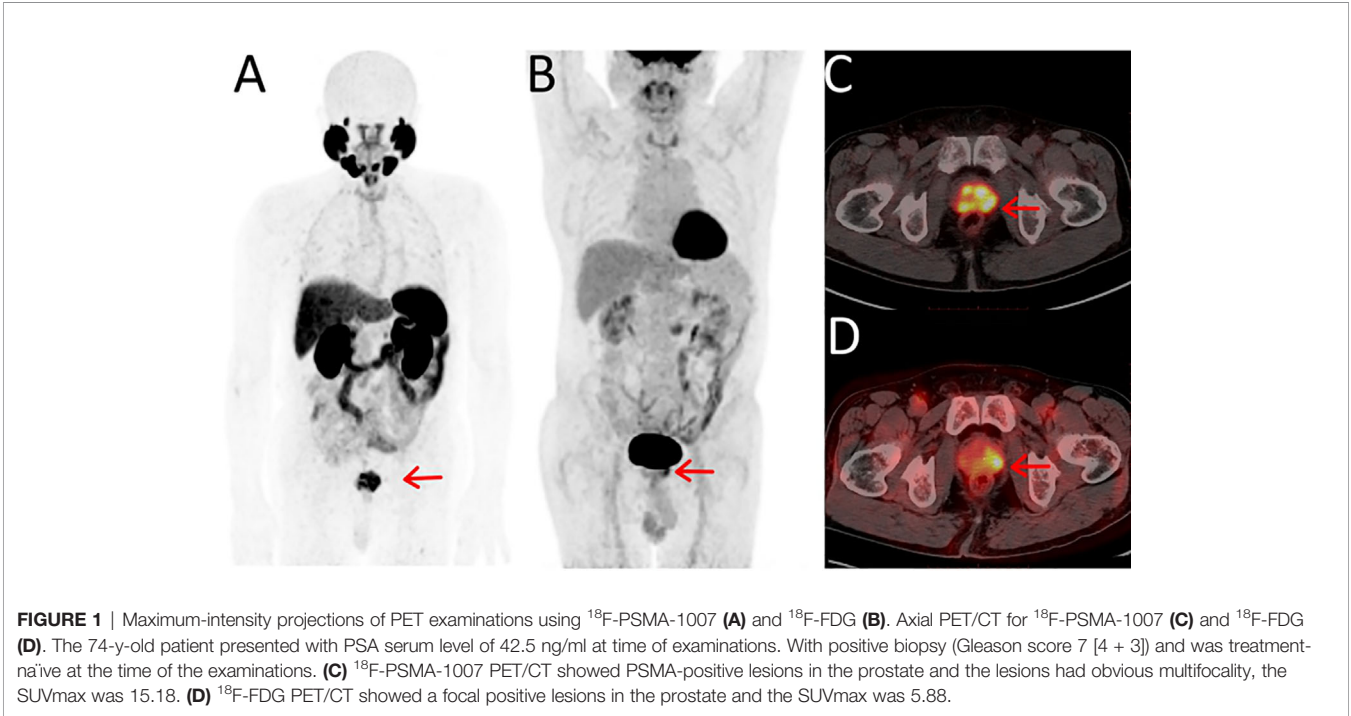
obvious multifocality. 14 of 21 cases (67%) was identified by 18F-FDG PET/CT, and none of them was found multifocality (**Table 1, Figure 1**). SUVmax, SUVmean of local lesions was significantly higher in 18F-PSMA-1007 PET/CT than in 18F-FDG PET/CT (median SUVmax of 15.20 (range 6.20–75.00) vs. 4.20 (range 2.80–10.50),  $P < 0.001$ ), (median SUVmean of 8.70 (range 3.80–43.00) vs. 2.80 (range 1.60–.30),  $P < 0.001$ ). TBR of local lesions was significantly higher in 18F-PSMA-1007 PET/CT than in 18F-FDG PET/CT (median TBR of 24.92 (range 8.41–117.06) vs. 4.82 (range 1.00–14.00),  $P < 0.001$ ) (**Table 2**).

Metastases Finding and Uptake

18F-PSMA-1007 PET/CT found 124 lesions with focal PSMA-ligand uptake, 49 (40%) of them attributed to benign origin (17 (35%) lesions suspicious of ganglia, 12 (24%) lesions attributed to unspecific lymph nodes, five (10%) lesions for fracture, five (10%) lesions attributed to degenerative changes, three (6%) lesions for unspecific soft tissue, seven (15%) lesions showed focal increased radiotracer-uptake above normal surroundings in PSMA PET without corresponding morphological changes in CT (two lesions for bone, five for others); 75(60%) attributed to metastases [50

(67%) lesions for bone metastases (**Table 3**), 25(33%) for lymph node metastases, no other soft tissue metastases was found]. For details see **Figure 2**. The SUVmax, SUVmean for suspicious metastases was significantly higher than probably benign (median SUVmax of 10.72 (range 1.42–79.70) vs. 3.14 (range 1.26–12.98),  $P < 0.001$ ), (median SUVmean of 6.67 (range 0.89–50.16) vs. 1.91 (range 0.89–8.30),  $P < 0.001$ ). (**Table 2, Figure 4**). ROC showed that optimal cut-off values of SUV in metastases vs. benign lesions was SUVmax = 7.71, (Areas under curve (AUC) = 0.795,  $P < 0.001$ ), SUVmean = 5.35 (AUC = 0.791,  $P < 0.001$ ) (**Figure 3**).

18F-FDG PET/CT detected a total of 68 FDG-positive lesions, 14 (21%) with benign origin [seven (50%) lesions attributed to unspecific lymph nodes, three (22%) lesions for fracture, two (14%) for degenerative changes, two (14%) for others], 54 (79%) with metastases [32 (59%) lesions attributed to bone metastases, 22 (41%) lesions suspicious of LN metastases]. For details see **Table 3**. The SUVmax, SUVmean for suspicious metastases was significantly higher than probably benign [median SUVmax of 4.42 (range 1.05–12.41) vs. 3.04 (range 1.71–5.60),  $P = 0.036$ ), (median SUVmean of 2.59 (range 0.86–7.81) vs. 1.75 (range 0.86–3.38),  $P = 0.014$ ] (**Table 2**).



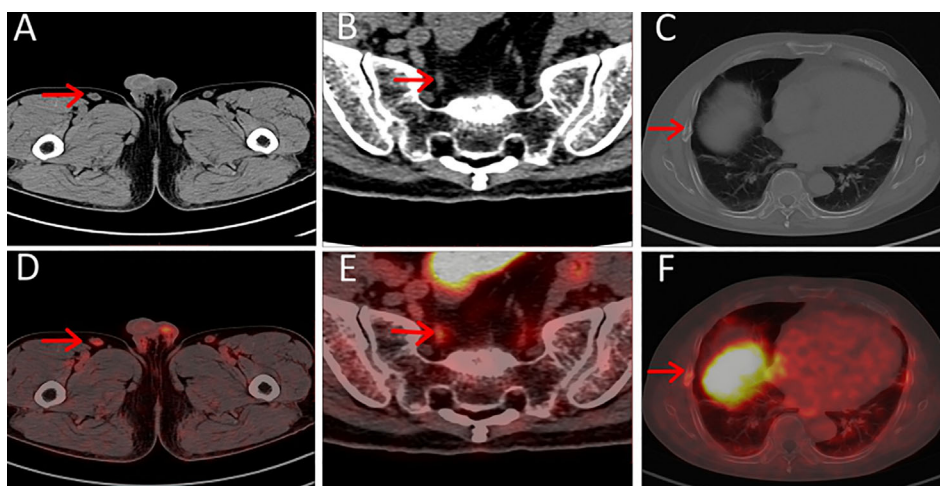


**FIGURE 2 | (A–C)** Axial CT, **(D–F)** axial PET/CT of pitfalls in  $^{18}\text{F}$ -PSMA-1007. Unspecific PSMA-ligand uptake in right inguinal lymph node **(A, D)**, PSMA-ligand uptake in pelvic ganglia **(B, E)** and PSMA-ligand uptake in right non-displaced rib fracture **(C, F)**.

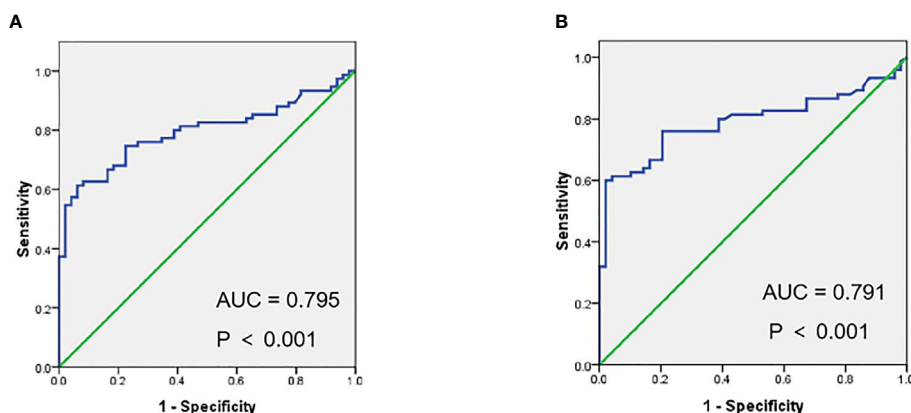


**FIGURE 3 |** Receiver operating characteristic curves (ROC) of SUVmax **(A)**, SUVmean **(B)** in metastases vs. benign lesions for  $^{18}\text{F}$ -PSMA-1007 PET/CT.

**TABLE 3 |** The distribution of PSMA-positive lesions and FDG-positive lesions.

Distribution	18F-PSMA-1007	18F-FDG
All	124	68
<b>metastase</b>	75 (60%)	54 (79%)
Bone metastase	50	32
Soft tissue metastase	25	22
<b>benign lesions</b>	49 (40%)	14 (21%)
ganglia	17	
unspecific lymph nodes	12	7
fracture	5	3
degenerative changes	5	2
unspecific soft tissue	3	2
increasly PSMA-ligand uptake without correlate on CT images	7	

No statistically significant was found when comparing the SUVs of lesions attributed to benign with  $^{18}\text{F}$ -PSMA-1007 and  $^{18}\text{F}$ -FDG (median SUVmax 3.14 vs. 3.04,  $P > 0.05$ ), SUVmean

(median SUVmean 1.91 vs. 1.75,  $P > 0.05$ ). SUVmax, SUVmean of metastases was significantly higher for  $^{18}\text{F}$ -PSMA-1007 PET/CT than for  $^{18}\text{F}$ -FDG PET/CT (median SUVmax of 10.72 (range 1.42–79.70) vs. 4.42 (range 1.05–12.41),  $P < 0.001$ ), (median SUVmean of 6.67 (range 0.89–50.16) vs. 2.59 (range 0.86–7.81),  $P < 0.001$ ). TBR of metastases was significantly higher in  $^{18}\text{F}$ -PSMA-1007 PET/CT than in  $^{18}\text{F}$ -FDG PET/CT (median TBR of 13.3 (range 1.61–96.02) vs. 7.91 (range 1.28–96.02),  $P < 0.001$ ) (**Figure 4**).

## DISCUSSION

This retrospective study mainly focused on comparing the detection rate of local lesions and metastases (both LN and bone metastases) in  $^{18}\text{F}$ -FDG PET/CT and  $^{18}\text{F}$ -PSMA-1007 PET/CT. Simultaneously, performing a comparison of lesions

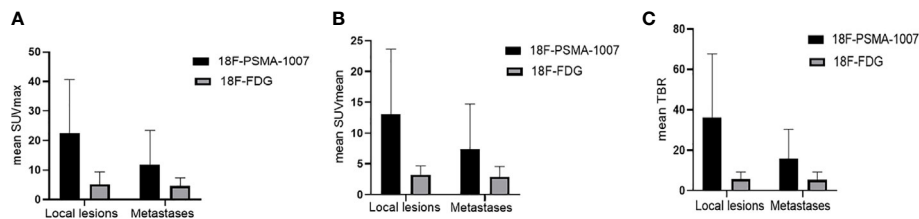


**FIGURE 4 | (A)** Comparison of mean SUVmax and its SD of  $^{18}\text{F}$ -PSMA-1007 and  $^{18}\text{F}$ -FDG for local lesions and metastases. **(B)** Comparison of mean SUVmean and its SD of  $^{18}\text{F}$ -PSMA-1007 and  $^{18}\text{F}$ -FDG for local lesions and metastases. **(C)** Comparison of mean TBR (tumor-to-background ratio) and its SD of  $^{18}\text{F}$ -PSMA-1007 and  $^{18}\text{F}$ -FDG for local lesions and metastases.

attributed to benign origin and lesions attributed to metastases in 18F-FDG PET/CT and 18F-PSMA-1007 PET/CT, respectively.

Detection rate for local lesions in 18F-PSMA-1007 PET/CT was higher than in 18F-FDG PET/CT (100% (21/21) for 18F-PSMA-1007 PET/CT, 67% (14/21) for 18F-FDG PET/CT) and 18F-PSMA-1007 PET/CT was more likely to find lesions with multifocality (eight cases for 18F-PSMA-1007 PET/CT, none for 18F-FDG PET/CT). This might be explained by the following reasons: Firstly, PSMA is a type II transmembrane glycoprotein that is strongly overexpressed in PCa cells (both primary tumor and metastases) and low in benign prostate tissue (22–24), making 18F-PSMA-1007 PET/CT a promising technique for detecting and locating prostate cancer. Furthermore, hepatobiliary elimination seems to be another advantage for 18F-PSMA-1007, while 18F-FDG mainly excreted *via* urinary tract (17, 25); low bladder/ureter activity in 18F-PSMA-1007 PET/CT make it possible to differentiate primary tumor and pelvic lymph node metastases from the bladder urinalysis activity (26). In present study, we found 18F-PSMA-1007 PET/CT was more likely to detect metastases (both LN and bone metastases) than 18F-FDG PET/CT (75 lesions for 18F-PSMA-1007 PET/CT, 54 for 18F-FDG PET/CT). However, a recently published study shows no significant difference was found when comparing the detection rate in 18F-PSMA-1007 and 18F-DCFPyL (27). Both tracers belong to the same family of PSMA ligands and labelled by the same radioisotope ( $^{18}\text{F}$ ) may explain the phenomenon (28).

Consistent with previous studies, we found that 18F-PSMA-1007 PET/CT shows high tumor-to-background ratios (TBR) in lesions with prostate cancer (6), median TBR of 24.92 in local lesions with prostate cancer, median TBR of 13.30 in lymph node metastases and bone metastases with prostate cancer. The median TBR of 18F-FDG PET/CT in local lesions with prostate cancer, lymph node metastases, and bone metastases with prostate cancer was 4.82 and 7.91, respectively. After injection of 18F-PSMA-1007 for 3 h, the uptake of radio-tracer in prostate cancer lesions demonstrated a remarkable increasing and leading to the improvement of tumor-to-background ratios (5), it makes tumor lesions more visible in 18F-PSMA-1007 PET/CT than in 18F-FDG PET/CT.

Recent studies suggest that PSMA-target PET shows some pitfalls in clinical application, especially in 18F labeled PSMA, as it may be expressed in other malignant and benign pathologies, even some normal tissues (6, 13, 14, 29) and these findings are in

line with ours. We found that some PSMA-positive lesions attributed to benign origin (e.g., benign lymph nodes, ganglia, and skeletal fracture) and the reason of this phenomenon is unclear yet. To our knowledge, salivary glands, liver, gallbladder, etc. non-prostate tissues show uptake in 18F-PSMA-1007 PET (5, 7), providing the possibility of PSMA-uptaking in benign lesions. Moreover, PSMA present both in peri-tumoral capillaries and inflammatory-associated neovasculature may explain the uptake of benign lesions (14). The arising of these pitfalls leads to an increasing in false positive and brings us challenges. Differentiating suspicious metastases from these potential diagnostic pitfalls may be of increased importance.

In present study, we found that the uptake of PSMA ligand tracer in probable Pca metastases was significantly higher than in benign lesions (10.72 vs. 3.14 for SUV max, 6.67 vs. 1.91 for SUVmean), which was consistent with previous studies (15). And ROC shows that SUVmax  $\geq 7.71$  was more likely to be Pca metastases (AUC = 0.795,  $P < 0.001$ ) than SUVmax  $< 7.71$ , SUVmean  $\geq 5.35$  was more likely to be Pca metastases (AUC = 0.791,  $P < 0.001$ ) than SUVmax  $< 5.35$ . These findings make it possible to differentiate suspicious metastases and benign lesions. Furthermore, lesions attributed to benign origin can be identified by CT (with 80% in benign lesions, 96% in coeliac ganglia) (14, 30), due to their typical shapes and locations. More importantly, the clinical medical records (e.g., other imaging data, history of fracture, inflammation) providing essential information when evaluating benign lesions.

In accordance with previous study (13, 14), we found that the most prevalent pitfall in 18F-PSMA-1007 PET/CT was non-specific radiotracer uptake in ganglia, with 17 (35%) lesions attributed to ganglia (including cervical, coeliac, or sacral ganglia). A recent study publication by Krohn et al. demonstrated that up to 94.0% of prostate cancer patients with PSMA-PET/CT show intense PSMA-ligand uptake in at least one coeliac ganglia (15). In current study, the distribution of radio-tracer uptake in other benign lesion with 18F-PSMA-1007 PET/CT was as follows, unspecific lymph nodes, fracture, degenerative changes, unspecific soft tissues, focal increasingly PSMA-ligand uptake showing no clear correlate on CT images, which were along with the previous study (12–14). Recently, a study found that a high number of PSMA-ligand uptake in the ribs without corresponding morphological changes in CT (14), which was different from our finding [only two (28%) lesions].

Small population was involved in present study may be the reason leading to this difference.

Lacking histopathology verification of the PSMA-positive lesions is the major limitation in present study. However, the uptake of lesions, CT images, and clinical medical records provide the possibility to identify benign lesions. Additionally, small patient population is another limitation, larger comparison trials will be needed in future studies.

## CONCLUSION

The study demonstrated that 18F-PSMA-1007 showed superiority in detecting Pca lesions (both primary and metastases) than 18F-FDG and the uptaking in benign lesions was more likely to be found in 18F-PSMA-1007. Emphasizing the known of pitfalls, evaluating PET and CT images as well as clinical medical records make it available to avoid a misdiagnosis in 18F-PSMA-1007 PET/CT.

## DATA AVAILABILITY STATEMENT

The datasets presented in this article are not readily available. Requests to access the datasets should be directed to zxing94@126.com.

## REFERENCES

- Bray F, Ferlay J, Soerjomataram I, Siegel RL, Torre LA, Jemal A. Global cancer statistics 2018: GLOBOCAN estimates of incidence and mortality worldwide for 36 cancers in 185 countries. *CA: Cancer J Clin* (2018) 68(6):394–424. doi: 10.3322/caac.21492
- Perera M, Papa N, Christidis D, Wetherell D, Hofman MS, Murphy DG, et al. Sensitivity, Specificity, and Predictors of Positive (68)Ga-Prostate-specific Membrane Antigen Positron Emission Tomography in Advanced Prostate Cancer: A Systematic Review and Meta-analysis. *Eur Urol* (2016) 70(6):926–37. doi: 10.1016/j.eururo.2016.06.021
- Afshar-Oromieh A, Babich JW, Kratochwil C, Giesel FL, Eisenhut M, Kopka K, et al. The Rise of PSMA Ligands for Diagnosis and Therapy of Prostate Cancer. *J Nucl Med* (2016) 57(Suppl 3):79s–89s. doi: 10.2967/jnumed.115.170720
- Sterzing F, Kratochwil C, Fiedler H, Katayama S, Hahl G, Kopka K, et al. (68)Ga-PSMA-11 PET/CT: a new technique with high potential for the radiotherapeutic management of prostate cancer patients. *Eur J Nucl Med Mol Imaging* (2016) 43(1):34–41. doi: 10.1007/s00259-015-3188-1
- Giesel FL, Hadaschik B, Cardinale J, Radtke J, Vinsensia M, Lehnert W, et al. F-18 labelled PSMA-1007: biodistribution, radiation dosimetry and histopathological validation of tumor lesions in prostate cancer patients. *Eur J Nucl Med Mol Imaging* (2017) 44(4):678–88. doi: 10.1007/s00259-016-3573-4
- Cardinale J, Schäfer M, Benešová M, Bauder-Wüst U, Leotta K, Eder M, et al. Preclinical Evaluation of (18)F-PSMA-1007, a New Prostate-Specific Membrane Antigen Ligand for Prostate Cancer Imaging. *J Nucl Med* (2017) 58(3):425–31. doi: 10.2967/jnumed.116.181768
- Rahbar K, Afshar-Oromieh A, Bögemann M, Wagner S, Schäfers M, Stegger L, et al. (18)F-PSMA-1007 PET/CT at 60 and 120 minutes in patients with prostate cancer: biodistribution, tumor detection and activity kinetics. *Eur J Nucl Med Mol Imaging* (2018) 45(8):1329–34. doi: 10.1007/s00259-018-3989-0
- Giesel FL, Kesch C, Yun M, Cardinale J, Haberkorn U, Kopka K, et al. 18F-PSMA-1007 PET/CT Detects Micrometastases in a Patient With Biochemically Recurrent Prostate Cancer. *Clin Genitourinary Cancer* (2017) 15(3):e497–e9. doi: 10.1016/j.clgc.2016.12.029

## ETHICS STATEMENT

The study was ethically approved by Sichuan Cancer Hospital Ethics Committee and in accordance to the local regulations of China. All patients signed a written informed consent form.

## AUTHOR CONTRIBUTIONS

XZ, YL, XJ, XW, and ZZ designed the project, XZ and YL wrote the manuscript. HLu, HLi, and ZL organized data. SC and TS analyzed data. JY and ZC reviewed the data and the manuscript. All authors contributed to the article and approved the submitted version.

## FUNDING

This study was supplied by the Sichuan Science and Technology program (2019YJ0574; 2020YFS0421) and the Health research project of Sichuan Province (20PJ117).

## ACKNOWLEDGMENTS

We thank all members of our department for helpful discussions.

- Giesel FL, Will L, Kesch C, Freitag M, Kremer C, Merkle J, et al. Biochemical Recurrence of Prostate Cancer: Initial Results with [(18)F]PSMA-1007 PET/CT. *J Nucl Med* (2018) 59(4):632–5. doi: 10.2967/jnumed.117.196329
- Giesel FL, Knorr K, Spohn F, Will L, Maurer T, Flechsig P, et al. Detection Efficacy of (18)F-PSMA-1007 PET/CT in 251 Patients with Biochemical Recurrence of Prostate Cancer After Radical Prostatectomy. *J Nucl Med* (2019) 60(3):362–8. doi: 10.2967/jnumed.118.212233
- Jadvar H. Prostate cancer: PET with 18F-FDG, 18F- or 11C-acetate, and 18F- or 11C-choline. *J Nucl Med* (2011) 52(1):81–9. doi: 10.2967/jnumed.110.077941
- Keidar Z, Gill R, Goshen E, Israel O, Davidson T, Morgulis M, et al. 68Ga-PSMA PET/CT in prostate cancer patients - patterns of disease, benign findings and pitfalls. *Cancer Imaging* (2018) 18(1):39. doi: 10.1186/s40644-018-0175-3
- Sheikhabaei S, Afshar-Oromieh A, Eiber M, Solnes LB, Javadi MS, Ross AE, et al. Pearls and pitfalls in clinical interpretation of prostate-specific membrane antigen (PSMA)-targeted PET imaging. *Eur J Nucl Med Mol Imaging* (2017) 44(12):2117–36. doi: 10.1007/s00259-017-3780-7
- Rauscher I, Krönke M, König M, Gafita A, Maurer T, Horn T, et al. Matched-Pair Comparison of (68)Ga-PSMA-11 PET/CT and (18)F-PSMA-1007 PET/CT: Frequency of Pitfalls and Detection Efficacy in Biochemical Recurrence After Radical Prostatectomy. *J Nucl Med* (2020) 61(1):51–7. doi: 10.2967/jnumed.119.229187
- Krohn T, Verburg FA, Pufe T, Neuhuber W, Vogg A, Heinzel A, et al. [(68)Ga]PSMA-HBED uptake mimicking lymph node metastasis in coeliac ganglia: an important pitfall in clinical practice. *Eur J Nucl Med Mol Imaging* (2015) 42(2):210–4. doi: 10.1007/s00259-014-2915-3
- Zhou X, Shen TP, Yao YT, Lu H, Chen SR, Xiao DQ, et al. Synthesis of 18F-PSMA-1007 by one-step method and PET/CT imaging in prostate cancer. *Chin J Nucl Med Mol Imaging* (2019) 39(10):606–9. doi: 10.3760/cma.j.issn.2095-2848.2019.10.007
- Gallagher BM, Ansari A, Atkins H, Casella V, Christman DR, Fowler JS, et al. Radiopharmaceuticals XXVII. 18F-labeled 2-deoxy-2-fluoro-D-glucose as a radiopharmaceutical for measuring regional myocardial glucose metabolism



- in vivo: tissue distribution and imaging studies in animals. *J Nucl Med* (1977) 18(10):990–6.
18. Miccò M, Vargas HA, Burger IA, Kollmeier MA, Goldman DA, Park KJ, et al. Combined pre-treatment MRI and 18F-FDG PET/CT parameters as prognostic biomarkers in patients with cervical cancer. *Eur J Radiol* (2014) 83(7):1169–76. doi: 10.1016/j.ejrad.2014.03.024
  19. Uprimny C, Kroiss AS, Decristoforo C, Fritz J, von Guggenberg E, Kendler D, et al. (68)Ga-PSMA-11 PET/CT in primary staging of prostate cancer: PSA and Gleason score predict the intensity of tracer accumulation in the primary tumour. *Eur J Nucl Med Mol Imaging* (2017) 44(6):941–9. doi: 10.1007/s00259-017-3631-6
  20. Eiber M, Maurer T, Souvatzoglou M, Beer AJ, Ruffani A, Haller B, et al. Evaluation of Hybrid  $^{68}\text{Ga}$ -PSMA Ligand PET/CT in 248 Patients with Biochemical Recurrence After Radical Prostatectomy. *J Nucl Med* (2015) 56(5):668–74. doi: 10.2967/jnumed.115.154153
  21. Fendler WP, Schmidt DF, Wenter V, Thierfelder KM, Zach C, Stief C, et al. 68Ga-PSMA PET/CT Detects the Location and Extent of Primary Prostate Cancer. *J Nucl Med* (2016) 57(11):1720–5. doi: 10.2967/jnumed.116.172627
  22. Demirci E, Sahin OE, Ocak M, Akovali B, Nematyazar J, Kabasakal L. Normal distribution pattern and physiological variants of 68Ga-PSMA-11 PET/CT imaging. *Nucl Med Commun* (2016) 37(11):1169–79. doi: 10.1097/mnm.0000000000000566
  23. Mease RC, Foss CA, Pomper MG. PET imaging in prostate cancer: focus on prostate-specific membrane antigen. *Curr Top Med Chem* (2013) 13(8):951–62. doi: 10.2174/1568026611313080008
  24. Afshar-Oromieh A, Malcher A, Eder M, Eisenhut M, Linhart HG, Hadaschik BA, et al. PET imaging with a [68Ga]gallium-labelled PSMA ligand for the diagnosis of prostate cancer: biodistribution in humans and first evaluation of tumour lesions. *Eur J Nucl Med Mol Imaging* (2013) 40(4):486–95. doi: 10.1007/s00259-012-2298-2
  25. Rahbar K, Weckesser M, Ahmadzadehfard H, Schäfers M, Stegger L, Bögemann M. Advantage of (18)F-PSMA-1007 over (68)Ga-PSMA-11 PET imaging for differentiation of local recurrence vs. urinary tracer excretion. *Eur J Nucl Med Mol Imaging* (2018) 45(6):1076–7. doi: 10.1007/s00259-018-3952-0
  26. Kuten J, Fahoum I, Savin Z, Shamni O, Gitstein G, Hershkovitz D, et al. Head-to-Head Comparison of (68)Ga-PSMA-11 with (18)F-PSMA-1007 PET/CT in Staging Prostate Cancer Using Histopathology and Immunohistochemical Analysis as a Reference Standard. *J Nucl Med* (2020) 61(4):527–32. doi: 10.2967/jnumed.119.234187
  27. Giesel FL, Will L, Lawal I, Lengana T, Kratochwil C, Vorster M, et al. Intraindividual Comparison of (18)F-PSMA-1007 and (18)F-DCFPyL PET/CT in the Prospective Evaluation of Patients with Newly Diagnosed Prostate Carcinoma: A Pilot Study. *J Nucl Med* (2018) 59(7):1076–80. doi: 10.2967/jnumed.117.204669
  28. Kopka K, Benešová M, Bařinka C, Haberkorn U, Babich J. Glu-Ureido-Based Inhibitors of Prostate-Specific Membrane Antigen: Lessons Learned During the Development of a Novel Class of Low-Molecular-Weight Theranostic Radiotracers. *J Nucl Med* (2017) 58(Suppl 2):17s–26s. doi: 10.2967/jnumed.116.186775
  29. Jochumsen MR, Dias AH, Bouchelouche K. Benign Traumatic Rib Fracture: A Potential Pitfall on 68Ga-Prostate-Specific Membrane Antigen PET/CT for Prostate Cancer. *Clin Nucl Med* (2018) 43(1):38–40. doi: 10.1097/rlu.0000000000001871
  30. Wang ZJ, Webb EM, Westphalen AC, Coakley FV, Yeh BM. Multi-detector row computed tomographic appearance of celiac ganglia. *J Comput Assist Tomogr* (2010) 34(3):343–7. doi: 10.1097/RCT.0b013e3181d26ddd

**Conflict of Interest:** The authors declare that the research was conducted in the absence of any commercial or financial relationships that could be construed as a potential conflict of interest.

Copyright © 2021 Zhou, Li, Jiang, Wang, Chen, Shen, You, Lu, Liao, Li and Cheng. This is an open-access article distributed under the terms of the Creative Commons Attribution License (CC BY). The use, distribution or reproduction in other forums is permitted, provided the original author(s) and the copyright owner(s) are credited and that the original publication in this journal is cited, in accordance with accepted academic practice. No use, distribution or reproduction is permitted which does not comply with these terms.



# Comparison of Radiomic Models Based on Low-Dose and Standard-Dose CT for Prediction of Adenocarcinomas and Benign Lesions in Solid Pulmonary Nodules

Jieke Liu<sup>†</sup>, Hao Xu<sup>†</sup>, Haomiao Qing, Yong Li, Xi Yang, Changjiu He, Jing Ren and Peng Zhou<sup>\*</sup>

Department of Radiology, Sichuan Cancer Hospital & Institute, Sichuan Cancer Center, School of Medicine, University of Electronic Science and Technology of China, Chengdu, China

## OPEN ACCESS

### Edited by:

Min Wu,  
Sichuan University, China

### Reviewed by:

Yang Hai,  
Thomas Jefferson University,  
United States  
Jianying Wang,  
Sichuan University, China

### \*Correspondence:

Peng Zhou  
penghyzhou@126.com

<sup>†</sup>These authors have contributed  
equally to this work

### Specialty section:

This article was submitted to  
Cancer Imaging and  
Image-directed Interventions,  
a section of the journal  
Frontiers in Oncology

**Received:** 27 November 2020

**Accepted:** 14 December 2020

**Published:** 02 February 2021

### Citation:

Liu J, Xu H, Qing H, Li Y, Yang X,  
He C, Ren J and Zhou P (2021)  
Comparison of Radiomic Models  
Based on Low-Dose and  
Standard-Dose CT for Prediction of  
Adenocarcinomas and Benign Lesions  
in Solid Pulmonary Nodules.  
Front. Oncol. 10:634298.  
doi: 10.3389/fonc.2020.634298

**Objectives:** This study aimed to develop radiomic models based on low-dose CT (LDCT) and standard-dose CT to distinguish adenocarcinomas from benign lesions in patients with solid solitary pulmonary nodules and compare the performance among these radiomic models and Lung CT Screening Reporting and Data System (Lung-RADS). The reproducibility of radiomic features between LDCT and standard-dose CT were also evaluated.

**Methods:** A total of 141 consecutive pathologically confirmed solid solitary pulmonary nodules were enrolled including 50 adenocarcinomas and 48 benign nodules in primary cohort and 22 adenocarcinomas and 21 benign nodules in validation cohort. LDCT and standard-dose CT scans were conducted using same acquisition parameters and reconstruction method except for radiation dose. All nodules were automatically segmented and 104 original radiomic features were extracted. The concordance correlation coefficient was used to quantify reproducibility of radiomic features between LDCT and standard-dose CT. Radiomic features were selected to build radiomic signature, and clinical characteristics and radiomic signature were combined to develop radiomic nomogram for LDCT and standard-dose CT, respectively. The performance of radiomic models and Lung-RADS was assessed by area under curve (AUC) of receiver operating characteristic curve, sensitivity, and specificity.

**Results:** Shape and first order features, and neighboring gray tone difference matrix features were highly reproducible between LDCT and standard-dose CT. No significant differences of AUCs were found among radiomic signature and nomogram of LDCT and standard-dose CT in both primary and validation cohort (0.915 vs. 0.919 vs. 0.898 vs. 0.909 and 0.976 vs. 0.976 vs. 0.985 vs. 0.987, respectively). These radiomic models had higher specificity than Lung-RADS (all correct  $P < 0.05$ ), while there were no significant differences of sensitivity between Lung-RADS and radiomic models.

**Conclusions:** The diagnostic performance of LDCT-based radiomic models to differentiate adenocarcinomas from benign lesions in solid pulmonary nodules were equivalent to that of standard-dose CT. The LDCT-based radiomic model with higher specificity and lower false-positive rate than Lung-RADS might help reduce overdiagnosis and overtreatment of solid pulmonary nodules in lung cancer screening.

**Keywords:** radiomics, low-dose computed tomography, lung cancer screening, lung adenocarcinoma, benign lesion, solid pulmonary nodule

## INTRODUCTION

Lung cancer is the leading cause of cancer-related death worldwide (1–3). Low-dose computed tomography (LDCT) has been widely recommended for lung cancer screening as it can reduce the mortality (4, 5), but concerns about the high false-positive rate of diagnosis and the following overtreatment are also emerging (4, 6–8). Radiomics, *via* high-throughput extraction of features from imaging data, has been applied to risk prediction, diagnostic discrimination, and disease progression, and improves decision-making in oncology (9–11). In recent years, a large number of studies build radiomic models using either LDCT (12–17) or standard-dose CT data (18–20) to predict malignancy of solitary pulmonary nodules, however, one key question that remains unanswered is whether the performance of LDCT-based radiomic model and underlying significant features are equivalent to that of standard-dose CT.

Concurrent with the recent prosperities on radiomics, the effect of scan acquisition parameters on the reproducibility of quantitative radiomic features aroused concerns of researchers. Studies in phantom and *in vivo* demonstrated that scanner variability, radiation dose, reconstruction method, and slice thickness did affect the quantification of many radiomic features (21–25). Therefore, the LDCT-based radiomic model may be not identical to that of standard-dose CT due to radiation dose reduction even though the other acquisition parameters are consistent. To study the effect of radiation dose reduction on radiomic features *in vivo*, Lo et al. applied the noise addition methods to simulate dose reduction conditions (22), while Solomon et al. repeated scan with half standard dose (23). Their results indicated some texture features were not reproducible when reducing radiation dose. However, the reproducibility of radiomic features of solitary pulmonary nodules between LDCT for lung cancer screening and standard-dose CT examinations remains unaddressed.

Adenocarcinoma is the most prevalent histologic type of lung cancer (26, 27), making it the most common true-positive finding in lung cancer screening (4, 5). Granulomas often appear as spiculated or lobulated solid nodules and are fluorodeoxyglucose avid, and therefore mimic invasive adenocarcinomas, representing the most confounding false-positive findings in lung cancer screening (4, 28). Many investigators attempted to distinguish granulomas from adenocarcinomas using radiomic features (29–33), but none of them used low-dose acquisition parameters. Besides, the radiomic model without including non-specific inflammation, hamartoma, and other benign lesions might limit its utility in lung cancer screening.

Thus, the present study aimed to develop radiomic models based on LDCT and standard-dose CT from same subjects to distinguish adenocarcinomas from benign lesions in patients with solid solitary pulmonary nodules and compare the performance among these radiomic models and Lung CT Screening Reporting and Data System (Lung-RADS). We also assessed the reproducibility of radiomic features of solid solitary pulmonary nodules between LDCT and standard-dose CT examinations.

## MATERIALS AND METHODS

### Pulmonary Nodules

This study was approved by the Institutional Review Board and the requirement for informed consent was waived as the data were analyzed retrospectively and anonymously.

A total of 141 solid solitary pulmonary nodules (72 adenocarcinomas and 69 benign nodules) were consecutively included in this study from April 2019 and May 2020, according to the following inclusion criteria: 1) detection of solid solitary pulmonary nodule without calcification for typical benign lesion; 2) LDCT obtained from lung cancer screening; 3) standard-dose CT obtained within 24 h after LDCT to evaluate hilar and mediastinal lymph nodes; 4) pathologically confirmed. The exclusion criteria were as follows: 1) history of cancer in previous 5 years; 2) images of poor quality with respiratory and movement artifacts; 3) nodules with undefined border resulting in poor segmentation.

We divided the nodules into two independent cohorts according to a ratio of 7:3 and the date of inclusion. Fifty adenocarcinomas and 48 benign nodules enrolled between April 2019 and November 2019 constituted the primary cohort, and 22 adenocarcinomas and 21 benign nodules enrolled between November 2019 and May 2020 constituted the validation cohort. The radiologist (HQ, with 7 years of experience in thoracic radiology) who was blinded to the final diagnosis performed categorization on nodules according to Lung-RADS (34).

### Image Acquisition

All LDCT and standard-dose CT scans were performed on a 256-slice multi-detector CT scanner (Brilliance iCT, Philips Healthcare, Amsterdam, Netherlands), using the following acquisition parameters: tube voltage of 100 kV and tube current of 20 or 30 mAs for LDCT, tube voltage of 120 kV and

tube current of 100 to 250 mAs for standard-dose CT, standard resolution mode, detector collimation of  $128 \times 0.625$  mm, helical pitch of 0.915, and gantry rotation time of 0.4 s. All the raw datasets were then reconstructed using the hybrid iterative reconstruction method (iDose4, level 6, Philips Healthcare, Amsterdam, Netherlands) with standard reconstruction filter for body, slice thickness of 0.625 mm, slice increment of 0.625 mm, field of view of  $350 \text{ mm} \times 350 \text{ mm}$ , and matrix of  $1,024 \times 1,024$ . The estimated effective dose of LDCT scan for all subjects was  $0.68 \pm 0.11$  mSv (range from 0.40 to 0.93).

## Segmentation and Radiomic Features Extraction

All target nodules were automatically detected and segmented using uAI platform (United Imaging Healthcare, Shanghai, China), an artificial intelligence software basing on deep learning method (35, 36). No manual adjustments of the segmentation results were performed to avoid inter-observer and intra-observer variability. The representative segmentation results were shown in **Figure 1**. A total of 104 original radiomic features, including first order, shape, and texture features, were extracted from the target nodules using an open-source Python package (PyRadiomics, version 3.0, <https://pyradiomics.readthedocs.io>) (37). Further details of radiomic features are provided in the **Supplementary Material**.

## Quantifying Feature Reproducibility

The concordance correlation coefficient (CCC) was used to quantify reproducibility of extracted radiomic features between LDCT and standard-dose CT in the combined primary and validation cohorts (38). A radiomic feature with  $\text{CCC} \geq 0.90$  was then defined as a reproducible feature, as previously described (39–41). The percentage of features in each category with a CCC of  $\geq 0.85$ ,  $\geq 0.90$ , and  $\geq 0.95$  was calculated, respectively.

## Feature Selection and Radiomic Signature Construction

Features were standardized using z-score normalization and then selected to build radiomic signature in the primary cohort of LDCT and standard-dose CT dataset respectively. Firstly, the Mann-Whitney U test was employed to select the features that were statistically different between groups (unadjusted  $P < 0.05$ ), as the quantitative radiomic features did not have a normal distribution. Secondly, Spearman correlation analysis and minimum redundancy-maximum relevance (mRMR) (42) were sequentially conducted to exclude redundant radiomic features. Highly correlated features (Spearman correlation coefficient  $> 0.9$ ) were excluded and the top ranked 10 features were reserved. Thirdly, the least absolute shrinkage and selection operator (LASSO) method was used to select the most predictive features from the primary cohort (43). Finally, multivariate logistic regression with backward stepwise selection was applied to construct radiomic score (Rad-score), in which the stopping rule

was the likelihood ratio test with Akaike's information criterion (44). Rad-score of each patient in was calculated *via* a linear combination of the selected features and weighted by the respective coefficients.

## Radiomic Nomogram Construction

Independent factors for differentiating adenocarcinomas from benign nodules among Rad-score and clinical variables were identified by inputting significant variables found using univariate logistic regression analysis. Multivariable logistic regression analysis was applied to build radiomic nomogram for LDCT and standard-dose CT respectively, which was a visualized and individual tool that integrated independent factors to predict the probability of adenocarcinoma in the primary cohort.

## Performance of Radiomic Signature and Nomogram

The area under the curve (AUC) of receiver operating characteristic (ROC) curve was determined to evaluate the discrimination performance of the radiomic signature and radiomic nomogram of LDCT and standard-dose CT in both primary and validation cohorts. The sensitivity, specificity, accuracy, positive predictive value (PPV), and negative predictive value (NPV) were also calculated. To evaluate the calibration performance of radiomic nomogram, calibration curves were plotted. The Hosmer-Lemeshow (H-L) test was performed to assess the goodness-of-fit of radiomic nomogram.

## Clinical Utility

Decision curve analyses were conducted to estimate the clinical utility of the radiomic models and Lung-RADS by calculating the net benefits at a range of threshold probabilities in the combined primary and validation cohorts (45).

## Statistical Analysis

Statistical analysis was performed by R software (version 4.0.0, <http://www.r-project.org>), SPSS software (version 19.0, <https://www.ibm.com>), and MedCalc (v. 18.21, <https://www.medcalc.org>). The chi-squared test was used to compare the differences in gender, and group comparisons of age was performed using independent sample t-test.  $P < 0.05$  was considered statistically significant.

The performance of Lung-RADS was also evaluated. The ROC of Lung-RADS was performed in both primary and validation cohorts according to that nodules of category 4A, 4B, and 4X were labeled as malignancy while category 2 and 3 as benign nodules. The corresponding sensitivity, specificity, accuracy, PPV, and NPV were calculated. Then comparisons of AUCs among radiomic models and Lung-RADS were performed using the Delong test in the primary and validation cohorts (46). In these pairwise models with significant difference in AUC, further comparisons of sensitivity and specificity were performed using the McNemar test in the combined cohort (47). Analyses were corrected for multiple comparisons using the false discovery rate (FDR) method (48).



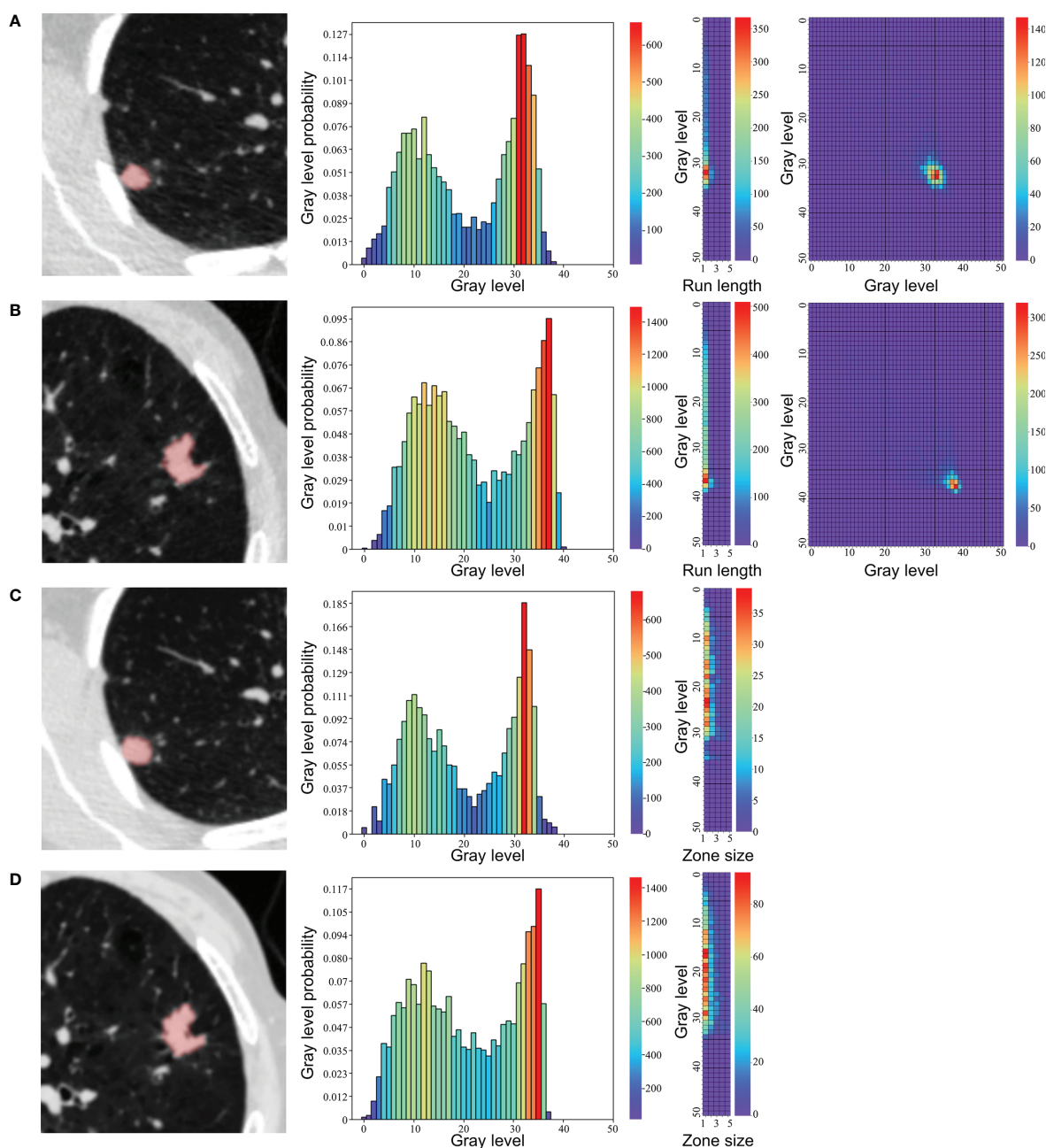


**FIGURE 1** | Representative segmentation results and texture feature maps of nodules. **(A, C)** A 43-year-old female with a granuloma, **(B, D)** A 75-year-old male with an adenocarcinoma. From left to right: **(A, B)** segmentation in low-dose CT, neighboring gray tone difference matrix, gray-level run length matrix, gray-level cooccurrence matrix. **(C, D)** segmentation in standard-dose CT, neighboring gray tone difference matrix, gray level size zone matrix.

## RESULTS

### Clinical Characteristics

The baseline clinical-pathologic characteristics, including gender, age, Lung-RADS category, and histologic subtype of benign nodules in the primary and validation cohorts are listed in **Table 1**. There was no difference in gender between the adenocarcinoma group and the benign group in the primary or

validation cohorts. Significant differences were found in age between the two groups in primary and validation cohorts ( $P = 0.003$  and  $P < 0.0001$ , respectively).

### Feature Reproducibility

The reproducibility of radiomic features between LDCT and standard-dose CT regarding different feature categories is

**TABLE 1 |** Characteristics of adenocarcinomas and benign nodules in the primary and validation cohorts.

Characteristic	Primary cohort (n = 98)			Validation cohort (n = 43)		
	Adenocarcinoma (n = 50)	Benign (n = 48)	P	Adenocarcinoma (n = 22)	Benign (n = 21)	P
Gender			0.69			0.55
Female	22	19		9	11	
Male	28	29		13	10	
Age (years)	61.32 ± 1.30	53.96 ± 1.44	0.0003	65.45 ± 1.70	53.33 ± 1.59	<0.0001
Lung-RADS category						
2, 3	2	27		0	14	
4A, 4B, 4X	48	21		22	7	
Histologic subtype						
Inflammation		17			10	
Granulomas		17			7	
Hamartoma		6			1	
PSP		5			0	
Other benign entities		3			3	

Age is shown in means ± standard deviation, and the other data are the number of nodules. Granulomas are caused by *Mycobacterium tuberculosis*, *Cryptococcus neoformans*, and other unspecified conditions. Other benign entities include intrapulmonary lymph node, fibroplasia, and lymphoid hyperplasia. Lung-RADS, Lung CT Screening Reporting and Data System; PSP, pulmonary sclerosing pneumocytoma.

presented in the **Supplementary Material**. Shape and neighboring gray tone difference matrix (NGTDM) features were most reproducible (100%), followed by first order features (n = 16/18, 89%). Besides, 57% gray-level cooccurrence matrix (GLCM, n = 12/21), 50% gray level size zone matrix (GLSZM, n = 8/16), and 43% gray level dependence matrix (GLDM, n = 6/14) features were reproducible. Gray-level run length matrix (GLRLM) features were least reproducible (n = 5/16, 31%).

## Feature Selection and Radiomic Signature Construction

The process of feature selection is presented in the **Supplementary Material**. Finally, three features in LDCT (GLCM\_DifferenceVariance, GLRLM\_RunEntropy, and NGTDM\_Strength) and two features in standard-dose CT (GLSZM\_ZoneEntropy and NGTDM\_Strength) were selected in the primary cohort. The representative maps of these texture feature were shown in **Figure 1**. The calculation formulas of Rad-score basing on these features with nonzero coefficients are presented in the **Supplementary Material**. Distributions of the Rad-score in the adenocarcinoma and benign groups in the primary and validation cohorts are shown in the **Supplementary Material**.

## Radiomic Nomogram Construction

According to univariate logistic regression analysis, age, Rad\_score of LDCT, and Rad\_score of standard-dose CT were significant independent differentiators of adenocarcinomas and benign nodules (**Table 2**), and they were integrated to develop the radiomic nomograms for predicting the probability of adenocarcinoma of LDCT and standard-dose CT respectively (**Figures 2A, B**). The calculation formulas of radiomic nomogram are presented in the **Supplementary Material**.

## Performance of Radiomic Signature, Radiomic Nomogram, and Lung-RADS

The ROC curves of radiomic models and Lung-RADS are shown in **Figure 3**. The AUC, sensitivity, specificity, accuracy, PPV, and NPV of each model are shown in **Table 3**.

The calibration curves of the radiomics nomogram of LDCT and standard-dose CT for the probability of adenocarcinoma demonstrated good agreement between prediction and observation in the primary and validation cohorts (**Figures 2C, D**). The H-L test yielded non-significant results in the both primary and validation cohorts of LDCT ( $P = 0.650$  and  $0.998$ ) and standard-

**TABLE 2 |** Univariate and multivariate logistic regression analysis of factors for differentiating adenocarcinomas from benign nodules in the primary cohort.

Variables		Odds ratio	95% confidence interval	P
Univariate logistic regression				
Age		1.085	1.035–1.137	0.0008
Gender		1.199	0.537–2.680	0.658
Rad_score of low-dose CT		2.718	1.718–4.302	<0.0001
Rad_score of standard-dose CT		2.718	1.785–4.410	<0.0001
Multivariate logistic regression				
Low-dose CT	Rad_score	2.601	1.643–4.118	<0.0001
	Age	1.052	0.990–1.117	0.104
Standard-dose CT	Rad_score	2.638	1.713–4.061	0.088
	Age	1.053	0.992–1.118	<0.0001

Rad\_score, radiomic score.

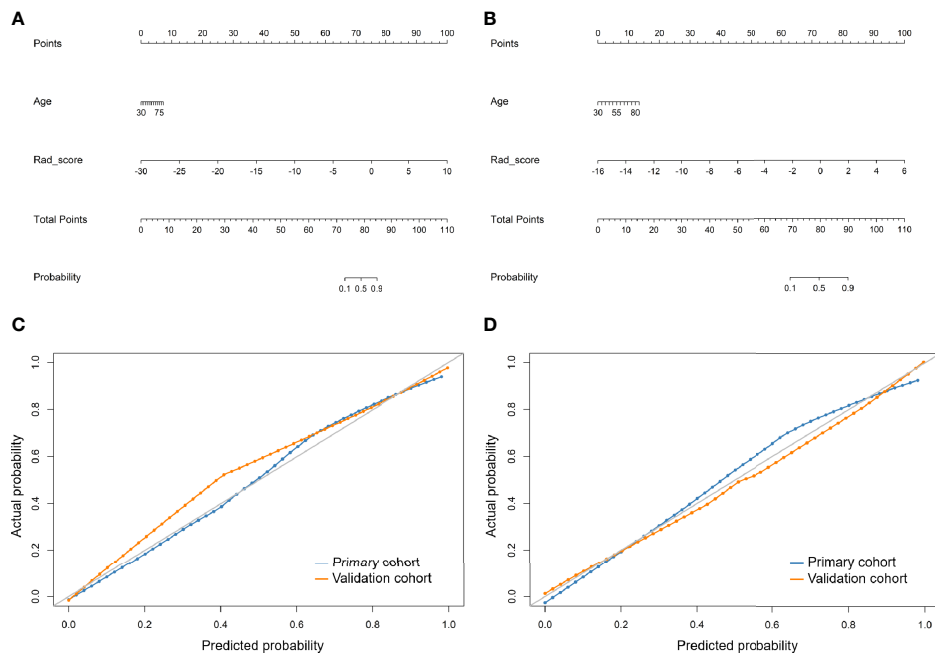


**FIGURE 2 |** Developed radiomic nomograms and calibration curves for predicting the probability of adenocarcinoma. **(A)** Radiomic nomogram of low-dose CT. **(B)** Radiomic nomogram of standard-dose CT. **(C)** Calibration curve of radiomic nomogram of low-dose CT. **(D)** Calibration curve of radiomic nomogram of standard-dose CT. Rad\_score, radiomic score.

dose CT ( $P = 0.151$  and  $0.988$ ), which suggested no departure from a perfect fit.

According to the DeLong test, the AUCs of the radiomic models were higher than that of Lung-RADS in the primary and validation cohorts (all correct  $P < 0.05$ ), while there were no significant differences among the radiomic models (Table 4). The McNemar test results further showed the radiomic models had higher specificity than Lung-RADS in the combined cohort (all correct  $P < 0.05$ ), while there were no significant differences of sensitivity between Lung-RADS and radiomic models (Table 5).

## Clinical Utility

The results of decision curve analyses for the radiomic models and Lung-RADS are presented in Figure 4. The decision curves showed that the model of radiomic signature of low-dose CT, radiomic nomogram of low-dose CT, radiomic signature of standard-dose CT, and radiomic nomogram of standard-dose CT added more net benefit than Lung-RADS in differentiating adenocarcinomas from benign nodules within the range of the threshold probability of 0.02 to 0.84, 0.02 to 0.85, 0.02 to 0.74, and 0.02 to 0.79, respectively.

## DISCUSSION

In the present study, we investigated the ability of radiomic models based on LDCT and standard-dose CT to distinguish adenocarcinomas from benign lesions in patients with solid solitary pulmonary nodules. We found the AUCs of LDCT-based radiomic

models were equivalent to that of standard-dose CT. All the radiomic models showed higher specificity than the Lung-RADS approach, which was consistent with previous report (12, 17). We also assessed the reproducibility of radiomic features of solid solitary pulmonary nodules between LDCT and standard-dose CT examinations *in vivo*. Generally, shape and first order features were more reproducible than texture features except for NGTDM features.

Radiologists usually stratify pulmonary nodules in lung cancer screening by interpreting characteristics such as location, attenuation, diameter, volume, and margin. The differential diagnosis of solitary solid nodules may be more difficult than that of sub-solid nodules. More than 90% of pathologically confirmed sub-solid nodules were malignant in China (49), while the malignancy rate of solid nodules was 66.6% in previous study (50) and 51.1% in our study. Several possible reasons may lead to the overtreatment of solid nodules in China. First, with high tuberculosis incidence in this country, indeterminate solid nodules caused by granulomas or other inflammations were usually larger than 8 mm with irregular shape and border. These benign nodules had overlapping characteristics with adenocarcinomas in location, size, and morphology (51–53). Thus, the Lung-RADS categorization of these benign nodules were equal to or beyond 4A, resulting in low specificity. The radiomic models developed in this study had higher specificity and lower false-positive rate in distinguishing adenocarcinomas from benign lesions than the Lung-RADS, and they might help clinicians avoid choosing too aggressive approach. Second, 41 of 69 benign nodules in this study were categorized as Lung-RADS 2 or 3, and they were all pathologically confirmed by surgery. The result indicated the great fear of missing malignant

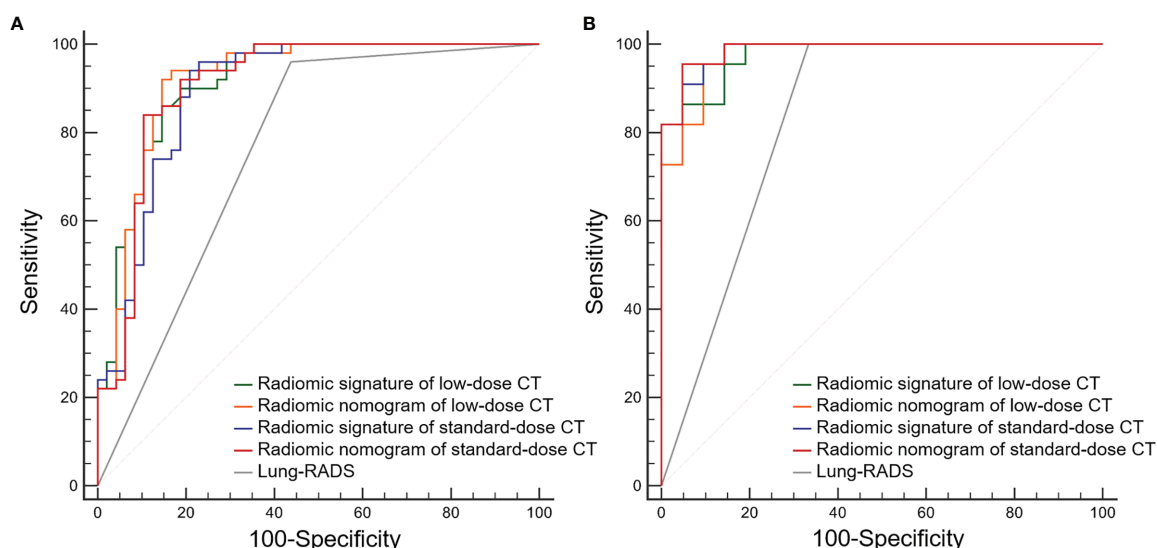


**FIGURE 3 |** Receiver operating characteristic (ROC) curves of the radiomic models and Lung CT Screening Reporting and Data System (Lung-RADS) for differentiating adenocarcinomas from benign nodules. **(A)** Primary cohort. **(B)** Validation cohort.

**TABLE 3 |** Diagnostic performance the radiomic signature and radiomic nomogram of low-dose CT and standard-dose CT, and Lung-RADS for differentiating adenocarcinomas from benign nodules in the primary and validation cohorts.

	AUC (95% CI)	Sensitivity	Specificity	Accuracy	PPV	NPV
Primary cohort						
Radiomic signature of low-dose CT	0.915 (0.859–0.972)	0.860 (43/50)	0.854 (41/48)	0.857 (84/98)	0.860 (43/50)	0.854 (41/48)
Radiomic nomogram of low-dose CT	0.919 (0.861–0.977)	0.920 (46/50)	0.854 (41/48)	0.888 (87/98)	0.868 (46/53)	0.911 (41/45)
Radiomic signature of standard-dose CT	0.898 (0.833–0.963)	0.940 (47/50)	0.792 (38/48)	0.867 (85/98)	0.825 (47/57)	0.927 (38/41)
Radiomic nomogram of standard-dose CT	0.909 (0.946–0.972)	0.840 (42/50)	0.896 (43/48)	0.867 (85/98)	0.894 (42/47)	0.843 (43/51)
Lung-RADS	0.761 (0.685–0.837)	0.960 (48/50)	0.562 (27/48)	0.765 (75/98)	0.696 (48/69)	0.931 (27/29)
Validation cohort						
Radiomic signature of low-dose CT	0.976 (0.944–1.000)	0.864 (19/22)	0.857 (18/21)	0.860 (37/43)	0.864 (19/22)	0.857 (18/21)
Radiomic nomogram of low-dose CT	0.976 (0.941–1.000)	0.909 (20/22)	0.905 (19/21)	0.907 (39/43)	0.909 (20/22)	0.905 (19/21)
Radiomic signature of standard-dose CT	0.985 (0.960–1.000)	0.955 (21/22)	0.905 (19/21)	0.930 (40/43)	0.913 (21/23)	0.950 (19/20)
Radiomic nomogram of standard-dose CT	0.987 (0.965–1.000)	0.909 (20/22)	0.952 (20/21)	0.930 (40/43)	0.952 (20/21)	0.909 (20/22)
Lung-RADS	0.833 (0.730–0.937)	1.000 (22/22)	0.667 (14/21)	0.837 (36/43)	0.759 (22/29)	1.000 (14/14)

Unless otherwise specified, numbers in the parentheses were used to calculate percentages. Lung-RADS, Lung CT Screening Reporting and Data System; AUC, area under curve; CI, confidence interval; PPV, positive predictive value; NPV, negative predictive value.

nodules for both patients and surgeons in China, especially in the cancer hospital. Because the medical environment of China tends to favor cautiousness from both patients and clinicians (54).

This study also addressed a very important question that radiomic models based on LDCT and standard-dose CT had equivalent diagnostic performance to differentiate adenocarcinomas from benign lesions in solid nodules. NGTDM\_Strength was highly reproducible and thus the common significant texture feature

related to benign nodules in both LDCT and standard-dose CT models. Higher value of NGTDM\_Strength indicates an image with slower change in intensity but larger coarse differences in gray level intensities. It suggested benign nodules were more homogeneous than adenocarcinomas. Besides, the other significant texture features related to adenocarcinomas included GLCM\_DifferenceVariance and GLRLM\_RunEntropy in LDCT model and GLSZM\_Zone Entropy in standard-dose CT model. They all indicated that



**TABLE 4** | Comparisons of area under the curves among the radiomic models and Lung-RADS in the primary and validation cohorts.

Pairwise comparison	Primary cohort		Validation cohort	
	Z	P	Z	P
Lung-RADS vs. Radiomic signature of low-dose CT	4.012	0.0001*	2.643	0.0082*
Lung-RADS vs. Radiomic nomogram of low-dose CT	4.123	<0.0001*	2.679	0.0074*
Lung-RADS vs. Radiomic signature of standard-dose CT	3.329	0.0009*	2.732	0.0063*
Lung-RADS vs. Radiomic nomogram of standard-dose CT	3.713	0.0002*	2.798	0.0051*
Radiomic signature of low-dose CT vs. Radiomic nomogram of low-dose CT	0.354	0.7236	<0.001	0.999
Radiomic signature of low-dose CT vs. Radiomic signature of standard-dose CT	1.058	0.2903	0.707	0.4794
Radiomic signature of low-dose CT vs. Radiomic nomogram of standard-dose CT	0.385	0.7003	0.928	0.3534
Radiomic nomogram of low-dose CT vs. Radiomic signature of standard-dose CT	1.037	0.2998	0.599	0.5492
Radiomic nomogram of low-dose CT vs. Radiomic nomogram of standard-dose CT	0.663	0.5075	0.841	0.4003
Radiomic signature of standard-dose CT vs. Radiomic nomogram of standard-dose CT	1.019	0.3084	0.402	0.6877

\*Differences are significant at  $P < 0.05$  corrected with false discovery rate. Lung-RADS, Lung CT Screening Reporting and Data System.

**TABLE 5** | Comparisons of sensitivity and specificity between Lung-RADS and radiomic models in the combined cohort.

Pairwise comparison	Sensitivity		Specificity	
	$\chi^2$	P	$\chi^2$	P
Lung-RADS vs. Radiomic signature of low-dose CT	4.900	0.0269	12.042	0.0005*
Lung-RADS vs. Radiomic nomogram of low-dose CT	0.167	0.6831	9.375	0.0022*
Lung-RADS vs. Radiomic signature of standard-dose CT	1.500	0.2207	14.087	0.0002*
Lung-RADS vs. Radiomic nomogram of standard-dose CT	4.900	0.0269	16.962	<0.0001*

\*Differences are significant at  $P < 0.05$  corrected with false discovery rate. Lung-RADS, Lung CT Screening Reporting and Data System.

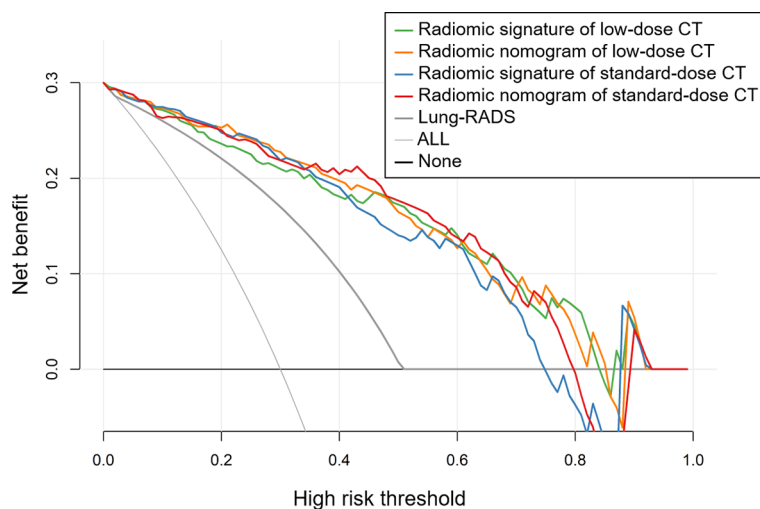


**FIGURE 4** | Decision curves of the radiomic models and Lung CT Screening Reporting and Data System (Lung-RADS). The decision curves showed that the model of radiomic signature of low-dose CT, radiomic nomogram of low-dose CT, radiomic signature of standard-dose CT, and radiomic nomogram of standard-dose CT added more net benefit than Lung-RADS in differentiating adenocarcinomas from benign nodules within the range of the threshold probability of 0.02 to 0.84, 0.02 to 0.85, 0.02 to 0.74, and 0.02 to 0.79, respectively.

adenocarcinomas had more heterogeneity than benign nodules in the texture patterns. The shape and first order features, representing the morphology and attenuation characteristics, were highly reproducible as radiation dose changed. However, they were not included in LDCT or standard-dose CT models, suggesting the deficiency of traditional image features to stratify the indeterminate solid nodules.

We acknowledged several limitations in this study. First, this was a single-center retrospective study with relatively small sample size. The advantage was the standardization of acquisition parameters, avoiding potential confounding variability caused by heterogeneous parameters and image preprocessing (21, 25). Further multi-center study with larger datasets is needed to validate the reported radiomic models. Second, only pathologically confirmed nodules

were enrolled and nodules with undefined border resulting in poor segmentation were excluded, leading to potential selection bias. Third, nodule segmentation was performed with an artificial intelligence software basing on deep learning method and the underlying parameters were inherently in black box. The advantage of automatic segmentation method was high reproducibility, avoiding inter-observer and intra-observer variability that resulting from manual segmentation.

In conclusion, the diagnostic performance of radiomic models based on LDCT and standard-dose CT to differentiate adenocarcinomas from benign lesions in solid pulmonary nodules were equivalent. These radiomic models had higher specificity and lower false-positive rate than Lung-RADS. The LDCT-based radiomic model might be an effective tool for reducing overdiagnosis and overtreatment of solid pulmonary nodules in lung cancer screening.

## DATA AVAILABILITY STATEMENT

The original contributions presented in the study are included in the article/**Supplementary Material**. Further inquiries can be directed to the corresponding author.

## ETHICS STATEMENT

The studies involving human participants were reviewed and approved by the Ethics Review Board of Sichuan Cancer Hospital

& Institute, School of Medicine, University of Electronic Science and Technology of China. Written informed consent for participation was not required for this study in accordance with the national legislation and the institutional requirements.

## AUTHOR CONTRIBUTIONS

JL, JR, and PZ conceived and designed the study. HQ, YL, XY, and CH collected the data. JL and HX analyzed the data and drafted the manuscript. All authors reviewed the manuscript and PZ revised the final manuscript. HQ and PZ provided funding for the study. All authors contributed to the article and approved the submitted version.

## FUNDING

This study was supported by Sichuan Science and Technology Program (grant numbers 2019YJ0585, 2021YFS0075) and Chengdu Science and Technology Program (grant number 2018-YF05-01134-SN).

## SUPPLEMENTARY MATERIAL

The Supplementary Material for this article can be found online at: <https://www.frontiersin.org/articles/10.3389/fonc.2020.634298/full#supplementary-material>

## REFERENCES

1. Siegel RL, Miller KD, Jemal A. Cancer statistics, 2020. *CA Cancer J Clin* (2020) 70(1):7–30. doi: 10.3322/caac.21590
2. GBD Causes of Death Collaborators. Global, regional, and national age-sex-specific mortality for 282 causes of death in 195 countries and territories, 1980–2017: a systematic analysis for the Global Burden of Disease Study 2017. *Lancet* (2018) 392(10159):1736–88. doi: 10.1016/S0140-6736(18)32203-7
3. Gao S, Li N, Wang S, Zhang F, Wei W, Li N, et al. Lung Cancer in People's Republic of China. *J Thorac Oncol* (2020) 15(10):1567–76. doi: 10.1016/j.jtho.2020.04.028
4. National Lung Screening Trial Research T, Aberle DR, Adams AM, Berg CD, Black WC, Clapp JD, et al. Reduced lung-cancer mortality with low-dose computed tomographic screening. *N Engl J Med* (2011) 365(5):395–409. doi: 10.1056/NEJMoa1102873
5. de Koning HJ, van der Aalst CM, de Jong PA, Scholten ET, Nackaerts K, Heuvelmans MA, et al. Reduced Lung-Cancer Mortality with Volume CT Screening in a Randomized Trial. *N Engl J Med* (2020) 382(6):503–13. doi: 10.1056/NEJMoa1911793
6. Bach PB, Mirkin JN, Oliver TK, Azzoli CG, Berry DA, Brawley OW, et al. Benefits and harms of CT screening for lung cancer: a systematic review. *JAMA* (2012) 307(22):2418–29. doi: 10.1001/jama.2012.5521
7. Veronesi G, Maisonneuve P, Bellomi M, Rampinelli C, Durli I, Bertolotti R, et al. Estimating overdiagnosis in low-dose computed tomography screening for lung cancer: a cohort study. *Ann Intern Med* (2012) 157(11):776–84. doi: 10.7326/0003-4819-157-11-201212040-00005
8. Patz EF Jr, Pinsky P, Gatsonis C, Sicks JD, Kramer BS, Tammemagi MC, et al. Overdiagnosis in low-dose computed tomography screening for lung cancer. *JAMA Intern Med* (2014) 174(2):269–74. doi: 10.1001/jamainternmed.2013.12738
9. Lambin P, Rios-Velazquez E, Leijenaar R, Carvalho S, van Stiphout RG, Granton P, et al. Radiomics: extracting more information from medical images using advanced feature analysis. *Eur J Cancer* (2012) 48(4):441–6. doi: 10.1016/j.ejca.2011.11.036
10. Gillies RJ, Kinahan PE, Hricak H. Radiomics: Images Are More than Pictures, They Are Data. *Radiology* (2016) 278(2):563–77. doi: 10.1148/radiol.2015151169
11. Lambin P, Leijenaar RTH, Deist TM, Peerlings J, de Jong EEC, van Timmeren J, et al. Radiomics: the bridge between medical imaging and personalized medicine. *Nat Rev Clin Oncol* (2017) 14(12):749–62. doi: 10.1038/nrclinonc.2017.141
12. Hawkins S, Wang H, Liu Y, Garcia A, Stringfield O, Krewer H, et al. Predicting Malignant Nodules from Screening CT Scans. *J Thorac Oncol* (2016) 11(12):2120–8. doi: 10.1016/j.jtho.2016.07.002
13. Paul R, Hawkins SH, Schabath MB, Gillies RJ, Hall LO, Goldgof DB. Predicting malignant nodules by fusing deep features with classical radiomics features. *J Med Imaging (Bellingham)* (2018) 5(1):11021. doi: 10.1117/1.JMI.5.1.011021
14. Choi W, Oh JH, Riyahi S, Liu CJ, Jiang F, Chen W, et al. Radiomics analysis of pulmonary nodules in low-dose CT for early detection of lung cancer. *Med Phys* (2018) 45(4):1537–49. doi: 10.1002/mp.12820
15. Peikert T, Duan F, Rajagopalan S, Karwowski RA, Clay R, Robb RA, et al. Novel high-resolution computed tomography-based radiomic classifier for screen-identified pulmonary nodules in the National Lung Screening Trial. *PLoS One* (2018) 13(5):e0196910. doi: 10.1371/journal.pone.0196910
16. Delzell DAP, Magnuson S, Peter T, Smith M, Smith BJ. Machine Learning and Feature Selection Methods for Disease Classification With Application to Lung Cancer Screening Image Data. *Front Oncol* (2019) 9:1393. doi: 10.3389/fonc.2019.01393
17. Mao L, Chen H, Liang M, Li K, Gao J, Qin P, et al. Quantitative radiomic model for predicting malignancy of small solid pulmonary nodules detected by low-dose CT screening. *Quant Imaging Med Surg* (2019) 9(2):263–72. doi: 10.21037/qims.2019.02.02

18. Chen CH, Chang CK, Tu CY, Liao WC, Wu BR, Chou KT, et al. Radiomic features analysis in computed tomography images of lung nodule classification. *PLoS One* (2018) 13(2):e0192002. doi: 10.1371/journal.pone.0192002
19. Digumarthy SR, Padole AM, Rastogi S, Price M, Mooradian MJ, Sequist LV, et al. Predicting malignant potential of subsolid nodules: can radiomics preempt longitudinal follow up CT? *Cancer Imaging* (2019) 19(1):36. doi: 10.1186/s40644-019-0223-7
20. Xu Y, Lu L, E LN, Lian W, Yang H, Schwartz LH, et al. Application of Radiomics in Predicting the Malignancy of Pulmonary Nodules in Different Sizes. *AJR Am J Roentgenol* (2019) 213(6):1213–20. doi: 10.2214/AJR.19.21490
21. Mackin D, Fave X, Zhang L, Fried D, Yang J, Taylor B, et al. Measuring Computed Tomography Scanner Variability of Radiomics Features. *Invest Radiol* (2015) 50(11):757–65. doi: 10.1097/RLI.0000000000000180
22. Lo P, Young S, Kim HJ, Brown MS, McNitt-Gray MF. Variability in CT lung-nodule quantification: Effects of dose reduction and reconstruction methods on density and texture based features. *Med Phys* (2016) 43(8):4854. doi: 10.1118/1.4954845
23. Solomon J, Mileto A, Nelson RC, Roy Choudhury K, Samei E. Quantitative Features of Liver Lesions, Lung Nodules, and Renal Stones at Multi-Detector Row CT Examinations: Dependency on Radiation Dose and Reconstruction Algorithm. *Radiology* (2016) 279(1):185–94. doi: 10.1148/radiol.2015150892
24. Zhao B, Tan Y, Tsai WY, Qi J, Xie C, Lu L, et al. Reproducibility of radiomics for deciphering tumor phenotype with imaging. *Sci Rep* (2016) 6:23428. doi: 10.1038/srep23428
25. Berenguer R, Pastor-Juan MDR, Canales-Vazquez J, Castro-García M, Villas MV, Mansilla Legorburo F, et al. Radiomics of CT Features May Be Nonreproducible and Redundant: Influence of CT Acquisition Parameters. *Radiology* (2018) 288(2):407–15. doi: 10.1148/radiol.2018172361
26. Lewis DR, Check DP, Caporaso NE, Travis WD, Devesa SS. US lung cancer trends by histologic type. *Cancer* (2014) 120(18):2883–92. doi: 10.1002/cncr.28749
27. Nakamura H, Saji H. Worldwide trend of increasing primary adenocarcinoma of the lung. *Surg Today* (2014) 44(6):1004–12. doi: 10.1007/s00595-013-0636-z
28. Murrmann GB, van Vollenhoven FH, Moodley L. Approach to a solid solitary pulmonary nodule in two different settings—"Common is common, rare is rare". *J Thorac Dis* (2014) 6(3):237–48. doi: 10.3978/j.issn.2072-1439.2013.11.13
29. Dennie C, Thornhill R, Sethi-Virmani V, Souza CA, Bayanati H, Gupta A, et al. Role of quantitative computed tomography texture analysis in the differentiation of primary lung cancer and granulomatous nodules. *Quant Imaging Med Surg* (2016) 6(1):6–15. doi: 10.3978/j.issn.2223-4292.2016.02.01
30. Orooji M, Alilou M, Rakshit S, Beig N, Khorrami MH, Rajiah P, et al. Combination of computer extracted shape and texture features enables discrimination of granulomas from adenocarcinoma on chest computed tomography. *J Med Imaging (Bellingham)* (2018) 5(2):24501. doi: 10.1117/1.JMI.5.2.024501
31. Yang X, He J, Wang J, Li W, Liu C, Gao D, et al. CT-based radiomics signature for differentiating solitary granulomatous nodules from solid lung adenocarcinoma. *Lung Cancer* (2018) 125:109–14. doi: 10.1016/j.lungcan.2018.09.013
32. Beig N, Khorrami M, Alilou M, Prasanna P, Braman N, Orooji M, et al. Perinodular and Intranodular Radiomic Features on Lung CT Images Distinguish Adenocarcinomas from Granulomas. *Radiology* (2019) 290(3):783–92. doi: 10.1148/radiol.2018180910
33. Chen X, Feng B, Chen Y, Liu K, Li K, Duan X, et al. A CT-based radiomics nomogram for prediction of lung adenocarcinomas and granulomatous lesions in patient with solitary sub-centimeter solid nodules. *Cancer Imaging* (2020) 20(1):45. doi: 10.1186/s40644-020-00320-3
34. American College of Radiology. *Lung CT Screening Reporting and Data System (Lung-RADS, Version 1.1)*. (2019). Available at: <https://www.acr.org/Clinical-Resources/Reporting-and-Data-Systems/Lung-Rads>.
35. Mu G, Chen Y, Wu D, Zhan Y, Zhou X, Gao Y. "Relu Cascade of Feature Pyramid Networks for CT Pulmonary Nodule Detection". In: HI Suk, M Liu, P Yan, C Lian, editors. *Machine Learning in Medical Imaging, MLMI 2019. Lecture Notes in Computer Science, vol 11861*. Springer (2019). p. 444–52.
36. Wang Q, Zhou X, Wang C, Liu Z, Huang J, Zhou Y, et al. WGAN-Based Synthetic Minority Over-Sampling Technique: Improving Semantic Fine-Grained Classification for Lung Nodules in CT Images. *IEEE Access* (2019) 7:18450–63. doi: 10.1109/ACCESS.2019.2896409
37. van Griethuysen JJM, Fedorov A, Parmar C, Hosny A, Aucoin N, Narayan V, et al. Computational Radiomics System to Decode the Radiographic Phenotype. *Cancer Res* (2017) 77(21):e104–e7. doi: 10.1158/0008-5472.CAN-17-0339
38. Lin LI. A concordance correlation coefficient to evaluate reproducibility. *Biometrics* (1989) 45(1):255–68. doi: 10.2307/2532051
39. Hunter LA, Krafft S, Stingo F, Choi H, Martel MK, Kry SF, et al. High quality machine-robust image features: identification in nonsmall cell lung cancer computed tomography images. *Med Phys* (2013) 40(12):121916. doi: 10.1118/1.4829514
40. Balagurunathan Y, Kumar V, Gu Y, Kim J, Wang H, Liu Y, et al. Test-retest reproducibility analysis of lung CT image features. *J Digit Imaging* (2014) 27(6):805–23. doi: 10.1007/s10278-014-9716-x
41. Baessler B, Weiss K, Pinto Dos Santos D. Robustness and Reproducibility of Radiomics in Magnetic Resonance Imaging: A Phantom Study. *Invest Radiol* (2019) 54(4):221–8. doi: 10.1097/RLI.0000000000000530
42. Hanchuan P, Fuhui L, Ding C. Feature selection based on mutual information criteria of max-dependency, max-relevance, and min-redundancy. *IEEE Trans Pattern Anal Mach Intell* (2005) 27(8):1226–38. doi: 10.1109/TPAMI.2005.159
43. Sauerbrei W, Royston P, Binder H. Selection of important variables and determination of functional form for continuous predictors in multivariable model building. *Stat Med* (2007) 26(30):5512–28. doi: 10.1002/sim.3148
44. Pan W. Akaike's information criterion in generalized estimating equations. *Biometrics* (2001) 57(1):120–5. doi: 10.1111/j.0006-341x.2001.00120.x
45. Vickers AJ, Cronin AM, Elkin EB, Gonen M. Extensions to decision curve analysis, a novel method for evaluating diagnostic tests, prediction models and molecular markers. *BMC Med Inform Decis Mak* (2008) 8:53. doi: 10.1186/1472-6947-8-53
46. DeLong ER, DeLong DM, Clarke-Pearson DL. Comparing the areas under two or more correlated receiver operating characteristic curves: a nonparametric approach. *Biometrics* (1988) 44(3):837–45. doi: 10.2307/2531595
47. Hawass NE. Comparing the sensitivities and specificities of two diagnostic procedures performed on the same group of patients. *Br J Radiol* (1997) 70(832):360–6. doi: 10.1259/bjr.70.832.9166071
48. Benjamini Y, Hochberg Y. Controlling the False Discovery Rate - a Practical And Powerful Approach To Multiple Testing. *J R Stat Soc Ser B-Methodol* (1995) 57(1):289–300. doi: 10.1111/j.2517-6161.1995.tb02031.x
49. Yang W, Sun Y, Fang W, Qian F, Ye J, Chen Q, et al. High-resolution Computed Tomography Features Distinguishing Benign and Malignant Lesions Manifesting as Persistent Solitary Subsolid Nodules. *Clin Lung Cancer* (2018) 19(1):e75–83. doi: 10.1016/j.clcc.2017.05.023
50. She Y, Zhao L, Dai C, Ren Y, Jiang G, Xie H, et al. Development and validation of a nomogram to estimate the pretest probability of cancer in Chinese patients with solid solitary pulmonary nodules: A multi-institutional study. *J Surg Oncol* (2017) 116(6):756–62. doi: 10.1002/jso.24704
51. Xu DM, van Klaveren RJ, de Bock GH, Leusveld A, Zhao Y, Wang Y, et al. Limited value of shape, margin and CT density in the discrimination between benign and malignant screen detected solid pulmonary nodules of the NELSON trial. *Eur J Radiol* (2008) 68(2):347–52. doi: 10.1016/j.ejrad.2007.08.027
52. Khan AN, Al-Jahdali HH, Irion KL, Arabi M, Koteyar SS. Solitary pulmonary nodule: A diagnostic algorithm in the light of current imaging technique. *Avicenna J Med* (2011) 1(2):39–51. doi: 10.4103/2231-0770.90915
53. Gould MK, Donington J, Lynch WR, Mazzone PJ, Midthun DE, Naidich DP, et al. Evaluation of individuals with pulmonary nodules: when is it lung cancer? Diagnosis and management of lung cancer, 3rd ed: American College of Chest Physicians evidence-based clinical practice guidelines. *Chest* (2013) 143(5 Suppl):e93S–e120S. doi: 10.1378/chest.12-2351

54. Oudkerk M, Liu S, Heuvelmans MA, Walter JE, Field JK. Lung cancer LDCT screening and mortality reduction - evidence, pitfalls and future perspectives. *Nat Rev Clin Oncol* (2020). doi: 10.1038/s41571-020-00432-6

**Conflict of Interest:** The authors declare that the research was conducted in the absence of any commercial or financial relationships that could be construed as a potential conflict of interest.

*Copyright © 2021 Liu, Xu, Qing, Li, Yang, He, Ren and Zhou. This is an open-access article distributed under the terms of the Creative Commons Attribution License (CC BY). The use, distribution or reproduction in other forums is permitted, provided the original author(s) and the copyright owner(s) are credited and that the original publication in this journal is cited, in accordance with accepted academic practice. No use, distribution or reproduction is permitted which does not comply with these terms.*





# The MRI-Visible Nanocomposite Facilitates the Delivery and Tracking of siRNA Loaded DC Vaccine in the Breast Cancer Model

Changqiang Wu<sup>1,2</sup>, Wencheng Zhu<sup>3,4</sup>, Rongrong Jin<sup>3</sup>, Hua Ai<sup>3</sup> and Ye Xu<sup>1\*</sup>

<sup>1</sup> Department of Radiology, Children's Hospital of Chongqing Medical University, National Clinical Research Center for Child Health and Disorders, Ministry of Education Key Laboratory of Child Development and Disorders, Chongqing Key Laboratory of Pediatrics, Chongqing, China, <sup>2</sup> Sichuan Key Laboratory of Medical Imaging and School of Medical Imaging, North Sichuan Medical College, Nanchong, China, <sup>3</sup> National Engineering Research Center for Biomaterials Sichuan University, Chengdu, China, <sup>4</sup> Shanghai Institute of Biochemistry and Cell Biology, Chinese Academy of Sciences, Shanghai, China

## OPEN ACCESS

### Edited by:

Pilar López-Larrubia,  
Consejo Superior de Investigaciones  
Científicas (CSIC), Spain

### Reviewed by:

Afshin Namdar,  
University of Alberta, Canada  
Kun Zheng,  
Peking Union Medical College Hospital  
(CAMS), China

### \*Correspondence:

Ye Xu  
yexu@cqmu.edu.cn

### Specialty section:

This article was submitted to  
Cancer Imaging and  
Image-directed Interventions,  
a section of the journal  
Frontiers in Oncology

Received: 26 October 2020

Accepted: 14 December 2020

Published: 05 February 2021

### Citation:

Wu C, Zhu W, Jin R, Ai H and  
Xu Y (2021) The MRI-Visible  
Nanocomposite Facilitates  
the Delivery and Tracking  
of siRNA Loaded DC Vaccine  
in the Breast Cancer Model.  
Front. Oncol. 10:621642.  
doi: 10.3389/fonc.2020.621642

Dendritic cell (DC) vaccines have recently been developed for the treatment of various cancers but often do not function as well as expected, primarily due to the highly complex *in vivo* immune environment. This proof-of-principle study aimed to test the feasibility of modulating the *in vivo* behaviors of DC vaccines (DCVs) by introducing siRNA-laden magnetic resonance (MR) imaging nanovectors into cells, while providing visible information on their homing to lymph nodes. The N-alkyl-PEI2k-LAC/SPIO nanocomposites were prepared and characterized, showing favorable properties of siRNA transfection and MRI labeling efficiency in DCs. Cell viability assays revealed no observable effects on the survival and phenotype of DCs if the concentration of the complex was within 8  $\mu$ g Fe/ml. An orthotopic mouse model of breast cancer was developed. The DCVs transfected with *IDO* siRNA contained nanocomposites were adoptively transferred to start the treatment. MR imaging clearly visualized the homing of DCVs into lymph nodes. At the end of the treatment, DCVs presented significantly better tumor suppression than DCs or PBS ( $P < 0.05$ ). Generally, the N-alkyl-PEI2k-LAC/SPIO nanocomposites represent a highly efficient MR imaging platform for siRNA transfection that is potentially useful for *in vivo* tracking of vaccine cells.

**Keywords:** dendritic cell, anticancer immunotherapy, gene transfection, nanocomposite, magnetic resonance imaging

## INTRODUCTION

Dendritic cells (DCs) have been recruited as a cellular vaccine for tumor immunotherapy but their performance *in vivo* is generally unsatisfactory (1). Factors such as the weak antigenicity of tumors, failure of vaccine cells to migrate into lymph nodes (LNs) and drive T cell priming, and immune evasion of tumors, *etc.*, are considered the culprits (2). Among these factors, tumor immune evasion may play a key role. Recent studies revealed that up-regulated expression of indoleamine 2, 3-dioxygenase (IDO), a major rate-limiting enzyme of tryptophan catabolism, in DCs would induce

naïve CD4<sup>+</sup> T cells to differentiate into regulatory T cells (Tregs), thus impeding antitumor immunity (3). A small interfering RNA (siRNA) targeting IDO has been transfected into DCs to block the immunosuppression induced by the IDO mRNA, which exhibited potent tumor growth inhibition in animal models (4–6). As a promising RNA interference (RNAi) strategy, it involves the processes of delivering synthetic siRNAs into cells, incorporating these siRNAs into the silencing complex and subsequent degradation of sequence-specific mRNA. Unfortunately, exogenous siRNAs are easily degraded by nuclease *in vivo*, restricting the application of RNAi. Therefore, the preparation of an effective gene delivery system for loading and protecting gene fragments from nuclease damage and for improving gene transfection efficiency is very important (7). Previously, our research group synthesized an aqueous-phase magnetic resonance (MR) nanovector, N-alkyl-PEI2k/SPIO, with superior properties in subsequent experiments for MR imaging and as a nanocarrier for gene transfection (8, 9). Moreover, because the nanocomposites are modified by lactose, they hold superior MR imaging properties, improved biocompatibility by inducing protective autophagy and enhanced therapeutic immune activation of DC (10, 11). This study aimed to employ this lactosylated analog as a gene delivery platform for carrying IDO siRNA to transfect antitumor DC vaccines (DCVs) and to use it for the treatment of orthotopic 4T1 breast cancer in mouse models while using MR imaging to track the *in vivo* homing of DCVs to the draining LNs (**Figure 1**). To our best knowledge, this study utilizes a self-made, MRI-visible gene transfection vector to modulate the anticancer functions of DCVs by gene silencing while tracking their migration *in vivo*. Few studies have been reported on this topic previously.

## MATERIALS AND METHODS

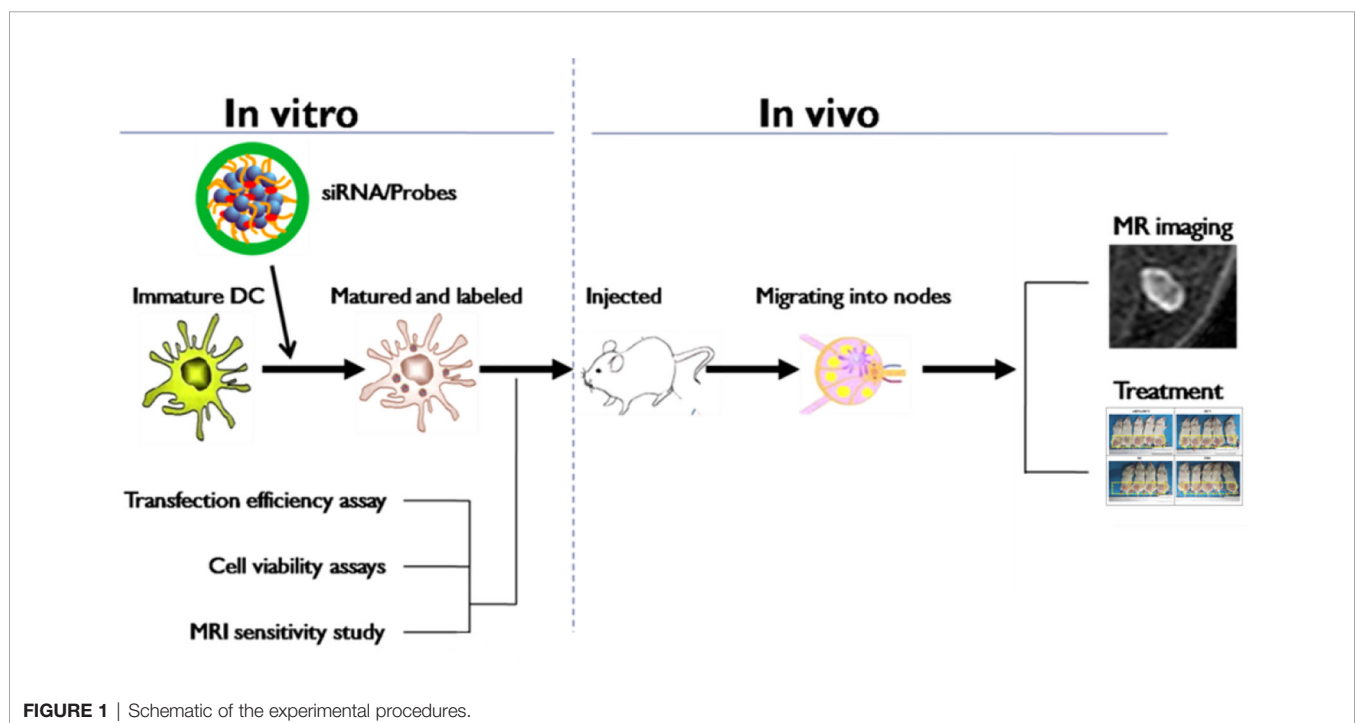
### Preparation of N-alkyl-PEI2k-LAC-Stabilized SPIO Nanoparticles

Branched PEI2k (MW: 2 kD) was reacted with 1-iodododecane as previously reported (8). The product was treated with NaOH and dialyzed against water to obtain N-alkyl-PEI2k upon freeze-drying. The product N-alkyl-PEI2k was dissolved in methanol and added dropwise to a DL-glycidol methanol solution (12). The mixture was stirred for 3 days and dialyzed in water, yielding N-alkyl-PEI2k-LAC.

Hydrophobic SPIO nanoparticles were synthesized using the methods described by Sun et al. (13). After drying under argon gas, SPIO nanoparticles were redispersed in chloroform and mixed with N-alkyl-PEI2k-LAC at a mass ratio of 1:0.6. The mixture was transferred to water under sonication and shaken for 24 h, followed by rotary evaporation to obtain chloroform-free N-alkyl-PEI2k-LAC/SPIO nanocomposites.

### Characterization of N-alkyl-PEI2k-LAC/SPIO Nanocomposites

Water-soluble N-alkyl-PEI2k-LAC/SPIO nanocomposites were characterized using dynamic light scattering (DLS) and electron microscopy (SEM).  $T_2$  relaxation times were measured with a 1.5 T MR system (Siemens Sonata) at room temperature. Briefly, the Fe concentration of the nanocomposites in water was detected using atomic absorption spectrometry; then, gelatin phantoms containing gradient Fe concentrations of the nanocomposite were prepared. The  $T_2$  relaxation time was detected using MR imaging with a spin echo sequence (TR of 5,000 ms, TE ranging from 6 to 500 ms). The relaxivity value ( $r_2$ ) was calculated from a



curve of  $1/T_2$  relaxation time ( $s^{-1}$ ) vs. the iron concentration (mM Fe) (12).

### Characterization of the N-alkyl-PEI2k-LAC/SPIO/siRNA Complex

According to the target gene sequence selection methods described in literature (14), an siRNA targeting the *IDO* mRNA was synthesized by Ruibo Biological Co., Ltd. The antisense strand is 5'GUUCUAGAAGGAUCCUUGA3'. Alkyl-PEI2K-LAC/SPIO was mixed with the siRNA in PBS at different N:P molar ratios (0, 2.5, 5, 7.5, 10, 12.5, and 15, respectively). The complexes were subjected to gel electrophoresis to detect the optimal binding concentration. Then, alkyl-PEI2k-LAC/SPIO and siRNA were mixed at an N:P ratio of five for 20 min. A gradient mass of heparin or serum was separately added to the mixture to test siRNA-release capacity and stability of the complex in serum.

### Preparation of Cells and siRNA-Transfected Dendritic Cell Vaccines

The generation of murine DCs has been described in our previous report (12). Briefly, the bone marrow of Balb/C female mice was washed into RPMI-1640 medium and centrifuged to collect the cell pellet. The cells were cultured in flasks and stimulated with GM-CSF (20 ng/ml). On day 8, the non-adherent population was harvested. LPS (100 ng/ml, Sigma-Aldrich) and TNF- $\alpha$  (20 ng/ml, Peprotech) were added and cells were cultured for another 2 days to obtain mature DCs. The purity of DCs was determined by measuring CD11c expression using fluorescence activated cell sorting (FACS).

The 4T1 cells were cultured in RPMI-1640 medium containing 10% fetal bovine serum and 5% penicillin-streptomycin at 37°C in the presence of 5% CO<sub>2</sub>. Approximately 3 days later, the cells in the logarithmic growth phase were sub-cultured.

Using preparation methods described in the literature (15), the cultured 4T1 breast cancer cells were lysed by subjecting them to six freeze-thaw cycles and a 30 min incubation in a water bath with ultrasound exposure before being passed over a 0.2  $\mu$ m filter on the benchtop to collect the filtrate. On day 8 of culture, DCs were co-incubated with the N-alkyl-PEI2k-LAC/SPIO/siRNA complexes at 6  $\mu$ g Fe/ml for 6 h; the 4T1 lysate was added at a ratio of 3:1 (4T1 cells:DCs) and incubated for 48 h, and then cells were treated with LPS (100 ng/ml) for 12 h before harvest to promote maturation.

### In Vitro Transfection of N-Alkyl-PEI2k-LAC/SPIO/siRNA

FITC-conjugated N-alkyl-PEI2k-LAC/SPIO was mixed with the siRNA at an N:P ratio of five for 20 min to determine if the complexes would be successfully engulfed by the cells. The complexes were collected and added to the culture medium of immature DCs at 6  $\mu$ g Fe/ml. After a 6 h incubation, cells were collected and fixed, incubated with DAPI for 15 min, and then washed with PBS. Fifty microliters of the cell suspension were dropped on a slide for confocal laser scanning microscopy (CLSM). For the analysis of the transfection efficiency, immature DCs were

plated in a 48-well plate at a density of  $2 \times 10^5$  cells/ml; then, N-alkyl-PEI2k-LAC/SPIO/siRNA ( $n = 5$ ) was added at Fe concentrations of 0, 2, 4, 6, 8, 10, and 12  $\mu$ g/ml. After a 6 h incubation the plates were cooled to room temperature, the iron reaction reagent was added, and the absorbance was read at 570 nm using a plate reader (Varioskan Flash, Thermo Scientific). The N-alkyl-PEI2k-LAC/SPIO/siRNA complexes were added to immature DCs at 6  $\mu$ g Fe/ml to determine potential unwanted effects on DCs. Six hours later, the medium was replaced with three volumes of 4T1 breast tumor cell lysate, as described in detail below. After a 48 h incubation, DCVs transfected with N-alkyl-PEI2k-LAC/SPIO/siRNA complexes were obtained. The siRNA-laden DCVs were collected and transferred to a 1.5 ml centrifuge tube, with siRNA-free and immature DCs and siRNA-free DCVs as controls, and then incubated with antibodies to detect the expression of the surface molecular markers MHC-II, CD11c, CD80, CD86, and CCR7 using FACS.

### Western Blotting

On day 8 of culture, DCs were divided into two groups, one was incubated with IFN- $\gamma$  (200 U/ml), LPS (100 ng/ml) and TNF- $\alpha$  (20 ng/ml), and the other was treated only with LPS (100 ng/ml) and TNF- $\alpha$  (20 ng/ml). Forty-eight hours later, the cells were collected for Western blotting to analyze the expression of IDO (16).

### Dendritic Cell Vaccine Treatment Protocols for 4T1 Mice and In Vivo Magnetic Resonance Imaging

After hair removal, the mammary fat pads of 6-week-old Balb/C female mice were injected with  $1 \times 10^6$  4T1 cells. Vaccines were injected using previously reported procedures (17). Briefly, TNF- $\alpha$  (100 ng/ml) was subcutaneously injected into the left posterior footpad of the mice to pre-sensitize the local tissues. After 48 h, PBS, DC, DCV, and *IDO* siRNA-laden DCV were injected at the same sites, respectively. About 100  $\mu$ l of PBS,  $3 \times 10^6$  cells/ft of DC, or  $3 \times 10^6$  cells/ft DCV were injected on the day of tumor inoculation and thereafter repeated once a week for two times. Mice with breast cancer were randomly grouped into four ( $n = 5$  mice per group). The following treatment regimens were planned: (1) PBS injected into the left footpad; (2) N-alkyl-PEI2k-LAC/SPIO DCs, activated by LPS (100 ng/ml) and TNF- $\alpha$  (20 ng/ml), injected into the left footpad; (3) N-alkyl-PEI2k-LAC/SPIO DCVs injected into the left footpad; and (4) *IDO* siRNA-laden DCVs injected into the left footpad. The mice were imaged under a Philips 3.0 T MR scanner using a 25 mm small animal coil at 24 h before and 48 h after each injection. Echoes of popliteal lymph nodes (LNs) were measured primarily using a  $T_2$ -weighted fast spin echo (TSE) sequence (TR = 2300 ms, TE = 121 ms, matrix =  $148 \times 148$ , slice thickness = 0.6/0.0 mm, FOV = 30 mm, flip angle = 90°, NSA = 10).

### Evaluation of the Therapeutic Effects of Indoleamine 2, 3-Dioxygenase siRNA-Laden Dendritic Cell Vaccines on Tumors

After the inoculation of 4T1 cells, the tumor sizes were measured on day 3 and repeated every 3 days thereafter for 4 repeats.

The tumor volume  $S$  was calculated using the formula,  $S = 0.5 \times a^2 \times b$ , where  $a$  represents the short diameter of the tumor and  $b$  represents the long diameter of the tumor (18).

## Statistical Analysis

SPSS 13.0 software was employed for statistical analyses. Independent sample T-test was used to test the statistical significance of differences between two groups, and one-way analysis of variance was used to determine the statistical significance of differences among more groups.  $P < 0.05$  indicates a significant difference.

## RESULTS

### Characterization of the Nanocomposites

The chemical structures of amphiphilic N-alkyl-PEI2k-LAC and N-alkyl-PEI2k were characterized using  $^1\text{H}$  NMR and elemental analysis (Figure 2). N-alkyl-PEI2k:  $^1\text{H}$  NMR (400 MHz,  $\text{CDCl}_3$ )  $\delta$  3.15–2.21 (m,  $-\text{CH}_2\text{CH}_2\text{NH}-$ ,  $-\text{CH}_2\text{CH}_2(\text{CH}_2)_9\text{CH}_3$ ), 1.41 (br,  $-\text{CH}_2\text{CH}_2(\text{CH}_2)_9\text{CH}_3$ ), 1.25 (s,  $-\text{CH}_2\text{CH}_2(\text{CH}_2)_9\text{CH}_3$ ), 0.88 (t,  $-\text{CH}_2(\text{CH}_2)_{10}\text{CH}_3$ ); Elemental analysis: C, 56.489%; N, 19.07%; H, 9.209%. N-alkyl-PEI2k-LAC:  $^1\text{H}$  NMR (300 MHz, DMSO)  $\delta$  4.55–3.21 (m, LAC), 3.19–2.25 (m,  $-\text{CH}_2\text{CH}_2\text{NH}-$ ,  $-\text{CH}_2\text{CH}_2(\text{CH}_2)_9\text{CH}_3$ ), 1.39 (br,  $-\text{CH}_2\text{CH}_2(\text{CH}_2)_9\text{CH}_3$ ), 1.22 (s,  $-\text{CH}_2\text{CH}_2(\text{CH}_2)_9\text{CH}_3$ ), 0.84 (s,  $-\text{CH}_2(\text{CH}_2)_{10}\text{CH}_3$ ). Elemental analysis: C, 46.188%; N, 11.499%; H, 10.223%. Grafting ratio of alkyl and lactose were separately 12.1 and 10.3%, calculated upon elemental analysis results.

The monodisperse SPIO nanocrystals and amphiphilic material (mass ratio: N-alkyl-PEI2k-LAC : SPIO = 0.6) were used to form N-alkyl-PEI2k-LAC/SPIO nanocomposites in the water phase. The nanocomposites dispersed in water stably, with a diameter of  $83.0 \pm 26.5$  nm obtained using DLS (Figure 3). The dry sample presented as spherical particles in SEM images, and SPIO nanocrystals aggregated into nanoclusters in the composites in TEM images (Figure 4). The surface charge of the SPIO nanocomposites remained positive with a zeta potential of  $34.6 \pm 1.1$  mV, a value that is lower than N-alkyl-PEI2k/SPIO nanocomposites (approximately 40 mV), due to lactose partially shielding the positive electric charge on PEI.

Gelatin phantoms containing gradient Fe concentrations of the nanocomposite were detected using spin echo  $T_2$ WI at different echo times with a clinical 1.5 T MR imager at room temperature to measure the  $T_2$  relaxivity of the nanocomposites. Signal intensities (SIs) were acquired to calculate the  $T_2$  relaxivity ( $r_2$ ) of the nanocomposites of  $481.3 \text{ mM}^{-1}\text{s}^{-1}$  (Figure 5).

### Characterization of the N-alkyl-PEI2k-LAC/SPIO/siRNA Complex

N-alkyl-PEI2k-LAC/SPIO was incubated with the siRNA at different N:P molar ratios and then subjected to gel electrophoresis. With the increase in the N:P ratio, siRNA electromigration was increasingly blocked, and electromigration was completely blocked at an N:P ratio  $\geq 5$ . Based on these results, the siRNA was successfully bound to the surface of the nanocomposites (Figure 6A).

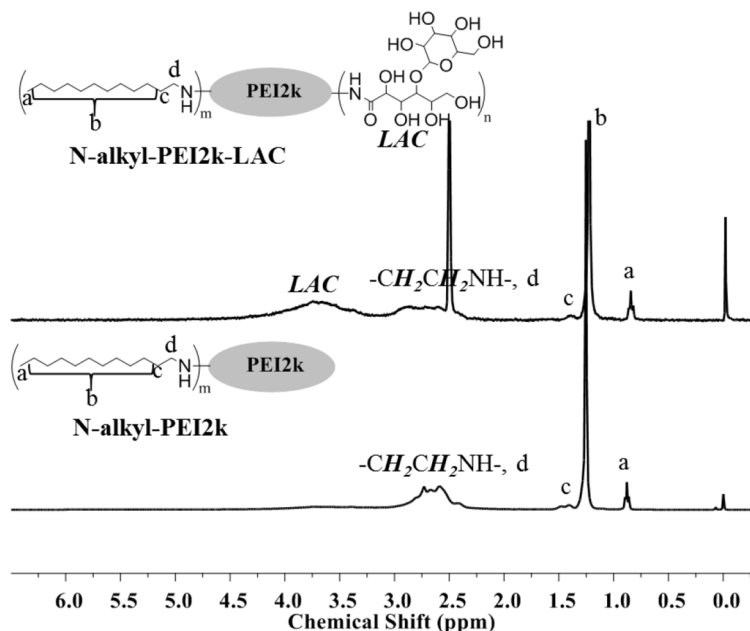
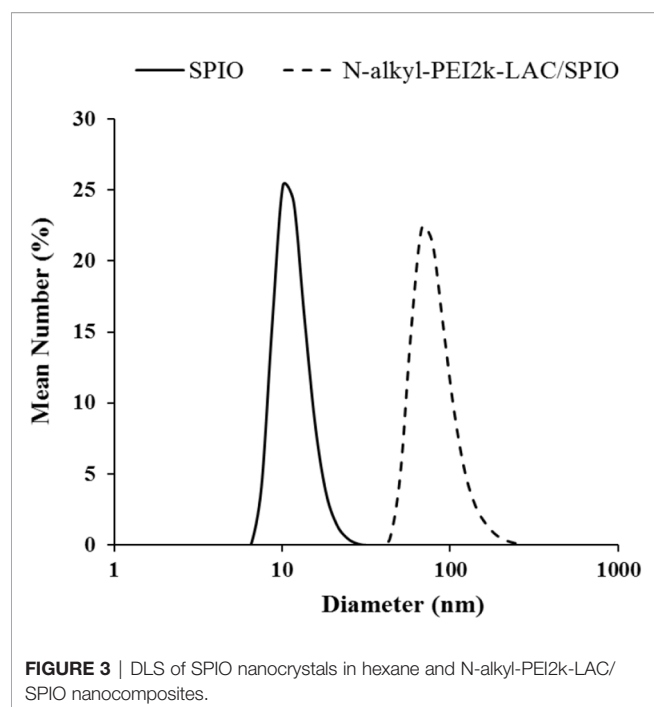


**FIGURE 2** |  $^1\text{H}$ -NMR spectra of N-alkyl-PEI2k-LAC (DMSO) and N-alkyl-PEI2k ( $\text{CDCl}_3$ ).





In a heparin decomplexation assay, N-alkyl-PEI2k-LAC/SPIO/siRNA complexes (N:P = 5) were loaded on agarose gel. The electrophoresis assay showed that the siRNA was released from the complexes when heparin was added. At a heparin: siRNA mass ratio  $\geq 5$ , the released siRNA tended to be stable and its concentration no longer increased (**Figure 6B**).

In a serum stability assay, N-alkyl-PEI2k-LAC/SPIO/siRNA complexes (N:P = 5) and the unbound siRNA were separately incubated with 50% fetal bovine serum (FBS) for different periods. As a result, the siRNA in the complexes was substantially more stable in serum than the unbound siRNA; and even after a 24 h incubation, the siRNA still stably resided on

the nanocomposite surface without observable degradation (**Figure 6C**).

### **In Vitro Transfection of N-alkyl-PEI2k-LAC/SPIO/siRNA**

FITC-conjugated N-alkyl-PEI2k-LAC/SPIO was mixed with the siRNA; then, the complexes were transfected into DCs by coinubation. CLSM revealed clusters of green fluorescent particles around the blue-stained nuclei. Differential interference contrast (DIC) imaging further showed pseudopodia of the cells, suggesting that they are siRNA-laden DCs (**Figure 7**).

The intracellular Fe content was measured using a colorimetric ferrozine assay. DCs took up the N-alkyl-PEI2k-LAC/SPIO/siRNA complexes in a time- and dose-dependent manner (**Figure 8**). After a 6 h incubation, the intracellular Fe content tended to be stable, indicating that at least 6 h is necessary for sufficient transfection. A slightly lower concentration of the N-alkyl-PEI2k-LAC/SPIO/siRNA complexes, 6  $\mu\text{g}$  Fe/ml, was adopted for subsequent *in vivo* studies to ensure ample antigen loading.

The surface phenotype of DCs was detected using a FACS assay to probe possible adverse effects of the transfection process on DC maturation. CD11c is a marker of the purity of DCs. Our culture produced approximately 90% CD11c positive cells. Four other biomarkers, MHC-II, CD80, CD86, and CCR7, showed similar expression on siRNA-laden mature DCs to siRNA-free mature DCs, but the expression of CD80, CD86, and CCR7 was significantly higher than on immature DCs ( $P < 0.05$  for all of them), suggesting the excellent biosafety of transfection (**Figure 9**).

### **Western Blot**

Western blotting was performed on two groups of mature DCs treated with or without IFN- $\gamma$  to analyze the expression of the target protein IDO in DCs. Replicate experiments revealed that IFN- $\gamma$ -induced DCs expressed slightly higher levels of IDO (**Figure 10**).

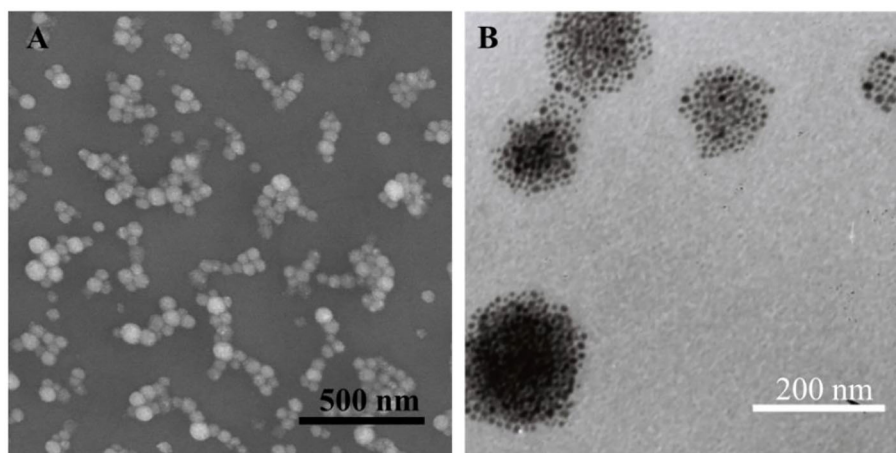


**FIGURE 4** | SEM (A) and TEM (B) images of N-alkyl-PEI2k-LAC/SPIO nanocomposites.

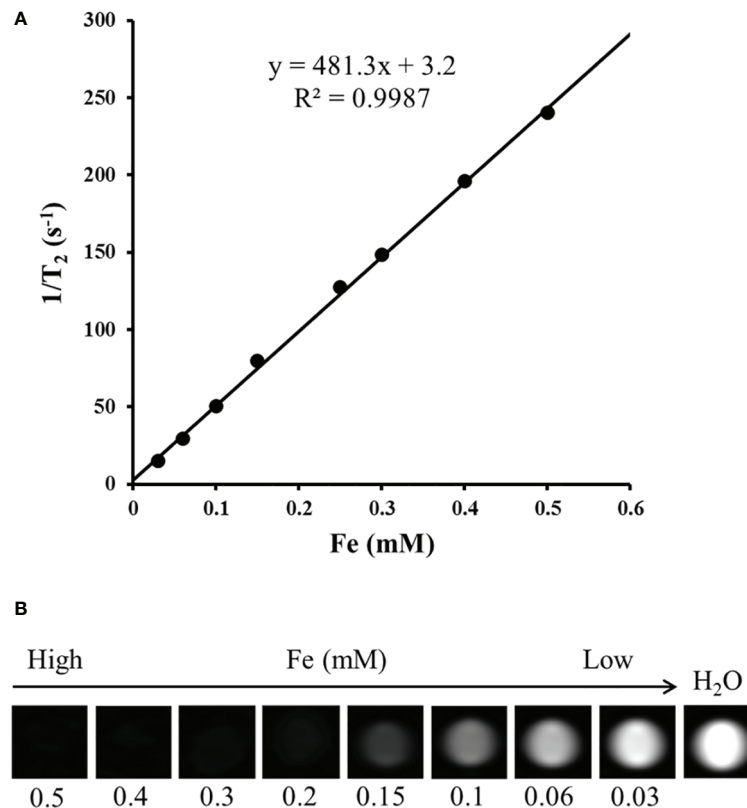


**FIGURE 5** |  $T_2$  relaxation rate as a function of the Fe concentration for N-alkyl-PEI2k-LAC/SPIO nanocomposites at 1.5 T **(A)**;  $T_2$ -weighted MR images of N-alkyl-PEI2k-LAC/SPIO nanocomposites in water **(B)**.

## In Vivo Magnetic Resonance Imaging of Tumors Treated With Indoleamine 2, 3-Dioxygenase siRNA-Laden Dendritic Cell Vaccines

MR imaging was performed to observe whether the injected vaccines migrated to the draining lymph nodes as expected and resulted in changes in SI. MR imaging of bilateral popliteal lymph nodes was performed on the four groups of tumor-bearing mice before and after each footpad injection. Vaccines were injected weekly for three injections, and MR images were correspondingly obtained at two time points, immediately before and 48 h after each injection. Left popliteal nodes of all DC groups were gradually enlarged. In particular, the nodes were strikingly enlarged 1 week after the first injection. On the TSE images captured 48 h after the first injection, the signal was clearly reduced within the nodes' central zone of all DC groups; at 48 h after the second or third injections, a focal signal reduction was still visible, but not as clear as after the first injection (Figure 11).

## Evaluation of the Antitumor Therapeutic Effects

By the end of the experiment, all mice survived, except for one mouse in the N-alkyl-PEI2k-LAC/SPIO DC group that died

unexpectedly. After the inoculation of 4T1 tumor cells, tumor volume was measured and calculated once every 3 days for five measurements. Tumor sizes increased gradually, regardless of treatment with PBS, DC, DCVs or *IDO* siRNA-laden DCVs. Notably, tumors in the PBS group grew the fastest, followed by the tumors in the DC group. Tumors in the two vaccine groups grew at similar rates (Figure 12). The tumor volume was analyzed using ANOVA, and the *IDO* siRNA-laden DCV group had comparable tumor volumes to the DCV group, but significantly larger volumes than the PBS or the DC group ( $P < 0.05$  for both) (Figure 13).

## DISCUSSION

### N-alkyl-PEI2k-LAC/SPIO as Magnetic Resonance Imaging-Visible Gene Nanovector Showed Favorable Properties

This study utilizes lactobionic acid to superficially modify N-alkyl-PEI2k/SPIO. The generated nanocomposites possess favorable physicochemical and MR imaging properties, as confirmed by  $^1\text{H}$  NMR, DLS, SEM and MR imaging. We studied their capabilities of binding or releasing the siRNA, the serum stability of the siRNA in the complexes, gene transfection efficiency, and their effects on DCs to obtain a better

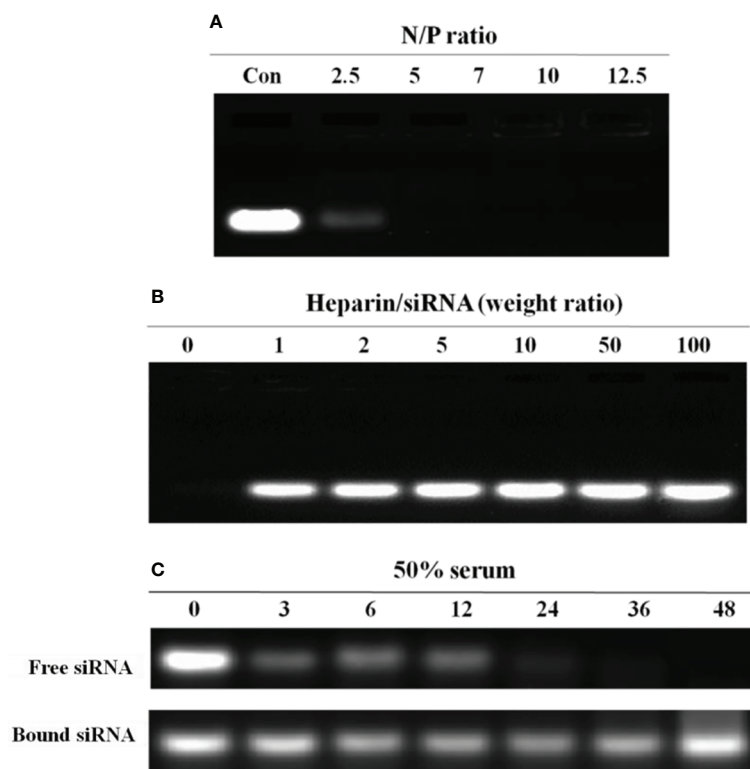


**FIGURE 6** | Agarose gel electrophoresis analysis of the N-alkyl-PEI2k-LAC/SPIO/siRNA complexes. **(A)** At an N:P ratio  $\geq 5$ , the nanocomposites completely bound the siRNA. **(B)** At a heparin/siRNA mass ratio  $\geq 5$ , a substantial amount of the siRNA was released. **(C)** Serum stability of the siRNA bound to or free from N-alkyl-PEI2k-LAC/SPIO. The free siRNA or N-alkyl-PEI2k-LAC/SPIO/siRNA complexes were incubated with 50% serum for the indicated times. Heparin was used to release the bound siRNA from the nanocomposites.

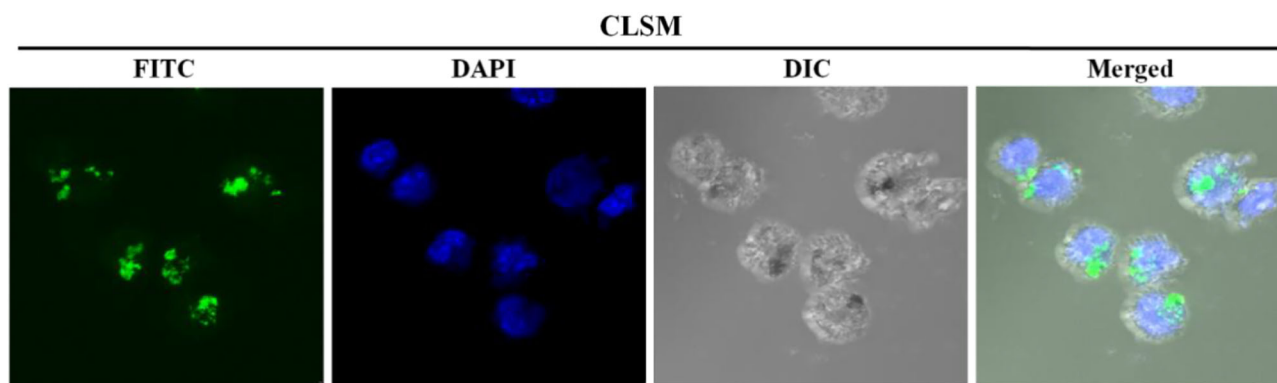


**FIGURE 7** | CLSM images of immature siRNA-laden DC showing clusters of green fluorescent particles around the DAPI blue-stained nuclei. DIC images display the pseudopodia of the cells.

understanding of their biological properties as nanocarriers for gene transfection. Similar to the previously reported N-alkyl-PEI2k/SPIO, at an N:P ratio  $\geq 5$ , N-alkyl-PEI2k-LAC/SPIO almost completely bound the siRNA, suggesting that the lactose modification method has little effect on the ability of

the nanocomplex to bind to siRNA (9, 19). At a heparin/siRNA mass ratio  $\geq 1$ , the siRNA was fully released to silence the target genes. Moreover, a high concentration of the siRNA persisted in serum even at 48 after the interaction with N-alkyl-PEI2k-LAC/SPIO, indicating that the nanocomposites provide reliably

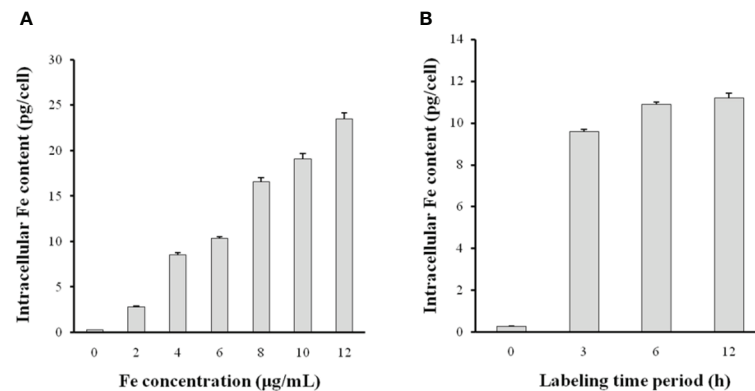


**FIGURE 8** | The siRNA transfection efficiency was altered by the N-alkyl-PEI2k-LAC/SPIO/siRNA concentration (A) and transfection time period (B). Higher concentrations of the complexes or a longer transfection time period increases the Fe content within DCs (n = 5).

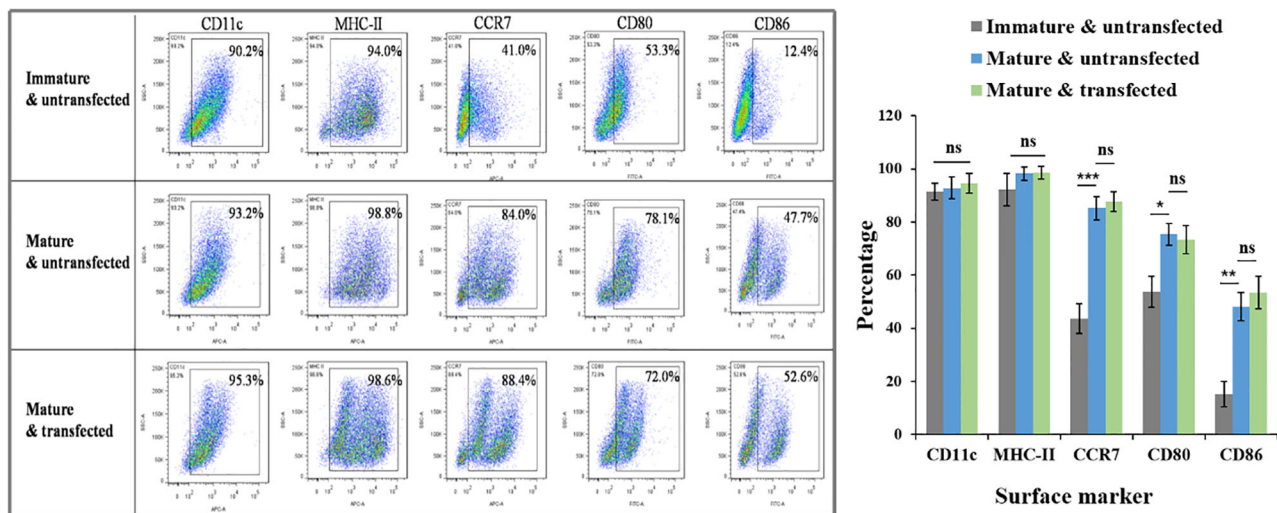
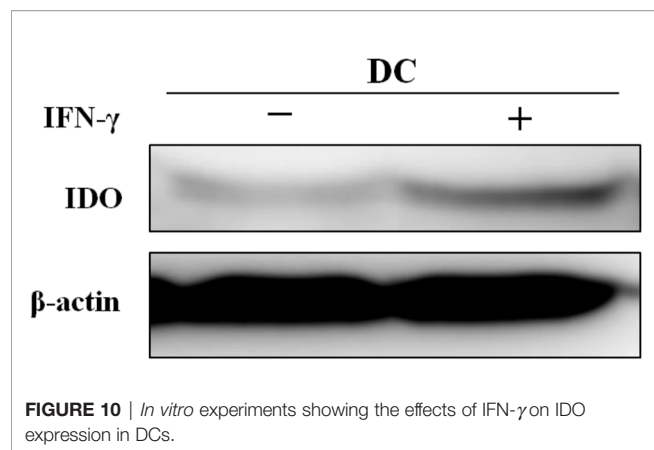


**FIGURE 9** | Effects of N-alkyl-PEI2k-LAC/SPIO/siRNA transfection on the maturation phenotype and marker expression of DCs. FACS assay showed that siRNA-laden mature DCs expressed similar levels in biomarkers MHC-II, CD80, CD86, and CCR7 to siRNA-free mature DCs, but significantly higher levels than immature DCs in CCR7, CD80 and CD86. A two-tailed unpaired Student's t test was performed for two-group comparisons, and the results with significant difference were marked in \*  $P < 0.05$ , \*\*  $P < 0.01$ , or \*\*\*  $P < 0.001$ , respectively. ns, no significance.

protect the siRNA from enzymolysis *in vivo*. Both CLSM and intracellular Fe content measurements showed that the transfection of N-alkyl-PEI2k-LAC/SPIO/IDO-siRNA was successful and depended on both the time and concentration. The molecular phenotype of a cell, to some extent, represents its properties and functions. FACS results showed that expression of four important molecular markers (MHC-II, CD80, CD86, and CCR7) on DCs transfected with the siRNA complex at 6 μg Fe/ml was not distinctly different from siRNA-free mature DCs. In recent years, some authors have noted that nanoparticles often facilitated maturation of DCs (20, 21). In a previous study, we also found that glycidol-modified alkyl-PEI/SPIO

nanocomposites up-regulated expression of MHC-II, CD80, CD86, and CCR7 if DCs were labeled prior to maturation (12). When DCs are matured, they exhibit function reduction in capturing antigens and function enhancement in migration and antigen-presentation. We do not think the effects of nanocomposites to DCs are conducive because the non-specific stimulation may lead to impaired capture of the antigens (12). In current study, the effect was not so evident for N-alkyl-PEI2k-LAC/SPIO nanocomposites, as shown by the FACS results. The improved properties perhaps partly attribute to the lactose modification that reduced surface cations of the nanocomposites. DCs are the cells highly sensitive to external





stimuli (12). The expression of their surface markers was not obviously affected in this study, suggesting the biological friendliness of the nanovector and the transfection process.

### In Vivo Homing of *Indoleamine 2, 3-Dioxygenase* siRNA-Laden Dendritic Cell Vaccines to Lymph Nodes Can Be Successfully Detected by Magnetic Resonance Imaging

During the treatment of 4T1 tumor-bearing mice with DCVs, MR imaging showed that *IDO* siRNA-laden DCVs that were injected into the murine left footpads successfully migrated to the draining lymph nodes after 48 h, resulting in nodal enlargement and darkening of the MR signal in the central zone. The central

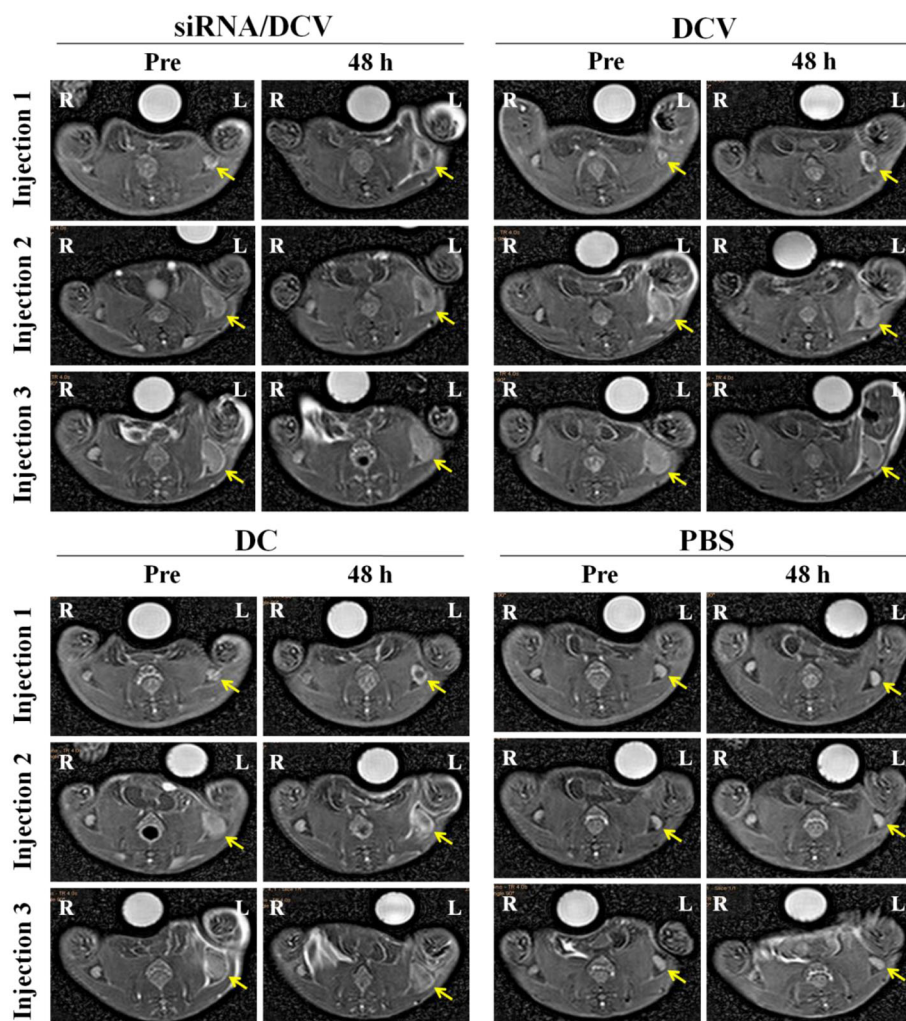


**FIGURE 11** | The left hind footpads were injected three times (1 injection/week) with the siRNA/DC vaccine (siRNA/DCVs), DC vaccine (DCVs), DC or PBS. At 24 h after each injection, MR images of all groups but the PBS group showed decreased signals within enlarged popliteal lymph nodes (yellow arrows).

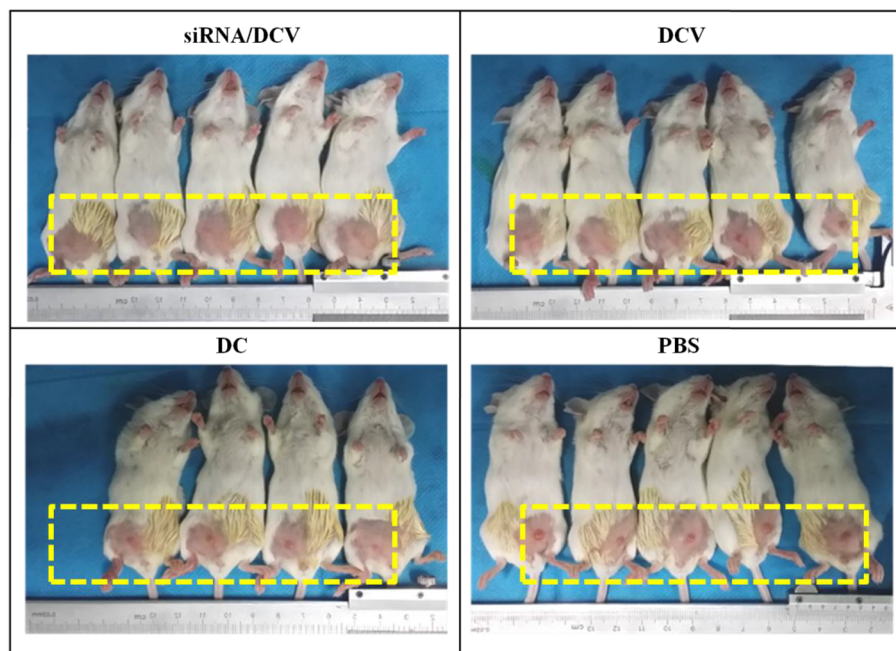


**FIGURE 12** | Photos taken on the 6<sup>th</sup> day after tumor cell inoculation. Tumors grew fastest in the PBS group, followed by the DC group and the two vaccine groups.

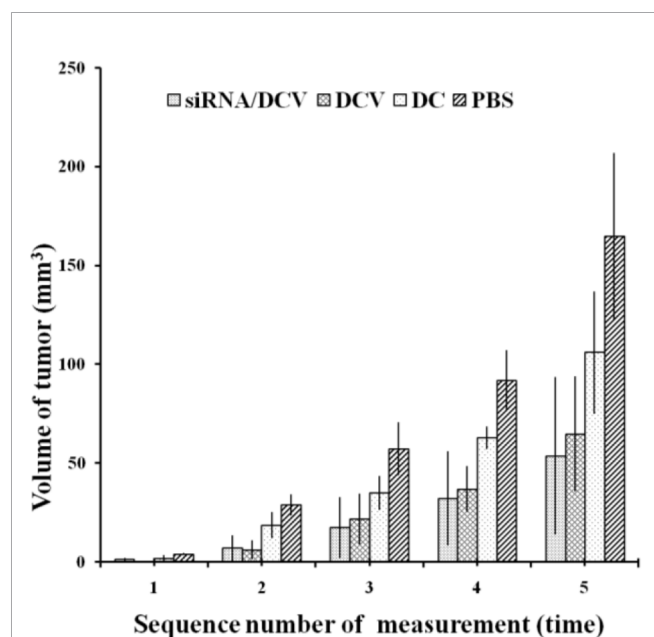


**FIGURE 13** | Tumor volumes were compared among the four groups. A significant difference was observed between the PBS group and the other groups ( $n = 5$ ,  $P < 0.05$ ). Moreover, measurements at the second to fifth time points showed that tumors in the siRNA/DCV group or the DCV group were both smaller than tumors in the DC group ( $n = 5$ ,  $P < 0.05$ ), suggesting the presence of a specific immune response.

distribution indicates a decrease in the MR signal caused by active homing of the N-alkyl-PEI2k-LAC/SPIO nanocomposite

containing DCVs rather than the nanocomposites themselves that are present mainly in the peripheral distribution (22). The tumor treatment adopted in this study mainly referred to the methodology reported by Hegmans JP (17). In the present study, regardless of the material that was injected, the tumors of the mice grew over time. However, the tumors of the PBS group grew fastest, followed by the DC group, indicating that both DCVs and IDO siRNA-laden DCVs actively inhibit tumor growth.

### Limitations of This Study and Possible Causes

Notably, in contrast to previous reports, DCVs transfected with or without IDO-siRNA produced similar levels of tumor inhibition in the present study. No significant difference in tumor size was observed between the two groups (23, 24). This lack of a difference in the tumor size is a major drawback of the study, as tumor is presumed to be regulated by the low expression of IDO in DCs, as verified by our repeated experiments. Typically, IFN- $\gamma$  induction alone is sufficient to up-regulate IDO expression in DCs, but accumulating evidence showed that the up-regulation of IDO in DCs required 'two signals', *i.e.*, IFN- $\gamma$  stimulation followed a second stimulus (such as IL-10, CD40 or LPS) (25, 26). In the present study, DCs underwent a two-stage stimulation with IFN- $\gamma$  and LPS, but to our surprise, the expression of IDO in DCs remained low. We have not yet determined a rational explanation for these outcomes but presume that they may be associated with the factors listed below. a) The subtype of DCs. The DCs cultured in this study were mainly cDCs, not pDCs, which may partially explain the low expression of IDO. b) The method used for DC

culture. We cultured DCs mainly using the methodology reported by Lutz MB (27). Vaccines prepared using the method described by Lutz MB have been reported to exert the best anticancer effect (17). A good therapeutic effect may require IDO low expression. c) The microenvironment in which DCs reside. The DCs cultured in the present study were obtained from normal tumor-free mice. However, tumor-mediated modulation of the humoral immune environment has been reported to contribute to the up-regulation of IDO in DCs (28). Nevertheless, the main purpose of this study was to show that an IDO siRNA could be successfully introduced into DCs with lab-made gene nanovectors and used as *in vivo* imaging tracer. This purpose has been achieved. Moreover, our research group has previously used vectors in an analogous molecular skeleton to repeatedly confirm that the transfection of an siRNA with these vectors effectively silences the target genes in cells (9, 19). In subsequent studies, we plan to select more suitable targets such as PD-L, A20 and DlgR2 to verify the validity of siRNA-mediated silencing.

## CONCLUSIONS

In this study we used, with success, the lactosylated nanocomposites N-alkyl-PEI2k-LAC/SPIO as an MRI-visible gene nanovector for IDO siRNA transfection into DCs. After the IDO siRNA-laden DCVs were adoptively transferred to the mice with 4T1 tumors, *in vivo* MR imaging clearly showed them homing into the draining lymph nodes. In summary, N-alkyl-PEI2k-LAC/SPIO, a gene delivery system, is able to transfect nucleic acid fragments and track cell migration *in vivo* using MR imaging.

## REFERENCES

- Zhang S, Wang Q, Miao B. Review: dendritic cell-based vaccine in the treatment of patients with advanced melanoma. *Cancer Biother Radiopharm* (2007) 22:501–7. doi: 10.1089/cbr.2007.354
- Zhang X, Gordon JR, Xiang J. Advances in dendritic cell-based vaccine of cancer. *Cancer Biother Radiopharm* (2002) 17:601–19. doi: 10.1089/108497802320970217
- Munn DH, Sharma MD, Lee JR, Jhaveri KG, Johnson TS, Keskin DB, et al. Potential regulatory function of human dendritic cells expressing indoleamine 2,3-dioxygenase. *Science* (2002) 297:1867–70. doi: 10.1126/science.1073514
- Endo R, Nakamura T, Kawakami K, Sato Y, Harashima H. The silencing of indoleamine 2,3-dioxygenase 1 (IDO1) in dendritic cells by siRNA-loaded lipid nanoparticles enhances cell-based cancer immunotherapy. *Sci Rep* (2019) 9:11335. doi: 10.1038/s41598-019-47799-w
- Yen MC, Lin CC, Chen YL, Huang SS, Yang HJ, Chang CP, et al. A novel cancer therapy by skin delivery of indoleamine 2,3-dioxygenase siRNA. *Clin Cancer Res* (2009) 15(2):641–9. doi: 10.1158/1078-0432.CCR-08-1988
- Chen D, Koropatnick J, Jiang N, Zheng X, Zhang X, Wang H, et al. Targeted siRNA silencing of indoleamine 2,3-dioxygenase in antigen-presenting cells using mannose-conjugated liposomes: a novel strategy for treatment of melanoma. *J Immunother* (2014) 37(2):123–34. doi: 10.1097/CJL.0000000000000022
- Chen Y, Wang W, Lian G, Qian C, Wang L, Zeng L, et al. Development of an MRI-visible nonviral vector for siRNA delivery targeting gastric cancer. *Int J Nanomed* (2012) 7:359–68. doi: 10.2147/IJN.S24083
- Wang Z, Liu G, Sun J, Wu B, Gong Q, Song B, et al. Self-assembly of magnetite nanocrystals with amphiphilic polyethylenimine: structures and

## DATA AVAILABILITY STATEMENT

The raw data supporting the conclusions of this article will be made available by the authors, without undue reservation.

## ETHICS STATEMENT

All animal procedures were performed in accordance with the Guidelines for Care and Use of Laboratory Animals of North Sichuan Medical College, and experiments were approved by the Animal Ethics Committee of North Sichuan Medical College (P20191226).

## AUTHOR CONTRIBUTIONS

HA, as the consultant, was responsible for the guiding of the experimental research. YX took charge of the overall design of the project as well as the quality and schedule control. CW prepared and tested the MRI nanocomposites, and CW, WZ and RJ implemented the biological experiments. All authors contributed to the article and approved the submitted version.

## FUNDING

This work was funded by the National Natural Science Foundation of China (81601490), Chongqing Science and Technology Foundation, and Chongqing Science and Technology Commission (cstc2018jcsx-msybX0069 and cstc2016 shmszx130009).

- applications in magnetic resonance imaging. *J Nanosci Nanotechnol* (2009) 9:378–85. doi: 10.1166/jnn.2009.j033
- Lin G, Zhu W, Yang L, Wu J, Lin B, Xu Y, et al. Delivery of siRNA by MRI-visible nanovehicles to overcome drug resistance in MCF-7/ADR human breast cancer cells. *Biomaterials* (2014) 35:9495–507. doi: 10.1016/j.biomaterials.2014.07.049
- Shen T, Zhu W, Yang L, Liu L, Jin R, Duan J, et al. Lactosylated N-Alkyl polyethylenimine coated iron oxide nanoparticles induced autophagy in mouse dendritic cells. *Regenerative Biomater* (2018) 5:141–9. doi: 10.1093/rb/rbx032
- Du J, Zhu W, Yang L, Wu C, Lin B, Wu J, et al. Reduction of polyethylenimine-coated iron oxide nanoparticles induced autophagy and cytotoxicity by lactosylation. *Regenerative Biomater* (2016) 3:223–9. doi: 10.1093/rb/rbw023
- Xu Y, Wu C, Zhu W, Xia C, Wang D, Zhang H, et al. Superparamagnetic MRI probes for *in vivo* tracking of dendritic cell migration with a clinical 3 T scanner. *Biomaterials* (2015) 58:63–71. doi: 10.1016/j.biomaterials.2015.04.016
- Sun SH, Zeng H, Robinson DB, Raoux S, Rice PM, Wang SX, et al. Monodisperse MFe<sub>2</sub>O<sub>4</sub> (M = Fe, Co, Mn) nanoparticles. *J Am Chem Soc* (2004) 126:273–9. doi: 10.1021/ja0380852
- Steinman RM. Dendritic cells: understanding immunogenicity. *Eur J Immunol* (2007) 37 Suppl 1:S53–60. doi: 10.1002/eji.200737400
- Akita H, Kogure K, Moriguchi R, Nakamura Y, Higashi T, Nakamura T, et al. Nanoparticles for *ex vivo* siRNA delivery to dendritic cells for cancer vaccines: programmed endosomal escape and dissociation. *J Controlled Release Off J Controlled Release Society* (2010) 143:311–7. doi: 10.1016/j.jconrel.2010.01.012
- Jurgens B, Hainz U, Fuchs D, Felzmann T, Heitger A. Interferon-gamma-triggered indoleamine 2,3-dioxygenase competence in human monocyte-

- derived dendritic cells induces regulatory activity in allogeneic T cells. *Blood* (2009) 114:3235–43. doi: 10.1182/blood-2008-12-195073
17. Hegmans JP, Hemmes A, Aerts JG, Hoogsteden HC, Lambrecht BN. Immunotherapy of murine malignant mesothelioma using tumor lysate-pulsed dendritic cells. *Am J Respir Crit Care Medicine* (2005) 171:1168–77. doi: 10.1164/rccm.200501-057OC
  18. Silva MA, Jury J, Sanz Y, Wiepjes M, Huang X, Murray JA, et al. Increased bacterial translocation in gluten-sensitive mice is independent of small intestinal paracellular permeability defect. *Digest Dis Sci* (2012) 57:38–47. doi: 10.1007/s10620-011-1847-z
  19. Liu G, Xie J, Zhang F, Wang Z, Luo K, Zhu L, et al. N-Alkyl-PEI-functionalized iron oxide nanoclusters for efficient siRNA delivery. *Small* (2011) 7:2742–9. doi: 10.1002/smll.201100825
  20. Jia J, Zhang Y, Xin Y, Jiang C, Yan B, Zhai S. Interactions between nanoparticles and dendritic cells: from the perspective of cancer immunotherapy. *Front Oncol* (2018) 8:404. doi: 10.3389/fonc.2018.00404
  21. Dong H, Wen ZF, Chen L, Zhou N, Liu H, Dong S, et al. Polyethyleneimine modification of aluminum hydroxide nanoparticle enhances antigen transportation and cross-presentation of dendritic cells. *Int J Nanomed* (2018) 13:3353–65. doi: 10.2147/IJN.S164097
  22. Cho NH, Cheong TC, Min JH, Wu JH, Lee SJ, Kim D, et al. A multifunctional core-shell nanoparticle for dendritic cell-based cancer immunotherapy. *Nat Nanotechnol* (2011) 6:675–82. doi: 10.1038/nnano.2011.149
  23. Flatekval GF, Sioud M. Modulation of dendritic cell maturation and function with mono- and bifunctional small interfering RNAs targeting indoleamine 2,3-dioxygenase. *Immunology* (2009) 128:e837–48. doi: 10.1111/j.1365-2567.2009.03093.x
  24. Sioud M, Saeboe-Larssen S, Hetland TE, Kaern J, Mobergslien A, Kvalheim G. Silencing of indoleamine 2,3-dioxygenase enhances dendritic cell immunogenicity and antitumour immunity in cancer patients. *Int J Oncol* (2013) 43:280–8. doi: 10.3892/ijo.2013.1922
  25. Yanagawa Y, Iwabuchi K, Onoe K. Co-operative action of interleukin-10 and interferon-gamma to regulate dendritic cell functions. *Immunology* (2009) 127:345–53. doi: 10.1111/j.1365-2567.2008.02986.x
  26. Jung ID, Lee JS, Lee CM, Noh KT, Jeong YI, Park WS, et al. Induction of indoleamine 2,3-dioxygenase expression via heme oxygenase-1-dependant pathway during murine dendritic cell maturation. *Biochem Pharmacol* (2010) 80:491–505. doi: 10.1016/j.bcp.2010.04.025
  27. Lutz MB, Kukutsch N, Ogilvie AL, Rossner S, Koch F, Romani N, et al. An advanced culture method for generating large quantities of highly pure dendritic cells from mouse bone marrow. *J Immunol Methods* (1999) 223:77–92. doi: 10.1016/s0022-1759(98)00204-x
  28. Kuaes MA, Wenzel J, Schmid-Wendtner MH, Bieber T, Von Bubnoff D. Myeloid CD11c+ S100+ dendritic cells express indoleamine 2,3-dioxygenase at the inflammatory border to invasive lower lip squamous cell carcinoma. *Histol Histopathol* (2011) 26:997–1006. doi: 10.14670/HH-26.997

**Conflict of Interest:** The authors declare that the research was conducted in the absence of any commercial or financial relationships that could be construed as a potential conflict of interest.

Copyright © 2021 Wu, Zhu, Jin, Ai and Xu. This is an open-access article distributed under the terms of the Creative Commons Attribution License (CC BY). The use, distribution or reproduction in other forums is permitted, provided the original author(s) and the copyright owner(s) are credited and that the original publication in this journal is cited, in accordance with accepted academic practice. No use, distribution or reproduction is permitted which does not comply with these terms.





# Use of Radiomics to Improve Diagnostic Performance of PI-RADS v2.1 in Prostate Cancer

Mou Li<sup>1</sup>, Ling Yang<sup>1</sup>, Yufeng Yue<sup>1</sup>, Jingxu Xu<sup>2</sup>, Chencui Huang<sup>2</sup> and Bin Song<sup>1\*</sup>

<sup>1</sup> Department of Radiology, West China Hospital of Sichuan University, Chengdu, China, <sup>2</sup> Department of Research Collaboration, R&D Center, Beijing Deepwise & League of PHD Technology Co., Ltd, Beijing, China

## OPEN ACCESS

### Edited by:

Changqiang Wu,  
North Sichuan Medical College, China

### Reviewed by:

Junqiang Lei,  
First Hospital of Lanzhou University,  
China  
Haiyi Wang,  
Chinese People's Liberation Army  
General Hospital, China

### \*Correspondence:

Bin Song  
songlab\_radiology@163.com

### Specialty section:

This article was submitted to  
Cancer Imaging and  
Image-directed Interventions,  
a section of the journal  
Frontiers in Oncology

Received: 21 November 2020

Accepted: 30 December 2020

Published: 17 February 2021

### Citation:

Li M, Yang L, Yue Y, Xu J, Huang C  
and Song B (2021) Use of Radiomics  
to Improve Diagnostic Performance of  
PI-RADS v2.1 in Prostate Cancer.  
Front. Oncol. 10:631831.  
doi: 10.3389/fonc.2020.631831

**Objective:** To investigate whether a radiomics model can help to improve the performance of PI-RADS v2.1 in prostate cancer (PCa).

**Methods:** This was a retrospective analysis of 203 patients with pathologically confirmed PCa or non-PCa between March 2015 and December 2016. Patients were divided into a training set ( $n = 141$ ) and a validation set ( $n = 62$ ). The radiomics model (Rad-score) was developed based on multi-parametric MRI including T2 weighted imaging (T2WI), diffusion weighted imaging (DWI), apparent diffusion coefficient (ADC) imaging, and dynamic contrast enhanced (DCE) imaging. The combined model involving Rad-score and PI-RADS was compared with PI-RADS for the diagnosis of PCa by using the receiver operating characteristic curve (ROC) analysis.

**Results:** A total of 112 (55.2%) patients had PCa, and 91 (44.8%) patients had benign lesions. For PCa versus non-PCa, the Rad-score had a significantly higher area under the ROC curve (AUC) [0.979 (95% CI, 0.940–0.996)] than PI-RADS [0.905 (0.844–0.948),  $P = 0.002$ ] in the training set. However, the AUC between them was insignificant in the validation set [0.861 (0.749–0.936) vs. 0.845 (0.731–0.924),  $P = 0.825$ ]. When Rad-score was added to PI-RADS, the performance of the PI-RADS was significantly improved for the PCa diagnosis (AUC = 0.989,  $P < 0.001$  for the training set and AUC = 0.931,  $P = 0.038$  for the validation set).

**Conclusions:** The radiomics based on multi-parametric MRI can help to improve the diagnostic performance of PI-RADS v2.1 in PCa.

**Keywords:** artificial intelligence, radiomics, prostate cancer, multi-parametric MRI, PI-RADS v2.1

## INTRODUCTION

Prostate cancer (PCa) remains the most commonly diagnosed malignancy among men in the western world (1). The frequency of PCa in Asia has increased rapidly in years (2). Accurate detection and diagnosis of PCa are key factors to improve its therapeutic response and prognosis. Currently, magnetic resonance imaging (MRI) is generally considered the best modality for the detection and localization of PCa, and are thus becoming increasingly important (3). A recently developed multi-parametric (mp) MRI protocols including T2-weighted (T2W), diffusion-weighted

(DWI), and dynamic contrast-enhanced (DCE) imaging, appears to have good performance for PCa diagnosis, when associated with the Prostate Imaging Reporting and Data System (PI-RADS) (4).

In 2012, the initial version (v1) of PI-RADS was released to promote standardized MRI techniques and image interpretation. However, limitations of version 1 were soon evident. In 2015, version 2 was described to further improve reporting accuracy, and now has seen a broad uptake (4, 5). In 2019, PI-RADS version 2.1 was newly described, with several studies suggesting that version 2.1 could be preferable than version 2 for the evaluation of transition zone PCa (6–8). PI-RADS is now playing an increasingly prominent role in PCa diagnosis (9, 10). However, PI-RADS seems to have limitations of relatively low specificities, and inter-reader reproducibility. Thus a quantitative diagnostic method is needed to improve the performance of PI-RADS for the definite diagnosis of PCa (11, 12).

Radiomics can provide large-scale radiological image analysis by using a large number of quantitative features (13). Compared with genomics and proteomics, radiomics has the advantages of non-invasion assessments, comprehensive views of whole tumor and convenience in routine practice; thus, this technique has great potential for application in individualized diagnosis and treatment. Two studies (4, 14) have shown that radiomics can be used to detect PCa. However, it's uncertain whether radiomics can add value to PI-RADS in the diagnosis of PCa. Therefore, this study aimed to determine whether radiomics of mpMRI can enhance the performance of PI-RADS v2.1 in PCa diagnosis.

## MATERIALS AND METHODS

### Patients

This study was approved by the local Institutional Review Boards (No. 2019-1209, Date: December 30, 2019) and the need for written informed consent was waived.

The institutional database of medical records was searched for suitable patients between March 2015 and December 2016. A total of 203 patients (mean age 66 years, age range 36–85 years) who met the following criteria were finally enrolled. The inclusion criteria: (1) Men with suspicious lesions on mpMRI; (2) These lesions were histologically confirmed by biopsy or radical prostatectomy; (3) no prior prostate endocrine therapy, biopsy, surgery, or radiation therapy before MRI examination. The exclusion criteria: (1) lesions with maximum transverse diameter <5 mm, which could hardly be delineated on MRI; (2) poor mpMRI quality. The patient recruitment pathway was shown in **Figure 1**.

The baseline characteristics, pathological data, and radiographic evaluation of each patient, including age, size, location, Gleason score, PI-RADS v2.1 score and prostate-specific antigen (PSA) were shown in **Table 1**. The patients were divided into two groups (the training and validation sets) at a ratio of 7:3 according to the scanning date.

### MRI Examination

All MRI examinations were performed on the same 3.0 T MRI scanner (Skyra, Siemens Healthcare Sector, Germany) with a pelvic phased array coil. Scan sequences included T2WI in the axial and sagittal planes, DWI with b values of 0, 200, 400, and 1,000 s/mm<sup>2</sup>, and DCE. ADC maps were calculated on a designated workstation. **Supplementary Material** summarizes the parameters of mpMRI sequences, including the type, repetition time/echo time (TR/TE), section thickness, field of view (FoV), and bandwidth.

### Reference Standard for Pathology

All lesions were histopathologically proven based on biopsy (transrectal ultrasound [TRUS]-guided 12-core systematic biopsy) or surgical specimens (radical prostatectomy). Pathological confirmatory reports were acquired from medical records of the Department of Pathology.

### PI-RADS Evaluation

Two experienced radiologists (more than 5 years of experience in the diagnosis of PCa) were assigned to review the mpMRI. The patient identification was removed from all images, and the readers were blinded to all clinicopathological information. The mpMRI including T2WI, DWI with corresponding ADC map, and DCE of the largest lesion in each patient was scored with a scale of 1–5 using PI-RADS v2.1. PI-RADS scores obtained by the two readers were assessed by a weighted Kappa statistics test to evaluate the inter-observer variability. Then any disagreement between the two readers was solved by discussion during the image interpretation.

### Texture Feature Extraction and Model-Building

The images were normalized before feature calculation. In detail, each image was subtracted by the mean value and was divided by the standard deviation value. Then the image was multiplied by 100, and resampled to the same resolution.

Two radiologists drew volume of interest (VOI) independently on MR images of 30 patients to evaluate the stability of the features. Only the features with inter- and intra-class correlation coefficient (ICC) > 0.75 can be included in the following analysis. The entire VOI of the tumor were drawn on the base of radiologic-histologic correlation slice by slice (the radiologists were blinded to the histopathology results). For the patient with multiple lesions, only the dominant lesion (the largest lesion) was segmented.

Radiomic features of the lesions were extracted using PyRadiomics. Three types of features (first-order statistics, texture features, and shape features) for a total of 1,304 features were extracted from each sequence of mpMRI. To eliminate the differences in the value scales of radiomics features, all of the features were normalized before feature selection. Each feature was subtracted by the mean value of the training group and was divided by the standard deviation value. The same normalization method was applied to the validation set. Redundant features were removed by One-way analysis of variance (ANOVA). Then, the least

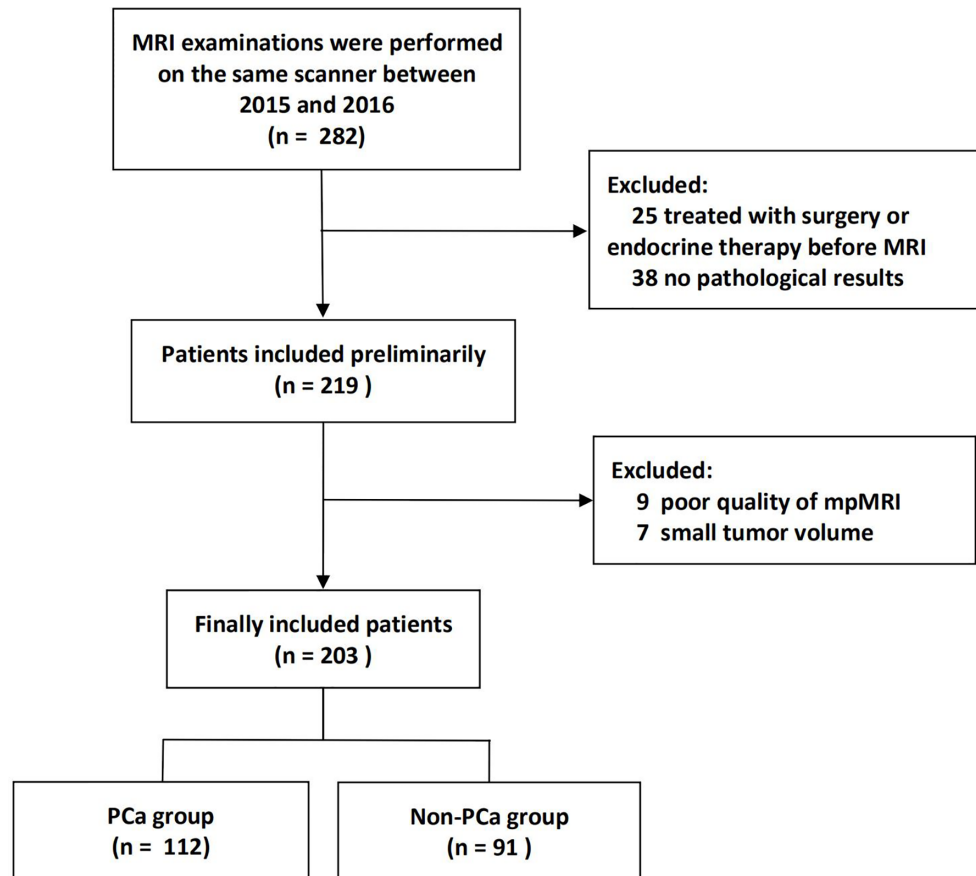


**FIGURE 1** | Flow chart of patients' recruitment pathway.

**TABLE 1** | Patient and tumor characteristics.

Characteristics	PCa (n = 112)	Non-PCa (n = 91)	P value	Training cohort (n = 141)	Validation cohort (n = 62)	P value
Age (y)	66.0 ± 7.6	66.0 ± 10.3	0.970	66.5 ± 8.6	64.9 ± 9.42	0.245
Size (long axis, mm)	2.22 ± 1.08	1.56 ± 0.88	0.001	1.86 ± 0.96	2.07 ± 1.21	0.194
Location			0.023			0.479
Transitional zone	51	56		72	35	
Peripheral zone	61	35		69	27	
PSA (ng/ml)			0.000			0.749
PSA ≤ 10	15	41		37	19	
10 < PSA ≤ 20	31	37		47	21	
PSA > 20	66	13		57	22	
Gleason score (6/7/8/9)	11/69/8/24	–		8/50/5/15	3/19/3/9	0.797
Extracapsular invasion on MRI (+/–)	74/38	6/85	0.000	58/83	22/40	0.448
PI-RADS v2.1 score			0.000			0.651
1	0	3		1	2	
2	0	26		18	8	
3	6	30		24	12	
4	32	25		42	15	
5	74	7		56	25	

This table summarized the integrated PI-RADS scoring results for the two readers. The weighted Kappa between two readers was 0.722 [95% CI 0.651–0.794], which indicated strong consistency. PCa, prostate cancer; PSA, prostate-specific antigen.

absolute shrinkage and selection operator (LASSO) regression method was applied to select the most distinguishable features.

Each clinical feature was assessed by univariate logistic regression. The features revealed as statistically significant with univariate logistic regression analysis were then analyzed with multivariate logistic regression analysis for model-building. A nomogram was generated for model visualization. Receiver operating characteristic (ROC) curve analyses were conducted to estimate the diagnostic performance of the models for the diagnosis of PCa.

## Statistical Analysis

All statistical analyses were performed on R software, Statistic Package for Social Science version 21, Stata 15.0, and Medcalc 15.2.2. Differences in **Table 1** were assessed by the chi-square test, the Mann-Whitney test, or *t*-test. The AUCs between different models were compared by DeLong's test. The confidence level was set at  $P < 0.05$ .

## RESULTS

A total of 203 patients were included in this study, in which 112 patients had PCa, and 91 patients had benign lesions [84 benign prostatic hyperplasia (BPH), and 7 high-grade prostatic intraepithelial neoplasia (HGPIN)]. For the lesion origin, 96 lesions originated from the peripheral zone, and 107 lesions were located in the transitional zone. The PCa had a larger size than non-PCa (long axis,  $2.22 \pm 1.08$  mm vs.  $1.56 \pm 0.88$  mm,  $P = 0.001$ ). As shown in **Table 1**. As for the reference standard, 82 patients with benign lesions did not undergo radical prostatectomy, and the pathological results were determined by TRUS-guided biopsy.

## Feature Selection and Model-Building

For the consistency test of VOIs, the number of features with ICC  $> 0.75$  were 522 for DWI, 655 for ADC, 471 for DCE, and 266 for T2WI, as shown in **Figure 2A**. A total of 45 features (5, 19, 10, and 11 features were extracted from T2WI, DWI, ADC, and DCE images, respectively) were selected by LASSO method (**Figure 2B**). These features all had high ICC ( $> 0.75$ ). The radiomics model (Rad-score) was comprised of these features in a formula shown in **Supplementary Material**. Rad-score had statistical difference between PCa and non-PCa groups (Rad-score =  $0.85 \pm 0.29$  vs.  $0.12 \pm 0.25$ ,  $P < 0.001$ ). Then the combined models were built by combining PI-RADS (odds ratio [OR] = 6.4,  $P = 0.001$ ) with Rad-score (OR = 14.5,  $P < 0.001$ ) or PSA using multivariate logistic regression analysis.

A nomogram was generated for the combined model (PI-RADS + Rad-score) visualization (**Figure 3A**). To use the nomogram, find the point for each feature on the corresponding axis, add the points for all features, and draw a line from the total points axis to the risk axis to determine the risk of PCa. Higher total score was associated with greater risk of PCa. The model yielded satisfactory fit measurement based on the training set

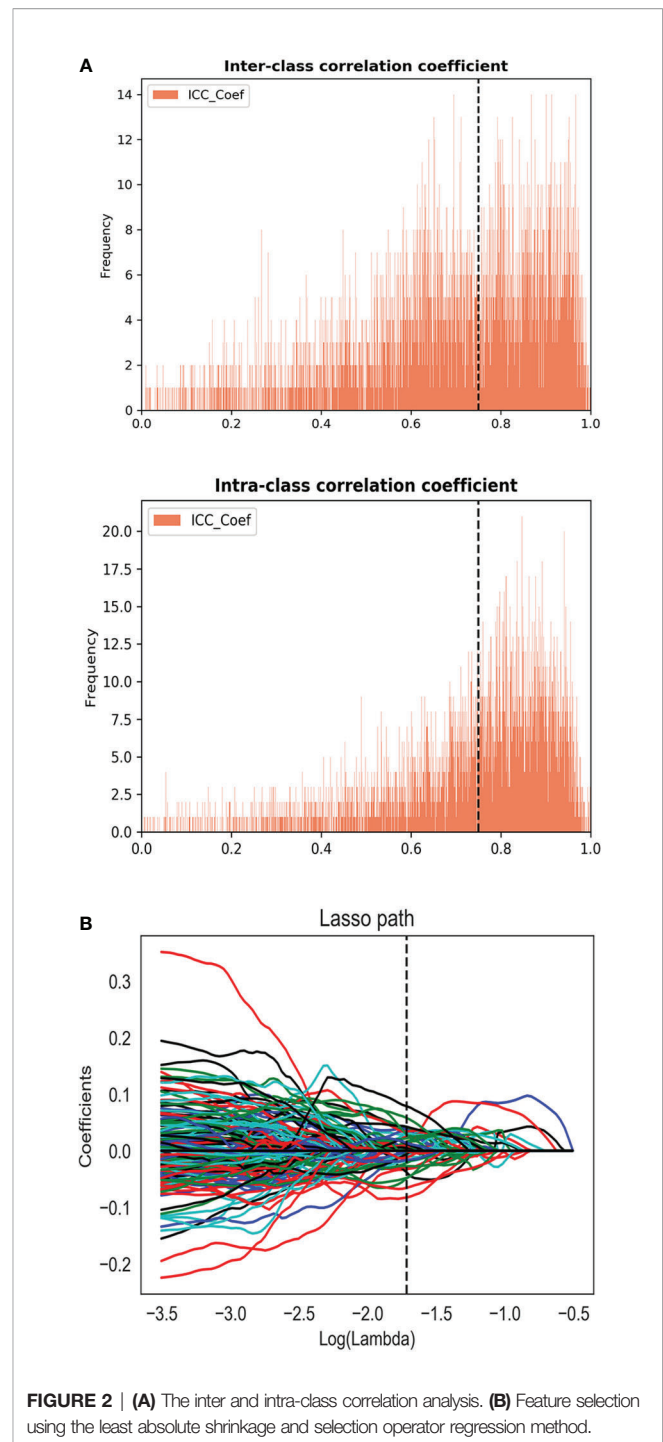


**FIGURE 2 | (A)** The inter and intra-class correlation analysis. **(B)** Feature selection using the least absolute shrinkage and selection operator regression method.

(Hosmer-Lemeshow test,  $P = 0.943$ ). Moreover, there were also good calibration curves for the risk estimation (**Figures 3B, C**).

## PCa vs. Non-PCa Classification

Rad-score had a significantly higher AUC [0.979 (95% CI, 0.940–0.996)] than PI-RADS [0.905 (0.844–0.948),  $P = 0.002$ ] in the training set. However, the AUC between them was insignificant in the validation set [0.861 (0.749–0.936) vs. 0.845 (0.731–0.924),



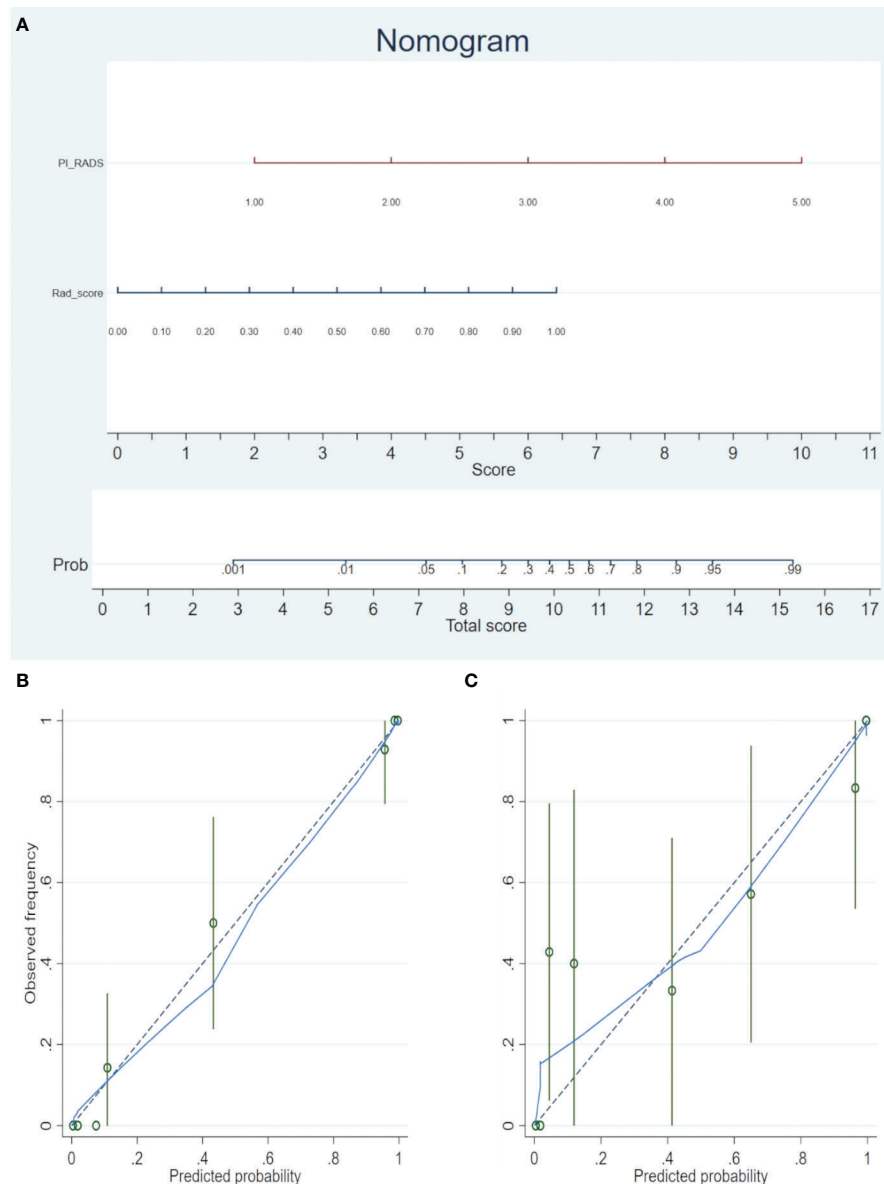


**FIGURE 3 | (A)** The radiomics nomogram was developed in the training cohort, with the Rad-score and PI-RADS incorporated. **(B)** Calibration curve of the nomogram in the training set. **(C)** Calibration curve of the nomogram in the validation set. Calibration curves depict the calibration of the model in terms of the agreement between the predicted risks of PCa (the x-axis) and observed outcomes of PCa (the y-axis). The blue solid line represents the performance of the nomogram (Note: a closer fit to the diagonal dotted line represents a better prediction).

$P = 0.825$ ]. When Rad-score was added to PI-RADS, the performance of PI-RADS was significantly improved for the PCa diagnosis (AUC = 0.989,  $P < 0.001$  for the training set and AUC = 0.931,  $P = 0.038$  for the validation set). As shown in **Table 2** and **Figure 4**.

In the case of clinical features, PSA, location, size, and extracapsular invasion were selected by univariate logistic regression analysis. However, only PSA was included in the combined model by multivariate logistic regression analysis. However, the addition of PSA to the combined model failed to

show incremental diagnostic value (AUC = 0.990 vs. 0.989 for the training set; AUC = 0.937 vs. 0.931 for the validation set). As shown in **Table 2** and **Figure 4**.

For differentiating the peripheral zone lesions, the AUC of the combined model was higher than that of PI-RADS (AUC = 0.995 vs. 0.891,  $P = 0.002$  for the training cohort; AUC = 0.941 vs. 0.753,  $P = 0.046$  for the validation cohort; AUC = 0.987 vs. 0.860,  $P < 0.001$  in the whole cohort). For differentiating lesions in the transitional zone, the AUC of the combined model was higher than that of PI-RADS (AUC = 0.981 vs. 0.909,  $P = 0.007$  for the

**TABLE 2 |** ROC analyses of PI-RADS v2.1, Rad-score, and the combined models in the training and validation cohorts.

Model	The training cohort			P value	The validation cohort			P value
	AUC	SEN	SPE		AUC	SEN	SPE	
PI-RADS*	0.905	96.2%	63.5%		0.845	91.2%	67.9%	
Rad-score	0.979	89.7%	95.2%	0.002	0.861	82.4%	82.1%	0.825
PI-RADS + Rad-score	0.989	92.3%	98.4%	<0.001	0.931	79.4%	96.4%	0.038
PI-RADS + Rad-score + PSA	0.990	92.3%	98.4%	<0.001	0.937	79.4%	96.4%	0.026

\*When PI-RADS v2.1 score of the lesion  $\geq 4$ , this lesion was diagnosed as PCa.

P value, compared with PI-RADS.

AUC, Area under the curve; SEN, sensitivity; SPE, specificity.

training cohort; AUC = 0.926 vs. 0.861,  $P = 0.170$  in the validation cohort; AUC = 0.960 vs. 0.894,  $P = 0.006$  in the whole cohort).

## Classification of PI-RADS 3 Lesions

Thirty-six patients in this study had PI-RADS 3 lesions on prostate MRI, in which 6 patients had PCa, and 30 patients had non-PCa. The Rad-score, and the combined model (Rad-score + PI-RADS) both had good diagnostic performance for the identification of PI-RADS 3 lesions (both AUC = 0.944), which was shown in **Table 3** and **Figure 5**.

## DISCUSSION

In this study, we proposed a combined model (PI-RADS combined with Rad-score) to significantly improve the diagnostic value of PI-RADS v2.1. By adding Rad-score to PI-RADS, the combined model outperformed PI-RADS in the diagnosis of PCa (AUC = 0.989 vs. 0.905,  $P < 0.001$  for the training set; AUC = 0.931 vs. 0.845,  $P = 0.038$  for the validation set). Thus adding quantitative Rad-score can benefit radiologists in the diagnosis of PCa.

PI-RADS v2 is designed to improve lesion detection, localization, characterization, and risk stratification in patients with suspected cancer (15). It is known that PI-RADS v2 generally benefits from its highly structured criteria, making relatively high diagnostic sensitivity in PCa diagnosis (14). However, the specificity and inter-reader reproducibility are moderate (16–18). To address these limitations of PI-RADS v2, an updated version (PI-RADS v2.1) was developed in 2019. One of the major modifications in version 2.1 is the diagnostic criteria for the transitional zone PCa of low T2WI scores. When comparing the performance between version 2 and 2.1 for characterization of suspected PCa, several studies suggested that AUC tended to be higher in version 2.1 than in version 2 without statistical significance (6–8). It must be noted that PI-RADS v2.1 still showed a high false positive rate (moderate specificity) for PCa diagnosis, similar to that with PI-RADS v2. Moreover, PI-RADS 3 lesions are frequently encountered (22–32%), and carry a moderate malignant potential (up to 20–30%), the stratification of these lesions is still challenging when using PI-RADS (19). Therefore, quantitative parameters, such as radiomics, may help to prevent misdiagnoses and improve performance of PI-RADS v2.1.

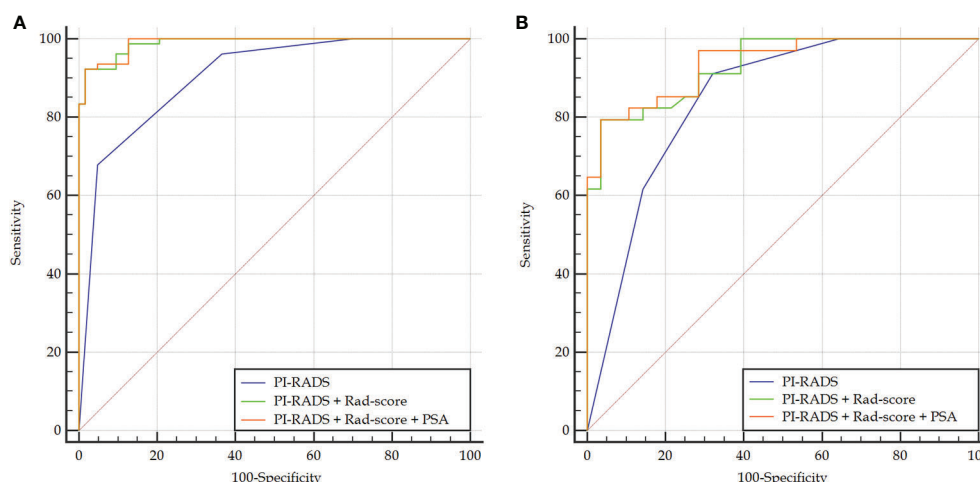


**FIGURE 4 |** Comparison of ROC curves between PI-RADS v2.1 and the combined models in the training (A) and validation (B) sets. The combined models both had significantly higher AUCs than PI-RADS.

**TABLE 3 |** ROC analyses of PI-RADS, Rad-score, and the combined models for identifying PI-RADS 3 lesions.

Model	PI-RADS 3 lesions (n = 36)			P value
	AUC	SEN	SPE	
PI-RADS*	0.500	0	100%	
Rad-score	0.944	100%	80%	<0.001
PI-RADS + Rad-score	0.944	100%	80%	<0.001
PI-RADS + Rad-score + PSA	0.911	83.3%	90.0%	<0.001

\*When PI-RADS v2.1 score of the lesion  $\geq 4$ , this lesion was diagnosed as PCa.

P value, compared with PI-RADS.

AUC, Area under the curve; SEN, sensitivity; SPE, specificity.

Compared with qualitative or subjective explanation of radiological images, radiomics permits high-throughput extraction of quantitative features to evaluate the degree of intratumor heterogeneity (20). In recent years, radiomics analysis has appeared as a potent tool for constructing decision-support models. A number of studies have used radiomics analysis to automate PCa diagnosis and risk stratification (21, 22). While few studies (4, 14) focused on the comparison of the diagnostic value between radiomics and PI-RADS. Our results suggested that the AUC of radiomics was higher than that of PI-RADS in the training set, which was consistent with previous studies. However, the difference of AUC was insignificant in the validation set, which was not entirely consistent with the previous studies. This finding showed that radiomics might not replace PI-RADS currently. The building methods between our study and those of previous studies were all machine learning, and all these studies lacked external validation. However, there were still some differences that need to be explained. Firstly, the version of PI-RADS in our study was 2.1, which was different from version 2 in previous studies (4, 14). Secondly, Chen et al. (14) only used T2WI and ADC images, in which lack of enhanced images reduced the effectiveness of mpMRI and radiomics. Finally, prior studies (4, 14) had the smaller sample sizes than ours, especially Wang et al. (14).

In our study, extracapsular invasion, location of lesions, and tumor diameter did not present enough predictive power for the differentiation of benign and malignant lesions. Thus, we integrated PSA into the combined model (Rad-score + PI-RADS). However, adding PSA failed to show incremental diagnostic value. This might be because the AUC of the combined model was high enough. In our work, when Rad-score were added, the diagnostic performance of PI-RADS was prominently improved: the specificity increased from 63.5 to 98.4% in the training set, and from 67.9 to 96.4% in the validation set. Adding Rad-score to PI-RADS might overcome the challenge of moderate specificity of PI-RADS. For the individual zone-based analysis, the combined model outperformed PI-RADS in the training, validation, and whole sets for differentiating lesions in the peripheral zone. However, the combined model failed to show significantly higher diagnostic performance in differentiating transitional zone lesions for the validation cohort ( $P = 0.170$ ). We speculated that this might be related to the small sample size of transitional zone lesions in the validation set.

For PI-RADS 3 lesions classification, our exploratory results may provide preliminary evidence to justify the use of radiomics in this field. In clinical practice of the future, the validation of radiomics is important for the challenging PI-RADS 3 lesions, including biopsy or short-term follow-up in these lesions with high risk of PCa indicated by radiomics.

Our study had several limitations. First, due to its retrospective design, there might be selection bias between PCa and non-PCa groups, and the high b-value images ( $b \text{ value} \geq 1,400 \text{ s/mm}^2$ ) failed to be obtained. Second, prospective and external validation was not performed. Third, all mpMRI images were obtained from a single institution. In the future, multicenter verification is needed to extend the versatility of the experimental results.

In conclusion, although the radiomics model cannot replace PI-RADS currently, adding radiomics to PI-RADS has the potential to improve the performance of the structured PI-RADS scheme by providing radiologists with quantitative and

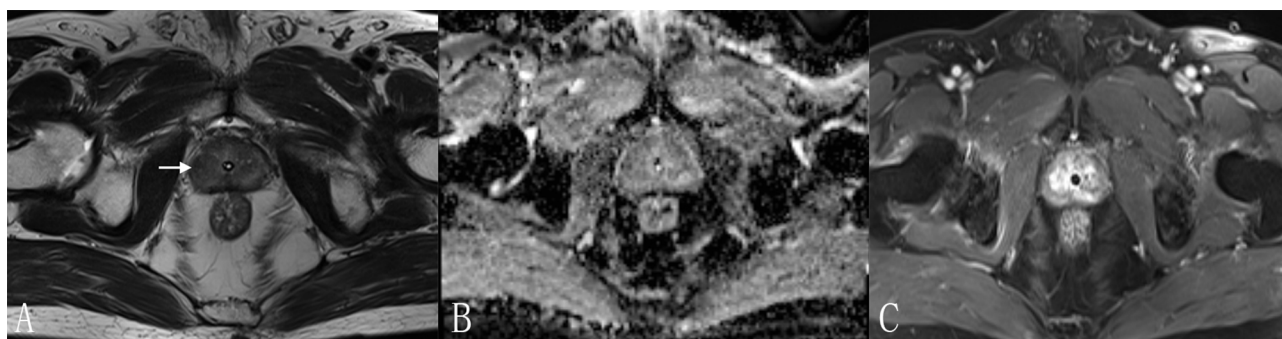


**FIGURE 5 |** A 70-year-old man with a PI-RADS 3 lesion. **(A)** T2WI, heterogeneous signal intensity with obscured margins (arrow), which indicated 3 points according to PI-RADS v2.1; **(B)** ADC with 3 points, focal hypointense (discrete and different from the background); **(C)** DCE, contemporaneously with enhancement of adjacent normal prostatic tissues. According to **(A–C)**, this lesion was classified as PI-RADS 3, indicating this lesion had an intermediate likelihood of clinically significant cancer. However, considering Rad-score (value = 0.97) and PI-RADS (score = 3), the risk of PCa was very high (the probability was about 85%) according to the nomogram. Finally, this lesion was proven to be PCa pathologically, with Gleason score = 3 + 4.

standardized criteria, thereby enabling us to more confidentially detect prostate cancer.

## DATA AVAILABILITY STATEMENT

The original contributions presented in the study are included in the article/**Supplementary Material**. Further inquiries can be directed to the corresponding author.

## ETHICS STATEMENT

The studies involving human participants were reviewed and approved by West China Hospital of Sichuan University Biomedical Research Ethics Committee. Written informed consent for participation was not required for this study in accordance with the national legislation and the institutional requirements. Written informed consent was not obtained from the individual(s) for the publication of any potentially identifiable images or data included in this article.

## REFERENCES

- Cheung E, Wadhera P, Dorff T, Pinski J. Diet and prostate cancer risk reduction. *Expert Rev Anticancer Ther* (2008) 8(1):43–50. doi: 10.1586/14737140.8.1.43
- Boettcher AN, Usman A, Morgans A, VanderWeele DJ, Sosman J, Wu JD. Past, Current, and Future of Immunotherapies for Prostate Cancer. *Front Oncol* (2019) 9:884. doi: 10.3389/fonc.2019.00884
- Tian JY, Guo FJ, Zheng GY, Ahmad A. Prostate cancer: updates on current strategies for screening, diagnosis and clinical implications of treatment modalities. *Carcinogenesis* (2018) 39(3):307–17. doi: 10.1093/carcin/bgx141
- Chen T, Li M, Gu Y, Zhang Y, Yang S, Wei C, et al. Prostate Cancer Differentiation and Aggressiveness: Assessment With a Radiomic-Based Model vs. PI-RADS v2. *J Magn Reson Imag* (2019) 49(3):875–84. doi: 10.1002/jmri.26243
- Hoffmann R, Logan C, O'Callaghan M, Gormly K, Chan K, Foreman D. Does the Prostate Imaging-Reporting and Data System (PI-RADS) version 2 improve accuracy in reporting anterior lesions on multiparametric magnetic resonance imaging (mpMRI)? *Int Urol Nephrol* (2018) 50(1):13–9. doi: 10.1007/s11255-017-1753-1
- Tamada T, Kido A, Takeuchi M, Yamamoto A, Miyaji Y, Kanomata N, et al. Comparison of PI-RADS version 2 and PI-RADS version 2.1 for the detection of transition zone prostate cancer. *Eur J Radiol* (2019) 121:108704. doi: 10.1016/j.ejrad.2019.108704
- Xu L, Zhang G, Zhang D, Zhang X, Bai X, Yan W, et al. Comparison of PI-RADS version 2.1 and PI-RADS version 2 regarding interreader variability and diagnostic accuracy for transition zone prostate cancer. *Abdom Radiol (NY)* (2020) 45(12):4133–41. doi: 10.1007/s00261-020-02738-6
- Byun J, Park KJ, Kim MH, Kim JK. Direct Comparison of PI-RADS Version 2 and 2.1 in Transition Zone Lesions for Detection of Prostate Cancer: Preliminary Experience. *J Magn Reson Imag* (2020) 52(2):577–86. doi: 10.1002/jmri.27080
- Bjurlin MA, Carroll PR, Eggener S, Fulgham PF, Margolis DJ, Pinto PA, et al. Update of the Standard Operating Procedure on the Use of Multiparametric Magnetic Resonance Imaging for the Diagnosis, Staging and Management of Prostate Cancer. *J Urol* (2020) 203(4):706–12. doi: 10.1097/JU.0000000000000617
- Zhang L, Tang M, Chen S, Lei X, Zhang X, Huan Y. A meta-analysis of use of Prostate Imaging Reporting and Data System Version 2 (PI-RADS V2) with multiparametric MR imaging for the detection of prostate cancer. *Eur Radiol* (2017) 27(12):5204–14. doi: 10.1007/s00330-017-4843-7

## AUTHOR CONTRIBUTIONS

BS and LY conceived of the presented idea. ML and YY collected the data. ML, JX, and CH analyzed the data. ML drafted the manuscript. All authors reviewed the manuscript and BS made corrections to the manuscript. All authors contributed to the article and approved the submitted version.

## FUNDING

This work was supported by grants from China International Medical Foundation (2019 SKY Imaging Research Funds, NO. Z-2014-07-1912).

## SUPPLEMENTARY MATERIAL

The Supplementary Material for this article can be found online at: <https://www.frontiersin.org/articles/10.3389/fonc.2020.631831/full#supplementary-material>

- Mussi TC, Yamauchi FI, Tridente CF, Tachibana A, Tonso VM, Recchimuzzi DR, et al. Interobserver Agreement and Positivity of PI-RADS Version 2 Among Radiologists with Different Levels of Experience. *Acad Radiol* (2019) 26(8):1017–22. doi: 10.1016/j.acra.2018.08.013
- Chen F, Cen S, Palmer S. Application of Prostate Imaging Reporting and Data System Version 2 (PI-RADS v2): Interobserver Agreement and Positive Predictive Value for Localization of Intermediate- and High-Grade Prostate Cancers on Multiparametric Magnetic Resonance Imaging. *Acad Radiol* (2017) 24(9):1101–6. doi: 10.1016/j.acra.2017.03.019
- Avanzo M, Stancanelli J, El Naqa I. Beyond imaging: The promise of radiomics. *Phys Med* (2017) 38:122–39. doi: 10.1016/j.ejmp.2017.05.071
- Wang J, Wu CJ, Bao ML, Zhang J, Wang XN, Zhang YD. Machine learning-based analysis of MR radiomics can help to improve the diagnostic performance of PI-RADS v2 in clinically relevant prostate cancer. *Eur Radiol* (2017) 27(10):4082–90. doi: 10.1007/s00330-017-4800-5
- Hassanzadeh E, Glazer DI, Dunne RM, Fennessy FM, Harisinghani MG, Tempany CM. Prostate imaging reporting and data system version 2 (PI-RADS v2): a pictorial review. *Abdom Radiol (NY)* (2017) 42(1):278–89. doi: 10.1007/s00261-016-0871-z
- Smith CP, Türkbey B. PI-RADS v2: Current standing and future outlook. *Turk J Urol* (2018) 44(3):189–94. doi: 10.5152/tud.2018.12144
- Kasel-Seibert M, Lehmann T, Aschenbach R, Guettler FV, Abubrig M, Grimm MO, et al. Assessment of PI-RADS v2 for the Detection of Prostate Cancer. *Eur J Radiol* (2016) 85(4):726–31. doi: 10.1016/j.ejrad.2016.01.011
- Rosenkrantz AB, Ginocchio LA, Cornfeld D, Froemming AT, Gupta RT, Turkbey B, et al. Interobserver Reproducibility of the PI-RADS Version 2 Lexicon: A Multicenter Study of Six Experienced Prostate Radiologists. *Radiology* (2016) 280(3):793–804. doi: 10.1148/radiol.2016152542
- Giambelluca D, Cannella R, Vernuccio F, Comelli A, Pavone A, Salvaggio L, et al. PI-RADS 3 Lesions: Role of Prostate MRI Texture Analysis in the Identification of Prostate Cancer. *Curr Probl Diagn Radiol* (2019) 50(2):175–85. doi: 10.1067/j.cpradiol.2019.10.009
- Li M, Zhu YZ, Zhang YC, Yue YF, Yu HP, Song B. Radiomics of rectal cancer for predicting distant metastasis and overall survival. *World J Gastroenterol* (2020) 26(33):5008–21. doi: 10.3748/wjg.v26.i33.5008
- Stanzione A, Gambardella M, Cuocolo R, Ponsiglione A, Romeo V, Imbriaco M. Prostate MRI radiomics: A systematic review and radiomic quality score assessment. *Eur J Radiol* (2020) 129:109095. doi: 10.1016/j.ejrad.2020.109095
- Patel N, Henry A, Scarsbrook A. The value of MR textural analysis in prostate cancer. *Clin Radiol* (2019) 74(11):876–85. doi: 10.1016/j.crad.2018.11.007



**Conflict of Interest:** Authors JX and CH were employed by the company Beijing Deepwise & League of PHD Technology Co., Ltd.

The remaining authors declare that the research was conducted in the absence of any commercial or financial relationships that could be construed as a potential conflict of interest.

*Copyright © 2021 Li, Yang, Yue, Xu, Huang and Song. This is an open-access article distributed under the terms of the Creative Commons Attribution License (CC BY). The use, distribution or reproduction in other forums is permitted, provided the original author(s) and the copyright owner(s) are credited and that the original publication in this journal is cited, in accordance with accepted academic practice. No use, distribution or reproduction is permitted which does not comply with these terms.*



# Case Report: Extra-Articular Diffuse Tenosynovial Giant Cell Tumor of the Temporomandibular Joint

Xibiao Yang<sup>1†</sup>, Li Yao<sup>1†</sup>, Tianping Yu<sup>2</sup>, Xiaoli Du<sup>3</sup> and Qiang Yue<sup>1\*</sup>

<sup>1</sup> Department of Radiology, West China Hospital, Sichuan University, Chengdu, China, <sup>2</sup> Department of Pathology, West China Hospital, Sichuan University, Chengdu, China, <sup>3</sup> Department of Radiology, Chengdu First People's Hospital, Chengdu, China

## OPEN ACCESS

### Edited by:

Changqiang Wu,  
North Sichuan Medical College, China

### Reviewed by:

Yuchuan Hu,  
Tangdu Hospital, China  
Weelic Chong,  
Thomas Jefferson University,  
United States

### \*Correspondence:

Qiang Yue  
scu\_yq@163.com

<sup>†</sup>These authors have contributed  
equally to this work

### Specialty section:

This article was submitted to  
Cancer Imaging and  
Image-directed Interventions,  
a section of the journal  
Frontiers in Oncology

**Received:** 18 December 2020

**Accepted:** 18 January 2021

**Published:** 26 February 2021

### Citation:

Yang X, Yao L, Yu T, Du X and Yue Q  
(2021) Case Report: Extra-Articular  
Diffuse Tenosynovial Giant Cell Tumor  
of the Temporomandibular Joint.  
Front. Oncol. 11:643635.  
doi: 10.3389/fonc.2021.643635

Diffuse tenosynovial giant cell tumor (D-TSGCT) is a benign but locally destructive tumor of synovium that may involve joints, tendon sheaths, and bursae. Its occurrence in the temporomandibular joint (TMJ) is extremely rare. The authors reported a case of 48-year-old man with an extra-articular D-TSGCT in the TMJ with medial cranial fossa extension. computed tomography (CT) and magnetic resonance imaging (MRI) features are described. The lesion was a cystic-solid mass centered at the temporal bone without involvement of the condylar head, and its solid component presented high-density on CT and hypointensity on MRI. No signs of recurrence or metastasis was observed during 12-months of follow-up. The present report suggested the potential characteristics of radiologic imaging of D-TSGCT in TMJ.

**Keywords:** diffuse tenosynovial giant cell tumor, temporomandibular joint, computed tomography, magnetic resonance imaging, imaging features

## INTRODUCTION

Diffuse tenosynovial giant cell tumor (D-TSGCT), also referred to as pigmented villonodular synovitis (PVNS), is benign disorder arising from the synovium of the joints, bursa, and tendon sheath (1). It often involves the large joints of the extremities (2), among which knee joint is most commonly affected, followed by the hip joint and the foot joint (3). According to the anatomical site of involvement, D-TSGCT are classified as intra-articular or extra-articular, and the latter has a higher recurrence rate (4).

Although any synovium can be affected, only more than 100 cases of D-TSGCT involving the temporomandibular joint (TMJ) region have been reported, only 10 cases were classified as the extra-articular form (5–9). Due to the non-specific clinical manifestations and limited knowledge of the radiological features, D-TSGCT of TMJ is easily misdiagnosed as others tumors arising from bone and cartilage, or ear diseases which manifested as bone destruction (10). In the present study, we described a rare case of an extra-articular D-TSGCT in the right TMJ without the involvement of condylar head.

## CASE PRESENTATION

The patient was diagnosed with D-TSGCT at 48 years of age in West China Hospital. He started experiencing mild unilateral tinnitus, hearing loss from 3 years ago, the symptoms exacerbated gradually and trismus presented 6 months ago. Three months ago, the patient was diagnosed as cholesteatoma in the community hospital and no intervention was received. Soon afterwards, the patient presented to the otolaryngology clinic of our hospital. No facial numbness, facial muscle dysfunction, dysphagia, diplopia, or vision loss was reported, and the patient stated that there was no history of trauma to the face or jaw. A hard, non-tender, non-movable and poorly defined soft tissue mass in the right temporal area was revealed by physical examination. The high-resolution computed tomography (HRCT) of the temporal bone was performed first and suspected diagnosis of giant cell tumor (GCT) of the bone was made. The diffusion-enhanced Magnetic resonance imaging (MRI) was performed for further diagnosis, GCT of the bone or D-TSGCT was suspected diagnosed. The patient was then treated with surgery and the pathological examination was conducted. According to the histopathological features, in combination with radiological manifestations and clinical history, the final diagnosis of D-TSGCT was made. The timeline of diagnosis and treatment was showed in **Supplementary Figure 1**.

## Imaging Examinations

The HRCT revealed a mixed-density mass with soft tissue density and slightly hypodensity ( $5.2\text{ cm} \times 3.2\text{ cm} \times 3.3\text{ cm}$ ) in the right temporal squama. Incomplete bone shell was visible, and the articular surface of temporal bone was eroded while the condylar head was not involved (**Figure 1**). The fossa media was invaded through the defective temporal bone, and the temporal lobe was compressed. MRI plan scan identified an irregular and heterogeneous mass, which showed cystic components with slightly hypointensity in T1-weighted imaging (T1WI), water-like hyperintensity T2-weighted imaging (T2WI), and solid components with hypointensity both T1WI and T2WI (**Figure 2**). Hypointense signal was observed on diffusion-weighted images

(DWI) (**Figure 2**). After contrast agent (Gd-DTPA) administration, slightly enhancement was present at the wall of the cystic part, no enhancement was observed in the solid part (**Figure 2**). The effusion was also observed in the adjacent mastoid.

## Surgical Findings and Pathological Examination Results

The patient underwent surgical resection on September of 2019 and the mass was completely removed. The lesion was extradural, and its texture was mixed with hard and soft component. The external auditory canal and the bone of skull base were eroded. The mass showed adhesion to the adjacent dura and adhered tightly to the surrounding tissues. The cross-section of the lesion was dark red with hard capsule.

Microscopically, the lesion mainly composed of small, round to spindle-shaped mononuclear cells, accompanied by varying numbers of osteoclast-like giant cells, foamy cells, and hemosiderin pigments. The mononuclear cells are characterized by round or reniform nuclei, and pale cytoplasm. Osteoclast-like giant cells are usually readily apparent, which contain a variable number of nuclei. Hemosiderin deposits are virtually identified. Mitotic activity reaches up to 10 mitoses per 10 high power field (HPF). Focal necrosis and foamy cells are rarely seen. No cellular atypia was reported (**Figure 3**). A diagnosis of diffuse, extra-articular TGCT was made.

## Post-Operative Course

During 12-months of follow-up, the patient had no signs of recurrence or metastasis, the clinical symptoms were ameliorated obviously. The last time MRI data was showed in **Supplementary Figure 2**.

## DISCUSSION

The etiology of D-TSGCT remains unclear and some possible pathogenetic theories include trauma, osteoclastic proliferation, infection, immune mechanisms, inflammation, neoplasia, and metabolic disturbances are proposed (11). The theory introduced

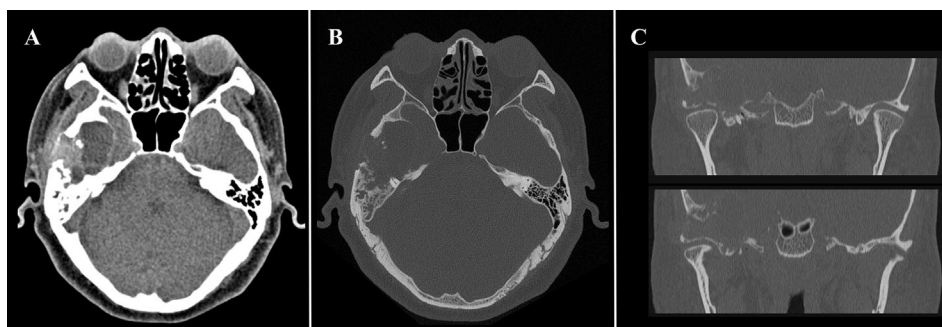


**FIGURE 1** | Computed tomography (CT) of a 48-year-old man with diffuse tenosynovial giant cell tumor (D-TSGCT) in right temporomandibular joint (TMJ). **(A)** A heterogeneous-density mass in the right temporomandibular joint region (soft tissue window, axial view). **(B)** Involvement of the temporal squamous and petrosal bones (bone window, axial view). **(C)** Erosion of the temporal bone while the condylar head was preserved (bone window, coronal view).

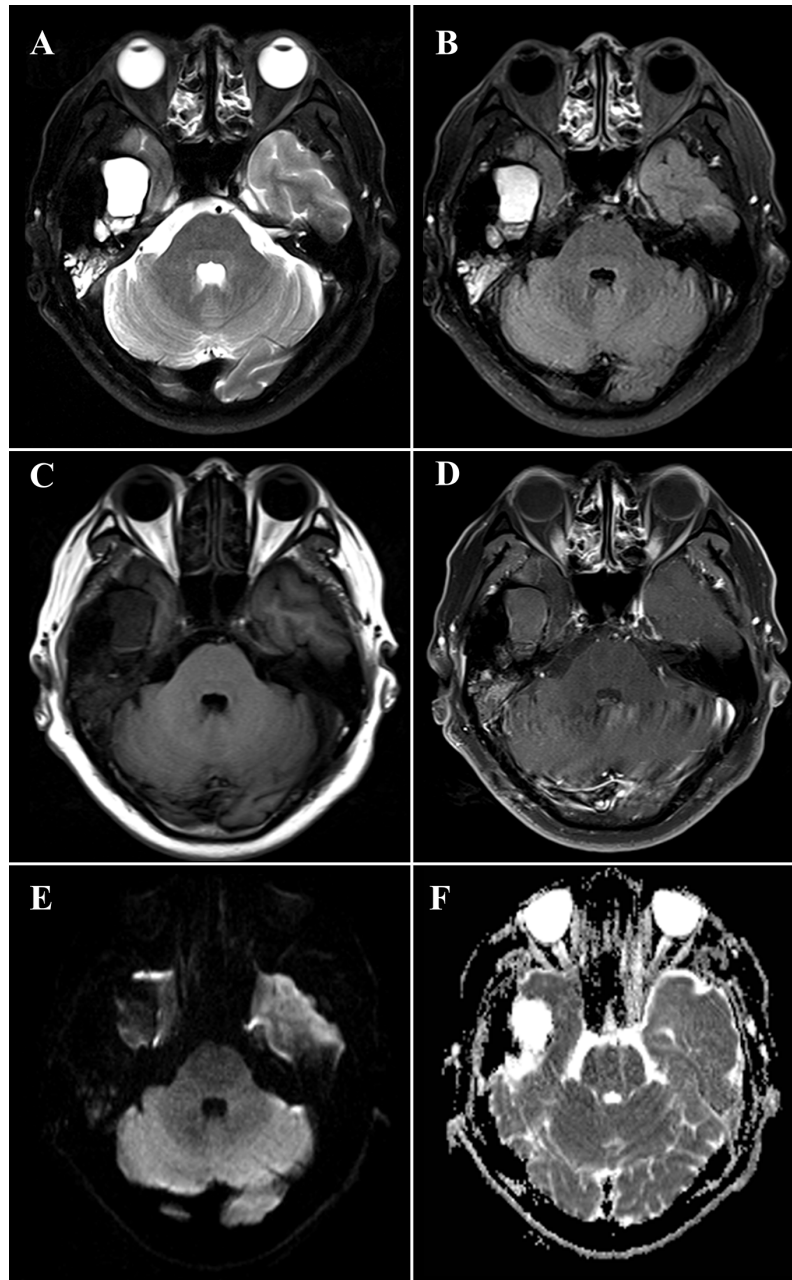


**FIGURE 2 |** Magnetic resonance imaging (MRI) of a 48-year-old man with diffuse tenosynovial giant cell tumor (D-TSGCT) in right temporomandibular joint (TMJ). MRI reveals a predominantly hypointense lesion with focal cystic changes on T2-weight imaging (**A**), fluid-attenuated inversion recovery (FLAIR) sequence (**B**) and T1-weighted imaging (**C**), which infiltrates the medial cranial fossa. Mild enhancement at the wall of the cystic part and no enhancement of the solid part was observed after administration of contrast agent (**D**). The lesion is hypointense on diffusion-weighted imaging (DWI) (**E**) and displays heterogeneous intensity on the apparent diffusion coefficient (ADC) map (**F**).

by Jaffe is that of a reactive inflammation is most widely accepted (12), however, by the findings of clonal chromosomal aberrations (13), D-TSGCT is categorized as fibrohistiocytic tumor in the current World Health Organization (WHO) classification (14). D-TSGCT can occur at any age, but the adults aged 30-50 years are predominantly affected, with equal gender prevalence (15). D-TSGCT involving TMJ is rare, with the incidence of only 1.8

cases per one million population (16). Symptoms are nonspecific including painful or painless preauricular mass, TMJ symptoms (including click sound or trismus), and dysaudia (including hearing loss, ear fullness, and tinnitus) (17). Depression on the trigeminal and facial nerve may cause local numbness in some cases. The onset age (48 years old) and gradually aggravated dysaudia and TMJ symptoms are typical in the present case.



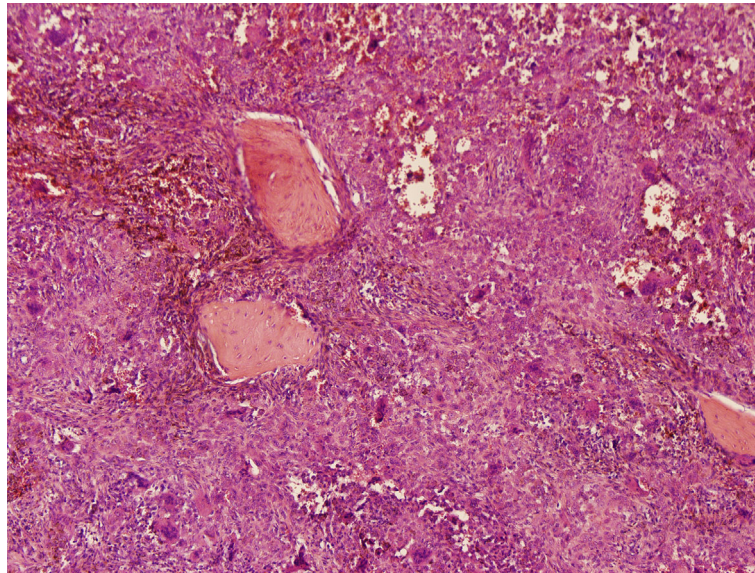


**FIGURE 3 |** Histology of a diffuse tenosynovial giant cell tumor (D-TSGCT) of the temporomandibular joint (TMJ). Microscopic examination reveals large amount of mononuclear cells, irregularly distributed osteoclast-like giant cells, and hemosiderin pigments (hematoxylin-eosin [HE], original magnification  $\times 100$ ).

Macroscopically, D-TSGCT are usually large, firm or sponge-like. It has a multi-nodular appearance, with ranging in color from yellow to dark red or brown. Microscopically, most lesions are infiltrative and grow as diffuse, expansile sheets. The cellularity varies depending on the relative proportion of mononuclear cells, multinucleate giant cells, foam cells and the amount of fibrous stroma. The mononuclear component comprises larger cells and small histiocyte-like cells. Osteoclast-like giant cells, which contain a variable number of nuclei, are usually readily apparent, but may be inconspicuous in highly cellular tumors. Large amounts of haemosiderin are frequently observed in most cases and sheets of foam cells are commonly identified in the periphery of lesions. The stromal fibrosis may appear hyalinized, although it is less marked than in the localized type (18, 19).

CT and MRI provide valuable information in the diagnosis and developing treatment plan of D-TSGCT, delineating the extent of lesion as well as destruction of bone (20). Classical radiological features of the disease include high-density noncalcifying soft tissue mass on CT owing to extensive iron deposition (20). The MRI presentation of lesion varied according to the component proportions of hemosiderin, lipids, fibrous, stroma, and cellular elements (21). The lesion usually generates a low to intermediate signal in both T1WI and T2WI because of the paramagnetic effect caused by hemosiderin concentration (22). The low signal intensity caused by the presence of hemosiderin on MRI that is accentuated on gradient-recalled echo (GRE) or susceptibility-weighted imaging (SWI) sequences is also termed as the “blooming effect” (23), which is a typical feature of D-TSGCT. All these typical features are also prominent in our present case. Comparing to the lesion in the large joints which commonly involve both sides of the joint and affect joint cavity or surrounding soft tissues, the D-TSGCT in

the TMJ can be centered in the bone and leads to destruction of the mandibular condyle, temporal bone, and intracranial extension (9). Cyst formation with water-like hyperintense signal at T2WI can be observed at the edge of the lesion in some cases, with non or minimal wall-like enhancement (3). Consistently, the present case manifested as heterogeneous mass centered at the temporal bone, and lateral cyst was also observed. It is worth noting that, uniquely, condylar head was preserved in this lesion.

The classification of the lesion type regarding to intra- or extra-articular can be difficult in clinical practice, because the anatomy of the TMJ region is complex (9). Wang et al. categorized the D-TSGCT involving the TMJ into 3 types on the basis of the imaging features, including bone-centered type, intraosseous type, and soft tissue type. The imaging findings of the present case were consistent with the bone-centered type, which is usually centered at the craniofacial bone around the TMJ, showing expansive bone erosion with incomplete bone shell and soft tissue mass adjacent to the bone erosion (9). The present case and previous reports (8, 9) demonstrated that, the bone-centered type lesions were relatively larger than other types which may attribute to longer illness duration. The joint surface was preserved in the early course of this type of disease, non-affected TMJ function and other mild symptoms may delayed the patient’s visit to the clinic.

The main differential diagnosis of D-TSGCT at TMJ includes GCT of the bone, synovial chondromatosis, aneurysmal bone cyst (ABCs), rheumatoid arthritis (RA), and cholesteatoma. GCT of bone characteristically involves extremities of long bones, usually manifests as expanded and soap bubble like inner structure with no calcification or mineralization. Synovial chondromatosis usually occurs in the synovium of large joints,

characterized by multiple calcified nodules in the lesion area on CT. Uncalcified bodies generates hypointensity on T1WI and hyperintensity on T2WI. There is no hemosiderin deposition in the above two diseases. RA often invades multiple joints with demineralization and narrowing of the joint space. On CT or MRI, ABCs demonstrate as expansile osteolytic lesions with thin sclerotic margins, and the typical features are fluid-fluid levels with low signal intensity in the inferior layer and high signal intensity in the superior layer on T2WI. Cholesteatoma commonly affects the petrous part of temporal bone, presenting as bone destruction, accompanying with homogenous density soft tissue mass on CT, and the lesion manifests as remarkable high intensity on T2WI. Other diseases addressing preauricular swelling such as brown tumor, and synovial sarcoma are also needed to be taken into differential diagnosis. With the rare incidence, accurate diagnosis can be challenging before operation. Solid mass generating high-density on CT and hypointensity on MRI with cystic changes may be of some specificity to D-TSGCT of TMJ, in combination with clinical history and histopathological features suggest the diagnosis.

Recurrence rates of D-TSGCT after treatment varied ranging from 9 to 46%, depending on the joint affected and the length of follow-up (24, 25). The main treatment strategy of D-TSGCT is complete surgical excision of involved bones and wide synovectomy (23). However, the complete removal is challenging due to the infiltrative nature of the disease and the need to preserve the adjacent joint function. Therefore, adjuvant external beam radiation therapy (EBRT) is necessary when the surgical margin is inadequate. Additional treatments including cryosurgery, total joint arthroplasty, immunotherapy, and targeted therapy might be alternative when the complete removal is considered mutilating, but the effect of these treatments remains controversial due to the rarity of the disease and heterogeneity of the patients (26). The D-TSGCT is considered a tumor with uncertain behavior, and histologically benign D-TSGCT can rarely develop metastasis (27).

## PATIENT PERSPECTIVE

“Four years ago, I started to find hearing loss in my right ear, the symptoms worsened gradually, and the mouth opening was restricted. I went to the community hospital first and was diagnosed as cholesteatoma. Afterwards, I went to the department of otorhinolaryngology, orthopedics and neurosurgery of West China Hospital, hoping to receive thorough treatment. After various examinations, the doctor told me that my disease might be a benign bone tumor and suggested the surgery to remove the mass. After the pathological examination, I knew that my disease is a rare tumor that occurs in the temporomandibular joint. My symptoms gradually improved after the operation and there are no signs of recurrence so far. The doctors and nurses in West China Hospital were nice, and the attention and care I received was well-organized and excellent. I do not mind my case being reported and happy that other doctors learning from that.”

## CONCLUSION

We describe a rare case of D-TSGCT in the TMJ without involvement of the condyle head and its CT and MRI characteristic, which is highly valuable in establishing the diagnosis.

## DATA AVAILABILITY STATEMENT

The original contributions presented in the study are included in the article/**Supplementary Material**. Further inquiries can be directed to the corresponding author.

## ETHICS STATEMENT

Written informed consent was obtained from the individual(s) for the publication of any potentially identifiable images or data included in this article.

## AUTHOR CONTRIBUTIONS

XY and LY performed the data acquisition. XY, LY, and XD performed the radiological analysis of MRI and CT images. TY performed the histopathological observation. XY, LY, and QY performed the manuscript preparation. All authors contributed to the article and approved the submitted version.

## FUNDING

This work was supported by the Sichuan Provincial Foundation of Science and Technology (Grant No. 2019YFS0428 and 2021YFS0077), the Foundation of the National Research Center of Geriatrics (Grant No. Z2018A07) and Science and Technology Project of the Health Planning Committee of Sichuan (19PJ078 and 19PJ247).

## SUPPLEMENTARY MATERIAL

The Supplementary Material for this article can be found online at: <https://www.frontiersin.org/articles/10.3389/fonc.2021.643635/full#supplementary-material>

**Supplementary Figure 1** | The timeline of diagnosis and treatment of the case.

**Supplementary Figure 2** | Magnetic resonance imaging (MRI) after 12-months follow-up, no signs of recurrence were found. A: T1-weighted imaging; B: T2-weight imaging; C: Enhanced T1-weighted imaging, axial view; D: Enhanced T1-weighted imaging, coronal view.

## REFERENCES

- Garner HW, Bestic JM. Benign synovial tumors and proliferative processes. *Semin Musculoskelet Radiol* (2013) 17(2):177–8. doi: 10.1055/s-0033-1343095
- Somerhausen NS, Fletcher CD. Diffuse-type giant cell tumor: clinicopathologic and immunohistochemical analysis of 50 cases with extraarticular disease. *Am J Surg Pathol* (2000) 24(4):479–92. doi: 10.1097/0000478-200004000-00002
- Nomura F, Ariizumi Y, Kiyokawa Y, Tasaki A, Tateishi Y, Koide N, et al. Pigmented villonodular synovitis occurring in the temporomandibular joint. *Auris Nasus Larynx* (2019) 46(4):609–17. doi: 10.1016/j.anl.2018.10.021
- Gouin F, Noailles T. Localized and diffuse forms of tenosynovial giant cell tumor (formerly giant cell tumor of the tendon sheath and pigmented villonodular synovitis). *Orthop Traumatol Surg Res* (2017) 103(1S):S91–S7. doi: 10.1016/j.otsr.2016.11.002
- Gong ZC, Lin ZQ, Moming A, Ling B, Liu H, Hu M, et al. Extra-articular diffuse tenosynovial giant cell tumour of the infratemporal fossa: report of a case and literature review. *Int J Oral Maxillofac Surg* (2010) 39(8):820–4. doi: 10.1016/j.ijom.2010.02.026
- Lee JH, Kim YY, Seo BM, Baek SH, Choi JY, Choung PH, et al. Extra-articular pigmented villonodular synovitis of the temporomandibular joint: case report and review of the literature. *Int J Oral Maxillofac Surg* (2000) 29(6):408–15. doi: 10.1034/j.1399-0020.2000.290603.x
- Chow LT, Kumta SM, King WW. Extra-articular pigmented villonodular synovitis of the temporomandibular joint. *J Laryngol Otol* (1998) 112(2):182–5. doi: 10.1017/s0022215100140265
- Son SM, Park YS, Choi CH, Lee HC, Lee OJ, Woo CG. Extra-articular tenosynovial giant cell tumor of diffuse type in the temporal area with brain parenchymal invasion: a case report. *Br J Neurosurg* (2018) 32(6):688–90. doi: 10.1080/02688697.2018.1426729
- Wang JG, Liu J, He B, Gao L, Zhang L, Liu J. Diffuse Tenosynovial Giant Cell Tumor Around the Temporomandibular Joint: An Entity With Special Radiologic and Pathologic Features. *J Oral Maxillofac Surg* (2019) 77(5):1022.e1–22.e39. doi: 10.1016/j.joms.2019.01.025
- Carlson ML, Osetinsky LM, Alon EE, Inwards CY, Lane JJ, Moore EJ. Tenosynovial giant cell tumors of the temporomandibular joint and lateral skull base: Review of 11 cases. *Laryngoscope* (2017) 127(10):2340–6. doi: 10.1002/lary.26435
- Kerfant N, Bardin T, Roulot E. Multiple Giant Cell Tumors of the Tendon Sheath : Separate Volar and Dorsal Lesions Involving Three Digits of the Same Hand Following Repetitive Trauma. *J Handb Microsurg* (2015) 7(1):233–5. doi: 10.1007/s12593-015-0185-3
- Jaffe HL, Lichtenstein L, Sutro CJ. Pigmented Villonodular Synovitis, Bursitis and Tenosynovitis. *Arch Pathol* (1941) 31:731–65.
- Righi A, Gambarotti M, Sbaraglia M, Frisoni T, Donati D, Vanel D, et al. Metastasizing tenosynovial giant cell tumour, diffuse type/pigmented villonodular synovitis. *Clin Sarcoma Res* (2015) 5:15. doi: 10.1186/s13569-015-0030-2
- Somerhausen N, van den Rijn M. Tenosynovial giant cell tumour, diffuse type. In: C Fletcher, JA Bridge, PCW Hogendoorn, F Mertens, editors. *WHO classification of tumours of soft tissue and bone*, 4. Lyon: IARC Press (2013). p. 102–3.
- Cascone P, Rinna C, Ungari C, Poladas G, Filiaci F. Pigmented villonodular synovitis of the temporomandibular joint. *J Craniofac Surg* (2005) 16(4):712–6. doi: 10.1097/01.scs.0000159085.67672.2d
- Myers BW, Masi AT. Pigmented villonodular synovitis and tenosynovitis: a clinical epidemiologic study of 166 cases and literature review. *Med (Baltimore)* (1980) 59(3):223–38. doi: 10.1097/00005792-198005000-00004
- Joshi K, Huang B, Scanga L, Buchman C, Chera BS. Postoperative radiotherapy for diffuse pigmented villonodular synovitis of the temporomandibular joint. *Am J Otolaryngol* (2015) 36(1):106–13. doi: 10.1016/j.amjoto.2014.10.017
- Hoch BL, Garcia RA, Smalberger GJ. Chondroid tenosynovial giant cell tumor: a clinicopathological and immunohistochemical analysis of 5 new cases. *Int J Surg Pathol* (2011) 19(2):180–7. doi: 10.1177/1066896910381899
- Lu DY, Zhang L, Apple SK, Dry SM, Moatamed NA. Fine needle aspiration of pigmented villonodular synovitis of the temporomandibular joint. *Diagn Cytopathol* (2011) 39(1):45–8. doi: 10.1002/dc.21362
- Bemporad JA, Chaloupka JC, Putman CM, Roth TC, Tarro J, Mitra S, et al. Pigmented villonodular synovitis of the temporomandibular joint: diagnostic imaging and endovascular therapeutic embolization of a rare head and neck tumor. *AJNR Am J Neuroradiol* (1999) 20(1):159–62.
- Lynskey SJ, Pianta MJ. MRI and thallium features of pigmented villonodular synovitis and giant cell tumours of tendon sheaths: a retrospective single centre study of imaging and literature review. *Br J Radiol* (1056) 2015:88:20150528. doi: 10.1259/bjr.20150528
- Wan JM, Magarelli N, Peh WC, Guglielmi G, Shek TW. Imaging of giant cell tumour of the tendon sheath. *Radiol Med* (2010) 115(1):141–51. doi: 10.1007/s11547-010-0515-2
- Romanach MJ, Brasileiro BF, Leon JE, Alves DB, de Almeida OP, Vargas PA. Pigmented villonodular synovitis of the temporomandibular joint: case report and review of the literature. *Oral Surg Oral Med Oral Pathol Oral Radiol Endod* (2011) 111(3):e17–28. doi: 10.1016/j.tripleo.2010.11.019
- Byers PD, Cotton RE, Deacon OW, Lowy M, Newman PH, Sissons HA, et al. The diagnosis and treatment of pigmented villonodular synovitis. *J Bone Joint Surg Br* (1968) 50(2):290–305. doi: 10.1302/0301-620X.50B2.290
- Schwartz HS, Unni KK, Pritchard DJ. Pigmented villonodular synovitis. A retrospective review of affected large joints. *Clin Orthop Relat Res* (1989) 247:243–55. doi: 10.1097/00003086-198910000-00034
- Verspoor FG, van der Geest IC, Vegt E, Veth RP, van der Graaf WT, Schreuder HW. Pigmented villonodular synovitis: current concepts about diagnosis and management. *Future Oncol* (2013) 9(10):1515–31. doi: 10.2217/fon.13.124
- Asano N, Yoshida A, Kobayashi E, Yamaguchi T, Kawai A. Multiple metastases from histologically benign intraarticular diffuse-type tenosynovial giant cell tumor: a case report. *Hum Pathol* (2014) 45(11):2355–8. doi: 10.1016/j.humpath.2014.06.025

**Conflict of Interest:** The authors declare that the research was conducted in the absence of any commercial or financial relationships that could be construed as a potential conflict of interest.

Copyright © 2021 Yang, Yao, Yu, Du and Yue. This is an open-access article distributed under the terms of the Creative Commons Attribution License (CC BY). The use, distribution or reproduction in other forums is permitted, provided the original author(s) and the copyright owner(s) are credited and that the original publication in this journal is cited, in accordance with accepted academic practice. No use, distribution or reproduction is permitted which does not comply with these terms.





# Is Additional Systematic Biopsy Necessary in All Initial Prostate Biopsy Patients With Abnormal MRI?

Xueqing Cheng<sup>1†</sup>, Jinshun Xu<sup>2†</sup>, Yuntian Chen<sup>1</sup>, Zhenhua Liu<sup>3</sup>, Guangxi Sun<sup>3</sup>, Ling Yang<sup>1</sup>, Jin Yao<sup>1</sup>, Hao Zeng<sup>3\*</sup> and Bin Song<sup>1\*</sup>

<sup>1</sup> Department of Radiology, West China Hospital, Sichuan University, Chengdu, China, <sup>2</sup> Department of Ultrasound, West China Hospital, Sichuan University, Chengdu, China, <sup>3</sup> Department of Urology, West China Hospital, Sichuan University, Chengdu, China

## OPEN ACCESS

### Edited by:

Changqiang Wu,  
North Sichuan Medical College, China

### Reviewed by:

Haoran Sun,  
Tianjin Medical University General  
Hospital, China  
Gang Huang,  
Gansu Provincial Hospital, China

### \*Correspondence:

Bin Song  
songlab\_radiology@163.com  
Hao Zeng  
kucaizeng@163.com

<sup>†</sup>These authors have contributed  
equally to this work

### Specialty section:

This article was submitted to  
Cancer Imaging and  
Image-directed Interventions,  
a section of the journal  
Frontiers in Oncology

**Received:** 17 December 2020

**Accepted:** 14 January 2021

**Published:** 26 February 2021

### Citation:

Cheng X, Xu J, Chen Y, Liu Z, Sun G,  
Yang L, Yao J, Zeng H and Song B  
(2021) Is Additional Systematic Biopsy  
Necessary in All Initial Prostate Biopsy  
Patients With Abnormal MRI?  
Front. Oncol. 11:643051.  
doi: 10.3389/fonc.2021.643051

**Purpose:** To determine whether additional systematic biopsy is necessary in all biopsy naïve patients with MRI visible lesions by taking PI-RADS score and prostate volume into consideration.

**Materials and Methods:** Patients who underwent combined systematic biopsy (SB) and cognitive MRI-targeted biopsy (TB) in our hospital between May 2018 and June 2020 were retrospectively reviewed. The detection rate of clinical significant prostate cancer (csPCa), biopsy grade group (GG) concordance, and disease upgrading rate on radical prostatectomy were compared between SB and TB and further stratified by PI-RADS v2.0 category and prostate volume.

**Results:** A total of 234 patients were analyzed in this study. TB alone detected more csPCa and less clinically insignificant prostate cancer (cisPCa) than SB alone in the whole cohort (57.3 vs 53%,  $P = 0.041$ ; 3.8 vs 7.7%,  $P = 0.049$  respectively). The additional SB indicated only a marginal increase of csPCa detection but a remarkable increase of cisPCa detection compared with targeted biopsy (59.4 vs 57.3%,  $P = 0.064$ ; 3.8 vs 7.7%,  $P = 0.012$ ). As stratified by PI-RADS category, the difference of csPCa detection rate between TB and SB was not significant either in PI-RADS 5 subgroup (83.8 vs 76.3%,  $P = 0.07$ ) or in PI-RADS 3–4 subgroup (43.5 vs 40.9%,  $P = 1.0$ ). Additional SB decreased the rate of disease upgrading on radical prostatectomy (RP) than TB alone in PI-RADS 3–4 subgroup (14.5 vs 25.5%,  $P = 0.031$ ) other than PI-RADS 5 subgroup (6 vs 6%,  $P = 1.0$ ). When stratified by prostate volume (PV), TB alone detected more csPCa than SB in small prostate (PV < 30 ml) group (81.0 vs 71.0%,  $P = 0.021$ ) but not in large prostate (PV ≥ 30 ml) group (44.0 vs 42.7%,  $P = 0.754$ ). The additional SB did not significantly decrease the rate of disease upgrading on RP than TB alone in either small or large prostate (6.4 vs 8.5%,  $P = 1.0$ ; 13.8 vs 22.4%,  $P = 0.063$ ).

**Conclusion:** The combination biopsy method was no superior than targeted biopsy alone in PI-RADS 5 or in small volume prostate subgroup.

**Keywords:** prostate cancer, prostate biopsy, targeted biopsy, MRI, PI-RADS



## INTRODUCTION

The standard 10 or 12 cores systematic transrectal ultrasound biopsy (TRUS) was the most common diagnostic method for men suspected with prostate cancer (PCa) on the basis of elevated prostate-specific antigen (PSA) level or an abnormal digital rectal examination (1). But this random sampling strategy is lacking reliability and associated with missed clinically significant PCa (csPCa) and substantial inaccurate risk stratification (2, 3). In addition, systematic biopsy can inadvertently detect indolent PCa causing overdiagnosis and eventually overtreatment.

With recent advances, prostate multiparametric magnetic resonance imaging (mpMRI) has been widely used as a triage test before biopsy in clinical practice, which could reduce unnecessary prostate biopsies (4). Meanwhile, MRI-targeted biopsy allows better sampling of cancer through accurate localization of suspicious prostate lesions just as other solid organs tumors (5–10). Many studies demonstrated that MRI-targeted biopsy improved csPCa detection and cancer risk stratification compared with systematic biopsy (6, 9, 11–14). Although the NICE and the EAU guidelines recommend combined targeted and systematic biopsies in case of positive MRI findings, particularly for repeat biopsies (15, 16), questions about the necessity for additional systematic biopsy still persist. As reported, for every one additional csPCa detected, 60 patients need systematic biopsy in addition to targeted biopsy (17). While this combined biopsy strategy leads to a large number of cores being taken, thus further increasing the risk of complication and injury inherent to prostate biopsies as well as the economic burden. Therefore, it is of clinical importance to assess the clinical implications of targeted biopsy with additional systematic biopsy.

Prostate volume and PI-RADS category are the major two factors taken into consideration to perform initial prostate biopsy in men with suspected prostate cancer based on elevated PSA, but whether they could be incorporated to the selection of optimal biopsy method is unknown. In this study, we assessed the use of cognitive MRI guided targeted, systematic, or combined prostate biopsy in an attempt to determine whether the systematic biopsy is necessary in all initial biopsy naïve patients with abnormal MRI and whether PI-RADS score and prostate volume should affect the type of biopsy method that is selected.

## MATERIALS AND METHODS

### Patients

This study was a retrospective study approved by the institutional review board with a waiver of informed consent. Patients suspected with prostate cancer for elevated prostate-specific antigen (PSA) level or abnormal digital rectal examination and subsequently underwent combined systematic biopsy and cognitive MRI-targeted biopsy in our hospital between May 2018 and June 2020 were included. The prebiopsy mpMRI indicated suspicious prostate lesions (PI-RADS  $\geq 3$ ). The exclusion criteria include: a) previous prostate

biopsy, prostate surgery, or neoadjuvant hormonal therapy before biopsy; b) missing PSA or PSA  $>100$  ng/ml; c) MRI not performed at our institution; d) interval between MRI and biopsy longer than 6 months.

### Image Acquisition and Interpretation

Multiparametric MRI was performed using 3.0-T MRIs (Magnetom Skyra, Siemens) with phased-array body surface coil. All images were obtained with 3-mm section thickness. T2-weighted images in the sagittal, coronal, and axial planes, diffusion weighted images (b value up to  $1,500 \text{ s/mm}^2$ ) in the axial plane, and dynamic contrast-enhanced images were acquired according to the international prostate MRI guidelines (18). MRI lesions were assigned a Prostate Imaging Reporting and Data System Version 2 (PI-RADS v2.0) score of 1 to 5. Two radiologists with respectively 3 and 10 years of experience in abdominal imaging read the images for each patient separately (18). Radiologists were not blinded to clinical information. The lesion with the highest PI-RADS score on mpMRI was defined as the index lesion. If there were two or more foci of equally high PI-RADS score, then the largest one was designated the index lesion.

### Biopsy Technique and Histological Evaluation

All prostate biopsies were performed transperineally under local anesthesia using TRUS guidance with a bi-planar ultrasound probe (BK Medical, USA). A standard 10 or 12 cores systematic biopsy (SB) was obtained including transitional, peripheral, anterior zone from base to apex followed by cognitive MRI-guided targeted biopsy (TB). The MR images were available for direct review during the biopsy. Each lesion with a PI-RADS score of 3–5 was biopsied using two or three cores (a maximum of five cores per patient). All biopsy procedures were performed by two experienced urologists with more than 10 years of experience in prostate biopsy, and guided by an experienced urological radiologist (with more than 10 years' experience in TRUS guiding prostate biopsy). Where a lesion was visible at TRUS, it was targeted by using the core for the relevant prostate zone (no additional cores were performed).

All prostate biopsy cores were individually labeled and were analyzed by two dedicated uropathologists. For patients diagnosed as PCa, the number of positive cores, proportion of cancer involvement, as well as grade group (GG) and Gleason score (GS) were determined using the 2014 International Society of Urologic Pathology (ISUP) criteria (19). A GG  $\geq 2$  (GS  $\geq 3 + 4$ ) was defined as clinically significant prostate cancer (csPCa), whereas others were defined as clinically insignificant prostate cancer (cisPCa) (19).

### Statistical Analysis

Comparisons of categorical variable were performed using the chi-square test and continuous variables were evaluated with the Student t test after evaluating normality of the data using a one-sample Kolmogorov-Smirnov test. One way ANOVA was used

for comparison of continuous variables between groups unless the data were not normally distributed, in which case the Kruskal-Wallis test was used. Wilcoxon's matched-pairs signed-rank test was used to compare number of biopsy cores, number of positive cores, and percentage of cancer involvement. The McNemar test was used to evaluate differences in cancer detection rates and upgrading rates on radical prostatectomy between each biopsy method. A  $P < 0.05$  was considered to indicate statistical significance. The statistical analysis was performed using SPSS (ver. 19.0; SPSS Inc., Chicago, IL, USA).

## RESULTS

### Clinical Characteristics

There were 290 patients performed systematic combined with targeted biopsy (TB+SB), and 56 of them were excluded because of prior prostate biopsy or surgery ( $n = 33$ ), MRI not performed at our institution ( $n = 5$ ); missing PSA or PSA  $>100$  ng/ml ( $n = 10$ ), and duration between biopsy and MRI longer than 6 months ( $n = 8$ ). Finally, there were 234 patients included in this study (Figure 1), 48 (20.5%) of them had a PI-RADS v2.0 score of 3, 106 (45.3%) had a score of 4, and 80 (34.2%) had a score of 5. The median number of MRI lesions detected was 1, with a median of 3 targeted cores and 12 systematic cores taken per patient. Patient demographics are shown in Table 1.

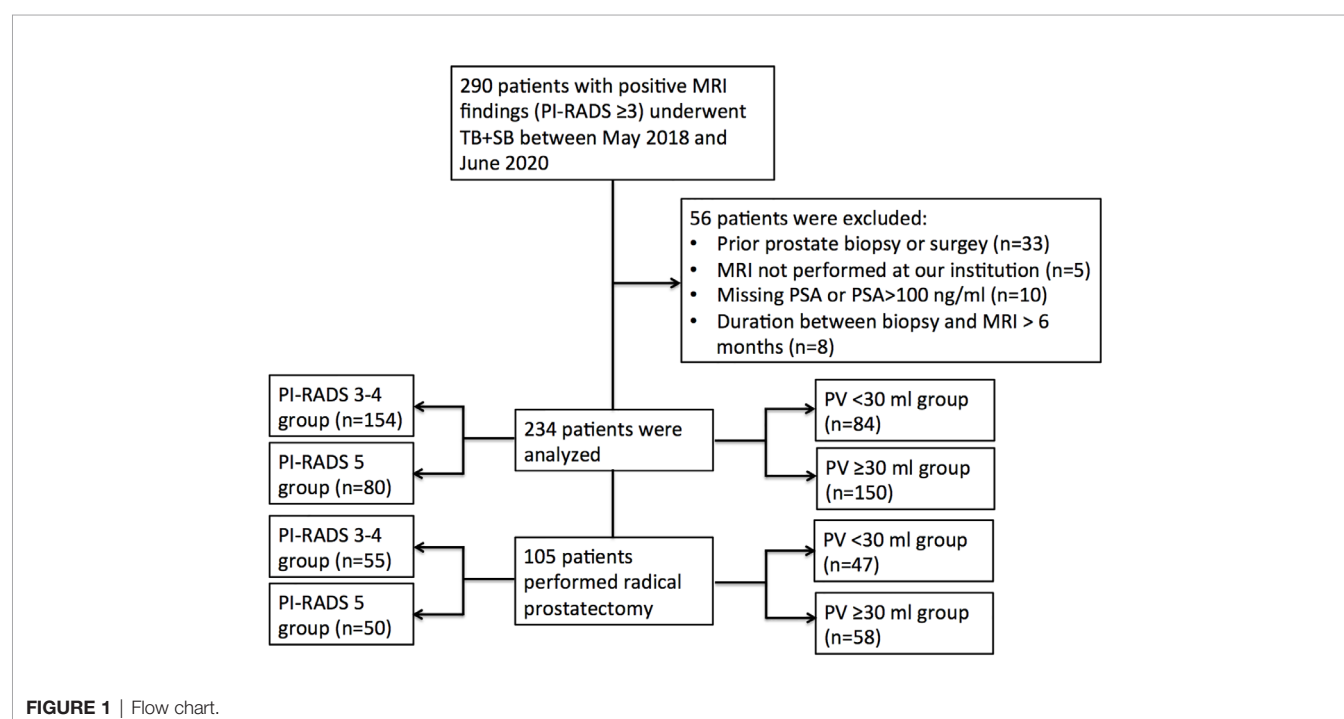
### Targeted Versus Systematic Cancer Detection and Risk Stratification for the Whole Cohort

The two biopsy methods were compared in terms of the highest GG detected per patient, and the highest GG that was detected by

**TABLE 1 |** Patient characteristics.

Characteristics	Total
No. of patients	234
Age (y)	66.3 $\pm$ 8.95
PSA (ng/ml)	12.5 $\pm$ 9.94
Prostate volume on MRI (ml)	42.2 $\pm$ 23.65
No. of MRI lesions	1 (1, 2)
Maximum diameter of index lesion (cm)	1.5 $\pm$ 0.61
PI-RADS Score	
3	48 (20.5%)
4	106 (45.3%)
5	80 (34.2%)
Combined biopsy results	
No cancer	77
GG1 (GS 3 + 3)	18
GG2 (GS 3 + 4)	61
GG3 (GS 4 + 3)	50
GG4 (GS 4 + 4/3+5)	13
GG5 (GS 4 + 5)	15
No. of cores on TB	3 (3, 5)
No. of cores on SB	12 (12, 12)
No. of positive samples on TB	2 (0, 3)
No. of positive samples on SB	1 (0, 4)
Cancer involvement on TB (%)	30 (15, 60)
Cancer involvement on SB (%)	17.5 (10, 30)

either biopsy method was considered as the GG detected on combined biopsy as shown in Table 2. There was a significant difference in the number of positive cores and percentage of cancer involvement of positive core (Table 1, both  $P < 0.001$ ). Among 234 patients who underwent combined biopsy, 139 (59.4%) were diagnosed of csPCa, 18 (7.7%) were cisPCa, and 77 (33.5%) were not cancer. When each method was used alone, the detection rate of csPCa decreased to 57.3% (134 of 234 men) for TB and 53% (124 of 234 men) for SB (Figure 2). TB had a

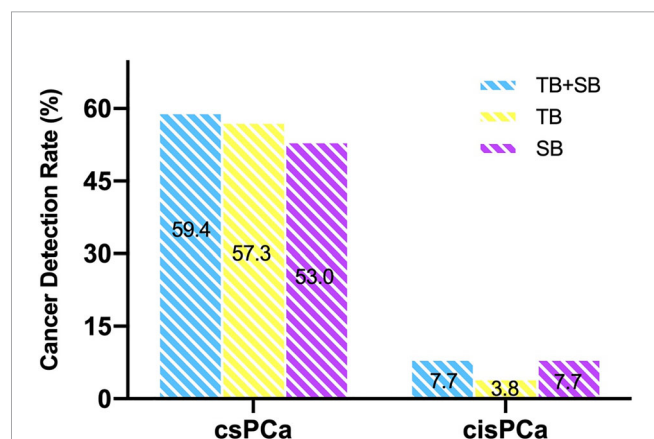


**FIGURE 1 |** Flow chart.

**TABLE 2** | Cross-tabulation of highest grade group detected by biopsy method.

		No. of Patients in Grade Group (GG) with SB						
		No cancer	GG1	GG2	GG3	GG4	GG5	Total
No. of Patients in Grade Group (GG) with TB	No cancer	77	10	4	0	0	0	91
	GG1	3	5	1	0	0	0	9
	GG2	6	3	47	0	1	0	57
	GG3	3	0	9	38	0	1	51
	GG4	2	0	0	3	7	2	14
	GG5	1	0	0	3	0	8	12
	Total	92	18	61	44	8	11	234

The blue shading means upgrading by TB, the grey shading means upgrading by both biopsy methods, and the green shading means upgrading by SB.

**FIGURE 2** | Comparison of csPCa and cisPCa detection rate between TB+SB, TB alone, and SB alone in the whole cohort.

significantly greater csPCa detection rate than SB ( $P = 0.041$ ), and similar csPCa detection rate with TB+SB ( $P = 0.063$ ). While, the cisPCa detection rate of TB was significantly lower than TB+SB

and SB ( $P = 0.012$ ,  $P = 0.049$  respectively; **Figure 2**). Among the 14 (6.0%) prostate cancer missed by TB, only 4 (28.6%) was GG2, and the other was all GG1 with no more than 2 cores positive on SB (**Table 2**). But SB alone missed 6  $GG \geq 3$ , 6 GG2, and 3 GG1 cancers.

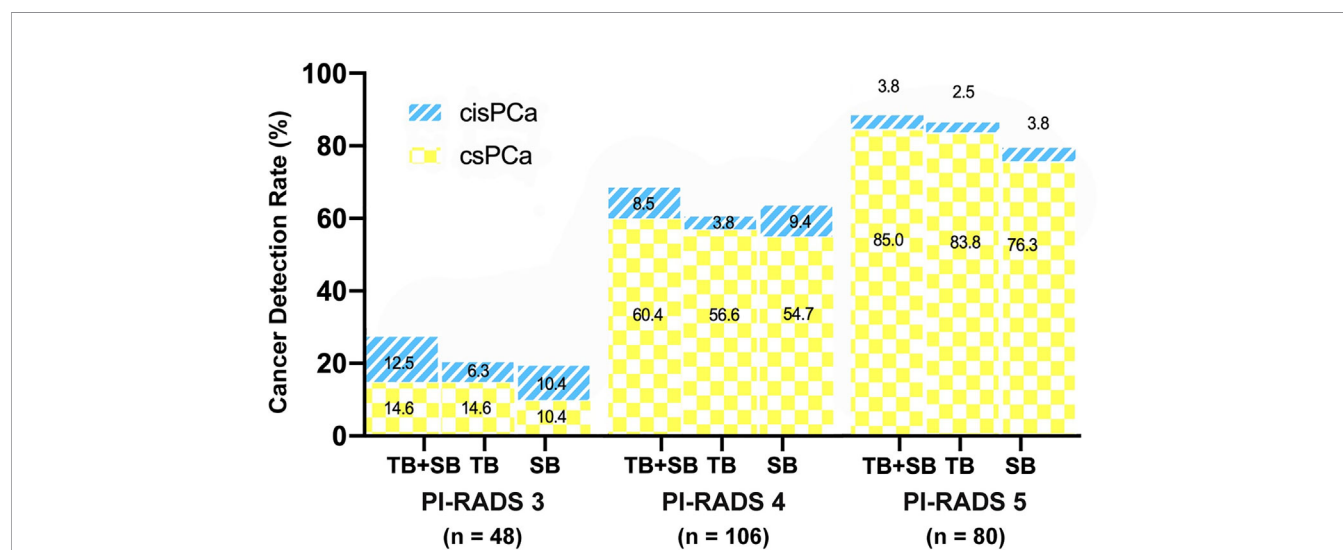
Among 157 patients diagnosed as prostate cancer by combined biopsy, 105 (66.9%) had concordant grade group between TB and SB, 33 (21%) patients had upgraded GG on TB over SB, and 19 (12.1%) had upgraded GG on SB over TB. Omission of SB would lead a reclassification to lower risk stratification in three patients. But the omission of targeted biopsy would make 9 prostate cancers reclassified to lower stratification (**Table 2**).

## Relationship of PI-RADS, Prostate Volume With CDR

As shown in **Figure 3**, the csPCa detection rate increased significantly with a greater PI-RADS score ( $P < 0.001$ ), with no significant difference between biopsy methods. This finding was not seen in cisPCa detection by any of TB+SB ( $P = 0.182$ ), TB ( $P = 0.565$ ), and SB ( $P = 0.259$ ). Taking prostate volume into consideration, there was a significant trend in increased detection of csPCa with decreased prostate volume by all methods (**Figure 4**, all  $P < 0.001$ ).

## Targeted Versus Systematic Cancer Detection and Risk Stratification Stratified by PI-RADS Score

To evaluate cancer detection and risk stratification by PI-RADS score, patients were split into PI-RADS 5 ( $n = 80$ ) and PI-RADS 3–4 group ( $n = 154$ ). The conjunction of SB detected additional one and four csPCa in PI-RADS 5 and PI-RADS 3–4 group respectively, but didn't lead to a higher csPCa detection rate compared than TB alone in both groups ( $P = 1.0$ ,  $P = 0.125$  respectively, **Table 3**). Meanwhile, the difference of csPCa detection rate between TB and SB was not significant either in

**FIGURE 3** | Comparison of csPCa ( $GS \geq 7$ ) and cisPCa ( $GS \geq 6$ ) cancer detection between TB+SB, TB alone, and SB alone stratified by PI-RADS score.

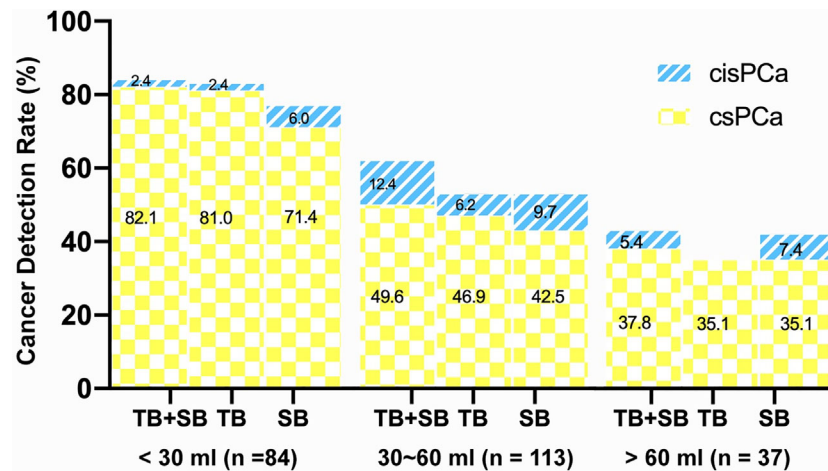


**FIGURE 4** | Comparison of csPCa (GS≥7) and cisPCa (GS6) cancer detection between TB+SB, TB alone, and SB alone stratified by prostate volume.

**TABLE 3** | Characteristics of the study population stratified by PI-RADS.

Parameter	PI-RADS 5	PI-RADS 3-4	P
Number	80	154	
Age	68.5 ± 9.35	65.1 ± 8.54	0.232
PSA	16.8 ± 13.84	10.3 ± 5.89	0.000
Prostate volume	39.7 ± 18.5	43.5 ± 25.89	0.073
csPCa detection (%)			
TB+SB	68 (85%)	71 (46.1%)	0.000
TB alone	67 (83.8%)	67 (43.5%)	0.000
SB alone	61 (76.3%)	63 (40.9%)	0.000
GG concordant between TB and SB	47 (66.2%)	58 (67.4%)	0.869
GG discordant between TB and SB	24 (33.8%)	28 (32.6%)	—
Upgrading on TB	19 (79.2%)	14 (50%)	0.029
Upgrading on SB	5 (20.8%)	14 (50%)	0.029
Radical prostatectomy	50	55	
Upgrading over TB+SB	3 (6%)	8 (14.5%)	0.153
Upgrading over TB	3 (6%)	14 (25.5%)	0.003
Upgrading over SB	14 (28%)	12 (21.8%)	0.464

PI-RADS 5 group (83.8 vs 76.3%,  $P = 0.07$ ) or in PI-RADS 3-4 group (43.5 vs 40.9%,  $P = 1.0$ ).

With respect to the GG concordance between TB and SB, the concordant rate was similar in PI-RADS 5 and PI-RADS 3-4 subgroup (66.2 vs 67.4%,  $P = 0.869$ , **Table 3**). Patients with PI-RADS 5 lesions were more likely to experience upgrading on TB than PI-RADS 3-4 patients (79.2 vs 50%,  $P = 0.029$ ). Conversely, patients with PI-RADS 3-4 lesions were more likely to experience upgrading on SB compared to PI-RADS 5 patients (50 vs 20.8%,  $P = 0.029$ ).

## Targeted Versus Systematic Cancer Detection and Risk Stratification Stratified by Prostate Volume

When the whole cohort was stratified by prostate volume (PV), TB alone detected significantly more csPCa than SB in small prostate (PV <30 ml) group (81.0 vs 71.0%,  $P = 0.021$ ) but not in large prostate (PV ≥30 ml) group (44 vs 42.7%,  $P = 0.754$ ). The conjunction with SB detected additional one and four csPCa in

small and large prostate group respectively, but didn't increase the csPCa detection rate compared with TB alone in each subgroup (82.1 vs 81%,  $P = 1.0$ ; 46.7 vs 44%,  $P = 0.125$ ).

As for GG concordance between the two methods, men with small prostate seems more likely to experience upgrading on TB than men with large prostate (78.9 vs 54.5%, **Table 4**), but the difference was of no significance ( $P = 0.078$ ).

## Pathological Concordance on Radical Prostatectomy

Out of 157 prostate cancer patients detected by combined biopsy, 105 subsequently underwent radical prostatectomy (RP) at our institution. In total, 11 (10.5%) of 105 patients had upgraded GG on RP. There were four men upgraded from GG1 to GG2 ( $n = 4$ ), two from GG2 to GG3, one from GG3 to GG4, and two from GG3 to GG5. The other two patients were misdiagnosed as no cancer in

**TABLE 4** | Characteristics of the study population stratified by prostate volume.

Parameter	PV <30 ml	PV ≥30 ml	P
Number	84	150	
Age	63.3 ± 8.43	68.0 ± 8.80	0.354
PSA	12.1 ± 9.57	12.8 ± 10.16	0.649
PI-RADS			
3	8 (9.5%)	40 (26.7%)	0.008
4	43 (51.2%)	63 (42%)	
5	33 (39.3%)	47 (31.3%)	
csPCa detection (%)			
TB+SB	69 (82.1%)	70 (46.7%)	0.000
TB alone	68 (81%)	66 (44%)	0.000
SB alone	60 (71%)	64 (42.7%)	0.000
GG concordant between TB and SB	52 (73.2%)	53 (61.6%)	0.124
GG discordant between TB and SB	19 (26.8%)	33 (38.4%)	0.124
Upgrading on TB	15 (78.9%)	18 (54.5%)	0.078
Upgrading on SB	4 (21.1%)	15 (45.5%)	0.078
Radical prostatectomy	47	58	
Upgrading over TB+SB	3 (6.4%)	8 (13.8%)	0.218
Upgrading over TB	4 (8.5%)	13 (22.4%)	0.054
Upgrading over SB	7 (14.9%)	19 (32.8%)	0.035



initial biopsy but detected GG2 cancer in the second biopsy and subsequent radical prostatectomy, therefore upgraded from no cancer to GG2. Either TB alone or SB alone would lead 17 (16.2%) and 26 (24.8%) men upgraded on RP respectively, with a significantly greater rate of disease upgrading than combined biopsy ( $P = 0.031$ ,  $P < 0.001$  respectively). Difference in rates of upgrading between TB alone and SB alone was not significant ( $P = 0.078$ ).

When stratified by PI-RADS score, patients in PI-RADS 3–4 group had significant greater GG upgrading on RP over TB than PI-RADS 5 group (25.5 vs 6%,  $P = 0.003$ ). The omission of SB would lead six more patients' Gleason score upgraded on RP in PI-RADS 3–4 group, but not lead any disease upgrading in PI-RADS 5 group as compared to combined biopsy (Table 3). In other words, combined biopsy was superior to TB alone in PI-RADS 3–4 patients (14.5 vs 25.5%,  $P = 0.031$ ), but was no superior to TB alone in PI-RADS 5 patients (6 vs 6%,  $P = 1.0$ ) for decreasing the rate of Gleason upgrading on RP. TB had a significantly lower rate disease upgrading on RP than SB in PI-RADS 5 group (6 vs 28%,  $P = 0.001$ ), and a similar upgrading rate with SB in PI-RADS 3–4 group (25.5 vs 21.8%,  $P = 0.754$ ).

As stratified by prostate volume, men with large prostate seem more likely to experience disease upgrading on RP than small prostate by any of TB+SB, TB, or SB, but with no significant difference except for SB (Table 4). The addition of SB would not significantly decrease the upgrading rate on RP compared with TB alone in either small prostate group (6.4 vs 8.5%,  $P = 1.0$ ) or large prostate group (13.8 vs 22.4%,  $P = 0.063$ ). Also, the upgrading rate of TB was not significantly lower than that of SB in each group (8.5 vs 14.9%,  $P = 0.21$ ; 22.4 vs 32.8%,  $P = 0.375$  for small and large prostate group respectively). However, combined biopsy significantly decreased the risk of disease upgrading on RP compared with SB alone in large prostate group (13.8 vs 32.8%,  $P = 0.001$ ) other than small prostate group (6.4 vs 14.9%,  $P = 0.125$ ). These data suggest that those who have large prostate would benefit from combined biopsy in reducing disease upgrading on RP.

## DISCUSSION

There has been considerable concern regarding whether additional systematic biopsy is required for MRI-visible lesions (13, 20–22). Several previous studies demonstrated that the combination of MRI-targeted and systematic biopsy obtain the maximal detection of csPCa than either biopsy method alone (21, 23). Systematic biopsy beneficially detected additional 3.5–13% csPCa in MRI-positive men (24), while approximately 6% csPCa had the risk stratification upgrading by systematic biopsy over targeted biopsy (25). In the present study, cognitive MRI-guided targeted biopsy showed greater csPCa detection rate and lower cisPCa detection rate with greater percentage of cancer involvement than systematic biopsy. Although systematic biopsy beneficially detected additional 6% prostate cancers in the whole cohort, only 28.6% of them were csPCa. The additional systematic biopsy indicated only a marginal increase of csPCa detection but a remarkable increase of cisPCa detection compared with targeted biopsy in the whole study population. While, the rate of Gleason upgrading on RP was lowest

in combined biopsy (6.4%), followed by TB (8.5%) and SB (14.9%). This raises the question about the necessity of performing systematic biopsy among all patients with MRI-visible lesions.

It has been reported that the utility of MRI/US fusion-targeted biopsy was especially relevant at enlarged prostate, higher MRI suspicious and higher PSA level (21, 26–28). However, few of the previous studies indicate if systematic biopsy can be omitted dependent on these variables. To our knowledge, this is the first study to evaluate the performance of additional systematic biopsy in biopsy naïve patients taking PI-RADS scores and prostate volume into consideration.

PI-RADS score was suggested as a predict factor of csPCa. In this study, we found that the probability of csPCa detection increased as PI-RADS score increased (Figure 3), which was consistent with earlier studies (21, 26). When stratified by PI-RADS score, GG upgrading on targeted biopsy was more commonly observed in PI-RADS 5 subgroup, while GG upgrading on systematic biopsy was more commonly observed in PI-RADS 3–4 subgroup. Among patients with PI-RADS 3–4 lesions, they had equal probability of upgrading on either targeted or systematic biopsy. Moreover, the combined biopsy method showed the same rate of disease upgrading on radical prostatectomy in PI-RADS 5 subgroup, and a significantly decreased upgrading rate in PI-RADS 3–4 subgroup, as compared to targeted biopsy alone. These findings suggest that additional systematic biopsy could be avoided in patients with PI-RADS 5 lesions, but is required for accurate risk stratification of prostate cancer in patients with PI-RADS 3–4 lesions. Previously, Ahmad et al.'s study also came to the similar findings in a repeated biopsy cohort study (29).

Prostate volume is another important variable taken into consideration for prostate biopsy decision (30, 31). The risk of sampling error for systematic biopsy increased, thus resulted in lower detection rate of prostate cancer as prostate volume increased. Large prostate volume has also been reported to be associated with disease upgrading based by systematic biopsy over MRI/US Fusion-guided targeted biopsy due to increased operator-dependent deformation during the biopsy procedure (25). Herein, we found that both targeted and systematic biopsy had a decreased csPCa detection rate as prostate volume increased (Figure 4), which is consistent with prior findings (21, 27). Among those cases with discordant GG between the two biopsies, men with large volume prostate seem more likely to be upgraded by systematic biopsy over targeted biopsy. Prior study by De et al. showed that MRI/US fusion-guided targeted biopsy outperformed systematic biopsy for detection of csPCa in large volume prostate (>40 ml) compared to smaller volume prostate and suggested systematically perform MRI-US fusion biopsies rather than systematic biopsies as a first line approach in prostate volume greater than 40 ml (27). But the present study showed that cognitive MRI-guided targeted biopsy showed significantly higher csPCa detection rate (81%) than systematic biopsy (71%) in small volume prostate (<30 ml), rather than in large volume prostate ( $\geq 30$  ml). This result was in consistent with Wysock et al.'s study which demonstrated that smaller prostate volume was a predicted factor of increased cancer detection rate on

targeted biopsy, likely because of decreased sampling error and needle deflection (32). Moreover, we also found that disease upgrading on radical prostatectomy over each biopsy was more commonly observed in large prostate than small prostate. Notably, the distribution of PI-RADS score was not equal between small and large PV group due to the prevalence of csPCa, which may make a potential effect on these results. These findings suggest that the additional systematic biopsy benefit more in large prostate than small prostate, which could not be omitted in men with large prostate ( $\geq 30$  ml).

This study has several limitations. Firstly, this is retrospective study in a large referral institution, which may lead potential selection biases. Secondly, lesion-to-lesion comparison in patients with multiple MRI suspicious lesions was not available in the study. The comparisons of biopsy methods were performed per patient rather than per lesion. Thirdly, we used cognitive MRI-guided targeted biopsy instead of MRI/US fusion targeted biopsy, which may reduce the performance of MRI guided targeted biopsy. But all the cognitive targeted prostate biopsies were performed by two experienced urologists and guided by an experienced urological radiologist. The findings should be further validated in large, prospective, multi-center studies.

In conclusion, the combination biopsy method was no superior than targeted biopsy alone in PI-RADS 5 or in small volume prostate subgroup in initial prostate biopsy patients with abnormal MRI. Large volume prostate ( $\geq 30$  ml) and lower PI-RADS categories (PI-RADS 3–4) may benefit more from the addition of systematic biopsy than the converse.

## REFERENCES

1. Smeenge M, de la Rosette JJ, Wijkstra H. Current status of transrectal ultrasound techniques in prostate cancer. *Curr Opin Urol* (2012) 22(4):297–302. doi: 10.1097/MOU.0b013e3283548154
2. Bjurlin MA, Carter HB, Schellhammer P, Cookson MS, Gomella LG, Troyer D, et al. Optimization of initial prostate biopsy in clinical practice: sampling, labeling and specimen processing. *J Urol* (2013) 189(6):2039–46. doi: 10.1016/j.juro.2013.02.072
3. Siddiqui MM, Rais-Bahrami S, Truong H, Stamatakis L, Vourganti S, Nix J, et al. Magnetic Resonance Imaging/Ultrasound–Fusion Biopsy Significantly Upgrades Prostate Cancer Versus Systematic 12-core Transrectal Ultrasound Biopsy. *Eur Urol* (2013) 64(5):713–9. doi: 10.1016/j.eururo.2013.05.059
4. Ahmed HU, El-Shater Bosaily A, Brown LC, Gabe R, Kaplan R, Parmar MK, et al. Diagnostic accuracy of multi-parametric MRI and TRUS biopsy in prostate cancer (PROMIS): a paired validating confirmatory study. *Lancet* (2017) 389(10071):815–22. doi: 10.1016/S0140-6736(16)32401-1
5. Bjurlin MA, Taneja SS. Prediagnostic Risk Assessment with Prostate MRI and MRI-Targeted Biopsy. *Urol Clin North Am* (2017) 44(4):535–46. doi: 10.1016/j.ucl.2017.07.012
6. Patel U, Dasgupta P, Challacombe B, Cahill D, Brown C, Patel R, et al. Pre-biopsy 3-Tesla MRI and targeted biopsy of the index prostate cancer: correlation with robot-assisted radical prostatectomy. *BJU Int* (2017) 119(1):82–90. doi: 10.1111/bju.13525
7. Tonttila PP, Lantto J, Pääkkö E, Piippo U, Kauppila S, Lammintausta E, et al. Prebiopsy Multiparametric Magnetic Resonance Imaging for Prostate Cancer Diagnosis in Biopsy-naïve Men with Suspected Prostate Cancer Based on Elevated Prostate-specific Antigen Values: Results from a Randomized Prospective Blinded Controlled Trial. *Eur Urol* (2016) 69(3):419–25. doi: 10.1016/j.eururo.2015.05.024

## DATA AVAILABILITY STATEMENT

The raw data supporting the conclusions of this article will be made available by the authors, without undue reservation.

## ETHICS STATEMENT

The studies involving human participants were reviewed and approved by the Institutional Review Board of West China Hospital of Sichuan University. Written informed consent for participation was not required for this study in accordance with the national legislation and the institutional requirements.

## AUTHOR CONTRIBUTIONS

XC and YC designed the study. GS and ZL acquired the data. LY and JY analyzed and interpreted the data. XC and JX wrote the manuscript. HZ and BS reviewed the manuscript. All authors contributed to the article and approved the submitted version.

## FUNDING

This work was funded by Science and Technology Innovation Talent of Sichuan (20CXRC0065) and Science and Technology Project of Chengdu(2019-YF05-00376-SN).

8. Radtke JP, Schwab C, Wolf MB, Freitag MT, Alt CD, Kesch C, et al. Multiparametric Magnetic Resonance Imaging (MRI) and MRI–Transrectal Ultrasound Fusion Biopsy for Index Tumor Detection: Correlation with Radical Prostatectomy Specimen. *Eur Urol* (2016) 70(5):846–53. doi: 10.1016/j.eururo.2015.12.052
9. Kasivisvanathan V, Rannikko AS, Borghi M, Panebianco V, Mynderse LA, Vaarala MH, et al. MRI-Targeted or Standard Biopsy for Prostate-Cancer Diagnosis. *New Engl J Med* (2018) 378(19):1767–77. doi: 10.1056/NEJMoa1801993
10. Rouvière O, Puech P, Renard-Penna R, Claudon M, Roy C, Mège-Lechevallier F, et al. Use of prostate systematic and targeted biopsy on the basis of multiparametric MRI in biopsy-naïve patients (MRI-FIRST): a prospective, multicentre, paired diagnostic study. *Lancet Oncol* (2019) 20(1):100–9. doi: 10.1016/S1470-2045(18)30569-2
11. Woo S, Suh CH, Eastham JA, Zelefsky MJ, Morris MJ, Abida W, et al. Comparison of Magnetic Resonance Imaging-stratified Clinical Pathways and Systematic Transrectal Ultrasound-guided Biopsy Pathway for the Detection of Clinically Significant Prostate Cancer: A Systematic Review and Meta-analysis of Randomized Controlled Trials. *Eur Urol Oncol* (2019) 2(6):605–16. doi: 10.1016/j.euo.2019.05.004
12. Delongchamps NB, Peyromaure M, Schull A, Beuvon F, Bouazza N, Flam T, et al. Prebiopsy Magnetic Resonance Imaging and Prostate Cancer Detection: Comparison of Random and Targeted Biopsies. *J Urol* (2013) 189(2):493–9. doi: 10.1016/j.juro.2012.08.195
13. van der Leest M, Cornel E, Israël B, Hendriks R, Padhani AR, Hoogenboom M, et al. Head-to-head Comparison of Transrectal Ultrasound-guided Prostate Biopsy Versus Multiparametric Prostate Resonance Imaging with Subsequent Magnetic Resonance-guided Biopsy in Biopsy-naïve Men with Elevated Prostate-specific Antigen: A Large Prospective Multicenter Clinical Study. *Eur Urol* (2019) 75(4):570–8. doi: 10.1016/j.eururo.2018.11.023

14. Schoots IG, Roobol MJ, Nieboer D, Bangma CH, Steyerberg EW, Hunink MG. Magnetic Resonance Imaging-targeted Biopsy May Enhance the Diagnostic Accuracy of Significant Prostate Cancer Detection Compared to Standard Transrectal Ultrasound-guided Biopsy: A Systematic Review and Meta-analysis. *Eur Urol* (2015) 68(3):438–50. doi: 10.1016/j.eururo.2014.11.037
15. Mottet N, van den Bergh RCN, Briers E, Van den Broeck T, Cumberbatch MG, De Santis M, et al. EAU-EANM-ESTRO-ESUR-SIOG Guidelines on Prostate Cancer-2020 Update. Part 1: Screening, Diagnosis, and Local Treatment with Curative Intent. *Eur Urol* (2021) 79(2):243–62. doi: 10.1016/j.eururo.2020.09.042
16. NICE Guidance. Prostate cancer: diagnosis and management: (c) NICE (2019) Prostate cancer: diagnosis and management. *BJU Int* (2019) 124(1):9–26. doi: 10.1111/bju.14809
17. Siddiqui MM, Rais-Bahrami S, Turkbey B, George AK, Rothwax J, Shakir N, et al. Comparison of MR/Ultrasound Fusion-Guided Biopsy With Ultrasound-Guided Biopsy for the Diagnosis of Prostate Cancer. *Jama* (2015) 313(4):390–7. doi: 10.1001/jama.2014.17942
18. Weinreb JC, Barentsz JO, Choyke PL, Cornud F, Verma S. PI-RADS Prostate Imaging - Reporting and Data System: 2015, Version 2. *Eur Urol* (2015) 69(1):16–40. doi: 10.1016/j.eururo.2015.08.052
19. Epstein JI, Egevad L, Amin MB, Delahunt B, Srigley JR, Humphrey PA, et al. The 2014 International Society of Urological Pathology (ISUP) Consensus Conference on Gleason Grading of Prostatic Carcinoma: Definition of Grading Patterns and Proposal for a New Grading System. *Am J Surg Pathol* (2016) 29:244–52. doi: 10.1097/PAS.0000000000000530
20. Barentsz J, Futterer JJ, Padhani AR. Will Magnetic Resonance Imaging-guided Biopsy Replace Systematic Biopsy? *Eur Urol Focus* (2015) 1(2):152–5. doi: 10.1016/j.euf.2015.07.008
21. Elkhoury FF, Felker ER, Kwan L, Sisk AE, Delfin M, Natarajan S, et al. Comparison of Targeted vs Systematic Prostate Biopsy in Men Who Are Biopsy Naive: The Prospective Assessment of Image Registration in the Diagnosis of Prostate Cancer (PAIREDCAP) Study. *JAMA Surg* (2019) 154(9):811–8. doi: 10.1001/jamasurg.2019.1734
22. Marra G, Ploussard G, Futterer J, Valerio M, Party E.-Y.P.C.W. Controversies in MR targeted biopsy: alone or combined, cognitive versus software-based fusion, transrectal versus transperineal approach? *World J Urol* (2019) 37(2):277–87. doi: 10.1007/s00345-018-02622-5
23. Lee AYM, Yang XY, Lee HJ, Law YM, Huang HH, Lau WKO, et al. Multiparametric MRI-ultrasonography software fusion prostate biopsy: initial results using a stereotactic robotic-assisted transperineal prostate biopsy platform comparing systematic vs targeted biopsy. *BJU Int* (2020) 126(5):568–76. doi: 10.1016/S2666-1683(20)34155-0
24. Schoots IG, Padhani AR, Rouvière O, Barentsz JO, Richenberg J. Analysis of Magnetic Resonance Imaging-directed Biopsy Strategies for Changing the Paradigm of Prostate Cancer Diagnosis. *Eur Urol Oncol* (2019) 3(1):32–41. doi: 10.1016/j.euo.2019.10.001
25. Muthigi A, George AK, Sidana A, Kongnyuy M, Simon R, Moreno V, et al. Missing the Mark: Prostate Cancer Upgrading by Systematic Biopsy over Magnetic Resonance Imaging/Transrectal Ultrasound Fusion Biopsy. *J Urol* (2017) 197(2):327–34. doi: 10.1016/j.juro.2016.08.097
26. Walton Diaz A, Hoang AN, Turkbey B, Hong CW, Truong H, Sterling T, et al. Can magnetic resonance-ultrasound fusion biopsy improve cancer detection in enlarged prostates? *J Urol* (2013) 190(6):2020–5. doi: 10.1016/j.juro.2013.05.118
27. de Gorski A, Roupêt M, Peyronnet B, Le Cossec C, Granger B, Comperat E, et al. Accuracy of Magnetic Resonance Imaging/Ultrasound Fusion Targeted Biopsies to Diagnose Clinically Significant Prostate Cancer in Enlarged Compared to Smaller Prostates. *J Urol* (2015) 194(3):669–73. doi: 10.1016/j.juro.2015.03.025
28. Shakir NA, George AK, Siddiqui MM, Rothwax JT, Rais-Bahrami S, Stamatakis L, et al. Identification of Threshold Prostate Specific Antigen Levels to Optimize the Detection of Clinically Significant Prostate Cancer by Magnetic Resonance Imaging/Ultrasound Fusion Guided Biopsy. *J Urol* (2014) 192(6):1642–9. doi: 10.1016/j.juro.2014.08.002
29. Arabi A, Deebajah M, Yaguchi G, Pantelic M, Williamson S, Gupta N, et al. Systematic Biopsy Does Not Contribute to Disease Upgrading in Patients Undergoing Targeted Biopsy for PI-RADS 5 Lesions Identified on Magnetic Resonance Imaging in the Course of Active Surveillance for Prostate Cancer. *Urology* (2019) 134:168–72. doi: 10.1016/j.urology.2019.08.035
30. Xu N, Wu YP, Li XD, Lin MY, Zheng QS, Chen SH, et al. Risk of upgrading from prostate biopsy to radical prostatectomy pathology: Is magnetic resonance imaging-guided biopsy more accurate? *J Cancer* (2018) 9(19):3634–9. doi: 10.7150/jca.26791
31. Freedland SJ, Isaacs WB, Platz EA, Terris MK, Aronson WJ, Amling CL, et al. Prostate size and risk of high-grade, advanced prostate cancer and biochemical progression after radical prostatectomy: a search database study. *J Clin Oncol* (2005) 23(30):7546–54. doi: 10.1200/JCO.2005.05.525
32. Wysock JS, Rosenkrantz AB, Huang WC, Stifelman MD, Lepor H, Deng FM, et al. A prospective, blinded comparison of magnetic resonance (MR) imaging-ultrasound fusion and visual estimation in the performance of MR-targeted prostate biopsy: the PROFUS trial. *Eur Urol* (2014) 66(2):343–51. doi: 10.1016/j.eururo.2013.10.048

**Conflict of Interest:** The authors declare that the research was conducted in the absence of any commercial or financial relationships that could be construed as a potential conflict of interest.

Copyright © 2021 Cheng, Xu, Chen, Liu, Sun, Yang, Yao, Zeng and Song. This is an open-access article distributed under the terms of the Creative Commons Attribution License (CC BY). The use, distribution or reproduction in other forums is permitted, provided the original author(s) and the copyright owner(s) are credited and that the original publication in this journal is cited, in accordance with accepted academic practice. No use, distribution or reproduction is permitted which does not comply with these terms.



# Advances in Research on the Cardiovascular Complications of Acromegaly

Han Yang<sup>1,2†</sup>, Huiwen Tan<sup>1†</sup>, He Huang<sup>3</sup> and Jianwei Li<sup>1\*</sup>

<sup>1</sup> Department of Endocrinology and Metabolism, West China Hospital, Sichuan University, Chengdu, China, <sup>2</sup> Department of Endocrinology and Metabolism, Chongqing Sixth People's Hospital, Chongqing, China, <sup>3</sup> Department of Cardiology, West China Hospital, Sichuan University, Chengdu, China

## OPEN ACCESS

### Edited by:

Changqiang Wu,  
North Sichuan Medical College, China

### Reviewed by:

Giovanna Aparecida Balarini Lima,  
Fluminense Federal University, Brazil  
Renata Simona Auriemma,  
University of Naples Federico II, Italy  
Andrew Hoffman,  
Stanford University, United States

### \*Correspondence:

Jianwei Li  
jerryli678@yahoo.com

<sup>†</sup>These authors have contributed  
equally to this work and share first  
authorship

### Specialty section:

This article was submitted to  
Cancer Imaging and  
Image-directed Interventions,  
a section of the journal  
Frontiers in Oncology

**Received:** 13 December 2020

**Accepted:** 16 March 2021

**Published:** 02 April 2021

### Citation:

Yang H, Tan H, Huang H and Li J  
(2021) Advances in Research  
on the Cardiovascular  
Complications of Acromegaly.  
Front. Oncol. 11:640999.  
doi: 10.3389/fonc.2021.640999

Cardiovascular-related complications are one of the most common complications in patients with acromegaly, and can lead to an increased risk of death. Hypertension and cardiomyopathy are the main cardiovascular complications. The characteristics of acromegalic cardiomyopathy are concentric biventricular hypertrophy and diastolic dysfunction. In addition, arrhythmia and heart valve disease are common cardiac complications in acromegaly. Although the underlying pathophysiology has not been fully elucidated, the spontaneous overproduction of GH and IGF-1, increasing age, prolonged duration of disease and the coexistence of other cardiovascular risk factors are crucial to cardiac complications in patients with acromegaly. Early diagnosis and appropriate treatment of acromegaly might be beneficial for the prevention of cardiomyopathy and premature death.

**Keywords:** acromegaly, hypertension, cardiomyopathy, cardiac systolic and diastolic function, echocardiography

Acromegaly is a chronic neuroendocrine disease with a prevalence of 83-133 cases per one million people (1–7). Approximately 98% are caused by pituitary adenomas that secrete growth hormone (GH) (8, 9), and 2% are caused by pituitary hyperplasia, ectopic growth hormone or ectopic growth hormone releasing hormone (GHRH) secretion. Excessive growth hormone stimulates the liver to produce high levels of insulin-like growth factor-1 (IGF-1). Excessive secretion of GH and IGF-1 has a long-term effect on tissues and multiple organs, which will lead to the excessive proliferation of soft tissues, bones and cartilage of the whole body, causing facial changes, enlarged hands and feet, thick skin, enlarged internal organs, bone and joint disease and obstructive sleep apnea syndrome (OSAS). The quality of life of patients with acromegaly is seriously affected by these disorders. In addition, pituitary tumors can not only cause compression symptoms, but also cause a corresponding increase in the incidence of cardiovascular-related diseases, growth hormone-related metabolic abnormalities, high blood pressure, respiratory diseases, and malignant tumors such as thyroid nodules/thyroid cancer and colon cancer (10), resulting in a shortened life of patients with acromegaly. Compared with the general population, the risk of death in patients with acromegaly had been increased by 61%, and cardiovascular-related complications are the main risk factors affecting the survival rate of patients with acromegaly (11). The common cardiovascular complications in patients with acromegaly mainly include hypertension, acromegalic cardiomyopathy, valvular disease, and arrhythmia (12, 13). The main features of acromegalic cardiomyopathy are ventricular concentric hypertrophy and impaired diastolic function. Autopsy



results found that up to 93% of patients with acromegaly had myocardial hypertrophy (14), and up to 60% of patients with acromegaly had arrhythmia, hypertension or valvular heart disease (12). The occurrence of cardiovascular complications may triple the chance of hospitalization for patients with acromegaly and significantly increase the average annual medical expenses (15). More importantly, the presence of any cardiovascular disease at the time of diagnosis of acromegaly indicates a significant increase in the risk of death, and the mortality rate may even reach 100% within 15 years (12). The treatment of acromegaly has been developed in many medical centers, and with the increase in the use of surgery, drugs and stereotactic radiotherapy to enable faster and better clinical and biochemical control, the quality of life and survival of patients with acromegaly has been greatly improved. Recent studies have shown that strict control of GH and IGF-1 levels has reduced the death risk of acromegaly to a level comparable to that of the general population (13, 16–18). However, if GH and IGF-1 remain uncontrolled in patients with acromegaly, systolic dysfunction and even heart failure may eventually occur, which will seriously affect the survival of patients. However, the mechanism of abnormal heart structure and function in acromegaly has not yet been fully elucidated. The present article will review the occurrence, mechanism and related risk factors for common cardiovascular diseases in patients with acromegaly.

## HYPERTENSION

Hypertension is considered one of the most relevant negative prognostic factors for mortality in acromegaly (12, 19). The incidence of hypertension in patients with acromegaly was 11.9%–54.7%, with an average of 33.6% (20). During ACROSTUDY (ACROSTUDY™ is a global non-interventional surveillance study of long-term treatment with pegvisomant initiated in 2004 for evaluating outcomes in patients with acromegaly), 68 patients of acromegaly deaths were reported in the hypertension cohort, while 10 in the cohort without hypertension (19). However, studies have shown that the incidence may be overestimated (21, 22). Minnit et al. observed that, in 40 patients with acromegaly, the incidence of hypertension was 42.5% as assessed by the average of three consecutive random measurements of blood pressure by a standard mercury blood pressure meter, while the incidence of hypertension as assessed by ambulatory blood pressure monitoring (ABPM) was 17.5% (21). A similar result was recently reported by Costenaro et al., with ABPM being assessed at 22.9% in 37 patients with acromegaly, compared with an average rate of hypertension of 32.4% with two random blood pressure tests (22). Therefore, ABPM is more objective and accurate to evaluate the blood pressure, which should be recommended in acromegaly.

Acromegaly-associated hypertension is characterized by special manifestations, with low systolic blood pressure and high diastolic blood pressure (23, 24). Vitale and colleagues found that compared with age- and sex-matched

nonacromegalic patients with hypertension, patients with acromegaly had lower systolic blood pressure than nonacromegalic hypertensive controls, while diastolic blood pressure was higher than nonacromegalic hypertension, which suggested that increased vascular resistance may be related to the excessive GH and IGF-1 induced growth of vascular smooth muscle cells (23), and it may also be related to water and sodium retention caused by GH and IGF-1 (24). Additionally, compared with hypertension patients with non-acromegaly, ABPM results showed that approximately 50% of acromegaly hypertension is nondipper hypertension (nocturnal blood pressure drop is less than 10%), which might be related to acromegaly patients' overreaction to sympathetic nerve stimulation (25).

At present, there are still controversies about the risk factors for hypertension in patients with acromegaly. Studies had found that blood pressure level was positively correlated with IGF-I level (26). Costenaro et al. observed that patients with uncontrolled acromegaly had a higher incidence of hypertension than those with remission of acromegaly and nonacromegalic controls (22). Sardella had pointed out that patients with uncontrolled acromegaly had a 6-fold increase in the risk of hypertension compared with patients who achieved remission after treatment (27). The meta-analysis of Schutte et al. included 3 prospective RCT studies, 14 cross-sectional studies, and 3 case-control studies. A total of 11704 acromegaly subjects and 912 healthy controls were included. The results showed that when the concentration of IGF-1 exceeded 191 ng/ml, blood pressure was significantly positively correlated with IGF-1 ( $r=0.31$ ,  $P<0.001$ ), when IGF-1 was lower than 191 ng/ml, blood pressure was negatively correlated with IGF-1 (28). This study suggested that in patients with acromegaly who had not yet been completely controlled, blood pressure might be positively correlated with IGF-I level. Therefore, partial or complete remission of acromegaly will be beneficial for blood pressure control. However, in another study, blood pressure was not found to be related to IGF-1 level (23). And patient age and body mass index (BMI) may also be important determinants of hypertension in patients with acromegaly. Sardella and her colleagues observed that the blood pressure of patients with acromegaly was positively correlated with BMI and age (27). However, whether family history of hypertension and sex were related to hypertension in acromegaly is still controversial. A study included 200 patients with acromegaly and 200 subjects with nonacromegaly matched by sex, age, BMI, and smoking habits to assess the prevalence and risk factors for hypertension. And the results suggested that patients with acromegaly have a higher prevalence of hypertension than the control group [hazard ratio (HR) 1.9,  $P=0.0002$ ], and the risk of hypertension increases with age. And the study also found that 62% of nonacromegalic patients with hypertension had a family history, while only 30% of patients with acromegaly had a family history (23).

The mechanism of hypertension in patients with acromegaly has not yet been fully elucidated (24–29). The occurrence of hypertension may be due to the comprehensive effects of long-term high levels of GH/IGF-1 on the cardiovascular system,

kidneys and other organs, which ultimately leads to an increase in extracellular fluid volume and peripheral vascular resistance. Moreover, the accompanying myocardial hypertrophy, OSAS, and insulin resistance in patients with acromegaly can also cause or aggravate hypertension. And the direct or indirect effects of GH/IGF-I cause water and sodium retention. Half a century ago, researchers proposed that GH and IGF-1 could promote water and sodium retention by activating the renin-angiotensin-aldosterone system (RAAS), but there were still controversies. Some studies showed that GH could increase the levels of renin and aldosterone, but other studies found that without relying on the action of plasma renin, excessive GH could directly stimulate the rise in aldosterone levels, leading to hypertension in patients with acromegaly (20). Bielohuby et al. found that aldosterone was increased with chronic GH excess, and the aldosterone level decreased significantly after acromegaly was controlled, but renin concentrations were unaffected, which suggesting that GH might directly promote the secretion of aldosterone (29). The precise mechanism by which chronic excess GH increases aldosterone is unclear, but this study showed that it was unrelated to increased renin, excess IGF-1, or increased adrenal aldosterone synthase expression. Actually, aldosterone synthase is also expressed in some extra-adrenal tissues (30, 31). And excessive growth hormone may affect the synthesis of extra-adrenal aldosterone. GH/IGF-I can also directly act on the sodium channel (epithelial sodium channel, ENaC) of the kidney and renal tubular epithelial cells to increase its activity and cause water and sodium retention (32). There is another mechanism of hypertension in patients with acromegaly, which is increased peripheral vascular resistance. Maison et al. compared 10 patients with acromegaly with normal blood pressure and 10 healthy controls. The results showed that nitric oxide (NO)-mediated vascular endothelium-dependent diastolic function was impaired in patients with acromegaly (33). Nitric oxide is a powerful vasodilator that can also reduce platelet aggregation and activation, inhibit the proliferation and migration of vascular smooth muscle cells, and reduce the adhesion of white blood cells and endothelial cells. Ronconi et al. compared the blood of 13 patients with acromegaly and 12 sex- and age-matched normal blood pressure controls and found that the NO concentration decreased in platelets of patients with acromegaly, which was mainly related to the decreased expression of endothelial NO synthase, and the internal NO concentration was negatively correlated with GH/IGF-1 levels and the duration of acromegaly (34).

## ACROMEGALIC CARDIOMYOPATHY

When constantly high levels of GH and IGF-1 stimulated the hearts of patients with acromegaly, and combined with the GH and IGF-1 receptors on the surface of cardiomyocytes, the myocardial contractility changed with increasing the intracellular calcium concentration and sensitivity to calcium, and led to myocardium interstitial collagen precipitation, muscle

fiber disorder, and interstitial lymphocyte infiltration of cardiomyocytes, which eventually progressed to acromegaly cardiomyopathy (12, 35). The most common features of acromegaly cardiomyopathy are biventricular concentric hypertrophy, myocardial fibrosis and diastolic dysfunction. In addition, excessive growth hormone may also upset the local water balance of the myocardium and increase the myocardial water content. Excluding other heart diseases, heart changes in acromegaly were first defined as acromegaly cardiomyopathy at the end of the 19th century (36). The development of acromegaly cardiomyopathy is usually divided into three stages. In the early stage, it is mainly myocardial concentric hypertrophy, increasing heart rate and increased cardiac output, which are manifestations of hyperkinetic syndrome generally in younger patients with a shorter duration of disease. Acromegaly cardiomyopathy at this stage is still reversible. In the middle stage, myocardial hypertrophy becomes more obvious and severe, ventricular diastolic function is impaired, and the left ventricular ejection fraction decreases during exercise. If acromegaly is untreated or not effectively controlled, it will progress to the final stage, during which systolic dysfunction at rest and heart failure may occur. At this stage, even if acromegaly is treated, heart disease becomes irreversible (37, 38). In addition, patients with acromegaly often have hypertension, valvular heart disease, arrhythmia, as well as vascular endothelial dysfunction and glucose and lipid metabolism disorders, which may potentially aggravate cardiomyopathy.

## Cardiomyopathy

In 2004, Colao et al. from Italy reviewed the systemic complications of acromegaly and proposed that the most common cardiac change in patients with acromegaly is biventricular concentric hypertrophy. Most patients showed obvious left ventricular hypertrophy at the time of diagnosis. Left ventricular hypertrophy is observed in the early stage of acromegaly, and the histology of acromegaly is mainly manifested as myocardial interstitial fibrosis (12). An autopsy report of 27 patients with acromegaly showed that 93% of patients had left ventricular hypertrophy (LVH), and 85% had myocardial fibrosis (14). At present, most studies exploring changes in cardiac structure and function are conducted through echocardiography (ECHO). **Table 1** summarizes related research on the evaluation of cardiac structure and function in acromegaly with echocardiography from 2002 to 2020 in PubMed. In general, the incidence of myocardial hypertrophy in patients with acromegaly is 10.8–78.9%, and the average incidence is 41.9% (16, 39–59) (**Table 1**). The estimation of the incidence of myocardial hypertrophy is quite different, which may be related to the different definitions of myocardial hypertrophy and the different research designs (retrospective, prospective or cross-sectional) and the different study populations in different studies.

In recent years, studies have found that early pathologies such as reduced myocardial perfusion, myocardial edema, myocardial fibrosis, and regional myocardial movement incoordination greatly affect the quality of life and long-term survival rate of patients, and the application of echocardiography cannot make

an accurate assessment (45). Cardiac magnetic resonance imaging (CMRI) has been regarded as the gold standard for the assessment of cardiac lesions in acromegaly (60, 61). At present, there are few studies using cardiac MRI to study acromegaly cardiomyopathy (43, 51, 59, 62–64), and the conclusions are still inconsistent. Bogazzi et al. included 14 patients with acromegaly. CMRI found that 73% of the patients had left ventricular hypertrophy, which was higher than the 36% observed using echocardiography in the same study population. But myocardial fibrosis had not been found in their study (62). However, dos santos Silva et al. (51) included 40 patients and used both CMRI and ECHO to evaluate cardiac structure and function in acromegaly. At baseline, CMRI only found that 5% of patients with acromegaly had LVH, and in delayed myocardial enhancement analysis, 13.5% of patients had myocardial fibrosis, while ECHO found that 31% of patients had LVH. Therefore, the study believed that echocardiography might overestimate the incidence of myocardial hypertrophy. And recently Guo et al. analyzed the CMRI results of 61 patients with acromegaly, found that the incidence of LVH, IVSH, LVSD, RVSD, and myocardial fibrosis were 26.2%, 27.9%, 8.2%, 9.8%, and 14.8%, respectively (59). The main reason for the inconsistency in the diagnosis rate of LVH between the two research centers was the different diagnostic criteria. Different countries and races have dissimilar diagnostic criteria. The study by dos santos Silva et al. defined LVH as left ventricular mass index (LVMI) in males >135 g/m<sup>2</sup> and females >110 g/m<sup>2</sup>, while Bogazzi et al. defined as males >86 g/m<sup>2</sup> and females >67 g/m<sup>2</sup>. The diagnostic criteria of LVH were not mentioned in the report of Guo et al. However, the average LVMI in the study by Guo et al. was very close to the results of studies originating from Brazil, but much lower than the result of European studies (59).

The risk factors for myocardial hypertrophy in patients with acromegaly are still controversial. A retrospective study analyzed the cardiovascular-related complications of 205 newly diagnosed patients with active acromegaly and 410 gender- and age-matched nonacromegalic patients. The results showed that the prevalence of LVH in patients with acromegaly was 11.9-fold higher than that of nonacromegalic patients. The duration of acromegaly was the main risk factor for cardiomyopathy. And the relative risk of cardiomyopathy in patients with a duration of 10 years was 3-fold higher than that of patients with a duration of 5 years (45). A study by Xiaopeng Guo and others from Peking Union Medical College Hospital included 108 patients with acromegaly and found that age and increased BMI were independent risk factors for acromegaly cardiomyopathy (53). In addition, multivariate analysis, such as that performed by Casini, showed that hypertension and IGF-1 levels were determinants of left ventricular hypertrophy (41). However, multivariate logistic regression analysis by Nascimento et al. showed that acromegaly uncontrolled as an independent risk factor for left ventricular hypertrophy (49).

## Heart Function

Increased GH, directly and *via* IGF-1, induces myocardial hypertrophy and fibrosis. LVH causes diastolic and more rarely

systolic dysfunction. Diastolic dysfunction is common in patients with acromegaly. According to previous studies, its incidence was approximately 11.3–100%, with an average incidence of 46.3% (40–45, 47, 49, 51, 53, 56, 58) (**Table 1**). Decreased diastolic function is mainly manifested as insufficient cardiac filling capacity, significantly prolonged isovolumic relaxation time (IVRT) and mitral deceleration time (MDT), reduced peak E of mitral valve anterior blood flow, increased peak A of mitral valve anterior blood flow, and reduced E/A ratio, but these situations are usually mild (56). Age and the coexistence of diabetes (diabetics accounted for 19% of patients in this group) are independent risk factors for diastolic dysfunction, regardless of the duration of the disease. Another prospective study involving 19 cases of acromegaly also suggested that age was the most important predictor of diastolic dysfunction (39).

In a national study in Denmark, a total of 405 patients with acromegaly and 4,050 age- and gender-matched healthy subjects were included. The average follow-up was 10.6 years. It was found that the risk of acromegaly heart failure was 2.5 times that of the general population (1). In most studies, impaired systolic function was rare in patients with acromegaly. A comprehensive study of 3,173 patients with acromegaly from the database of 14 medical centers in Europe showed that 1.6% of patients had heart failure when they were diagnosed with acromegaly (55). To date, studies have reported that the highest incidence of impaired systolic function was 26.3%. A total of 205 patients with acromegaly were included in the study. Systolic dysfunction was defined as an echocardiographic examination of cardiac ejection fraction less than 50% (45), but the authors did not clarify whether the patient has clinical manifestations of heart failure. Recently, Guo et al. analyzed the CMRI results of 61 patients with acromegaly. And LVSD was detected in 5 patients (8.2%), 3 of whom had an LVEF higher than 40%. Two patients were diagnosed with severe LVSD and exhibited remarkably decreased LVEF (13.7% and 21.3%). Interestingly, all 5 patients with LVSD were males (59). However, earlier studies used CMRI to evaluate cardiac function did not find patients with acromegaly combined with systolic dysfunction (43, 51, 62). This may be related to the lack of data on the hearts of patients with acromegaly using CMRI assessment. The actual incidence of heart failure of acromegaly in the clinic may be very low. This is due to the continuous improvement in the diagnosis and treatment of acromegaly, which reduces the probability of its terminal stage. It is worthy of attention by clinicians that once patients develop heart failure, they often face a higher risk of death and increased hospitalization costs. In a retrospective study of 330 patients with acromegaly from two centers in France and Belgium (65), 9 patients (2.7%) developed chronic congestive heart failure, which was stage III–IV when rated by the New York Heart Association diagnostic criteria. Echocardiography showed dilated cardiomyopathy with left ventricular systolic dysfunction, and the left ventricular ejection fraction was less than 45%. Among them, 3 patients underwent heart transplantation due to end-stage heart failure. In addition, it was also suggested that if chronic symptomatic congestive heart failure occurred, the 1-year and 5-year mortality

**TABLE 1 |** Echocardiographic assessment of changes in cardiac structure and function in patients with acromegaly from 2002 to 2019.

Author, Published year	Country	Case Number	Sex (M, %)	Age (years)	Duration of illness (years)	GH ( $\mu\text{g/l}$ )	IGF-1 ( $\mu\text{g/l}$ )	Myocardial hypertrophy (%)	Impaired diastolic function (%)	Impaired systolic function (%)
Lombardi et al., 2002 (39)	Italy	19	9 (47.4)	41.7 $\pm$ 11.5	N/A	37.6 $\pm$ 47.9	865.7 $\pm$ 75.9	78.9	N/A	0
Bogazzi et al., 2005 (40)	Italy	22	13 (59.1)	50.1 $\pm$ 10.3	13.1 $\pm$ 5.6	14.1 $\pm$ 16.7	695.9 $\pm$ 291.5	77.2	100%	N/A
Casini et al., 2006 (41)	Brazil	40	14 (35.0)	45 $\pm$ 11	8.4 $\pm$ 5.1	7.42	2.21 $\pm$ 1.28 <sup>1</sup>	57.5	30.0	5
Pivonello et al., 2007 (42)	Italy	17	8 (47.1)	46.4 $\pm$ 11.1	1.3 $\pm$ 0.4	19.8 $\pm$ 22.7	731.2 $\pm$ 175.8	52.9	58.8	11.8
Bogazzi et al., 2008 (43)	Italy	14	8 (57.14)	46 $\pm$ 10	7 $\pm$ 5	6.4 $\pm$ 9.9	724.8 $\pm$ 212	35.7	28.6	0
De Marinis et al., 2008 (44)	Italy	48	18 (37.5)	N/A	N/A	N/A	N/A	70.8	75.0	N/A
Colao et al., 2011 (45)	Italy	205	97 (47.32)	47 $\pm$ 15	9.3 $\pm$ 6.4	52.1 $\pm$ 40.3	2.5 $\pm$ 0.9 <sup>1</sup>	78.0	43.9	26.3
Jayasena et al., 2011 (46)	UK	116	62 (53.45)	44 $\pm$ 2	N/A	N/A	N/A	20	N/A	N/A
Akdeniz et al., 2012 (47)	Turkey	42	15 (35.71)	50.3 $\pm$ 12.7	3.8(4.3, 8.9) <sup>2</sup>	N/A	454.7 $\pm$ 390.2	33.3	35.7	0
Annamalai et al., 2013 (48)	UK	24	N/A	N/A	N/A	N/A	N/A	58.3	N/A	N/A
Nascimento et al., 2013 (49)	Brazil	37	12 (35.14)	46.9 $\pm$ 12.8	N/A	N/A	2.06 $\pm$ 0.28 <sup>1</sup>	56.8	51.4	0
Mercado et al., 2014 (50)	Mexico	167	N/A	N/A	N/A	N/A	N/A	26.0	N/A	2.4
dos Santos Silva et al., 2015 (51)	Brazil	29	N/A	N/A	N/A	N/A	N/A	31.0	41.3	0
Sanchez-Ortiga et al., 2015 (52)	Spain	32	14 (43.8)	50.3 $\pm$ 11.4	6.2 $\pm$ 4.8	N/A	N/A	25.0	58.1	N/A
Guo et al., 2015 (53)	China	108	44 (40.74)	41.2 $\pm$ 12.7	6.5 $\pm$ 5.3	27.4 $\pm$ 44.6	802.7 $\pm$ 337.5	17.6	20.4	N/A
Kuhn et al., 2015 (54)	France	35	N/A	N/A	N/A	N/A	N/A	20	N/A	N/A
Petrossians et al., 2017 (55)	Europe	3173	1444 (45.5)	45.2(34.9,55)	N/A	N/A	N/A	15.5	N/A	1.6
Cansu et al., 2017 (56)	Turkey	53	21 (39.62)	45 $\pm$ 11	6.7 $\pm$ 5.9	2.16 $\pm$ 3.06 <sup>3</sup>	285 $\pm$ 204	50.1	11.3	N/A
Carmichael et al., 2017 (57)	US	121	54 (44.63)	55.4 $\pm$ 16.7	N/A	N/A	N/A	10.8	N/A	5
Maione et al., 2017 (16)	France	85	N/A	N/A	N/A	N/A	N/A	42.4	N/A	N/A
Natchev et al., 2019 (58)	Bulgaria	146	56 (38.37)	50.6 $\pm$ 12.5	N/A	N/A	N/A	48.9	47.0	5.4
Guo et al., 2020 (59)	China	61	34 (55.7)	43.2 $\pm$ 13.3	6.5 $\pm$ 4.8	36.3 $\pm$ 43.7	896.4 $\pm$ 253.9	14.8	N/A	3.3

N/A, means not mentioned in the study; %, means the incidence rate; <sup>1</sup>IGF-1 means a multiple of the upper limit of normal for each age group; <sup>2</sup>median disease duration; <sup>3</sup>the unit is ng/ml.



rates were 25% and 37.5%, respectively (65). Therefore, when chronic congestive heart failure develops in patients with acromegaly, their condition and prognosis are often poor.

Since obvious impairment of systolic function is rare, some studies have attempted to evaluate the early damage of the myocardium in patients with acromegaly. At present, there are studies using speckle tracking echocardiography (STE) to study the early changes in the left ventricular systolic function of the heart in patients with acromegaly (66–69). STE can analyze the local and overall systolic deformation capacity of the left ventricle, and its average value reflects the global longitudinal strain (GLS) of the left ventricular systolic function. Impaired GLS has been used as a sign of early and subclinical left ventricular systolic dysfunction (66). GLS is also recognized as the main predictor of heart-related events, and its accuracy is even higher than that of LVEF (66). Popielarz-Grygalewicz and colleagues evaluated the GLS of 140 patients with acromegaly, and 65% of the patients in this group were women, and the average age was  $50.5 \pm 13.8$  years old. Compared with age- and sex-matched healthy controls, patients with acromegaly had significant subclinical systolic dysfunction (67). Similarly, Uziębło-Życzkowska et al. recently compared 30 cases of acromegaly with 30 cases of a control group matched by sex, age, and blood pressure and found that the left ventricular systolic function of patients with acromegaly was significantly impaired, the GLS value was significantly reduced, and patients with acromegaly had higher left ventricular weight, larger left atrium anteroposterior diameter and left atrium volume index (69). However, Volschan et al. evaluated the GLS of 37 patients with acromegaly and 48 controls (matched by sex, age, hypertension, and diabetes) and found no differences between patients and controls (66). The different conclusions of these studies may be related to sample selection and sample size. At present, there are few studies on GLS in patients with acromegaly, and the early cardiomyopathy of patients with acromegaly needs further study.

## HEART VALVE DISEASE

Previous studies have shown (67, 70–73) that patients with acromegaly often have heart valve disease, among which the mitral valve and aortic valve are the most commonly involved parts, mainly manifested by valve regurgitation. Heart valve disease is an important part of ventricular insufficiency, but there are few reports of valvular disease of acromegaly that are studied separately (70–72). In 1997, Ohtsuka et al. performed valve replacement on 5 patients with severe valve disease and left heart failure and acromegaly. They found that patients with acromegaly had degeneration of heart valves with mucopolysaccharide deposition, increased ring fragility, and valve leaflet disorder. Therefore, regurgitation and stenosis of the mitral valve and aortic valve occurred (73). The cause of valvular disease in patients with acromegaly is not clear. It may be related to the increased expression of matrix

metalloproteinases (MMPs), the synthesis of proteoglycans, the deposition of collagen and mucopolysaccharides, and the abnormal regulation of extracellular matrix. In addition, elevated levels of proinflammatory cytokines in patients with active acromegaly could also increase the gene expression of MMPs (70). MMPs are a group of endogenous  $Zn^{2+}$ -dependent proteolytic enzymes that can degrade collagen, elastin and proteoglycan; can synthesize collagen and connective tissue that do not have normal structure and function by regulating the formation of matrix elements and the bioactive factors released by the degradation of extracellular matrix; and can participate in the remodeling of heart valve tissue (74). Another factor that may cause aortic regurgitation is dilation of the aortic root, which is reported in up to 26% of patients with acromegaly (75, 76).

Patients with acromegaly are prone to various valve diseases, but most valve diseases are mild (70, 71). Colao et al. (71) compared 42 patients with newly diagnosed acromegaly, 22 patients with successful pituitary tumor resection and remission for at least 1 year, and 64 patients with gender- and age-matched nonacromegaly. Mitral and aortic valve calcification, fibrosis, thickening of the valve leaflets and regurgitation were observed. It was found that 86% of patients in the active disease stage had valve abnormalities, while only 24% of the control group had valve abnormalities. After acromegaly was controlled by treatment, 73% of patients had valve abnormalities, while only 9% of the control group had valve abnormalities. However, the degree of valve disease observed in this group of patients was mild to moderate, which was of little clinical significance. Since the prevalence of mild mitral and tricuspid regurgitation is higher in the general population, while the prevalence of aortic regurgitation is much lower, it is generally believed that pathological mitral and tricuspid regurgitation flow is defined as more than moderate regurgitation, and pathological aortic regurgitation is defined as more than mild. Pereira et al. (70) evaluated the pathological significance of valvular regurgitation in patients with acromegaly. The study included 40 patients with acromegaly and 120 in the control group with age, sex, hypertension, and left ventricular systolic function matching. Valve regurgitation with pathological significance was common in patients with acromegaly, and 30% of whom had aortic valve regurgitation, while the incidence rate in the control group was only 7%. Moderate or above mitral regurgitation occurred in 5% of patients with acromegaly, but it was not found in the control group (70).

The duration of acromegaly is considered to be an independent risk factor for valvular disease (70). Study by Pereira et al. suggested that for every additional year of disease duration, the risk of valvular disease increased by 19%, regardless of the levels of GH and IGF-1, whether there was impaired left ventricular function, or hypertension. There was no pathological regurgitation in patients with a duration of less than 6 years, but aortic regurgitation occurred in 12.5% of patients with a duration of 6–10 years, and aortic regurgitation occurs in 40% of patients with a duration of more than 16 years. Moderate and above

mitral regurgitation was not observed in the nonacromegalic control group matched for age, gender, hypertension and left ventricular systolic function, but in patients with acromegaly with a duration of more than 16 years, 20% had moderate or more mitral regurgitation (70). Furthermore, the progression of valve disease is related to the failure to effectively control the levels of GH and IGF-I. A prospective study included 18 patients with active acromegaly and patients with acromegaly who were in remission after treatment. It was found that patients with uncontrolled acromegaly had an increased incidence of mitral regurgitation during follow-up; at baseline, 39% had mitral regurgitation, which increased to 78% after an average of 1.9 years of follow-up. However, there was no increase in the incidence of regurgitation in patients with remission of acromegaly (72). However, few studies have assessed the risk factors for valve diseases, especially prospective studies, and more clinical evidence is needed in the future.

## ARRHYTHMIA

In previous studies, 7-40% of patients with acromegaly might have arrhythmia, especially during exercise (37). Arrhythmias mainly manifest as ectopic beats, paroxysmal atrial fibrillation, paroxysmal supraventricular tachycardia, sick sinus syndrome, ventricular tachycardia and bundle branch block. Malignant ventricular tachyarrhythmia may be the cause of repeated syncope and sudden cardiac death in patients with acromegaly (77). The incidence of premature ventricular contractions and complex ventricular arrhythmia in patients with acromegaly is higher than that of the general population (78). In 1992, a clinical observation study included 32 patients found that 48% of patients with acromegaly had complex ventricular arrhythmias (79). In 2002, Lombardi et al. performed a 24-hour dynamic electrocardiogram on 19 patients with acromegaly, and the results showed that approximately 16.6% of patients with acromegaly had supraventricular premature beats, and 35% of patients had ventricular premature beats (39). However, in recent years, relatively few studies had used Holter to assess arrhythmia in acromegaly (80, 81). Recently, a study from Russia found that 42% patients with acromegaly had arrhythmias and cardiac conduction disorders, and 61% of patients with arrhythmia who underwent CMRI had the signs of myocardial fibrosis (82). But Warszawski et al. observed 36 patients with acromegaly and found no persistent arrhythmia at baseline and 1 year after treatment with somatostatin analogs (SSAs), and no arrhythmia-related symptoms were observed (64). The authors speculated that this phenomenon might be related to the fact that there was no significant myocardial fibrosis or myocardial hypertrophy in this group. Another study conducted 24-hour dynamic ECG monitoring on 47 patients with acromegaly and found that the average heart rate and variability of patients with acromegaly increased, but no significant clinical arrhythmia was observed (83).

One study suggested that the duration of acromegaly was a main risk factor of arrhythmias and cardiac conduction disorders

(82). In addition, the occurrence of ventricular arrhythmia may be related to left ventricular hypertrophy and fibrosis (63). Some recent studies suggested that the QT interval prolongation or an increase in QT dispersion (84, 85), the frequency of late potentials (81), may increase the risk of acromegaly arrhythmia. The actual reduction in severe arrhythmia in the clinic may be related to the adoption of stricter diagnostic criteria for acromegaly and early intervention in recent years, as well as to the treatment of complications (mainly hypertension and diabetes) that increase the risk of heart disease (64).

## ATHEROSCLEROSIS AND CORONARY HEART DISEASE

There is still controversy about whether patients with acromegaly are at increased risk of atherosclerosis and coronary heart disease (13). Because acromegaly is prone to being associated with hypertension, diabetes and other metabolic-related diseases, the risk of atherosclerosis and coronary heart disease may increase. However, some studies suggested that IGF-1 has anti-inflammatory and antioxidant properties, so IGF-1 was believed to have a protective effect on atherosclerosis (86). Von der Thüsen and colleagues observed the effect of IGF-1 on mouse arterial smooth muscle cells cultured in activated macrophage media. IGF-1 in atherosclerotic plaques could prevent plaque instability by regulating the renewal of smooth muscle cells and changing the phenotype of smooth muscle cells (87). Some studies have shown that patients with acromegaly have not found an increased risk of coronary heart disease (88-91). dos Santos Silva et al. compared the coronary artery calcium scores (CACs) and Framingham risk score (FS) of 56 patients with acromegaly and the control group (matched by sex, age, smoking habits, hypertension, diabetes and hypercholesterolemia). Interestingly, no difference was found. According to the FS and CACs to assess the risk of ischemic events, 91% of patients with acromegaly were classified as low-risk (88). Similarly, the study by Akutsu et al. suggested that CACs in patients with acromegaly were lower, and no cardiovascular events occurred after an average follow-up of 4.6 years (89). A prospective study by Bogazzi et al. used the Agatston score (AS) to evaluate the coronary calcium content of 52 patients with acromegaly and stratified them according to the FS. It was found that 71% of patients had a low risk of coronary heart disease, 27% had moderate risk, and 2% had high risk. In all AS-positive patients with calcified plaques in the coronary arteries, myocardial exercise stress SPECT was used to detect ischemia. Amazingly, all patients were negative. During the 5-year follow-up period, no major cardiovascular events occurred (90). Meanwhile, many evidence supports that acromegaly is associated with an increased risk of coronary artery disease (92-95). A study by Ragonese et al. enrolled 39 patients with acromegaly. According to a comprehensive assessment of the FS and AS, 41% of patients with acromegaly were at risk of coronary atherosclerosis (92). A recent meta-analysis of preclinical markers of atherosclerosis in patients with acromegaly also

showed that IMT of patients with acromegaly increased, and that both FMD and arterial stiffness were affected, which indicated that these patients had an increased risk of atherosclerosis. But in patients with biochemical remission, IMT and FMD were significantly improved (93). In addition, Ozkan used early markers of atherosclerosis, common carotid artery intima media thickness (IMT), flow-mediated dilation (FMD), and epicardial adipose tissue thickness (EAT) to detect whether patients with acromegaly had early atherosclerosis. The results showed that compared with the control group (matched by age, sex, BMI, diabetes, hypertension, and hyperlipidemia), patients with acromegaly had significantly higher IMT and EAT, while FMD significantly decreased. However, compared with the control group the patients with acromegaly presented lower levels of highly sensitive C reactive protein (hsCRP) and oxidative stress parameters, which suggested that inflammation and oxidative stress did not seem to contribute to the development of atherosclerosis in these patients (94).

There are still controversies about the duration of acromegaly and whether GH and IGF-1 are related to the increased risk of coronary heart disease. Some previous studies have suggested that the risk of coronary heart disease in patients with acromegaly is mainly related to metabolic complications such as diabetes, hypertension, and hyperlipidemia (89, 90). Tellatin and colleagues recently evaluated coronary flow reserve (CFR) as an indicator of coronary microvascular function in patients with asymptomatic acromegaly. The results suggested that patients with acromegaly had lower CFR. CFR and IGF-1 levels were negatively correlated. In the multiple logistic regression analysis, IGF-1 independently increased the probability of  $\text{CFR} \leq 2.5$  (96). The study by Herrmann et al. suggested that the duration of acromegaly and the subsequent metabolic disorders seemed to affect the CAC degree of patients with acromegaly (97).

However, the incidence of coronary heart disease in patients with acromegaly does not seem to increase. A study by Schöfl et al. observed 479 patients with acromegaly in 7 German endocrine centers and found that the incidence of myocardial infarction in patients with acromegaly was very close to that of the general population (SIR: 0.89, 95% CI: 0.47-1.52),  $P=0.80$  (98). Similarly, a national cohort study in Denmark did not find an increase in myocardial infarction in patients with acromegaly (HR: 1.0, 95% CI: 0.5-1.9) (1). Therefore, more prospective studies are needed on the incidence of atherosclerosis and coronary heart disease in patients with acromegaly.

## THE POTENTIAL BENEFITS OF ACROMEGALY CONTROL FOR RELATED HEART DISEASE

At present, surgical removal of tumors is still the preferred treatment for patients with acromegaly. Approximately 50% of patients are controlled by surgical treatment, total tumor resection can be easily achieved for microadenoma, and up to 85% of microadenoma is completely removed by surgery. The experience of the neurosurgeon has a great influence on the

success rate of the surgery (10, 99). For patients with high-risk surgery or who refuse surgery, and patients whose tumor is located in the cavernous sinus, which may be difficult to cure through surgery, medications (somatostatin analogs, growth hormone receptor antagonist, and dopamine agonist) and radiation therapy could be considered as treatment options (100).

A large number of clinical observation studies have shown that the heart structure and function of patients with acromegaly are significantly improved after the condition is controlled. It has been reported that surgical treatment can reduce the mass of the left ventricle and improve the diastolic and systolic function of patients (44, 101). Patients with acromegaly who had biochemical control after surgery showed reduced heart rate and blood pressure and improved endothelial diastolic dysfunction (102, 103). Minniti and colleagues included 30 newly diagnosed patients with acromegaly and completed echocardiography before and 6 months after transsphenoidal surgery. The results showed that LVM, LVMI, interventricular septum diastolic thickness (IVSDT) and posterior wall diastolic thickness (PWDT) were significantly reduced within 6 months after surgery. Furthermore, diastolic function was significantly improved compared with preoperative function (101).

At present, drugs such as somatostatin analogs, GH receptor antagonists and dopamine receptor agonists are often used as adjuvant treatments for surgery to achieve biochemical control in patients with acromegaly (10, 39, 61, 100, 103, 104). Many studies have suggested that somatostatin analogs can benefit the heart in treating acromegaly (39, 61, 104). Lombardi and colleagues enrolled 19 patients. After 6 months of treatment with lanreotide, LVM was significantly reduced, and the proportion of patients with ventricular premature beats decreased by 50%. Holter results showed that the heart rate in 24 hours was significantly reduced after 6 months of lanreotide treatment (39). Bogazzi et al. used CMRI to evaluate heart changes in 14 patients with untreated active acromegaly before and after a 6-month duration of treatment with lanreotide. The authors found that short-term treatment with lanreotide reduced the LVMI, reversing LV hypertrophy in most patients. However, no correlation was found between changes in the LVMI and changes in the serum IGF-I concentration. Notably, patients with controlled disease showed greater reduction of the LVMI than those with uncontrolled acromegaly (62). Octreotide and lanreotide may have a direct beneficial effect on the cardiovascular system through somatostatin receptors on cardiomyocytes. Cardiac fibroblasts express somatostatin receptors (SSTRs) 1, 2, 4, and 5. Cardiomyocytes express SSTR1 and SSTR2, and octreotide and lanreotide can bind to SSTR2 and SSTR5 and have a direct effect on cardiac fibroblasts and cardiomyocytes (105, 106). Thus, regardless of whether the administration of somatostatin in patients with acromegaly achieves biochemical control, it may significantly reduce LVMI and improve cardiomyopathy. Meanwhile, somatostatin analog therapy may improve mortality in patients with acromegaly. In 2019, a meta-analysis evaluating the mortality of acromegaly revealed that in 6 clinical intervention studies that used



somatostatin analogs as an adjuvant treatment for patients after surgery, the mortality of acromegaly did not increase (SMR: 0.98, CI: 0.83-1.15), and only in patients who received surgery and/or radiotherapy without the use of somatostatin analogs as adjuvant treatment did the mortality rate significantly increase (SMR: 2.11; CI: 1.54-2.91) (11).

When SSAs treatment alone cannot achieve biochemical control of acromegaly, the SSAs can be replaced or combined with the growth hormone receptor antagonist pegvisomant (PEG) (107). When SSAs fail to control acromegaly, PEG normalized serum IGF1 levels in 70–97% of cases (54). Studies have suggested that long-term SSAs and PEG combined therapy can improve the cardiac structure and function in patients with acromegaly resistant to SSAs, especially patients with diastolic dysfunction (54, 108). Auriemma et al. evaluated 36 patients undergoing high-dose single-drug-resistant SSA therapy. These patients received SSA treatment for a median duration of 36 months and further received SSA+PEG treatment for a median duration of 60 months. Comparison of the cardiac structure and function after using an SSA alone, using an SSA+PEG for 12 months, and using an SSA+PEG for 60 months suggested that short-term and long-term SSA+PEG treatment could significantly improve the LVMi and E/A. The study also suggested that the improvement was mainly related to IGF-1 normalization, and the IGF-1 concentration in 83% patients was controlled to the normal range (108). Because GH receptors are expressed on cardiomyocytes, PEG might have a direct effect on the heart; however, this remains to be elucidated (109). Few studies to date have focused on the changes in cardiac structure or function in patients with acromegaly using PEG alone (42, 54). A study by Pivonello et al. suggested that the LVM decreased after long-term use of PEG in 12 patients with acromegaly, both diastolic and systolic function improved, and a correlation was found between changes in the IGF-I concentration and changes in the left ventricular ejection fraction (42). However, a study by Kuhn et al. indicated that the LVM decreased and that the LVEF did not change significantly overall. Notably, they found that the LVEF significantly improved in patients with a baseline LVEF of <60% but decreased in patients with an LVEF of >70% (54). In addition to improving the structure and function of the heart, PEG can also improve arrhythmias (95) and reduce the Framingham risk score (110).

For patients with acromegaly who have not achieved biochemical remission after surgery, dopamine receptor agonist therapy is also a treatment options, especially for those patients with only a mildly elevated serum IGF-1 concentration. Previous studies have shown that high-dose cabergoline is related to valve disease in patients with Parkinson's disease (111, 112). A recent meta-analysis showed that patients with hyperprolactinemia treated with cabergoline were at increased risk of regurgitation of the tricuspid valve. This study analyzed data from 13 published studies of 836 patients with hyperprolactinemia treated with cabergoline and 1388 healthy controls. The results suggested that there was no difference in the risk of aortic or mitral regurgitation between the cabergoline-treated patients and the control group (113). To the best of our knowledge, only one

study has evaluated the effects of cabergoline on cardiac valves in patients with acromegaly (114). Maione et al. compared the prevalence and incidence of heart valve disease and regurgitation in a series of patients with acromegaly treated with cabergoline and matched patients who had never received this drug. The authors found no increase in the prevalence of valve regurgitation or remodeling relative to a matched cohort of patients with acromegaly who had never received cabergoline. The valve abnormalities observed here are more likely to have been related to acromegaly itself than to cabergoline (114). However, the cumulative doses and treatment durations in patients with acromegaly and patients with hyperprolactinemia were consistently lower than those in patients with Parkinson's disease. One study suggested that for patients who need high-dose cabergoline (>3 mg/week) for a long period of time, echocardiography may be needed to evaluate valve abnormalities, whereas patients who receive low-dose cabergoline (1–2 mg/week) may not need routine echocardiography (115). However, whether cabergoline might be harmful to the cardiac structure in patients with acromegaly requires further evaluation.

## SUMMARY

In summary, cardiovascular complications are the most common complication in patients with acromegaly, and also the main factors affecting the quality of life and survival time of patients. Patients with acromegaly often have cardiovascular diseases such as hypertension, myocardial hypertrophy, diastolic insufficiency, and arrhythmia. At present, the underlying physiopathology of various cardiac complications has not been fully elucidated, but the coexistence of GH/IGF-I over secretion, older age at diagnosis, prolonged disease duration, and other cardiovascular risk factors may be the most important factors for cardiovascular complications. Once acromegaly is diagnosed, the patient's heart condition should be thoroughly evaluated immediately. Clinicians should carefully screen each patient for hypertension, cardiomyopathy, valvular heart disease, and arrhythmia. More importantly, active intervention is necessary. Surgery is the first-line choice for patients with acromegaly to remove GH pituitary adenomas and control GH/IGF-1 levels. For patients who have not remitted after surgery and cannot be operated on, radiotherapy and/or drug therapy should be considered to achieve biochemical remission of GH/IGF-1 levels in patients with acromegaly as soon as possible. Early diagnosis and treatment can help reduce the risk of severe cardiac complications in patients with acromegaly, improve the quality of life of patients, and prolong the survival time.

## AUTHOR CONTRIBUTIONS

HY and HT designed, viewed, and collected the literature, analyzed the data, wrote and revised the draft, and



contributed equally to this work. HH analyzed and summarized the research progress of cardiac imaging, JL designed and analyzed, and contributed to the revision of the manuscript. All authors contributed to the article and approved the submitted version.

## REFERENCES

- Dal J, Feldt-Rasmussen U, Andersen M, Kristensen LØ, Laurberg P, Pedersen L, et al. Acromegaly incidence, prevalence, complications and long-term prognosis: a nationwide cohort study. *Eur J Endocrinol* (2016) 175:181–90. doi: 10.1530/EJE-16-0117
- Matsubayashi K, Kawakami K. Prevalence, incidence, comorbidities, and treatment patterns among Japanese patients with acromegaly: a descriptive study using a nationwide claims database. *Endocr J* (2020) 67:10(10). doi: 10.1507/endocrj.EJ20-0129
- Caputo M, Ucciero A, Mele C, De Marchi L, Magnani C, Cena T, et al. Use of administrative health databases to estimate incidence and prevalence of acromegaly in Piedmont Region, Italy. *J Endocrinol Invest* (2019) 424(4):397–402. doi: 10.1007/s40618-018-0928-7
- Raappana A, Koivukangas J, Ebeling T, Pirilä T. Incidence of pituitary adenomas in Northern Finland in 1992–2007. *J Clin Endocrinol Metab* (2010) 95:4268–75. doi: 10.1210/jc.2010-0537
- Hoskuldottir GT, Fjalldal SB, Sigurjonsdottir HA. The incidence and prevalence of acromegaly, a nationwide study from 1955 through 2013. *Pituitary* (2015) 18:803–7. doi: 10.1007/s11102-015-0655-4
- Daly AF, Rixhon M, Adam C, Demegioti A, Tichomirowa MA, Beckers A, et al. High prevalence of pituitary adenomas: a cross-sectional study in the province of Liege, Belgium. *J Clin Endocrinol Metab* (2006) 91:4769–75. doi: 10.1210/jc.2006-1668
- Fernandez A, Karavitaki N, Wass JA. Prevalence of pituitary adenomas: a community-based, cross-sectional study in Banbury (Oxfordshire, UK). *Clin Endocrinol (Oxf)* (2010) 72:377–82. doi: 10.1111/j.1365-2265.2009.03667.x
- Ben-Shlomo A, Melmed S. Acromegaly. *Endocrinol Metab Clin North Am* (2008) 37:101–22. doi: 10.1016/j.ecl.2007.10.002
- Melmed S. Medical progress: Acromegaly. *N Engl J Med* (2006) 355:2558–73. doi: 10.1056/NEJMr062453
- Katznelson L, Laws ER, Melmed S. Acromegaly: an endocrine society clinical practice guideline. *J Clin Endocrinol Metab* (2014) 99(11):3933–51. doi: 10.1210/jc.2014-2700
- Bolfi F, Neves AF, Boguszewski CL, Nunes-Nogueira VS. Mortality in acromegaly decreased in the last decade: a systematic review and meta-analysis. *Eur J Endocrinol* (2019) 181(5):59–71. doi: 10.1530/EJE-19-0509
- Colao A, Ferone D, Marzullo P, Lombardi G. Systemic Complications of Acromegaly: Epidemiology, Pathogenesis, and Management. *Endocr Rev* (2004) 25(1):102–52. doi: 10.1210/er.2002-0022
- Gadelha MR, Kasuki L, Lim DST, Fleseriu M. Systemic Complications of Acromegaly and the Impact of the Current Treatment Landscape: An Update. *Endocr Rev* (2019) 40(1):268–332. doi: 10.1210/er.2018-00115
- Lie JT. Pathology of the heart in acromegaly: anatomic findings in 27 autopsied patients. *Am Heart J* (1980) 100:41–52. doi: 10.1016/0002-8703(80)90277-x
- Broder MS, Neary MP, Chang E, Cherepanov D, Katznelson L. Treatments, complications, and healthcare utilization associated with acromegaly: a study in two large United States databases. *Pituitary* (2014) 17:333–41. doi: 10.1007/s11102-013-0506-0
- Maione L, Brue T, Beckers A, Delemer B, Petrossians P, Borson-Chazot F, et al. Changes in the management and comorbidities of acromegaly over three decades: the French Acromegaly Registry. *Eur J Endocrinol* (2017) 176:645–55. doi: 10.1530/EJE-16-1064
- Colao A, Vandevas P, Pivonello R, Grasso LF, Nachev E, Auriemma RS, et al. Could different treatment approaches in acromegaly influence life expectancy? A comparative study between Bulgaria and Campania (Italy). *Eur J Endocrinol* (2014) 171:263–73. doi: 10.1530/EJE-13-1022
- Arosio M, Reimondo G, Malchiodi E, Berchiolla P, Borraicino A, De Marinis L, et al. Predictors of morbidity and mortality in acromegaly: an Italian survey. *Eur J Endocrinol* (2012) 167:189–98. doi: 10.1530/EJE-12-0084
- Vila G, Luger A, van der Lely AJ, Neggers SJMM, Webb SM, Biller BMK, et al. Hypertension in Acromegaly in Relationship to Biochemical Control and Mortality: Global ACROSTUDY Outcomes. *Front Endocrinol (Lausanne)* (2020) 11:577173. doi: 10.3389/fendo.2020.577173
- Puglisi S, Terzolo M. Hypertension and Acromegaly. *Endocrinol Metab Clin N Am* (2019) 48:779–93. doi: 10.1016/j.ecl.2019.08.008
- Minniti G, Moroni C, Jaffrain-Rea ML, Bondanini F, Gulino A, Cassone R, et al. Prevalence of hypertension in acromegalic patients: clinical measurement versus 24-hour ambulatory blood pressure monitoring. *Clin Endocrinol (Oxf)* (1998) 48:149–52. doi: 10.1046/j.1365-2265.1998.3611177.x
- Costenaro F, Martin A, Horn RF, Czepielewski MA, Rodrigues TC. Role of ambulatory blood pressure monitoring in patients with acromegaly. *J Hypertens* (2016) 34:1357–63. doi: 10.1097/HJH.0000000000000962
- Vitale G, Pivonello R, Auriemma RS, Guerra E, Milone F, Savastano S, et al. Hypertension in acromegaly and in the normal population: prevalence and determinants. *Clin Endocrinol (Oxf)* (2005) 63:470–6. doi: 10.1111/j.1365-2265.2005.02370.x
- Brevetti G, Marzullo P, Silvestro A, Pivonello R, Oliva G, Savastano S, et al. Early vascular alterations in acromegaly. *J Clin Endocrinol Metab* (2002) 87:3174–9. doi: 10.1210/jcem.87.7.8643
- Sardella C, Urbani C, Lombardi M, Nuzzo A, Manetti L, Lupi I, et al. The beneficial effect of acromegaly control on blood pressure values in normotensive patients. *Clin Endocrinol* (2014) 81:573–81. doi: 10.1111/cen.12455
- Ohtsuka H, Komiya I, Aizawa T, Yamada T. Hypertension in acromegaly: hereditary hypertensive factor produces hypertension by enhancing IGF-I production. *Endocr J* (1995) 42(6):781–7. doi: 10.1507/endocrj.42.781
- Sardella C, Cappellani D, Urbani C, Manetti L, Marconcini G, Tomisti L, et al. Disease activity and lifestyle influence comorbidities and cardiovascular events in patients with acromegaly. *Eur J Endocrinol* (2016) 175:443–53. doi: 10.1530/EJE-16-0562
- Schutte AE, Volpe M, Tocci G, Conti E. Revisiting the Relationship Between Blood Pressure and Insulin-Like Growth Factor-1. *Hypertension* (2014) 63(5):1070–7. doi: 10.1161/HYPERTENSIONAHA.113.03057
- Bielohuby M, Roemmler J, Manolopoulou J, Johnsen I, Sawitzky M, Schopohl J, et al. Chronic growth hormone excess is associated with increased aldosterone: a study in patients with acromegaly and in growth hormone transgenic mice. *Exp Biol Med (Maywood)* (2009) 234:1002–9. doi: 10.3181/0901-RM-34
- Davies E, MacKenzie SM. Extra-adrenal production of corticosteroids. *Clin Exp Pharmacol Physiol* (2003) 30:437–45. doi: 10.1046/j.1440-1681.2003.03867.x
- Ye P, Kenyon CJ, Mackenzie SM, Nichol K, Seckl JR, Fraser R, et al. Effects of ACTH, dexamethasone, and adrenalectomy on 11 $\beta$ -hydroxylase (CYP11B1) and aldosterone synthase (CYP11B2) gene expression in the rat central nervous system. *J Endocrinol* (2008) 196:305–11. doi: 10.1677/JOE-07-0439
- Kamenicky P, Blanchard A, Frank M, Salenave S, Letierce A, Azizi M, et al. Body fluid expansion in acromegaly is related to enhanced epithelial sodium channel (ENaC) activity. *J Clin Endocrinol Metab* (2011) 96:2127–35. doi: 10.1210/jc.2011-0078
- Maison P, De 'molis P, Young J, Schaison G, Giudicelli JF, Chanson P. Vascular reactivity in acromegalic patients: preliminary evidence for regional endothelial dysfunction and increased sympathetic

## FUNDING

This study was supported by Grant 1.3.5 project for Disciplines of Excellence Clinical Research Incubation Project, West China Hospital Sichuan University (Grant No. 2020HXXFH034).

- vasoconstriction. *Clin Endocrinol (Oxf)* (2000) 53:445–51. doi: 10.1046/j.1365-2265.2000.01127.x
34. Ronconi V, Giacchetti G, Mariniello B, Camilletti A, Mantero F, Boscaro M, et al. Reduced nitric oxide levels in acromegaly: cardiovascular implications. *Blood Press* (2005) 14:227–32. doi: 10.1080/08037050510034293
  35. Powlson AS, Gurnell M. Cardiovascular Disease and Sleep-Disordered Breathing in Acromegaly. *Neuroendocrinology* (2016) 103(1):75–85. doi: 10.1159/000438903
  36. Huchard H. Anatomie pathologique, lesions et trouble cardiovasculaires de l'acromegalie. *J Practiciens* (1895) 9:249–50.
  37. Ramos-Leví AM, Marazuela M. Cardiovascular comorbidities in acromegaly: an update on their diagnosis and management. *Endocrine* (2017) 55(2):346–59. doi: 10.1007/s12020-016-1191-3
  38. Pivonello R, Auriemma RS, Grasso LF, Pivonello C, Simeoli C, Patalano R, et al. Complications of acromegaly: cardiovascular, respiratory and metabolic comorbidities. *Pituitary* (2017) 20:46–62. doi: 10.1007/s11102-017-0797-7
  39. Lombardi G, Colao A, Marzullo P, Biondi B, Palmieri E, Fazio S, et al. Improvement of left ventricular hypertrophy and arrhythmias after lanreotide-induced GH and IGF-I decrease in acromegaly. A prospective multi-center study. *J Endocrinol Invest* (2002) 25:971–6. doi: 10.1007/BF03344070
  40. Bogazzi F, Di Bello V, Palagi C, Donne MG, Di Cori A, Gavioli S, et al. Improvement of intrinsic myocardial contractility and cardiac fibrosis degree in acromegalic patients treated with somatostatin analogues: a prospective study. *Clin Endocrinol (Oxf)* (2005) 62:590–6. doi: 10.1111/j.1365-2265.2005.02265.x
  41. Casini AF, Araujo PB, Fontes R, Xavier SS, Gadelha MR. Cardiac morphology and performance alterations and analysis of determinant factors of left ventricular hypertrophy in 40 patients with acromegaly. *Arq Bras Endocrinol Metabol* (2006) 50:82–90. doi: 10.1590/s0004-27302006000100012
  42. Pivonello R, Galderisi M, Auriemma RS, De Martino MC, Galdiero M, Ciccarelli A, et al. Treatment with growth hormone receptor antagonist in acromegaly: effect on cardiac structure and performance. *J Clin Endocrinol Metab* (2007) 92(2):476–82. doi: 10.1210/jc.2006-1587
  43. Bogazzi F, Lombardi M, Strata E, Aquaro G, Di Bello V, Cosci C, et al. High prevalence of cardiac hypertrophy without detectable signs of fibrosis in patients with untreated active acromegaly: an *in vivo* study using magnetic resonance imaging. *Clin Endocrinol (Oxf)* (2008) 68:361–8. doi: 10.1111/j.1365-2265.2007.03047.x
  44. De Marinis L, Bianchi A, Mazziotti G, Mettimano M, Milardi D, Fusco A, et al. The long-term cardiovascular outcome of different GH-lowering treatments in acromegaly. *Pituitary* (2008) 11:13–20. doi: 10.1007/s11102-007-0062-6
  45. Colao A, Pivonello R, Grasso LF, Auriemma RS, Galdiero M, Savastano S, et al. Determinants of cardiac disease in newly diagnosed patients with acromegaly: results of a 10 years survey study. *Eur J Endocrinol* (2011) 165(5):713–21. doi: 10.1530/EJE-11-0408
  46. Jayasena CN, Comninou AN, Clarke H, Donaldson M, Meeran K, Dhillon WS. The effects of long-term growth hormone and insulin-like growth factor-1 exposure on the development of cardiovascular, cerebrovascular and metabolic co-morbidities in treated patients with acromegaly. *Clin Endocrinol (Oxf)* (2011) 75:220–5. doi: 10.1111/j.1365-2265.2011.04019.x
  47. Akdeniz B, Gedik A, Turan O, Ozpelit E, Ikiz AO, Itil O, et al. Evaluation of Left Ventricular Diastolic Function According to New Criteria and Determinants in Acromegaly. *Int Heart J* (2012) 53:299–305. doi: 10.1536/ihj.53.299
  48. Annamalai AK, Webb A, Kandasamy N, Elkhawad M, Moir S, Khan F, et al. A comprehensive study of clinical, biochemical, radiological, vascular, cardiac, and sleep parameters in an unselected cohort of patients with acromegaly undergoing presurgical somatostatin receptor ligand therapy. *J Clin Endocrinol Metab* (2013) 98:1040–50. doi: 10.1210/jc.2012-3072
  49. Nascimento GC, de Oliveira MT, Carvalho VC, Lopes MH, Guimares Sá AM, Souza MT, et al. Acromegalic cardiomyopathy in an extensively admixed population: is there a role for GH/IGF-I axis? *Clin Endocrinol (Oxf)* (2013) 78:94–101. doi: 10.1111/j.1365-2265.2012.04472.x
  50. Mercado M, Gonzalez B, Vargas G, Claudia R, Monteros ALE, Sosa E, et al. Successful mortality reduction and control of comorbidities in patients with acromegaly followed at a highly specialized multidisciplinary clinic. *J Clin Endocrinol Metab* (2014) 99:4438–46. doi: 10.1210/jc.2014-2670
  51. dos Santos Silva CM, Gottlieb I, Volschan I, Kasuki L, Warszawski L, Balarini Lima GA, et al. Low Frequency of Cardiomyopathy Using Cardiac Magnetic Resonance Imaging in an Acromegaly Contemporary Cohort. *J Clin Endocrinol Metab* (2015) 100:4447–55. doi: 10.1210/jc.2015-2675
  52. Sanchez-Ortega R, Climent V, Sanchez-Tejada L, Candela A, Pico A. Severe sleep apnea-hypopnea syndrome is related to left ventricle dysfunction and hypertension in acromegalic patients. *Endocrinol Nutr* (2015) 62:366–72. doi: 10.1016/j.endonu.2015.05.007
  53. Guo XP, Gao L, Zhang S, Li Y, Wu Y, Fang L, et al. Cardiovascular System Changes and Related Risk Factors in Acromegaly Patients: A Case-Control Study. *Int J Endocrinol* (2015) 2015:573643. doi: 10.1155/2015/573643
  54. Kuhn E, Maione L, Bouchachi A, Rozière M, Salenave S, Salenave S, et al. Long-term effects of pegvisomant on comorbidities in patients with acromegaly: a retrospective single-center study. *Eur J Endocrinol* (2015) 173:693–702. doi: 10.1530/EJE-15-0500
  55. Petrossians P, Daly AF, Natchev E, Maione L, Blijdorp K, Sahnoun-Fathallah M, et al. Acromegaly at diagnosis in 3173 patients from the Liege Acromegaly Survey (LAS) Database. *Endocr Relat Cancer* (2017) 24:505–18. doi: 10.1530/ERC-17-0253
  56. Cansu GB, Yilmaz N, Yanıkoğlu A, Özdem S, Yıldırım AB, Süleymanlar G, et al. Assessment of Diastolic Dysfunction, Arterial Stiffness, and Carotid Intima-Media Thickness in Patients with Acromegaly. *Endocr Pract* (2017) 23:536–45. doi: 10.4158/EP161637.OR
  57. Carmichael JD, Broder MS, Cherepanov D, Chang E, Mamelak A, Said Q, et al. The association between biochemical control and cardiovascular risk factors in acromegaly. *BMC Endocr Disord* (2017) 17:15. doi: 10.1186/s12902-017-0166-6
  58. Natchev E, Kundurdjiev A, Zlatareva N, Vandeva S, Kirilov G, Kundurzhiev T, et al. Echocardiographic myocardial changes in acromegaly: a cross-sectional analysis in a tertiary center bulgaria. *Endocr Care* (2019) 15(1):52–61. doi: 10.4183/aeb.2019.52
  59. Guo X, Cao J, Liu P, Cao Y, Li X, Kundurzhiev T, et al. Cardiac Abnormalities in Acromegaly Patients: A Cardiac Magnetic Resonance Study. *Int J Endocrinol* (2020) 2020:2018464. doi: 10.1155/2020/2018464
  60. Guo XP, Xing B. Progress in magnetic resonance research on heart disease in patients with acromegaly. *J Med Res* (2018) 47(8):7–10. doi: 10.11969/j.jissn.1673-548X.2018.08.003
  61. Grothues F, Smith GC, Moon JC, Bellenger NG, Collins P, Klein HU, et al. Comparison of interstudy reproducibility of cardiovascular magnetic resonance with two-dimensional echocardiography in normal subjects and in patients with heart failure or left ventricular hypertrophy. *Am J Cardiol* (2002) 90:29–34. doi: 10.1016/S0002-9149(02)02381-0
  62. Bogazzi F, Lombardi M, Strata E, Aquaro G, Lombardi M, Urbani C, et al. Effects of somatostatin analogues on acromegalic cardiomyopathy: Results from a prospective study using cardiac magnetic resonance. *J Endocrinol* (2010) 33:103–8. doi: 10.1007/BF03346562
  63. Andreassen M, Faber J, Kjaer A, Petersen CL, Kristensen LØ. Cardiac effects of 3 months treatment of acromegaly evaluated by magnetic resonance imaging and B-type natriuretic peptides. *Pituitary* (2010) 13:329–36. doi: 10.1007/s11102-010-0240-9
  64. Warszawski L, Kasuki L, Sá R, Dos Santos Silva CM, Volschan I, Gottlieb I, et al. Low frequency of cardiac arrhythmias and lack of structural heart disease in medically-naïve acromegaly patients: a prospective study at baseline and after 1 year of somatostatin analogs treatment. *Pituitary* (2016) 19(6):582–9. doi: 10.1007/s11102-016-0749-7
  65. Bihan H, Espinosa C, Valdes-Socin H, Salenave S, Young J, Levasseur S, et al. Long-term outcome of patients with acromegaly and congestive heart failure. *J Clin Endocrinol Metab* (2004) 89:5308–13. doi: 10.1210/jc.2004-0821
  66. Volschan IC, Kasuki L, Silva CM, Alcantara ML, Saraiva RM, Xavier SS, et al. Two-dimensional speckle tracking echocardiography demonstrates no effect of active acromegaly on left ventricular strain. *Pituitary* (2017) 20:349–57. doi: 10.1007/s11102-017-0795-9

67. Popielarz-Grygalewicz A, Gąsior JS, Konwicka A, Grygalewicz P, Stelmachowska-Banaś M, Zgliczyński W, et al. Heart in Acromegaly: The Echocardiographic Characteristics of Patients Diagnosed with Acromegaly in Various Stages of the Disease. *Int J Endocrinol* (2018) 2018:6935054. doi: 10.1155/2018/6935054
68. Di Bello V, Bogazzi F, Di Cori A, Palagi C, Delle Donne MG, Gavioli S, et al. Myocardial systolic strain abnormalities in patients with acromegaly: a prospective color Doppler imaging study. *J Endocrinol Invest* (2006) 29:544–50. doi: 10.1007/BF03344145
69. Uziębło-Życzkowska B, Jurek A, Witek P, Zieliński G, Gielera G, Krzesiński P. Left Heart Dysfunction in Acromegaly Revealed by Novel Echocardiographic Methods. *Front Endocrinol* (2020) 11:418. doi: 10.3389/fendo.2020.00418
70. Pereira AM, van Thiel SW, Lindner JR, Roelfsema F, van der Wall EE, Morreau H, et al. Increased prevalence of regurgitant valvular heart disease in acromegaly. *J Clin Endocrinol Metab* (2004) 89:71–5. doi: 10.1210/jc.2003-030849
71. Clao A, Spinelli L, Marzullo P, Pivonello R, Petretta M, Di Somma C, et al. High Prevalence of Cardiac Valve Disease in Acromegaly: An Observational, Analytical, Case-Control Study. *J Clin Endocrinol Metab* (2003) 88(7):3196–201. doi: 10.1210/jc.2002-021099
72. van der Klaauw AA, Bax JJ, Roelfsema F, Bleeker GB, Holman ER, Corssmit EP, et al. Uncontrolled acromegaly is associated with progressive mitral valvular regurgitation. *Growth Horm IGF Res* (2006) 16:101–7. doi: 10.1016/j.jghir.2006.02.002
73. Ohtsuka G, Aomi S, Koyanagi H, Tsukui H, Tomizawa Y, Hashimoto A, et al. Heart valve operation in acromegaly. *Ann Thor Surg* (1997) 64:390–3. doi: 10.1016/S0003-4975(97)00788-1
74. Fondard O, Detaint D, Lung B, Choqueux C, Adle-Biasette H, Jarraya M, et al. Extracellular matrix remodelling in human aortic valve disease: the role of matrix metalloproteinases and their tissue inhibitors. *Eur Heart J* (2005) 26:1333–41. doi: 10.1093/eurheartj/ehi248
75. van der Klaauw AA, Bax JJ, Smit JW, Holman ER, Delgado V, Bleeker GB, et al. Increased aortic root diameters in patients with acromegaly. *Eur J Endocrinol* (2008) 159:97–103. doi: 10.1530/EJE-08-0138
76. Casini AF, Neto LV, Fontes R, Franca RF, Xavier SS, Gadelha MR, et al. Aortic root ectasia in patients with acromegaly: experience at a single center. *Clin Endocrinol (Oxf)* (2011) 75:495–500. doi: 10.1111/j.1365-2265.2011.04067.x
77. Arias MA, Pachón M, Rodríguez-Padial L. Ventricular tachycardia in acromegaly. *Rev Port Cardiol* (2011) 30:223–6. doi: 10.1016/S0196-0644(99)70109-5
78. Hayward RP, Emanuel RW, Nabarro JD. Acromegalic heart disease: influence of treatment of acromegaly on the heart. *Q J Med* (1987) 62:41–58. doi: 10.1093/oxfordjournals.qjmed.a068078
79. Kahaly G, Olshausen KV, Mohr-Kahaly S, Erbel R, Boor S, Beyer J, et al. Arrhythmia profile in acromegaly. *Eur Heart J* (1992) 13:51–6. doi: 10.1093/oxfordjournals.eurheartj.a060047
80. Chemla D, Attal P, Maione L, Veyer AS, Mroue G, Baud D, et al. Impact of successful treatment of acromegaly on overnight heart rate variability and sleep apnea. *J Clin Endocrinol Metab* (2014) 99:2925–31. doi: 10.1210/jc.2013-4288
81. Maffei P, Martini C, Milanesi A, Corfini A, Mioni R, de Carlo E, et al. Late potentials and ventricular arrhythmias in acromegaly. *Int J Cardiol* (2005) 104:197–203. doi: 10.1016/j.ijcard.2004.12.010
82. Melkozerov KV, Przhlyakovskaya EG, Tarbaeva NV, Almaskhanova AA, Kuklina MD, Alferova PA, et al. Heart arrhythmias and conduction disorders in patients with acromegaly: the role of cardiac magnetic resonance imaging. *Ter Arkh* (2020) 92(10):70–7. doi: 10.26442/00403660.2020.10.000787
83. Comunello A, Dassi F, Martini C, De Carlo E, Mioni R, Battocchio M, et al. Heart rate variability is reduced in acromegaly patients and improved by treatment with somatostatin analogues. *Pituitary* (2015) 18:525–34. doi: 10.1007/s11102-014-0605-6
84. Unubol M, Eryilmaz U, Guney E, Ture M, Akgullu C. QT dispersion in patients with acromegaly. *Endocrine* (2013) 43:419–23. doi: 10.1007/s12020-012-9828-3
85. Orosz A, Csajbók E, Czékus C, Gavallér H, Magony S, Valkusz Z, et al. Increased Short-Term Beat-To-Beat Variability of QT Interval in Patients with Acromegaly. *PLoS One* (2015) 10:e0125639. doi: 10.1371/journal.pone.0125639
86. Higashi Y, Sukhanov S, Anwar A, Shai SY, Delafontaine P. IGF-1, oxidative stress and atheroprotection. *Trends Endocrinol Metab* (2010) 21:245–54. doi: 10.1016/j.tem.2009.12.005
87. von der Thüsen JH, Borensztajn KS, Moimas S, van Heiningen S, Teeling P, van Berkel TJ, et al. IGF-1 has plaque-stabilizing effects in atherosclerosis by altering vascular smooth muscle cell phenotype. *Am J Pathol* (2011) 178:924–34. doi: 10.1016/j.ajpath.2010.10.007
88. dos Santos Silva CM, Lima GA, Volschan IC, Gottlieb I, Kasuki L, Neto LV, et al. Low risk of coronary artery disease in patients with acromegaly. *Endocrine* (2015) 50(3):749–55. doi: 10.1007/s12020-015-0628-4
89. Akutsu H, Kreutzer J, Wasmeier G, Ropers D, Schfl C. Acromegaly per se does not increase the risk for coronary artery disease. *Eur J Endocrinol* (2010) 162:879–86. doi: 10.1530/EJE-09-0945
90. Bogazzi F, Battolla L, Spinelli C, Rossi G, Gavioli S, Di Bello V, et al. Risk factors for development of coronary heart disease in patients with acromegaly: a five-year prospective study. *J Clin Endocrinol Metab* (2007) 92:4271–7. doi: 10.1210/jc.2007-1213
91. Otsuki M, Kasayama S, Yamamoto H, Saito H, Sumitani S, Kouhara H, et al. Characterization of premature atherosclerosis of carotid arteries in acromegalic patients. *Clin Endocrinol (Oxf)* (2001) 54:791–6. doi: 10.1046/j.1365-2265.2001.01281.x
92. Ragonese M, Alibrandi A, Di Bella G, Salamone I, Puglisi S, Cotta OR, et al. Cardiovascular events in acromegaly: distinct role of Agatston and Framingham score in the 5-year prediction. *Endocrine* (2014) 47(1):206–12. doi: 10.1007/s12020-013-0115-8
93. Parolin M, Dassi F, Martini C, Mioni R, Russo L, Fallo F, et al. Preclinical markers of atherosclerosis in acromegaly: a systematic review and meta-analysis. *Pituitary* (2018) 21(6):653–62. doi: 10.1007/s11102-018-0911-5
94. Ozkan C, Altinova AE, Cerit ET, Yayla C, Sahinarslan A, Sahin D, et al. Markers of early atherosclerosis, oxidative stress and inflammation in patients with acromegaly. *Pituitary* (2015) 18(5):621–9. doi: 10.1007/s11102-014-0621-6
95. Berg C, Petersenn S, Lahner H, Herrmann BL, Buchfelder M, Droste M, et al. Cardiovascular risk factors in patients with uncontrolled and long-term acromegaly: comparison with matched data from the general population and the effect of disease control. *J Clin Endocrinol Metab* (2010) 95(8):3648–56. doi: 10.1210/jc.2009-2570
96. Tellatin S, Maffei P, Osto E, Dassi F, Famoso G, Montisci R, et al. Coronary microvascular dysfunction may be related to IGF-1 in acromegalic patients and can be restored by therapy. *Atherosclerosis* (2018) 269:100–5. doi: 10.1016/j.atherosclerosis.2017.12.019
97. Herrmann BL, Severing M, Schermund A, Berg C, Budde T, Erbel R, et al. Impact of Disease Duration on Coronary Calcification in Patients with Acromegaly. *Exp Clin Endocrinol Diabetes* (2009) 117:417–22. doi: 10.1055/s-0029-1214386
98. Schöfl C, Petroff D, Tönjes A, Grussendorf M, Droste M, Stalla G, et al. Incidence of myocardial infarction and stroke in acromegaly patients: results from the German Acromegaly Registry. *Pituitary* (2017) 20:635–42. doi: 10.1007/s11102-017-0827-5
99. Wang YY, Higham C, Kearney T, Davis JR, Trainer P, Gnanalingham KK. Acromegaly surgery in Manchester revisited—the impact of reducing surgeon numbers and the 2010 consensus guidelines for disease remission. *Clin Endocrinol (Oxf)* (2012) 76:399–406. doi: 10.1111/j.1365-2265.2011.04193.x
100. Giustina A, Barkhoudarian G, Beckers A, Ben-Shlomo A, Biermasz N, Biller B, et al. Multidisciplinary management of acromegaly: A consensus. *Rev Endocr Metab Disord* (2020) 21(4):667–78. doi: 10.1007/s11154-020-09588-z
101. Minniti G, Moroni C, Jaffrain-Rea ML, Esposito V, Santoro A, Affricano C, et al. Marked improvement in cardiovascular function after successful transphenoidal surgery in acromegalic patients. *Clin Endocrinol(Oxf)* (2001) 55:307–13. doi: 10.1046/j.1365-2265.2001.01343.x
102. Sakai H, Tsuchiya K, Nakayama C, Iwashima F, Izumiyama H, Doi M, et al. Improvement of endothelial dysfunction in acromegaly after

- transsphenoidal surgery. *Endocr J* (2008) 55:853–9. doi: 10.1507/endocrj.k07e-125
103. Colao A, Pivonello R, Galderisi M, Cappabianca P, Auriemma RS, Galdiero M, et al. Impact of treating acromegaly first with surgery or somatostatin analogs on cardiomyopathy. *J Clin Endocrinol Metab* (2008) 93:2639–46. doi: 10.1111/j.1478-3231.2004.0912.x
  104. Maison P, Tropeano AI, Macquin-Mavier I, Giustina A, Chanson P. Impact of somatostatin analogs on the heart in acromegaly: a metaanalysis. *J Clin Endocrinol Metab* (2007) 92:1743–7. doi: 10.1210/jc.2006-2547
  105. Colao A. Improvement of cardiac parameters in patients with acromegaly treated with medical therapies. *Pituitary* (2012) 15:50–8. doi: 10.1111/j.1478-3231.2004.0912.x
  106. Smith WH, Nair RU, Adamson D, Kearney MT, Ball SG, Balmforth AJ. Somatostatin receptor subtype expression in the human heart: differential expression by myocytes and fibroblasts. *J Endocrinol* (2005) 187:379–86. doi: 10.1677/joe.1.06082
  107. Strasburger CJ, Mattsson A, Wilton P, Aydin F, Hey-Hadavi J, Biller BM. Increasing frequency of combination medical therapy in the treatment of acromegaly with the GH receptor antagonist pegvisomant. *Eur J Endocrinol* (2018) 178(4):321–9. doi: 10.1530/EJE-17-0996
  108. Auriemma RS, Grasso LF, Galdiero M, Galderisi M, Pivonello C, Simeoli C, et al. Effects of long-term combined treatment with somatostatin analogues and pegvisomant on cardiac structure and performance in acromegaly. *Endocrine* (2017) 553(3):872–84. doi: 10.1007/s12020-016-0995-5
  109. Delafontaine P. Insulin-like growth factor I and its binding proteins in the cardiovascular system. *Cardiovasc Res* (1995) 30:825–34. doi: 10.1016/S0008-6363(95)00163-8
  110. Auriemma RS, Pivonello R, De Martino MC, Cudemo G, Grasso LF, Galdiero M, et al. Treatment with GH receptor antagonist in acromegaly: effect on cardiac arrhythmias. *Eur J Endocrinol* (2012) 168:15–22. doi: 10.1530/EJE-12-0596
  111. Zanettini R, Antonini A, Gatto G, Gentile R, Pezzoli G, Tesei S. Valvular heart disease and the use of dopamine agonists for Parkinson's disease. *N Engl J Med* (2007) 356:39–46. doi: 10.1056/NEJMoa054830
  112. Schade R, Andersohn F, Suissa S, Haverkamp W, Garbe E. Dopamine agonists and the risk of cardiac-valve regurgitation. *N Engl J Med* (2007) 356(1):29–38. doi: 10.1056/NEJMoa062222
  113. Stiles CE, Tetteh-Wayoe ET, Bestwick J, Steeds RP, Drake WM. A Meta-Analysis of the Prevalence of Cardiac Valvulopathy in Patients With Hyperprolactinemia Treated With Cabergoline. *J Clin Endocrinol Metab* (2019) 104(2):523–38. doi: 10.1210/jc.2018-01071
  114. Maione L, Garcia C, Bouchachi A, Kallel N, Maison P, Salenave S, et al. No evidence of a detrimental effect of cabergoline therapy on cardiac valves in patients with acromegaly. *J Clin Endocrinol Metab* (2012) 97(9):E1714 – E1719. doi: 10.1210/jc.2012-1833
  115. Auriemma RS, Pivonello R, Ferreri L, Priscitelli P, Colao A. Cabergoline Use for Pituitary Tumors and Valvular Disorders. *Endocrinol Metab Clin N Am* (2015) 44:89–97. doi: 10.1016/j.ecl.2014.10.007

**Conflict of Interest:** The authors declare that the research was conducted in the absence of any commercial or financial relationships that could be construed as a potential conflict of interest.

Copyright © 2021 Yang, Tan, Huang and Li. This is an open-access article distributed under the terms of the Creative Commons Attribution License (CC BY). The use, distribution or reproduction in other forums is permitted, provided the original author(s) and the copyright owner(s) are credited and that the original publication in this journal is cited, in accordance with accepted academic practice. No use, distribution or reproduction is permitted which does not comply with these terms.





# Intravoxel Incoherent Motion Model in Differentiating the Pathological Grades of Esophageal Carcinoma: Comparison of Mono-Exponential and Bi-Exponential Fit Model

Nian Liu<sup>1†</sup>, Xiongxiang Yang<sup>2†</sup>, Lixing Lei<sup>1</sup>, Ke Pan<sup>1</sup>, Qianqian Liu<sup>1</sup> and Xiaohua Huang<sup>1\*</sup>

<sup>1</sup> Department of Radiology, Affiliated Hospital of North Sichuan Medical College, Nanchong, China, <sup>2</sup> Department of Radiology, Nanchong Hospital of Traditional Chinese Medicine, Nanchong, China

## OPEN ACCESS

### Edited by:

Lu Yang,  
Sichuan University, China

### Reviewed by:

Jiayu Sun,  
Sichuan University, China  
Yongshu Lan,  
Affiliated Hospital of Southwest  
Medical University, China

### \*Correspondence:

Xiaohua Huang  
15082797553@163.com

<sup>†</sup>These authors have contributed  
equally to this work

### Specialty section:

This article was submitted to  
Cancer Imaging and  
Image-directed Interventions,  
a section of the journal  
Frontiers in Oncology

**Received:** 04 November 2020

**Accepted:** 15 March 2021

**Published:** 12 April 2021

### Citation:

Liu N, Yang X, Lei L, Pan K, Liu Q  
and Huang X (2021) Intravoxel  
Incoherent Motion Model in  
Differentiating the Pathological  
Grades of Esophageal  
Carcinoma: Comparison  
of Mono-Exponential  
and Bi-Exponential  
Fit Model.  
Front. Oncol. 11:625891.  
doi: 10.3389/fonc.2021.625891

**Purpose:** To compare the diagnostic efficiency of the mono-exponential model and bi-exponential model deriving from intravoxel incoherent motion diffusion-weighted imaging (IVIM-DWI) in differentiating the pathological grade of esophageal squamous cell carcinoma (ESCC).

**Methods:** Fifty-four patients with ESCC were divided into three groups of poorly-differentiated (PD), moderately-differentiated (MD), and well-differentiated (WD), and underwent the IVIM-DWI scan. Mono-exponential ( $D_{\text{mono}}$ ,  $D_{\text{mono}}^*$ , and  $f_{\text{mono}}$ ) and bi-exponential fit parameters ( $D_{\text{bi}}$ ,  $D_{\text{bi}}^*$ , and  $f_{\text{bi}}$ ) were calculated using the IVIM data for the tumors. Mean parameter values of three groups were compared using a one-way ANOVA followed by *post hoc* tests. The receiver operating characteristic curve was drawn for differentiating pathological grade of ESCC. Correlations between pathological grades and IVIM parameters were analyzed.

**Results:** There were significant differences in  $f_{\text{mono}}$  and  $f_{\text{bi}}$  among the PD, MD and WD ESCC groups (all  $p < 0.05$ ). The  $f_{\text{mono}}$  were  $0.32 \pm 0.07$ ,  $0.23 \pm 0.08$ , and  $0.16 \pm 0.05$ , respectively, and the  $f_{\text{bi}}$  were  $0.35 \pm 0.08$ ,  $0.26 \pm 0.10$ , and  $0.18 \pm 0.07$ , respectively. There was a significant difference in the  $D_{\text{mono}}$  between the WD and the PD group ( $1.48 \pm 0.51 \times 10^{-3} \text{ mm}^2/\text{s}$  versus  $1.05 \pm 0.44 \times 10^{-3} \text{ mm}^2/\text{s}$ ,  $p < 0.05$ ), but there was no significant difference between the WD and MD groups, MD and PD groups (all  $p > 0.05$ ). The  $D_{\text{mono}}^*$ ,  $D_{\text{bi}}$ , and  $D_{\text{bi}}^*$  showed no significant difference among the three groups (all  $p > 0.05$ ). The area under the curve (AUC) of  $D_{\text{mono}}$ ,  $f_{\text{mono}}$  and  $f_{\text{bi}}$  in differentiating WD from PD ESCC were 0.764, 0.961 and 0.932, and the sensitivity and specificity were 92.9% and 60%, 92.9% and 90%, 85.7% and 100%, respectively. The AUC of  $f_{\text{mono}}$  and  $f_{\text{bi}}$  in differentiating MD from PD ESCC were 0.839 and 0.757, and the sensitivity and specificity were 78.6% and 80%, 85.7% and 70%, respectively. The AUC of  $f_{\text{mono}}$  and  $f_{\text{bi}}$  in differentiating MD from WD ESCC were 0.746 and 0.740, and the sensitivity and specificity were 65% and 85%, 80% and 60%, respectively. The pathologically differentiated grade was correlated with all IVIM parameters (all  $p < 0.05$ ).

**Conclusions:** The mono-exponential IVIM model is superior to the bi-exponential IVIM model in differentiating pathological grades of ESCC, which may be a promising imaging method to predict pathological grades of ESCC.

**Keywords:** esophageal squamous cell carcinoma, intravoxel incoherent motion, bi-exponential model, diffusion-weighted imaging, pathological grade, mono-exponential model

## INTRODUCTION

Diffusion-weighted imaging (DWI) is a quantitative technology for evaluating the water motion of tissues without injecting contrast agents (1). It is a mono-compartmental model of water diffusion, and signal attenuation is mono-exponential as a function of b value in traditional DWI (2, 3). Subsequently, le Bihan et al. (4) proposed a bi-exponential mathematical model that can surpass the traditional mono-compartmental model to quantify the effect of intravoxel incoherent motion (IVIM). IVIM-DWI has the advantage of separate evaluation of diffusion and perfusion changes in tissues (4). At present, the IVIM-DWI has been used to evaluate the pathological or blood perfusion status in the brain (5, 6) and abdominal organs (7–11). However, few studies (12–14) have been performed regarding the diagnosis and pathological grade of esophageal carcinoma with MRI, because conventional MRI is limited in its ability to resolve the early esophageal cancer. As the constant progress achieved in this field, IVIM-DWI demonstrated the potential value for the diagnosis and pathological grade of esophageal carcinoma (12, 14, 15).

Despite these promising studies, the accuracy and reliability of IVIM parameters are still challenged by a variety of fitting methods, such as the full fitting and segmented fitting method (16–19). The bi-exponential IVIM model adopts the full fitting method to reflect the organizational information of multi-component perfusion (3, 18). The mono-exponential IVIM model estimates IVIM parameters by the segmented fitting method, which was a classical IVIM model and different from the traditional DWI of mono-exponential diffusion model (3, 17, 18). The mono-exponential IVIM model is only suitable for the tissues with few perfusion components (3). Previous studies (17, 18) have suggested the accuracy and reliability of the mono-exponential IVIM model with segmented fitting are superior to the bi-exponential IVIM model with full fitting in the liver and the pancreas, but the full fitting method provided a better fit at very low and low b-values in the liver (18). Different fitting models have a different application for tissue components, especially for the prediction of different pathological differentiated tissues (20–22). To date, no studies have evaluated the different fitting models of IVIM-DWI for esophageal carcinoma. Therefore, it is still unclear whether the

mono-exponential fit model or bi-exponential fit model in IVIM is suitable for esophageal carcinoma.

Therefore, the purpose of the present study is to determine whether the bi-exponential or mono-exponential fit model of IVIM can be used to distinguish the pathological grade of esophageal squamous cell carcinoma (ESCC), and which fitting model is more suitable for the pathological grade of ESCC.

## MATERIALS AND METHODS

### Study Population

The study was approved by the ethics committee of the Affiliated Hospital of North Sichuan Medical College. Written informed consent was obtained from each participant. From January 2016 to February 2018, 68 consecutive patients with ESCC were enrolled in the present study according to the following inclusion criteria: patients with ESCC were confirmed by endoscopic pathology; and patients have not undergone any treatment for this disease before, such as radiotherapy, chemotherapy, and surgery; and MRI scan and IVIM-DWI were performed using the same magnetic resonance instrument. Fourteen patients were excluded, and the exclusion criteria were as follows: the patients had contraindications to MRI, or patients had a greater area of internal necrosis caused by lesions, or the images had severe motion artifacts. Finally, 54 cases of ESCC were included in this study.

The degree of pathological differentiation of the tumors was divided into poorly-differentiated (PD), moderately-differentiated (MD), and well-differentiated (WD) ESCC groups, and the T stage of tumors and tumor location (upper, middle, and lower esophagus) were determined according to the seventh edition guidelines of American Joint Committee on Cancer Stage (23).

### MR Imaging Techniques

MRI was performed using a 3.0T magnetic resonance instrument (Discovery MR 750, GE Medical Systems, Waukesha, WI, U.S.A.) with 32-channel phased-array body coil. Before the examination, patients were asked to fast for six hours and conduct shallow slow breath training, and to remove all metal objects. The patients were in a supine position and did not swallow during the examination. Patients were placed foot first, and supine with arms extended above their heads. The shimming was adopted to reduce gas interference before IVIM-DWI scanning. The respiratory-triggered technique and saturation suppression technology were used to avoid motion artifacts and guarantee the image quality of IVIM-DWI scans. The

**Abbreviations:** IVIM, intravoxel incoherent motion; DWI, diffusion-weighted imaging; ESCC, esophageal squamous cell carcinoma; PD, poorly-differentiated; MD, moderately-differentiated; WD, well-differentiated; D, true diffusion coefficient; D\*, pseudo-diffusion coefficient; f, pseudo diffusion fraction; mono, mono-exponential fitting; bi, bi-exponential fitting; T2WI, T2-weighted imaging; ROC, Receiver Operating Curve; AUC, area under curve.

scanning parameters of IVIM-DWI are as follows: repetition time = 6315.8 ms, echo time = 58.2 ms, the thickness of layer 4 mm, interlay spacing 1.0 mm, the field of view = 34 cm × 34 cm, and matrix = 96 × 128. The ten  $b$  values were 0, 30, 50, 80, 150, 200, 400, 600, 800, 1000 s/mm<sup>2</sup>, respectively. The corresponding number of excitations were 2, 2, 2, 2, 2, 2, 2, 4, 6, 8, respectively. The total scan time of IVIM-DWI was about 8 minutes.

Other sequences, such as the axial acquisition with volume acceleration-flexible T1-weighted imaging, respiratory-triggered axial propeller T2-weighted imaging (T2WI) with fat suppression, and axial single-shot fast spin-echo T2WI were also performed as routine work.

## Measurement and Calculation of Data

All the IVIM-DWI data were sent to GE Advantage Windows 4.5 Workstation for processing, using FuncTool software to obtain the ADC map in post-processing. IVIM-DWI and MADC maps were obtained after the images of adjacent fat, bone and gas were removed based on the definition of the diagnostic threshold. The region of interest (ROI) was drawn on the solid tumor components per MR image and three consecutive sections were selected by T2WI imaging for the measurement. Three ROIs were drawn on each section. Meanwhile, identification of a selection of the representative tumor tissue for ROI positioning was defined with the most cellularity part, and ROI was placed to cover as much of the solid part of the tumors as possible and to avoid cystic degeneration, necrosis, hemorrhage, and normal vessels to the greatest extent (12). The areas of ROI ranged from 53 mm<sup>2</sup> to 55 mm<sup>2</sup>. Then, the software automatically generated the true diffusion coefficient ( $D$ ) map, pseudo-diffusion coefficient ( $D^*$ ) map, and pseudo diffusion fraction ( $f$ ) map and the corresponding parameters derived from the IVIM model. The deriving parameters of the mono-exponential model include  $D_{\text{mono}}$ ,  $D^*_{\text{mono}}$ , and  $f_{\text{mono}}$ , and the deriving parameters of the bi-exponential model include  $D_{\text{bi}}$ ,  $D^*_{\text{bi}}$ , and  $f_{\text{bi}}$ . It was measured by radiologists with 5 years of experience, and the average values of each parameter were taken.

IVIM parameters have a variety of calculation methods, including the Levenberg-Marquardt algorithm, segmentation constrained, bayesian probability, etc (16, 24). The Mono-exponential model used the segmentation constrained algorithm, and the bi-exponential model was fitted by nonlinear least-square based on the Levenberg-Marquardt algorithm (18). The mono-exponential model in IVIM adopted the method of asymptotic fitting, which can be obtained by using the fit equation [1] (18, 25):

$$S_b/S_0 = f \times \exp(-bD^*) + (1-f) \times \exp(-bD) \quad [1]$$

$S_b$  is the signal intensity under a given  $b$  value,  $S_0$  is the signal intensity without diffusion weighting. The  $D$  represents the true diffusion coefficient,  $D^*$  represents the pseudo-diffusion coefficient, and  $f$  represents the microvascular volume fraction.

The mono-exponential model IVIM-derived parameters used the segmentation constrained algorithm, which is divided into a high  $b$ -value part (usually  $b > 200$  s/mm<sup>2</sup>) and a relatively low  $b$ -value part (usually  $b < 200$  s/mm<sup>2</sup>) (18). When the  $b$ -value is large

( $>200$  s/mm<sup>2</sup>), since  $D^*$  is significantly greater than  $D$ , the effects of  $D^*$  on the signal attenuation can be ignored (4, 25, 26). So Eq. [1] can be simplified as follows:

$$S_b/S_0 = (1-f) \times \exp(-bD) \quad [2]$$

The curve of the high  $b$ -value data is considered as mono-exponential decay by equation [2], and the  $D$  value can be acquired with a simple linear fitting by equation [2]. The fitted curve was then extrapolated to get the intercept at  $b = 0$ . The  $f$  value was given through equation  $f = (S_0 - S_b)/S_0$  by the ratio of the intercept to the DWI data point at  $b = 0$  (27). After substituting  $D$  and  $f$  value into the Equation [1] (26),  $D^*$  values can be derived from the mono-exponential model with segmented fitting  $b$ -values.

The bi-exponential IVIM model is a full fitting of DWI signals to the bi-exponential function (18, 19, 28, 29). All  $b$  values are used to calculate IVIM parameters at the same time. First, high  $b$  values are used to calculate  $D$  values using Eq. [1]. Then, we fitted  $S_b$  for low  $b$  values using Eq. [1] after removing the effects of  $D$  value, and the  $f$  and  $D^*$  simultaneously were obtained (28).

## Statistical Analysis

Statistical analyses were performed by SPSS22.0 software (Chicago, IL, USA) and MedCalc software Version 18.11 (MedCalcsoftware, Ostend, Belgium). Quantitative data were expressed in terms of mean  $\pm$  standard deviation ( $\bar{x} \pm SD$ ). The Shapiro-Wilks test was used to test the normality of distributions. If the data was a normal distribution, analysis of variance (ANOVA) was used to test the significant difference of IVIM parameters among three groups, and then *post hoc* with the least significant difference test was used. If the data was not a normal distribution, the Kruskal-Wallis test was used. Spearman's rank correlation was used to analyze the correlation between IVIM parameters and pathological grade. Receiver Operating Curve (ROC) was drawn to evaluate the diagnostic efficiency of each parameter and to determine the diagnostic threshold value for the grading of ESCC. If the AUC is ranged from 0.5 to 0.7, then it is regarded as a low diagnostic value. If the AUC is ranged from 0.7 to 0.9, it is regarded as a moderate diagnostic value. If the AUC is greater than 0.9, it is regarded as a high diagnostic value. The two-tailed  $p$ -value less than 0.05 is considered statistically significant.

## RESULTS

### General Characteristics of Patients

There were 54 patients with diagnosed ESCC (forty-three men and 11 women; mean age, 62.59  $\pm$  6.65 years; age range, 49-76 years). There were 14 PD, 20 MD, and 20 WD ESCC by pathologically differentiated grade. There were 25 cases in stage T3, and 29 in stage T4. The tumors were located in the lower esophagus in 14 cases, the middle esophagus in 35, and the upper esophagus in 5.

## The Differences Between Mono-Exponential and Bi-Exponential Fitting Model Parameters Distinguishing the Pathological Grade of ESCC

The ANOVA tests showed that there were significant differences in  $D_{\text{mono}}$ ,  $f_{\text{mono}}$ , and  $f_{\text{bi}}$  among the WD group, MD group, and PD group (all  $p < 0.05$ ), whereas there was no difference in  $D^*_{\text{mono}}$ ,  $D_{\text{bi}}$ , and  $D^*_{\text{bi}}$  (all  $p > 0.05$ ). Detailed results were shown in **Table 1**.

For the mono-exponential fit parameters, there were significant differences in  $f_{\text{mono}}$  among the PD, MD, and WD groups ( $0.32 \pm 0.07$ ,  $0.23 \pm 0.08$ , and  $0.16 \pm 0.05$ , respectively; all  $p < 0.05$ ; **Figure 1**). A significant difference was found in the  $D_{\text{mono}}$  between the WD and the PD group ( $1.48 \pm 0.51 \times 10^{-3} \text{ mm}^2/\text{s}$  versus  $1.05 \pm 0.44 \times 10^{-3} \text{ mm}^2/\text{s}$ ,  $p < 0.05$ ; **Figure 1**), but no significant difference was found between the WD and MD groups, MD and PD groups ( $1.48 \pm 0.51 \times 10^{-3} \text{ mm}^2/\text{s}$  versus  $1.22 \pm 0.39 \times 10^{-3} \text{ mm}^2/\text{s}$ ,  $1.22 \pm 0.39 \times 10^{-3} \text{ mm}^2/\text{s}$  versus  $1.05 \pm 0.44 \times 10^{-3} \text{ mm}^2/\text{s}$ , respectively; all  $p > 0.05$ ).

For the bi-exponential fit parameters, there were significant differences in  $f_{\text{bi}}$  among the PD, MD, and WD ESCC groups ( $0.35 \pm 0.08$ ,  $0.26 \pm 0.10$ , and  $0.18 \pm 0.07$ , respectively; all  $p < 0.05$ ).

## The Diagnostic Efficacy Between the Two Models for the Pathological Grade of ESCC

The area under curve (AUC) values of  $D_{\text{mono}}$ ,  $f_{\text{mono}}$ , and  $f_{\text{bi}}$  in differentiating WD from PD ESCC were 0.764, 0.961, and 0.932 (**Figure 2**). The sensitivity of  $D_{\text{mono}}$ ,  $f_{\text{mono}}$ , and  $f_{\text{bi}}$  was 92.9%, 92.9%, and 85.7%, and specificity was 60%, 90%, and 100%, respectively. The AUC value of  $f_{\text{mono}}$  and  $f_{\text{bi}}$  in differentiating MD from PD ESCC were 0.839 and 0.757 (**Figure 2**). The sensitivity of  $f_{\text{mono}}$  and  $f_{\text{bi}}$  was 78.6% and 85.7%, and specificity was 80% and 70%, respectively. The AUC of  $f_{\text{mono}}$  and  $f_{\text{bi}}$  in differentiating MD from WD ESCC were 0.746 and 0.740 (**Figure 2**). The sensitivity of  $f_{\text{mono}}$  and  $f_{\text{bi}}$  were 65% and 80%, and specificity was 85% and 60%, respectively. The AUC, sensitivity, specificity, and cut-off values of  $D_{\text{mono}}$ ,  $f_{\text{mono}}$ , and  $f_{\text{bi}}$  for differentiating pathological grade of ESCC were listed in **Table 2**.

## Correlations Between Mono-Exponential, Bi-Exponential Model Parameters, and Pathological Grade

For the mono-exponential model parameters, the pathologically differentiated grade correlated positively with the  $D_{\text{mono}}$  ( $r = 0.370$ ,  $p = 0.006$ ) and  $D^*_{\text{mono}}$  ( $r = 0.278$ ,  $p = 0.042$ ), and correlated negatively with  $f_{\text{mono}}$  values ( $r = -0.679$ ,  $p < 0.001$ ).

For the bi-exponential model parameters, the pathologically differentiated grade correlated positively with the  $D_{\text{bi}}$  ( $r = 0.489$ ,  $p = 0.001$ ),  $D^*_{\text{bi}}$  ( $r = 0.321$ ,  $p = 0.018$ ), and correlated negatively with  $f_{\text{bi}}$  values ( $r = -0.619$ ,  $p < 0.001$ ).

## DISCUSSION

The present study evaluated the pathologically differentiated grade of ESCC by comparing the mono-exponential model and bi-exponential model in the post-processing of IVIM-DWI. The results demonstrated that the mono-exponential model parameters showed higher diagnostic value than the bi-exponential model parameters in differentiating pathologically grade of ESCC. Both the mono-exponential and bi-exponential fit parameter values correlated with pathologically differentiated grades. This finding provides a basis for the application of the IVIM-DWI model in the pathologically differentiated grade of ESCC. In our study, the mono-exponential model of IVIM was different from the traditional DWI model, and the traditional DWI with mono  $b$  value in these previous studies (4, 30–32) were used to detect the degree and direction of limitation in the *in vivo* water molecules movement. For reasons that capillary perfusion and the diffusion associated with microcirculation perfusion have a great effect on signal attenuation (4, 27), ADC of traditional mono-exponential diffusion model cannot reflect the diffusion of *in vivo* water molecules exactly and properly (33, 34). Previous studies (34–36) indicated that the IVIM-DWI model has higher accuracy than the traditional DWI with mono  $b$  value in the diagnosis of esophageal carcinoma. Therefore, our study compares the mono-exponential IVIM model and bi-exponential IVIM model parameters in differentiating the pathologically differentiated grade of ESCC rather than

**TABLE 1 |** The differences between the mono-exponential IVIM model and bi-exponential IVIM model distinguishing the pathological grade of ESCC ( $\bar{x} \pm \text{SD}$ ).

Model parameters	WD (n=20)	MD (n=20)	PD (n=14)	Post-hoc by LSD			
	Mean $\pm$ SD	Mean $\pm$ SD	Mean $\pm$ SD	ANOVA p value	PD vs WD p value	PD vs MD p value	MD vs WD p value
<b>Mono-exponential IVIM model</b>							
$D_{\text{mono}}$ ( $10^{-3} \text{ mm}^2/\text{s}$ )	$1.48 \pm 0.51$	$1.22 \pm 0.39$	$1.05 \pm 0.44$	0.031*	0.010*	0.277	0.090
$D^*_{\text{mono}}$ ( $10^{-2} \text{ mm}^2/\text{s}$ )	$2.65 \pm 1.96$	$1.88 \pm 1.26$	$1.25 \pm 0.56$	0.147	NA	NA	NA
$f_{\text{mono}}$	$0.16 \pm 0.05$	$0.23 \pm 0.08$	$0.32 \pm 0.07$	<0.001***	<0.001***	<0.001***	<0.001***
<b>Bi-exponential IVIM model</b>							
$D_{\text{bi}}$ ( $10^{-3} \text{ mm}^2/\text{s}$ )	$1.33 \pm 0.54$	$1.17 \pm 0.51$	$0.91 \pm 0.45$	0.065	NA	NA	NA
$D^*_{\text{bi}}$ ( $10^{-2} \text{ mm}^2/\text{s}$ )	$2.82 \pm 1.63$	$2.21 \pm 1.41$	$1.67 \pm 0.78$	0.059	NA	NA	NA
$f_{\text{bi}}$	$0.18 \pm 0.07$	$0.26 \pm 0.10$	$0.35 \pm 0.08$	<0.001***	<0.001***	0.005**	0.003**

\* $P < 0.05$ , \*\* $P < 0.01$ , \*\*\* $P < 0.001$ .

ESCC, esophageal squamous cell carcinoma; IVIM, intravoxel incoherent motion;  $D^*$ , pseudo-diffusion coefficient;  $D$ , true diffusion coefficient;  $f$ , pseudo diffusion fraction; mono, mono-exponential fitting model; bi, bi-exponential fitting model; LSD, least significant difference; WD, well-differentiated; MD, moderately-differentiated; PD, poorly-differentiated.



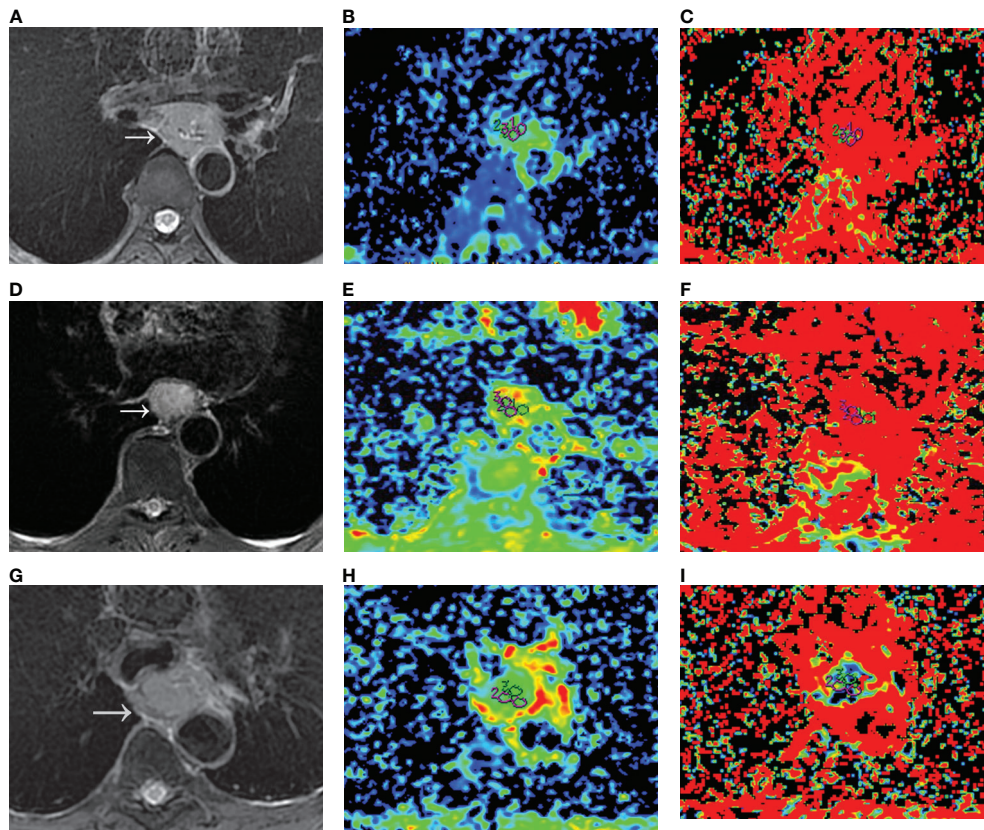


**FIGURE 1** |  $D_{mono}$  and  $f_{mono}$  values derived from mono-exponential IVIM-DWI of ESCC with different pathologically differentiated grades. **(A–C)** PD ESCC in a 48-year-old man. The regions of interest are selected by **(A)** T2-weighted image and drawn on **(B)**  $D_{mono}$  map ( $0.958 \times 10^{-3} \text{ mm}^2/\text{s}$ ) and **(C)**  $f_{mono}$  map ( $0.381 \times 100\%$ ). **(D–F)** MD ESCC in a 64-year-old man. The regions of interest are selected by **(D)** T2-weighted image and drawn on **(E)**  $D_{mono}$  map ( $1.450 \times 10^{-3} \text{ mm}^2/\text{s}$ ) and **(F)**  $f_{mono}$  map ( $0.290 \times 100\%$ ). **(G–I)** WD ESCC in a 61-year-old man. The regions of interest are selected by **(G)** T2-weighted image and drawn on **(H)**  $D_{mono}$  map ( $1.54 \times 10^{-3} \text{ mm}^2/\text{s}$ ) and **(I)**  $f_{mono}$  map ( $0.120 \times 100\%$ ). IVIM, intravoxel incoherent motion; DWI, diffusion-weighted imaging; ESCC, esophageal squamous cell carcinoma; PD, poorly-differentiated; MD, moderately-differentiated; WD, well-differentiated; D, true diffusion coefficient; f, pseudo diffusion fraction.

comparing the IVIM-DWI model and traditional mono-exponential DWI. These will help clinicians find a better fitting model for the pathologically differentiated grade of ESCC, and provide a reference for the selection of the optimal IVIM fitting model for tumor staging and evaluating prognosis.

In the present study, we found that the  $f_{mono}$  and  $D_{mono}$  value of mono-exponential IVIM model have higher diagnostic performance for differentiation of ESCC, whereas the bi-exponential IVIM model only had  $f_{bi}$  values. One of the possible reasons is that the mono-exponential model used the segmentation constrained algorithm, and the bi-exponential model used a full fitting based on the Levenberg-Marquardt algorithm. Though both the two fitting methods have similar repeatability (17). Previous studies (18, 19) have proved that the mono-exponential fitting model demonstrated a more accurate estimation of D in signal prediction for high b-values in the abdomen relative to the bi-exponential fitting model, but tending to underestimate  $D^*$  (18). The bi-exponential fitting model should allow more flexibility and provided a better fit and a more accurate estimation of  $D^*$  at low b-values (18), so it is possible to produce results closer to the true physiological value

of IVIM parameters. Therefore, the different fitting methods of the two models in our study may explain the difference. The second possibility is that the mono-exponential IVIM model may detect one or a few perfusion components, while the bi-exponential IVIM model reflects the organizational information of multi-component perfusion (3). A collection of vessels with similar physiological properties can be usually regarded as one perfusion component, such as vascular size, blood flow velocity, and vascular spatial configuration (3, 37). Therefore, it can be inferred that the mono-exponential IVIM model could more truly reflect the perfusion component and diffusion information of esophageal carcinoma, and the mono-exponential IVIM model may be more suitable for predicting the pathological grade of ESCC.

It is noteworthy that both the  $f_{mono}$  and  $f_{bi}$  can help differentiate PD, MD, and WD ESCC. The mean  $f_{mono}$  and  $f_{bi}$  values decreased gradually from the PD group to the WD group. The  $f_{mono}$  and  $f_{bi}$  were correlated negatively with the pathologically differentiated grade of ESCC. The previous study (12) supported our results, and they also reported that the f value was a gradually decreasing trend from the PD group to the WD

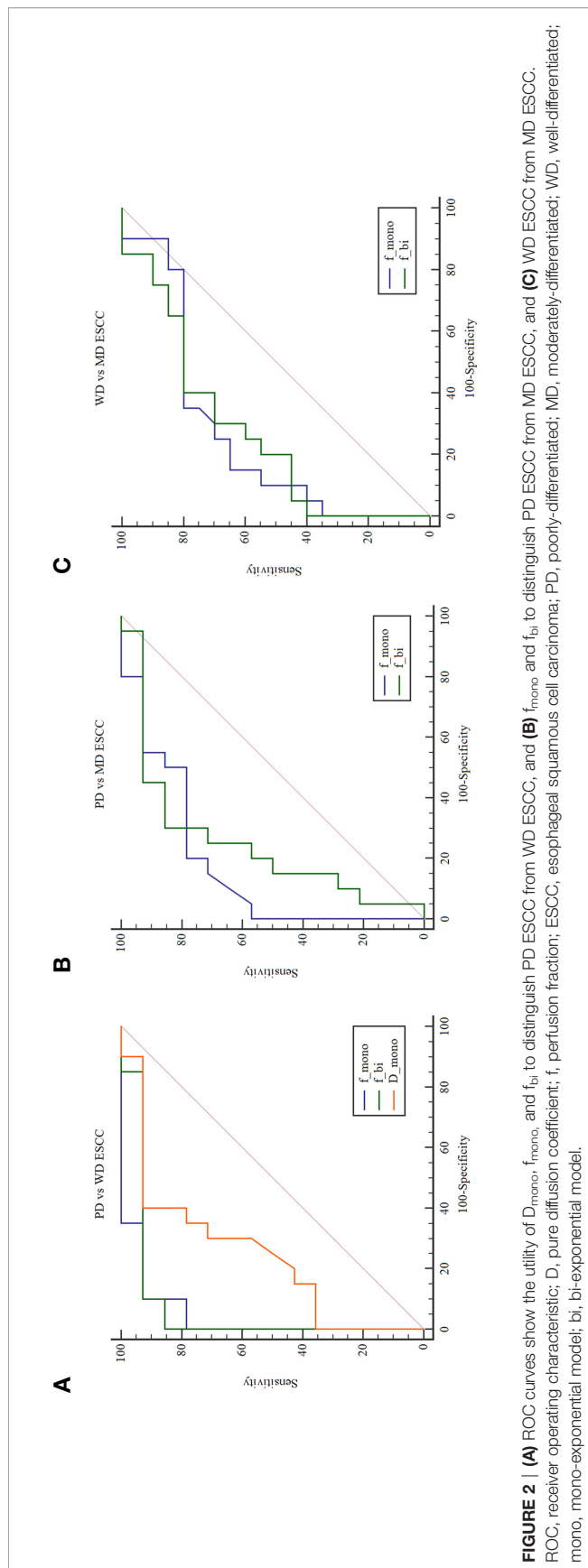


**FIGURE 2 |** (A) ROC curves show the utility of  $D_{\text{mono}}$ ,  $f_{\text{mono}}$ , and  $f_{\text{bi}}$  to distinguish PD ESCC from MD ESCC, and (B)  $f_{\text{mono}}$  and  $f_{\text{bi}}$  to distinguish PD ESCC from WD ESCC, and (C) WD ESCC from MD ESCC. ROC, receiver operating characteristic; D, pure diffusion coefficient; f, perfusion fraction; ESCC, esophageal squamous cell carcinoma; PD, poorly-differentiated; MD, moderately-differentiated; WD, well-differentiated; mono, mono-exponential model; bi, bi-exponential model.

**TABLE 2 |** The diagnostic efficacy between the two models for the pathological grade of ESCC.

Differentiations	Variable	Cut-off value	AUC	Sensitivity	Specificity
PD vs WD	$D_{\text{mono}}$	$1.26 \times 10^{-3} \text{ mm}^2/\text{s}$	0.764	0.929	0.600
	$f_{\text{mono}}$	0.214	0.961	0.929	0.900
	$f_{\text{bi}}$	0.289	0.932	0.857	1.000
PD vs MD	$f_{\text{mono}}$	0.301	0.839	0.786	0.800
	$f_{\text{bi}}$	0.312	0.757	0.857	0.700
WD vs MD	$f_{\text{mono}}$	0.193	0.746	0.650	0.850
	$f_{\text{bi}}$	0.208	0.740	0.800	0.600

ESCC, esophageal squamous cell carcinoma; D, true diffusion coefficient; f, pseudo diffusion fraction; mono, mono-exponential fitting model; bi, bi-exponential fitting model; PD, poorly-differentiated; MD, moderately-differentiated; WD, well-differentiated.

group. Still,  $f$  values showed no statistical difference among the three groups. The  $f$  value represents microcapillary perfusion and reflects the vascularity in tissue, which is helpful to assess the pathological differentiation grade of the tumor (28, 38). The  $f$  value was positively correlated with microvessel density (39). Previous studies (40, 41) have reported that the microvessel density of moderately- or well-differentiated esophageal carcinoma was lower than that of poorly-differentiated esophageal carcinoma. These findings further support our study. Therefore, both the  $f_{\text{mono}}$  and  $f_{\text{bi}}$  can be used in differentiating well-differentiated, moderately-differentiated, and poorly-differentiated ESCC.

Our study also demonstrated that both the  $D^*_{\text{mono}}$  and  $D^*_{\text{bi}}$  were not statistically significant in differentiating the PD, MD, and WD ESCC, which was similar to previous studies (12, 42). Previous studies (3, 16, 27, 43) have shown that the  $D^*$  often suffers from high variance and standard deviation, which can obscure or misinterpret pathologies in clinical applications. The parameter variance of the IVIM model is easy to be disturbed by many factors (16, 44). For example, they are susceptible to four major factors (3, 17, 45, 46), such as the noise in DWI, the different  $b$  values, the fitting techniques or model, and the artifact of cardiac and breathing motions. However, there is no uniform standard for the selection of  $b$  values in clinical practice so far. So long as the distribution of  $b$  values is reasonable, the parameters of the IVIM model may be no longer affected by  $b$  values (7, 45). At the same time, we avoided and excluded the artifacts of cardiac and breathing motions by respiratory gating and shimming. Also, the  $D^*$  value is associated with blood flow velocity and vascular length (3). The blood supply of the esophageal tumors varies greatly, which is mainly related to the anatomical location of the esophagus (12) and may influence the perfusion of the tumor. Therefore,  $D^*$  was not useful for the evaluation of the pathological differentiation grade of ESCC.

In our study, the pathologically differentiated grade of ESCC was correlated negatively with the  $f_{\text{mono}}$  and  $f_{\text{bi}}$  and correlated positively with the  $D_{\text{mono}}$ ,  $D^*_{\text{mono}}$ ,  $D_{\text{bi}}$ , and  $D^*_{\text{bi}}$ , which indicated that the parameters derived from IVIM-DWI could well reflect the differentiation grade of esophageal carcinoma. The lower the degree of tumor differentiation pathologically, the larger the cell

atypia and the tumor cell density (28). With the lower the degree of differentiation of esophageal carcinoma, the increase of tumor cell density will lead to a more limited spread and finally lead to the decrease of D value (28). The differentiation grade of ESCC is an important prognostic indicator (47, 48), and it is also one of the indicators to choose the best therapeutic alternative (49, 50). Therefore, IVIM-DWI could be a promising and non-invasive imaging method in predicting the pathological grade of ESCC.

There are several limitations to this study. First, the sample size was relatively small, especially in the poorly differentiated ESCC. And the sample lack T1 and T2 stage ESCC, because most patients don't have any symptoms until the T3 or T4 stage. We will enlarge the sample size to analyze the correlation between the two IVIM models and the stage in the further. Second, we did not compare mono-exponential IVIM and bi-exponential IVIM models between different pathological types of esophageal cancers, but samples containing only ESCC eliminated other confounding factors for the findings. Therefore, we need larger different pathological types of sample size in further studies. Third, the correlation between the tumor's location and two IVIM models were not investigated. Fourth, the accuracy of the parameters may differ according to the different b-value ranges for target lesions. But the analysis of signal intensities averages over an ROI approach and segmented fitting method combined with the reasonable b value distributions could lead to considerable improvement in accuracy (17, 45). Finally, esophageal peristalsis or glandular secretion can cause signal decay, which may be difficult to differentiate from perfusion effects (15). Though we ask the patient not to swallow during the examination and use the respiratory-triggered and saturation suppression technique, these issues need to be considered when interpreting our findings. Despite these limitations, the present study depicted the difference between mono-exponential IVIM and bi-exponential IVIM fitting models in the evaluation of pathological differentiation grade of ESCC.

## CONCLUSION

In conclusion, the  $f_{\text{mono}}$  derived from mono-exponential IVIM-DWI shows higher diagnostic performance than  $f_{\text{bi}}$  derived from bi-exponential IVIM-DWI in differentiating WD, MD, and PD

ESCC, and  $D_{\text{mono}}$  derived from mono-exponential IVIM-DWI can distinguish PD from WD ESCC. The mono-exponential fit parameters derived from IVIM are superior to the bi-exponential fit parameters in differentiating pathologically differentiated grades of ESCC, which may be a promising non-invasive imaging method to predict the pathological grade of ESCC. The findings may help to select an appropriate fitting model for the application of IVIM in ESCC and improve the diagnostic accuracy.

## DATA AVAILABILITY STATEMENT

The raw data supporting the conclusions of this article will be made available by the authors, without undue reservation.

## ETHICS STATEMENT

The studies involving human participants were reviewed and approved by Affiliated Hospital of North Sichuan Medical College. The patients/participants provided their written informed consent to participate in this study.

## AUTHOR CONTRIBUTIONS

NL, XY and LL collected the cases and analyzed the data. KP and QL performed the MRI scan. NL and XY wrote the manuscript, and XH made substantial contributions to the conception and revised the manuscript. All authors contributed to the article and approved the submitted version.

## FUNDING

This study was supported by the Bureau of Science & Technology and Intellectual Property Nanchong City (NO. 19SXHZ0429, XH), and the Science and Technology Development Plan of North Sichuan Medical College (No. CBY14-A-ZD06, NL).

## REFERENCES

1. Sun H, Liu K, Liu H, Ji Z, Yan Y, Jiang L, et al. Comparison of bi-exponential and mono-exponential models of diffusion-weighted imaging for detecting active sacroiliitis in ankylosing spondylitis. *Acta Radiol* (2018) 59:468–77. doi: 10.1177/0284185117722811
2. Le Bihan D. Intravoxel incoherent motion perfusion MR imaging: a wake-up call. *Radiology* (2008) 249:748–52. doi: 10.1148/radiol.2493081301
3. Kuai ZX, Liu WY, Zhu YM. Effect of multiple perfusion components on pseudo-diffusion coefficient in intravoxel incoherent motion imaging. *Phys Med Biol* (2017) 62:8197–209. doi: 10.1088/1361-6560/aa8d0c
4. Le Bihan D, Breton E, Lallemand D, Aubin ML, Vignaud J, Laval-Jeantet M. Separation of diffusion and perfusion in intravoxel incoherent motion MR imaging. *Radiology* (1988) 168:497–505. doi: 10.1148/radiology.168.2.3393671
5. Wu WC, Yang SC, Chen YF, Tseng HM, My PC. Simultaneous assessment of cerebral blood volume and diffusion heterogeneity using hybrid IVIM and DK MR imaging: initial experience with brain tumors. *Eur Radiol* (2017) 27:306–14. doi: 10.1007/s00330-016-4272-z
6. Federau C, Wintermark M, Christensen S, Mlynash M, Marcellus DG, Zhu G, et al. Collateral blood flow measurement with intravoxel incoherent motion perfusion imaging in hyperacute brain stroke. *Neurology* (2019) 92:e2462–2462e2471. doi: 10.1212/WNL.00000000000007538
7. Koh DM, Collins DJ, Orton MR. Intravoxel incoherent motion in body diffusion-weighted MRI: reality and challenges. *AJR Am J Roentgenol* (2011) 196:1351–61. doi: 10.2214/AJR.10.5515
8. Klauss M, Mayer P, Maier-Hein K, Laun FB, Mehrabi A, Kauczor HU, et al. IVIM-diffusion-MRI for the differentiation of solid benign and malign hypervascular liver lesions-Evaluation with two different MR scanners. *Eur J Radiol* (2016) 85:1289–94. doi: 10.1016/j.ejrad.2016.04.011



9. Taimouri V, Afacan O, Perez-Rossello JM, Callahan MJ, Mulkern RV, Warfield SK, et al. Spatially constrained incoherent motion method improves diffusion-weighted MRI signal decay analysis in the liver and spleen. *Med Phys* (2015) 42:1895–903. doi: 10.1118/1.4915495
10. Mao W, Zhou J, Zeng M, Ding Y, Qu L, Chen C, et al. Chronic kidney disease: Pathological and functional evaluation with intravoxel incoherent motion diffusion-weighted imaging. *J Magn Reson Imaging* (2018) 47:1251–9. doi: 10.1002/jmri.25861
11. Kim B, Lee SS, Sung YS, Cheong H, Byun JH, Kim HJ, et al. Intravoxel incoherent motion diffusion-weighted imaging of the pancreas: Characterization of benign and malignant pancreatic pathologies. *J Magn Reson Imaging* (2017) 45:260–9. doi: 10.1002/jmri.25334
12. Zhu S, Wei Y, Gao F, Li L, Liu Y, Huang Z, et al. Esophageal carcinoma: Intravoxel incoherent motion diffusion-weighted MRI parameters and histopathological correlations. *J Magn Reson Imaging* (2019) 49:253–61. doi: 10.1002/jmri.26172
13. Yamada I, Hikishima K, Miyasaka N, Kawano T, Tokairin Y, Ito E, et al. Esophageal carcinoma: ex vivo evaluation with diffusion-tensor MR imaging and tractography at 7 T. *Radiology* (2014) 272:164–73. doi: 10.1148/radiol.14132170
14. Kumbasar B. Carcinoma of esophagus: radiologic diagnosis and staging. *Eur J Radiol* (2002) 42:170–80. doi: 10.1016/s0720-048x(02)00030-x
15. Huang YC, Chen TW, Zhang XM, Zeng NL, Li R, Tang YL, et al. Intravoxel incoherent motion diffusion-weighted imaging of resectable oesophageal squamous cell carcinoma: association with tumour stage. *Br J Radiol* (2018) 91:20170421. doi: 10.1259/bjr.20170421
16. Orton MR, Collins DJ, Koh DM, Leach MO. Improved intravoxel incoherent motion analysis of diffusion weighted imaging by data driven Bayesian modeling. *Magn Reson Med* (2014) 71:411–20. doi: 10.1002/mrm.24649
17. Park HJ, Sung YS, Lee SS, Lee Y, Cheong H, Kim YJ, et al. Intravoxel incoherent motion diffusion-weighted MRI of the abdomen: The effect of fitting algorithms on the accuracy and reliability of the parameters. *J Magn Reson Imaging* (2017) 45:1637–47. doi: 10.1002/jmri.25535
18. Chevallier O, Zhou N, Cercueil JP, He J, Loffroy R, Wang Y. Comparison of tri-exponential decay versus bi-exponential decay and full fitting versus segmented fitting for modeling liver intravoxel incoherent motion diffusion MRI. *NMR Biomed* (2019) 32:e4155. doi: 10.1002/nbm.4155
19. Cercueil JP, Petit JM, Nougaret S, Soyfer P, Fohlen A, Pierredon-Foulongne MA, et al. Intravoxel incoherent motion diffusion-weighted imaging in the liver: comparison of mono-, bi- and tri-exponential modelling at 3.0-T. *Eur Radiol* (2015) 25:1541–50. doi: 10.1007/s00330-014-3554-6
20. van Baalen S, Leemans A, Dik P, Lilien MR, Ten Haken B, Froeling M. Intravoxel incoherent motion modeling in the kidneys: Comparison of mono-, bi-, and triexponential fit. *J Magn Reson Imaging* (2017) 46:228–39. doi: 10.1002/jmri.25519
21. Barbieri S, Donati OF, Froehlich JM, Thoeny HC. Impact of the calculation algorithm on biexponential fitting of diffusion-weighted MRI in upper abdominal organs. *Magn Reson Med* (2016) 75:2175–84. doi: 10.1002/mrm.25765
22. Gurney-Champion OJ, Collins DJ, Wetscherek A, Rata M, Klaassen R, van Laarhoven H, et al. Principal component analysis for fast and model-free denoising of multi b-value diffusion-weighted MR images. *Phys Med Biol* (2019) 64:105015. doi: 10.1088/1361-6560/ab1786
23. Edge SB, Byrd DR, Compton CC. *AJCC cancer staging manual*. 7th edn. Chicago: American Joint Committee on Cancer. (2010)
24. Iima M, Yano K, Kataoka M, Umehana M, Murata K, Kanao S, et al. Quantitative non-Gaussian diffusion and intravoxel incoherent motion magnetic resonance imaging: differentiation of malignant and benign breast lesions. *Invest Radiol* (2015) 50:205–11. doi: 10.1097/RLI.0000000000000094
25. Hayashi T, Miyati T, Takahashi J, Fukuzawa K, Sakai H, Tano M, et al. Diffusion analysis with triexponential function in liver cirrhosis. *J Magn Reson Imaging* (2013) 38:148–53. doi: 10.1002/jmri.23966
26. Luciani A, Vignaud A, Cavet M, Nhieu JT, Mallat A, Ruel L, et al. Liver cirrhosis: intravoxel incoherent motion MR imaging—pilot study. *Radiology* (2008) 249:891–9. doi: 10.1148/radiol.2493080080
27. Dyvorne HA, Galea N, Nevers T, Fiel MI, Carpenter D, Wong E, et al. Diffusion-weighted imaging of the liver with multiple b values: effect of diffusion gradient polarity and breathing acquisition on image quality and intravoxel incoherent motion parameters—a pilot study. *Radiology* (2013) 266:920–9. doi: 10.1148/radiol.12120686
28. Ma W, Zhang G, Ren J, Pan Q, Wen D, Zhong J, et al. Quantitative parameters of intravoxel incoherent motion diffusion weighted imaging (IVIM-DWI): potential application in predicting pathological grades of pancreatic ductal adenocarcinoma. *Quant Imaging Med Surg* (2018) 8:301–10. doi: 10.21037/qims.2018.04.08
29. Yan R, Haopeng P, Xiaoyuan F, Jinsong W, Jiawen Z, Chengjun Y, et al. Non-Gaussian diffusion MR imaging of glioma: comparisons of multiple diffusion parameters and correlation with histologic grade and MIB-1 (Ki-67 labeling) index. *Neuroradiology* (2016) 58:121–32. doi: 10.1007/s00234-015-1606-5
30. Song Y, Yoon YC, Chong Y, Seo SW, Choi YL, Sohn I, et al. Diagnostic performance of conventional MRI parameters and apparent diffusion coefficient values in differentiating between benign and malignant soft-tissue tumours. *Clin Radiol* (2017) 72:691.e1–691.e10. doi: 10.1016/j.crad.2017.02.003
31. Ding Y, Tan Q, Mao W, Dai C, Hu X, Hou J, et al. Differentiating between malignant and benign renal tumors: do IVIM and diffusion kurtosis imaging perform better than DWI. *Eur Radiol* (2019) 29:6930–9. doi: 10.1007/s00330-019-06240-6
32. Ding Y, Zeng M, Rao S, Chen C, Fu C, Zhou J. Comparison of Biexponential and Monoexponential Model of Diffusion-Weighted Imaging for Distinguishing between Common Renal Cell Carcinoma and Fat Poor Angiomyolipoma. *Korean J Radiol* (2016) 17:853–63. doi: 10.3348/kjr.2016.17.6.853
33. Dijkstra H, Baron P, Kappert P, Oudkerk M, Sijens PE. Effects of microperfusion in hepatic diffusion weighted imaging. *Eur Radiol* (2012) 22:891–9. doi: 10.1007/s00330-011-2313-1
34. Sukstanskii AL, Yablonskiy DA. Effects of restricted diffusion on MR signal formation. *J Magn Reson* (2002) 157:92–105. doi: 10.1006/jmre.2002.2582
35. Cheng B, Yu J. Predictive value of diffusion-weighted MR imaging in early response to chemoradiotherapy of esophageal cancer: a meta-analysis. *Dis Esophagus* (2019) 32:1–6. doi: 10.1093/dote/doy065
36. Zhang JL, Sigmund EE, Chandarana H, Rusinek H, Chen Q, Vivier PH, et al. Variability of renal apparent diffusion coefficients: limitations of the monoexponential model for diffusion quantification. *Radiology* (2010) 254:783–92. doi: 10.1148/radiol.09090891
37. Moteki T, Horikoshi H. Evaluation of noncirrhotic hepatic parenchyma with and without significant portal vein stenosis using diffusion-weighted echoplanar MR on the basis of multiple-perfusion-components theory. *Magn Reson Imaging* (2011) 29:64–73. doi: 10.1016/j.mri.2010.07.008
38. Le Bihan D. Diffusion, confusion and functional MRI. *Neuroimage* (2012) 62:1131–6. doi: 10.1016/j.neuroimage.2011.09.058
39. Lee HJ, Rha SY, Chung YE, Shim HS, Kim YJ, Hur J, et al. Tumor perfusion-related parameter of diffusion-weighted magnetic resonance imaging: correlation with histological microvessel density. *Magn Reson Med* (2014) 71:1554–8. doi: 10.1002/mrm.24810
40. Yang X, Zhai N, Sun M, Zhao Z, Yang J, Chen K, et al. Influence of lymphatic endothelial cells on proliferation and invasiveness of esophageal carcinoma cells *in vitro* and lymphangiogenesis *in vivo*. *Med Oncol* (2015) 32:222. doi: 10.1007/s12032-015-0662-3
41. Inoue K, Ozeki Y, Suganuma T, Sugiura Y, Tanaka S. Vascular endothelial growth factor expression in primary esophageal squamous cell carcinoma. Association with angiogenesis and tumor progression. *Cancer* (1997) 79:206–13. doi: 10.1002/(sici)1097-0142(19970115)79:2<206::aid-cnrc2>3.0.co;2-i
42. Zheng H, Ren W, Pan X, Zhang Q, Liu B, Liu S, et al. Role of intravoxel incoherent motion MRI in early assessment of the response of esophageal squamous cell carcinoma to chemoradiotherapy: A pilot study. *J Magn Reson Imaging* (2018) 48:349–58. doi: 10.1002/jmri.25934
43. Wurnig MC, Donati OF, Ulbrich E, Filli L, Kenkel D, Thoeny HC, et al. Systematic analysis of the intravoxel incoherent motion threshold separating perfusion and diffusion effects: Proposal of a standardized algorithm. *Magn Reson Med* (2015) 74:1414–22. doi: 10.1002/mrm.25506
44. Barbieri S, Donati OF, Froehlich JM, Thoeny HC. Comparison of Intravoxel Incoherent Motion Parameters across MR Imagers and Field Strengths: Evaluation in Upper Abdominal Organs. *Radiology* (2016) 279:784–94. doi: 10.1148/radiol.2015151244



45. Lemke A, Stieltjes B, Schad LR, Laun FB. Toward an optimal distribution of b values for intravoxel incoherent motion imaging. *Magn Reson Imaging* (2011) 29:766–76. doi: 10.1016/j.mri.2011.03.004
46. Pang Y, Turkbey B, Bernardo M, Kruecker J, Kadoury S, Merino MJ, et al. Intravoxel incoherent motion MR imaging for prostate cancer: an evaluation of perfusion fraction and diffusion coefficient derived from different b-value combinations. *Magn Reson Med* (2013) 69:553–62. doi: 10.1002/mrm.24277
47. Kyriazanos ID, Tachibana M, Shibakita M, Yoshimura H, Kinugasa S, Dhar DK, et al. Pattern of recurrence after extended esophagectomy for squamous cell carcinoma of the esophagus. *Hepatogastroenterology* (2003) 50:115–20.
48. Wang Y, Bai G, Guo L, Chen W. Associations Between Apparent Diffusion Coefficient Value With Pathological Type, Histologic Grade, and Presence of Lymph Node Metastases of Esophageal Carcinoma. *Technol Cancer Res Treat* (2019) 18:1533033819892254. doi: 10.1177/1533033819892254
49. Salem ME, Puccini A, Xiu J, Raghavan D, Lenz HJ, Korn WM, et al. Comparative Molecular Analyses of Esophageal Squamous Cell Carcinoma, Esophageal Adenocarcinoma, and Gastric Adenocarcinoma. *Oncologist* (2018) 23:1319–27. doi: 10.1634/theoncologist.2018-0143
50. Arnold M, Soerjomataram I, Ferlay J, Forman D. Global incidence of oesophageal cancer by histological subtype in 2012. *Gut* (2015) 64:381–7. doi: 10.1136/gutjnl-2014-308124

**Conflict of Interest:** The authors declare that the research was conducted in the absence of any commercial or financial relationships that could be construed as a potential conflict of interest.

Copyright © 2021 Liu, Yang, Lei, Pan, Liu and Huang. This is an open-access article distributed under the terms of the Creative Commons Attribution License (CC BY). The use, distribution or reproduction in other forums is permitted, provided the original author(s) and the copyright owner(s) are credited and that the original publication in this journal is cited, in accordance with accepted academic practice. No use, distribution or reproduction is permitted which does not comply with these terms.



# Preoperative Assessment for Event-Free Survival With Hepatoblastoma in Pediatric Patients by Developing a CT-Based Radiomics Model

Yi Jiang<sup>1</sup>, Jingjing Sun<sup>1</sup>, Yuwei Xia<sup>2</sup>, Yan Cheng<sup>1</sup>, Linjun Xie<sup>1</sup>, Xia Guo<sup>1\*</sup> and Yingkun Guo<sup>1\*</sup>

<sup>1</sup> West China Second University Hospital, Sichuan University, Chengdu, China, <sup>2</sup> Huiying Medical Technology, Beijing, China

## OPEN ACCESS

### Edited by:

Changqiang Wu,  
North Sichuan Medical College, China

### Reviewed by:

Bin Yang,  
Nanjing University, China  
Tianwu Chen,  
North Sichuan Medical College, China

### \*Correspondence:

Xia Guo  
guoxkl@163.com  
Yingkun Guo  
gykpanda@163.com

### Specialty section:

This article was submitted to  
Cancer Imaging and Image-directed  
Interventions,  
a section of the journal  
Frontiers in Oncology

**Received:** 22 December 2020

**Accepted:** 11 February 2021

**Published:** 16 April 2021

### Citation:

Jiang Y, Sun J, Xia Y, Cheng Y, Xie L,  
Guo X and Guo Y (2021) Preoperative  
Assessment for Event-Free Survival  
With Hepatoblastoma in Pediatric  
Patients by Developing a CT-Based  
Radiomics Model.  
Front. Oncol. 11:644994.  
doi: 10.3389/fonc.2021.644994

**Objective:** To explore a CT-based radiomics model for preoperative prediction of event-free survival (EFS) in patients with hepatoblastoma and to compare its performance with that of a clinicopathologic model.

**Patients and Methods:** Eighty-eight patients with histologically confirmed hepatoblastoma (mean age:  $2.28 \pm 2.72$  years) were recruited from two institutions between 2002 and 2019 for this retrospective study. They were divided into a training cohort (65 patients from institution A) and a validation cohort (23 patients from institution B). Radiomics features were extracted manually from pretreatment CT images in the portal venous (PV) phase. The least absolute shrinkage and selection operator (LASSO) Cox regression model was applied to construct a “radiomics signature” and radiomics score (Rad-score) for EFS prediction. Then, a nomogram incorporating the Rad-score, updated staging system, and significant variables of clinicopathologic risk (age, alpha-fetoprotein (AFP) level, histology subtype, tumor diameter) as the radiomic model, clinicopathologic model, and combined clinicopathologic-radiomic model were built for EFS estimation in the training cohort, the performance of which was assessed in an external-validation cohort with respect to clinical usefulness, discrimination, and calibration.

**Results:** Nine survival-relevant features were selected for a radiomics signature and Rad-score building. Multivariable analysis revealed that histology subtype ( $P = 0.01$ ), PV ( $P = 0.001$ ) invasion, and metastasis ( $P = 0.047$ ) were independent risk factors of EFS. Patients were divided into low- and high-risk groups based on the Rad-score with a cutoff of 0.08 according to survival outcome. The radiomics signature-incorporated nomogram showed good performance ( $P < 0.001$ ) for EFS estimation (C-Index: 0.810; 95% CI: 0.738–0.882), which was comparable with that of the clinicopathologic model for EFS estimation (C-Index: 0.81 vs. 0.85). The radiomics-based nomogram failed to show incremental prognostic value compared with that using the clinicopathologic model. The combined model (radiomics signature plus clinicopathologic parameters) showed significant improvement in the discriminatory accuracy, along with good calibration and

greater net clinical benefit, of EFS (C-Index: 0.88; 95% CI: 0.829–0.933).

**Conclusion:** The radiomics signature can be used as a prognostic indicator for EFS in patients with hepatoblastoma. A combination of the radiomics signature and clinicopathologic risk factors showed better performance in terms of EFS prediction in patients with hepatoblastoma, which enabled precise clinical decision-making.

**Keywords:** pediatric, hepatoblastoma, computer tomography imaging, prognosis, radiomics, nomogram

## INTRODUCTION

Hepatoblastoma (HB) is the primary hepatic malignancy that occurs in childhood worldwide. With the prevalence of HB being on the rise, an annual incidence of 1.5 cases/million people has been documented (1, 2). Complete resection of the liver is the first-line treatment for early-stage HB with localized lesions (3–5). However, a considerable proportion of patients with unresectable advanced-stage HB requires preoperative chemotherapy (3). The survival outcomes of pediatric patients with HB have improved substantially over recent decades, primarily due to developments in surgical methods and therapy intensification (3, 6). Nevertheless, the optimal combination strategy of chemotherapy and surgery and the increased risk of toxicities from cumulative chemotherapy have not been addressed (7, 8). Thus, therapy should be based on the identification of patients at high risk of a poor outcome in HB.

In recent decades, several prognostic and risk factors of HB have been reported (9–13). Several prospective studies have been conducted by four major research teams: the Children's Oncology Group (COG); the International Childhood Liver Tumors Strategy Group (SIOPEL); the Japanese Study Group for Pediatric Liver Tumors (JPLT); and the German Society for Pediatric Oncology and Hematology (GPOH). These teams have developed risk-stratified stratagems to improve survival outcomes (14). One remarkable achievement was the Pretreatment Extension of Disease (PRETEXT) system introduced by SIOPEL, which is used widely for the preoperative diagnosis of HB based on imaging assessment (15). However, each study has used different risk-stratification strategies, which yielded dissimilar outcome predictions. In 2018, a final, uniform, global hepatoblastoma stratification (HS) system was established by the Children's Hepatic tumors International Collaboration (CHIC) based on pooled trial data from cooperative groups (1,605 patients from JPLT, GPOH, COG, and SIOPEL). The system refined the individual prognostic variables with age and the PRETEXT stage, together with annotation factors, alpha-fetoprotein (AFP) concentration, metastases, and tumor resectability (4). Gradually, patients with HB benefitted from better stratification to select the most appropriate therapeutic option. Notwithstanding this accomplishment, this risk-stratification model was neither finalized with regard to the histology type nor adapted to the treatment response, as it was somewhat complex in terms of clinical utility in smaller patient cohorts (4, 10, 11, 16). Meanwhile, preoperative PRETEXT has moderate accuracy with a tendency of over-staging, and its diagnostic accuracy is dependent upon imaging

technology/equipment to some extent (4, 17). The creation of a feasible, simple, and practical prognostic stratification model to identify risks in patients with HB remains a major challenge.

Medical imaging is vital in clinical management to aid in decision-making and guide “individualized” treatment (18). Over recent years, rapid advances in “big data” and artificial intelligence have led to breakthroughs in “data mining” during analyses of medical images. These advances have created the field of “radiomics,” which has allowed the prediction of clinical endpoints in various types of cancer (19–23). A nomogram model incorporating radiomics features and clinicopathologic factors seems to improve the prognostic accuracy (24, 25). Taking into consideration the heterogeneity of HB is crucial for risk stratification and the prognosis (16). Also, the limitation of histology samples means that the full information about a histological type within a tumor is lacking, which can compromise management (26). Also, patients with an identical PRETEXT stage can show variations in recurrence and survival outcomes (27). These observations demonstrate that the current staging system for HB does not provide adequate prognostic information about the biological heterogeneity of HB. In this regard, radiomics (i.e., characterizing tumor phenotypes by extracting information about the biological processes of tumors from medical images) could facilitate the prediction of tumor progression.

We have no evidence of obtaining a “radiomics signature” to predict the survival outcome of HB. We developed a predictive model comprising radiomics based on CT-derived images and clinical features to forecast event-free survival (EFS) in patients with HB and to assess its additional value to the staging system.

## MATERIALS AND METHODS

### Ethical Approval of the Study Protocol

The protocol for this retrospective multicenter study was approved by the Ethics Committee of the West China Second University Hospital within Sichuan University (Sichuan, China). The requirement for written informed consent was waived.

### Inclusion Criteria

The criteria for study inclusion were as follows: (i) age <18 years; (ii) histopathologic diagnosis of HB; (iii) preoperative CT of the abdomen and imaging of sufficient quality for analyses; and (iv) complete medical records with data on the surgical procedure and follow-up.

## Patients

The database of our institution was used to collect medical records from January 2009 to August 2019. The internal training cohort comprised 65 patients with HB confirmed by histology who underwent hepatectomy or needle biopsy at the West China Second University Hospital. The data for the external validation cohort were from 23 consecutive patients from the West China Second University Hospital of Sichuan University between January 2012 and December 2019 with identical enrolment criteria. In total, 88 patients were enrolled (57 males and 31 females; mean age,  $2.28 \pm 2.72$  years; age range, 0.1–12.9 years) in the present study. Clinicopathologic data were recorded for each patient. Surgical excisions or tumor-biopsy samples were reviewed by a very experienced pathologist to assess the histology subtype of the tumor. Histopathology confirmation was done with a surgical specimen in 68 patients and with core-needle biopsy in 20 patients.

Clinical information (sex, age, tumor diameter, AFP concentration, clinical stage, surgical notes, treatment regimen, chemotherapy, survival at the time of final follow-up, CT-reported imaging features) at baseline was documented. Tumor stage and preoperative risk assessment were reclassified according to the CHIC- Hepatoblastoma Stratification (HS) and the 2017 PRETEXT systems (4, 13).

## Follow-Up

Event-free survival was the primary endpoint in this study (28). EFS is defined as the period from the date of CT examination to the date of the first relapse, of development of a second malignancy, of disease progression, of death, or of final follow-up, as appropriate (4). The minimum duration of follow-up for EFS was 10 months. The maximum duration of follow-up was 143 (median, 27) months. CT scan of the chest and abdomen was done every 2 months in the first year, every 3 months in the second year, and every 6 months in the third year after surgery, and was also done annually; this strategy was in line with the follow-up procedure of West China Second University Hospital.

## CT Image Acquisition and Feature Analysis

Contrast-enhanced CT of the abdomen was conducted <7 days before surgery. The data of CT images were obtained using two multidetector-row CT systems (NeuViz 128, Neusoft, Beijing, China; Discovery CT750 HD, GE Healthcare, Piscataway, NJ, USA) at two institutions. The detailed imaging protocol is described in **Supplementary Material I**. The morphologic characteristics of HB lesions on CT images were documented as CT-reported features for the possible prognostic factors of EFS. These factors were the diameter, location, morphology (round/lobulated vs. irregular), margin (well-circumscribed vs. ill-defined), and density modification (homogeneous vs. heterogeneous) of the tumor, as well as the presence of hemorrhage, cystic/necrotic components and calcifications, capsular retraction, tumor vessels, perihepatic effusion, collateral veins, and vascular invasion. Distant metastasis in remote organs was also recorded. In addition, an imaging-based 2017 PRETEXT staging system and related annotation factors were applied for the grouping of tumor extent and analyses of image features (4).

The factors were vascular involvement (V, hepatic vein/inferior vena cava; P, portal vein), multifocality (F), tumor rupture (R), extrahepatic tumor extension (E), the involvement of the caudate lobe (C), lymph-node metastases (N), and distant metastases (M). CT scans of the chest and MRI of the brain were done in all patients to investigate distant metastases before treatment.

## Collection of Clinicopathologic Risk Factors

We collected the clinicopathologic characteristics recognized as being significant risk factors according to the risk stratification for HB set by CHIC-HS (15). That is, the risk stratification of patients was classified into three groups (very low risk/low risk; intermediate risk; high risk), and the age was divided into three groups ( $\leq 2$ , 3–7, and  $\geq 8$  years). Groups for the serum AFP concentration ( $\leq 100$ , 101–1,000, and  $> 1,000$  ng/ml) were not included in the analyses because the AFP concentration was much more than 100 ng/ml for most patients and only three patients had an AFP concentration in the range of 101–1,000 ng/ml. We combined the very-low-risk group and the low-risk group into one group because of the identical EFS in these two groups. In addition, a combined factor of VPEFR was identified as positive (VPEFR+) if one of the V, P, E, F, or R factors, as described by CHIC-HS, were present (4). The 2014 International Consensus Histology Classification for HB (29) was used for the reallocation of histology subtypes for patients in our study.

## Analyses of Radiomics Features Based on CT

Tumor segmentation and extraction of radiomics features were carried out on the Radcloud platform 3.1.0 (<http://radcloud.cn/>; Huiying Medical Technology, Beijing, China). CT scans were done at different centers. Hence, the corresponding image preprocessing along with filtering of image data for normalization of CT images was undertaken to obtain more robust radiomics features (**Supplementary Material II**). To segment the volume of interest (VoI) of tumors for further analyses, two radiologists (JY and CY, with 8 and 12 years of experience in the interpretation of abdominal CT images in children, respectively) delineated the region of interest (RoI) manually (30) along the contour of the lesion in layers on the portal venous (PV)-phase image in a blinded manner. All depicted RoIs were delineated strictly using identical criteria and validated visually by the same expert (JY). The “pyradiomics” package within Python 3.8.1 (<https://pyradiomics.readthedocs.io/>) was employed to extract 1,409 quantitative imaging features from images of the PV-phase on CT. The detailed information of radiomics features are depicted in **Supplementary Material III**. All radiomics features were complied with definitions as delineated by the Imaging Biomarker Standardization Initiative (30).



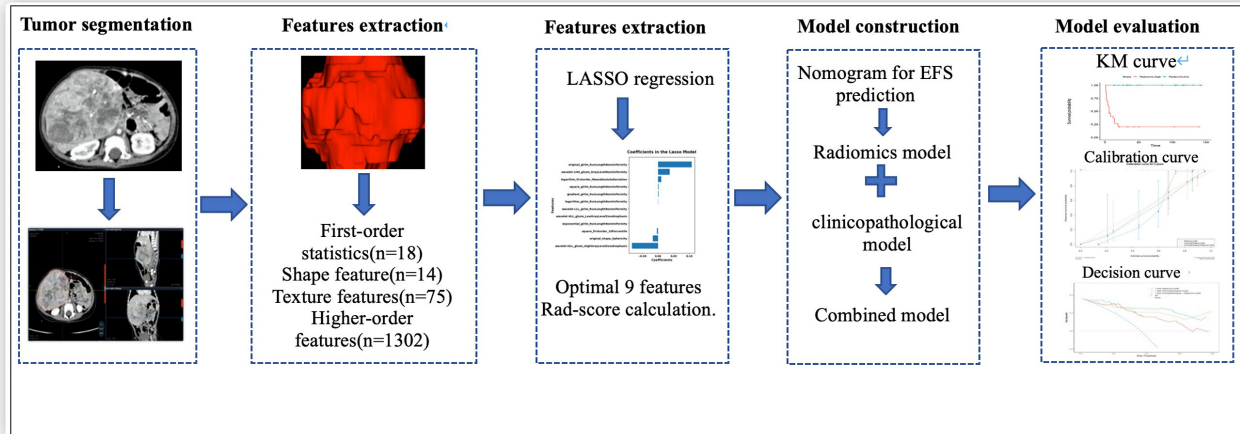


**FIGURE 1 |** Radiomics framework of predicting the EFS of patients with hepatoblastoma.

## Feature Selection and Building of a Prediction Model

The least absolute shrinkage and selection operator (LASSO) Cox regression model was adopted to reduce the redundancy of high-dimensional features and to select the most useful prognostic features correlated to EFS. Then, the radiomics score (“Rad-score”) based on a selected radiomics signature was built using a Cox regression model for predicting the risk of disease progression in the training cohort. In addition to the radiomics model, independent prognostic factors were selected gradually by univariate and multivariate Cox regression analyses carried out in the training cohort to form a clinicopathologic model and an incorporated clinicopathologic-Rad-score (CR) model for EFS prediction. Then, a nomogram was created for the visualization of EFS prediction.

## Survival Analysis Based on the Radiomics Signature

The difference in EFS between the Rad-score and clinicopathological risk-factor groups was analyzed using the Kaplan–Meier survival curves and the log-rank test in the training cohort. Then, the result was applied to the validation cohort. Meanwhile, the radiomics signature was used to divide patients of the training cohort into low- and high-risk groups based on the optimal Rad-score cutoff point (which was identified in log-rank statistics), and verification was done in the validation cohort.

## Evaluation of the Model Using a Radiomics Signature

The prediction performance of our model was evaluated according to discrimination, calibration, and clinical usefulness. The discrimination performance was quantified using Harrell’s Concordance Index (C-Index). A C-Index of  $\sim 0.7$  indicates a good predictive value. Calibration was explored based on consistency between estimated 3-year survival and actual 3-year

survival in the corresponding calibration curves in the training and validation cohorts. Analyses of decision curves denoted clinical usefulness based on the net benefit of the model across different threshold probabilities. The study workflow, comprising of image collection, lesion segmentation, extraction of radiomics features, feature selection, construction of models in the training cohort, and evaluation of the performance of prediction models in the test cohort, is elaborated in **Figure 1**.

## Statistical Analysis

Normalization of features, selection of features, and model construction were undertaken using Python 3.8.1 ([www.python.org/](http://www.python.org/)). The “scikit-learn” (<https://scikit-learn.org/>), “pyradiomics” (<https://pyradiomics.readthedocs.io/>), and “matplotlib” (<https://matplotlib.org/>) packages were applied. Other statistical analyses were accomplished with SPSS 26.0 (IBM, Armonk, NY, USA) and R 4.0.3 ([www.R-project.org/](http://www.R-project.org/)).  $P < 0.05$  was considered significant. EFS was analyzed by the Kaplan–Meier method. The log-rank test was employed to compare the outcome between patients with different risk factors. Characteristics at baseline in the training and validation cohorts were assessed by an independent-sample  $t$ -test, the two-tailed  $\chi^2$ -test, or the Fisher’s exact test as appropriate. Univariate and multivariate Cox regression analyses were undertaken to screen for the significant predictors of EFS. Factors with  $p < 0.10$  in the univariable analysis were provided as input to the multivariable analysis. The variable risk was denoted as a hazard ratio (HR) with a corresponding 95% confidence interval (CI).

## RESULTS

### Patient Characteristics at Baseline

The characteristics of the patients at baseline in the training and validation cohorts are detailed in **Table 1**. Of the 88 patients included in this study at final follow-up, the mean duration of follow-up was 42.43 months and the median duration of EFS was 19 months. The shortest duration of EFS was 1 month. The

**TABLE 1 |** Baseline patient and tumor characteristics according to the radiomics score in the training and validation cohorts.

Characteristic	Category	Training	Validation	P-value
Number of patients		65	23	
Age at initial diagnosis (years)	Mean age (y)	2.99 ± 2.44	3.09 ± 3.32	0.407
	≤2	53 (81.5%)	13 (56.5%)	
	3–7	8 (12.3%)	8 (34.7%)	
	≥8	4 (6.1%)	2 (8.6%)	
Sex				0.648
	Male	43 (14%)	14 (60.8%)	
	Female	22 (33.8%)	9 (39.1%)	
Serum AFP concentration, ng/mL				0.395
	≤100	0	0	
	101–1,000	2 (3%)	1 (4.3%)	
	>1,000	63 (96.9%)	22 (95.6%)	
Histological subtype				0.903
	Fetal	23 (35.3%)	7 (30.4%)	
	Embryonal	2 (3%)	1 (4.3%)	
	Epithelial mixed	16 (24.6%)	5 (21.7%)	
	Mixed epithelial/mesenchymal	24 (36.9%)	10 (43.4%)	
PRETEXT group				0.196
	I	9 (13.8%)	7 (30.4%)	
	II	31 (47.6%)	9 (39.1%)	
	III	14 (21.5%)	4 (17.3%)	
	IV	11 (16.9%)	3 (13.0%)	
Annotation factors				
V (HV or IVC involvement)	Yes	12 (18.4%)	1 (4.3%)	0.101
P (PV involvement)	Yes	17 (26.1%)	2 (8.6%)	0.08
E (extrahepatic tumor extension)	Yes	2 (3%)	2 (8.6%)	
F (multifocality)	Yes	17 (26.1%)	4 (17.3%)	0.397
R (tumor rupture)	Yes	3 (4.6%)	2 (8.6%)	0.468
C (caudate involvement)	Yes	9 (13.8%)	2 (8.6%)	0.073
N (lymph node metastasis)	Yes	6 (9.2%)	1 (4.3%)	0.457
M (distant metastasis)	Yes	10 (15.3%)	4 (17.3%)	0.662
One or more of V, P, E, F, R	Yes	26 (40%)	6 (26%)	0.233
CHIC-HS risk stratification				0.615
	Very low/low	35 (53.8)	15 (65.2%)	
	Intermediate	13 (20%)	3 (13.0%)	
	High	17 (26.1%)	5 (21.7%)	
Number of deaths		17 (26.1%)	5 (21.7%)	0.674
Follow-up time (month)	Median	30	27	0.391
	Maximum	143	97	
EFS	Median (month)	19	20	0.569
	Event	27 (41.5%)	7 (30%)	0.347
	No event	38 (58.4%)	16 (69.5%)	
Preoperative chemotherapy		13 (20%)	5 (21.7%)	
Surgical resection		46 (70%)	15 (65.2%)	
Orthotopic liver transplantation		1	0	
Resection of pulmonary metastases		1	0	

AFP, alpha-fetoprotein; PRETEXT, 2017 PRE-Treatment EXTent of tumor; HV, hepatic vein; IVC, inferior vena cava; PV, portal vein; CHIC-HS, Children's Hepatic tumors International Collaboration-Hepatoblastoma Stratification; EFS, event-free survival.

**TABLE 2 |** Univariate and multivariate analysis of event-free survival for patients in training cohort.

Variables	Univariate		Multivariate	
	HR (95% CI)	P	HR (95% CI)	P
CHIC-HS risk stratification		0.005	2.07 (0.759–5.640)	0.026
Very low/low	1.000 (Reference)	0.004	NA	
Intermediate	1.856 (0.543–6.341)	0.023	NA	
High	5.437 (1.870–12.551)	0.011	NA	
PRETEXT group	1.007 (1.335–4.841)	0.003	2.542 (1.335–4.841)	0.004
Histological subtype		<0.001		0.010
Fetal	1.000 (Reference)		1.000 (Reference)	
Embryonal	2.124 (0.027–0.576)	0.008	1.364 (1.075–1.731)	
Epithelial mixed	2.234 (0.046–0.698)	0.002	2.459 (0.370–16.344)	
Mixed epithelial/mesenchymal	4.492 (0.151–1.603)	0.019	3.354 (1.524–27.434)	
M (distant metastasis)	5.387 (2.131–13.620)	<0.01	0.150 (0.023–0.977)	0.047
F (multifocality)	4.527 (1.828–11.209)	0.001	NA	
P (PV involvement)	5.404 (2.167–13.474)	0.002	7.43 (2.134–25.911)	0.001
R (tumor rupture)	4.681 (1.071–10.465)	0.009	NA	
VPERF+	4.559 (1.726–12.040)	0.002	0.09 (0.010–0.967)	
Tumor vessel	2.503 (1.012–6.190)	0.040	NA	
Effusion	2.776 (1.112–6.927)	0.029	NA	
Radiomics signature	3.009 (1.963–4.613)	0.006	5.138 (1.268–16.495)	0.024

HR, hazard ratio; CI, confidence interval; CHIC-HS, Children's Hepatic tumors International Collaboration-Hepatoblastoma systems; PV, portal vein; CHIC-HS, Children's Hepatic tumors International Collaboration-Hepatoblastoma Stratification; EFS, event-free survival.

percentage of EFS at 5 years was 73.8% in the training cohort and 78.3% in the validation cohort. Thirty-four events were observed for the EFS calculation: 29 patients had disease progression, 17 patients relapsed, and 16 died after surgery. Most patients (85/88) had a serum AFP of >1,000 ng/ml. Only three patients had a serum AFP level between 100 and 1,000 ng/ml. Of these 88 patients, 14 (16.6%) were diagnosed with distant metastasis upon their first evaluation. Lung metastases were documented in 13 patients, and one patient had mandibular-bone metastases. The histology subtype was available for all patients. There was no significant difference between the two cohorts with respect to clinicopathologic characteristics or survival ( $P = 0.073$ – $0.903$ ).

The inter- and intra-observer reproducibility of extraction of radiomic features were high. Therefore, all outcomes were based on the measurements taken by the first radiologist (JY).

## CT Features

The mean value for the maximum dimension of the tumor was 10.7 cm (range: 4.2–19). The tumors had delineated boundaries (41/88, 46.6%), capsules (79/88, 89.8%), collateral circulation (17/88, 19.3%), bleeding (17/88, 19.3%), and vessels (35/88, 39.8%), and some tumors were heterogeneous (79/88, 89.8%) at presentation. Also, 21/88 (23.9%) tumors were multifocal, whereas 21/88 (23.9%) had perihepatic effusion. Cystic/necrotic components were present in 83/88 (94.362%) tumors, and calcifications were present in 39/88 (44.3%) lesions. The calcifications were punctate, coarse, or speckled. The capsular retraction was noted in 67/88 (76.1%) of tumors.

## Collection of Clinicopathologic Prognostic Factors

The identified significant association factors for EFS were determined by univariable and multivariable logistic regression analysis. We found that CHIC-HS risk stratification; PRETEXT grade; histology subtype; the PRETEXT annotation factors, M and P; and VPERF+ were independent of clinical prognostic risk factors (Table 2). Multivariable Cox proportional hazard analysis showed that the PRETEXT annotation factor P was the strongest predictor (HR, 7.43; 95% CI: 2.134–25.911;  $P = 0.001$ ). The histology subtype showed a similar significance in predicting EFS (HR, 1.364; 95% CI: 1.075–1.731;  $P = 0.010$ ) whereas distant metastasis showed borderline significance for EFS prediction (HR, 0.150; 95% CI: 0.023–0.977;  $P = 0.047$ ).

## Construction of a Rad-Score Based on a Radiomics Signature

Nine potential survival-related radiomics features from 92 significant features ( $p < 0.05$ ) were documented. The nine features, namely, “TotalEnergy,” “LowGrayLevelZoneEmphasis,” “GrayLevelNonUniformity,” “LowGrayLevelZoneEmphasis,” “SmallAreaLowGrayLevelEmphasis,” “LowGrayLevelZoneEmphasis,” “ZoneEntropy,” “SizeZoneNonUniformityNormalized,” and “RunLengthNonUniformity,” were identified in the training cohort for the construction of a radiomics model and the calculation of Rad-score by the LASSO Cox regression analysis (Supplementary Table 1). The HR for the Rad-score was 3.009 (95% CI: 1.963–4.613) in the training cohort. According to the distribution of the Rad-score, we classified patients further

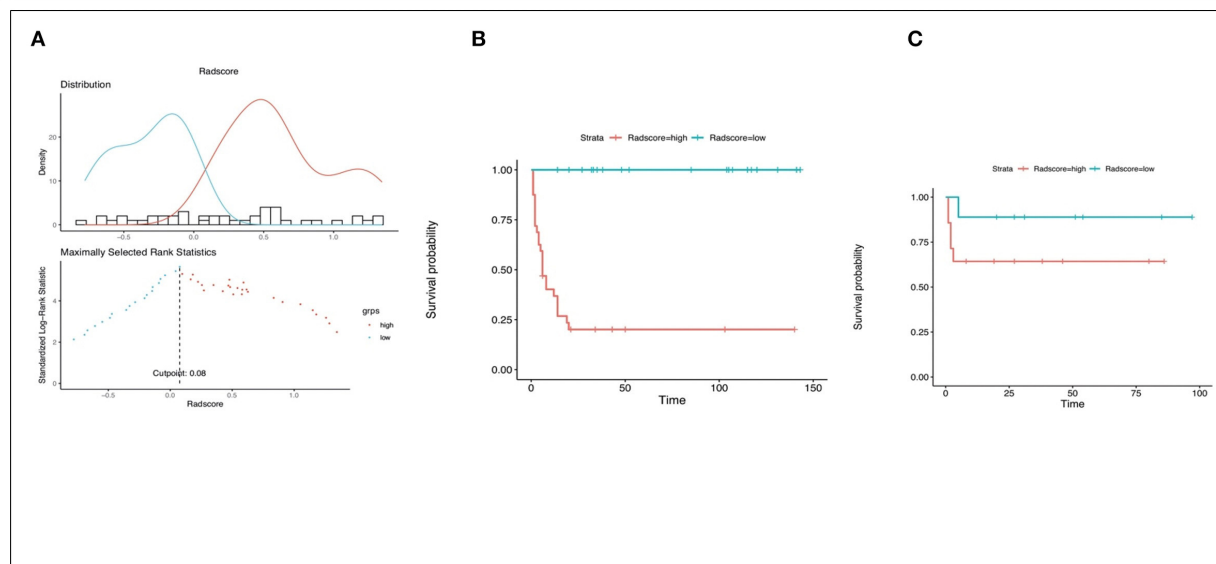


**FIGURE 2 |** Kaplan-Meier survival analysis of event-free survival of patients with HB. Graphs show results of Kaplan-Meier survival analyses according to the radiomics score cutoff value (A) for patients in the training data set (B) and those in the validation data set (C). A significant association of the radiomics score with the EFS was shown in the training data set, which was then confirmed in the validation data set.

into low-risk (Rad-score  $<0.08$ ) and high-risk (Rad-score  $>0.08$ ) groups using an optimal cutoff of 0.08 (Figure 2A). Survival analyses revealed a significant difference between these two risk-stratification groups ( $P < 0.001$ ) in the training and validation cohorts (Figures 2B,C). Furthermore, survival analyses applied in all clinicopathologic subgroups (CHIC-HS, histology subtype, M, P, F, VPERF) demonstrated that these risk factors were significant for disease progression ( $p < 0.01$ ) (Supplementary Figure 1).

### Performance of the Radiomics Nomogram Compared With the Clinical-Pathological Nomogram in Predicting EFS

Based on the multivariate Cox regression analysis, three nomograms that incorporated the Rad-score and independent clinicopathologic factors and CR were generated (Figure 3). The radiomics nomogram exhibited good discrimination performance (C-Index: 0.810; 95% CI: 0.738–0.882) in the validation cohort, which was comparable with clinicopathologic factors (C-Index: 0.855; 95% CI: 0.790–0.920) without improvement in performance in EFS estimation. The combined model with Rad-score and clinicopathological factors achieved a significant incremental value (C-Index: 0.881; 95% CI: 0.829–0.933) for the accuracy of prognosis relative to the radiomics signature alone and the clinicopathologic factors alone. The estimates of the C-Index, of concordance probability, and of the Akaike information criterion (AIC) for the different prediction models are listed in Table 3. Moreover, the calibration curve indicated a satisfactory agreement between the outcome of survival prediction and actual survival at 3-year follow-up in

the internal-validation cohort and external-validation cohort (Figure 4).

Analyses of decision curves showed that the combined model integrating the Rad-score and the clinicopathologic nomogram obtained higher clinical utility relative to that obtained using the radiomics signature alone or the clinicopathologic factors alone (Figure 5).

## DISCUSSION

Patients with advanced HB carry a substantial risk of local relapse and distant metastasis even after resection. Indeed, only about one-thirds of patients with HB have a resectable tumor at initial presentation (2). Whether an optimal treatment regimen with adjuvant chemotherapy and surgery provides survival benefit is controversial and is largely dependent on the assessment of prognostic risk.

We developed a quantitative radiomics approach with CT for accurate pretreatment risk stratification in HB to assist in decision-making for clinical treatment. A LASSO Cox-based radiomics signature was demonstrated to be an independent risk factor for EFS in patients with HB. A radiomics model with specific radiomics features using pretreatment of CT-enhanced images showed similar performance to that of a postoperative clinicopathologic model for predicting EFS of HB. The combination of a nomogram with the Rad-score and clinicopathologic factors achieved better performance than that using the radiomics nomogram and the clinicopathologic nomogram for individualized EFS estimation. The result supports another possibility of preoperative evaluation before



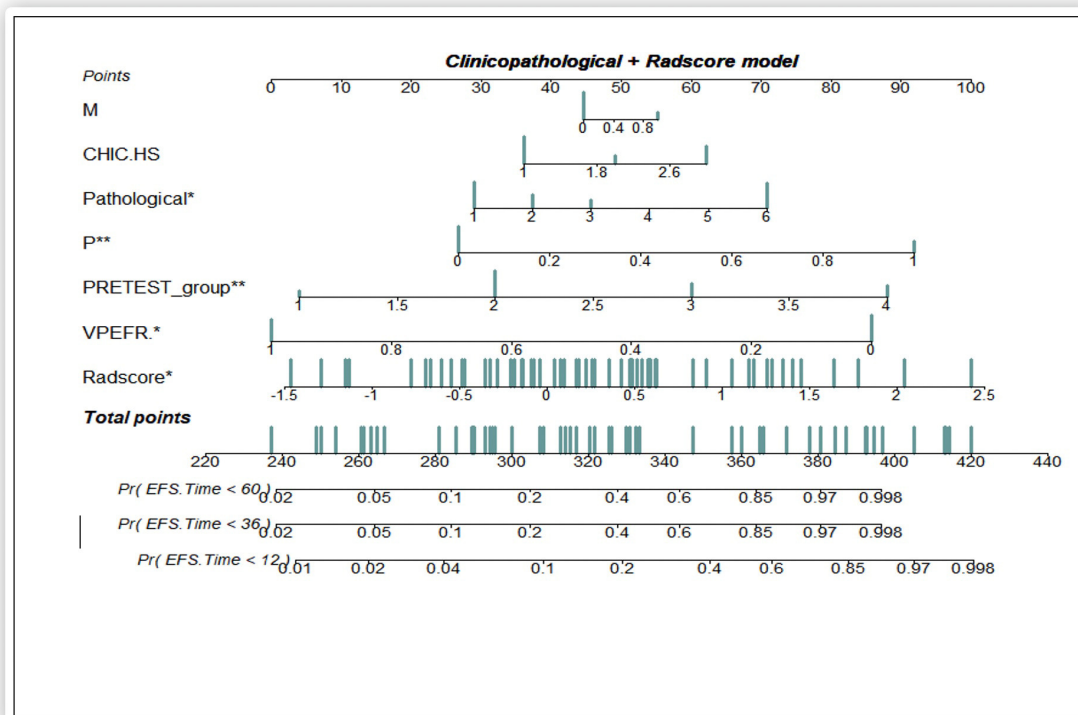


**FIGURE 3 |** A prediction performance analysis with combined clinicopathologic-Rad-score of patients with HB. Significant codes: \*\*\*0; \*\*0.001; \*0.01; .0.05; ' 0.1; 1.

**TABLE 3 |** Models performance.

Model	C-index (95% CI)	Se (C-index)	P-value	AIC
Rad-score (1)	0.810 (0.738~0.882)	0.037	0.256 (1,2)	162.650
Clinicopathological (2)	0.855 (0.790~0.920)	0.033	0.211 (2,3)	154.446
Clinicopathological+Rad-score (3)	0.881 (0.829~0.933)	0.026	0.006 (1,3)	149.025

surgical pathology when Evans' surgical staging is used based on exploratory surgery for patients with HB (9). In addition, the patients were categorized into low- and high-risk groups by using the multiple feature-based Rad-score with significant differences in EFS, which would be an important supplement to the present PRETEXT and CHIC-HS systems for the evaluation of clinical risk factors. We investigated, for the first time, the use of radiomics features using quantitative CT images to predict disease progression in pediatric patients with HB.

In recent years, much attention has been paid to developing high-throughput screening to extract many quantitative features in medical imaging to assist the clinical diagnosis. Also, the radiomics signature has been shown to be validated robustly, be cost-effective, and be powerfully predictive of survival from solid tumors in several studies (18–22, 24, 25, 31–34). The selected radiomics signature provides a non-invasive, simple, and reproducible method for acquiring phenotypic information, which is not available using conventional imaging and which can be employed to predict survival outcomes. Reviews by

scholars have suggested that intratumoral heterogeneity could be demonstrated by radiomics, which would imply a worse prognosis with relapse and metastasis (35, 36). A quantitative radiomics analysis by Aerts and colleagues revealed the radiomics signature and the interpretation of intratumor heterogeneity associated with the underlying gene expression (37). In the present study, the features of conventional CT images were extracted, and the analysis of dimensionality reduction was carried out by a LASSO regression algorithm to select the features that could best reflect the different components in HB. The LASSO approach was able to acquire all features with non-zero coefficients, which enhanced the interpretation and prediction accuracy of the model. The subset of the selected optimal features contained several first-order statistics features (which reflect the internal voxel intensity of lesions) and texture features (which reflect the gray-distribution characteristics in dimensional space and suggest the heterogeneity composition or distribution of lesions in the dimensional space). However, interpretation of the complex associations between radiomics

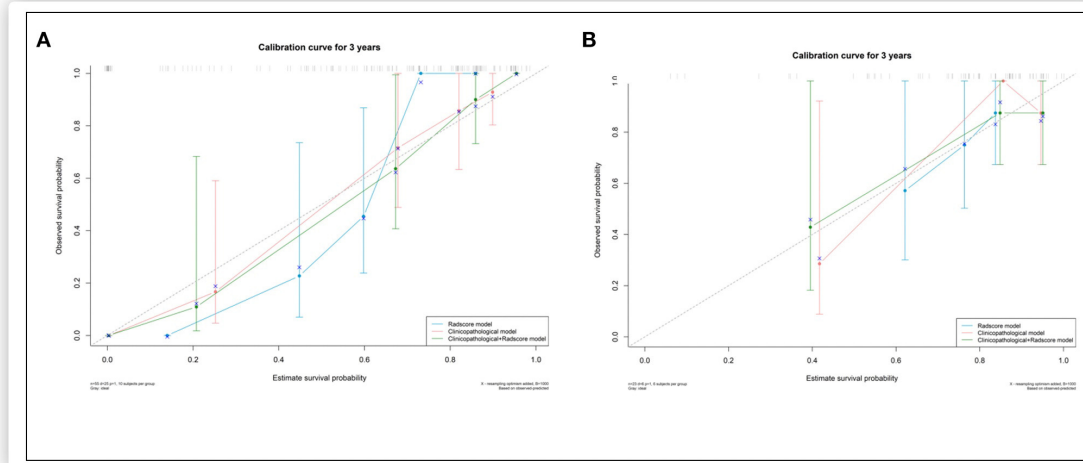


**FIGURE 4** | Calibration curves for each model in the internal validation (A) and external validation (B) set.

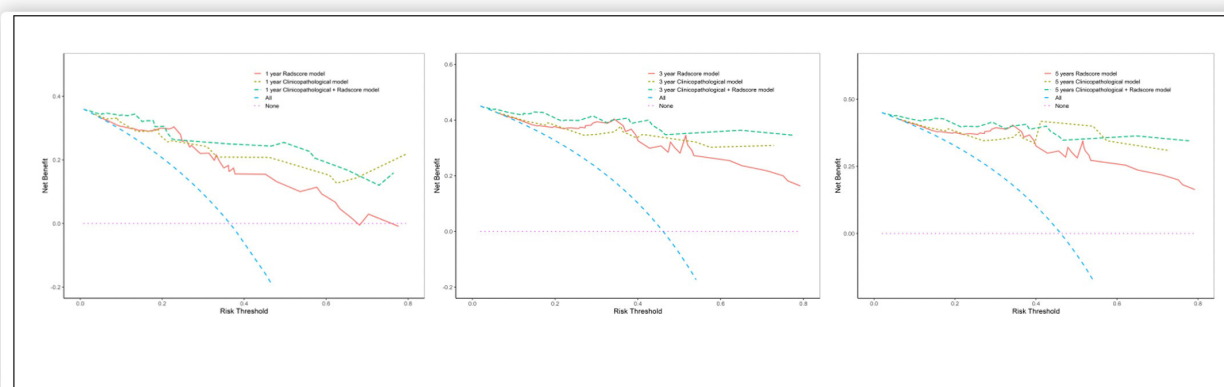


**FIGURE 5** | Decision curve analysis for each model between the observed 1-, 3-, and 5-year outcomes.

features and biological processes in a tumor remains a challenge (38). Besides, considering the complex intervention, multiple interacting components, in the biological processes and the nature of malignancy, it is hard to correlate a single radiomics-based factor with a pathophysiological change in an intuitive manner. Hence, the multiple features based on the radiomics signature show significantly greater estimation outcome than that of any selected feature alone. In the present study, nine features of a radiomics signature in 88 patients achieved a favorable performance for the assessment of survival from HB. In addition, the multiple-component radiomics signature from the training cohort was externally validated in the test cohort using different device brands and at different institutions, thereby illustrating the repeatability and stability of this model.

In recent decades, an increasing number of studies focusing on the association between several risk factors and HB survival have been published (9–12). Although prognostic factors and

outcomes were stated, the studies failed to provide a new prognostic model (2). The CHIC group developed unified risk stratification for patients with HB. Several factors, namely AFP, PRETEXT group, and PRETEXT annotation factors, were shown to affect patient survival (4). However, the present CHIC-HS system may be awkward to use in clinical practice because there are many variables in its complex stratification system. Also, the reasons for some factors eliciting a worse outcome (e.g., older age) are not entirely clear. In addition, the prognostic importance of pathological subtypes has not been included in study groups. Some histology types have been associated with the prognosis in clinical trials (9, 39). Hence, comparisons between any outcome and prognostic factors between groups are challenging and unreliable (13). In accordance with the CHIC-HS, we defined identical risk factors in the present study as well as histology types. Although histology subtypes were incomplete (small-cell undifferentiated and macrotrabecular types were absent),

the results are consistent with data from studies that reported a better prognosis with a pure fetal well-differentiated type and a worse prognosis with a non-pure fetal type (40). We also investigated the performance of morphologic characteristics using conventional imaging as a preoperative prognostic factor for potential association with outcome of HB, as described in an earlier study (17, 41). However, none of the morphologic features on imaging were included in the regression models in the present study; their prognostic value and the association with EFS should be validated in additional studies. We incorporated CHIC-HS-related risk factors and morphologic features into a clinicopathologic model. We found that all variables remained as predictors to identify an increased risk, except the PRETEXT annotation factor E; these observations are in accordance with the results of previous studies (4, 13). The multivariate Cox regression analysis indicated that the PRETEXT annotation factor, P, was the strongest negative independent prognostic factor and that factor M showed borderline significance in our cohort; these data are consistent with results from other similar studies (27).

Nomograms have been developed for some cancers and are accepted as reliable tools for the prediction of risk for individuals (42, 43). Based on the abovementioned risk factors, we incorporated the radiomics signature and clinicopathologic characteristics to develop and validate a radiomics–clinicopathologic nomogram to improve the accuracy of prognosis prediction for patients with HB. Overall, the results from the combined nomogram displayed more robust power for predicting EFS in HB than that of the radiomics model alone or the clinicopathologic model alone, with a higher C-index, better calibration, and improvement in the net reclassification. Furthermore, the decision curve analysis indicated the benefit of using combined model beyond the clinical staging system across the appropriate range of reasonable threshold probabilities. This result suggested that the radiomics signature reinforced the prognostic ability of the staging system, thereby adding prognostic value to clinicopathologic risk factors. The concept of this combination model has been described previously (34, 44). However, the combination model mentioned earlier was employed to facilitate personalized treatment for patients with HB and provide pediatricians with a powerful tool for making clinical decisions. The radiomics nomogram (which contained the Rad-score) yielded a C-Index of 0.810 (95% CI: 0.738–0.882) for EFS prediction in the validation cohort, and this C-Index was similar to that of the clinicopathologic model. This observation suggested that the Rad-score might contain clinical information due to the extraction of high-dimensional features that can capture prognostic information. Thus, the Rad-score could be used as a surrogate biomarker to improve the prognostic ability before treatment. In addition, the Rad-score could be used to stratify patients into low- and high-risk groups. Patients with higher Rad-scores had worse EFS, which suggested that low-risk patients would receive radical hysterectomy. For the high-risk group, intensive treatment could elicit greater survival benefits. Thus, the Rad-score may be an efficient tool to enable personalized treatment before surgery.

The present study had five main limitations. First, the sample size was small (particularly the external-validation cohort). Second, the study was retrospective. Third, missing information and a small number of clinicopathologic factors [e.g., age group (>8 years) or histology subtypes] may have led to a performance bias. Fourth, the underlying connection between the radiomics signature and biological information was not investigated. Finally, delineation of RoIs was processed using a manual method. The exploitation of auto-segmentation could be an efficient and accurate method for lesion identification in future radiomics research.

In conclusion, a radiomics signature can be used as a biomarker for risk stratification in patients with HB. A nomogram integrating the radiomics signature, the staging system, and other clinicopathologic risk factors for EFS estimation may be a valuable tool for guiding individual pretreatment for patients with HB.

## DATA AVAILABILITY STATEMENT

The raw data supporting the conclusions of this article will be made available by the authors, without undue reservation.

## ETHICS STATEMENT

The studies involving human participants were reviewed and approved by Institution Ethics Committee of China West second hospital of Sichuan University. Written informed consent to participate in this study was provided by the participants' legal guardian/next of kin. Written informed consent was obtained from the individual(s), and minor(s)' legal guardian/next of kin, for the publication of any potentially identifiable images or data included in this article.

## AUTHOR CONTRIBUTIONS

YJ, YX, and YG: conceptualization. JS: data curation. JS and YC: formal analysis. YC: investigation. LX and XG: methodology. YG: project administration and YG: supervision. YJ: writing—original draft. YJ and YG: writing—review and editing. All authors: contributed to the article and approved the submitted version.

## FUNDING

This research was supported by grants from the National Natural Science Foundation of China (81760331), Fund of Science and Technology of Sichuan Province (Nos. 19ZDYF1202 and 2020YFS0253), and Fund of Chengdu Science and Technology Bureau (No. 2019-YF05-01140-SN).

## SUPPLEMENTARY MATERIAL

The Supplementary Material for this article can be found online at: <https://www.frontiersin.org/articles/10.3389/fonc.2021.644994/full#supplementary-material>

## REFERENCES

- Darbari A, Sabin KM, Shapiro CN, Schwarz KB. Epidemiology of primary hepatic malignancies in U.S. children. *Hepatology*. (2003) 38:560–6. doi: 10.1053/jhep.2003.50375
- Feng J, Polychronidis G, Heger U, Frongia G, Mehrabi A, Hoffmann K. Incidence trends and survival prediction of hepatoblastoma in children: a population-based study. *Cancer Commun*. (2019) 39:62. doi: 10.1186/s40880-019-0411-7
- Hiyama E. Pediatric hepatoblastoma: diagnosis and treatment. *Transl Pediatr*. (2014) 3:293–9. doi: 10.3978/j.issn.2224-4336.2014.09.01
- Meyers RL, Maibach R, Hiyama E, Häberle B, Krailo M, Rangaswami A, et al. Risk-stratified staging in paediatric hepatoblastoma: a unified analysis from the Children's Hepatic tumors International Collaboration. *Lancet Oncol*. (2017) 18:122–31. doi: 10.1016/S1470-2045(16)30598-8
- Kim EF, Shatalov KV, Filin AV, Arnautova IV, Galyan TN, Tarba NS, et al. Surgical treatment of hepatoblastoma PRETEXT/POST-TEXT III and IV. *Khirurgiya*. (2017) 12:70–4. doi: 10.17116/hirurgia20171270-74
- Czauderna P, Lopez-Terrada D, Hiyama E, Häberle B, Malogolowkin MH, Meyers RL. Hepatoblastoma state of the art: pathology, genetics, risk stratification, and chemotherapy. *Curr Opin Pediatr*. (2014) 26:19–28. doi: 10.1097/MOP.0000000000000046
- Häberle B, Rangaswami A, Krailo M, Czauderna P, Hiyama E, Maibach R, et al. The importance of age as prognostic factor for the outcome of patients with hepatoblastoma: analysis from the Children's Hepatic tumors International Collaboration (CHIC) database. *Pediatric Blood Cancer*. (2020) 67:e28350. doi: 10.1002/pbc.28350
- Zsiros J, Brugieres L, Brock P, Roebuck D, Maibach R, Zimmermann A, et al. Dose-dense cisplatin-based chemotherapy and surgery for children with high-risk hepatoblastoma (SIOPEL-4): a prospective, single-arm, feasibility study. *Lancet Oncol*. (2013) 14:834–42. doi: 10.1016/S1470-2045(13)70272-9
- Meyers RL, Rowland JR, Krailo M, Chen Z, Katzenstein HM, Malogolowkin MH. Predictive power of pretreatment prognostic factors in children with hepatoblastoma: a report from the Children's Oncology Group. *Pediatr Blood Cancer*. (2009) 53:1016–22. doi: 10.1002/pbc.22088
- Aronson DC, Schnater JM, Staalman CR, Weverling GJ, Plaschkes J, Perilongo G, et al. Predictive value of the pretreatment extent of disease system in hepatoblastoma: results from the International Society of Pediatric Oncology Liver Tumor Study Group SIOPEL-1 study. *J Clin Oncol*. (2005) 23:1245–52. doi: 10.1200/JCO.2005.07.145
- Maibach R, Roebuck D, Brugieres L, Capra M, Brock P, Dall'Igna P, et al. Prognostic stratification for children with hepatoblastoma: the SIOPEL experience. *Eur J Cancer*. (2012) 48:1543–9. doi: 10.1016/j.ejca.2011.12.011
- Fuchs J, Rydzynski J, Von Schweinitz D, Bode U, Hecker H, Weinl P, et al. Pretreatment prognostic factors and treatment results in children with hepatoblastoma: a report from the German Cooperative Pediatric Liver Tumor Study HB 94. *Cancer*. (2002) 95:172–82. doi: 10.1002/cncr.10632
- Czauderna P, Häberle B, Hiyama E, Rangaswami A, Krailo M, Maibach R, et al. The Children's Hepatic tumors International Collaboration (CHIC): novel global rare tumor database yields new prognostic factors in hepatoblastoma and becomes a research model. *Eur J Cancer*. (2016) 52:92–101. doi: 10.1016/j.ejca.2015.09.023
- Meyers RL, Tiao G, de Ville de Goyet J, Superina R, Aronson DC. Hepatoblastoma state of the art: pre-treatment extent of disease, surgical resection guidelines and the role of liver transplantation. *Curr Opin Pediatr*. (2014) 26:29–36. doi: 10.1097/MOP.0000000000000042
- Towbin AJ, Meyers RL, Woodley H, Miyazaki O, Weldon CB, Morland B, et al. 2017 PRETEXT: radiologic staging system for primary hepatic malignancies of childhood revised for the Paediatric Hepatic International Tumour Trial (PHITT). *Pediatr Radiol*. (2018) 48:536–54. doi: 10.1007/s00247-018-4078-z
- Shaikh F. A common global risk stratification system for hepatoblastoma. *Lancet Oncol*. (2017) 18:13–5. doi: 10.1016/S1470-2045(16)30579-4
- Voss SD. Staging and following common pediatric malignancies: MRI versus CT versus functional imaging. *Pediatr Radiol*. (2018) 48:1324–36. doi: 10.1007/s00247-018-4162-4
- Lambin P, Leijenaar, RTH, Deist TM, Peerlings J, de Jong, EEC, van Timmeren J, et al. Radiomics: the bridge between medical imaging and personalized medicine. *Nat Rev Clin Oncol*. (2017) 14:749–62. doi: 10.1038/nrclinonc.2017.141
- Zhang N, Liang R, Gensheimer MF, Guo M, Zhu H, Yu J, et al. Early response evaluation using primary tumor and nodal imaging features to predict progression-free survival of locally advanced non-small cell lung cancer. *Theranostics*. (2020) 10:11707–18. doi: 10.7150/thno.50565
- Zhang J, Wang X, Zhang L, Yao L, Xue X, Zhang S, et al. Radiomics predict postoperative survival of patients with primary liver cancer with different pathological types. *Ann Transl Med*. (2020) 8:820. doi: 10.21037/atm-19-4668
- Yan BC, Li Y, Ma FH, Feng F, Sun MH, Lin GW, et al. Preoperative assessment for high-risk endometrial cancer by developing an MRI- and clinical-based radiomics nomogram: a multicenter study. *J Magn Reson Imaging*. (2020) 52:1872–1882. doi: 10.1002/jmri.27289
- Fang J, Zhang B, Wang S, Jin Y, Wang F, Ding Y, et al. Association of MRI-derived radiomic biomarker with disease-free survival in patients with early-stage cervical cancer. *Theranostics*. (2020) 10:2284–92. doi: 10.7150/thno.37429
- Dai W, Mo S, Han L, Xiang W, Li M, Wang R, et al. Prognostic and predictive value of radiomics signatures in stage I–III colon cancer. *Clin Transl Med*. (2020) 10:288–93. doi: 10.1002/ctm2.31
- Xie D, Wang TT, Huang SJ, Deng JJ, Ren YJ, Yang Y, et al. Radiomics nomogram for prediction disease-free survival and adjuvant chemotherapy benefits in patients with resected stage I lung adenocarcinoma. *Transl Lung Cancer Res*. (2020) 9:1112–23. doi: 10.21037/tlcr-19-577
- Huang Y, Liu Z, He L, Chen X, Pan D, Ma Z, et al. Radiomics signature: a potential biomarker for the prediction of disease-free survival in early-stage (I or II) non-small cell lung cancer. *Radiology*. (2016) 281:947–57. doi: 10.1148/radiol.2016152234
- Baheti AD, Luana Stanescu A, Li N, Chapman T. Contrast-enhanced CT features of hepatoblastoma: can we predict histopathology? *Clin Imaging*. (2017) 44:33–7. doi: 10.1016/j.clinimag.2017.03.023
- Yoon HM, Hwang J, Kim KW, Namgoong JM, Kim DY, Koh KN, et al. Prognostic factors for event-free survival in pediatric patients with hepatoblastoma based on the 2017 PRETEXT and CHIC-HS systems. *Cancers*. (2019) 11:1387. doi: 10.3390/cancers11091387
- Brown J, Perilongo G, Shafford E, Keeling J, Pritchard J, Brock P, et al. Pretreatment prognostic factors for children with hepatoblastoma—results from the International Society of Paediatric Oncology (SIOP) study SIOPEL 1. *Eur J Cancer*. (2000) 36:1418–25. doi: 10.1016/S0959-8049(00)00074-5
- López-Terrada D, Alaggio R, de Dávila MT, Czauderna P, Hiyama E, Katzenstein H, et al. Towards an international pediatric liver tumor consensus classification: proceedings of the Los Angeles COG liver tumors symposium. *Mod Pathol*. (2014) 27:472–91. doi: 10.1038/modpathol.2013.80
- Zwanenburg A, Vallières M, Abdalah MA, Aerts H, Andrearczyk V, Apte A, et al. The image biomarker standardization initiative: standardized quantitative radiomics for high-throughput image-based phenotyping. *Radiology*. (2020) 295:328–38. doi: 10.1148/radiol.2020191145
- Choe J, Lee SM, Do KH, Kim S, Choi S, Lee JG, et al. Outcome prediction in resectable lung adenocarcinoma patients: value of CT radiomics. *Eur Radiol*. (2020) 30:4952–63. doi: 10.1007/s00330-020-06872-z
- Zauchar JM, Chauvie S, Zaucha R, Biggii A, Gallamini A. The role of PET/CT in the modern treatment of Hodgkin lymphoma. *Cancer Treat Rev*. (2019) 77:44–56. doi: 10.1016/j.ctrv.2019.06.002
- Kim S, Shin J, Kim DY, Choi GH, Kim MJ, Choi JY. Radiomics on gadoteric acid-enhanced magnetic resonance imaging for prediction of postoperative early and late recurrence of single hepatocellular carcinoma. *Clin Cancer Res*. (2019) 25:3847–55. doi: 10.1158/1078-0432.CCR-18-2861
- Jiang Y, Chen C, Xie J, Wang W, Zha X, Lv W, et al. Radiomics signature of computed tomography imaging for prediction of survival and chemotherapeutic benefits in gastric cancer. *EBioMedicine*. (2018) 36:171–82. doi: 10.1016/j.ebiom.2018.09.007
- Banerjee S, Wang DS, Kim HJ, Sirlin CB, Chan MG, Korn RL, et al. A computed tomography radiogenomic biomarker predicts microvascular invasion and clinical outcomes in hepatocellular carcinoma. *Hepatology*. (2015) 62:792–800. doi: 10.1002/hep.27877
- Kuo MD, Jamshidi N. Behind the numbers: decoding molecular phenotypes with radiogenomics-guiding principles and technical considerations. *Radiology*. (2014) 270:320–5. doi: 10.1148/radiol.13132195



37. Aerts HJ, Velazquez ER, Leijenaar RT, Parmar C, Grossmann P, Carvalho S, et al. Decoding tumour phenotype by noninvasive imaging using a quantitative radiomics approach. *Nat Commun.* (2014) 5:4006. doi: 10.1038/ncomms5644
38. Tran B, Dancey JE, Kamel-Reid S, McPherson JD, Bedard PL, Brown AM, et al. Cancer genomics: technology, discovery, and translation. *J Clin Oncol.* (2012) 30:647–60. doi: 10.1200/JCO.2011.39.2316
39. Malogolowkin MH, Katzenstein HM, Meyers RL, Krailo MD, Rowland JM, Haas J, et al. Complete surgical resection is curative for children with hepatoblastoma with pure fetal histology: a report from the Children's Oncology Group. *J Clin Oncol.* (2011) 29:3301–6. doi: 10.1200/JCO.2010.29.3837
40. Czauderna P, Garnier H. Hepatoblastoma: current understanding, recent advances, and controversies. *F1000Res.* (2018) 7:53. doi: 10.12688/f1000research.12239.1
41. Baheti AD, Chapman T, Rudzinski E, Albert CM, Stanescu AL. Diagnosis, histopathologic correlation and management of hepatoblastoma: what the radiologist needs to know. *Clin Imaging.* (2018) 52:273–9. doi: 10.1016/j.clinimag.2018.08.009
42. Tang LQ, Li CF, Li J, Chen WH, Chen QY, Yuan LX, et al. Establishment and validation of prognostic nomograms for endemic nasopharyngeal carcinoma. *J Natl Cancer Inst.* (2016) 108:djv291. doi: 10.1093/jnci/djv291
43. Yang P, Qiu J, Li J, Wu D, Wan X, Lau WY, et al. Nomograms for pre- and postoperative prediction of long-term survival for patients who underwent hepatectomy for multiple hepatocellular carcinomas. *Ann Surg.* (2016) 263:778–86. doi: 10.1097/SLA.0000000000001339
44. Yang J, Wu Q, Xu L, Wang Z, Su K, Liu R, et al. Integrating tumor and nodal radiomics to predict lymph node metastasis in gastric cancer. *Radiother Oncol.* (2020) 150:89–96. doi: 10.1016/j.radonc.2020.06.004

**Conflict of Interest:** The authors declare that the research was conducted in the absence of any commercial or financial relationships that could be construed as a potential conflict of interest.

Copyright © 2021 Jiang, Sun, Xia, Cheng, Xie, Guo and Guo. This is an open-access article distributed under the terms of the Creative Commons Attribution License (CC BY). The use, distribution or reproduction in other forums is permitted, provided the original author(s) and the copyright owner(s) are credited and that the original publication in this journal is cited, in accordance with accepted academic practice. No use, distribution or reproduction is permitted which does not comply with these terms.



# Cancer or Tuberculosis: A Comprehensive Review of the Clinical and Imaging Features in Diagnosis of the Confusing Mass

Yufan Xiang<sup>†</sup>, Chen Huang<sup>†</sup>, Yan He and Qin Zhang<sup>\*</sup>

Department of Neurosurgery, Department of Oncology, Department of Postgraduate Students, West China School of Medicine, Sichuan University, Chengdu, China

## OPEN ACCESS

### Edited by:

Changqiang Wu,  
North Sichuan Medical College, China

### Reviewed by:

Ke Xie,  
Sichuan Academy of Medical  
Sciences and Sichuan Provincial  
People's Hospital, China  
Peng Zhou,  
Sichuan Cancer Hospital, China

### \*Correspondence:

Qin Zhang  
76690830@qq.com

<sup>†</sup>These authors have contributed  
equally to this work

### Specialty section:

This article was submitted to  
Cancer Imaging and Image-directed  
Interventions,  
a section of the journal  
Frontiers in Oncology

Received: 20 December 2020

Accepted: 23 February 2021

Published: 28 April 2021

### Citation:

Xiang Y, Huang C, He Y and Zhang Q  
(2021) Cancer or Tuberculosis: A  
Comprehensive Review of the Clinical  
and Imaging Features in Diagnosis of  
the Confusing Mass.  
Front. Oncol. 11:644150.  
doi: 10.3389/fonc.2021.644150

Confusing masses constitute a challenging clinical problem for differentiating between cancer and tuberculosis diagnoses. This review summarizes the major theories designed to identify factors associated with misdiagnosis, such as imaging features, laboratory tests, and clinical characteristics. Then, the clinical experiences regarding the misdiagnosis of cancer and tuberculosis are summarized. Finally, the main diagnostic points and differential diagnostic criteria are explored, and the characteristics of multimodal imaging and radiomics are summarized.

**Keywords:** clinical diagnosis, cancer, tuberculosis, clinical feature, imaging feature, multimodal imaging, radiomics

## INTRODUCTION

Cancer and tuberculosis are two of the most common diseases affecting health worldwide. According to a recent World Health Organization (WHO) report, tuberculosis has one of the highest mortalities among all infectious diseases worldwide, causing an estimated 1.5 million deaths in 2018 (1). In 2020, an estimated 1,806,590 new cancer cases and 606,520 cancer-related deaths were estimated to occur in the USA. Tuberculosis is a great mimicker and diagnostic chameleon and is prone to be diagnosed as cancer (2). Moreover, due to its unusual presentations and lack of specific diagnostic tests, patients with cancer have been misdiagnosed with tuberculosis (3, 4). Therefore, these confusing masses represent a substantial clinical problem in the differential diagnosis of cancer and tuberculosis. Although many reports have addressed the differences between tuberculosis and cancer, comprehensive summaries are very rare (5).

Multimodal imaging involves the combination of at least two imaging tools to obtain more detailed, accurate images for diagnosis. Radiomics is a newly emerging form of computational medical imaging which involves the analysis and translation of medical images into quantitative data and have been rapidly developed in recent years. The analysis begins with acquiring a sufficient number of multimodal images of good quality and diversity. After extracting imaging features using a computer, trained algorithms can provide diagnostic aid or exact quantitative information by calculating the extracted features (6–9). Thus, the combination use of multimodal imaging and radiomics may enable a more accurate differential diagnosis for confused masses.

This review summarizes major theories designed to identify the factors associated with misdiagnosis and highlights key findings related to these confusing features to enhance diagnostic accuracy in clinical practice. Additionally, the potential for using multimodal imaging and radiomics in differentiating cancer and tuberculosis was also discussed.

## METHODS

We searched PubMed for reported cases associated with the misdiagnosis of cancer and tuberculosis using the search strategy (“diagnostic errors” [Mesh]) AND (“tuberculosis” [Mesh]) AND (“neoplasms” [Mesh]) from 2000 to 2020. Among these patients, 11 of 37 were misdiagnosed with tuberculosis, and 26 of 37 were misdiagnosed with tuberculosis. Notably, these confusing diseases can involve any organ, such as the liver, salivary glands (10), kidneys (11), nasopharynx (12), pancreas (13), and gallbladder (14). The diagnoses of 33 of these patients were confirmed by biopsy of the lesion, while three were diagnosed based on their body fluid cultures, and one patient was diagnosed based on empiric antituberculosis treatment.

In summary, the clinical manifestations of these cases are non-specific. The main characteristics leading to the misdiagnosis of tuberculosis as cancer included false-positive positron emission tomography/computerized tomography (PET/CT) findings, an oncologic history and elevated carbohydrate antigen 125 (CA 125) or carbohydrate antigen 19-9 (CA 19-9) levels, while the main reasons for misdiagnosing cancer as tuberculosis were a history of tuberculosis, a positive tuberculin test, and a history of a rare cancer. The features associated with the chosen cases are summarized in **Table 1**.

## RESULTS AND DISCUSSION

### Imaging Modalities

#### Computerized Tomography (CT)

Computerized tomography (CT) is commonly used in clinical practice to initially assess whether a mass is a malignant tumor or benign nodule according to the imaging features such as the size, shape, tumor border, and enhancement characteristics. A previous study reported a misdiagnosis case based on a head and neck CT scan showing a target sign with a ring enhancement around a central nidus of calcification, which led to the misdiagnosis of metastatic papillary adenocarcinoma (originating from primary lung carcinoma) as cerebral tuberculosis (36). The target sign of cerebral tuberculosis was first described in 1979 (43) and became a pathognomonic requirement for a cerebral tuberculosis diagnosis in 1988 (44). As a non-specific radiologic finding, the target sign most commonly indicated cerebral tuberculoma or metastatic adenocarcinoma, and recent clinical evidence suggested its specificity for tuberculosis (45, 46). Cerebral tuberculosis also shows a solid enhancing mass (47). Therefore, in the different clinical contexts, this target sign confuses clinicians (36).

Chest CT scans lead to higher rates of misdiagnosis between tuberculosis and cancer than head and neck CT and abdominal CT. The CT scan features of pulmonary tuberculosis include irregular linear opacity, discrete miliary nodules, calcified nodules or consolidation, parenchymal bands, and pericatricial emphysema (18). The most common findings of CT scans in patients with early bronchogenic spread of primary tuberculosis are 2–4 mm centrilobular nodules and branching linear lesions presenting as intrabronchiolar and peribronchiolar caseation necrosis. As the disease progresses, 2–4 mm centrilobular nodules

may coalesce and become lobular and consolidated or expand to 5–8 mm nodules (48). After antituberculous chemotherapy, resolution of the lesion occurs, resulting in bronchovascular distortion, bronchiectasis, emphysema, and fibrosis (49). CT scans of early miliary dissemination commonly feature ground-glass opacification with barely discernible nodules, followed by discrete miliary nodules representing round intrapulmonary lesions of <3 cm (50). Multiple pulmonary nodular lesions of varying sizes usually lead to misdiagnosis, especially when complemented by non-specific symptoms (2, 26, 32). In some tuberculosis cases, chest CTs showed multiple round nodules of different sizes, with clear boundaries and partial fusion (2). In addition, chest CT scans have also shown pneumonia in patients with cancer. A previous study reported that chest CT scans of a patient with large B cell non-Hodgkin's lymphoma showed pneumonia throughout the entire lung and diffuse ground glass opacities in both lung fields (26). Furthermore, in patients with histories of tuberculosis and cancer, the imaging manifestations are so similar that definitive diagnoses are difficult to make, and errors occur more frequently than in patients without histories of these diseases (38, 39).

The common features of abdominal CT scans related to misdiagnosis are the pancreatic head (13, 27) and peritoneum (15). The incidence of pancreatic tuberculosis is rare, and this disease may present as a heterogeneously enhanced structure in the pancreatic head with multiple enlarged lymph nodes surrounding the head of the pancreas (13). These findings lead to errors in the diagnosis of patients suspected of having a pancreatic neoplasm with multiple lymph node metastases (27). Regarding miliary tuberculosis of the abdomen, abdominal CT scans may show a solitary liver mass with an irregular enhancing rim and progressive enhancement, which likely leads to a radiographic diagnosis of intrahepatic cholangiocarcinoma (15).

In general, the CT imaging features of spinal tuberculosis include irregular lytic lesions and sclerosis, narrowing of the intervertebral disk space, disc collapse with eventual progression to kyphotic deformity, destruction of the anterior parts of adjacent vertebrae, formation of a large paravertebral abscess, and calcifications or sequestra within the paravertebral abscess (51). The clinical characteristics of spinal tuberculosis and cancer metastasis are non-specific. The imaging presentations of spinal metastatic adenocarcinoma are highly consistent with spinal tuberculosis, and misdiagnosis occurs (29). On the other hand, radiotherapy is often used for suspected malignant spinal lesions without histologic confirmation, and a definitive diagnosis of spinal tuberculosis was finally made (52). Therefore, in cases of spinal lesions of unknown origin, tuberculosis should be taken into consideration despite a previous diagnosis of cancer.

### Magnetic Resonance Imaging

Although the lung parenchyma was considered difficult to evaluate by magnetic resonance imaging (MRI) due to low proton density in the pulmonary tissue, susceptibility artifacts and respiratory motion artifacts (53), MRI would be helpful for discriminating pulmonary lesions because of its higher contrast resolution, absence of radiation, and multiple-parameter imaging (54). MRI has found relevant applications in the diagnosis

**TABLE 1** | Feature summary of related cases.

Study	Age	Gender	Misdiagnosis	Modified diagnosis	Clinical characters for leading misdiagnosis
Hang et al. (2)	73	M	Hematogenous spread of gastrointestinal tumor	Atypical systemic hematogenous disseminated tuberculosis	CA19-9↑↑; CT findings of the two lungs showed multiple round or round-like nodules of different sizes, with clear boundaries and partial fusion
Di Renzo et al. (15)	76	M	Peritoneal carcinomatosis	Miliary tuberculosis	PET-CT resulting, thick, FDG-avid ring surrounding the liver
	53	M	Intrahepatic cholangiocarcinoma	Miliary tuberculosis	CT showed a large hypoattenuating mass and multiple prominent retroperitoneal, pericaval, and periportal lymph nodes; MRI showed a large liver lesion in the setting of cirrhosis; PET/CT demonstrated the right hepatic lobe mass to be FDG-avid
Muhammad et al. (10)	44	F	Salivary gland neoplasm	Salivary gland tuberculosis	Fine-needle aspiration cytology (FNAC) showed few atypical cells and the possibility of salivary gland neoplasm could not be ruled out
Li et al. (16)	71	M	Tuberculous pleural effusion	Pleural mesothelial sarcoma	Elevated adenosine dehydrogenase (ADH) and positive tuberculin test
Gandhi et al. (17)	3	F	Tuberculosis	Maxillary myxoma	Elevated ADA and normal tumor markers in pericardial effusion
Chaker et al. (11)	52	F	Renal cell carcinoma	Renal tuberculosis	History of pulmonary tuberculosis
Lee et al. (18)	37	M	Metastasis of breast carcinoma	Tuberculosis	History of breast cancer; PET/CT also showed intense uptake
	49	M			
	60	M			
Narahari et al. (19)	19	F	Tuberculosis	Invasive mucinous adenocarcinoma	Young patients
Kumawat et al. (20)	22	M	Tuberculosis	Chronic myeloid leukemia	Brain imaging and cerebrospinal fluid analysis suspected to have tubercular meningitis
Feng et al. (3)	45	M	Tubercular meningitis	Primary central nervous system lymphoma	MR images disclosed the swollen cerebellum and cauda equina, with contrast enhancement in both meninges and nerve roots and extremely high protein level in CSF
Arora et al. (21)	25	F	Squamous cell carcinoma	Primary oral tuberculosis	Oral ulcer with chronic non-healing history
Nyunt et al. (22)	39	F	Tuberculosis	Diffuse large B cell lymphoma	Chest X-ray showed an anterior mediastinal mass and computed tomography (CT)-guided biopsy was reported as chronic granulomatous inflammation suggestive of tuberculosis
Zhang et al. (23)	30	F	Nasopharyngeal carcinoma	Tuberculosis	Fibrolaryngoscope examination suggested nasopharyngeal carcinoma
Tembani (24)	24	M	Tuberculous pericardial effusion	Pericardial angiosarcoma	Large fibrinous pericardial effusions
Mou et al. (25)	65	F	Submucosal tumor	Esophageal tuberculosis	Endoscopy suggested submucosal tumor
Naselli et al. (25)	1	F	Mediastinal malignant neoplasia	Tuberculosis	A large mediastinal mass dislocating and compressing the respiratory structures
Liu et al. (26)	64	F	Tuberculosis	Intravascular large B cell lymphoma	CT showed left upper lobe pneumonia and tuberculosis skin test (PPD test) was positive
Yang (27)	40	M	Pancreatic carcinoma	Pancreatic tuberculosis	Computed tomography revealed a pancreatic mass that mimicked a pancreatic head carcinoma
Moghadam (28)	43	M	Gastric cancer	Gastric tuberculosis	The detection of negative acid-fast bacilli in the histopathology specimen
Zheng et al. (29)	45	M	Spinal tuberculosis	Spinal metastatic adenocarcinoma	CT/MRI of the lumbar spine supported the initial diagnosis of spinal tuberculosis
Agoda et al. (30)	27	M	Testicular cancer	Testicular tuberculosis	Ultrasonography suggested testicular cancer
Suárez et al. (13)	42	M	Pancreatic carcinoma	Pancreatic tuberculosis	CT revealed a heterogeneously enhancing, multicystic structure in the pancreatic head
Kim et al. (12)	72	M	Nasopharyngeal carcinoma	Nasopharyngeal tuberculosis	A potentially false-positive PET/CT finding
Basu et al. (31)	17	M	Neck recurrence in differentiated thyroid carcinoma	Tuberculosis	PET/CT found intense FDG uptake in the nodal conglomerate
Ringshausen et al. (32)	67	M	Metastatic lung cancer	Tuberculosis	Had no history of previous TB or TB exposure; negative result supported tuberculosis

(Continued)



TABLE 1 | Continued

Study	Age	Gender	Misdiagnosis	Modified diagnosis	Clinical characters for leading misdiagnosis
Huang et al. (33)	44	F	Tuberculous spondylitis	Primary non-Hodgkin lymphoma	Primary non-Hodgkin lymphoma (PHL) of the spine is very rare
Bhatia et al. (34)	36	M	Branch-ducttype IPMT (BDT-IPMT), with liver metastasis	Pancreatic tuberculosis	Isolated pancreatic tuberculosis is a rare disease; CA19-9↑; The imaging features were suggestive of branch-ducttype IPMT (BDT-IPMT), with liver metastasis
Cantarella et al. (35)	52	F	Multifocal carcinoma	Glottic tuberculosis	Glottic tuberculosis is very rare
Ramia et al. (14)	64	M	Gallbladder cancer	Gallbladder tuberculosis	Gallbladder tuberculosis is very rare; false-positive PET/CT finding
Kong et al. (36)	74	M	Cerebral tuberculosis	Metastatic papillary adenocarcinoma	CT find a "target" lesion with a central core of calcification and a ring of enhancement.
Dursun et al. (37)	18	F	Endodermal sinus tumor	Peritoneal tuberculosis	Laboratory studies showed elevated CA125 and alpha fetoprotein levels suggesting an initial diagnosis of endodermal sinus tumor
Picolos et al. (38)	66	M	Metastasis of papillary thyroid carcinoma	Inactive pulmonary tuberculosis	History of thyroid cancer; positive result of radioiodine whole-body scintigraphy
Chen et al. (39)	80	F	Metastatic ovarian cancer	Pulmonary tuberculosis	Rapidly growing ovarian mass, elevated serum CA-125, and multiple pulmonary varying-sized nodular lesions
Gheorghe et al. (40)	63	F	Gastric cancer	Gastroduodenal tuberculosis	Gastroduodenal tuberculosis is a rare; endoscopy suggested gastric cancer
Kouraklis et al. (41)	35	F	Pancreatic carcinoma	Pancreatic tuberculosis	Frozen sections by direct trucut needle biopsy raised suspicions of a malignancy
O'Reilly et al. (42)	84	M	Breast carcinoma	Tuberculosis	Breast lump presenting clinically and radiologically as a carcinoma

↑ and ↑↑, Increase.

of chest diseases and the differential diagnosis of benign and malignant lung lesions (55, 56). Qi et al. (57) investigated the differences in the imaging features of mass-like tuberculosis and lung cancer on conventional MR sequences and found that most tuberculosis lesions showed low signal intensity on T2-weighted images while lung cancer showed high signal intensity; the signal of tuberculosis lesions was mostly uneven on T2-weighted images, but the signal of lung cancer was mostly uniform; most tuberculosis lesions showed high signal intensity on T1-weighted images while lung cancer showed low signal intensity. Besides, benign mediastinal lymph nodes in tuberculosis lesions showed a variety of signals on T2-weighted images, whereas the majority of metastatic mediastinal lymph nodes displayed slight homogeneous hyperintensity.

### Radiomics in Chest Imaging

Non-invasive and computer-aided alternatives have gradually been used in the differentiation of tuberculosis and lung cancer. In recent years, radiomics has attracted more and more attention due to its high-throughput extraction and distinguishing features from medical images, and to construct radiomics nomogram model to assist physicians to make the most accurate diagnosis (58–60). Cui et al. (61) developed and validated radiomics methods for distinguishing pulmonary tuberculosis from lung cancer based on CT images; they found the radiomics nomogram model exhibited good discrimination, with an AUC of 0.914 in the training cohort, and 0.900 in the validation cohort, showing that proposed radiomic methods can be used as a non-invasive tool for discrimination of tuberculosis and lung cancer on the basis of preoperative CT data. Another study (62) investigated the

preoperative differential diagnostic performance of a radiomics nomogram in tuberculous granuloma and lung adenocarcinoma appearing as solitary pulmonary solid nodules and found that the radiomics nomogram showed better diagnostic accuracy than any single model with the AUC 0.9660, 0.9342, and 0.9064 for the training, internal validation, and external validation cohorts, respectively, which similarly indicated the radiomics nomogram could preoperatively distinguish between lung cancer and tuberculosis.

### False-Positive PET/CT Findings

PET/CT is a powerful diagnostic method for characterizing masses, and it can more accurately assess mediastinal lymph nodes stages in cancer than CT (63). Many clinical conditions are now well-known to be responsible for false positives in oncological PET/CT scanning and are often related to uptake because of inflammation or infection processes. Infectious diseases, post-operative surgical conditions and radiation pneumonitis show as high fludeoxyglucose (FDG) uptake on PET/CT scans (64). Overexpression of glucose transporter-1 (GLUT-1) receptors in human macrophages, neutrophils, and lymphocytes following stimulation with cytokines or mutagens has been implicated in the intense uptake of FDG in inflammatory conditions. This highlights that standard uptake value (SUV) alone is an unreliable parameter for characterizing lesions in such a setting and should be used with caution and adequate correlation (31). A previous study showed that tuberculosis was mostly responsible (50%) for false positives in PET/CT (65). Tuberculosis at various locations, such as the gallbladder, nasopharynx, and peritoneum, is

usually misdiagnosed due to false-positive findings on PET/CT scans (14, 15). In a case of nasopharyngeal tuberculosis, PET/CT revealed intense activity in soft tissue masses in the nasopharynx and cervical lymph nodes (12). Combined with those of fibrolaryngoscope examination, the results may lead to misdiagnosis as nasopharyngeal carcinoma (23). In lymph node tuberculosis, PET/CT also showed intense uptake. Patients previously diagnosed with cancer with multifocal hypermetabolic lesions may confuse clinicians, leading to misdiagnosis (66). Thus, when PET/CT findings show increased FDG uptake in patients with cancer as well as suspected metastatic lesions, tuberculous lymphadenopathy should be considered a differential diagnosis.

## LABORATORY TESTS

### Non-Specificity of CA 19-9 Levels in Serum

CA 19-9 is synthesized by pancreatic, gastric, colon, biliary ductal, and endometrial tissues, and its serum levels are extremely low (67). As a tumor marker for pancreatic, hepatobiliary, and gastrointestinal cancer, high CA 19-9 levels are indicative of advanced disease and a poor prognosis (CA 19-9 level of >100 U/ml usually suggests unresectable or metastatic disease) (68, 69). In addition to cancer, overexpression of CA 19-9 has also been observed in some benign conditions, including gastrointestinal disorders, hepatobiliary system diseases, pneumonia, pleural effusion, renal failure, and systemic lupus erythematosus (SLE), and this phenomenon may be associated with glycan-mediated cell-cell interactions in mucosal immunity (67). Hence, this indicator has low specificity. In the misdiagnosis of cancer and tuberculosis, sharply increased CA 19-9 levels also play a key role (2). CA 19-9 was reportedly elevated in cases of pulmonary tuberculosis (70), hematogenous disseminated tuberculosis (2), and pancreatic tuberculosis (34, 71). In pulmonary disease, the median CA 19-9 level in patients with pulmonary tuberculosis (median CA 19-9 level: 5.85 U/ml) was significantly lower than that in patients with pulmonary non-tuberculous mycobacterial disease (median CA 19-9 level: 13.80 U/ml,  $p < 0.001$ ). Moreover, the CA 19-9 levels tended to decrease when pulmonary non-tuberculous mycobacterial disease was successfully treated, but this was not observed in pulmonary tuberculosis (70). Although the serum levels of CA 19-9 are commonly significantly lower in non-malignant diseases than in malignant diseases, CA 19-9 was reported to reach concentrations of 165 U/ml in hematogenous disseminated tuberculosis (2) and 66.84 U/ml in pancreatic tuberculosis (27). Therefore, although serum CA 19-9 levels lack specificity, CA 19-9 is the only marker of pancreatic cancer used in the clinic (69). When patients with increased CA 19-9 levels present atypically, tuberculosis may be the definitive diagnosis.

### Non-Specificity of Serum CA 125 Levels

Since the report on CA 125 expression in ovarian tumors published in the early 1980s, serum CA 125 levels have been utilized as a biomarker for the differential diagnosis of pelvic masses and have been widely used to monitor patients with ovarian cancer (72–74). Although the CA 125 levels in serum are elevated in over 80% of patients with ovarian cancer at the time of

initial diagnosis, using this parameter as a diagnostic marker can lead to clinical mistakes (75). In regard to peritoneal tuberculosis, patients with rapidly growing ovarian masses and elevated serum CA 125 levels usually lead to an initial diagnosis of ovarian cancer (37). Furthermore, tuberculosis is misdiagnosed as a metastatic ovarian cancer when patients show elevated serum CA 125 levels and multiple pulmonary nodular lesions (39). Thus, infectious diseases can mimic metastatic diseases and therefore increase the difficulty of diagnosis.

### Adenosine Deaminase Activity

Adenosine deaminase activity (ADA) activity is widely distributed in human tissues and is the highest in lymphoid tissues, and two isozymes of ADA exist, ADA1 and ADA2 (76). The serum concentrations of ADA1 are high in patients with tuberculosis, and previous evidence suggests that the increased ADA1 is the results of T cell lymphocyte stimulation by mycobacterial antigens (77). ADA has been developed and widely used for the diagnosis of tuberculosis. However, it is not a specific index for differentiating between tuberculosis and cancer diagnoses. Although elevated ADA levels usually indicate tuberculosis, the non-specific characteristics of cancer patients presenting with increased ADA levels and a positive tuberculin test can lead to misdiagnosis (16, 17).

### Carcinoembryonic Antigen and Cytokeratin Fraction 21-1 in Serum

Both carcinoembryonic antigen (CEA) and cytokeratin fraction 21-1 (CYFRA 21-1) are widely used as tumor markers and are not considered to be confusing indexes based on the reviewed literature above. What is more, Jia et al. report that the CEA and CYFRA 21-1 levels are very valuable for distinguishing between lung cancer and pulmonary tuberculosis (78).

### Fine-Needle Aspiration Cytology

The diagnosis of cancer is usually made based on histological analyses of excisional biopsies, fine-needle aspiration cytology, and liquid biopsy (16). Fine-needle aspiration cytology, a commonly used method that is minimally invasive, quick, and accurate, involves the use of a thin needle to acquire cellular material from a bodily lesion or mass for diagnostic purposes. However, fine-needle aspiration cytometry is less sensitive and specific for some malignant tumors, such as those of the parotid gland (6), pancreas (41), and malignant lymphoma (79). In the parotid gland, the sensitivity and specificity of fine-needle aspiration cytology are 79 and 96%, respectively (80). In lymphoma, the median rate at which fine-needle aspiration cytology yields a subtype-specific diagnosis of lymphoma is 74% (77). Several factors are related to the specificity of fine-needle aspiration cytometry. First, fine-needle aspiration is unsatisfactory, and only the inflammatory necrosis area is obtainable in cases of small amounts of tissue, deep locations, and hard masses. Determining whether necrosis is caused by tumor disease or simple inflammation is almost impossible (81). Second, during pathological examination, seriously degenerated tumor cells are poorly stained, leading to fuzzy chromatin staining and structures. In particular, it is easy to make a

misdiagnosis of tuberculosis when some carcinoma cells are spindle shaped, when nuclei exhibit vacuolar changes, and when lymphoma cells have lightly stained chromatin with obvious nucleoli and inflammatory necrosis (82). In addition, granulomatous inflammation often occurs in infectious diseases such as tuberculosis and mycosis and can also occur as a local inflammatory reaction in malignant tumors (83–85). Hence, although biopsy pathology is crucial for differentiating between cancer and tuberculosis, the findings of this examination may be a key factor underlying misdiagnosis.

## OTHER CHARACTERISTICS

### History of Previous Disease

Tuberculosis and cancer have a complex and dangerous liaison relationship (86). On the one hand, long-term chemotherapy, radiotherapy, and surgery will weaken the immune system in patients with cancer, which increases the risk of tuberculosis infection (87, 88). On the other hand, a large cohort study reported that pulmonary tuberculosis is associated with an increased risk of developing lung cancers (89). In clinical practice, without specific information, patients that have been previously diagnosed with cancer or tuberculosis may be misdiagnosed (38, 66).

### Definitive Diagnoses of Rare Diseases

Physicians usually do not apt to consider diagnosis of patients as rare diseases at first time, such as primary non-Hodgkin lymphoma of the spine (33), glottic tuberculosis (35), isolated pancreatic tuberculosis (34), and gallbladder tuberculosis (14). The limited knowledge and preconceived professional ideas may lead to errors in the diagnoses of these rare cancers and tuberculosis.

## CONCLUSIONS

CT is commonly used in clinical practice to initially assess diseases. However, the shortcomings of this technology also cause confusion. Fine-needle aspiration cytology is a commonly used biopsy method but not reliable. Excisional biopsies may be the best definitive diagnostic method for confusing masses. When

PET/CT findings show cancer patients with increased FDG uptake, tuberculosis should be considered a differential diagnosis, except in suspected cases of metastatic lesions. ADA and tumor markers are not specific indexes in the differential diagnosis of tuberculosis and metastasis. Thus, the following features are summarized to differentiate tuberculosis from cancer: (1) Fine-needle aspiration cytology has low sensitivity and specificity. (2) High FDG uptake on PET/CT scans can occur in cases of tuberculosis. (3) Tumor markers, including CA 19-9 and CA125, could be increased in tuberculosis patients. (4) ADA can be upregulated in cancer patients. (5) Histopathological examination and tuberculosis cultures are still the gold standards for diagnosis.

In the diagnosis of tuberculosis, multimodal imaging could offer high spatial resolution, soft tissue contrast, and biological information at the molecular level with high sensitivity. Radiomics technology use computers to extract numerous imaging features, especially the ones that cannot be distinguished by eyes directly, which may enable the ability of automatically distinguishing complex images and offer quantitative information. However, the characteristics and quality of the images cannot be automatically assessed, which means the extracted features should be calculated by using a computational-aided diagnostic algorithms before they can be used practically (7, 90). With well-trained algorithms, confusing masses can be identified based on the extracted features. Beig et al. provided an excellent example of using radiomic features on lung CT images to distinguish adenocarcinomas from granulomas (8).

In summary, although clinicians should conduct more studies on the special features of these diseases, a comprehensive review of misdiagnosis characteristics could also guide the plan for use of multimodal imaging and radiomics-based algorithms.

## AUTHOR CONTRIBUTIONS

QZ conceived and designed the experiments and revised the manuscript. YX, CH, and YH contributed reagents and materials and helped with the analysis. YX and CH wrote the manuscript. All authors contributed to the article and approved the submitted version.

## REFERENCES

- Harding E. WHO global progress report on tuberculosis elimination. *Lancet Respir Med.* (2020) 8:19. doi: 10.1016/S2213-2600(19)30418-7
- Hang TX, Fang G, Huang Y, Hu CM, Chen W. Misdiagnosis of a multi-organ involvement hematogenous disseminated tuberculosis as metastasis: a case report and literature review. *Infect Dis Poverty.* (2020) 9:66. doi: 10.1186/s40249-020-00681-8
- Feng M, Yang X, Ma Q, He Y. Retrospective analysis for the false positive diagnosis of PET-CT scan in lung cancer patients. *Medicine.* (2017) 96:e7415. doi: 10.1097/MD.00000000000007415
- Khurse BB, Kumar S, Deo S, Malik P, Kumar V, Kumar R, et al. Mediastinal nodal staging of non-small cell lung cancer using PET-CT in a tuberculosis-endemic country. *Ann Oncol.* (2017) 28:ii14. doi: 10.1093/annonc/mdx086.002
- Singh SK, Ahmad Z, Bhargava R, Pandey DK, Gupta V, Garg PK. Coincidence of tuberculosis and malignancy: a diagnostic dilemma. *South Med J.* (2009) 102:113. doi: 10.1097/SMJ.0b013e318188e32c
- Lee SY, Jeon SI, Jung S, Chung IJ, Ahn CH. Targeted multimodal imaging modalities. *Adv Drug Deliv Rev.* (2014) 76:60–78. doi: 10.1016/j.addr.2014.07.009
- Hosny A, Parmar C, Quackenbush J, Schwartz LH, Aerts HJWL. Artificial intelligence in radiology. *Nat Rev Cancer.* (2018) 18:500–10. doi: 10.1038/s41568-018-0016-5
- Beig N, Khorrami M, Alilou M, Prasanna P, Braman N, Orooji M, et al. Perinodular and intranodular radiomic features on lung CT images distinguish adenocarcinomas from granulomas. *Radiology.* (2019) 290:783–92. doi: 10.1148/radiol.2018180910
- Schwalbe N, Wahl B. Artificial intelligence and the future of global health. *Lancet.* (2020) 395:1579–86. doi: 10.1016/S0140-6736(20)30226-9

10. Muhammad T, Iftikhar H, Ikram M. Intraparotid tuberculosis misdiagnosed as neoplasm on FNAC. *J Coll Physicians Surg Pakistan*. (2019) 29:593–4. doi: 10.29271/jcpsp.2019.06.593
11. Chaker K, Chakroun M, Gharbi M, Chebil M. Renal tuberculosis mimicking renal cell carcinoma: a case report. *J Med Case Rep*. (2019) 13:139. doi: 10.1186/s13256-019-2073-0
12. Kim KS. Primary nasopharyngeal tuberculosis mimicking carcinoma: a potentially false-positive PET/CT finding. *Clin Nucl Med*. (2010) 35:346–8. doi: 10.1097/RLU.0b013e3181d624ff
13. Suárez-Moreno RM, Hernández-Ramírez DA, Madrazo-Navarro M, Salazar-Lozano CR, García-Álvarez KG, Espinoza-Álvarez A. Tuberculosis of the pancreas: an unsuspected cause of abdominal pain and fever. *Cir Cir*. (2010) 78:352–6. doi: 10.1016/j.ciresp.2009.12.024
14. Ramia JM, Muffak K, Fernández A, Villar J, Garrote D, Ferron JA. Gallbladder tuberculosis: False-positive PET diagnosis of gallbladder cancer. *World J Gastroenterol*. (2006) 12:6559–60. doi: 10.3748/wjg.v12.i40.6559
15. Di Renzo C, Tabrizian P, Kozuch DE, Fiel MI, Schwartz ME. Abdominal tuberculosis mimicking cancer clinically and on fluorodeoxyglucose (FDG)-positron emission tomography (PET) imaging: a two-case series. *Am J Case Rep*. (2020) 21:e918901. doi: 10.12659/AJCR.918901
16. Li WQ, Fu AS, Shao DF, Zhang Q, Wang MH, Wang HY, et al. Elevated adenosine dehydrogenase (ADH) and positive tuberculin test firstly misdiagnosed as tuberculous pleural effusion finally proved as pleural mesothelial sarcoma by thoracoscopic biopsy pathology: A case report and literature review. *Clin Lab*. (2019) 65:190323. doi: 10.7754/Clin.Lab.2019.190323
17. Gandhi D, Pawar V, Chandane P, Shah I. Maxillary myxoma misdiagnosed as tuberculosis. *Trop Doct*. (2019) 49:227–9. doi: 10.1177/0049475519829599
18. Lee JY, Lee KS, Jung KJ, Han J, Kwon OJ, Kim J, et al. Pulmonary tuberculosis: CT and pathologic correlation. *J Comput Assist Tomogr*. (2000) 24:691–8. doi: 10.1097/00004728-200009000-00005
19. Narahari NK, Uppin SG, Kapoor A, Stalin BJ, Paramjyothi GK. Invasive mucinous adenocarcinoma of the lung in a 19-year-old female. *Asian Cardiovasc Thorac Ann*. (2018) 26:635–9. doi: 10.1177/0218492318804951
20. Kumawat BL, Sharma CM, Saini PK, Garg A. Central nervous system blast crisis of chronic myeloid leukaemia misdiagnosed as tubercular meningitis. *BMJ Case Rep*. (2018) 2018:223923. doi: 10.1136/bcr-2017-223923
21. Arora KS, Garg S, Kaur P, Mohapatra S. Primary oral tuberculosis on the tongue mimicking squamous cell carcinoma. *Indian J Tuberc*. (2018) 65:84–6. doi: 10.1016/j.ijtb.2016.09.019
22. Nyunt WWT, Wong YP, Wan Jamaludin WF, Abdul Wahid SFS. Diffuse large B cell lymphoma with chronic granulomatous inflammation. *Malays J Pathol*. (2016) 38:55–9.
23. Zhang Y, Chen Y, Huang Z, Cai L, Wu J. Nasopharyngeal tuberculosis mimicking nasopharyngeal carcinoma on 18F-FDG PET/CT in a young patient. *Clin Nucl Med*. (2015) 40:518–20. doi: 10.1097/RLU.0000000000000656
24. Tembani-Munyandu NC, Katsidzira L, Makunike-Mutasa R, Chinogureyi A. An unusual cause of a large fibrinous pericardial effusion. *Cardiovasc J Afr*. (2015) 26:e7–e10. doi: 10.5830/CVJA-2014-075
25. Naselli A, Granata C, Garaventa A, Conte M, Losurdo G, Castagnola E. Tuberculosis diagnosed after chemotherapy for presumed mediastinal malignant neoplasia. *Pediatr Blood Cancer*. (2014) 61:1897–8. doi: 10.1002/pbc.25053
26. Liu C, Lai N, Zhou Y, Li S, Chen R, Zhang N. Intravascular large B-cell lymphoma confirmed by lung biopsy. *Int J Clin Exp Pathol*. (2014) 7:6301–6.
27. Yang Y-J. Pancreatic tuberculosis mimicking pancreatic carcinoma during anti-tuberculosis therapy: a case report. *World J Clin Cases*. (2014) 2:167–9. doi: 10.12998/wjcc.v2.i5.167
28. Moghadam AG, Alborzi A, Pouladfar G, Monabati A. Primary gastric tuberculosis mimicking gastric cancer: a case report. *J Infect Dev Ctries* (2013) 7(04):355–7. doi: 10.3855/jidc.2598
29. Zheng CY, Liu DX, Luo SW, Du SX. Imaging presentation highly manifested as tuberculosis in a case of spinal metastatic carcinoma. *Orthopedics*. (2011) 34:e436–8. doi: 10.3928/01477447-20110627-32
30. Agoda-Koussema L, Tchaou M, Adjénou V, Sonhayé L, Anoukoum T, Tengué K, et al. Heterogeneous testicle on ultrasonography: consider tuberculosis after cancer in endemic zone. *Med Trop*. (2011) 71:100.
31. Basu S, Menon S. FDG avid supraclavicular neck adenopathy of tubercular etiology masquerading as neck recurrence in differentiated thyroid carcinoma: potential source of false positive FDG-PET study. *Int J Oral Maxillofac Surg*. (2010) 39:628–9. doi: 10.1016/j.ijom.2010.01.021
32. Ringshausen FC, Tannapfel A, Nicolas V, Weber A, Duchna HW, Schultze-Werninghaus G, et al. A fatal case of spinal tuberculosis mistaken for metastatic lung cancer: recalling ancient Pott's disease. *Ann Clin Microbiol Antimicrob*. (2009) 8:32. doi: 10.1186/1476-0711-8-32
33. Huang B, Li CQ, Liu T, Zhou Y. Primary non-Hodgkin's lymphoma of the lumbar vertebrae mimicking tuberculous spondylitis: a case report. *Arch Orthop Trauma Surg*. (2009) 129:1621–5. doi: 10.1007/s00402-009-0835-7
34. Bhatia V, Garg PK, Arora VK, Sharma R. Isolated pancreatic tuberculosis mimicking intraductal pancreatic mucinous tumor. *Gastrointest Endosc*. (2008) 68:610–1. doi: 10.1016/j.gie.2007.12.022
35. Cantarella G, Pagani D, Fasano V, Scaramellini G. Glottic tuberculosis masquerading as early multifocal carcinoma. *Tumori J*. (2007) 93:302–4. doi: 10.1177/030089160709300315
36. Kong A, Koukourou A, Boyd M, Crowe G. Metastatic adenocarcinoma mimicking “target sign” of cerebral tuberculosis. *J Clin Neurosci*. (2006) 13:955–8. doi: 10.1016/j.jocn.2005.11.039
37. Dursun P, Ersoz S, Gultekin M, Aksan G, Yüce K, Ayhan A. Disseminated peritoneal tuberculosis mimicking advanced-stage endodermal sinus tumor: a case report. *Int J Gynecol Cancer*. (2006) 1:303–7. doi: 10.1111/j.1525-1438.2006.00205.x
38. Picolos MK, Habra M, Safdar A, Sarlis NJ. Inactive pulmonary tuberculosis mimicking metastasis from papillary thyroid carcinoma in diagnostic radioiodine whole-body scintigraphy. *Thyroid*. (2005) 15:1105–6. doi: 10.1089/thy.2005.15.1105
39. Chen CH, Huang CY, Chow SN. Early-stage ovarian carcinoma combined with pulmonary tuberculosis mimicking advanced ovarian cancer: a case report. *Int J Gynecol Cancer*. (2004) 14:1007–11. doi: 10.1111/j.1048-891X.2004.014543.x
40. Gheorghe L, Băncilă I, Gheorghe C, Herlea V, Vasilescu C, Aposteanu G. Antro-duodenal tuberculosis causing gastric outlet obstruction—a rare presentation of a protean disease. *Rom J Gastroenterol*. (2002) 11:149–52.
41. Kouraklis G, Glinavou A, Karayiannakis A, Karatzas G. Primary tuberculosis of the pancreas mimicking a pancreatic tumor. *Int J Pancreatol*. (2001) 29:151–3. doi: 10.1385/ijgc:29:3:151
42. O'Reilly M, Patel K, Cummins R. Tuberculosis of the breast presenting as carcinoma. *Mil Med*. (2000) 165:800–2. doi: 10.1159/000054256
43. Welchman JM. Computerised tomography of intracranial tuberculomata. *Clin Radiol*. (1979) 30:567–73. doi: 10.1016/S0009-9260(79)80199-3
44. van Dyk A. CT of intracranial tuberculomas with specific reference to the “target sign”. *Neuroradiology*. (1988) 30:329–36. doi: 10.1007/BF00328184
45. Schaller MA, Wicke F, Foerch C, Weidauer S. Central nervous system tuberculosis: etiology, clinical manifestations and neuroradiological features. *Clin Neuroradiol*. (2019) 29:3–18. doi: 10.1007/s00062-018-0726-9
46. Bernaerts A, Vanhoenacker FM, Parizel PM, Van Goethem JWM, van Altena R, Laridon A, et al. Tuberculosis of the central nervous system: overview of neuroradiological findings. *Eur Radiol*. (2003) 13:1876–90. doi: 10.1007/s00330-002-1608-7
47. Yanardag H, Uygun S, Yumuk V, Caner M, Canbaz B. Cerebral tuberculosis mimicking intracranial tumour. *Singapore Med J*. (2005) 46:731–3.
48. Skoura E, Zumla A, Bomanji J. Imaging in tuberculosis. *Int J Infect Dis*. (2015) 32:87–93. doi: 10.1016/j.ijid.2014.12.007
49. Im JG, Itoh H, Shim YS, Lee JH, Ahn J, Han MC, et al. Pulmonary tuberculosis: CT findings - Early active disease and sequential change with antituberculous therapy. *Radiology*. (1993) 186:653–60. doi: 10.1148/radiology.186.3.8430169
50. Setio AAA, Traverso A, de Bel T, Berens MSN, Bogaard C van den, Cerello P, et al. Validation, comparison, and combination of algorithms for automatic detection of pulmonary nodules in computed tomography images: the LUNA16 challenge. *Med Image Anal*. (2017) 42:1–13. doi: 10.1016/j.media.2017.06.015
51. Ansari S, Amanullah M, Ahmad K, Rauniyar RK. Pott's spine: diagnostic imaging modalities and technology advancements. *N Am J Med Sci*. (2013) 5:404–11. doi: 10.4103/1947-2714.115775
52. Jutte PC, van Altena R, Pras E, Thijn CJP. Causes of misdiagnosis and mistreatment of spinal tuberculosis with radiotherapy in nonendemic areas: a



- pitfall in diagnosis and treatment: hazards of radiotherapy on the tuberculous lesion. *Spine*. (2005) 30:E300–4. doi: 10.1097/01.brs.0000163886.20464.02
53. Kapur S, Bhalla A S, Jana M. Pediatric chest MRI: a review. *Indian J Pediatr*. (2019) 86:842–53. doi: 10.1007/s12098-018-02852-w
  54. Rizzi EB, Schinina V, Cristofaro M, Goletti D, Palmieri F, Bevilacqua N, et al. Detection of pulmonary tuberculosis: comparing MR imaging with HRCT. *BMC Infect Dis*. (2011) 11:243. doi: 10.1186/1471-2334-11-243
  55. Schaefer J F, Vollmar J, Schick F, Vonthein R, Seemann MD, Aebert H, et al. Solitary pulmonary nodules: dynamic contrast-enhanced MR imaging—perfusion differences in malignant and benign lesions. *Radiology*. (2004) 232:544–53. doi: 10.1148/radiol.2322030515
  56. Fujimoto K. Usefulness of contrast-enhanced magnetic resonance imaging for evaluating solitary pulmonary nodules. *Cancer imaging*. (2008) 8:36–44. doi: 10.1102/1470-7330.2008.0009
  57. Qi LP, Chen KN, Zhou XJ, Tang L, Liu YL, Li XT, et al. Conventional MRI to detect the differences between mass-like tuberculosis and lung cancer. *J Thorac Dis*. (2018) 10:5673–84. doi: 10.21037/jtd.2018.09.125
  58. Aerts HJWL, Velazquez ER, Leijenaar RTH, Parmar C, Grossmann P, Carvalho S, et al. Decoding tumour phenotype by noninvasive imaging using a quantitative radiomics approach. *Nat Commun*. (2014) 5:4006. doi: 10.1038/ncomms5006
  59. Lambin P, Rios-Velazquez E, Leijenaar R, Carvalho S, van Stiphout RGPM, Granton P, et al. Radiomics: extracting more information from medical images using advanced feature analysis. *Eur J Cancer*. (2012) 48:441–6. doi: 10.1016/j.ejca.2011.11.036
  60. Zhou H, Dong D, Chen B, Fang M, Cheng Y, Gan Y, et al. Diagnosis of distant metastasis of lung cancer: based on clinical and radiomic features. *Transl Oncol*. (2018) 11:31–6. doi: 10.1016/j.tranon.2017.10.010
  61. Cui EN, Yu T, Shang SJ, Wang XY, Jin YL, Dong Y, et al. Radiomics model for distinguishing tuberculosis and lung cancer on computed tomography scans. *World J Clin Cases*. (2020) 8:5203–12. doi: 10.12998/wjcc.v8.i21.5203
  62. Feng B, Chen X, Chen Y, Liu K, Li K, Liu X, et al. Radiomics nomogram for preoperative differentiation of lung tuberculoma from adenocarcinoma in solitary pulmonary solid nodule. *Eur J Radiol*. (2020) 128:109022. doi: 10.1016/j.ejrad.2020.109022
  63. Boland GWL, Dwamena BA, Sangwaiya MJ, Goehler AG, Blake MA, Hahn PF, et al. Characterization of adrenal masses by using FDG PET: a systematic review and meta-analysis of diagnostic test performance. *Radiology*. (2011) 259:117–26. doi: 10.1148/radiol.111100569
  64. Chang JM, Lee HJ, Goo JM, Lee HY, Lee JJ, Chung JK, et al. False positive and false negative FDG-PET scans in various thoracic diseases. *Korean J Radiol*. (2006) 7:57–69. doi: 10.3348/kjr.2006.7.1.57
  65. Yen RF, Chen KC, Lee JM, Chang YC, Wang J, Cheng MF, et al. 18F-FDG PET for the lymph node staging of non-small cell lung cancer in a tuberculosis-endemic country: Is dual time point imaging worth the effort? *Eur J Nucl Med Mol Imaging*. (2008) 35:1305–15. doi: 10.1007/s00259-008-0733-1
  66. Lee S, Woo SU, Kim WY, Lee JB, Eo JS. Lymphadenopathy by tuberculosis seemed like metastasis on FDG PET/CT in patients with breast carcinoma. *Breast J*. (2019) 25:723–5. doi: 10.1111/tbj.13248
  67. Pavai S, Yap SF. The clinical significance of elevated levels of serum CA 19-9. *Med J Malaysia*. (2003) 58:667–72.
  68. Ballehaninna UK, Chamberlain RS. Serum CA 19-9 as a biomarker for pancreatic cancer—a comprehensive review. *Indian J Surg Oncol*. (2011) 2:88–100. doi: 10.1007/s13193-011-0042-1
  69. Scarà S, Bottoni P, Scatena R. CA 19-9: biochemical and clinical aspects. *Adv Exp Med Biol*. (2015) 867:247–60. doi: 10.1007/978-94-017-7215-0\_15
  70. Hong JY, Jang SH, Kim SY, Chung KS, Song JH, Park MS, et al. Elevated serum CA 19-9 levels in patients with pulmonary nontuberculous mycobacterial disease. *Brazil J Infect Dis*. (2016) 20:26–32. doi: 10.1016/j.bjid.2015.09.005
  71. Falkowski AL, Graber J, Haack HG, Tarr PE, Rasch H. Isolated pancreatic tuberculosis: a case report and radiological comparison with cystic pancreatic lesions radiological comparison with cystic pancreatic lesions. *J Radiol Case Rep*. (2013) 7:1–11. doi: 10.3941/jrcr.v7i1.1292
  72. Karam AK, Karlan BY. Ovarian cancer: the duplicity of CA125 measurement. *Nat Rev Clin Oncol*. (2010) 7:335–9. doi: 10.1038/nrclinonc.2010.44
  73. Felder M, Kapur A, Gonzalez-Bosquet J, Horibata S, Heintz J, Albrecht R, et al. MUC16 (CA125): tumor biomarker to cancer therapy, a work in progress. *Mol Cancer*. (2014) 13:129. doi: 10.1186/1476-4598-13-129
  74. Duffy MJ, Bonfrer JM, Kulpa J, Rustin GJS, Soletormos G, Torre GC, et al. CA125 in ovarian cancer: European Group on Tumor Markers guidelines for clinical use. *Int J Gynecol Cancer*. (2005) 15:679–91. doi: 10.1111/j.1525-1438.2005.00130.x
  75. Dochez V, Caillon H, Vaucel E, Dimet J, Winer N, Ducarme G. Biomarkers and algorithms for diagnosis of ovarian cancer: CA125, HE4, RMI and ROMA, a review. *J Ovarian Res*. (2019) 12:28. doi: 10.1186/s13048-019-0503-7
  76. Kurata N. Adenosine deaminase. *Nihon Rinsho*. (1995) 53:1178–83. doi: 10.1042/bj0360478
  77. Barua R, Hossain M. Adenosine deaminase in diagnosis of tuberculosis: a review. *Anwer Khan Mod Med Coll J*. (2014) 52:43–8. doi: 10.3329/akmmcj.v5i2.21132
  78. Jia H, Zhang L, Wang B. The value of combination analysis of tumor biomarkers for early differentiating diagnosis of lung cancer and pulmonary tuberculosis. *Ann Clin Lab Sci*. (2019) 49:645–9.
  79. Frederiksen JK, Sharma M, Casulo C, Burack WR. Systematic review of the effectiveness of fine-needle aspiration and/or core needle biopsy for subclassifying lymphoma. *Arch Pathol Lab Med*. (2015) 139:245–51. doi: 10.5858/arpa.2013-0674-RA
  80. Kuan EC, Mallen-St. Clair J, St. John MA. Evaluation of parotid lesions. *Otolaryngol Clin North Am*. (2016) 49:313–25. doi: 10.1016/j.otc.2015.10.004
  81. Monaco SE. Fine needle aspiration cytology. *Pathobiol Hum Dis*. (2014) 3379–98. doi: 10.1016/B978-0-12-386456-7.06504-7
  82. Garg SK, Tiwari RP, Tiwari D, Singh R, Malhotra D, Ramnani VK, et al. Diagnosis of tuberculosis: available technologies, limitations, and possibilities. *J Clin Lab Anal*. (2003) 17:155–63. doi: 10.1002/jcla.10086
  83. Trinchieri G. Cancer and inflammation: an old intuition with rapidly evolving new concepts. *Annu Rev Immunol*. (2012) 30:677–706. doi: 10.1146/annurev-immunol-020711-075008
  84. Candido J, Hagemann T. Cancer-related inflammation. *J Clin Immunol*. (2013) 33(Suppl. 1):S79–84. doi: 10.1007/s10875-012-9847-0
  85. Grivennikov SI, Greten FR, Karin M. Immunity, inflammation, and cancer. *Cell*. (2010) 140:883–99. doi: 10.1016/j.cell.2010.01.025
  86. Vento S, Lanzafame M. Tuberculosis and cancer: a complex and dangerous liaison. *Lancet Oncol*. (2011) 12:520–2. doi: 10.1016/S1470-2045(11)70105-X
  87. Cheng MP, Chakra CNA, Yansouni CP, Cnossen S, Shrier I, Menzies D, et al. Risk of active tuberculosis in patients with cancer: a systematic review and metaanalysis. *Clin Infect Dis*. (2017) 64:635–44. doi: 10.1093/cid/ciw838
  88. Simonsen DE, Farkas DK, Horsburgh CR, Thomsen RW, Sørensen HT. Increased risk of active tuberculosis after cancer diagnosis. *J Infect*. (2017) 74:590–8. doi: 10.1016/j.jinf.2017.03.012
  89. Yu YH, Liao CC, Hsu WH, Chen HJ, Liao WC, Muo CH, et al. Increased lung cancer risk among patients with pulmonary tuberculosis: a population cohort study. *J Thorac Oncol*. (2011) 11:1899–906. doi: 10.1097/JTO.0b013e3181fb4fcc
  90. Kulkarni S, Jha S. Artificial intelligence, radiology, and tuberculosis: a review. *Acad Radiol*. (2020) 27:71–5. doi: 10.1016/j.acra.2019.10.003

**Conflict of Interest:** The authors declare that the research was conducted in the absence of any commercial or financial relationships that could be construed as a potential conflict of interest.

Copyright © 2021 Xiang, Huang, He and Zhang. This is an open-access article distributed under the terms of the Creative Commons Attribution License (CC BY). The use, distribution or reproduction in other forums is permitted, provided the original author(s) and the copyright owner(s) are credited and that the original publication in this journal is cited, in accordance with accepted academic practice. No use, distribution or reproduction is permitted which does not comply with these terms.



# Individualized Prediction of Colorectal Cancer Metastasis Using a Radiogenomics Approach

Qin Liu<sup>1†</sup>, Jie Li<sup>1†</sup>, Lin Xu<sup>2†</sup>, Jiasi Wang<sup>3†</sup>, Zhaoping Zeng<sup>1</sup>, Jiangping Fu<sup>1</sup>, Xuan Huang<sup>4</sup>, Yanpeng Chu<sup>1</sup>, Jing Wang<sup>5\*</sup>, Hong-Yu Zhang<sup>6\*</sup> and Fanxin Zeng<sup>1,7\*</sup>

<sup>1</sup> Department of Clinical Research Center, Dazhou Central Hospital, Dazhou, China, <sup>2</sup> Department of Radiology, Dazhou Central Hospital, Dazhou, China, <sup>3</sup> Department of Clinical Laboratory, Dazhou Central Hospital, Dazhou, China, <sup>4</sup> Department of Ophthalmology, Medical Research Center, Beijing Chaoyang Hospital, Capital Medical University, Beijing, China, <sup>5</sup> Department of Clinical Laboratory, Beijing Chaoyang Hospital, Capital Medical University, Beijing, China, <sup>6</sup> Hubei Key Laboratory of Agricultural Bioinformatics, College of Informatics, Huazhong Agricultural University, Wuhan, China, <sup>7</sup> School of Medical and Life Sciences, Chengdu University of Traditional Chinese Medicine, Chengdu, China

## OPEN ACCESS

### Edited by:

Peng Mi,  
Sichuan University, China

### Reviewed by:

Jiyan Zhou,  
Guangzhou Medical University, China  
Gang Li,  
Peking University First Hospital, China

### \*Correspondence:

Fanxin Zeng  
zengfx@pku.edu.cn  
Hong-Yu Zhang  
zhy630@mail.hzau.edu.cn  
Jing Wang  
kyc6636@126.com

<sup>†</sup>These authors have contributed  
equally to this work

### Specialty section:

This article was submitted to  
Cancer Imaging and Image-directed  
Interventions,  
a section of the journal  
Frontiers in Oncology

Received: 24 October 2020

Accepted: 15 February 2021

Published: 28 April 2021

### Citation:

Liu Q, Li J, Xu L, Wang J, Zeng Z,  
Fu J, Huang X, Chu Y, Wang J,  
Zhang H-Y and Zeng F (2021)  
Individualized Prediction of Colorectal  
Cancer Metastasis Using a  
Radiogenomics Approach.  
Front. Oncol. 11:620945.  
doi: 10.3389/fonc.2021.620945

**Objectives:** To evaluate whether incorporating the radiomics, genomics, and clinical features allows prediction of metastasis in colorectal cancer (CRC) and to develop a preoperative nomogram for predicting metastasis.

**Methods:** We retrospectively analyzed radiomics features of computed tomography (CT) images in 134 patients (62 in the primary cohort, 28 in the validation cohort, and 44 in the independent-test cohort) clinicopathologically diagnosed with CRC at Dazhou Central Hospital from February 2018 to October 2019. Tumor tissues were collected from all patients for RNA sequencing, and clinical data were obtained from medical records. A total of 854 radiomics features were extracted from enhanced venous-phase CT of CRC. Least absolute shrinkage and selection operator regression analysis was utilized for data dimension reduction, feature screen, and radiomics signature development. Multivariable logistic regression analysis was performed to build a multiscale predicting model incorporating the radiomics, genomics, and clinical features. The receiver operating characteristic curve, calibration curve, and decision curve were conducted to evaluate the performance of the nomogram.

**Results:** The radiomics signature based on 16 selected radiomics features showed good performance in metastasis assessment in both primary [area under the curve (AUC) = 0.945, 95% confidence interval (CI) 0.892–0.998] and validation cohorts (AUC = 0.754, 95% CI 0.570–0.938). The multiscale nomogram model contained radiomics features signatures, four-gene expression related to cell cycle pathway, and CA 19-9 level. The multiscale model showed good discrimination performance in the primary cohort (AUC = 0.981, 95% CI 0.953–1.000), the validation cohort (AUC = 0.822, 95% CI 0.635–1.000), and the independent-test cohort (AUC = 0.752, 95% CI 0.608–0.896) and good calibration. Decision curve analysis confirmed the clinical application value of the multiscale model.

**Conclusion:** This study presented a multiscale model that incorporated the radiological eigenvalues, genomics features, and CA 19-9, which could be conveniently utilized to facilitate the individualized preoperatively assessing metastasis in CRC patients.

**Keywords:** colorectal cancer, metastasis, radiomics, genomics, carbohydrate antigen 19-9

## INTRODUCTION

Colorectal cancer (CRC) is a common malignant tumor, for which the incidence of men is usually higher than women. In 2012, more than 690,000 people died of CRC worldwide (1). At present, the main treatment of CRC is surgical resection, supplemented by chemotherapy or radiotherapy. However, more than 20% of patients are still life-threatening because of disease metastasis (2). Accurate prediction of tumor metastasis is of great significance for the individualized treatment and prognosis of patients with CRC (3). Computed tomography (CT), a non-invasive imaging tool, has been used for screening and preoperative evaluation of various cancers (4–7). In CRC patients, the venous phase of enhanced CT scan shows a stronger resolution and good response to the size and scope of tumors (8). However, CT has limited specificity in the differential diagnosis of distal metastasis, metastatic lymph nodes, and lesions with smaller diameter (9, 10). Therefore, we need to find more specific method to distinguish CRC metastasis.

Quantitative high-throughput analysis of a large number of image data obtains radiomics eigenvalues, which allows for more in-depth mining of CT data (11, 12). Radiological eigenvalues can be used as predictive biomarkers to diagnose, treat, and evaluate the disease. Several investigators have shown that the radiomics is closely related to tumor stages and grades (13, 14), and the combined analysis of a set of biomarkers is more practical than single indicators (15). CA-19-9, known as a tumor marker, has been reported to be significantly increased in gastrointestinal cancers (16, 17). It is also used to combine with other clinical indicators evaluating the metastasis of CRC (18). A study has reported that combined radiomics signatures and clinical risk factors such as carcinoembryonic antigen (CEA) are valuable to evaluate the lymph node metastasis in CRC patients (19). Although these features obtained by radiomics that are combined with clinical indicators have been used as useful predictors to predict indeterminate pulmonary nodules and lymph node metastasis in CRC (19, 20), these biomarkers often focus on one or a few aspects of the progression in CRC. Few studies have combined more accurate predictors from different dimensions such as genomics, which may provide more available risk assessment information. In recent years, genomics plays an important role in the diagnosis and treatment of cancers (21). Some studies have explored the metastasis and precise treatment of CRC through genomics analysis (22, 23). The abnormal cell cycle is a typical characteristic of tumor (24). *CDKN2A*, *TP53*, *ATM*, and *MYC* play an important role in cell cycle, which regulates the cell growth and proliferation (25, 26). However, an optimal approach, combined with more dimensions, is needed to improve the prediction model performance.

Therefore, the aim of this study was to develop and validate a multiscale model by combining radiomics signatures, genomics features, and clinical risk factors for evaluation of preoperative metastasis in CRC patients.

## MATERIALS AND METHODS

### Patients

The study was approved by the ethics committee of Dazhou Central Hospital (IRB00000003-17003) and obtained informed consent from patients. The study retrospectively reviewed 267 patients clinicopathologically diagnosed with CRC from February 2018 to March 2019 as primary and validation cohorts and reviewed 116 patients from April 2019 to October 2019 as independent-test cohort. The participants underwent surgical resection for therapeutic purposes. Finally, 90 patients were included in primary and validation cohorts. Independent-test cohort included 44 CRC patients. All CRC tissue samples were obtained intraoperatively for RNA sequencing and stored in liquid nitrogen. The clinical stage of tumors was according to tumor–node–metastasis staging system [American Joint Committee on Cancer, 8th edition, staging system]. The metastasis was defined as patients with pathologically diagnosed CRC metastasis after surgery or within 3 months after surgery.

The 90 participants were randomly divided into a primary cohort and a validation cohort at a ratio of ~7:3. In total, the primary cohort comprised 62 patients (38 males and 24 females, 24 metastasis and 38 non-metastasis patients). There were 28 patients in the validation cohort (16 males and 12 female, 11 metastasis, and 17 non-metastasis patients). In the independent-test cohort, there were 25 metastasis and 19 non-metastasis patients (29 males and 15 females). Clinical data, including age, gender, preoperative histological grade, and CA 19-9, were obtained from medical records.

Serum CA 19-9 levels of the patients were detected by CA 19-9 test kit (Roche Diagnostics Corp., Switzerland) with cobas e601 system at the initial hospitalization. The recommended normal range of CA 19-9 is 0–27 ng/mL. The flowchart of the study is shown in **Figures 1A,B**. Inclusion criteria for the study were as follows: (1) patients with baseline and 2-weeks complete enhanced CT examinations; (2) CT images were obtained with 1-mm thickness; (3) the patient diagnosed with CRC by pathology; and (4) age 18–75 years. Exclusion criteria were as follows: (1) patients with inflammatory diseases, including infection, ischemic heart disease, collagen disease, intestinal perforation, or obstruction; (2) patients with familial adenomatous polyposis or hereditary nonpolyposis colon cancer; and (3) patients, lacking CT images or with poor image quality, could not extract radiomics features.

### CT Image Acquisition and Analysis

The imaging ensemble data acquisition was performed on the abdominal CT enhanced scan using Siemens Definition AS 64-row CT. The acquisition parameters were as follows: 100 kV, CAREdose4D, 0.5-s rotation time, detector collimation: 128 × 0.6 mm, field of view 380 × 380 mm, matrix: 512 × 512; after routine CT plain scan, 60–80 mL iodophor contrast agent (320 mg/mL) was used at a speed of 2–3 mL/s and with a high-pressure syringe (Ulrich, Germany), and then 40 mL of normal saline was injected, after 23 s. Arterial scan, 60-s postvenous scan, delayed the scan after 120 s; delayed prolonged scan time according to the lesion, contrast-enhanced CT reconstruction with thickness 1 mm. Then, the CT image of the portal vein (thickness 1.0 mm)

**Abbreviations:** CRC, colorectal cancer; CT, computed tomography; CA 19-9, carbohydrate antigen 19-9; AUC, area under curve; ROC, receiver operating characteristic curve; LASSO, least absolute shrinkage and selection operator; CI, confidence interval; PPV, positive predictive value; NPV, negative predictive value.

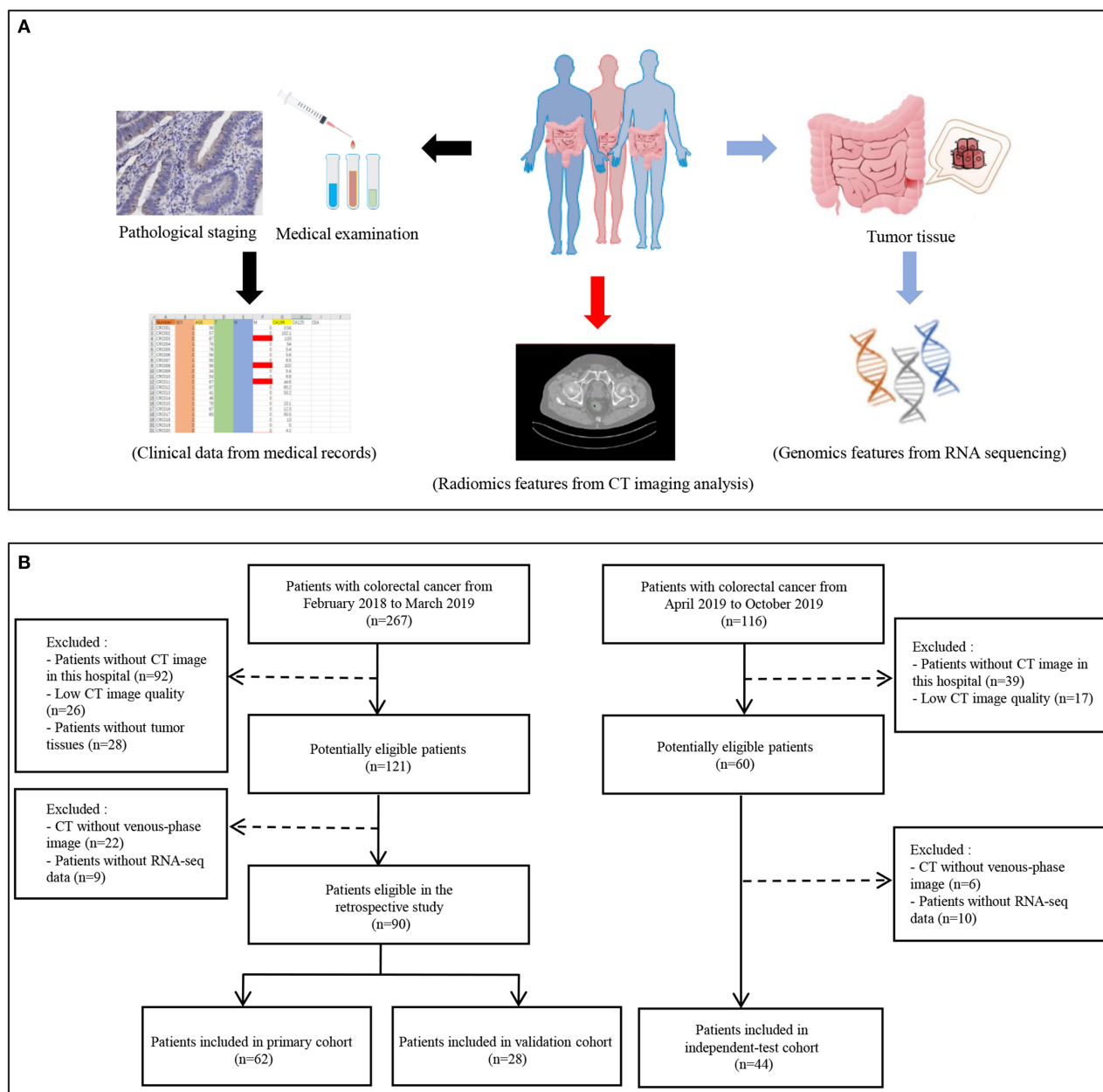


**FIGURE 1 |** Flowchart of study. **(A)** The data collection pipeline in this study. **(B)** Flowchart of patients' inclusion.

DICOM data was retrieved from CD Viewer (INFINITT, Seoul, South Korea). Two professional data readers used the 3D Slicer software (version 4.10.2) to delineate the tumor tissue under the guidance of a clinical imaging specialist for building a three-dimensional tumor tissue (27, 28). Finally, the eigenvalue results were derived from the SlicerRadiomics plug-in.

## Radiomics Signature Extraction

The primary cohort was used to establish the prediction models. The 10-fold cross-validation least absolute shrinkage and selection operator (LASSO) was used for selecting the

most valuable radiomics features via minimum criteria. The radiomics score was calculated for each participant by a linear combination of screened features weighted by their respective LASSO coefficients.

## Genomics Feature Selection

Total RNA of tumor tissues collected from CRC patients was extracted by TRIZOL reagent (Takara Biomedical Technology, Beijing, China). Eligible total RNA was purified and fragmented for further sequencing library construction. Qualified sequencing libraries were sequenced by Illumina with sequencing strategy



**TABLE 1** | Characteristics of patients in the primary and validation cohorts.

Characteristic	Primary cohort		P	Validation cohort		P
	Non-metastasis (n = 38)	Metastasis (n = 24)		Non-metastasis (n = 17)	Metastasis (n = 11)	
Age (mean ± SD), years	59.68 ± 10.84	58.46 ± 12.92	0.689	60.01 ± 12.24	61.64 ± 12.56	0.744
Sex, no. (%)			0.063			0.441
Male	27 (71.05)	11 (45.83)		11 (64.71)	5 (45.45)	
Female	11 (28.95)	13 (54.17)		6 (35.29)	6 (54.55)	
CA 19-9 level, no. (%)			0.008*			0.023*
Normal	31 (83.78)	11 (50.00)		14 (93.33)	5 (50.00)	
Abnormal	6 (16.22)	11 (50.00)		1 (6.67)	5 (50.00)	
Tumor stage, no. (%)			<0.001*			<0.001*
0	4 (10.53)	0 (0.00)		0 (0.00)	0 (0.00)	
I	18 (47.37)	0 (0.00)		7 (41.18)	0 (0.00)	
II	16 (42.11)	0 (0.00)		10 (58.82)	0 (0.00)	
III	0 (0.00)	20 (83.33)		0 (0.00)	6 (54.55)	
IV	0 (0.00)	4 (16.67)		0 (0.00)	5 (45.45)	
Tumor sites, no. (%)			0.077			0.254
Rectum	30 (78.95)	12 (50.00)		13 (76.47)	6 (54.54)	
Right colon	4 (10.53)	4 (16.67)		1 (5.88)	4 (36.36)	
Left colon	3 (7.89)	4 (16.67)		1 (5.88)	0 (0.00)	
Radiomics score (mean ± SD)	−3.71 ± 3.72	3.37 ± 5.17	<0.001*	−0.81 ± 4.35	4.15 ± 6.18	0.02*
Sigmoid colon	1 (2.63)	4 (16.67)		1 (5.88)	0 (0.00)	
Transverse colon	0 (0.00)	0 (0.00)		1 (5.88)	1 (9.10)	

*T* test or  $\chi^2$  test was used to compare characteristics differences between non-metastasis and metastasis groups in primary and validation cohorts. \**P* < 0.05. The upper reference limit value for CA 19-9 level was 27 ng/mL in clinic. Abnormal: CA 19-9 level >27 ng/mL; normal: CA 19-9 level ≤27 ng/mL.

SD, standard deviation; CA-19-9, carbohydrate antigen 19-9.

PE150. Clean reads were used for subsequent analysis. The differentially expressed genes between metastasis and non-metastasis groups were analyzed by DEseq2 package in R software. Protein–protein interaction network (<https://string-db.org/>) was applied to analyze the potential interaction.

## Construction and Performance of the Multiscale Nomogram

The prediction model was developed based on the selected radiomics features by using multivariable logistic regression analysis. The model was converted into prediction nomogram for providing clinicians with an easy-to-use tool to facilitate the individual probability of CRC preoperative metastasis. The predictive performance of the multivariate nomogram was assessed in the primary cohort and then verified in the validation cohort and independent-test cohort. The receiver operating characteristic curve (ROC) analysis was used as a performance indicator. In order to estimate the clinical usefulness of the prediction nomogram, the decision curve was conducted by calculating the net benefits for a range of threshold probabilities.

## Statistical Analysis

Statistical analysis was performed using R software [version R 3.6.1 for Windows (x64)] and IBM SPSS (version 20.0). The appropriate package and function to complete the corresponding statistical test were loaded. The “pROC” package (version 1.15.3)

was used to plot ROC curves. The “glmnet” package (version 2.0–18) was used to finish the LASSO model. The “rms” package (version 5.1–3.1) was performed for calibration curve. The “rmda” package (version 1.6) was performed for decision curve. At inspection level, *P* < 0.05 is considered statistically significant. The differences of the basic clinical information between metastasis and non-metastasis groups were performed by *t*-test or  $\chi^2$  test.

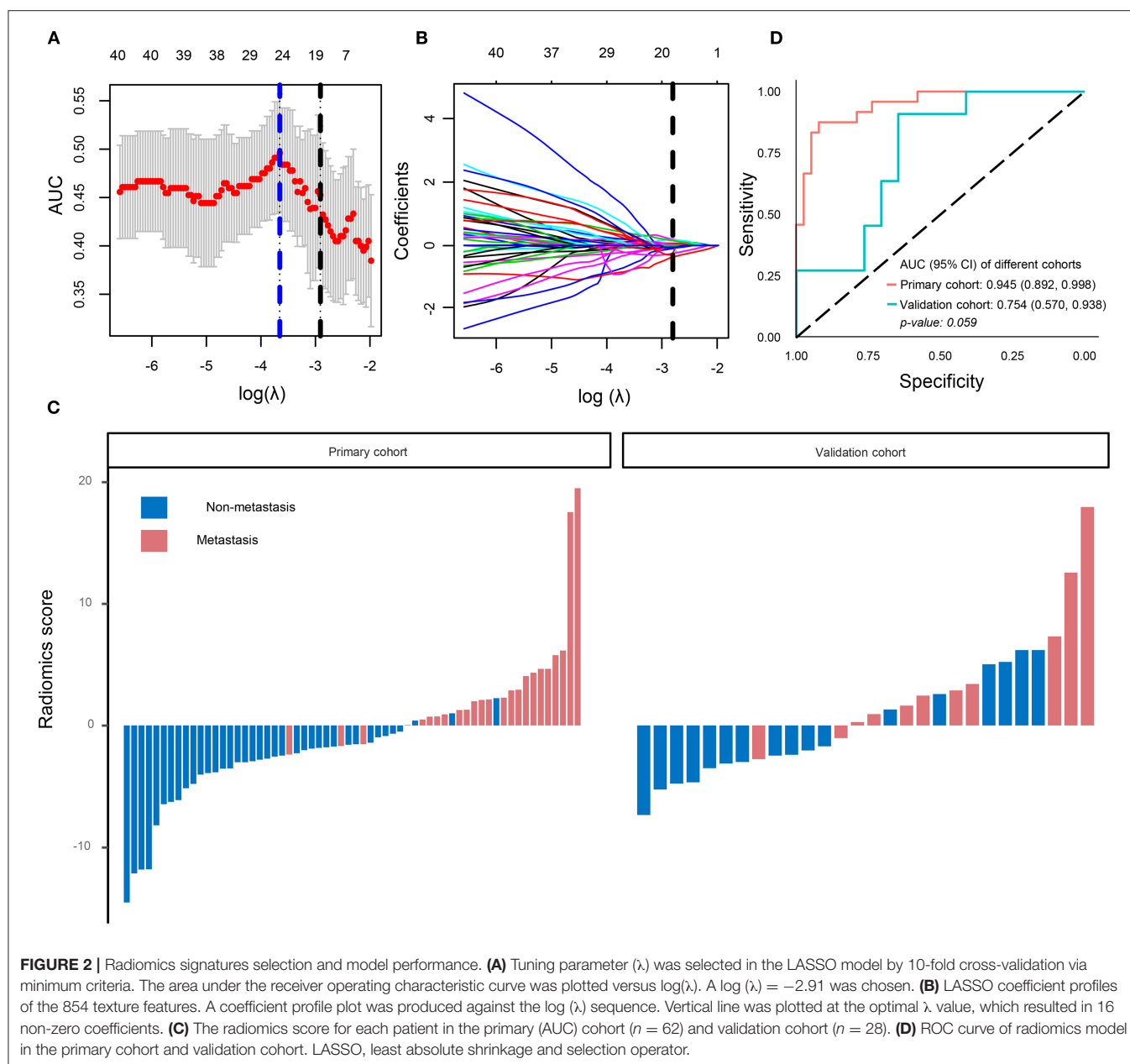
## RESULTS

### Clinical Phenotype Data

The characteristics of patients in the primary cohort, validation cohort, and independent-test cohort are shown in **Table 1**, **Supplementary Tables 1, 2**. There was no difference in clinical data between the primary and validation cohorts (**Supplementary Table 1**). CA 19-9 showed a significant difference between metastasis and non-metastasis groups in the primary cohort (*P* < 0.05), which was then confirmed in the validation cohort (*P* < 0.05) (**Table 1**).

### Radiomics Signature Building

Using the LASSO regression model, 854 texture features were reduced to 16 potential predictors (ratio 53:1; **Figures 2A,B**). The radiology eigenvalues were calculated by radiomics score calculation formula (**Supplementary File 1**). The radiomics

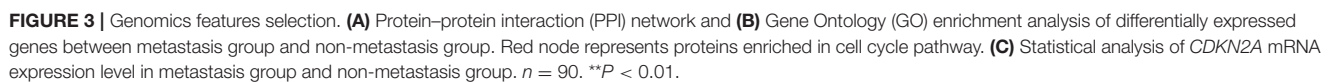


score was significantly different between metastasis and non-metastasis in the primary and validation cohorts ( $P < 0.05$ ) (Table 1, Figure 2C). The area under curve (AUC) of the radiomics model reached 0.945 [95% confidence interval (CI) 0.892–0.998] in the primary cohort and 0.754 (95% CI 0.570–0.938) in the validation cohort, respectively (Figure 2D). Typical cases of non-metastasis and metastasis are presented in Supplementary Figure 2.

## Development and Validation of the Multiscale Model

In order to improve the performance of the model, we combined multidimensional data. Genomics features and

clinical risk factors were screened for the construction of the multiscale radiogenomics model. The analysis of RNA sequencing results revealed that the cell cycle pathway was significantly different between the metastasis group and the non-metastasis group (Figures 3A,B). The four cell cycle-related genes (*CDKN2A*, *TP53*, *ATM*, and *MYC*) were identified by protein–protein interaction network. Among them, *CDKN2A* was notably increased in the metastasis group (Figure 3C). Previous studies have shown that CA 19-9 is a commonly used tumor marker in clinical practice (18). Remarkably, the multiscale model, combined radiomics with four cell cycle-related genes and clinical risk factor CA 19-9, had better discriminative capacity than the radiomics model. The AUC



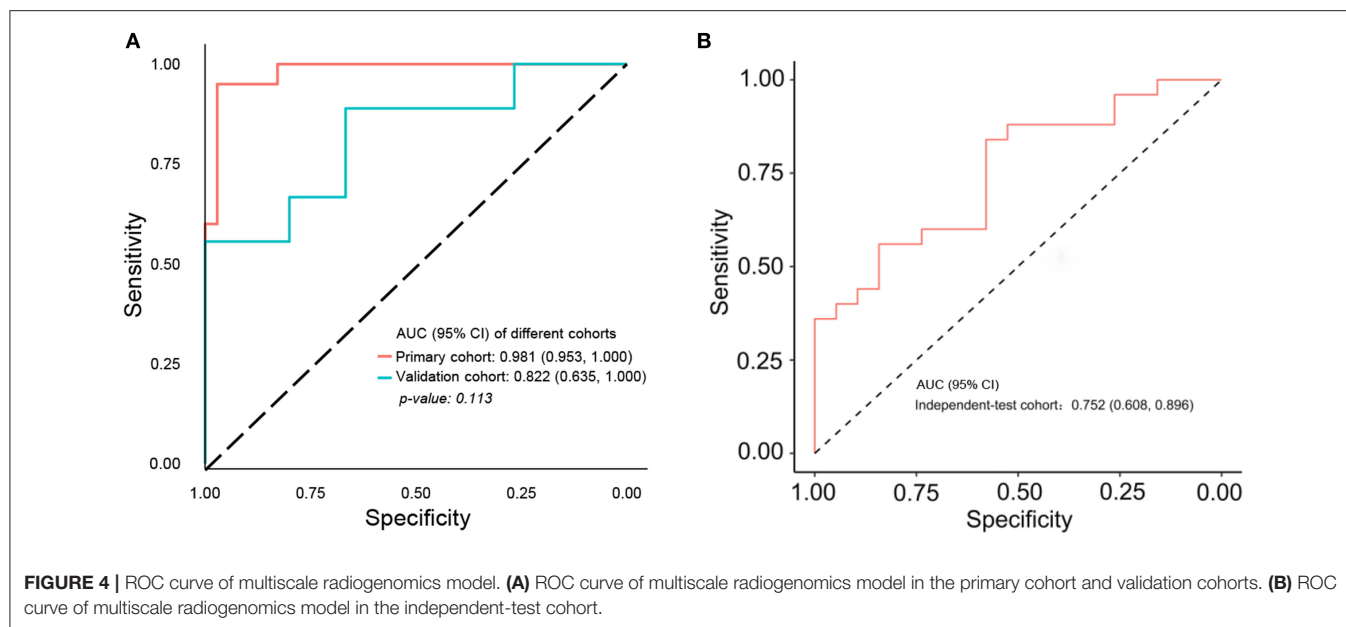


**TABLE 2 |** Performance of the radiomics model and multiscale radiogenomics model in primary and validation cohorts.

Item	Radiomics model		Multiscale radiogenomics model	
	Primary cohort	Validation cohort	Primary cohort	Validation cohort
Sensitivity (95% CI)	0.921 (0.786–0.983)	0.846 (0.546–0.981)	0.944 (0.813–0.993)	0.833 (0.516–0.979)
Specificity (95% CI)	0.875 (0.676–0.973)	0.600 (0.323–0.837)	0.947 (0.740–0.999)	0.538 (0.277–0.848)
PPV (95% CI)	0.921 (0.786–0.983)	0.647 (0.383–0.858)	0.971 (0.851–0.999)	0.667 (0.384–0.882)
NPV (95% CI)	0.875 (0.676–0.973)	0.818 (0.482–0.977)	0.900 (0.683–0.988)	0.778 (0.400–0.972)
AUC (95% CI)	0.945 (0.892–0.998)	0.754 (0.570–0.938)	0.981 (0.953–1.000)	0.822 (0.635–1.000)

PPV, positive predictive value; NPV, negative predictive value; AUC, area under the curve.

of the multiscale model reached 0.981 (95% CI 0.953–1.000) and 0.822 (95% CI 0.635–1.000) in the primary and validation cohorts, respectively (**Figure 4A**). In addition, as shown in **Table 2**, the multiscale model had better accuracy for assessing CRC preoperative metastasis (sensitivity: 94.4%, specificity: 94.7%, positive predictive value: 97.1%, negative predictive value: 90.0%). To further validate the generalization of multiscale model, we applied the model in an independent-test cohort. The AUC achieved 0.752 (95% CI 0.608–0.896) in the independent-test cohort (**Figure 4B**), which suggested that the model had good robustness and generalization.

## Clinical Use

Next, we further constructed the multiscale nomogram for clinical use, based on radiomics feature, genomics characteristics, and CA 19-9 (**Figure 5A**). Good calibration was observed for the probability of CRC metastasis (**Figure 5B**). The decision curve analyses of the radiomics model and the multiscale model are shown in **Figure 5C**. The decision curve illustrated that both models had relatively good performance for clinical application. Importantly, the multiscale model indicated higher benefit than

the radiomics model, which suggested that the multiscale model was a reliable clinical utility for assessment of preoperative metastasis in CRC patients.

## DISCUSSION

In this study, we established and validated a multiscale model for individualized preoperative metastasis assessment in patients with CRC. The multiscale nomogram incorporated radiomics features, genomics signatures, and clinical risk factor. The convenient multiscale nomogram facilitated the individualized evaluation of CRC preoperative metastasis.

Metastasis is the leading cause of reduced 5-years survival rate for patients with CRC (2). Accurate evaluation of metastasis is critical for optimizing the CRC treatment strategies. Currently, the discrimination of CRC metastasis based on the visual judgment of clinicians remains challenging. Quantitative high-throughput radiomics analysis provides many high-dimensional imaging characteristics based on medical imaging, and the main applications are diagnosis, treatment planning, and evaluations in the field of oncology (29). Previous studies have demonstrated



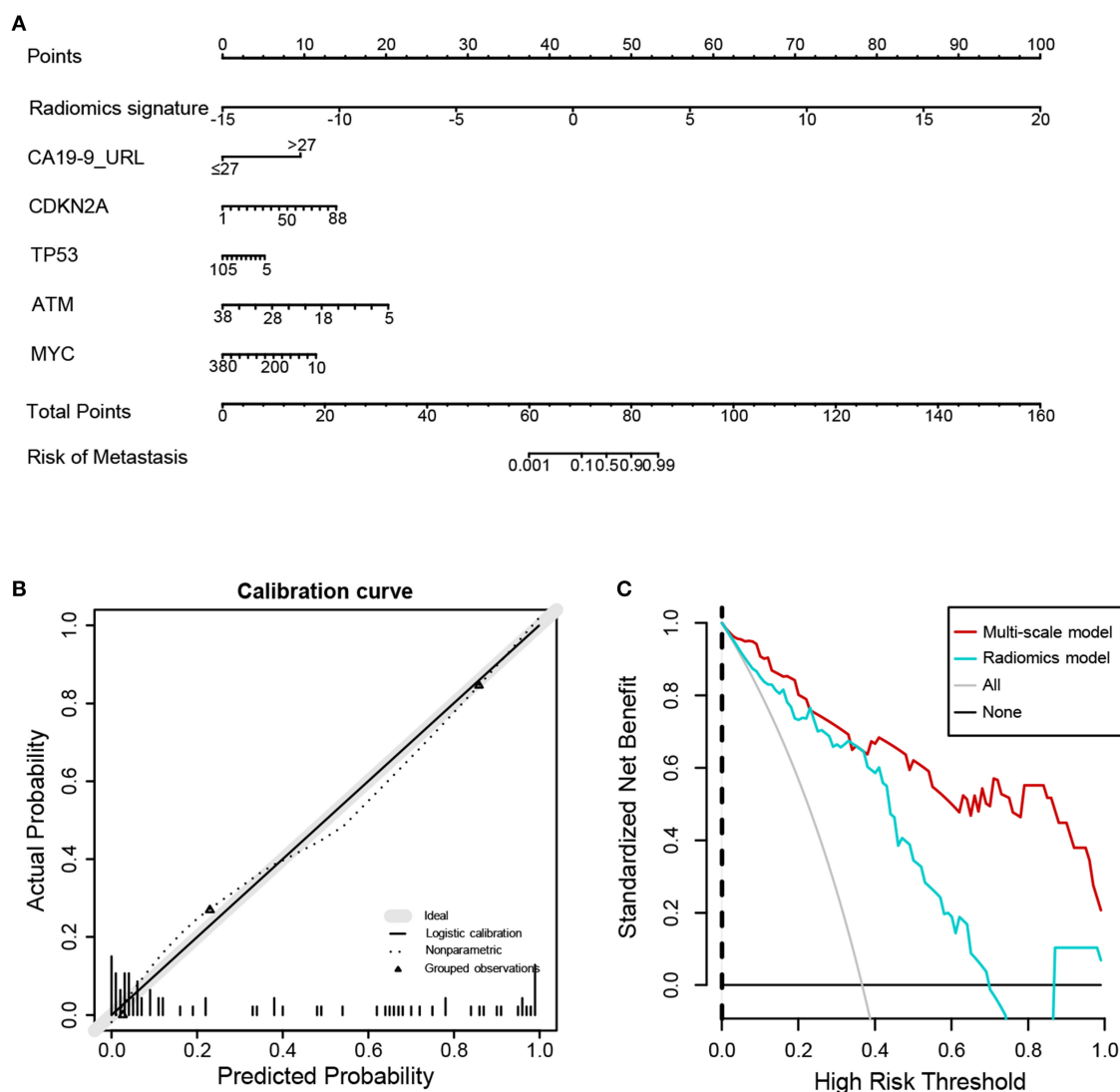


**FIGURE 5 |** Nomogram, calibration curve, and decision curve derived from the multiscale radiogenomics model. **(A)** Nomogram developed with the radiomics score, genomics, and CA-19-9. **(B)** Calibration curve analysis for the multiscale radiogenomics model. The y axis represents the actual probability of metastasis. The x axis represents the predicted probability of metastasis. **(C)** Decision curve analysis for the multiscale radiogenomics model.

that radiomics is used successfully in the prediction of lymph node metastasis and of outcomes (19, 30). Moreover, the combined analysis using multiple markers performs better than individual analysis in clinical practice (19, 31, 32). Meanwhile, risk stratification and clinical decision-making are better to assess the disease risk by polygenic risk score (33). Exploring the genomics of cancer patients might help to optimize therapeutic strategies. Previous study has proposed that the gene expression could be evaluated by radiomics features in CRC (34). However, the potential associations between radiomics, gene expression, and clinical risk remain unclear.

In this study, the regions of interest on enhanced venous-phase CT were delineated to screen for metastasis-related image

features. Eight hundred fifty-four radiomics features, extracted from enhanced venous-phase CT, were reduced to 16 potential predictors by LASSO. The AUCs of the radiomics model were 0.945 (95% CI 0.892–0.998) and 0.754 (95% CI 0.570–0.938) in the primary and validation cohorts, respectively. To enhance the performance of the model, we combined gene expression and clinical risk factors. The 90 CRC tissues were analyzed by RNA sequencing, and we selected four genes (*CDKN2A*, *TP53*, *ATM*, and *MYC*) closely related to the cell cycle based on the RNA sequencing analysis. Existing studies have shown that *CDKN2A*, *TP53*, *ATM*, and *MYC* play an important role in progression and metastasis of CRC diseases (35–38). Our study indicated that these four genes were identified as genomics risk features

for assessment of CRC metastatic status. Previous studies have shown that CA 19-9 could be used as an important indicator for the prognosis of patients with CRC (39). Moreover, it has been demonstrated that CA 19-9 could be used to monitor the disease development in the metastatic CRC patients without of CEA elevation (40). Therefore, CA 19-9 was kept as a predictor during the process of model establishment. In this study, we combined genomics features and CA 19-9 with radiomics signatures to develop a multiscale model for evaluating the metastasis of CRC. The AUC of the multiscale model [0.981 (95% CI 0.953–1.000) and 0.822 (95% CI 0.635–1.000) in the primary and validation cohorts, respectively] was higher than the radiomics model, indicating that the multiscale model had a better performance. These results give us some hints, that is, while focusing on radiomics, the convergence of multiple omics will be more valuable for disease prediction and diagnosis.

We utilized a nomogram as an individualized tool for CRC preoperative metastasis detection and evaluated whether the multiscale nomogram on the basis of decisions could benefit patients. Decision curve analysis was performed for estimating the clinical consequences of the multiscale nomogram based on threshold probability. The decision curves indicated that the threshold probability ranged from 0 to 100%, implying that applying the multiscale nomogram to assess CRC metastatic status adds more net benefit than the “treat-all” or “treat-none” scheme. As expected, the net benefit of the multiscale model was better than the radiomics model, suggesting that the multiscale model could preferably assist both clinicians and patients to evaluate the risk of CRC preoperative metastasis.

There are several limitations to our study that deserve recognition. First, this is a single-center study with limited generalizability. Second, the sample size of the study is relatively small. Third, the research period and follow-up time were not long enough; some metastasis may be omitted. A large sample of patients from multiple centers should be studied to improve the robustness and reproducibility of our developed multiscale model.

In conclusion, this study presented a multiscale model that incorporated the radiological eigenvalues, genomics features, and CA 19-9, which could be conveniently utilized to facilitate the individualized evaluation of CRC preoperative metastasis.

## REFERENCES

1. Torre LA, Bray F, Siegel RL, Ferlay J, Lortet-Tieulent J, Jemal A. Global cancer statistics, 2012. *CA Cancer J Clin.* (2015) 65:87–108. doi: 10.3322/caac.21262
2. Siegel RL, Miller KD, Jemal A. Cancer statistics, 2019. *CA Cancer J Clin.* (2019) 69:7–34. doi: 10.3322/caac.21551
3. Engstrom PF, Arnoletti JP, Benson AB, 3rd, Chen YJ, Choti MA, Cooper HS, et al. NCCN clinical practice guidelines in oncology: colon cancer. *J Natl Compr Canc Netw.* (2009) 7:778–831. doi: 10.6004/jncn.2009.0056
4. Deck MD, Messina AV, Sackett JF. Computed tomography in metastatic disease of the brain. *Radiology.* (1976) 119:115–20. doi: 10.1148/119.1.115
5. McWilliams A, Tammemagi MC, Mayo JR, Roberts H, Liu G, Soghrati K, et al. Probability of cancer in pulmonary nodules detected on first screening CT. *N Engl J Med.* (2013) 369:910–9. doi: 10.1056/NEJMc1312411

## DATA AVAILABILITY STATEMENT

The original contributions presented in the study are publicly available. This data can be found here: <https://bigd.big.ac.cn/gsa-human> under accession number HRA000235.

## ETHICS STATEMENT

The studies involving human participants were reviewed and approved by the ethics committee of Dazhou Central Hospital. The patients/participants provided their written informed consent to participate in this study.

## AUTHOR CONTRIBUTIONS

FZ, H-YZ, and JingW participated in the study design and manuscript preparation. QL, JL, LX, and JiaW performed radiomics features extraction. QL, JL, LX, ZZ, JF, XH, and YC performed the samples and clinical data acquisition. QL, JL, JiaW, and FZ analyzed the data. QL, ZZ, FZ, and H-YZ revised the manuscript. All authors contributed to the article and approved the submitted version.

## FUNDING

This study was supported by the National Natural Science Foundation of China (81902861 and 32000485), the Scientific Research Fund of Sichuan health and Health Committee (No. 18PJ361), and the Scientific Research Fund of Technology Bureau in Sichuan Province (Nos. 2018138 and 2018JY0324).

## SUPPLEMENTARY MATERIAL

The Supplementary Material for this article can be found online at: <https://www.frontiersin.org/articles/10.3389/fonc.2021.620945/full#supplementary-material>

**Supplementary Figure 1** | Typical cases of non-metastasis and metastasis.

**Supplementary Table 1** | Characteristics comparison between primary and validation cohorts.

**Supplementary Table 2** | Characteristic of independent-test cohort.

6. Inouye SK, Sox HC, Jr. Standard and computed tomography in the evaluation of neoplasms of the chest. A comparative efficacy assessment. *Ann Intern Med.* (1986) 105:906–24. doi: 10.7326/0003-4819-105-6-906
7. Byrom J, Widjaja E, Redman CW, Jones PW, Tebbly S. Can pre-operative computed tomography predict resectability of ovarian carcinoma at primary laparotomy? *BJOG.* (2002) 109:369–75. doi: 10.1111/j.1471-0528.2002.01216.x
8. Mainenti PP, Cirillo LC, Camera L, Persico F, Cantalupo T, Pace L, et al. Accuracy of single phase contrast enhanced multidetector CT colonography in the preoperative staging of colo-rectal cancer. *Eur J Radiol.* (2006) 60:453–9. doi: 10.1016/j.ejrad.2006.08.001
9. Rapoport ED, Loft A. Liver metastases from colorectal cancer: imaging with superparamagnetic iron oxide (SPIO)-enhanced MR imaging, computed tomography and positron emission tomography. *Abdom Imaging.* (2007) 32:624–34. doi: 10.1007/s00261-007-9297-y

10. Dighe S, Purkayastha S, Swift I, Tekkis PP, Darzi A, A'Hern R, et al. Diagnostic precision of CT in local staging of colon cancers: a meta-analysis. *Clin Radiol.* (2010) 65:708–19. doi: 10.1016/j.crad.2010.01.024
11. Aerts HJ, Velazquez ER, Leijenaar RT, Parmar C, Grossmann P, Carvalho S, et al. Decoding tumour phenotype by noninvasive imaging using a quantitative radiomics approach. *Nat Commun.* (2014) 5:4006. doi: 10.1038/ncomms5644
12. Gillies RJ, Kinahan PE, Hricak H. Radiomics: images are more than pictures, they are Data. *Radiology.* (2016) 278:563–77. doi: 10.1148/radiol.2015151169
13. Zhang Y, Moore GR, Laule C, Bjarnason TA, Kozlowski P, Traboulsee A, et al. Pathological correlates of magnetic resonance imaging texture heterogeneity in multiple sclerosis. *Ann Neurol.* (2013) 74:91–9. doi: 10.1002/ana.23867
14. Yoon HJ, Kim Y, Kim BS. Intratumoral metabolic heterogeneity predicts invasive components in breast ductal carcinoma in situ. *Eur Radiol.* (2015) 25:3648–58. doi: 10.1007/s00330-015-3761-9
15. Birkhahn M, Mitra AP, Cote RJ. Molecular markers for bladder cancer: the road to a multimarker approach. *Expert Rev Anticancer Ther.* (2007) 7:1717–27. doi: 10.1586/14737140.7.12.1717
16. Shi B, Wang L, Yan C, Chen D, Liu M, Li P. Nonlinear heart rate variability biomarkers for gastric cancer severity: a pilot study. *Sci Rep.* (2019) 9:13833. doi: 10.1038/s41598-019-50358-y
17. Feng B, Zheng MH, Zheng YF, Lu AG, Li JW, Wang ML, et al. Normal and modified urinary nucleosides represent novel biomarkers for colorectal cancer diagnosis and surgery monitoring. *J Gastroenterol Hepatol.* (2005) 20:1913–9. doi: 10.1111/j.1440-1746.2005.03888.x
18. Vukobrat-Bijedic Z, Husic-Selimovic A, Sofic A, Bijedic N, Bjelogrić I, Gogov B, et al. Cancer antigens (CEA and CA 19-9) as markers of advanced stage of colorectal carcinoma. *Med Arch.* (2013) 67:397–401. doi: 10.5455/medarh.2013.67.397-401
19. Huang YQ, Liang CH, He L, Tian J, Liang CS, Chen X, et al. Development and validation of a radiomics nomogram for preoperative prediction of lymph node metastasis in colorectal cancer. *J Clin Oncol.* (2016) 34:2157–64. doi: 10.1200/JCO.2015.65.9128
20. Hu T, Wang S, Huang L, Wang J, Shi D, Li Y, et al. A clinical-radiomics nomogram for the preoperative prediction of lung metastasis in colorectal cancer patients with indeterminate pulmonary nodules. *Eur Radiol.* (2019) 29:439–49. doi: 10.1007/s00330-018-5539-3
21. Lawrence MS, Stojanov P, Mermel CH, Robinson JT, Garraway LA, Golub TR, et al. Discovery and saturation analysis of cancer genes across 21 tumour types. *Nature.* (2014) 505:495–501. doi: 10.1038/nature12912
22. Kyrochristos ID, Roukos DH. Comprehensive intra-individual genomic and transcriptional heterogeneity: evidence-based colorectal cancer precision medicine. *Cancer Treat Rev.* (2019) 80:101894. doi: 10.1016/j.ctrv.2019.101894
23. Oga T, Yamashita Y, Soda M, Kojima S, Ueno T, Kawazu M, et al. Genomic profiles of colorectal carcinoma with liver metastases and newly identified fusion genes. *Cancer Sci.* (2019) 110:2973–81. doi: 10.1111/cas.14127
24. Malumbres M, Barbacid M. Cell cycle, CDKs and cancer: a changing paradigm. *Nat Rev Cancer.* (2009) 9:153–66. doi: 10.1038/nrc2602
25. Bertoli C, Skotheim JM, de Bruin RA. Control of cell cycle transcription during G1 and S phases. *Nat Rev Mol Cell Biol.* (2013) 14:518–28. doi: 10.1038/nrm3629
26. Aarts M, Linardopoulos S, Turner NC. Tumour selective targeting of cell cycle kinases for cancer treatment. *Curr Opin Pharmacol.* (2013) 13:529–35. doi: 10.1016/j.coph.2013.03.012
27. Bruns N. [3D Slicer: universal 3D visualization software]. *Unfallchirurg.* (2019) 122:662–3. doi: 10.1007/s00113-019-0654-4
28. Fedorov A, Beichel R, Kalpathy-Cramer J, Finet J, Fillion-Robin J-C, Pujol S, et al. 3D Slicer as an image computing platform for the Quantitative Imaging Network. *Magn Reson Imaging.* (2012) 30:1323–41. doi: 10.1016/j.mri.2012.05.001
29. Liu Z, Wang S, Dong D, Wei J, Fang C, Zhou X, et al. The applications of radiomics in precision diagnosis and treatment of oncology: opportunities and challenges. *Theranostics.* (2019) 9:1303–22. doi: 10.7150/thno.30309
30. Dohan A, Gallix B, Guiu B, Le Malicot K, Reinhold C, Soyer P, et al. Early evaluation using a radiomic signature of unresectable hepatic metastases to predict outcome in patients with colorectal cancer treated with FOLFIRI and bevacizumab. *Gut.* (2020) 69:531–9. doi: 10.1136/gutjnl-2018-316407
31. Huang Y, Liu Z, He L, Chen X, Pan D, Ma Z, et al. Radiomics signature: a potential biomarker for the prediction of disease-free survival in early-stage (I or II) non-small cell lung cancer. *Radiology.* (2016) 281:947–57. doi: 10.1148/radiol.2016152234
32. Zhang JX, Song W, Chen ZH, Wei JH, Liao YJ, Lei J, et al. Prognostic and predictive value of a microRNA signature in stage II colon cancer: a microRNA expression analysis. *Lancet Oncol.* (2013) 14:1295–306. doi: 10.1016/S1470-2045(13)70491-1
33. Zeggini E, Gloy AL, Barton AC, Wain IV. Translational genomics and precision medicine: Moving from the lab to the clinic. *Science.* (2019) 365:1409–13. doi: 10.1126/science.aax4588
34. Chu Y, Li J, Zeng Z, Huang B, Zhao J, Liu Q, et al. A novel model based on cxc18-derived radiomics for prognosis prediction in colorectal cancer. *Front Oncol.* (2020) 10:575422. doi: 10.3389/fonc.2020.575422
35. Park HE, Kim JH, Cho NY, Lee HS, Kang GH. Intratumoral Fusobacterium nucleatum abundance correlates with macrophage infiltration and CDKN2A methylation in microsatellite-unstable colorectal carcinoma. *Virchows Arch.* (2017) 471:329–36. doi: 10.1007/s00428-017-2171-6
36. Iacopetta B. TP53 mutation in colorectal cancer. *Hum Mutat.* (2003) 21:271–6. doi: 10.1002/humu.10175
37. Randon G, Fuca G, Rossini D, Raimondi A, Pagani F, Perrone F, et al. Prognostic impact of ATM mutations in patients with metastatic colorectal cancer. *Sci Rep.* (2019) 9:2858. doi: 10.1038/s41598-019-39525-3
38. Satoh K, Yachida S, Sugimoto M, Oshima M, Nakagawa T, Akamoto S, et al. Global metabolic reprogramming of colorectal cancer occurs at adenoma stage and is induced by MYC. *Proc Natl Acad Sci USA.* (2017) 114:E7697–06. doi: 10.1073/pnas.1710366114
39. Stikma J, Grootendorst DC, van der Linden PW. CA 19-9 as a marker in addition to CEA to monitor colorectal cancer. *Clin Colorectal Cancer.* (2014) 13:239–44. doi: 10.1016/j.clcc.2014.09.004
40. Zhang SY, Lin M, Zhang HB. Diagnostic value of carcinoembryonic antigen and carcinoma antigen 19-9 for colorectal carcinoma. *Int J Clin Exp Pathol.* (2015) 8:9404–9.

**Conflict of Interest:** The authors declare that the research was conducted in the absence of any commercial or financial relationships that could be construed as a potential conflict of interest.

Copyright © 2021 Liu, Li, Xu, Wang, Zeng, Fu, Huang, Chu, Wang, Zhang and Zeng. This is an open-access article distributed under the terms of the Creative Commons Attribution License (CC BY). The use, distribution or reproduction in other forums is permitted, provided the original author(s) and the copyright owner(s) are credited and that the original publication in this journal is cited, in accordance with accepted academic practice. No use, distribution or reproduction is permitted which does not comply with these terms.



# 3D DenseNet Deep Learning Based Preoperative Computed Tomography for Detecting Myasthenia Gravis in Patients With Thymoma

## OPEN ACCESS

### Edited by:

Min Wu,  
Sichuan University, China

### Reviewed by:

Bingsheng Huang,  
Shenzhen University, China  
Hai-Feng Li,  
Capital Medical University, China

### \*Correspondence:

Zunfu Ke  
kezunfu@mail.sysu.edu.cn  
Shiting Feng  
fengsht@mail.sysu.edu.cn  
Huiyu Feng  
fenghuiy@mail.sysu.edu.cn

<sup>†</sup>These authors have contributed  
equally to this work and share  
first authorship

### Specialty section:

This article was submitted to  
Cancer Imaging and  
Image-directed Interventions,  
a section of the journal  
Frontiers in Oncology

Received: 21 November 2020

Accepted: 13 April 2021

Published: 05 May 2021

### Citation:

Liu Z, Zhu Y, Yuan Y, Yang L,  
Wang K, Wang M, Yang X, Wu X,  
Tian X, Zhang R, Shen B, Luo H,  
Feng H, Feng S and Ke Z (2021)  
3D DenseNet Deep Learning  
Based Preoperative Computed  
Tomography for Detecting Myasthenia  
Gravis in Patients With Thymoma.  
Front. Oncol. 11:631964.  
doi: 10.3389/fonc.2021.631964

Zhenguo Liu<sup>1†</sup>, Ying Zhu<sup>2,3†</sup>, Yujie Yuan<sup>4†</sup>, Lei Yang<sup>1</sup>, Kefeng Wang<sup>5</sup>, Minghui Wang<sup>5</sup>,  
Xiaoyu Yang<sup>2</sup>, Xi Wu<sup>2</sup>, Xi Tian<sup>6</sup>, Rongguo Zhang<sup>6</sup>, Bingqi Shen<sup>2</sup>, Honghe Luo<sup>1</sup>,  
Huiyu Feng<sup>7\*</sup>, Shiting Feng<sup>2\*</sup> and Zunfu Ke<sup>3,8\*</sup>

<sup>1</sup> Department of Thoracic Surgery, The First Affiliated Hospital of Sun Yat-sen University, Guangzhou, China, <sup>2</sup> Department of Radiology, The First Affiliated Hospital of Sun Yat-sen University, Guangzhou, China, <sup>3</sup> Institution of Precision Medicine, The First Affiliated Hospital of Sun Yat-sen University, Guangzhou, China, <sup>4</sup> Center of Gastrointestinal Surgery, The First Affiliated Hospital of Sun Yat-sen University, Guangzhou, China, <sup>5</sup> Department of Thoracic Surgery, The Sun Yat-sen Memorial Hospital of Sun Yat-sen University, Guangzhou, China, <sup>6</sup> Advanced Institute, Infervision, Beijing, China, <sup>7</sup> Department of Neurology, The First Affiliated Hospital of Sun Yat-sen University, Guangzhou, China, <sup>8</sup> Department of Pathology, The First Affiliated Hospital of Sun Yat-sen University, Guangzhou, China

**Background:** Myasthenia gravis (MG) is the most common paraneoplastic syndromes of thymoma and closely related to thymus abnormalities. Timely detecting of the risk of MG would benefit clinical management and treatment decision for patients with thymoma. Herein, we developed a 3D DenseNet deep learning (DL) model based on preoperative computed tomography (CT) as a non-invasive method to detect MG in thymoma patients.

**Methods:** A large cohort of 230 thymoma patients in a hospital affiliated with a medical school were enrolled. 182 thymoma patients (81 with MG, 101 without MG) were used for training and model building. 48 cases from another hospital were used for external validation. A 3D-DenseNet-DL model and five radiomic models were performed to detect MG in thymoma patients. A comprehensive analysis by integrating machine learning and semantic CT image features, named 3D-DenseNet-DL-based multi-model, was also performed to establish a more effective prediction model.

**Findings:** By elaborately comparing the prediction efficacy, the 3D-DenseNet-DL effectively identified MG patients and was superior to other five radiomic models, with a mean area under ROC curve (AUC), accuracy, sensitivity, and specificity of 0.734, 0.724, 0.787, and 0.672, respectively. The effectiveness of the 3D-DenseNet-DL-based multi-model was further improved as evidenced by the following metrics: AUC 0.766, accuracy 0.790, sensitivity 0.739, and specificity 0.801. External verification results confirmed the feasibility of this DL-based multi-model with metrics: AUC 0.730, accuracy 0.732, sensitivity 0.700, and specificity 0.690, respectively.



**Interpretation:** Our 3D-DenseNet-DL model can effectively detect MG in patients with thymoma based on preoperative CT imaging. This model may serve as a supplement to the conventional diagnostic criteria for identifying thymoma associated MG.

**Keywords:** thymoma, myasthenia gravis, deep learning—artificial neural network, computed tomography, imaging—computed tomography

## INTRODUCTION

Thymoma is the most common neoplasm of the anterior mediastinum in adults and known for their frequent association with myasthenia gravis (MG) (1). MG, the most common syndrome of paraneoplastic syndromes (2), is an autoimmune disease, involving antibodies against the postsynaptic nicotinic acetylcholine receptors (AChRs) at neuromuscular junctions, resulting in variable weakness of the voluntary muscle (3). Patients with MG can experience severe cardiopulmonary complications (4, 5). One of the most severe complications of MG is myasthenic crisis after thymoma resection, which can rapidly worsen, leading to respiratory failure and even death (6–9). According to NCCN clinical guidelines for thymomas, all patients suspected of having thymomas (even those without symptoms) should be carefully evaluated for the presence of MG before surgical procedure in order to avoid respiratory failure during the operation (2, 10, 11). However, some MG symptoms are atypical or asymptomatic, leading to missed or delayed diagnosis of MG in patients experiencing mild weakness or in individuals with weakness restricted to only a few muscles (12). In addition, the current criteria for diagnosing MG (including immunological, electrophysiological, and pharmacological approaches) are usually complex and time-consuming (13). In the real world, a majority of thymoma patients did not receive careful evaluation of MG by a neurologist before surgery. Therefore, a simple, non-invasive and feasible screening method for detecting MG in thymoma patients prior to operation is necessary to ensure proper clinical management, especially for developing surgical strategies and reducing perioperative complications.

In recent years, deep learning (DL) and radiomics in the medical imaging field have been studied intensively to explore the potential of utilizing various medical images as diagnostic, predictive, or prognostic information of human diseases, including the possibility of identifying tumor pathological subtypes, tumor phenotypes, and the gene–protein signatures (14, 15). MG syndrome is closely related to the histopathological abnormalities of thymus, such as thymoma (16). Thymomas are usually stratified into six entities [types A, AB, B1, B2, B3, and TC (carcinoma)] on the basis of the morphology of epithelial cells and the lymphocyte-to-epithelial cell ratio (17). Thymoma

associated MG is more common in type B (B<sub>1</sub>, B<sub>2</sub>, and B<sub>3</sub>) than type A and AB thymomas and absent in TC (16, 18). Recently, Xiaowei Han et al. reported that some CT imaging characteristics were significantly related to histological classification of thymoma and MG status (19). Therefore, it is possible to identify the presence of MG in thymoma patients using deep learning model or radiomics based on preoperative routine CT scan of thymoma.

Here, we designed this study to explore the effectiveness of 3D-DenseNet-DL model and five radiomics as predictive methods for MG using preoperative chest CT image. The final optimal model, named as 3D-DenseNet-DL based multi-model integrating with semantic CT image features, was ultimately established to detect MG in thymoma patients.

## MATERIALS AND METHODS

### Patients

For this study, 182 patients diagnosed with thymoma who had undergone thymectomy at the First Affiliated Hospital of Sun Yat-sen University from Jan 1st, 2011 to Jun 31st, 2018 were included for analysis and model building (SYSUFH dataset, **Table 1**). Another 48 thymoma patients admitted to the Sun Yat-sen Memorial Hospital of Sun Yat-sen University from Jan 1st, 2017 to Mar 31st, 2019 were used as the external validation cohort (SYSUMH dataset, **Table 1**). All cases had undergone enhanced preoperative CT examination and had been clearly staged based on pathological examination and clinical manifestation. All patients in our study were evaluated by neurologists to determine the status of myasthenia gravis (MG) syndrome or other autoimmune diseases before operation and were followed up to 2 years after surgery. The diagnostic criteria of MG in this study includes: (1) typical clinical manifestations; (2) two or more of the following: (a) positive neostigmine test, (b) decline of >10% on electromyographic low-frequency repetitive nerve stimulation or increased jitter on single-fiber electromyography, (c) positive serum AChR-Ab or MuSK-Ab or LRP4-Ab. This project was approved by the Ethics Committee and Institutional Review Board of Sun Yat-sen University. Informed consent was waived due to the retrospective nature of this study.

### CT Imaging Characteristics and Scan Protocol

Enhanced chest CT images were acquired within one week prior to operation. Imaging features were carefully evaluated through PACS reading workstation by two experienced radiologists

**Abbreviations:** ACC, accuracy; AChR, acetylcholine receptors; AI, artificial intelligence; AUC, area under ROC curve; CNN, convolutional neural network; CT, computed tomography; DenseNet, densely connected convolutional networks; DL, deep learning; MG, myasthenia gravis; PNS, paraneoplastic syndromes; ROI, regions of interests; SN, sensitivity; SP, specificity; TC, thymic carcinoma; RF, random forest; LR, logistic regression.

**TABLE 1 |** Baseline characteristic of the 230 patients with thymoma from two medical centers.

Variables	SYSUFH Dataset (n = 182)				SYSUMH Dataset (n = 48)			
	Number	without MG (n = 101)	with MG (n = 81)	P-value*	Number	without MG (n = 34)	with MG (n = 14)	P-value*
Sex				0.500				0.230
Male	115(63.2%)	66	49		27(56.3%)	21	6	
Female	67(36.8%)	35	32		21(43.7%)	13	8	
Age (year, mean $\pm$ SD)	NA	51.5 $\pm$ 13.1	47.5 $\pm$ 12.1	0.035 <sup>†</sup>	NA	51.6 $\pm$ 13.8	50.4 $\pm$ 15.1	0.791 <sup>†</sup>
WHO histologic classification				<0.001				0.227
A	22(12.1%)	19	3		8(16.7%)	7	1	
AB	37(20.3%)	22	15		13(27.1%)	11	2	
B1	21(11.5%)	15	6		5(10.4%)	4	1	
B2	72(39.6%)	26	46		19(39.6%)	10	9	
B3	21(11.5%)	10	11		3(6.25%)	2	1	
C	9(4.95%)	9	0		0	0	0	
Masaoka staging				0.006				0.151
I	84(46.2%)	43	41		41(85.4%)	28	13	
IIA	40(22.0%)	24	16		1(2.08%)	0	1	
IIB	16(8.79%)	5	11		0	0	0	
IIIA	20(10.9%)	13	7		5(10.4%)	5	0	
IIIB	13(7.14%)	7	6		1(2.08%)	1	0	
IV	9(4.94%)	9	0		0	0	0	
Smoking history				0.215				0.835
No	161(88.5%)	92	69		35(72.9%)	24	11	
Yes	21(11.5%)	9	12		13(27.1%)	10	3	
Surgical approach#				<0.001				0.051
Thymoma resection	31(17.0%)	30	1		4(8.33%)	4	0	
Thymectomy	30(16.5%)	29	1		30(62.5%)	23	7	
Extended thymectomy	111(61.0%)	34	77		14(29.2%)	7	7	

\*Chi-square test or Fisher's exact test; <sup>†</sup>Student's t test; #Some patients' data were missing; NA, Not Applicable; SYSUFH, the First Affiliated Hospital of Sun Yat-sen University; SYSUMH, Sun Yat-sen Memorial Hospital of Sun Yat-sen University.

specializing in chest CT imaging that were blinded to the MG statuses of the patients. CT Imaging characteristics that were evaluated included (**Table 2**): maximum diameter (3-D Maximum diameter); degree of enhancement (increment of enhanced CT value, HU); enhancement (homogeneous or heterogeneous); necrosis/cystic component (divided into 0–25%, 26–50%, 51–75%, 75–100% according to its volume percentage); shape (round or oval, lobulated, irregular); contours (smooth or irregular); presence of calcification, adjacent organ invasion, effusion (pleural/pericardial), and lymphadenopathy. All preoperative enhanced chest CT images were obtained with a 64-row multidetector CT scanner (Aquilion 64; Toshiba Medical, Tokyo, Japan). Scan parameters: x-ray tube voltage of 120 kVp; maximum of 500 mA with automatic tube current modulation. Axial thin-section CT images of the whole lung were reconstructed with a section thickness and spacing of 1.0 mm. Iopromide at 80–100 ml/per patient (300 mg I/ml, Schering Pharmaceutical Ltd) was injected at 3–4 ml/s flow rate and applied to contrast enhanced scanning protocol.

## Machine Learning Datasets

Thymoma on CT images were segmented manually using the annotation tool “ITK-SNAP” ([www.itksnap.org](http://www.itksnap.org)) (20). “ITK-SNAP”, as a free software, is widely used for medical image annotation and labeling. In this work, ITK-SNAP was applied for thymoma lesion segmentation. The output from ITK-SNAP is NIFTI files containing mask information of the thymoma for each sequence of CT images. We then used the mask information

to extract the area of thymoma, namely the regions of interests (ROI) (**Figure S1**). For feature extraction in radiomic analysis, the segmented thymoma was used directly. For deep learning modeling, a further preprocessing step was designed to prepare the segmented data for the convolutional neural network.

## Radiomic Analysis

### Radiomic Analysis Procedure

Radiomic analysis involved several steps: feature extraction, feature selection and machine learning. First, feature extraction was performed to convert raw images to structural data with radiomic information that could be processed by machine learning algorithms. Then, several methods were applied to further select high-quality features based on variance or regression. Finally, the data with selected features are used as inputs for several mainstream machine learning algorithms to train and test the model.

### Radiomic Features

The radiomic features were extracted using open source PyRadiomics software (<http://pyradiomics.readthedocs.io>) (21). The categories of features include: shape descriptors (2D and 3D), First Order Statistics, Gray Level Matrices (GLM) based: Gray Level Cooccurrence Matrix (GLCM), Gray Level Run Length Matrix (GLRLM), Gray Level Size Zone Matrix (GLSZM) and Gray Level Dependence Matrix (GMDM). These features were extracted not only from original images, but also from derived images filtered using Laplacians of Gaussians (LoG), Wavelet Decompositions, Square, Square Root,

**TABLE 2 |** Image characteristics of patients with thymoma.

Variables	Number	With MG		P-value
		No (n = 101)	Yes (n = 81)	
Maximum diameter <sup>†</sup>	NA	6.13 ± 2.93	4.91 ± 2.27	0.065
Degree of enhancement (HU) <sup>†</sup>	NA	32.56 ± 22.17	30.86 ± 20.06	0.972
Enhancement				0.074
Homogeneous	81(44.5%)	39	42	
Heterogeneous	101(55.5%)	62	39	
Necrosis/cystic component				0.029
0–25%	71(39.0%)	36	35	
26–50%	78(42.9%)	39	39	
51–75%	16(8.79%)	12	4	
75–100%	17(9.34%)	14	3	
Shape				0.027
Round or oval	91(50.0%)	50	41	
Lobulated	37(20.3%)	27	10	
Irregular	54(29.7%)	24	30	
Contours				0.030
Smooth	163(89.6%)	86	77	
Irregular	19(10.4%)	15	4	
Calcification				0.827
No	147(80.8%)	81	66	
Yes	35(19.2%)	20	15	
Adjacent organ invasion				<0.001
No	157(86.3%)	79	78	
Yes	25(13.7%)	22	3	
Effusion (Pleural/Pericardial)				0.028
No	169(92.9%)	90	79	
Yes	13(7.14%)	11	2	
Lymphadenopathy				0.030
No	166(91.2%)	88	78	
Yes	16(8.79%)	13	3	

<sup>†</sup>Data are mean ± standard deviation; NA, Not Applicable.

Logarithm and Exponential filters. In total, 1,390 radiomic features were extracted, covering the popular features used in research.

### Radiomic Feature Selection

Feature selection was conducted to select a subset of features from all extracted features for use in model building. The aims of this step were to reduce the dimensions of features, simplify the model and enhance generalization by reducing overfitting. A multi-level selection approach was adopted, which involved three algorithms in the order of: variance threshold method, k-best method, and the least absolute shrinkage selection operator (LASSO). Variance based method was adopted at first to select features with variance larger than a threshold (threshold = 0.1 in this study, data were normalized to a range of –1 to 1). Then, top k (k = 300 in this paper) features were further selected based on top ANOVA F-value between feature and the label. Finally, LASSO with five-fold cross-validation was adopted to automatically select the more effective features (Figure S2).

### Radiomic Model Building

The performance of radiomic analysis was evaluated using five popular machine learning algorithms: Random Forest, XGBoost,

Multilayer Perceptron, Logistic Regression and Support Vector Machine.

## Deep Learning

### Data Preprocessing

For deep learning, images with fixed dimension 160 × 160 × 64 (pixels) were used as input of the model. The images were constructed with equal width and length of 160 pixels and channels of 64 pixels. The size of the input image was determined by statistical analysis of the region of all the thymomas in this dataset.

### 3D-DenseNet

DenseNet (22) is a type of convolutional neural network (CNN). DenseNet composes of four dense blocks, as shown in the schematic diagram. Dense connections between layers within dense blocks are present in DenseNet. We chose DenseNet as the base model in this study due to its various advantages. First, DenseNet can be used to reduce over-fitting. Second, DenseNet is computationally efficient as it requires less than half of the parameters of ResNet. Although DenseNet was first designed for two-dimensional images, our study targeted 3D CT sequences. As most medical images are three-dimensional, we designed a 3D-DenseNet where the kernel of each convolutional and pooling layer was modified to 3D versions. In the proposed 3D DenseNet model, rectified linear unit (ReLU) was used as activation function in each layer, and softmax function was applied in the last layer of our network to obtain the probability for each sample (Figure 1 and Table S1). Batch normalization was applied before activation layer. The loss function of our model was due to binary cross-entropy, which was optimized using Adam with mini-batch size of 16.

### Training Process Optimization

Two kinds of data augmentation were applied during the training stage of deep learning to avoid overfitting. First, random cropping (Figure S3) was implemented by randomly placing the segmented thymoma image in the fixed cube with shape. Second, a fixed window center (WC) and window width (WW) of 300 were applied for input images with original CT values. A random change was applied for the training data with WW value ranging from –10 to 10 and WC value from –5 to 5. Transfer learning was also applied to obtain benefit such as acceleration of the training stage from the pretrained model, which boosted the training speed significantly compared with the other initialization methods (such as Xavier).

### Evaluation Metrics of Machine Learning

Five radiomic models (RF, XGBoost, SVM, MLP, LR) and one deep learning model (3D-DenseNet-DL model) were evaluated in the training and validation cohort using stratified five-fold cross-validation, and the parameter alpha was chosen with Mean Square Error (MSE) at minimum value. In this study, all the consecutively enrolled patients in SYSUFH dataset were randomly split into 80% for training and the remaining 20% for internal-validation. The metrics Area Under ROC Curve (AUC), ACC (accuracy), Sensitivity (SN) and Specificity (SP) were used to compare the performance of these models.

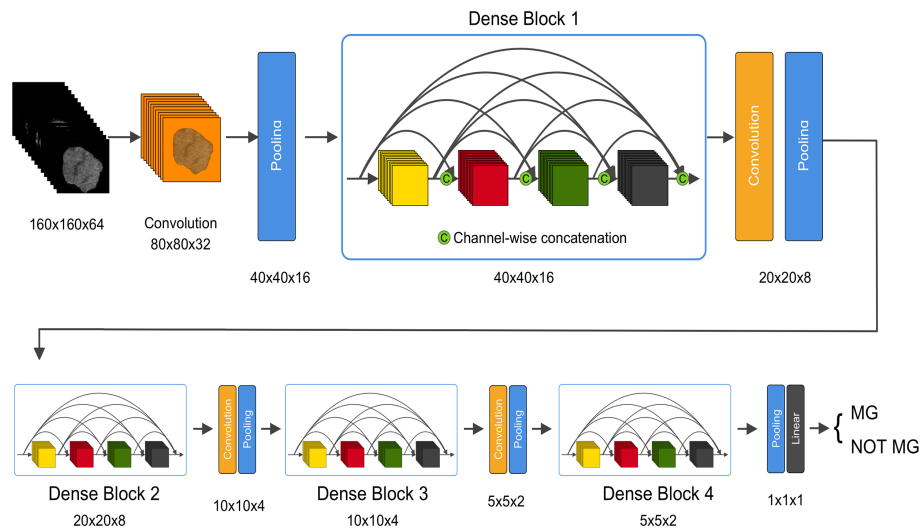


**FIGURE 1** | An illustration of the architecture of our 3D DenseNet deep learning model. Images with dimension  $160 \times 160 \times 64$  pixels are fed into the network, followed by multiple convolution and pooling operations, resulting in probability prediction for MG. In dense block, features with different levels are concatenated using skip connections. The dimension is halved after each transition layer.

The deep learning model was implemented using MXNet (version 1.2.0, Apache Software Foundation, Forest Hill, MD, USA) library (22), and the model was trained using four NVIDIA GeForce GTX 1080 GPUs (NVIDIA, Beijing, China).

## Statistical Analyses

Statistical analyses were performed using SPSS 22.0 (IBM, USA). Variables were grouped based on the presence of MG. Categorical variables were compared using the Chisq test. Continuous variables were compared using the T-test or Mann-Whitney U test for variable with abnormal distribution. Multivariate logistic regression analysis was used to explore independent predictors of MG. Variables included in this analysis included age, gender, enhancement heterogeneity, necrosis/cystic component rate, contours, shape, adjacent organ invasion, pleural/pericardial effusion, and lymphadenopathy.  $p < 0.05$  was considered as statistically significant. The area under the ROC curve (AUC), accuracy, sensitivity, and specificity were measured in order to evaluate the accuracy of models.

## RESULTS

### Clinical Characteristics of Patients

230 patients were included in this study; 182 (SYSUFH dataset) were used for training and model building, and an independent cohort of 48 cases (SYSUMH dataset) was used for external validation. The baseline characteristics of all patients from two medical centers were summarized in **Table 1**. In the SYSUFH cohort, a significant different ratio of histologic classification was

found between the two groups ( $P < 0.001$ ): MG patients with a lower A + AB ratio (22.2 vs. 40.6%) and higher  $B_1 + B_2 + B_3$  ratio (77.8 vs. 50.5%), compared to patients without MG. MG was not found in thymic carcinoma (TC), which is consistent with previous reports (18). In addition, MG patients showed significant association with younger age ( $47.5 \pm 12.1$  vs.  $51.5 \pm 13.1$  years,  $P = 0.035$ ) and relatively earlier thymoma Masaoka staging ( $P = 0.006$ ). There were no significant differences between the two groups in terms of gender and smoking history.

### Associations Between Semantic CT Image Characteristics and Status of MG

Ten common variables were used to describe the CT imaging features of thymomas included in this study (**Table 2**). The statistical differences between two groups were found in necrosis/cystic component rate ( $P = 0.029$ ), contours (smooth/irregular,  $P = 0.030$ ), shape ( $P = 0.027$ ), adjacent organ invasion ( $P < 0.001$ ), pleural/pericardial effusion ( $P = 0.028$ ), and lymphadenopathy ( $P = 0.030$ ). In general, thymoma patients with MG tend to have less enhancement heterogeneity, less lobulated shape, and lower rate of adjacent organ invasion.

### Detection of MG by Radiomic Analysis and 3D DenseNet DL Model

For the radiomic analysis and deep learning (DL) analysis, a total of 1,390 radiomic features were extracted from the Routine contrast enhanced chest CT image data. After applying Variance Threshold, K-best and LASSO methods, the remaining features after application of each method were 499, 300, and 16, respectively. The 16 features finally selected were listed in **Table S2**. To decipher the relationship between features,



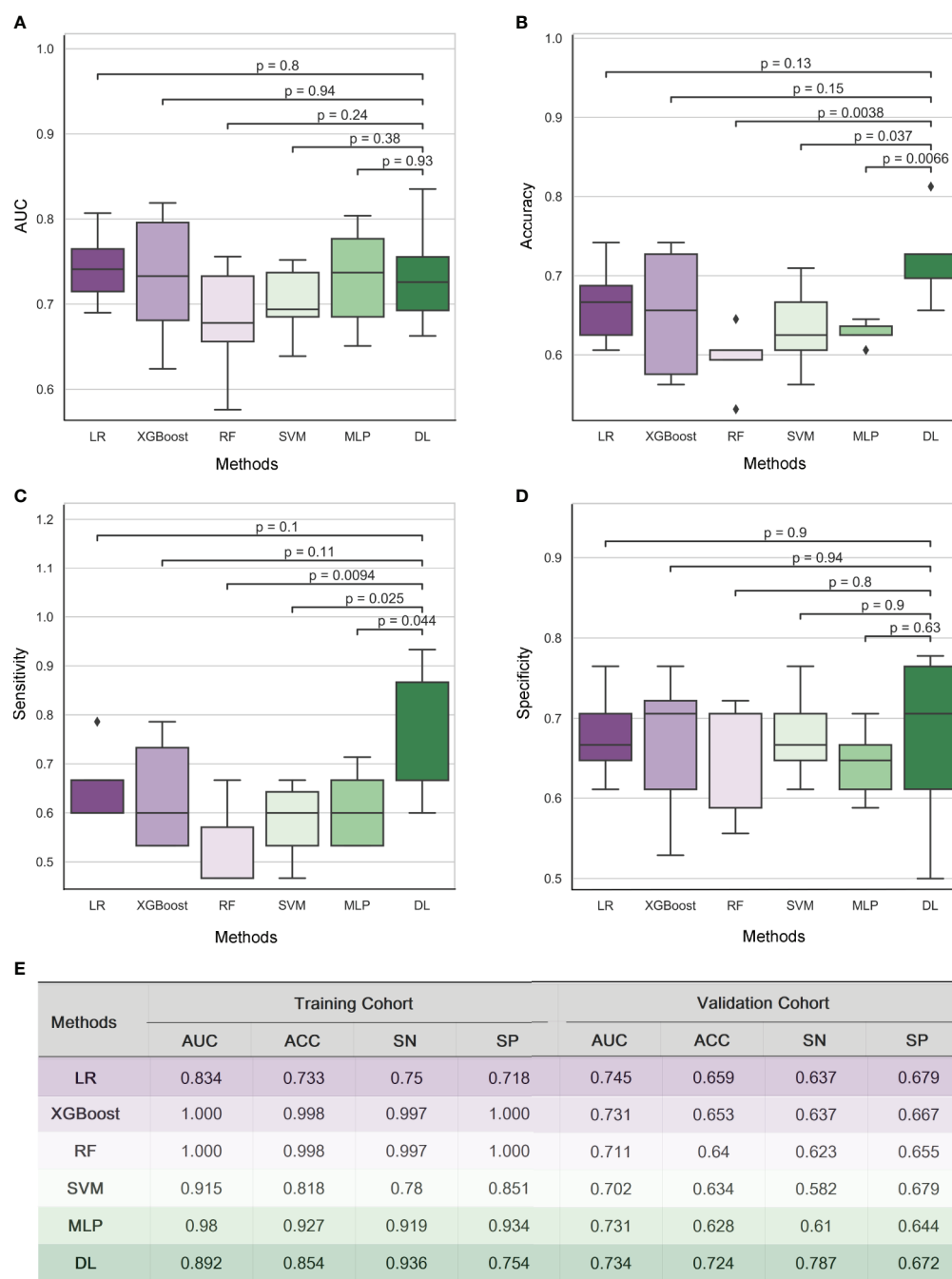


**FIGURE 2 |** Results of Radiomic analysis and 3D DenseNet deep learning model for detecting MG in a cohort of 182 thymoma patients. The performance of five radiomic models and 3D-DenseNet-DL model was compared using Area Under ROC Curve (AUC) (**A**), accuracy (**B**), sensitivity (**C**), and specificity (**D**). 3D DenseNet deep learning model for detecting MG showed similar results in AUC and specificity, but relatively better results in accuracy and sensitivity compared to five radiomic analysis models (**E**). “RF”, “LR”, and “DL” refer to “Random Forest”, “Logistic Regression”, and “Deep Learning” respectively; “AUC”, “ACC”, “SN”, and “SP” refer to the metrics Area Under ROC Curve, Accuracy, Sensitivity, and Specificity, respectively.

correlation analysis using the Pearson method was applied, and a heatmap was constructed for visualization (**Figure S4**).

Five radiomic models (RF, XGBoost, SVM, MLP, LR) and 3D-DenseNet-DL model were established to detect the status of TAMG,

and the values of each metric were shown in **Figure 2**. Compared with the other five radiomic models, the DL model showed the most favorable results with AUC 0.734, accuracy (ACC) 0.724, sensitivity (SN) 0.787 and specificity (SP) 0.672, respectively.

## Building of the 3D-DenseNet-DL Based Multi-Model for MG Detection

With the multivariable logistic regression analysis, only the shape of thymoma ( $P = 0.031$ ), the invasion rate of adjacent organ ( $P = 0.001$ ), and DL score ( $P < 0.001$ ) qualified as independent predictable factors (Table 3). To optimize the effectiveness of TAMG-detecting model, we further built 3D-DenseNet-DL based multi-model (DL plus two semantic CT features). With ROC curve analysis, the AUC of DL model, semantic CT feature model (the shape and the invasion rate of adjacent organ), and 3D-DenseNet-DL based multi-model were 0.734, 0.677, and 0.766, respectively (Figures 3A, B), suggesting that the 3D-DenseNet-DL based multi-model demonstrated better performance for detecting MG in thymoma patients.

**TABLE 3 |** Significant correlations of MG with semantic CT imaging features and DL score using Logistic Regression Forward Stepwise (Likelihood Ratio) method.

Characteristic	P &	P #	OR # (95% CI)
Shape	0.031	0.032	1.59 (1.04–2.43)
Adjacent organ invasion	0.001	0.007	0.11 (0.02–0.54)
DL score	0.000	0.000	147.84 (9.15–1238.51)

OR, odd ratio; CI, confidence interval; DL, deep learning; #, The P value was calculated by multivariable logistic regression analysis adjusted for age and gender; &, Unadjusted P value;  $P < 0.05$  was considered as statistically significant.

## The External Validation of 3D-DenseNet-DL Based Multi-Model

We further evaluated the 3D-DenseNet-DL model and the 3D-DenseNet-DL based multi-model in an external validation set composed of 48 thymoma patients from another medical center (SYSUMH). The results showed a comparable agreement in both datasets for the detection of TAMG, with an AUC of 0.730, ACC of 0.732, SN of 0.700, and SP of 0.690 for 3D-DenseNet-DL based multi-model; and AUC of 0.704, ACC of 0.690, SN of 0.760, and SP of 0.710 for 3D-DenseNet-DL model (Figure 3C). This favorable result further confirmed the reliability and efficacy of our 3D-DenseNet-DL based multi-model in screening TAMG in patients with thymoma.

## DISCUSSION

In this study, we proposed and validated a non-invasive method based on preoperative routine CT imaging of thymoma, referred to as “3D DenseNet deep learning (DL) based multi-model”, to detect MG before operation. With this model, we successfully filtered out most of MG patients in the internal validation set (AUC of 0.766), and further verified its reliability and efficacy in an external validation set (AUC of 0.730). We also established five radiomic models (RF, XGBoost, SVM, MLP, LR) to detect MG and compared the effectiveness in detecting disease with the DL model. Our results suggest our 3D-DenseNet-DL based

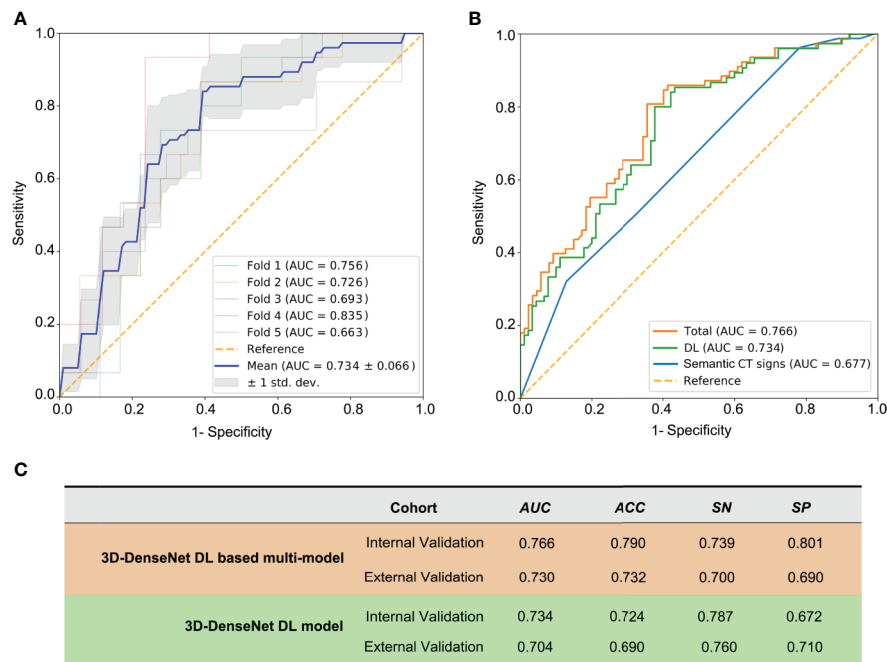


**FIGURE 3 |** The prediction metrics of 3D-DenseNet-DL and DL based multi-model. The metrics Area Under ROC Curve (AUC), ACC (accuracy), SN (sensitivity), and SP (specificity) were used to compare the performance of these models. (A) The prediction metrics of the deep learning results from training and five-fold cross-validation, a mean AUC of  $0.734 \pm 0.066$  was presented. (B) The comparison of three models of semantic CT signs model, 3D-DenseNet-DL model, and the comprehensive model (3D-DenseNet-DL based multi-model), with a mean AUC of 0.677, 0.734, and 0.766, respectively. (C) Values of 3D-DenseNet-DL model and 3D-DenseNet-DL based multi-model in external validation, with AUC 0.704, ACC 0.690, SN 0.760, and SP 0.710 for DL model, and AUC 0.730, ACC 0.732, SN 0.700, and SP 0.690 for our final 3D-DenseNet-DL based multi-model.

multi-model is an effective and non-invasive method for detecting MG in patients with thymoma. To our knowledge, this is the first study about the diagnosis of MG in thymoma patients by using machine learning based on CT imaging data.

Currently, a large number of diagnostic tests are available for MG diagnosis, including clinical, electrophysiological, and laboratory antibody tests (23). However, results from these tests can be negative in some patients, and diagnosing pure ocular MG can be a challenge (23). The anti-AChR antibody assay by radioimmunoassay kits is considered as the most reliable approach to diagnose MG (24, 25). However, these kits are expensive and not routinely available for most diagnostic laboratories. In China, commercial enzyme-linked immunosorbent assay (ELISA) kits are more widely used for anti-AChR test, which are inferior to radioimmunoassay in terms of both sensitivity and specificity (26). Therefore, although AChR antibody is found in nearly all of thymoma associated MG patients, the false positive rate was also high (16). Repetitive nerve stimulation (RNS) (27) and single-fiber electromyography (SFEMG) (28) are also used in electrophysiological confirmation for MG. However, SFEMG may not provide confirmation of the presence of MG unless weak muscles are tested, and the reliability of results is highly dependent on the experience of the technician (13). More importantly, as a relatively rare autoimmune disease, the diagnosis system of MG is mainly concentrated in large hospitals or medical centers, and a large number of patients with thymoma cannot be effectively screened for MG before surgery. Considering the limitations or unavailability of these classical diagnostic methods, a simple, easily available method with good efficacy is important in clinical practice for the preoperative detecting of MG in thymoma patients. CT examination, as a routine preoperative examination for patients with thymoma, is very popular. Therefore, our MG detecting DL model based on preoperative CT has great application prospects and clinical significance.

Nowadays, an increasing number of studies are performed to evaluate the potential relationship between CT imaging and biological features of solid tumors (29), such as glioblastoma (30), rectal and lung adenocarcinoma (31, 32). As the most common primary neoplasms of the mediastinum, the prediction of thymoma histology and stage by radiographic criteria has been mentioned in several previous reports. CT findings, such as smooth contours (33), calcification (33, 34), heterogeneous attenuation (34, 35), were interpreted as being of value in differentiating the various histologic subtypes of thymomas. Recently, Angelo Iannarelli and colleagues (36) found a relationship between radiomic parameters, histology, and grading of thymic tumors. More importantly, their study also demonstrated that MG syndrome was significantly associated with some parameters in quantitative texture analysis (QTA) (36). Although their study only included 16 patients (seven patients with MG), it represented an incentive for further evaluation of the value of radiographic analysis in detection of MG syndrome in thymoma patients. Based on these findings, we therefore proposed a machine learning model based on

preoperative CT imaging for screening MG in large cohort of thymoma patients and achieved the expected results. Moreover, our results further confirmed the superior reliability and efficacy of this developed 3D-DenseNet-DL model compared to the other five radiomic-based methods. These results also highlight the importance of radiographic analysis as diagnostic tools from the accurate characterization of the lesion itself to the detection of the paraneoplastic syndromes, which is a great stride in the application of AI in the medical field.

However, despite its satisfactory outcomes, this study has some limitations. First, given the retrospective nature of this analysis, a selection bias was unavoidable. Second, patients were not stratified into more detailed clinical status categories due to limited sample size. Third, the status of serum AChR binding antibodies was important for thymoma associated MG diagnosis, but the absence of such information in certain cases restrained further analysis. In addition, our deep learning model was built and validated only based on pathologically diagnosed thymoma, which limits the application scope of this model to some extent. Therefore, a perspective, multi-center clinical trial with larger cohort would be indispensable to further confirm and optimize the screening model for MG patients.

In conclusion, with a large sample data for modeling and an independent cohort for external validation, we firstly developed a 3D-DenseNet-DL based multi-model for MG screening in thymoma patients based on preoperative CT imaging and achieved favorable results.

## DATA AVAILABILITY STATEMENT

The raw data supporting the conclusions of this article will be made available by the authors, without undue reservation.

## AUTHOR CONTRIBUTIONS

Study concept and design, literature search, and writing: ZL, YZ, HF, HL, SF, and ZK. Data collection/interpretation: YZ, HF, YY, LY, BS, HL, KW, and MW. Data analysis: ZL, YZ, XY, XW, XT, SF, HL, and RZ. Approval of final version of submitted manuscript: all authors. Manuscript editing: all authors. All authors contributed to the article and approved the submitted version.

## FUNDING

The work was supported by grants from China National Natural Sciences Foundation (No.82001331) and Natural Sciences Foundation of Guangdong Province (No.2018A0303130250).

## SUPPLEMENTARY MATERIAL

The Supplementary Material for this article can be found online at: <https://www.frontiersin.org/articles/10.3389/fonc.2021.631964/full#supplementary-material>

## REFERENCES

- Detterbeck FC, Parsons AM. Thymic Tumors. *Ann Thorac Surg* (2004) 77:1860–9. doi: 10.1016/j.athoracsur.2003.10.001
- Lewis JE, Wick MR, Scheithauer BW, Bernatz PE, Taylor WF. Thymoma. A Clinicopathologic Review. *Cancer* (1987) 60:2727–43. doi: 10.1002/1097-0142(19871201)60:11<2727::AID-CNCR2820601125>3.0.CO;2-D
- Drachman DB. Myasthenia Gravis. *N Engl J Med* (1994) 330:1797–810. doi: 10.1056/NEJM199406233302507
- Gritti P, Sgarzi M, Carrara B, Lanterna LA, Novellino L, Spinelli L, et al. A Standardized Protocol for the Perioperative Management of Myasthenia Gravis Patients. Experience With 110 Patients. *Acta Anaesthesiol Scand* (2012) 56:66–75. doi: 10.1111/j.1399-6576.2011.02564.x
- Kanai T, Uzawa A, Sato Y, Suzuki S, Kawaguchi N, Himuro K, et al. A Clinical Predictive Score for Postoperative Myasthenic Crisis. *Ann Neurol* (2017) 82:841–9. doi: 10.1002/ana.25087
- Lacomis D. Myasthenic Crisis. *Neurocrit Care* (2005) 3:189–94. doi: 10.1385/LCCM.3.3:189
- Watanabe A, Watanabe T, Obama T, Mawatari T, Ohsawa H, Ichimiya Y, et al. Prognostic Factors for Myasthenic Crisis After Transsternal Thymectomy in Patients With Myasthenia Gravis. *J Thorac Cardiovasc Surg* (2004) 127:868–76. doi: 10.1016/j.jtcvs.2003.07.036
- Ando T, Omasa M, Kondo T, Yamada T, Sato M, Menju T, et al. Predictive Factors of Myasthenic Crisis After Extended Thymectomy for Patients With Myasthenia Gravis. *Eur J Cardio-Thoracic Surg* (2015) 48:705–9. doi: 10.1093/ejcts/ezu530
- Juel VC. Myasthenia Gravis: Management of Myasthenic Crisis and Perioperative Care. *Semin Neurol* (2004) 24:75–81. doi: 10.1055/s-2004-829595
- N.C.C. Network. Nccn Clinical Practice Guidelines in Oncology IEEE (Institute of Electrical and Electronics Engineers). In: *Thymomas and Thymic Carcinomas* (2019). Available at: <https://ieeexplore.ieee.org/document/8099726>.
- Cata JP, Lasala JD, Williams W, Mena GE. Myasthenia Gravis and Thymoma Surgery: A Clinical Update for the Cardiothoracic Anesthesiologist. *J Cardiothorac Vasc Anesth* (2018) 33(9):2537–45. doi: 10.1053/j.jvca.2018.07.036
- Evoli A, Iorio R, Bartocconi E. Overcoming Challenges in the Diagnosis and Treatment of Myasthenia Gravis. *Expert Rev Clin Immunol* (2016) 12:157–68. doi: 10.1586/1744666X.2016.1110487
- Keesey JC. Clinical Evaluation and Management of Myasthenia Gravis. *Muscle Nerve* (2004) 29:484–505. doi: 10.1002/mus.20030
- Bi WL, Hosny A, Schabath MB, Giger ML, Birkbak NJ, Mehrtash A, et al. Artificial Intelligence in Cancer Imaging: Clinical Challenges and Applications. *CA Cancer J Clin* (2019) 69:127–57. doi: 10.3322/caac.21552
- Choi JY. Radiomics and Deep Learning in Clinical Imaging: What Should We do? *Nucl Med Mol Imaging* (2018) 52:89–90. doi: 10.1007/s13139-018-0514-0
- Fujii Y. Thymus, Thymoma and Myasthenia Gravis. *Surg Today* (2013) 43:461–6. doi: 10.1007/s00595-012-0318-2
- Kondo K, Yoshizawa K, Tsuyuguchi M, Kimura S, Sumitomo M, Morita J, et al. Who Histologic Classification is a Prognostic Indicator in Thymoma. *Ann Thorac Surg* (2004) 77:1183–8. doi: 10.1016/j.athoracsur.2003.07.042
- Radovich M, Pickering CR, Felau I, Ha G, Zhang H, Jo H, et al. The Integrated Genomic Landscape of Thymic Epithelial Tumors. *Cancer Cell* (2018) 33:244–258 e10. doi: 10.1016/j.ccell.2018.01.003
- Han XW, Gao WW, Chen Y, Du L, Duan JH, Yu HW, et al. Relationship Between Computed Tomography Imaging Features and Clinical Characteristics, Masaoka-Koga Stages, and World Health Organization Histological Classifications of Thymoma. *Front Oncol* (2019) 9:1041. doi: 10.3389/fonc.2019.01041
- Yushkevich PA, Piven J, Hazlett HC, Smith RG, Ho S, Gee JC, et al. User-Guided 3d Active Contour Segmentation of Anatomical Structures: Significantly Improved Efficiency and Reliability. *Neuroimage* (2006) 31:1116–28. doi: 10.1016/j.neuroimage.2006.01.015
- van Griethuysen JJM, Fedorov A, Parmar C, Hosny A, Aucoin N, Narayan V, et al. Computational Radiomics System to Decode the Radiographic Phenotype. *Cancer Res* (2017) 77:e104–7. doi: 10.1158/0008-5472.CAN-17-0339
- Huang G, Liu Z, van der Maaten L, Weinberger KQ. Densely Connected Convolutional Networks. In: *30th Ieee Conference on Computer Vision and Pattern Recognition (Cvpr 2017)* (2017). p. 2261–9. doi: 10.1109/CVPR.2017.243
- Gilhus NE, Tzartos S, Evoli A, Palace J, Burns TM, Verschuuren J. Myasthenia Gravis. *Nat Rev Dis Primers* (2019) 5:30. doi: 10.1038/s41572-019-0079-y
- Lindstrom JM, Seybold ME, Lennon VA, Whittingham S, Duane DD. Antibody to Acetylcholine Receptor in Myasthenia Gravis. *Prevalence Clin correlates Diagn value Neurol* (1976) 26:1054–9. doi: 10.1212/WNL.26.11.1054
- Oger J, Kaufman R, Berry K. Acetylcholine Receptor Antibodies in Myasthenia Gravis: Use of a Qualitative Assay for Diagnostic Purposes. *Can J Neurol Sci* (1987) 14:297–302. doi: 10.1017/S0317167100026652
- Zisimopoulou P, Brenner T, Trakas N, Tzartos SJ. Serological Diagnostics in Myasthenia Gravis Based on Novel Assays and Recently Identified Antigens. *Autoimmun Rev* (2013) 12:924–30. doi: 10.1016/j.autrev.2013.03.002
- Keesey JC. Aae Minimonograph #33: Electrodiagnostic Approach to Defects of Neuromuscular Transmission. *Muscle Nerve* (1989) 12:613–26. doi: 10.1002/mus.880120802
- Sanders DB. Clinical Impact of Single-Fiber Electromyography. *Muscle Nerve* (2002) 11:S15–20. doi: 10.1002/mus.10141
- Colen R, Foster I, Gatenby R, Giger ME, Gillies R, Gutman D, et al. Nci Workshop Report: Clinical and Computational Requirements for Correlating Imaging Phenotypes With Genomics Signatures. *Transl Oncol* (2014) 7:556–69. doi: 10.1016/j.tranon.2014.07.007
- Jain R, Poisson LM, Gutman D, Scarpace L, Hwang SN, Holder CA, et al. Outcome Prediction in Patients With Glioblastoma by Using Imaging, Clinical, and Genomic Biomarkers: Focus on the Nonenhancing Component of the Tumor. *Radiology* (2014) 272:484–93. doi: 10.1148/radiol.14131691
- Rizzo S, Petrella F, Buscarino V, De Maria F, Raimondi S, Barberis M, et al. Ct Radiogenomic Characterization of EGFR, K-RAS, and ALK Mutations in Non-Small Cell Lung Cancer. *Eur Radiol* (2016) 26:32–42. doi: 10.1007/s00330-015-3814-0
- De Cecco CN, Ganeshan B, Ciolina M, Rengo M, Meinel FG, Musio D, et al. Texture Analysis as Imaging Biomarker of Tumoral Response to Neoadjuvant Chemoradiotherapy in Rectal Cancer Patients Studied With 3-T Magnetic Resonance. *Invest Radiol* (2015) 50:239–45. doi: 10.1097/RLI.0000000000000116
- Tomiyama N, Johkoh T, Mihara N, Honda O, Kozuka T, Koyama M, et al. Using the World Health Organization Classification of Thymic Epithelial Neoplasms to Describe Ct Findings. *AJR Am J Roentgenol* (2002) 179:881–6. doi: 10.2214/ajr.179.4.1790881
- Tomiyama N, Muller NL, Ellis SJ, Cleverley JR, Okumura M, Miyoshi S, et al. Invasive and Noninvasive Thymoma: Distinctive Ct Features. *J Comput Assist Tomogr* (2001) 25:388–93. doi: 10.1097/00004728-200105000-00010
- Han J, Lee KS, Yi CA, Kim TS, Shim YM, Kim J, et al. Thymic Epithelial Tumors Classified According to a Newly Established WHO Scheme: CT and MR Findings. *Korean J Radiol* (2003) 4:46–53. doi: 10.3348/kjr.2003.4.1.46
- Iannarelli A, Sacconi B, Tomei F, Anile M, Longo F, Bezzi M, et al. Analysis of CT Features and Quantitative Texture Analysis in Patients With Thymic Tumors: Correlation With Grading and Staging. *Radiol Med* (2018) 123:345–50. doi: 10.1007/s11547-017-0845-4

**Conflict of Interest:** Authors XT and RZ were employed by Advanced Institute, Infervision, Beijing.

The remaining authors declare that the research was conducted in the absence of any commercial or financial relationships that could be construed as a potential conflict of interest.

Copyright © 2021 Liu, Zhu, Yuan, Yang, Wang, Wang, Yang, Wu, Tian, Zhang, Shen, Luo, Feng, Feng and Ke. This is an open-access article distributed under the terms of the Creative Commons Attribution License (CC BY). The use, distribution or reproduction in other forums is permitted, provided the original author(s) and the copyright owner(s) are credited and that the original publication in this journal is cited, in accordance with accepted academic practice. No use, distribution or reproduction is permitted which does not comply with these terms.





# Arterial Spin Labeling MRI for Predicting Microvascular Invasion of T1 Staging Renal Clear Cell Carcinoma Preoperatively

Han-Mei Zhang<sup>1</sup>, Da-Guang Wen<sup>1</sup>, Yi Wang<sup>1</sup>, Yi-Ge Bao<sup>2</sup>, Yuan Yuan<sup>1</sup>, Yun-Tian Chen<sup>1</sup> and Bin Song<sup>1\*</sup>

<sup>1</sup> Department of Radiology, West China Hospital, Sichuan University, Chengdu, China, <sup>2</sup> Department of Urology, West China Hospital, Sichuan University, Chengdu, China

## OPEN ACCESS

### Edited by:

Changqiang Wu,  
North Sichuan Medical College, China

### Reviewed by:

Jing Chen,  
The Affiliated Hospital of Southwest  
Medical University, China  
Li Li,  
Chengde Hospital of Traditional  
Chinese Medicine, China

### \*Correspondence:

Bin Song  
songlab\_radiology@163.com

### Specialty section:

This article was submitted to  
Cancer Imaging and  
Image-directed Interventions,  
a section of the journal  
Frontiers in Oncology

Received: 22 December 2020

Accepted: 09 April 2021

Published: 18 May 2021

### Citation:

Zhang H-M, Wen D-G, Wang Y,  
Bao Y-G, Yuan Y, Chen Y-T and  
Song B (2021) Arterial Spin Labeling  
MRI for Predicting Microvascular  
Invasion of T1 Staging Renal Clear Cell  
Carcinoma Preoperatively.  
Front. Oncol. 11:644975.  
doi: 10.3389/fonc.2021.644975

**Background:** Microvascular invasion (MVI) is a valuable factor for T1 staging renal clear cell carcinoma (ccRCC) operation strategy decision, which is confirmed histopathologically post-operation. This study aimed to prospectively evaluate the performance of arterial spin labeling (ASL) MRI for predicting MVI of T1 staging ccRCC preoperatively.

**Methods:** 16 volunteers and 39 consecutive patients were enrolled. MRI examinations consisted of ASL (three post label delays separately) of the kidney, followed by T1 and T2-weighted imaging. Two sessions of ASL were used to evaluate the reproducibility on volunteers. Renal blood flow of renal cortex, medulla, the entire and solid part of the tumor were measured on ASL images. Conventional imaging features were extracted. MVI and WHO/ISUP classification were evaluated histopathologically. A paired t-test was used to compare the renal cortex and medulla between ASL 1 and ASL 2. The reproducibility was assessed using the intraclass correlation. Differences in mean perfusion between the entire and the solid parts of tumors with or without MVI were assessed separately using Student's t test. The diagnostic performance was assessed. Logistic regression analysis was used to indicate the independent prediction index for MVI.

**Results:** The two sessions of ASL showed no significant difference between the mean cortex values of RBF. The cortical RBF measurements demonstrated good agreement. 12 ccRCCs presented with MVI histopathologically. Mean perfusion of the solid part of tumors with MVI were  $536.4 \pm 154.8$  ml/min/100 g (PLD1),  $2912.5 \pm 939.3$  ml/min/100 g (PLD2),  $3280.3 \pm 901.2$  ml/min/100 g (PLD3). Mean perfusion of the solid part of tumors without MVI were  $453.5 \pm 87.2$  ml/min/100 g (PLD1),  $1043.6 \pm 695.8$  ml/min/100 g (PLD2),  $1577.6 \pm 1085.8$  ml/min/100 g (PLD3). These two groups have significant difference at all the PLDs ( $p < 0.05$ ). The RBF of PLD1 of the solid part of tumor perfusion showed well diagnostic performance for predicting MVI: sensitivity 75%, specificity 100%, positive predictive value 66.7%, and negative predictive value 95.7%.

The maximum diameter of the tumor, ill-defined margin, and the solid part of tumor perfusion were the independent prediction index for MVI.

**Conclusion:** ASL MR imaging has good reproducibility for renal cortex, and good diagnostic performance for predicting MVI for ccRCC.

**Keywords:** arterial spin labeling MRI, renal blood flow, microvascular invasion, diagnostic test (MeSH), renal clear cell carcinoma

## INTRODUCTION

With the imaging technology developing, the detection of renal cell carcinoma (RCC) has increased (1). RCC is the most common type of kidney solid tumor, accounting for 90% of malignant kidney tumors (2). For focal RCC T1/2N0M0, although cryoablation is an optional therapy, high quality evidence suggests that surgery is the best therapy strategy. The operation strategy mainly contains radical nephrectomy (RN) and partial nephrectomy (PN). Many retrospective studies (3–5) have shown that from the perspective of oncology and patient quality of life for RCC tumors less than 4 cm in diameter RCC, partial resection is more likely to be chosen. In the Kidney Cancer Management Guide, for RCC with a tumor diameter greater than 4 cm and less than 7 cm, there is no high-quality evidence to support which procedure (RN or PN) should be chosen.

It is also mentioned in the guidelines that for patients with venous tumor thrombus, radical nephrectomy is currently recommended (4). It has been suggested that RCC with a diameter greater than 4 cm has a larger proportion accompanied with renal vein thrombosis than RCC smaller than 4 cm (6). Sugino et al. (7) suggest that the first step in the invasion of tumor cells into large blood vessels is to grow in the efferent veins (*i.e.* venules) and then gradually spread to the large and medium veins. The venules belong to the category of microvascular, and the microvascular are blood vessels that can only be seen under the microscope. It should include tiny genus of large veins, tiny venous vessels in the tumor capsule, and tiny segments within the tumor fibers. This means that microvascular invasion is the former step of venous tumor thrombus. In this situation, radical nephrectomy is preferred. In particular, previous studies reported that MVI is an independent risk factor of tumor recurrence after surgical resection of hepatocellular carcinoma (8). Furthermore, multiple research studies (9–11) have shown that microvascular invasion is an important factor in the prognosis of renal cell carcinoma. Therefore, if microvascular invasion can be accurately predicted before surgery, the operation strategy for patients with renal cell carcinoma (especially the size larger than 4 cm and smaller than 7 cm) will be more confident; the management of renal cell carcinoma is a step closer; it can also provide more information for predicting the prognosis of patients before surgery.

**Abbreviations:** MVI, microvascular invasion; ASL, arterial spin labeling; ccRCC, clear cell renal cell carcinoma.

Some conventional MRI features have been reported to indirectly predict MVI, such as irregular tumor margins, capsule disruption, peritumoral enhancement (12), lack of the functional MRI features, which may occur before conventional MRI features and supply more functional information. Arterial spin labeling (ASL) is a magnetic resonance imaging (MRI) technique that allows the non-invasive quantitative assessment of tissue perfusion, using the magnetization of endogenous-labeled blood to provide contrast, without using of any exogenous contrast agent (13). The basis for the calculation of tissue perfusion is the difference between images acquired with and without labeling. Tissue perfusion obtained with ASL MRI is not affected by vessel permeability and is beneficial for eliminating the risk of nephrogenic systemic fibrosis in patients with renal impairment (14, 15). ASL for renal blood flow quantification in healthy kidneys, renal allografts, and renal masses has good feasibility and reliability (16, 17).

Since microvascular invasion is tightly related with the invasiveness of tumor, which are usually reflected from the perfusion of tumor, this study aimed to prospectively evaluate the performance of functional ASL imaging for predicting microvascular invasion of T1 staging (maximum diameter  $\leq 7$  cm) renal clear cell carcinoma which was confirmed histopathologically.

## MATERIALS AND METHODS

### Inclusion and Exclusion Criteria

The hospital institutional review board permitted this study, and all patients have signed the written informed consent. 16 volunteers and 39 consecutive patients were enrolled between August 2019 and June 2020. The inclusion criteria were: (1) renal lesion (maximum diameter  $\leq 7$  cm) was detected by abdominal computed tomography (CT) or ultrasound; (2) no treatment of the renal lesion; (3) age between 18 and 70 years old; (4) good image quality; and (5) radical nephrectomy. The exclusion criteria of the patients were as follows: (1) contraindication to MRI; (2) post-surgical histopathology indicated no ccRCCs (18).

### MRI Protocol

MRI examinations consisted of ASL MRI of the kidney, followed by T1-weighted and T2-weighted imaging of the abdomen, as described in **Table 1**. Ten healthy volunteers were scanned using a breath-hold renal perfusion imaging using Pseudocontinuous ASL (pCASL) scheme on a 3 T GE W750 scanner. Spin-echo (SE)-based Echo planar imaging (EPI) is used for readout

**TABLE 1** | Imaging parameters for ASL-MRI, T1WI, T2WI sequences.

Parameter	ASL imaging	Coronal T2WI	Axial T2WI	Axial T1WI
Repetition time (ms)	5,323.8	1,000	1,650	150
Echo time (ms)	18	68	26	1.4/2
Flip angle (degrees)	/	150	111	75
Section thickness (mm)	7	3	5	5
Matrix	64 × 96	320 × 256	320 × 256	256 × 205
Field of view (mm)	320 × 320	452 × 452	378 × 276	438 × 285
Acquisition time	2 min 13 s	27 s	1 min 7 s	33 s
Post label delay (ms)	500 (PLD1), 1,000 (PLD2), 2,000 (PLD3)	/	/	/

techniques. The time between the inversion pulse to the central k-space of the first slice was defined as post-label delay. Three different PLDs (500, 1,000, and 2,000 ms) were used separately. Seven slices covering both kidneys were acquired with an oblique-coronal image orientation. The total scanning time is 2 min 13 s.

A second identical scan session within 1 h after the first scan session (ASL 1 and ASL 2) for all volunteers (without eating or drinking) was conducted. Patients included in this study were scanned with the same protocol.

## Quantification of Renal Cortex Perfusion and Renal Mass

Analysis was performed using custom-written MATLAB programs (The MathWorks, Inc., Natick, MA, USA). ASL perfusion-weighted (PW) difference images were formed by subtracting the non-selective images from the selective images (19). PW difference images were inspected for motion, misaligned pairs discarded, and the remaining PW difference images averaged to form an average PW difference image ( $\Delta M$ ) for each slice. These were then normalized to the base M0 image. T1 maps were formed by fitting the inversion recovery data to a

two-parameter model.  $\Delta M$ , T1, and base M0 maps were used to generate a renal perfusion ( $f$ ) map, in units of ml/100 g/min, by fitting the data to a kinetic model. Each slice was fitted taking into account the exact post-label delay at which the slice was collected following the labeling pulse.

Renal blood flow in the area of renal cortex, medulla, the entire and solid parts of the tumor were measured on ASL images using region-of-interest (ROI) analysis by one reviewer (18). Image J was used to draw ROI to measure the perfusion and show the pseudocolor map. The reviewer was blinded to the histopathological analysis. The ROI of tumor was drawn covering the entire and solid parts (avoiding the necrosis area) of tumor and did not exceed the contour of the tumor. The ROI of the renal cortex was drawn covering the cortex.

## Conventional Imaging Features of Renal Mass

Conventional imaging features were extracted including the size of the tumor (which was quantified in the maximum section in axial image), signal features on T1WI and T2WI, the smooth/ill-defined margins, the shape (spherical, elliptical, irregular), presence of necrosis (20, 21) (Table 2).

## Histology

According to the “Guideline of Standardized Pathological Diagnosis of Primary Liver Cancer (2015 edition)”, MVI was defined as “a cancer cell nest with >50 cells in the endothelial vascular lumen under microscopy”, which was classified into three grades according to the number and distribution of MVI: M0, no MVI; M1 (the low-risk group),  $\leq 5$  MVI in adjacent liver tissue  $\leq 1$  cm away from the tumor; M2 (the high-risk group),  $> 5$  MVI or MVI in liver tissue  $> 1$  cm away from the tumor (22). This study used the above standard to evaluate the MVI of ccRCC. WHO/ISUP classification was also evaluated.

## Statistical Analyses

SPSS 19.0 software (SPSS, Chicago, IL, USA) was used for statistical analysis. The ASL perfusion values obtained were used for quantitative analysis. The mean, standard error of the

**TABLE 2** | Image features of kidney tumors.

Kidney Tumor Location		group1*	group2#	T1WI signal		group1	group2
left	20	7	13	low	20	7	13
right	19	5	14	medium	15	4	11
				high	4	1	3
T2WI signal		group1	group2	central necrosis		group1	group2
low	3	1	2	presence	17	5	12
medium	8	3	5	absence	22	7	15
high	28	8	20				
margin		group1	group2	the shape		group1	group2
smooth	17	8	9	spherical	15	5	10
ill-defined	22	4	18	elliptical	13	4	9
				irregular	11	3	8
the size of the tumor		group1	group2				
		3.6 ± 2.1	4.7 ± 1.8				

\*group1: kidney tumors with microvascular invasion.

#group2: kidney tumors without microvascular invasion.

mean and 95% confidence interval (CI) of perfusion of renal cortex perfusion and renal tumors were calculated.

Perfusion of the renal cortex and medulla was compared by a paired t-test between ASL 1 and ASL 2. The intraclass correlation (ICC) was used to assess the reproducibility (23).

Differences in mean perfusion between the entire and the solid parts of the tumors with or without microvascular invasion were assessed separately using Student's t-test. The receiver operating characteristic (ROC) curve analysis was conducted to assess the diagnostic power. The diagnostic performance of ASL imaging for predicting MVI of the ccRCC was assessed using the diagnostic test index: sensitivity, specificity, positive predictive value, and negative predictive value.

Logistic regression analysis included the entire and solid parts of tumor of perfusion, conventional MR imaging features, ISUP grading, and indicated which index was the independent prediction index for RCC accompanying with MVI.

## RESULTS

Image acquisition was completed successfully in 16 volunteers for 32 kidneys (eight males and eight females, age range, 31–58, mean age,  $44.3 \pm 13.9$  years) and 39 patients (22 males and 17 females, age range, 43–70, mean age,  $54.3 \pm 13.6$  years) for 39 renal lesions. Histopathological diagnosis was obtained by radical nephrectomy. The mean interval between MRI and histological analysis was  $2.1 \pm 1.2$  days. 39 patients with 39 lesions were diagnosed ccRCCs. 12 cases presented with MVI and the other 27 cases with no features of MVI. Within the 12 cases with MVI, 10 cases were classified into M1, 2 cases were classified into M2. 8, 20, 8, and 3 cases were classified into WHO/ISUP grades 1, 2, 3, and 4 separately.

## ASL Imaging

Perfusion weighted images were obtained from the ASL MRI in 32 kidneys for volunteers and 39 renal lesions for 39 patients.

In ASL 1, 32 kidneys were calculated for cortical RBF; the mean cortical RBF for the kidneys were  $1,207.2 \pm 715$  ml/min/100 g (PLD1),  $1,498 \pm 1,053.4$  ml/min/100 g (PLD2),  $2,093.2 \pm 1,316$  ml/min/100 g (PLD3), and only 14 kidneys were successfully calculated for medulla RBF in PLD1; 12 kidneys were successfully calculated for medulla RBF in PLD2, eight kidneys were successfully calculated for medulla RBF in PLD3. In ASL 2, 32 kidneys were calculated for cortical RBF; the mean cortical RBF for the kidneys were  $1,236.9 \pm 687.3$  ml/min/100 g (PLD1),  $1,598.6 \pm 978.4$  ml/min/100 g (PLD2),  $2,167.7 \pm 1,207.6$  ml/min/100 g (PLD3). Because of the poor image quality, the medulla RBF was not calculated. No significant difference of the mean values of RBF between ASL 1 and ASL 2 was shown. The cortical RBF measurements showed good agreement than the medulla and relatively lower variation (**Figure 1**). The ICC values for cortical and medulla RBF were 0.903 and 0.476 respectively.

The perfusion of the entire tumor was  $867.4 \pm 248.5$  ml/min/100 g (PLD1),  $1,085.3 \pm 146.9$  ml/min/100 g (PLD2),  $1,704.6 \pm 277.5$  ml/min/100 g (PLD3). The perfusion of the solid part of the tumor was  $1,251.1 \pm 323.5$  ml/min/100 g (PLD1),  $1,618.7 \pm 426.5$  ml/min/100 g (PLD2),  $2,101.4 \pm 344$  ml/min/100 g (PLD3). Mean perfusion of the solid part of the tumors with microvascular invasion was  $536.4 \pm 154.8$  ml/min/100 g (PLD1),  $2,912.5 \pm 939.3$  ml/min/100 g (PLD2),  $3,280.3 \pm 901.2$  ml/min/100 g (PLD3). Mean perfusion of the solid part of the tumors without microvascular invasion was  $453.5 \pm 87.2$  ml/min/100 g (PLD1),  $1,043.6 \pm 695.8$  ml/min/100 g (PLD2),  $1,577.6 \pm 1,085.8$  ml/min/100 g (PLD3) (**Figure 2**). These two groups have significant differences at all the PLDs ( $p < 0.05$ ).

## Diagnostic Performance

The diagnostic performance of the entire tumor perfusion for predicting microvascular invasion of the ccRCC was assessed; the AUC was 0.778 (PLD1), 0.741 (PLD2), 0.556 (PLD3); thus the RBF of PLD1 was used to access diagnostic performance: sensitivity 75%, specificity 56%, positive predictive value 45%, and negative predictive value 88%. The diagnostic performance

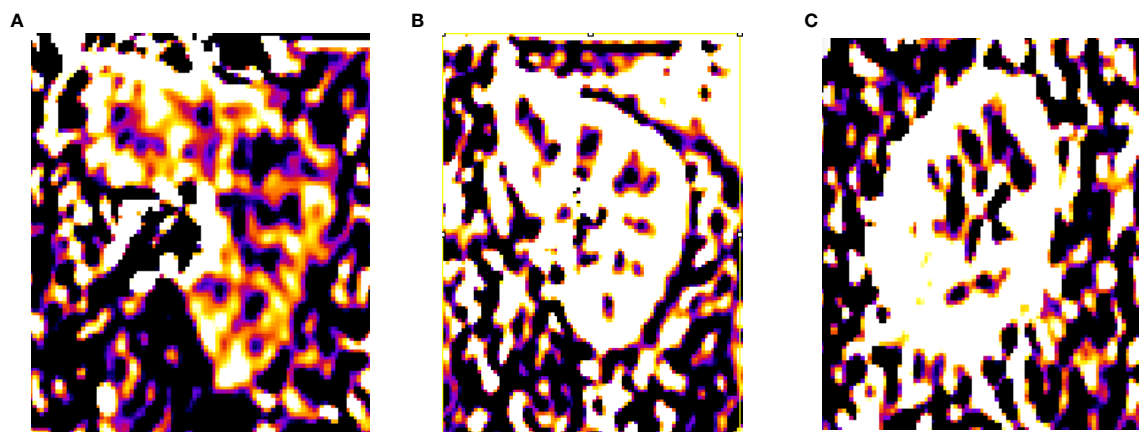


**FIGURE 1** | RBF of volunteers. (A) PLD = 500 ms, (B) PLD = 1,000 ms, (C) PLD = 2,000 ms.



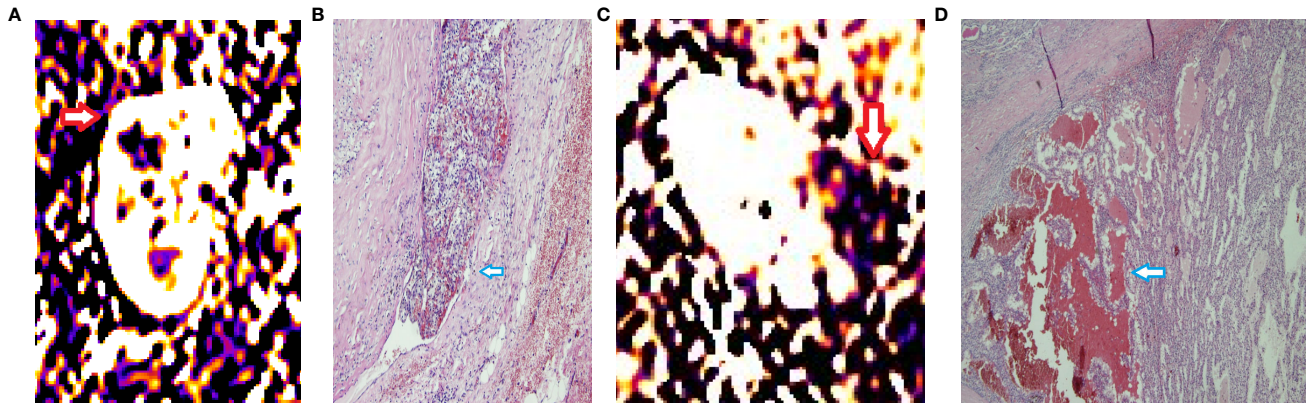


**FIGURE 2 |** RBF of ccRCCs with or without microvascular invasion. A 50-year-old man with a mass on right kidney (A, B). (A) RBF image showed a high-perfusion mass located on the upper section of right kidney (red arrow), with central low-perfusion, indicated the central necrosis. (B) Pathological section showed the cancer embolus (blue arrow) in the microvascular cavity. A 63-year-old woman with a mass on left kidney (C, D). (C) RBF image showed a low-perfusion mass located on the left kidney (red arrow). (D) Pathological section showed no microvascular invasion. There was hemorrhage within the tumor (blue arrow).

of the solid part of tumor perfusion for predicting MVI of the ccRCC was assessed; the AUC was 0.967 (PLD1), 0.924 (PLD2), 0.861 (PLD3); thus the RBF of PLD1 was used to assess diagnostic performance: sensitivity 75%, specificity 100%, positive predictive value 66.7%, and negative predictive value 95.7%.

Among MRI characteristics, ill-defined margin and the maximum diameter of the tumor were correlated with MVI. The tumor ISUP grade has no significant difference between tumors with or without MVI. Logistic regression analysis indicated the maximum diameter of the tumor (OR = 2.934,  $p < 0.01$ ), ill-defined margin (OR = 1.467,  $p < 0.01$ ), the solid part of tumor perfusion (OR = 2.245,  $p < 0.01$ ) were the independent prediction index for RCC accompanying MVI.

## DISCUSSION

This is the first study that used ASL MR imaging to predict microvascular invasion of T1 staging (maximum diameter  $\leq 7$  cm) renal cell carcinoma and indicated that perfusion of RCC has great diagnostic performance for predicting microvascular invasion. In the Kidney Cancer Management Guide for RCC with diameter greater than 4 cm and less than 7 cm, there is no high-quality evidence for choosing which operation procedure (RN or PN) should be conducted. It is also mentioned in the guidelines that for patients with venous tumor thrombus, radical nephrectomy is currently recommended. MVI is the former step of venous tumor thrombus. Thus, if the MVI can be predicted before operation, this will help doctors to prefer choosing radical nephrectomy as the suitable therapy; this will push the management of RCC a step further. MVI is tightly related with the invasiveness of tumor and which could be reflected from the perfusion of tumor. ASL MRI allows the non-invasive quantitative assessment of tissue perfusion without contrast media, which is safe and promising for the prediction of MVI.

The cortex RBF showed great image quality and stability in both ASL1 and ASL2; the cortex RBF elevated with the PLD increase. The medulla RBF showed poor image quality especially with longer PLD time. No significant difference between the two sections (ASL1 and ASL2) indicated good repeatability. Among MRI characteristics, the margin (clear or ill-defined) and maximum diameter of the tumor has significant difference between tumors with or without microvascular invasion.

Zhao et al. examined 139 RCC patients and aimed to explore the relationship between clinical and pathologic features with prognostic factors and indicated that microvascular invasion was a significant predictor of prognosis (24). Bernardos et al. retrospectively analyzed 153 pT3apN0cM0 kidney cancer patients and indicated that tumor necrosis and microvascular invasion were associated with tumor recurrence (25). Kim et al. reviewed 406 patients with localized or locally advanced ccRCC who underwent curative surgery and were followed up for  $>2$  years after surgery and indicated that tumor necrosis and MVI were independent risk factors for postoperative recurrence. Besides, microvascular invasion is the former step of venous tumor thrombus; the accurate pre-operative diagnosis can make the operation strategy be more confident.

Ma et al. (21) included 108 patients with surgically resected single intrahepatic cholangiocarcinoma to explore the association between preoperative MRI and MVI and indicated that arterial phase enhancement pattern and the enhancement ratio of arterial phase edge were associated with MVI. Vincenza Granata et al. (26) assessed major and ancillary MR parameters to explore which can be correlated with microvascular invasion of HCC and indicated that progressive pattern of contrast enhancement and satellite nodules surrounding tumors indicated presence of MVI. Wang et al. (27) analyzed 92 histopathologically confirmed HCCs with diffusion kurtosis imaging and conventional MRI features for predicting of microvascular invasion and indicated irregular surrounding enhancement as well as mean kurtosis value was associated

with MVI presence of HCC. Nebbia et al. included retrospectively 99 patients who were diagnosed with HCC to investigate MRI radiomics for predicting MVI status pre-surgery and indicated that the combination of T2 sequence and portal venous sequence yields the highest AUC for MVI status prediction (28). Since previous studies indicated enhancement of tumor usually correlated with MVI, this study used ASL to non-invasively evaluate perfusion. In this study, tumor with MVI has higher RBF than that without MVI, indicating that more invasive tumor had more blood supply; this was consistent with previous study.

PCASL MRI used for measuring renal cortical perfusion is feasible and reproducible. Main ASL imaging includes continuous ASL (CASL), pseudocontinuous ASL (PCASL), and pulsed ASL (PASL) based on different labeling methods; a single shorter RF pulse or a limited number of pulses are applied in PASL than in CASL and PCASL. The signal-to-noise ratio (SNR) of the PCASL method is higher than that of the PASL method because the PCASL method has longer temporal duration of the labeled bolus and higher labeled magnetization delivered than the PASL method. Since the SNR of ASL MRI is affected by both the labeling technique and respiration movement, breath-hold strategy was used in this study to overcome respiratory mismatch (23). SE-EPI is less influenced by any B0 field homogeneity than GE-EPI and has a short acquisition time. Perfusion was found to be lower for SE-based readouts than GE-based readouts. Despite the PWI-SNR being significantly lower for SE-EPI compared with other schemes, the highest tSNR of SE-EPI readout was considered to be the most reproducible scheme for the kidney cortex assessment, with a small coefficient of variation while minimizing variability for the whole-kidney perfusion assessment (13).

In this study, cortex perfusion is feasible by using ASL MRI. Cutajar et al. (29, 30) reported that cortical RBF measurement was repeatable, which was consistent with the results of the present study. In contrast, the medullary perfusion appears poorly reproducible, which might be due to the medullary perfusion complex physiology or the lower SNR conditions since the medullary perfusion obviously decreased than the cortex. In this study, cortical RBF is higher than in other studies, and the solid part of RCC is also higher than in some studies; the tendency (the solid part of RCC is similar to kidney cortex) is similar to the other studies.

Some studies reported that spherical shape tumors are more likely to be MVI-negative. In this study, the shape of RCC does not have a significant difference between MVI-negative and MVI-positive. T1 staging RCC may usually represent spherical than irregular shape; this may cause the no significant difference between the two groups. Chou et al. prospectively evaluated the association of preoperative multiphasic CT findings of HCC with MVI and found tumor margins on CT images were associated with MVI (31). The ill-defined margin may indicate the invasiveness of tumor, which has higher angiogenesis and more likely to have venous invasion.

In previous studies, the maximum diameter of the tumor was also considered to be a risk factor of MVI; tumor size increases

are usually associated with the presence of MVI. This may be meaningful in different staging than only in T1 staging.

A new WHO/ISUP grading system is recommended for use by the WHO. This is a four-grade system, mainly based on the different degrees of nucleolar prominence and the presence of sarcomatoid or rhabdoid morphology (32). Esnaola et al. (33) reported a cohort of 245 with hepatic cell cancer and indicated that tumor size and tumor grade had strong correlation with MVI. Since tumors in this study were stage T1, this may lead to a small difference of ISUP grade and lead to no significant difference between the group with or without MVI.

This study has some limitations. First, the sample size is relatively small. Studies with larger sample size could be conducted to validate the result. Second, some previous studies have used other MRI imaging reflecting perfusion such as dynamic contrast enhancement to predict MVI; the diagnostic performance of ASL and other MRI imaging techniques could be compared in future studies.

This study used PCASL MR imaging to predict microvascular invasion of T1 stage (maximum diameter  $\leq 7$ cm) renal clear cell carcinoma preoperatively and indicated that the PCASL MR imaging has good reproducibility for renal cortex and good diagnostic performance for predicting MVI for ccRCC, which could help doctors in making more suitable operation strategy.

## DATA AVAILABILITY STATEMENT

The raw data supporting the conclusions of this article will be made available by the authors, without undue reservation.

## ETHICS STATEMENT

The studies involving human participants were reviewed and approved by the ethics committee of West China Hospital, Sichuan University. The patients/participants provided their written informed consent to participate in this study.

## AUTHOR CONTRIBUTIONS

Guarantor of integrity of the entire study: H-MZ and BS. Protocol/project development: H-MZ. Data collection or management: D-GW, YW, Y-GB, and YY. Data analysis: D-GW and Y-TC. Manuscript writing/editing: H-MZ. All authors contributed to the article and approved the submitted version.

## FUNDING

This work was supported by the China National Institutes of Health [grant number: 81801671] and Sichuan Provincial Science and Technology plan Grants [grant number: 2019YFS0445].

## REFERENCES

- Nguyen MM, Gill IS, Ellison LM. The Evolving Presentation of Renal Carcinoma in the United States: Trends From the Surveillance, Epidemiology, and End Results Program. *J Urol* (2006) 176:2397–400. discussion 2400. doi: 10.1016/j.juro.2006.07.144
- MacLennan S, Imamura M, Lapitan MC, Omar MI, Lam TB, Hilvano-Cabungcal AM, et al. Systematic Review of Perioperative and Quality-of-Life Outcomes Following Surgical Management of Localised Renal Cancer. *Eur Urol* (2012) 62:1097–117. doi: 10.1016/j.eururo.2012.07.028
- MacLennan S, Imamura M, Lapitan MC, Omar MI, Lam TB, Hilvano-Cabungcal AM, et al. Systematic Review of Oncological Outcomes Following Surgical Management of Localised Renal Cancer. *Eur Urol* (2012) 61:972–93. doi: 10.1016/j.eururo.2012.02.039
- Ljungberg B, Bensalah K, Canfield S, Dabestani S, Hofmann F, Hora M, et al. EAU Guidelines on Renal Cell Carcinoma: 2014 Update. *Eur Urol* (2015) 67:913–24. doi: 10.1016/j.eururo.2015.01.005
- Capitanio U, Terrone C, Antonelli A, Minervini A, Volpe A, Furlan M, et al. Nephron-Sparing Techniques Independently Decrease the Risk of Cardiovascular Events Relative to Radical Nephrectomy in Patients With a T1a-T1b Renal Mass and Normal Preoperative Renal Function. *Eur Urol* (2015) 67:683–9. doi: 10.1016/j.eururo.2014.09.027
- Kirkali Z, Van Poppel H. A Critical Analysis of Surgery for Kidney Cancer With Vena Cava Invasion. *Eur Urol* (2007) 52:658–62. doi: 10.1016/j.eururo.2007.05.009
- Sugino T, Yamaguchi T, Hoshi N, Kusakabe T, Ogura G, Goodison S, et al. Sinusoidal Tumor Angiogenesis is a Key Component in Hepatocellular Carcinoma Metastasis. *Clin Exp Metastasis* (2008) 25:835–41. doi: 10.1007/s10585-008-9199-6
- Lim KC, Chow PK, Allen JC, Chia GS, Lim M, Cheow PC, et al. Microvascular Invasion is a Better Predictor of Tumor Recurrence and Overall Survival Following Surgical Resection for Hepatocellular Carcinoma Compared to the Milan Criteria. *Ann Surg* (2011) 254:108–13. doi: 10.1097/SLA.0b013e31821ad884
- Kwon SY, Lee JN, Kim BS, Ko YH, Song PH, Kim HT, et al. Impact of Microvascular Invasion and Tumor Necrosis on the Prognosis of Korean Patients With Pt1b Renal Cell Carcinoma. *Urol Int* (2015) 95:65–71. doi: 10.1159/000366138
- Huang H, Pan XW, Huang Y, Xu DF, Cui XG, Li L, et al. Microvascular Invasion as a Prognostic Indicator in Renal Cell Carcinoma: A Systematic Review and Meta-Analysis. *Int J Clin Exp Med* (2015) 8(7):10779–92.
- Santiago-Agredano B, Álvarez-Kindelán J, Font-Ugalde P, Blanca-Pedregosa A, López-Beltrán A, Requena-Tapia MJ. Prognostic Value of Microvascular Invasion in Predicting Survival in Renal Cell Carcinoma. *Actas Urol Esp* (2013) 37:504–12. doi: 10.1016/j.acuroe.2012.07.018
- Zhang X, Li J, Shen F, Lau WY. Significance of Presence of Microvascular Invasion in Specimens Obtained After Surgical Treatment of Hepatocellular Carcinoma. *J Gastroenterol Hepatol* (2018) 33:347–54. doi: 10.1111/jgh.13843
- Buchanan CE, Cox EF, Francis ST. Evaluation of 2D Imaging Schemes for Pulsed Arterial Spin Labeling of the Human Kidney Cortex. *Diagnostics (Basel)* (2018) 8(3):43. doi: 10.3390/diagnostics8030043
- Kiefer C, Schroth G, Gralla J, Diehm N, Baumgartner I, Husmann M. A Feasibility Study on Model-Based Evaluation of Kidney Perfusion Measured by Means of FAIR Prepared true-FISP Arterial Spin Labeling (ASL) on a 3-T MR Scanner. *Acad Radiol* (2009) 16:79–87. doi: 10.1016/j.acra.2008.04.024
- Pedrosa I, Rafatzand K, Robson P, Wagner AA, Atkins MB, Rofsky NM, et al. Arterial Spin Labeling MR Imaging for Characterisation of Renal Masses in Patients With Impaired Renal Function: Initial Experience. *Eur Radiol* (2012) 22:484–92. doi: 10.1007/s00330-011-2250-z
- Heusch P, Wittsack HJ, Blondin D, Ljijmani A, Nguyen-Quang M, Martirosian P, et al. Functional Evaluation of Transplanted Kidneys Using Arterial Spin Labeling MRI. *J Magn Reson Imaging* (2014) 40:84–9. doi: 10.1002/jmri.24336
- Heusch P, Wittsack HJ, Heusner T, Buchbender C, Quang MN, Martirosian P, et al. Correlation of Biexponential Diffusion Parameters With Arterial Spin-Labeling Perfusion MRI: Results in Transplanted Kidneys. *Invest Radiol* (2013) 48:140–4. doi: 10.1097/RLI.0b013e318277bfe3
- Zhang H, Wu Y, Xue W, Zuo P, Oesingmann N, Gan Q, et al. Arterial Spin Labelling MRI for Detecting Pseudocapsule Defects and Predicting Renal Capsule Invasion in Renal Cell Carcinoma. *Clin Radiol* (2017) 72:936–43. doi: 10.1016/j.crad.2017.06.003
- Cox EF, Buchanan CE, Bradley CR, Prestwich B, Mahmoud H, Taal M, et al. Multiparametric Renal Magnetic Resonance Imaging: Validation, Interventions, and Alterations in Chronic Kidney Disease. *Front Physiol* (2017) 8:696. doi: 10.3389/fphys.2017.00696
- Cuccurullo V, Di Stasio GD, Mazzarella G, Cascini GL. Microvascular Invasion in HCC: The Molecular Imaging Perspective. *Contrast Media Mol Imaging* (2018) 2018:9487938. doi: 10.1155/2018/9487938
- Ma X, Liu L, Fang J, Rao S, Lv L, Zeng M, et al. MRI Features Predict Microvascular Invasion in Intrahepatic Cholangiocarcinoma. *Cancer Imaging* (2020) 20:40. doi: 10.1186/s40644-020-00318-x
- Cong WM, Bu H, Chen J, Dong H, Zhu YY, Feng LH, et al. Practice Guidelines for the Pathological Diagnosis of Primary Liver Cancer: 2015 Update. *World J Gastroenterol* (2016) 22:9279–87. doi: 10.3748/wjg.v22.i42.9279
- Kim DW, Shim WH, Yoon SK, Oh JY, Kim JK, Jung H, et al. Measurement of Arterial Transit Time and Renal Blood Flow Using Pseudocontinuous ASL MRI With Multiple Post-Labeling Delays: Feasibility, Reproducibility, and Variation. *J Magn Reson Imaging* (2017) 46:813–9. doi: 10.1002/jmri.25634
- Zhao Y, Chen H, Xie Y, Zhang C, Hou Y, Jin M. Clinicopathologic Features and Prognostic Factors in Patients With Renal Cell Carcinoma With Sarcomatoid Differentiation. *APMIS* (2020) 128:378–86. doi: 10.1111/apm.13035
- Barbas Bernardos G, Herranz Amo F, Caño Velasco J, Cancho Gil MJ, Mayor de Castro J, Aragón Chamizo J, et al. Influence of Venous Tumour Extension on Local and Remote Recurrence of Stage pT3a pN0 cM0 Kidney Tumours. *Actas Urol Esp* (2019) 43:77–83. doi: 10.1016/j.acuroe.2019.01.001
- Granata V, Fusco R, Setola SV, Picone C, Vallone P, Belli A, et al. Microvascular Invasion and Grading in Hepatocellular Carcinoma: Correlation With Major and Ancillary Features According to LIRADS. *Abdom Radiol (NY)* (2019) 44:2788–800. doi: 10.1007/s00261-019-02056-6
- Wang WT, Yang L, Yang ZX, Hu XX, Ding Y, Yan X, et al. Assessment of Microvascular Invasion of Hepatocellular Carcinoma With Diffusion Kurtosis Imaging. *Radiology* (2018) 286:571–80. doi: 10.1148/radiol.2017170515
- Nebbia G, Zhang Q, Arefan D, Zhao X, Wu S. Pre-Operative Microvascular Invasion Prediction Using Multi-parametric Liver MRI Radiomics. *J Digit Imaging* (2020) 33:1376–86. doi: 10.1007/s10278-020-00353-x
- Cutajar M, Thomas DL, Banks T, Clark CA, Golay X, Gordon I. Repeatability of Renal Arterial Spin Labelling MRI in Healthy Subjects. *MAGMA* (2012) 25:145–53. doi: 10.1007/s10334-011-0300-9
- Cutajar M, Thomas DL, Hales PW, Banks T, Clark CA, Gordon I. Comparison of ASL and DCE MRI for the non-Invasive Measurement of Renal Blood Flow: Quantification and Reproducibility. *Eur Radiol* (2014) 24:1300–8. doi: 10.1007/s00330-014-3130-0
- Chou CT, Chen RC, Lin WC, Ko CJ, Chen CB, Chen YL. Prediction of Microvascular Invasion of Hepatocellular Carcinoma: Preoperative CT and Histopathologic Correlation. *AJR Am J Roentgenol* (2014) 203:W253–9. doi: 10.2214/AJR.13.10595
- Warren AY, Harrison D. WHO/ISUP Classification, Grading and Pathological Staging of Renal Cell Carcinoma: Standards and Controversies. *World J Urol* (2018) 36:1913–26. doi: 10.1007/s00345-018-2447-8
- Esnaola NF, Lauwers GY, Mirza NQ, Nagorney DM, Doherty D, Ikai I, et al. Predictors of Microvascular Invasion in Patients With Hepatocellular Carcinoma Who are Candidates for Orthotopic Liver Transplantation. *J Gastrointest Surg* (2002) 6:224–32. doi: 10.1016/s1091-255x(01)00015-4

**Conflict of Interest:** The authors declare that the research was conducted in the absence of any commercial or financial relationships that could be construed as a potential conflict of interest.

Copyright © 2021 Zhang, Wen, Wang, Bao, Yuan, Chen and Song. This is an open-access article distributed under the terms of the Creative Commons Attribution License (CC BY). The use, distribution or reproduction in other forums is permitted, provided the original author(s) and the copyright owner(s) are credited and that the original publication in this journal is cited, in accordance with accepted academic practice. No use, distribution or reproduction is permitted which does not comply with these terms.





# New TRUS Techniques and Imaging Features of PI-RADS 4 or 5: Influence on Tumor Targeting

Amy Inji Chang and Byung Kwan Park\*

Department of Radiology, Samsung Medical Center, Sungkyunkwan University School of Medicine, Seoul, South Korea

## OPEN ACCESS

### Edited by:

Lu Yang,  
Sichuan University, China

### Reviewed by:

DiMing Cai,  
Sichuan University, China  
Sung Woo Park,  
Pusan National University,  
South Korea

### \*Correspondence:

Byung Kwan Park  
1436park@gmail.com;  
rapark@skku.edu

### Specialty section:

This article was submitted to  
Cancer Imaging and  
Image-directed Interventions,  
a section of the journal  
Frontiers in Oncology

**Received:** 07 October 2020

**Accepted:** 17 May 2021

**Published:** 09 June 2021

### Citation:

Chang AI and Park BK (2021)  
New TRUS Techniques  
and Imaging Features of PI-RADS 4  
or 5: Influence on Tumor Targeting.  
Front. Oncol. 11:608409.  
doi: 10.3389/fonc.2021.608409

**Purpose:** To determine if the new transrectal ultrasound (TRUS) techniques and imaging features contribute to targeting Prostate Imaging and Reporting and Data System (PI-RADS) 4 or 5.

**Materials and Methods:** Between December 2018 and February 2020, 115 men underwent cognitive biopsy by radiologist A, who was familiar with the new TRUS findings and biopsy techniques. During the same period, 179 men underwent magnetic resonance imaging–TRUS image fusion or cognitive biopsy by radiologist B, who was unfamiliar with the new biopsy techniques. Prior to biopsy, both radiologists knew MRI findings such as the location, size, and shape of PI-RADS 4 or 5. We recorded how many target biopsies were performed without systematic biopsy and how many of these detected higher Gleason score (GS) than those detected by systematic biopsy. The numbers of biopsy cores were also obtained. Fisher Exact or Mann–Whitney test was used for statistical analysis.

**Results:** For PI-RADS 4, target biopsy alone was performed in 0% (0/84) by radiologist A and 0.8% (1/127) by radiologist B ( $p > 0.9999$ ). Target biopsy yielded higher GSs in 57.7% (30/52) by radiologist A and 29.5% (23/78) by radiologist B ( $p = 0.0019$ ). For PI-RADS 5, target biopsy alone was performed in 29.0% (9/31) by radiologist A and 1.9% (1/52) by radiologist B ( $p = 0.0004$ ). Target biopsy yielded higher GSs in 50.0% (14/28) by radiologist A and 18.2% (8/44) by radiologist B ( $p = 0.0079$ ). Radiologist A sampled fewer biopsy cores than radiologist B ( $p = 0.0008$  and  $0.0023$  for PI-RADS 4 and 5), respectively.

**Conclusions:** PI-RADS 4 or 5 can be more precisely targeted if the new TRUS biopsy techniques are applied.

**Keywords:** prostate adenocarcinoma, transrectal ultrasound, cognitive biopsy, fusion biopsy, magnetic resonance imaging



## INTRODUCTION

Prostate Imaging and Reporting and Data System (PI-RADS) 4 or 5 should be biopsied because these lesions have a much higher incidence of being confirmed as significant cancer than do lesions with PI-RADS 3 or less (1–5). When PI-RADS 4 or 5 is detected on magnetic resonance imaging (MRI), transrectal ultrasound (TRUS)-guided cognitive or MRI-TRUS fusion biopsy is performed to detect significant cancers.

Recently, several investigators reported the new TRUS features of peripheral or transition PI-RADS 4 or 5 lesions (6–11). They also introduced new TRUS techniques, such as how to choose the imaging sequence, control image contrast, compress the prostate, and localize a tumor (6–11). However, they did not determine whether being familiar with the new TRUS techniques and imaging features influenced on tumor targeting. Still, the utility of the new biopsy techniques in targeting cancer remains unclear.

Accordingly, we hypothesized that TRUS-guided cognitive biopsy using the new TRUS techniques and features would improve targeting PI-RADS 4 or 5. The study aim was to determine the effect of operator familiarity with the new biopsy techniques on tumor targeting.

## MATERIALS AND METHODS

### Patient Selection

Between December 2018 and February 2020, 557 men underwent TRUS-guided cognitive or MRI-TRUS fusion biopsy because of high (2.5 ng/ml or greater) prostate-specific antigen (PSA) after MRI was performed prior to all biopsies (**Figure 1**). Of these patients, 263 were excluded according to the following criteria: PI-RADS 1–2 ( $n = 39$ ), and 3 ( $n = 224$ ). The remaining 294 were included because an index lesion was categorized as PI-RADS 4 ( $n = 211$ ) or 5 ( $n = 83$ ) on pre-

biopsy MRI. Radiologist A performed TRUS-guided cognitive biopsy in 115 men, whose index lesion was PI-RADS 4 in 84 men and 5 in 31 men on pre-biopsy MRI. Radiologist B performed MRI-TRUS fusion biopsy ( $n = 176$ ) or TRUS-guided cognitive biopsy ( $n = 3$ ) in 179 men, whose index lesion was PI-RADS 4 in 127 men and 5 in 52 men on pre-biopsy MRI. Each radiologist, who interpreted pre-biopsy MR images in a patient, was supposed to perform a biopsy in the same patient.

### Biopsy Techniques

Radiologists A and B had already performed TRUS-guided cognitive or MRI-TRUS fusion biopsy in more than 500 men each before this study period began. Radiologist A alone was familiar with the following TRUS techniques and imaging features (6–9): First, fundamental imaging was performed instead of harmonic imaging (**Figure 2**). Second, the TRUS dynamic range was kept to 50 or less (**Figure 2**). Third, the prostate was not compressed until PI-RADS 4 or 5 was detected. Fourth, a TRUS lesion appeared more superiorly than an MRI lesion as it was nearer to the posterior capsule. Fifth, a TRUS lesion appeared more inferiorly than an MRI lesion as it was nearer to the anterior capsule (**Figure 2**). Sixth, peripheral and transition PI-RADS 4 or 5 looked hypoechoic and hyperechoic relative to neighboring normal tissue, respectively (**Figure 2**). Finally, PI-RADS 5 tended to be more hypoechoic or hyperechoic than PI-RADS 4 or less. However, radiologist B was not familiar with these new TRUS techniques and features for targeting PI-RADS 4 or 5 (**Figure 2**).

Both of two radiologists were fully aware of the location, size, and shape of an index lesion on MRI. Radiologist A, who performed cognitive biopsy alone, already knew how to use the new TRUS features and techniques. Radiologist B, who performed MRI-TRUS fusion biopsy or cognitive biopsy, did not know it.

Radiologists A and B used one of the following ultrasonography (US) scanners: EPIC (Philips Health Care, Bothell, WA, USA), IU22

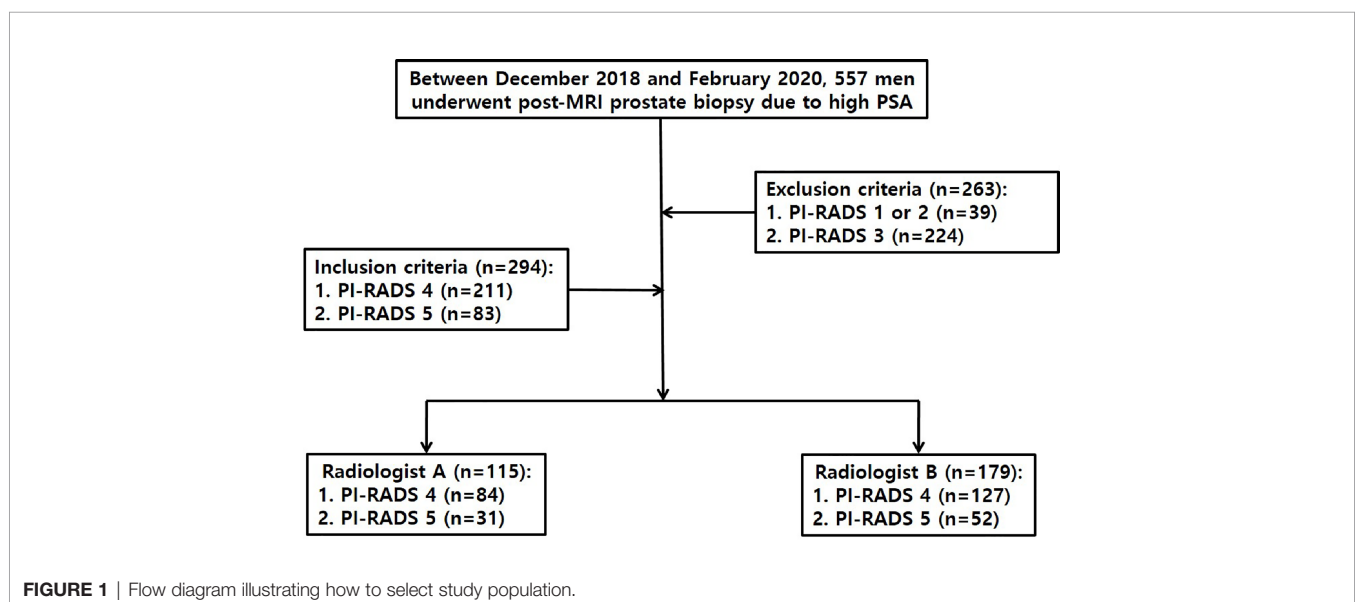




**FIGURE 2** | A 77-year-old man with PSA of 9.57 ng/ml. **(A)** T2-weighted axial magnetic resonance image showing a PI-RADS 4 transition mass (black arrow) in the left base. The tumor is contacting the anterior capsule. The white arrow indicates a small cyst in the neighboring hyperplastic nodule. **(B)** Transverse TRUS image scanned by radiologist A showing a slightly hyperechoic mass (black arrow) in the left mid-gland. The tumor was targeted with four cores of which three were GS 6 and one was negative. Sextant systematic biopsy was also performed, but all of the cores were negative. The white arrow indicates a small cyst in the neighboring hyperplastic nodule, which is the same imaging feature seen on T2-weighted MR image. This TRUS sequence is fundamental imaging with low dynamic range, resulting in good contrast between the PI-RADS 4 lesion and normal tissue. **(C)** Transverse TRUS image, which was scanned by radiologist B two months before beginning our study period, shows a slightly hypoechoic mass (black arrow) in the left base contacting the bladder base. The tumor was targeted with three cores of which all were negative. Systematic biopsy was also performed with 10 cores of which all were negative. Radiologist B did not detect the neighboring hyperplastic nodule with a small cyst that was seen on the T2-weighted MR image. This TRUS sequence is harmonic imaging with high dynamic range, subsequently leading to poor tissue contrast.

(Philips Health Care), or Aplio 500 (Toshiba Medical System, Japan). Radiologist A did not use MRI-TRUS fusion software, but radiologist B used Fly Thru and Smart Fusion (Toshiba Medical System) for MRI-TRUS fusion imaging.

## Data Analysis

Patients' ages, PSA levels, tumor sizes, and tumor locations were compared between the groups undergoing the biopsies performed by radiologist A or B. The sizes of PI-RADS 4 and 5 were measured on diffusion-weighted MR images for peripheral tumors or on T2-weighted MR images for transition tumors. The tumor locations were recorded as peripheral-to-transition ratios in each group.

The numbers of target and systematic biopsies were compared to identify how many patients underwent target biopsy alone without relying on systematic biopsy. Systematic biopsy was not performed only when the radiologists ensured that an index lesion was precisely targeted. However, systematic biopsy alone was performed only when an index lesion was invisible on TRUS or when software fusion of MRI-TRUS images was too poor to target an index lesion.

Target and systematic biopsies were compared in patients with cancer-proven PI-RADS 4 or 5 in terms of Gleason score (GS) to identify how many targeted biopsies were superior, equal, and inferior to systematic biopsies. These data were also compared between radiologists A and B to determine which biopsy technique was more accurate in targeting an index lesion.

The numbers of target or systematic cores that each radiologist sampled in each patient with cancer-proven PI-RADS 4 or 5 were compared to determine which radiologist took fewer cores. Positive to negative core ratios (PNCRs) were compared between radiologists A and B to assess how efficiently cancer was detected with the target or systematic cores.

The cancer detection rates (CDRs) were compared between radiologists A and B. The CDR was calculated as the number of cancer cases divided by the total number of cases. The significant CDR was calculated as the number of GS 7 or higher cases divided by the total number of cases.

## Standard Reference

The standard reference was histological examination of the prostate biopsies that were performed by radiologists A and B. Significant cancer was defined as a tumor with a GS  $\geq 7$  (3 + 4).

## Statistical Analysis

Mann-Whitney test was performed to compare the patients' ages, PSA levels, tumor sizes, and biopsy cores between the PI-RADS 4 or 5 group. Fisher exact test was also performed to compare tumor locations, target-to-systematic biopsy ratios, PNCRs, and CDRs. Commercial software (PASW Statistics, version 20.0; Chicago, IL, USA) was used for statistical analysis. A two-sided *p* value of less than 0.05 was considered statistical significance.

## RESULTS

The median PSA levels of the PI-RADS 4 groups biopsied by radiologists A and B were 4.58 ng/ml (2.50–16.44 ng/ml) and 5.81 ng/ml (2.50–46.70 ng/ml), respectively (**Table 1**) (*p* = 0.0001). However, there was no significant difference between the PI-RADS 4 or 5 groups in terms of the other patients' demographics (**Table 1**) (*p* = 0.4154–0.999).

For the PI-RADS 4 tumors, radiologists A performed target and systematic biopsies in all (100%, 84/84) patients, and radiologist B performed the combination biopsy in 126 (99.2%,

**TABLE 1 |** Patients' demographics.

	PI-RADS 4 (n = 211)		P values	PI-RADS 5 (n = 83)		P values
	RA group (n = 84)	RB group (n = 127)		RA group (n = 31)	RB group (n = 52)	
Age (years)	67.0 (43.0–80.0)	65.0 (42.0–83.0)	0.0763	67.0 (55.0–98.0)	68.5 (49.0–84.0)	0.5947
PSA (ng/ml)	4.58 (2.50–16.44)	5.81 (2.50–46.70)	0.0001	8.69 (3.34–747.30)	9.22 (2.50–84.6)	0.8323
Tumor size (mm)	9.5 (4.0–14.5)	10.0 (3.7–13.8)	0.8402	19.0 (15.7–58.0)	21.0 (15.0–42.0)	0.4154
PZ to TZ ratio	69:15	105:22	>0.9999	17:14	26:26	0.8207

PI-RADS, Prostate Imaging and Reporting and Data System; RA, Radiologist A; RB, Radiologist B; PSA, Prostate-specific antigen; PZ, Peripheral Zone; TZ, Transition Zone; All data except lesion location are shown as the median (range).

126/127) patients except one who had target biopsy alone ( $p > 0.9999$ ). The overall CDRs were 64.3% (54/84) for radiologist A and 61.4% (78/127) for radiologist B ( $p = 0.7715$ ). The significant CDRs were 40.5% (34/84) for radiologist A and 43.3% (55/127) for radiologist B ( $p = 0.2141$ ).

For the PI-RAD 5 tumors, however, radiologists A and B performed target biopsy alone in nine (29.0%, 9/31) patients and in one (1.9%, 1/52) patient, respectively ( $p = 0.0004$ ). The overall CDRs were 90.3% (28/31) for radiologist A and 84.6% (44/52) for radiologist B ( $p = 0.5249$ ). The significant CDRs were 83.9% (26/31) for radiologist A and 76.9% (40/52) for radiologist B ( $p = 0.5776$ ).

For the cancer-proven PI-RAD 4 cases, target biopsy was superior to systematic biopsy in 57.7% (30/52) by radiologist A and in 29.5% (23/78) by radiologist B (**Table 2**) ( $p = 0.0019$ ). Target biopsy was equal to systematic biopsy in 19.2% (10/52) by radiologist A and in 44.9% (35/78) by radiologist B (**Table 2**) ( $p = 0.0027$ ). However, there was no significant difference between radiologists A and B in the number of patients in which the target biopsy was inferior to systematic biopsy (**Table 2**) ( $p = 0.8365$ ). The median numbers of target and systematic cores were 11.0 (8.0–12.0) for radiologist A and 12.0 (8.0–14.0) for radiologist B ( $p = 0.0008$ ). The median numbers of target cores were 5.0 (2.0–6.0) for radiologist A and 2.0 (2.0–5.0) for radiologist B ( $p < 0.0001$ ), whereas those of the systematic cores were 6.0 (2.0–6.0) for radiologist A and 10.0 (5.0–10.0) for radiologist B ( $p < 0.0001$ ). The PNCRs were 248:330 for radiologist A and 338:561 for radiologist B ( $p = 0.0439$ ).

For the cancer-proven PI-RADS 5 cases, target biopsy was superior to systematic biopsy in 50.0% (14/28) by radiologist A and in 18.2% (8/44) by radiologist B (**Table 2**) ( $p = 0.0079$ ). However, there was no significant difference between radiologists A and B in the number of patients for whom target biopsy was equal or inferior to systematic biopsy (**Table 2**) ( $p = 0.0545$  or 0.5108). The median numbers of target and systematic cores

were 10.0 (3.0–13.0) for radiologist A and 11.0 (7.0–13.0) for radiologist B ( $p = 0.0023$ ). The median numbers of target cores were 5.0 (3.0–8.0) for radiologist A and 3.0 (0.0–7.0) for radiologist B ( $p < 0.0001$ ), whereas those of the systematic biopsy were 6.0 (0.0–6.0) for radiologist A and 9.0 (0.0–11.0) for radiologist B ( $p < 0.0001$ ). The PNCRs were 149:84 for radiologist A and 250:229 for radiologist B ( $p = 0.0037$ ).

Among the PI-RAD 4 groups, the overall and significant CDRs of target biopsies performed by radiologist A were 54.8% (46/84) and 35.7% (30/84), whereas those of target biopsies performed by radiologist B were 51.2% (65/127) and 34.6% (44/127), respectively. Among the PI-RAD 5 groups, the overall and significant CDRs of target biopsies performed by radiologist A were 87.1% (27/31) and 80.6% (25/31), whereas those of target biopsies performed by radiologist B were 82.7% (43/52) and 73.1% (38/52), respectively. The  $p$  values of overall CDRs in the PI-RADS 4 and 5 were 0.6733 and 0.7583, and those of significant CDRs in the PI-RADS 4 and 5 were 0.8838 and 0.5968, respectively.

## DISCUSSION

Our results showed that a greater number of target biopsies yielded higher GSs than did systematic biopsies by radiologist A who was familiar with the new TRUS techniques and features of PI-RADS 4 or 5. For this reason, a greater number of men with PI-RADS 5 underwent target biopsy alone by radiologist A than by radiologist B who did not know the new TRUS techniques and features of PI-RADS 4 or 5. Moreover, radiologist A was able to perform biopsies with fewer cores because of higher PNCRs than was radiologist B.

Recent US scanners recommend the use of harmonic imaging rather than fundamental imaging because the former provides better axial and lateral resolutions than does the latter (12–14).

**TABLE 2 |** Comparison of Gleason scores from target and systematic biopsies.

	Cancer-proven PI-RADS 4 (n = 130)		P values	Cancer-proven PI-RADS 5 (n = 72)		P values
	RA group (n = 52)	RB group (n = 78)		RA group (n = 28)	RB group (n = 44)	
T > S (%)	57.7 (30/52)	29.5 (23/78)	0.0019	50.0 (14/28)	18.2 (8/44)	0.0079
T = S (%)	19.2 (10/52)	44.9 (35/78)	0.0027	39.3 (11/28)	63.6 (28/44)	0.0545
T < S (%)	23.1 (12/52)	25.6 (20/78)	0.8365	10.7 (3/28)	18.2 (8/44)	0.5108

PI-RADS, Prostate Imaging and Reporting and Data System; RA, Radiologist A; RB, Radiologist B; T > S, T = S, and T < S indicates that the Gleason scores of the target biopsy were superior, equal, and inferior, respectively, to those of the systematic biopsy.

However, increasing tissue resolution inevitably results in decreasing tissue contrast between prostate cancer and normal tissue. Prostate cancer that is located near the transducer can be depicted with poor contrast because of the lack of harmonics in the incident ultrasound wave (15). Therefore, radiologist A did not use harmonic imaging but rather fundamental imaging. Moreover, he maintained lower dynamic range to enhance tissue contrast by sharpening the tumor edges (16).

Tumor locations appear so different between MRI and TRUS because of the different scan axes. Axial MRI images are scanned along the perpendicular axis of the prostate urethra, whereas axial TRUS images are scanned along the oblique axis of the prostate urethra (6, 7, 10, 17). For this reason, when PI-RADS 4 or 5 is closer to the anterior capsule, the tumor seems to be located more inferiorly on TRUS than on MRI. Given that PI-RADS 4 or 5 is closer to the posterior capsule, the tumor seems to be located more superiorly on TRUS than on MRI. Currently, urologists or radiologists who perform TRUS-guided cognitive biopsy try to find an index tumor at the same level that is seen on MRI. Therefore, their targeting is likely to be so poor that significant cancer cannot be sampled precisely. Another technical tip for achieving good lesion depiction is to not compress the prostate until PI-RADS 4 or 5 is detected. Compression deforms the shape of the PI-RADS 4 or 5 but also obscures a small tumor because it is frequently embedded in the normal tissue (6, 9, 10, 17).

Urologists or radiologists are used to know that the TRUS features of prostate cancer are hypoechoic regardless of lesion location. Peripheral cancer was hypoechoic compared with the neighboring normal tissue, but transition cancer was hyperechoic compared with the neighboring hyperplastic nodules. Several papers have reported that some prostate cancers are hyperechoic compared with adjacent tissue (18–20). The incidence of hyperechoic tumors is reported as high as 40% (20). Unfortunately, the researchers did not demonstrate that these cancers arise from transition cancers. However, Park et al. have showed that transition cancer tends to be more hyperechoic than does peripheral cancer (6).

Many papers have reported that significant CDRs range from 22.1% to 78.0% for PI-RADS 4 and 72.4% to 90.7% for PI-RADS 5 (3, 4, 21–23). Radiologist A achieved a relatively lower significant CDR (40.5%) for PI-RADS 4, although the new TRUS techniques and features were applied for biopsy. The median size of PI-RADS 4 was less than 10 mm, which subsequently led to a decreasing significant CDR (9). Moreover, the median PSA levels were lower in the PI-RADS 4 patients who were biopsied by radiologist A. However, radiologist A achieved a relatively higher significant CDR (83.9%) for PI-RADS 5 because there was no difference between the biopsy groups in the lesion sizes and PSAs.

Radiologist A could not avoid performing a systematic biopsy for PI-RADS 4 even though the tumor was clearly seen on TRUS. The main reason was that PI-RADS 4 was smaller than PI-RADS 5, and thus he could not ensure that it was targeted 100%. Moreover, the systematic biopsy achieved higher GSs than those of the target biopsy in a small number of PI-RADS 4 or 5 tumors. Because significant cancer can be detected in PI-RADS 3 or less, a systematic biopsy should be added to the target biopsy for PI-

RADS 4. However, radiologist A omitted the systematic biopsy in a substantial number of PI-RADS 5 tumors, especially for men who did not stop taking aspirin because of coronary artery stent. Therefore, the new techniques of TRUS biopsy may contribute not only to a decreasing number of biopsy cores but also to a reduction in the complication rate (6).

Indeed, the purpose of our investigation was not to compare cognitive fusion and image fusion biopsy in terms of tumor targeting. Whether or not a biopsy operator knows the new TRUS techniques and imaging features can influence tumor targeting. Radiologist A knew it, but radiologist B did not. Radiologist B as well as radiologist A also performed cognitive biopsy although the number of cognitive biopsies was small. Because he did not know the new TRUS techniques and imaging features, he was not able to precisely detect an index tumor, which is shown in **Figure 2**. Besides, the image quality of his TRUS was inferior to that of radiologist A's TRUS. In other words, the new TRUS techniques and imaging features help to improve image quality, cancer detection, and tumor targeting regardless of biopsy types (cognitive fusion or image fusion) if a biopsy operator is familiar with them. Many readers frequently misunderstand that our study was to compare cognitive fusion and image fusion biopsies in terms of tumor targeting.

Our current policy of TRUS biopsy is that systematic biopsy is routinely performed after an index tumor is targeted because it can detect additional significant cancers where PI-RADS 1 or 2 were diagnosed (11, 24). PI-RADS 1–2 does not indicate that CDR is 0% (23). Radiologist A achieved higher overall and significant CDRs of target biopsies than radiologist B even if the PSA levels and tumor sizes of PI-RADS 4 and 5 groups, which radiologist A performed biopsies, were lower/smaller than those of PI-RADS 4 and 5 groups, which radiologist A performed biopsies. Unfortunately, there was no significant difference between the groups in terms of CDR due to small number of biopsy cases. However, target biopsies of radiologist A are so likely to provide much lower underestimation of GS compared to prostatectomies because of good tumor targeting. GS underestimation frequently induces under-treatment of prostate cancer (25).

Our study had some limitations. First, the standard reference was not a prostatectomy but rather a biopsy examination because a substantial number of cancer-proven patients underwent active surveillance, hormone therapy, radiation therapy, or chemotherapy. Therefore, the biopsy GS did not correlate with the surgical GS in all patients. Second, the targeting of PI-RADS 2 or 3 between radiologists A and B were not compared. Lower PI-RADS scores appear to be more difficult to detect with TRUS. Further investigation is necessary to assess the utility of the new biopsy techniques in targeting lower PI-RADS scores. Third, the number of PI-RADS 4 or 5 lesions was relatively smaller for radiologist A than for radiologist B. However, the number of PI-RADS 3 lesions, which were excluded from the current study, was much larger for radiologist A than for radiologist B. Our urologists had previously recognized that the new biopsy techniques were better than the conventional MRI-TRUS fusion or cognitive biopsy techniques for tumor targeting.



Thus, they transferred a larger number of PI-RADS 3 cases to radiologist A because this category required more precise targeting. Fourth, the same biopsy modality was not used to compare radiologists A and B in terms of tumor targeting. Recent meta-analysis reported that there is no difference between MRI-TRUS cognitive fusion and MRI-TRUS image fusion biopsies in terms of cancer detection rate (26). Our study showed no significant difference between A and B in terms of cancer detection rate, either. However, whether or not radiologists or urologists are familiar with the new TRUS findings and techniques influence the tumor targeting significantly regardless of types of biopsies that they perform. For more than 10 years, radiologists A and B have performed MRI-TRUS cognitive fusion or MRI-TRUS image fusion biopsies. However, radiologist A discovered new TRUS findings and techniques, leading to improve tumor targeting four years ago. Since then, he has performed only MRI-TRUS cognitive fusion biopsy definitely based on the new TRUS findings and techniques in order to improve targeting an index lesion. In contrast, radiologist B insisted that MRI-TRUS image fusion biopsy is more reliable to tumor targeting. Therefore, this was the background of our research that being familiar with the new TRUS findings and techniques helps radiologists or urologists to have more precise tumor targeting regardless of types of biopsies. Our results and figures showed that there was no difference between A and B in terms of significant or insignificant cancer detection rate. Radiologist A demonstrated that the Gleason scores of target biopsies were significantly higher than those of systematic biopsies. Accordingly, he was able to omit the systematic biopsy in many cases or reduce the number of biopsy cores. In contrast, radiologists B showed that the Gleason scores of target biopsy were not different from those of systematic biopsy. Accordingly, he was not able to omit the systematic biopsy, resulting in increasing the number of biopsy cores and complication rates. If radiologist B had been familiar to the new TRUS findings and techniques, his tumor targeting could have been more precise. Recently, our urologists have transferred only to the radiologist A so many patients who cannot stop aspirin medication due to cardiovascular diseases because they ask him to perform a target biopsy alone in them. When we carefully see the **Figure 2** images, radiologist A detected a true lesion in the mid-gland and cancer was detected. However, radiologist B was not able to detect a true lesion because he did not know the new TRUS findings and techniques, and his biopsy results were negative. Fifth, there was different demographics between PI-RADS 4 or 5 groups. The PSA levels of PI-RADS 4 and 5 groups, who radiologist A biopsied, were lower than those of PI-RADS 4 and 5 groups, who radiologist B biopsied. Besides, the tumor sizes of PI-RADS 4 and 5 groups, who radiologist A biopsied, were smaller than those of PI-RADS 4 and 5 groups, who radiologist B biopsied. Generally, as PSA levels and tumor sizes increase, cancer detection rates (CDRs) also increase. Nonetheless, the CDRs of radiologist A were higher than those of radiologists B. Therefore,

we do not think that the different PSA levels or tumor sizes had influence on tumor targeting. Sixth, we did not perform inter-reader agreement between radiologist A and B in terms of MRI interpretation. We can indirectly identify the disagreement. Overall and significant CDRs of PI-RADS 4 and 5 are similar to those of PI-RADS 4 and 5, which were reported by previous investigations (10, 23). Besides, PI-RADS 4 and 5 provide lower inter-reader agreement between radiologists compared to PI-RADS 2 or 3. We do not think that disagreement will not be high. Finally, our study was a retrospective design. Accordingly, we cannot completely exclude a selection bias in including study population. MRI-TRUS fusion or cognitive biopsy does not fully obtain systemic puncture, and its accuracy or representativeness is still controversial.

## CONCLUSION

Radiologists or urologists can target PI-RADS 4 or 5 more precisely if they are familiar with the new TRUS techniques and imaging features. Systematic biopsy is considered as a routine procedure due to additional detection of prostate cancer. However, systematic biopsy might be omitted in PI-RAD 5 patients who have T3 or higher stage cancer, bleeding tendency, or anti-coagulant medication if the new TRUS techniques and imaging features are applied.

## DATA AVAILABILITY STATEMENT

The raw data supporting the conclusions of this article will be made available by the authors, without undue reservation.

## ETHICS STATEMENT

The studies involving human participants were reviewed and approved by Samsung Medical Center, Institutional Review Board. Written informed consent for participation was not required for this study in accordance with the national legislation and the institutional requirements.

## AUTHOR CONTRIBUTIONS

Conceptualization, BP. Methodology and software, BP. Formal analysis, AC. Investigation, BP. Resources, BP. Data curation, AC. Writing—original draft preparation, AC. Writing—review and editing, AC. and BP. Visualization, AC. Supervision, BP. Project administration, BP. All authors contributed to the article and approved the submitted version.

## REFERENCES

- Weinreb JC, Barentsz JO, Choyke PL, Cornud F, Haider MA, Macura KJ, et al. Pi-Rads Prostate Imaging - Reporting and Data System: 2015, Version 2. *Eur Urol* (2016) 69:16–40. doi: 10.1016/j.eururo.2015.08.052
- Turkbey B, Rosenkrantz AB, Haider MA, Padhani AR, Villeirs G, Macura KJ, et al. Prostate Imaging Reporting and Data System Version 2.1: 2019 Update of Prostate Imaging Reporting and Data System Version 2. *Eur Urol* (2019) 76:340–51. doi: 10.1016/j.eururo.2019.02.033
- Greer MD, Shih JH, Lay N, Barrett T, Kayat Bittencourt L, Borofsky S, et al. Validation of the Dominant Sequence Paradigm and Role of Dynamic Contrast-Enhanced Imaging in PI-RADS Version 2. *Radiology* (2017) 285:859–69. doi: 10.1148/radiol.2017161316
- Hofbauer SL, Maxeiner A, Kittner B, Heckmann R, Reimann M, Wiemer L, et al. Validation of Prostate Imaging Reporting and Data System Version 2 for the Detection of Prostate Cancer. *J Urol* (2018) 200:767–73. doi: 10.1016/j.juro.2018.05.003
- Thai JN, Narayanan HA, George AK, Siddiqui MM, Shah P, Mertan FV, et al. Validation of PI-RADS Version 2 in Transition Zone Lesions for the Detection of Prostate Cancer. *Radiology* (2018) 288:485–91. doi: 10.1148/radiol.2018170425
- Park BK, Park SY. New Biopsy Techniques and Imaging Features of Transrectal Ultrasound for Targeting PI-RADS 4 and 5 Lesions. *J Clin Med* (2020) 9:530–40. doi: 10.3390/jcm9020530
- Park BK. Ultrasound-Guided Genitourinary Interventions: Principles and Techniques. *Ultrasonography* (2017) 36:336–48. doi: 10.14366/usg.17026
- Park BK. Image-Guided Prostate Biopsy: Necessity for Terminology Standardization. *J Ultrasound Med* (2020) 39:191–6. doi: 10.1002/jum.15083
- Park SY, Park BK. Necessity of Differentiating Small (< 10 Mm) and Large (≥ 10 Mm) PI-RADS 4. *World J Urol* (2020) 38:1473–9. doi: 10.1007/s00345-019-02924-2
- An T, Park BK. Validation of New TRUS Biopsy Techniques for PI-RADS 4 or 5. *Precis Future Med* (2020) 4:141–8. doi: 10.23838/pfm.2020.00114
- An T, Park BK. Value of Systematic Biopsy Added to Target Biopsy for Detecting Significant Cancer in Men With Prostate Imaging and Reporting and Data System 5. *Precis Future Med* (2020) 4:107–13. doi: 10.23838/pfm.2020.00107
- Choudhry S, Gorman B, Charboneau JW, Tradup DJ, Beck RJ, Kofler JM, et al. Comparison of Tissue Harmonic Imaging With Conventional US in Abdominal Disease. *Radiographics* (2000) 20:1127–35. doi: 10.1148/radiographics.20.4.g00j371127
- Hohl C, Schmidt T, Haage P, Honnef D, Blaum M, Staatz G, et al. Phase-Inversion Tissue Harmonic Imaging Compared With Conventional B-mode Ultrasound in the Evaluation of Pancreatic Lesions. *Eur Radiol* (2004) 14:1109–17. doi: 10.1007/s00330-003-2191-2
- Schmidt T, Hohl C, Haage P, Honnef D, Mahnen AH, Krombach G, et al. Phase-Inversion Tissue Harmonic Imaging Compared to Fundamental B-mode Ultrasound in the Evaluation of the Pathology of Large and Small Bowel. *Eur Radiol* (2005) 15:2021–30. doi: 10.1007/s00330-005-2749-2
- Hedrick WR, Metzger L. Tissue Harmonic Imaging: A Review. *J Diagn Med Sonography* (2005) 21:183–89. doi: 10.1007/s00330-005-2749-2
- Thoires K. Physical and Technical Principles of Sonography: A Practical Guide for non-Sonographers. *Radiographer* (2012) 59:124–32. doi: 10.14366/usg.17026
- Chung JH, Park BK. Transrectal Ultrasound Features and Biopsy Outcomes of Transition PI-RADS 5. *Acta Radiol* (2021). doi: 10.1177/02841851211018775
- Salo JO, Rannikko S, Makinen J, Lehtonen T. Echogenic Structure of Prostatic Cancer Imaged on Radical Prostatectomy Specimens. *Prostate* (1987) 10:1–9. doi: 10.1002/pros.2990100103
- Egawa S, Wheeler TM, Greene DR, Scardino PT. Unusual Hyperechoic Appearance of Prostate Cancer on Transrectal Ultrasonography. *Br J Urol* (1992) 69:169–74. doi: 10.1111/j.1464-410x.1992.tb15490.x
- Spajic B, Eupic H, Tomas D, Stimac G, Kruslin B, Kraus O. The Incidence of Hyperechoic Prostate Cancer in Transrectal Ultrasound-Guided Biopsy Specimens. *Urology* (2007) 70:734–7. doi: 10.1016/j.urol.2007.06.1092
- Tan N, Lin WC, Khoshnoodi P, Asvadi NH, Yoshida J, Margolis DJ, et al. In-Bore 3-T MR-guided Transrectal Targeted Prostate Biopsy: Prostate Imaging Reporting and Data System Version 2-Based Diagnostic Performance for Detection of Prostate Cancer. *Radiology* (2017) 283:130–9. doi: 10.1148/radiol.2016152827
- Mehralivand S, Bednarova S, Shih JH, Mertan FV, Gaur S, Merino MJ, et al. Prospective Evaluation of PI-RADS Version 2 Using the International Society of Urological Pathology Prostate Cancer Grade Group System. *J Urol* (2017) 198:583–90. doi: 10.1016/j.juro.2017.03.131
- Kasivisvanathan V, Rannikko AS, Borghi M, Panebianco V, Mynderse LA, Vaarala MH, et al. Mri-Targeted or Standard Biopsy for Prostate-Cancer Diagnosis. *N Engl J Med* (2018) 378:1767–77. doi: 10.1056/NEJMoa1801993
- Kim HS, Park BK. Is Transrectal Ultrasound-Guided Systematic Biopsy Necessary After PI-RADS 4 is Targeted? *Precis Future Med* (2021). doi: 10.23838/pfm.2021.00030
- Epstein JI, Feng Z, Trock BJ, Pierorazio PM. Upgrading and Downgrading of Prostate Cancer From Biopsy to Radical Prostatectomy: Incidence and Predictive Factors Using the Modified Gleason Grading System and Factoring in Tertiary Grades. *Eur Urol* (2012) 61:1019–24. doi: 10.1016/j.eururo.2012.01.050
- Watts KL, Frechette L, Muller B, Ilinky D, Kovac E, Sankin A, et al. Systematic Review and Meta-Analysis Comparing Cognitive vs. Image-Guided Fusion Prostate Biopsy for the Detection of Prostate Cancer. *Urol Oncol* (2020) 38:734:e19–25. doi: 10.1016/j.urolonc.2020.03.020

**Conflict of Interest:** The authors declare that the research was conducted in the absence of any commercial or financial relationships that could be construed as a potential conflict of interest.

Copyright © 2021 Chang and Park. This is an open-access article distributed under the terms of the Creative Commons Attribution License (CC BY). The use, distribution or reproduction in other forums is permitted, provided the original author(s) and the copyright owner(s) are credited and that the original publication in this journal is cited, in accordance with accepted academic practice. No use, distribution or reproduction is permitted which does not comply with these terms.



## OPEN ACCESS

**Edited by:**

Changqiang Wu,  
North Sichuan Medical College,  
China

**Reviewed by:**

Junliang Han,  
Fourth Military Medical University,  
China  
Jian-hua Zhuang,  
Shanghai Changzheng Hospital, China

**\*Correspondence:**

Hong Zheng  
profzhenghong@163.com

**\*ORCID:**

Qingqing Dai  
orcid.org/0000-0003-3064-8310  
Qirong Chen  
orcid.org/0000-0002-8404-1189  
Meijun Zheng  
orcid.org/0000-0001-7258-3127  
Hong Zheng  
orcid.org/0000-0002-0199-2940

<sup>‡</sup>These authors have contributed  
equally to this work and  
share first authorship

<sup>§</sup>These authors have contributed  
equally to this work and  
share last authorship

**Specialty section:**

This article was submitted to  
Cancer Imaging and  
Image-directed Interventions,  
a section of the journal  
Frontiers in Oncology

**Received:** 06 November 2020

**Accepted:** 07 June 2021

**Published:** 29 June 2021

**Citation:**

Dai Q, Zheng M, Chen Q, Zheng H  
and Li B (2021) The Preoperative  
Diagnostic Value of MRI and Otoneural  
Tests in Acoustic Neuroma.  
Front. Oncol. 11:626485.  
doi: 10.3389/fonc.2021.626485

# The Preoperative Diagnostic Value of MRI and Otoneural Tests in Acoustic Neuroma

Qingqing Dai<sup>1†‡</sup>, Meijun Zheng<sup>1†‡</sup>, Qirong Chen<sup>1†</sup>, Hong Zheng<sup>1\*†§</sup> and Bilan Li<sup>2§</sup>

<sup>1</sup> Department of Otolaryngology, West China Hospital of Sichuan University, Chengdu, China, <sup>2</sup> Department of Otolaryngology-Head and Neck Surgery, Sichuan Provincial People's Hospital, University of Electronic Science and Technology of China, Chengdu, China

**Objectives:** To determine the preoperative diagnostic accuracy of MRI and otoneural tests (ONT) for acoustic neuroma (AN) in a cohort of unselected patients with pontocerebellar angle tumors. To find a convenient way to screening out the potential asymptomatic AN patient earlier.

**Design:** This diagnostic accuracy study was performed in a central hospital and included a consecutive sample of unilateral incipient pontocerebellar angle tumor patients referred for MRI and ONT before surgery. Different AN features of MRI and ONT were collected and concluded into preoperative diagnostic variables or variable combinations. Those of MRI and ONT are analyzed and compared with biopsy results by multivariable receiver operating characteristic (ROC) analysis. The early-stage group, the course of which is 1 year or less, was separately computed and compared.

**Results:** Eighty-three subjects were collected from June 2013 to June 2019; 62 were confirmed AN postoperatively by biopsy, whereas others are not AN. The area under the curve (AUC) of MRI was 0.611, whereas the AUC of ONT was 0.708. In the early-stage group, the AUC of MRI was 0.539, and the AUC of ONT was 0.744.

**Conclusions:** ONT was able to identify more subjects affected by unilateral incipient AN than MRI preoperatively. Given that ONT is a functional test for internal auditory canal nerves, it is an optimal screening test for AN patients because it provides more information than MRI for the further clinical plan. It is particularly noteworthy for identifying asymptomatic AN patients and for early stage. Therefore, it may help more patients from unnecessary surgery. Furthermore, an MRI follow-up is suggested if the patient was found alert in ONT.

**Keywords:** acoustic neuroma, magnetic resonance imaging, audiometry, vestibular, examination, ONT

## INTRODUCTION

Acoustic neuroma (AN), also termed vestibulocochlear schwannoma, from the Schwann cells of the vestibular division or the cochlear division, is the most common tumor in pontocerebellar angle. AN is shown to represent 6% to 8% of all intracranial tumors (1). The typically presenting complaints in AN patients are unilateral hearing loss, tinnitus, and disequilibrium. These disorders do not necessarily correlate close with tumor size or shape (2). As the natural history of the AN is variable (3), only less than 1% of AN exhibit sufficient growth to become clinically active. The patients with small tumors that do not compress the nerves and lead dysfunction may be asymptomatic. Thus, AN patients' managing options vary from observation, microsurgery, stereotactic radiosurgery to surgical debulking (4).

Nevertheless, it is an arduous task to differentiate AN from other tumors in the pontocerebellar angle before surgery (5). So the vital part for optimizing management, early diagnosis, is still under improvement. According to the guidelines of AN diagnosis, magnetic resonance imaging (MRI) will be performed to confirm the diagnosis after otoneural tests (ONT) (6, 7). Thus, ONT and MRI have assumed a significant role in the diagnosis of AN.

Otoneural tests (ONT) usually include audiological and vestibular examinations. Audiometry of AN is often characterized by unilateral or asymmetric sensorineural hearing loss and poor speech recognition (8), whereas vestibular examinations often found abnormal vestibulo-ocular reflex (VOR), or asymmetric caloric test, or spontaneous nystagmus (9).

MRI is currently the standard diagnostic test for AN besides pathology (10). With the extensive application of MRI, the early diagnosis rate of AN has been improved gradually. However, not all patients show the typical clinical traits of MRI in AN. Furthermore, as tumor size reduces, the sensitivity and specificity of this golden standard before surgery declines (11).

Because MRI is not sufficient enough, can we dig out more information from routine ONT tests? Besides the function of screening, are hearing and vestibular examinations helpful for the qualitative diagnosis of AN? This study aimed to assess the diagnostic accuracy of ONT for AN in a cohort of unselected pontocerebellar angle tumor patients. We studied the MRI and ONT tests that are commonly used in daily clinical practice, which are as follows: pure-tone test, speech reception threshold (SRT), speech discrimination score (SDS), videonystagmography (VNG), and caloric test. Moreover, we creatively comprehended the ONT tests to make out the score easily to diagnose and determine the preoperative diagnostic accuracy of MRI and ONT for AN.

## MATERIALS AND METHODS

This work was designed as a preoperative diagnostic accuracy study using otoneural tests in a cohort of unselected patients with

pontocerebellar angle tumors. The samples were collected prospectively among patients referred for vestibular testing at the balance laboratory of our department. We examined the medical records of all patients diagnosed with unilateral incipient pontocerebellar angle tumors based on their MRI imaging between June 2013 and June 2019 in the neurosurgery department at West China Hospital.

All the included patients were required to have otoneural tests and MRI examinations 1 week before surgery. The machine used in this study for ONT is the Ulmer VNG infrared nystagmus view system (Synapsys, France). Every patient has also undergone an enhanced MRI scan of the head in West China Hospital.

Complete otoneural tests consist of the following hearing function tests: pure tone audiometry, acoustic-conductivity resistance test, speech reception threshold (SRT), speech discrimination score (SDS); and vestibular function tests under VNG: VOR tests (including saccade test, smooth pursuit test, optokinetic test, gaze test, and spontaneous nystagmus), and caloric test. Patients with multiple neurofibromatosis and recurrent cerebellopontine angle tumor; or patients with visual impairment, severe systemic diseases, otitis media, or limited ocular movement who failed to complete the test were excluded from this study. All candidates were given informed consent following all the guidelines for investigation with human subjects required by the ethics committee of our hospital. The patients who agreed to sign it were included in the study.

Ultimately, 83 patients with unilateral incipient pontocerebellar angle tumors were included. Different AN features of MRI and ONT were collected and concluded into preoperative diagnostic variables or variable combinations. Those of MRI and ONT are analyzed and compared with after-surgery pathological results by multivariable receiver operating characteristic (ROC) analysis.

Variables of interest were as follows:

1. The final pathological result after surgery (pathol. for short): defined as the actual fact. AN for positive (1), other tumors for negative (0).
2. MRI result before surgery (MRI for short): If there is enlargement/enhancement of the inner auditory canal defined by experienced radiologists as positive (1), otherwise for negative (0).
3. Audiometry before surgery (speech. for short): acoustic-conductivity resistance test must be normal. So this variable includes pure-tone test, speech reception threshold (SRT), and speech discrimination score (SDS). 10 dBHL or more neural hearing impairment or speech discrimination impairment for positive (1). All tests are normal for negative (0).
4. VOR tests before surgery (oculom. for short): including saccade test, smooth pursuit test, optokinetic test, gaze test, and spontaneous nystagmus. If the VOR is impaired, or spontaneous nystagmus, or central positional nystagmus are defined as positive (1), all normal for negative (0).
5. Caloric test before surgery (Calori. for short): affected side impaired (UW>15%) for positive (1), normal for negative (0).



Our vestibular laboratory has set our own normal standard by recruiting normal local healthy control, and then set the UW >15% as abnormal.

6. Vestibular function impairment before surgery (vestib. for short): If there are two positives in VOR, nystagmus, or caloric test is defined as positive (1), all normal or only one positive for negative (0).

In this way, we transferred all results into binary variables.

We divided the patients into early-stage and late-stage groups by the course time of 1 year to mining more information about the early diagnosis of AN.

Statistical analysis was carried out with software MedCalc, version 13.0. General data are described by constituent ratios. Multiparametric receiver operating curve (ROC) analysis was adopted to achieve diagnostic accuracy. The methodology is by DeLong et al. (1988) and Binomial exact Confidence Interval for the AUC.

## RESULTS

### Patient Characteristics

Finally, 25 males and 58 females are recruited, sex ratio is 1:2.32. The average age is 48 years (17–75 years), and the average course is 3.1 years (1 month to 20 years) (**Table 1**). Forty-five cases are left side affected, side ratio is 1.18: 1, left-sided are slightly more than the right-sided. AN was found in 60 cases (72.29%). Other tumors include 14 meningiomas (16.87%) and 9 other types (10.84%) of pontocerebellar angle tumor (two cases of arachnoid cyst, two cases of epidermoid cyst, one case of ependymoma, one case of hemangioma, one case of hemangioblastoma, one case of trigeminal neuroma, and one case of poorly differentiated carcinoma).

### Diagnostic Results of the Variables

**Table 2** shows the diagnostic results of different tests for AN/non-AN groups. Audiometry seems to have the highest sensitivity for AN.

## Diagnostic Accuracy

### ROC for Variables' Comparison

Assuming an AN diagnosis based on the abovementioned single tests, ROC analysis revealed that no test achieved an accuracy ( $AUC \geq 0.75$ ) suitable for clinical use (**Table 3**), even though vestib. is a combination of oculom. and calori. tests. The highest diagnostic accuracy was obtained from audiometry (**Figure 1A**).

### ROC for Early-Stage Group

In the group of patients whose course is less than 1 year, MRI ( $AUC = 0.539$ ) is much less sensitive than the functional tests (**Table 3**). The greatest accuracy ( $AUC = 0.762$ ) for early-stage AN is still based on audiometry (**Figure 1B**), but the combination of vestibular function tests are all good ( $AUC > 0.7$ ).

### ROC for Late-Stage Group

In the group of patients whose course is more than 1 year, MRI ( $AUC = 0.717$ ) is much better than the functional tests (**Table 3**). The sensitivity of MRI for late-stage AN is still not satisfactory, but its specificity is much better than the functional tests this time (**Figure 1C**).

## DISCUSSION

As the retro-cochlear tumors in internal acoustic meatus, such as AN, can compress the vestibular nerve, there are further deterioration in the functions of nerves and diminishing of the blood supply of the inner ear (12). Therefore, AN should be detectable with the audial and vestibular tests and may be more sensitive (13). Both hearing and vestibular function tests are valuable for the diagnosis of AN (14). We usually call these tests altogether as otoneural tests.

In this study, we did not analyze the role of vestibular-evoked myogenic potentials (VEMP) in the diagnosis because VEMPs are not usual routine tests. Sometimes patients fail to produce VEMPs bilaterally, rendering these tests inconclusive, especially

**TABLE 1** | General data of age and course of all patients.

	Age (year)	Course (year)
Lowest value	17	0.1
Highest value	74	20
Arithmetic mean	47.95	3.08
95% CI for the mean	44.9774 to 50.9304	2.1488 to 4.0078
Median	48.56	1
Shapiro-Wilk test for normal distribution	W=0.98	W=0.67
	Accept normality (P=0.3007)	Reject normality (P<0.0001)

**TABLE 2** | Positive results of different tests in AN/non-AN groups.

Group	pathol	MRI	speech	oculom	calori	vestib
AN	60	42	56	33	47	51
non-AN	23	11	10	4	12	10

*pathol*, the final pathological result after surgery; *MRI*, MRI result before surgery; *speech*, audiometry before surgery; *oculom*, including saccade test, smooth pursuit test, optokinetic test, gaze test, and spontaneous nystagmus; *calori*, caloric test before surgery; *vestib*, vestibular function impairment before surgery.

**TABLE 3** | AUC of different variables in general/in early-stage group/in late-stage group.

		AUC	Standard Error <sup>a</sup>	95% CI <sup>b</sup>
In general	MRI	0.611	0.0610	0.498 to 0.716
	vestib	0.708	0.0577	0.598 to 0.802
	calori	0.631	0.0596	0.518 to 0.734
	speech	0.749	0.0553	0.642 to 0.838
In early-stage group	MRI	0.539	0.0794	0.381 to 0.692
	vestib	0.744	0.0730	0.588 to 0.865
	speech	0.762	0.0714	0.608 to 0.878
	calori	0.711	0.0751	0.552 to 0.839
In late-stage group	MRI	0.717	0.101	0.550 to 0.849
	vestib	0.580	0.0969	0.412 to 0.736
	calori	0.554	0.0813	0.386 to 0.713
	speech	0.643	0.0922	0.474 to 0.789

<sup>a</sup>DeLong et al., 1988.<sup>b</sup>Binomial exact.

MRI, MRI result before surgery; vestib, vestibular function impairment before surgery; calori, caloric test before surgery; speech, audiometry before surgery.

when testing oVEMP (15). Although increasing attention has been focused on the role of VEMP in the assessment of patients with AN, there is no consensus about the use of VEMPs in detecting AN (14), maybe because the positive rate of VEMP is highly related to the tumor size (12). Moreover, researchers found that VEMP can be normal with tumors under 1.5 cm (16).

MRI is required in patients with positive ONT results. Of course, MRI is still advisable even if the otoneural tests are negative (6). Although the progress of MRI made it possible to diagnose smaller and asymptomatic tumors than were previously, after a pontocerebellar angle tumor is found from MRI, an optimal treatment plan will be produced. However, different kinds of pontocerebellar angle tumors require different management (4, 17), so the specificity of diagnosis is vital for AN

management. Sometimes, it can be tough to differentiate AN from other symptoms because the symptoms vary (18). It is reported that AN's symptoms may relate to the tumor characteristics (tumor size or distribution), patient age or gender, and also the medical level (2). Therefore, predicting the potential diagnoses, depending on the clinical features, is not reliable. Nevertheless, the signs of AN in MRI are unsatisfactory, especially in patients with similar clinical and radiological features (10). The qualitative diagnosis of AN from MRI is only approximately 70% (18), which is similar to our result (71.7% in the late group).

Furthermore, there are similar shortcomings of radiological examinations in AN diagnosis: the low specificity (**Figure 1A**), especially in the early stage (**Figure 1B**), because the smaller

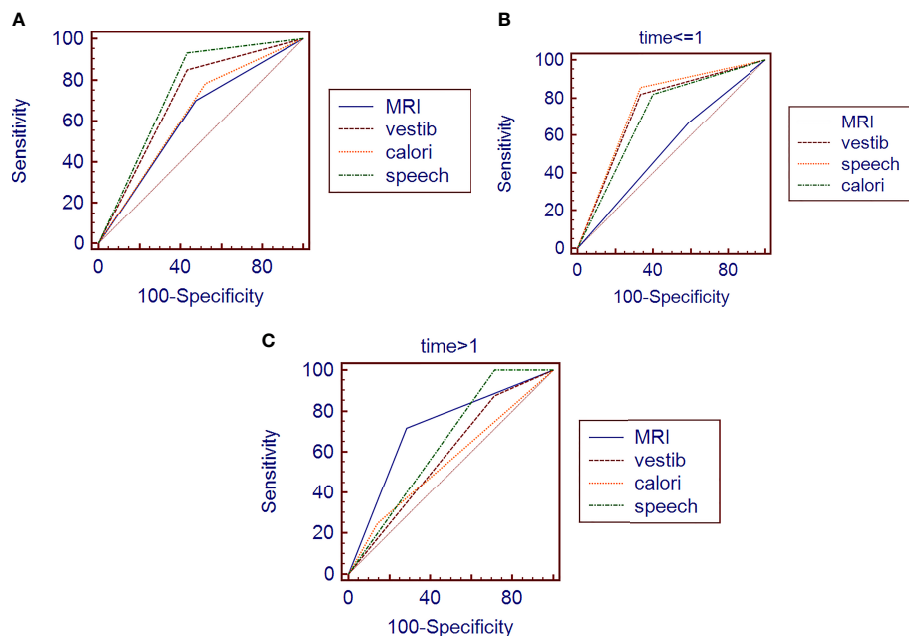


**FIGURE 1** | ROC of different variables in general (**A**) /in early-stage group (**B**) /in late-stage group (**C**). MRI, MRI result before surgery; vestib, vestibular function impairment before surgery; calori, caloric test before surgery; speech, audiometry before surgery time, the course of disease (we divided the patients into early-stage and late-stage groups by the course time of one year).

tumors are usually asymptomatic, making it complicated for early diagnosis. Some researchers already thought about this misdiagnosis and tried to use a hearing test to help the diagnostic value of MRI (19). However, adding a new test is a new burden for the economy and time-consuming.

Patients' initial examinations are always functional signs using ONT tests before MRI (7), maybe because most of the AN patients visited the otolaryngology department because of hearing loss, tinnitus, speech resolution, and other symptoms (5). Therefore, we may use these data to help differentiate AN from other pontocerebellar angle tumors. However lots of papers found that the significance of a single test for diagnosis is limited. We creatively combined them as a parameter to help diagnose, and our study shows the high accuracy of ONT in detecting AN among patients with pontocerebellar angle tumors, especially for the early stage. This is of clinical relevance, considering that most AN are found from MRI as pontocerebellar angle tumors but were only diagnosed after surgery. However, as it is hard for us to remove the tumors without any complications, even for experienced surgeons, surgery is not always the best choice for AN (20). Hence, the importance of ONT accuracy for AN is further emphasized because it may help avoid misdiagnosis and unnecessary surgery or suboptimal treatment.

On the other hand, this result may suggest an MRI follow-up if the patient was found alert in ONT.

## CONCLUSIONS

Among the lesions found by MRI in the pontocerebellar angle, preoperative ONT was able to get further insight into AN's features and identify more subjects affected by unilateral incipient AN than preoperative MRI. Given that ONT is a routine functional test for internal auditory canal lesions, it is an optimal screening test for AN patients and guides in the follow-up treatment. It is particularly noteworthy for identifying early-stage AN patients, given that it provides meaningful guidance for reducing operation rate, guiding radiotherapy, evaluating prognosis, and improving patients' quality of life.

## REFERENCES

1. Tos M, Thomsen J, Charabi S. Incidence of Acoustic Neuromas. *Ear Nose Throat J* (1992) 71(9):391–3. doi: 10.1177/014556139207100907
2. Nadol JB, Diamond PF, Thornton AR. Correlation of Hearing Loss and Radiologic Dimensions of Vestibular Schwannomas (Acoustic Neuromas). *Am J Otol* (1996) 17(2):312. doi: 10.1016/S0196-0709(96)90011-3
3. Winn HR, Youmans JR (eds). *Youmans & Winn Neurological Surgery*. Beijing: Peking University Medical Press (2020).
4. Hasegawa T. Stereotactic Radiosurgery for Nonvestibular Schwannomas. *Neurosurg Clinics N Am* (2013) 24(4):531–42. doi: 10.1016/j.nec.2013.05.003
5. Roos DE, Patel SG, Potter AE, Zacest AC. When is an Acoustic Neuroma Not an Acoustic Neuroma? Pitfalls for Radiosurgeons. *J Med Imaging Radiat Oncol* (2015) 59(4):474–9. doi: 10.1111/1754-9485.12328
6. Association OHAN and Surgery EBOC. Guidelines for Diagnosis and Treatment of Acoustic Neuroma. *Chin J Otorhinolaryngol Head Neck Surg* (2014) 49(3):181–6. doi: 10.3760/cma.j.issn.1673-0860.2014.03.002
7. Foundation MAOO Committee on Hearing and Equilibrium Guidelines for the Evaluation of Hearing Preservation in Acoustic Neuroma (Vestibular Schwannoma). American Academy of Otolaryngology-Head and Neck Surgery Foundation, Inc. *Otolaryngol - Head Neck Surg* (1995) 113(3):179–80. doi: 10.1016/S0194-5998(95)70101-X
8. Samii M, Matthies C. Management of 1000 Vestibular Schwannomas (Acoustic Neuromas): Hearing Function in 1000 Tumor Resections. *Neurosurgery* (1997) 40(2):248–60, 260–262. doi: 10.1097/00006123-199702000-00005
9. Okada Y, Takahashi M, Saito A, Kanzaki J. Electronystagmographic Findings in 147 Patients With Acoustic Neuroma. *Acta Otolaryngol Suppl* (1991) 487:150–6. doi: 10.3109/00016489109130461
10. Fortnum H, O'Neill C, Taylor R, Lenthall R, Nikolopoulos T, Lightfoot G, et al. The Role of Magnetic Resonance Imaging in the Identification of Suspected Acoustic Neuroma: A Systematic Review of Clinical and Cost Effectiveness and Natural History. *Health Technol Assess* (2009) 13(18):iii. doi: 10.3310/hta13180
11. Inoue Y, Ogawa K, Momoshima S, Kanzaki J. The Diagnostic Significance of the 3D-Reconstructed MRI in Vestibular Schwannoma Surgery: Prediction of Tumor Origin. *Eur Arch Otorhinolaryngol* (2002) 259(2):73–6. doi: 10.1007/s00405-001-0426-x
12. Ushio M, Iwasaki S, Chihara Y, Kawahara N, Morita A, Saito N, et al. Is the Nerve Origin of the Vestibular Schwannoma Correlated With Vestibular Evoked

## DATA AVAILABILITY STATEMENT

The raw data supporting the conclusions of this article will be made available by the authors, without undue reservation.

## ETHICS STATEMENT

The studies involving human participants were reviewed and approved by the Ethics Committee of West China Hospital. The patients/participants provided their written informed consent to participate in this study.

## AUTHOR CONTRIBUTIONS

MZ, QD, BL, and HZ carried out the study. QD, MZ, and HZ conceived the study and participated in its design and coordination. QD, MZ, and BL drafted the manuscript. QC, QD, and MZ participated in patient collecting and data works. QC, QD, and BL performed the statistical analyses. All authors contributed to the article and approved the submitted version.

## FUNDING

This study was supported by the Chinese Twelfth Five-Year National Science and Technology Support Program project (project number: 2012BAI12B00).

## ACKNOWLEDGMENTS

The authors thank Yanmei Liu for statistical analysis, Rongping He for database collecting, and our neurosurgeons for patient management. You are the best colleagues always!

- Myogenic Potential, Caloric Test, and Auditory Brainstem Response? *Acta Oto-Laryngol* (2009) 129(10):1095–100. doi: 10.1080/00016480802552543
13. Hirvonen M, Aalto H, Hirvonen TP. Motorized Head Impulse Rotator in Patients With Vestibular Schwannoma. *Acta Oto-Laryngol* (2008) 128(11):1215–20. doi: 10.1080/00016480801908027
  14. Constantin VK, Robert G. Audiovestibular Function Deficits in Vestibular Schwannoma. *BioMed Res Int* (2016) 2016:1–9. doi: 10.1155/2016/4980562
  15. Kjærsgaard Jb SMHD. Vestibular Deficits Correlating to Dizziness Handicap Inventory Score, Hearing Loss, and Tumor Size in a Danish Cohort of Vestibular Schwannoma Patients. *Otol Neurotol* (2019) 6(40):813–9. doi: 10.1097/MAO.0000000000002236
  16. Wu Z, Zhang S, Ji F, Zhao J, Yang W, Han D, et al. Manifestation of Vestibular Evoked Myogenic Potentials in Cerebello-Pontine Angle Occupying Lesions. *Chin J Otorhinolaryngol Head Neck Surg* (2005) 40(5):380. doi: 10.3760/j.issn:1673-0860.2005.05.016
  17. Moura Da Silva LF, Buffon VA, Coelho Neto M, Ramina R. Non-Schwannomatosis Lesions of the Internal Acoustic Meatus—a Diagnostic Challenge and Management: A Series Report of Nine Cases. *Neurosurg Rev* (2015) 38(4):641–8. doi: 10.1007/s10143-015-0638-y
  18. Calzada AP, Go JL, Tschirhart DL, Brackmann DE, Schwartz MS. Cerebellopontine Angle and Intracanalicular Masses Mimicking Vestibular Schwannomas. *Otol Neurotol* (2015) 36(3):491–7. doi: 10.1097/MAO.0000000000000567
  19. Metselaar M, Demirtas G, van Immerzeel T, Schroeffer M. Evaluation of Magnetic Resonance Imaging Diagnostic Approaches for Vestibular Schwannoma Based on Hearing Threshold Differences Between Ears: Added Value of Auditory Brainstem Responses. *Otol Neurotol* (2015) 36(10):1610–5. doi: 10.1097/MAO.0000000000000876
  20. Roos DE, Potter AE, Brophy BP. Stereotactic Radiosurgery for Acoustic Neuromas: What Happens Long Term? *Int J Radiat Oncol Biol Phys* (2012) 82(4):1352–5. doi: 10.1016/j.ijrobp.2011.04.068

**Conflict of Interest:** The authors declare that the research was conducted in the absence of any commercial or financial relationships that could be construed as a potential conflict of interest.

Copyright © 2021 Dai, Zheng, Chen, Zheng and Li. This is an open-access article distributed under the terms of the Creative Commons Attribution License (CC BY). The use, distribution or reproduction in other forums is permitted, provided the original author(s) and the copyright owner(s) are credited and that the original publication in this journal is cited, in accordance with accepted academic practice. No use, distribution or reproduction is permitted which does not comply with these terms.





# Artificial Intelligence in the Imaging of Gastric Cancer: Current Applications and Future Direction

Yun Qin<sup>1†</sup>, Yiqi Deng<sup>2†</sup>, Hanyu Jiang<sup>1</sup>, Na Hu<sup>1\*</sup> and Bin Song<sup>1\*</sup>

<sup>1</sup> Department of Radiology, West China Hospital, Sichuan University, Chengdu, China, <sup>2</sup> Department of Laboratory Medicine, State Key Laboratory of Biotherapy, West China Hospital, Sichuan University, Chengdu, China

## OPEN ACCESS

### Edited by:

Changqiang Wu,  
North Sichuan Medical College, China

### Reviewed by:

Subathra Adithan,  
Jawaharlal Institute of Postgraduate  
Medical Education and Research  
(JIPMER), India  
Hsin Wu Tseng,  
University of Arizona, United States

### \*Correspondence:

Na Hu  
nahu\_wch@163.com  
Bin Song  
anicesong@vip.sina.com

<sup>†</sup>These authors have contributed  
equally to this work

### Specialty section:

This article was submitted to  
Cancer Imaging and  
Image-directed Interventions,  
a section of the journal  
Frontiers in Oncology

**Received:** 20 November 2020

**Accepted:** 07 July 2021

**Published:** 21 July 2021

### Citation:

Qin Y, Deng Y, Jiang H, Hu N and  
Song B (2021) Artificial Intelligence in  
the Imaging of Gastric Cancer: Current  
Applications and Future Direction.  
Front. Oncol. 11:631686.  
doi: 10.3389/fonc.2021.631686

Gastric cancer (GC) is one of the most common cancers and one of the leading causes of cancer-related death worldwide. Precise diagnosis and evaluation of GC, especially using noninvasive methods, are fundamental to optimal therapeutic decision-making. Despite the recent rapid advancements in technology, pretreatment diagnostic accuracy varies between modalities, and correlations between imaging and histological features are far from perfect. Artificial intelligence (AI) techniques, particularly hand-crafted radiomics and deep learning, have offered hope in addressing these issues. AI has been used widely in GC research, because of its ability to convert medical images into minable data and to detect invisible textures. In this article, we systematically reviewed the methodological processes (data acquisition, lesion segmentation, feature extraction, feature selection, and model construction) involved in AI. We also summarized the current clinical applications of AI in GC research, which include characterization, differential diagnosis, treatment response monitoring, and prognosis prediction. Challenges and opportunities in AI-based GC research are highlighted for consideration in future studies.

**Keywords:** gastric cancer, artificial intelligence, deep learning, hand-crafted radiomics, methodologies, clinical applications and challenges

## INTRODUCTION

As one of the most common cancers, gastric cancer (GC) ranks as the top three in terms of mortality rate (1). The American Joint Commission on Cancer (8th Edition) for Gastric Cancer recommends computed tomography (CT) and endoscopic ultrasound for pretreatment TNM classification, whereas magnetic resonance imaging (MRI) and Positron Emission Tomography – Computed Tomography (PET-CT) are effective alternatives for metastasis evaluation. Despite the introduction of new techniques, the pretreatment diagnostic accuracy of GC varies from 40.8% to 98.1% (2–4). Efforts have also been made toward the prediction of histological type such as tumor differentiation grade and Lauren classification, based on enhancement pattern analysis, perfusion analysis, and spectral analysis, which have moderate discriminating performance and area under the curve (AUC) ranging from 0.697 to 0.891 (5–7). Given the importance of accurate pretreatment imaging evaluation and prognostic value of histopathological features, there is an urgent need for better diagnostic methods for treatment planning.

Fortunately, there has been considerable progress in artificial intelligence (AI) during the past decade, which offers promise for meeting these needs. Of all the AI techniques, hand-crafted radiomics and deep learning (DL) are the two most frequently applied methods for medical imaging and have shown the powerful capacity for converting mass medical images into minable data. With the ability to detect features that are invisible to human readers, hand-crafted radiomics and DL have demonstrated promising performance in tumor detection, characterization, and monitoring (8).

Therefore, we reviewed the published AI methodologies utilized in studies on GC imaging to provide an overview of the latest developments. This included data acquisition, lesion segmentation, feature design, and model construction. Furthermore, we summarize the representative clinical applications, knowledge gaps, and future directions. A total of 47 published AI studies on gastric cancer imaging were selected through MEDLINE (June, 2021), of which 45 were retrospective in design (36 single-center and 9 multicenter studies), while the remaining two were single-center prospective studies (**Table 1**). Imaging modalities varied across the studies. Specifically, 39 studies were performed using CT with only one studies based on dual-energy CT, six used MRI, and two used PET-CT (**Table 1**).

## METHODOLOGIES OF AI STUDIES ON GASTRIC CANCER

### Data Acquisition

Image preprocessing accounts for the substantial heterogeneity introduced by different imaging modalities, scanning protocols, machine types, and manufacturers. Image intensity normalization and resampling are two mathematical techniques that are used widely for this purpose. Specifically, image intensity normalization is performed to transform the original image into a standardized form to reduce data variability between cohorts and to generate appropriate inputs for quantitative radiomic feature calculation (20, 27). Resampling is used to adapt the input shape of the model by transforming the original image into the target size by upsampling or downsampling (32, 33, 36, 44).

In addition to imaging data, clinicopathological data also play an important role in AI-based modeling and can be used to improve model performance. These factors included patient age, gender, body mass index, cancer antigen 72-4 (CA72-4), CA199, CA242, carcinoembryonic antigen, alpha-fetoprotein, tumor location, tumor size, and TNM stages (9–13, 15, 17, 18, 20–22, 24–28, 30–36, 38–45, 54).

### Lesion Segmentation

Segmentation of region of interests (ROIs) in AI analysis can be performed using manual, automatic, or semiautomatic methods. Among the included AI-based GC studies, 42 (89%) studies utilized manual segmentation methods, four (9%) applied

semiautomatic methods (25, 30, 38, 39), and only one study (2%) used automatic method (48).

Manual segmentation, which is usually carried out by radiologists, involves placing rectangular/circular boxes that delineate the two-/three-dimensional (2D/3D) boundary of the whole lesion. In Di Dong et al.'s study, 2D ROIs were placed to cover the largest tumor area for predicting lymph node metastasis in locally advanced GC (32). Yue Wang et al. segmented the entire tumor and built a 3D-based hand-crafted radiomics model to diagnose intestinal-type gastric adenocarcinomas (39). In addition, Wenjuan Zhang et al. constructed a DL model on 18 layers of residual convolutional neural network (CNN) with squared segmentation of CT images to predict overall survival (OS) in GC patients (44). It is important to note that because subjective judgments regarding tumor boundaries can vary substantially among radiologists, manual segmentations by multiple radiologists at multiple time points are required to minimize intra- and inter-rater variability. In addition, intra- and interclass correlation coefficients and coefficients of variation are often calculated to evaluate the robustness and reproducibility of the extracted features (12, 14, 17, 22, 30, 31, 34, 36, 39, 41).

In contrast to manual segmentation, semiautomatic segmentation usually comprises two steps. First, several labeling points are marked by radiologists. Thereafter, the entire ROIs are generated automatically by computing devices, based on the labeling points. Satisfactory gastric lesion segmentation performance has been achieved using this approach (25, 30, 38, 39). All the four studies using semiautomatic segmentation employed the same software package (Frontier, Syngo via, Siemens healthcare), which applies a dichotomic classification algorithm to semiautomatically segment lesions from perinormal areas.

### Feature Extraction

After lesion segmentation, quantitative handcrafted engineer features can be calculated to profile the intrinsic characteristics of the ROI. Handcrafted engineer features can be categorized as first-order statistics, shape-based, or texture-based features. First-order statistics are used to describe the distribution of pixel/voxel intensities in the ROIs, shape-based features show the geometric properties of the ROIs, and texture-based features are gray level matrices that represent textural patterns in an image region. Commonly used manual engineered features are presented in **Table 2**.

As opposed to handcrafted features, DL features are derived directly from the artificial neural networks, which encode medical images into a series of feature maps to extract features that represent high-dimensional information that cannot be detected by human readers. Using this method, Yuan Gao et al. achieved a mean average precision value and AUC of 0.7801 and 0.9541 in predicting perigastric lymph node metastasis, based on faster region-based CNN (24).

Handcrafted features describe the morphology, intensity, and textural patterns of ROIs, whereas deep learning network can automatically learn non-handcrafted feature representations from sample images.

**TABLE 1** | Summary of published hand-crafted radiomics and deep learning studies on gastric cancer imaging.

No.	Authors	Year	Study objectives	Study design	No. of patients	Imaging Modality	Radiomics/ Deep learning	Statistical analysis (feature selection and modelling)	Segmentation
1	Ba-Ssalamah et al. (9)	2013	Gastric tumors differentiation prediction	Retrospective, Single-center	48	CT	Radiomics	LDA+kNN	Manual
2	Sung Hyun Yoon et al. (10)	2016	HER2-positive and survival prediction	Retrospective, Single-center	26	CT	Radiomics	NA	Manual
3	Zelan Ma et al. (11)	2017	Gastric cancer and lymphoma differentiation	Retrospective, Single-center	70	CT	Radiomics	LASSO	Manual
4	Song Liu et al. (12)	2017	T and N staging prediction	Prospective, Single-center	80	MRI	Radiomics	ICC	Manual
5	Francesco Giganti et al. (13)	2017	Therapy response prediction	Retrospective, Single-center	34	CT	Radiomics	RF, LOOCV, Univariate analysis, Multivariate analysis	Manual
6	Shunli Liu et al. (14)	2017	Differentiation degree and Lauren classification prediction	Retrospective, Single-center	107	CT	Radiomics	ICC	Manual
7	Yujuan Zhang et al. (15)	2017	Histological differentiation prediction	Retrospective, Single-center	78	MRI	Radiomics	AOV, Spearman correlation analysis	Manual
8	Song Liu et al. (16)	2017	Nodal status prediction	Prospective, Single-center	87	MRI	Radiomics	Spearman correlation test, ICC	Manual
9	Song Liu et al. (17)	2017	Aggressiveness assessment	Retrospective, Single-center	64	MRI	Radiomics	Spearman correlation test	Manual
10	Francesco Giganti et al. (18)	2017	Association investigation between preoperative texture and OS	Retrospective, Single-center	56	CT	Radiomics	RSF, Cox	Manual
11	Zhenhui Li et al. (19)	2018	Neoadjuvant chemotherapy response prediction	Retrospective, Single-center	47	CT	Radiomics	RF, NB, KNN, NNET, SVM, LDA, LASSO	Manual
12	Yuming Jiang et al. (20)	2018	Chemotherapy response and survival prediction	Retrospective, Multi-center	1591	CT	Radiomics	LASSO-Cox	Manual
13	Remy Klaassen et al. (21)	2018	Treatment response prediction	Retrospective, Single-center	196	CT	Radiomics	RF, Pearson correlation	Manual
14	Zhen Hou et al. (22)	2018	Treatment response prediction	retrospective, Single-center	43	MRI	Radiomics	ICC, ACC, KNN, ANN	Manual
15	Yuming Jiang et al. (23)	2018	Survival and chemotherapy benefit prediction	Retrospective, Single-center	214	PET/CT	Radiomics	LASSO-Cox	Manual
16	Yuan Gao et al. (24)	2019	Metastatic lymph nodes prediction	Retrospective, Single-center	602	CT	Deep Learning	FR-CNN	Manual
17	Qiong Li et al. (25)	2019	Adverse histopathological status prediction	Retrospective, Single-center	554	CT	Radiomics	LASSO	Semiautomatic
18	Wujie Chen et al. (26)	2019	Metastatic lymph nodes prediction	Retrospective, Single-center	146	MRI	Radiomics	LASSO, LVQ	Manual
19	Yumin Jiang et al. (27)	2019	pN stage Prediction	Retrospective, Multi-center	1689	CT	Radiomics	LASSO	Manual
20	Qiu-Xia Feng et al. (28)	2019	Metastatic lymph nodes prediction	Retrospective, Single-center	490	CT	Radiomics	SVM	Manual
21	Yue Wang et al. (29)	2019	Tumor invasion prediction	Retrospective, Single-center	244	CT	Radiomics	ICC, RF	Semiautomatic
22	Wuchao Li et al. (30)	2019	OS prediction	Retrospective, Single-center	181	CT	Radiomics	ICC, LASSO-Cox	Manual
23	Xujie Gao et al. (31)	2020	Metastatic lymph nodes prediction	Retrospective, Single-center	463	CT	Radiomics	ICC, LASSO	Manual
24	Di Dong et al. (32)	2020	Prediction of the number of lymph nodes metastasis	Retrospective, Multi-center	679	CT	Radiomics, Deep learning	SVM, ANN, RF, DLRN	Manual
25	Xujie Gao et al. (33)	2020	Tumor-infiltrating Treg cells and outcome prediction	Retrospective, Single-center	165	CT	Radiomics	ICC, LASSO	Manual
26	Xiaofeng Chen et al. (34)	2020	Lymphovascular invasion and clinical outcome prediction	Retrospective, Single-Center	160	CT	Radiomics	ICC, SPM, LASSO	Manual
27	Na Wang et al. (35)	2020	HER2 over-expression status prediction	Retrospective, Single-Center	460	CT	Radiomics	ICC, Logistic	Manual
28	Xujie Gao et al. (36)	2020	Metastatic lymph nodes prediction	Retrospective, Single-center	768	CT	Radiomics	ICC, LASSO	Manual
29	Jing Li et al. (37)	2020	Lymph node metastasis risk prediction	Retrospective, Single-Center	204	CT	Radiomics, Deep Learning	ICC, ANN, KNN, RF, SVM	Manual
30	Yue Wang et al. (38)	2020	Lymph node metastasis prediction	Retrospective, Single-Center	247	CT	Radiomics	ICC, RF	Semiautomatic
31	Yue Wang et al. (39)	2020	Intestinal-type gastric adenocarcinomas distinction	Retrospective, Single-Center	187	CT	Radiomics	ICC, RF	Semiautomatic
32	Shunli Liu et al. (40)	2020	Occult peritoneal metastasis prediction	Retrospective, Single-center	233	CT	Radiomics	ICC, ACC, multivariate logistic regression	Manual
33	Aytul Hande Yardimci et al. (41)	2020	T and N stages and tumor grade prediction	Retrospective, Single-center	114	CT	Radiomics	ICC, LDA	Manual

(Continued)

TABLE 1 | Continued

No.	Authors	Year	Study objectives	Study design	No. of patients	Imaging Modality	Radiomics/Deep learning	Statistical analysis (feature selection and modelling)	Segmentation
34	Jing Yang et al. (42)	2020	Lymph node metastasis prediction	Retrospective, Single-center	170	CT	Radiomics	Pearson correlation analysis , SFFS, logistic	Manual
35	Kai-YuSun et al. (43)	2020	Neoadjuvant chemotherapy response and survival prediction	Retrospective, Single-center	106	CT	Radiomics	SVM, PCA, Cox	Manual
36	Xiaofeng Chen et al. (34)	2020	Lymphovascular invasion and outcome prediction	Retrospective, Single-center	160	CT	Radiomics	ICC,SPM,LASSO	Manual
37	Wenjuan Zhang et al. (44)	2020	Early recurrence prediction	Retrospective, Multi-center	669	CT	Radiomics, Deep Learning	ICC, CV, DCNN	Manual
38	Yuming Jiang et al. (45)	2020	Tumor immune microenvironment and outcome prediction	Retrospective,Multi-center	1778	CT	Radiomics	Logistic	Manual
39	Liwen Zhang et al. (46)	2020	OS prediction	Retrospective, Multi-center	518	CT	Radiomics, Deep Learning	Cox	Manual
40	Xiao-Xiao Wang et al. (47)	2020	Lauren classification prediction	Retrospective, Single-center	539	CT	Radiomics	LASSO, logistic regression	Manual
41	Bao Feng et al. (48)	2021	Primary gastric lymphoma and Borrmann type IV gastric cancer differentiation	Retrospective, Multi-center	189	CT	Radiomics, Deep Learning	U-net based DL model, ICC, LASSO logistic regression	Automated
42	Yi-Wen Sun et al. (49)	2021	Gastric cancer and gastric lymphoma differentiation	Retrospective, Single-center	79	PET/CT	Radiomics	NA	Manual
43	Rui Wang et al. (50)	2021	Gastric neuroendocrine carcinomas and gastric adenocarcinomas differentiation	Retrospective, Single-center	63	CT	Radiomics	LASSO	Manual
44	Rui-Jia Sun et al. (51)	2021	Serosa invasion evaluation	Retrospective, Single-center	572	CT	Deep Learning	ICC, LASSO,DCNNs	Manual
45	Xiang Wang et al. (23)	2021	Prognosis prediction	Retrospective, Single-center	243	CT	Radiomics	multivariate COX regression analysis, LASSO	Manual
46	Yuming Jiang et al. (52)	2021	Occult peritoneal metastasis prediction	Retrospective, Multi-center	1225	CT	Deep Learning	PMetNet	Manual
47	Siwen Wang et al. (53)	2021	Disease-free survival prediction	Retrospective, Multi-center	353	CT	Radiomics	LASSO, multivariate Cox regression	Manual

LDA, Linear Discriminant Analysis; knn, k-Nearest Neighbors; NA, Not Available; LASSO, Least Absolute Shrinkage and Selection Operator; ICC, Intra-class Correlation Coefficient; RF, Random Forest; LOOCV, Leave One Out Cross Validation; AOV, Analysis Of Variance; NB, Naive Bayes; NNET, Neural Networks; SVM, Support Vector Machine; ACC, Absolute Correlation Coefficient; ANN, Artificial Neural Networks; FR-CNN, Faster Region-based Convolutional Neural Networks; LVQ, Learning Vector Quantization; DLRN, Deep Learning Radiomic Nomogram; SPM, Spearman correlation analysis; SFFS, Sequential Forward Floating Selection; PCA, Principal Component Analysis; RSF, Random Survival Forest; DCNN, Deep Convolutional Neural Networks; pmetnet, Peritoneal Metastasis Network; OS, Overall Survival.



**TABLE 2 |** Commonly used manual engineered features in gastric cancer.

No.	Shape-based 3D features (n=17)	Shape-based 2D features (n=10)	Histogram features (n=19)	Textural features (n=75)				
				Gray Level Co-occurrence Matrix (GLCM) Features (n=24)	Gray Level Run Length Matrix (GLRLM) Features (n=16)	Gray Level Size Zone Matrix (GLSZM) Features (n=16)	Neighbouring Gray Tone Difference Matrix (NGTDM) Features (n=5)	Gray Level Dependence Matrix (GLDM) Features (n=14)
1	Mesh Volume	Mesh Surface	Energy	Autocorrelation	Short Run Emphasis (SRE)	Small Area Emphasis (SAE)	coarseness	Small Dependence Emphasis (SDE)
2	Voxel Volume	Pixel Surface	Total Energy	Joint Average	Long Run Emphasis (LRE)	Large Area Emphasis (LAE)	contrast	Large Dependence Emphasis (LDE)
3	Surface Area	Perimeter	Entropy	Cluster Prominence	Gray Level Non-Uniformity (GLN)	Gray Level Non-Uniformity (GLN)	busyness	Gray Level Non-Uniformity (GLN)
4	Surface Area to Volume ratio	Perimeter to Surface ratio	Minimum	Cluster Shade	Gray Level Non-Uniformity Normalized (GLNN)	Gray Level Non-Uniformity Normalized (GLNN)	complexity	Dependence Non-Uniformity (DN)
5	Sphericity	Sphericity	10th percentile	Cluster Tendency	Run Length Non-Uniformity (RLN)	Size-Zone Non-Uniformity (SZN)	strength	Dependence Non-Uniformity Normalized (DNN)
6	Compactness 1	Spherical Disproportion	90th percentile	Contrast	Run Length Non-Uniformity Normalized (RLNN)	Size-Zone Non-Uniformity Normalized (SZNN)		Gray Level Variance (GLV)
7	Compactness 2	Maximum 2D diameter	Maximum	Correlation	Run Percentage (RP)	Zone Percentage (ZP)		Dependence Variance (DV)
8	Spherical Disproportion	Major Axis Length	Mean	Difference Average	Gray Level Variance (GLV)	Gray Level Variance (GLV)		Dependence Entropy (DE)
9	Maximum 3D diameter	Minor Axis Length	Median	Difference Entropy	Run Variance (RV)	Zone Variance (ZV)		Low Gray Level Emphasis (LGLLE)
10	Maximum 2D diameter (Slice)	Elongation	Interquartile Range	Difference Variance	Run Entropy (RE)	Zone Entropy (ZE)		High Gray Level Emphasis (HGLE)
11	Maximum 2D diameter (Column)		Range	Joint Energy	Low Gray Level Run Emphasis (LGLRE)	Low Gray Level Zone Emphasis (LGLZE)		Small Dependence Low Gray Level Emphasis (SDLGLE)
12	Maximum 2D diameter (Row)		Mean Absolute Deviation (MAD)	Joint Entropy	High Gray Level Run Emphasis (HGLRE)	High Gray Level Zone Emphasis (HGLZE)		Small Dependence High Gray Level Emphasis (SDHGLE)
13	Major Axis Length		Robust Mean Absolute Deviation (rMAD)	Informational Measure of Correlation (IMC) 1	Short Run Low Gray Level Emphasis (SRLGLE)	Small Area Low Gray Level Emphasis (SALGLE)		Large Dependence Low Gray Level Emphasis (LDLGLE)
14	Minor Axis Length		Root Mean Squared (RMS)	Informational Measure of Correlation (IMC) 2	Short Run High Gray Level Emphasis (SRHGLE)	Small Area High Gray Level Emphasis (SAHGLE)		Large Dependence High Gray Level Emphasis (LDHGLE)
15	Least Axis Length		Standard Deviation	Inverse Difference Moment (IDM)	Long Run Low Gray Level Emphasis (LRLGLE)	Large Area Low Gray Level Emphasis (LALGLE)		
16	Elongation		Skewness	Maximal Correlation Coefficient (MCC)	Long Run High Gray Level Emphasis (LRHGLE)	Large Area High Gray Level Emphasis (LAHGLE)		
17	Flatness		Kurtosis	Inverse Difference Moment Normalized (IDMN)				
18			Variance	Inverse Difference (ID)				
19			Uniformity	Inverse Difference Normalized (IDN)				
20				Inverse Variance				
21				Maximum Probability				
22				Sum Average				
23				Sum Entropy				
24				Sum of Squares				

Furthermore, studies combining handcrafted engineer and DL features have been carried out to maximize model efficiency. In Wenjuan Zhang et al.'s study, three handcrafted features, six DL features, and several clinical factors were combined to construct a nomogram, which demonstrated AUCs of 0.806–0.831 in predicting postoperative early recurrence in GC patients (44).

## Feature Selection

Most commonly used feature selection methods are categorized into the filter, wrapper, or embedded methods. Among these approaches, filter-based methods (e.g., correlation analysis, analysis of variance) are the simplest methods and select features according to a mutual information criterion (12, 14, 42, 55). Wrappers (e.g., recursive feature elimination, sequential feature selection algorithms, and genetic algorithms) extract useful features based on classifier performance. Filters and wrappers are frequently combined to improve feature selection ability. Using Pearson correlation analysis and the sequential forward floating selection algorithm, Jing Yang et al. obtained optimal tumor and nodal hand-crafted radiomics features to construct a model, which demonstrated good predictive performance for GC metastasis (42). Embedded methods perform variable selection during the model training process. The least absolute shrinkage and selection operator (LASSO) is a classical and widely applied embedded method (11, 19, 25, 27, 31, 33, 34, 36, 45). Unlike the aforementioned methods, LASSO regression adds a penalty against complexity, which can enable the construction of a simple, yet effective model with a small number of features.

## Model Construction

Regarding modeling strategy, logistic regression models (e.g., multivariate logistic regression, LASSO regression) have been widely used in AI-based GC studies. Random forest and support vector machines (SVM) are also effective alternatives for model construction (19, 28, 32, 36, 43). In a multicenter study, Di Dong

et al. proposed an AI model that integrated DL, hand-crafted radiomics, and clinical factors. Their model used various modeling methods, including SVM, artificial neural networks, random forest, Spearman's correlation analysis, logistic regression analysis, and linear regression analysis, and demonstrated good predictive performance for lymph node metastasis in locally advanced GC (32).

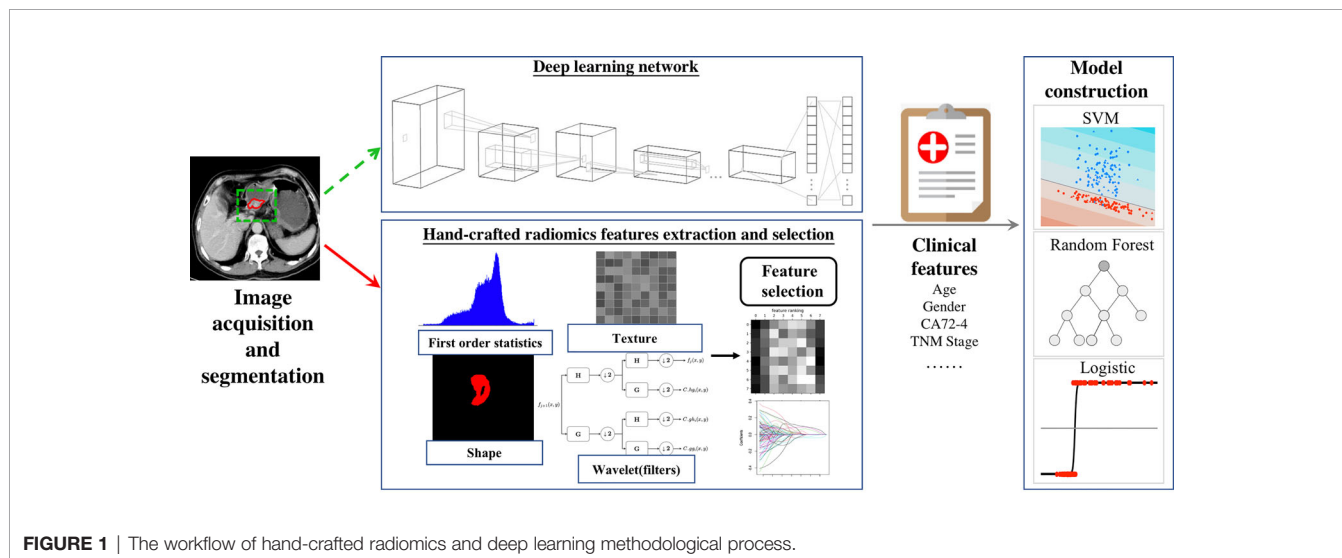
The above workflow and key methodologies of AI techniques in GC imaging are summarized in **Figure 1**.

## CLINICAL APPLICATIONS OF HAND-CRAFTED RADIOMICS AND DEEP LEARNING IN GASTRIC CANCER

Major clinical applications of AI in GC research are shown in **Figure 2**.

### Characterization

The TNM classification is the most widely used staging system in GC, and pretreatment CT/MRI is vital for making optimal treatment decisions (56, 57). Considering its widespread application, most hand-crafted radiomics and DL studies have utilized CT images for preoperative prediction of TNM stages (24, 27, 28, 31, 32, 36–38, 40–42, 51, 52). Precise pretreatment TNM staging of lymph node metastasis is plagued by major obstacles because of discrepancies in traditional imaging features, such as shape, size, and enhancement patterns. Therefore, many researchers have been developing AI-based models to accurately predict lymph node status in GC patients (24, 27, 28, 31, 32, 36–38, 41, 42). While Yang et al.'s study combined tumor and nodal hand-crafted radiomics features (42), other studies selected only the tumor for the ROI (24, 27, 28, 31, 32, 36–38, 41). Of the 10 studies focusing on lymph node status, seven were designed to discriminate between N+ and N- (28, 31, 36–38, 41, 42), two to discriminate specific N stages (N0–3) (27, 32), and one with



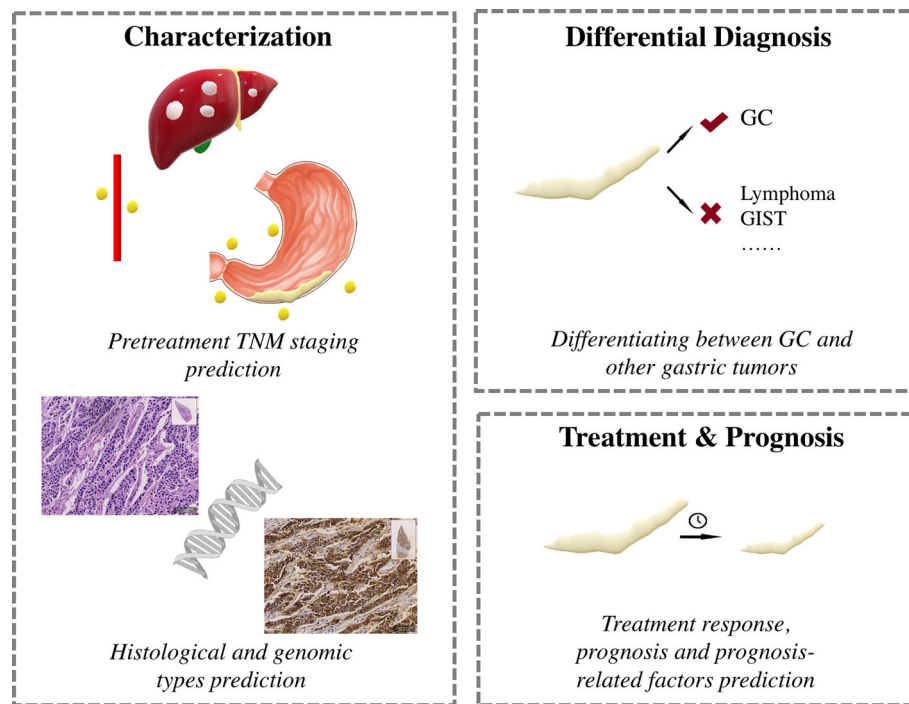


**FIGURE 2** | Clinical application of hand-crafted radiomics and deep learning in gastric cancer.

ambiguous lymph node status (24). Models based on hand-crafted radiomics, DL, or the combination of the two have shown AUC and C-indices of 0.79–0.95 in the training and 0.76–0.89 in the validation cohorts, respectively (24, 27, 28, 31, 32, 36–38, 41, 42). Three studies tested model efficacies for T stage prediction, where two aimed to discriminate T1/2 from T3/4 (29, 30, 41), and one to classify all T1–4 stages (25), with all yielding good discriminatory performance with AUCs ranging from 0.82 to 0.90. Liu et al. investigated venous CT images of primary tumors in advanced GC and built a hand-crafted radiomics model to predict occult peritoneal metastasis (40). Because of the popularity of CT, MRI has been used less frequently in GC patients, with only four studies focused on MRI-based prediction of TNM staging (12, 16, 17, 26). Using hand-crafted radiomics analysis, the authors found that diffusion-weighted imaging and apparent diffusion coefficient maps demonstrate potential in preoperative T and N staging for GC.

Using histopathological results as a reference, six studies explored the correlation between AI-based models and prognosis-related factors of tumor differentiation grade (9, 14, 15, 25), Lauren classification (14, 39, 47), and lymphovascular and neural invasion (14, 17, 25, 34). Two studies were based on MRI images (15, 17) and four were on CT images (14, 25, 34, 39), and all models exhibited good predictive ability for GC before operation. In addition, researchers carrying out immunohistochemistry studies have developed hand-crafted radiomics models to predict human epidermal receptor 2 status, which could serve as a noninvasive prediction tool for

GC for selecting candidates suitable for Herceptin (10, 35). Furthermore, Gao's hand-crafted radiomics model showed good performance in estimating tumor-infiltrating regulatory T (TITreg) cells, with AUCs of 0.85–0.88 in various cohorts (33).

## Differential Diagnosis

Five studies were conducted to differentiate between different gastric tumors (9, 11, 48–50). By applying texture analysis, Ba-Ssalamah et al. classified adenocarcinomas, lymphomas, and gastrointestinal stromal tumors from artery and portal venous CT images, respectively, and misclassification rates ranged from 0%–10% (9). Ma, Feng and Sun et al. focused specifically on differentiating Borrmann type IV GC from primary gastric lymphoma. By combining hand-crafted radiomics signatures, subjective CT findings, age, and gender, Ma's model achieved a diagnostic accuracy of 87.1% (11). All these models demonstrated potential for accurate gastric tumor discrimination.

## Treatment Response and Prognosis

Neoadjuvant chemotherapy (NAC) can decrease tumor size and reduce mortality (58) and is recommended for potentially resectable advanced GCs. However, response rates of NAC vary among studies (59). In patients who do not benefit from NAC, the delay in surgery can lead to tumor progression and poor prognosis. Therefore, noninvasive selection of NAC responders before treatment is crucial for treating patients with advanced GCs. Three studies have utilized CT-based hand-crafted radiomics analysis build models to predict non-

responders, which have yielded AUCs of 0.65–0.82 (13, 19, 43). Notably, Sun et al. demonstrated that their hand-crafted radiomics model performed better for NAC response prediction compared with a clinical model (43).

Chemotherapy and radiation therapy are two mainstays for advanced GCs. Three studies have been carried out to predict chemotherapy response (20, 21, 23). Jiang et al.'s model showed that higher scores of their CT-based hand-crafted radiomics signature indicated a favorable response to chemotherapy for stage II–III patients (20). Similarly, Jiang et al. built a Rad-score system based on hand-crafted radiomics features from PET images, where higher scores indicated chemotherapy responders (23). Klaassen et al. focused on individual liver metastases in esophagogastric cancers and developed a CT-based hand-crafted radiomics model to predict responsive lesions; the resulting AUCs ranged between 0.65–0.87 in various cohorts (21). Only one study tested model efficacy for radiotherapy responders in GC patients with abdominal cavity metastasis. Based on pretreatment CT images, Hou et al. constructed two prediction models with high accuracies ranging from 0.71 to 0.82 (22).

Prognosis is the research highlight of AI-based studies and numerous researchers have explored the potential of hand-crafted radiomics and DL features for prognosis prediction (10, 18, 20, 23, 25, 30, 33, 34, 43–46, 53, 60). Nine studies directly correlated hand-crafted radiomics and DL features with prognosis (10, 18, 20, 23, 30, 44, 46, 53, 60), and five constructed AI-based models to predict certain clinicopathological features, which were shown to be related to prognosis (25, 33, 34, 43, 45). Only one study extracted hand-crafted radiomics features from PET images (23), whereas all others used CT images (10, 13, 18–22, 25, 30, 33, 34, 43–46, 53, 60). Earlier studies reported OS-related hand-crafted radiomics features (10, 18), with later studies building hand-crafted radiomics and DL models that integrated hand-crafted radiomics features with and without clinicopathological features; these achieved good performance in OS, disease-free survival (DFS), and early recurrence prediction (20, 23, 30, 33, 44). Furthermore, hand-crafted radiomics models to predict clinicopathological features, such as TITreg cells, lymphovascular invasion, adverse histopathological status, tumor immune microenvironment, and NAC response have also been developed, which have yielded AUCs of 0.75–0.89 for predicting OS, DFS, and progression-free survival (25, 33, 34, 43, 45).

## FUTURE CHALLENGES AND OPPORTUNITIES

To date, numerous studies have demonstrated the prediction potential of hand-crafted radiomics and DL in GC characterization, differential diagnosis, treatment response, and prognosis. Despite the frequent application of MRI in clinical practice, it is not routinely recommended for GC evaluation. Most studies have focused on CT images and few have used MRI

images. Considering its excellent resolution of soft tissue, MRI images may reveal more intrinsic tumor features and improve prediction. Therefore, future investigations should aim to include more patients undergoing MRI examinations for GC evaluation. Lymph node metastasis status is a key component of pretreatment and postoperative evaluation, and many studies have developed methods for pretreatment AI-based prediction, which include prediction of the existence of lymph node metastasis and N stage. However, there have not been any studies that have focused on individual lymph nodes, which is fundamental for precise pretreatment N stage evaluation and treatment plan modification during follow-up. We encourage future studies to focus on individual lymph node metastasis status prediction based on rigid pathological correlations. Moreover, few studies have analyzed the relationship between imaging features and treatment response. There is still a considerable knowledge gap in this field; further research is needed to improve patient selection and develop better treatment plans.

In addition, future efforts should continue to be actively pursued regarding the methodologies of AI. More intensive and standardized quality controls throughout the entire workflow of AI are warranted to meet this requirement. By analyzing a total of 77 hand-crafted radiomics-based oncology researches, Park et al. reported insufficient overall scientific quality of current hand-crafted radiomics studies (61). Similar dilemmas arose at every stage of GC from data acquisition, segmentation, feature extraction, feature selection, model construction to model performance reporting. In this context, compliance with widely-accepted quality systems [e.g. Hand-crafted radiomics Quality Score (RQS) (62), Transparent Reporting of a multivariable prediction model for Individual Prognosis Or Diagnosis (TRIPOD) (63), etc.] may offer appeal. In addition, prospective multi-institutional collaborations to establish well-curated databases and networks are encouraged in future studies. Furthermore, considering the inherent capacity of AI in analyzing parallel streams of information, including clinical and genomics characteristics (64–66), multi-omics studies which integrate these data may pave the way for better personalized and precision medicine. Collectively, we hope the fruit of these efforts could help to shift the landscape of AI in GC from exploratory research settings to routine clinical settings.

## CONCLUSION

GC has a high incidence and mortality rate, which have been the clinical research emphasis over the past decades. Hand-crafted radiomics and DL are emerging quantitative subsets of AI that have been widely utilized in medicine. The exploration of GC using hand-crafted radiomics and DL has led to promising results for every step of the clinical pathway. However, most studies have been retrospective, conducted in a single center, and analyzed using a single image modality, which have limited the utility of the constructed AI models. Therefore, further prospective and multicenter studies are needed to validate the models. Moreover,



other imaging modalities, such as endoscopic ultrasound may be integrated into the models to further improve model efficacy.

## AUTHOR CONTRIBUTIONS

BS and NH designed and supervised this study. YQ, YD, and HJ conducted the literature search, article selection, data extraction, data analyses and data interpretation. YQ and YD contributed to the conception of the study and drafted the manuscript. All authors contributed to writing of the manuscript and approved the final manuscript. YQ and YD contributed equally to this work. All authors contributed to the article and approved the submitted version.

## REFERENCES

- Bray F, Ferlay J, Soerjomataram I, Siegel RL, Torre LA, Jemal A. Global Cancer Statistics 2018: GLOBOCAN Estimates of Incidence and Mortality Worldwide for 36 Cancers in 185 Countries. *CA Cancer J Clin* (2018) 68 (6):394–424. doi: 10.3322/caac.21492
- Li J, Fang M, Wang R, Dong D, Tian J, Liang P, et al. Diagnostic Accuracy of Dual-Energy CT-Based Nomograms to Predict Lymph Node Metastasis in Gastric Cancer. *Eur Radiol* (2018) 28(12):5241–9. doi: 10.1007/s00330-018-5483-2
- Yang L, Zheng R, Wang N, Yuan Y, Liu S, Li H, et al. Incidence and Mortality of Stomach Cancer in China, 2014. *Chin J Cancer Res* (2018) 30(3):291–8. doi: 10.21147/j.issn.1000-9604.2018.03.01
- Seevaratnam R, Cardoso R, McGregor C, Lourenco L, Mahar A, Sutradhar R, et al. How Useful Is Preoperative Imaging for Tumor, Node, Metastasis (TNM) Staging of Gastric Cancer? A Meta-Analysis. *Gastric Cancer* (2011) 15 (S1):3–18. doi: 10.1007/s10120-011-0069-6
- Tsurumaru D, Miyasaka M, Muraki T, Asayama Y, Nishie A, Oki E, et al. Diffuse-Type Gastric Cancer: Specific Enhancement Pattern on Multiphasic Contrast-Enhanced Computed Tomography. *Jpn J Radiol* (2017) 35(6):289–95. doi: 10.1007/s11604-017-0631-1
- Li R, Li J, Wang X, Liang P, Gao J. Detection of Gastric Cancer and Its Histological Type Based on Iodine Concentration in Spectral CT. *Cancer Imaging* (2018) 18(1):42. doi: 10.1186/s40644-018-0176-2
- Lee DH, Kim SH, Joo I, Han JK. CT Perfusion Evaluation of Gastric Cancer: Correlation With Histologic Type. *Eur Radiol* (2017) 28(2):487–95. doi: 10.1007/s00330-017-4979-5
- Bi WL, Hosny A, Schabath MB, Giger ML, Birkbak NJ, Mehrtash A, et al. Artificial Intelligence in Cancer Imaging: Clinical Challenges and Applications. *CA: A Cancer J Clin* (2019) 69(2):127–57. doi: 10.3322/caac.21552
- Ba-Ssalamah A, Muin D, Scherthaner R, Kulinna-Cosentini C, Bastati N, Stift J, et al. Texture-Based Classification of Different Gastric Tumors at Contrast-Enhanced CT. *Eur J Radiol* (2013) 82(10):e537–43. doi: 10.1016/j.ejrad.2013.06.024
- Yoon SH, Kim YH, Lee YJ, Park J, Kim JW, Lee HS, et al. Tumor Heterogeneity in Human Epidermal Growth Factor Receptor 2 (HER2)-Positive Advanced Gastric Cancer Assessed by CT Texture Analysis: Association With Survival After Trastuzumab Treatment. *PLoS One* (2016) 11(8):e0161278. doi: 10.1371/journal.pone.0161278
- Ma Z, Fang M, Huang Y, He L, Chen X, Liang C, et al. CT-Based Radiomics Signature for Differentiating Borrmann Type IV Gastric Cancer From Primary Gastric Lymphoma. *Eur J Radiol* (2017) 91:142–7. doi: 10.1016/j.ejrad.2017.04.007
- Liu S, Zhang Y, Chen L, Guan W, Guan Y, Ge Y, et al. Whole-Lesion Apparent Diffusion Coefficient Histogram Analysis: Significance in T and N Staging of Gastric Cancers. *BMC Cancer* (2017) 17(1):665. doi: 10.1186/s12885-017-3622-9
- Giganti F, Marra P, Ambrosi A, Salerno A, Antunes S, Chiari D, et al. Pre-Treatment MDCT-Based Texture Analysis for Therapy Response Prediction in Gastric Cancer: Comparison With Tumour Regression Grade at Final Histology. *Eur J Radiol* (2017) 90:129–37. doi: 10.1016/j.ejrad.2017.02.043
- Liu S, Liu S, Ji C, Zheng H, Pan X, Zhang Y, et al. Application of CT Texture Analysis in Predicting Histopathological Characteristics of Gastric Cancers. *Eur Radiol* (2017) 27(12):4951–9. doi: 10.1007/s00330-017-4881-1
- Zhang Y, Chen J, Liu S, Shi H, Guan W, Ji C, et al. Assessment of Histological Differentiation in Gastric Cancers Using Whole-Volume Histogram Analysis of Apparent Diffusion Coefficient Maps. *J Magn Reson Imaging* (2017) 45 (2):440–9. doi: 10.1002/jmri.25360
- Liu S, Zhang Y, Xia J, Chen L, Guan W, Guan Y, et al. Predicting the Nodal Status in Gastric Cancers: The Role of Apparent Diffusion Coefficient Histogram Characteristic Analysis. *Magn Reson Imaging* (2017) 42:144–51. doi: 10.1016/j.mri.2017.07.013
- Liu S, Zheng H, Zhang Y, Chen L, Guan W, Guan Y, et al. Whole-Volume Apparent Diffusion Coefficient-Based Entropy Parameters for Assessment of Gastric Cancer Aggressiveness. *J Magn Reson Imaging* (2018) 47(1):168–75. doi: 10.1002/jmri.25752
- Giganti F, Antunes S, Salerno A, Ambrosi A, Marra P, Nicoletti R, et al. Gastric Cancer: Texture Analysis From Multidetector Computed Tomography as a Potential Preoperative Prognostic Biomarker. *Eur Radiol* (2017) 27(5):1831–9. doi: 10.1007/s00330-016-4540-y
- Li Z, Zhang D, Dai Y, Dong J, Wu L, Li Y, et al. Computed Tomography-Based Radiomics for Prediction of Neoadjuvant Chemotherapy Outcomes in Locally Advanced Gastric Cancer: A Pilot Study. *Chin J Cancer Res* (2018) 30(4):406–14. doi: 10.21147/j.issn.1000-9604.2018.04.03
- Jiang Y, Chen C, Xie J, Wang W, Zha X, Lv W, et al. Radiomics Signature of Computed Tomography Imaging for Prediction of Survival and Chemotherapeutic Benefits in Gastric Cancer. *EBioMedicine* (2018) 36:171–82. doi: 10.1016/j.ebiom.2018.09.007
- Tian J, Klaassen R, Larue RTHM, Mearadji B, van der Woude SO, Stoker J, et al. Feasibility of CT Radiomics to Predict Treatment Response of Individual Liver Metastases in Esophagogastric Cancer Patients. *PLoS One* (2018) 13(11):e0207362. doi: 10.1371/journal.pone.0207362
- Hou Z, Yang Y, Li S, Yan J, Ren W, Liu J, et al. Radiomic Analysis Using Contrast-Enhanced CT: Predict Treatment Response to Pulsed Low Dose Rate Radiotherapy in Gastric Carcinoma With Abdominal Cavity Metastasis. *Quant Imaging Med Surg* (2018) 8(4):410–20. doi: 10.21037/qims.2018.05.01
- Jiang Y, Yuan Q, Lv W, Xi S, Huang W, Sun Z, et al. Radiomic Signature of (18)F Fluorodeoxyglucose PET/CT for Prediction of Gastric Cancer Survival and Chemotherapeutic Benefits. *Theranostics* (2018) 8(21):5915–28. doi: 10.7150/thno.28018
- Gao Y, Zhang ZD, Li S, Guo YT, Wu QY, Liu SH, et al. Deep Neural Network-Assisted Computed Tomography Diagnosis of Metastatic Lymph Nodes From Gastric Cancer. *Chin Med J (Engl)* (2019) 132(23):2804–11. doi: 10.1097/CM9.0000000000000532
- Li Q, Qi L, Feng QX, Liu C, Sun SW, Zhang J, et al. Machine Learning-Based Computational Models Derived From Large-Scale Radiographic-Radiomic Images Can Help Predict Adverse Histopathological Status of Gastric Cancer.

## FUNDING

This work was supported by grants from the National Natural Science Foundation of China (82002569, 81902437); 1.3.5 Project for Disciplines of Excellence, West China Hospital, Sichuan University (ZYJC21006, ZYYC20003).

## SUPPLEMENTARY MATERIAL

The Supplementary Material for this article can be found online at: <https://www.frontiersin.org/articles/10.3389/fonc.2021.631686/full#supplementary-material>

- Clin Transl Gastroenterol* (2019) 10(10):e00079. doi: 10.14309/ctg.00000000000000079
26. Chen W, Wang S, Dong D, Gao X, Zhou K, Li J, et al. Evaluation of Lymph Node Metastasis in Advanced Gastric Cancer Using Magnetic Resonance Imaging-Based Radiomics. *Front Oncol* (2019) 9:1265. doi: 10.3389/fonc.2019.01265
  27. Jiang Y, Wang W, Chen C, Zhang X, Zha X, Lv W, et al. Radiomics Signature on Computed Tomography Imaging: Association With Lymph Node Metastasis in Patients With Gastric Cancer. *Front Oncol* (2019) 9:340. doi: 10.3389/fonc.2019.00340
  28. Feng QX, Liu C, Qi L, Sun SW, Song Y, Yang G, et al. An Intelligent Clinical Decision Support System for Preoperative Prediction of Lymph Node Metastasis in Gastric Cancer. *J Am Coll Radiol* (2019) 16(7):952–60. doi: 10.1016/j.jacr.2018.12.017
  29. Wang Y, Liu W, Yu Y, Liu J-J, Jiang L, Xue H-D, et al. Prediction of the Depth of Tumor Invasion in Gastric Cancer: Potential Role of CT Radiomics. *Acad Radiol* (2019) 27(8):1077–84. doi: 10.1016/j.acra.2019.10.020
  30. Li W, Zhang L, Tian C, Song H, Fang M, Hu C, et al. Prognostic Value of Computed Tomography Radiomics Features in Patients With Gastric Cancer Following Curative Resection. *Eur Radiol* (2019) 29(6):3079–89. doi: 10.1007/s00330-018-5861-9
  31. Gao X, Ma T, Cui J, Zhang Y, Wang L, Li H, et al. A CT-Based Radiomics Model for Prediction of Lymph Node Metastasis in Early Stage Gastric Cancer. *Acad Radiol* (2020) 28(6):e155–64. doi: 10.1016/j.acra.2020.03.045
  32. Dong D, Fang MJ, Tang L, Shan XH, Gao JB, Giganti F, et al. Deep Learning Radiomic Nomogram can Predict the Number of Lymph Node Metastasis in Locally Advanced Gastric Cancer: An International Multicenter Study. *Ann Oncol* (2020) 31(7):912–20. doi: 10.1016/j.annonc.2020.04.003
  33. Gao X, Ma T, Bai S, Liu Y, Zhang Y, Wu Y, et al. A CT-Based Radiomics Signature for Evaluating Tumor Infiltrating Treg Cells and Outcome Prediction of Gastric Cancer. *Ann Transl Med* (2020) 8(7):469. doi: 10.21037/atm.2020.03.114
  34. Chen X, Yang Z, Yang J, Liao Y, Pang P, Fan W, et al. Radiomics Analysis of Contrast-Enhanced CT Predicts Lymphovascular Invasion and Disease Outcome in Gastric Cancer: A Preliminary Study. *Cancer Imaging* (2020) 20(1):24. doi: 10.1186/s40644-020-00302-5
  35. Wang N, Wang X, Li W, Ye H, Bai H, Wu J, et al. Contrast-Enhanced CT Parameters of Gastric Adenocarcinoma: Can Radiomic Features Be Surrogate Biomarkers for HER2 Over-Expression Status? *Cancer Manag Res* (2020) 12:1211–9. doi: 10.2147/CMAR.S230138
  36. Gao X, Ma T, Cui J, Zhang Y, Wang L, Li H, et al. A Radiomics-Based Model for Prediction of Lymph Node Metastasis in Gastric Cancer. *Eur J Radiol* (2020) 129:109069. doi: 10.1016/j.ejrad.2020.109069
  37. Li J, Dong D, Fang M, Wang R, Tian J, Li H, et al. Dual-Energy CT-Based Deep Learning Radiomics Can Improve Lymph Node Metastasis Risk Prediction for Gastric Cancer. *Eur Radiol* (2020) 30(4):2324–33. doi: 10.1007/s00330-019-06621-x
  38. Wang Y, Liu W, Yu Y, Liu JJ, Xue HD, Qi YF, et al. CT Radiomics Nomogram for the Preoperative Prediction of Lymph Node Metastasis in Gastric Cancer. *Eur Radiol* (2020) 30(2):976–86. doi: 10.1007/s00330-019-06398-z
  39. Wang Y, Liu W, Yu Y, Han W, Liu JJ, Xue HD, et al. Potential Value of CT Radiomics in the Distinction of Intestinal-Type Gastric Adenocarcinomas. *Eur Radiol* (2020) 30(5):2934–44. doi: 10.1007/s00330-019-06629-3
  40. Liu S, He J, Liu S, Ji C, Guan W, Chen L, et al. Radiomics Analysis Using Contrast-Enhanced CT for Preoperative Prediction of Occult Peritoneal Metastasis in Advanced Gastric Cancer. *Eur Radiol* (2020) 30(1):239–46. doi: 10.1007/s00330-019-06368-5
  41. Yardimci AH, Sel I, Bektas CT, Yarikaya E, Dursun N, Bektas H, et al. Computed Tomography Texture Analysis in Patients With Gastric Cancer: A Quantitative Imaging Biomarker for Preoperative Evaluation Before Neoadjuvant Chemotherapy Treatment. *Jpn J Radiol* (2020) 38(6):553–60. doi: 10.1007/s11604-020-00936-2
  42. Yang J, Wu Q, Xu L, Wang Z, Su K, Liu R, et al. Integrating Tumor and Nodal Radiomics to Predict Lymph Node Metastasis in Gastric Cancer. *Radiother Oncol* (2020) 150:89–96. doi: 10.1016/j.radonc.2020.06.004
  43. Sun K-Y, Hu H-T, Chen S-L, Ye J-N, Li G-H, Chen L-D, et al. CT-Based Radiomics Scores Predict Response to Neoadjuvant Chemotherapy and Survival in Patients With Gastric Cancer. *BMC Cancer* (2020) 20(1):468. doi: 10.1186/s12885-020-06970-7
  44. Zhang W, Fang M, Dong D, Wang X, Ke X, Zhang L, et al. Development and Validation of a CT-Based Radiomic Nomogram for Preoperative Prediction of Early Recurrence in Advanced Gastric Cancer. *Radiother Oncol* (2020) 145:13–20. doi: 10.1016/j.radonc.2019.11.023
  45. Jiang Y, Wang H, Wu J, Chen C, Yuan Q, Huang W, et al. Noninvasive Imaging Evaluation of Tumor Immune Microenvironment to Predict Outcomes in Gastric Cancer. *Ann Oncol* (2020) 31(6):760–8. doi: 10.1016/j.annonc.2020.03.295
  46. Zhang L, Dong D, Zhang W, Hao X, Fang M, Wang S, et al. A Deep Learning Risk Prediction Model for Overall Survival in Patients With Gastric Cancer: A Multicenter Study. *Radiother Oncol* (2020) 150:73–80. doi: 10.1016/j.radonc.2020.06.010
  47. Wang XX, Ding Y, Wang SW, Dong D, Li HL, Chen J, et al. Intratumoral and Peritumoral Radiomics Analysis for Preoperative Lauren Classification in Gastric Cancer. *Cancer Imaging* (2020) 20(1):83. doi: 10.1186/s40644-020-00358-3
  48. Feng B, Huang L, Li C, Quan Y, Chen Y, Xue H, et al. A Heterogeneity Radiomic Nomogram for Preoperative Differentiation of Primary Gastric Lymphoma From Borrmann Type IV Gastric Cancer. *J Comput Assist Tomogr* (2021) 45(2):191–202. doi: 10.1097/RCT.0000000000001117
  49. Sun YW, Ji CF, Wang H, He J, Liu S, Ge Y, et al. Differentiating Gastric Cancer and Gastric Lymphoma Using Texture Analysis (TA) of Positron Emission Tomography (PET). *Chin Med J (Engl)* (2020) 134(4):439–47. doi: 10.1097/CM9.0000000000001206
  50. Wang R, Liu H, Liang P, Zhao H, Li L, Gao J. Radiomics Analysis of CT Imaging for Differentiating Gastric Neuroendocrine Carcinomas From Gastric Adenocarcinomas. *Eur J Radiol* (2021) 138:109662. doi: 10.1016/j.ejrad.2021.109662
  51. Sun RJ, Fang MJ, Tang L, Li XT, Lu QY, Dong D, et al. CT-Based Deep Learning Radiomics Analysis for Evaluation of Serosa Invasion in Advanced Gastric Cancer. *Eur J Radiol* (2020) 132:109277. doi: 10.1016/j.ejrad.2020.109277
  52. Jiang Y, Liang X, Wang W, Chen C, Yuan Q, Zhang X, et al. Noninvasive Prediction of Occult Peritoneal Metastasis in Gastric Cancer Using Deep Learning. *JAMA Netw Open* (2021) 4(1):e2032269. doi: 10.1001/jamanetworkopen.2020.32269
  53. Wang S, Feng C, Dong D, Li H, Zhou J, Ye Y, et al. Preoperative Computed Tomography-Guided Disease-Free Survival Prediction in Gastric Cancer: A Multicenter Radiomics Study. *Med Phys* (2020) 47(10):4862–71. doi: 10.1002/mp.14350
  54. Parmar C, Rios Velazquez E, Leijenaar R, Jermoumi M, Carvalho S, Mak RH, et al. Robust Radiomics Feature Quantification Using Semiautomatic Volumetric Segmentation. *PLoS One* (2014) 9(7):e102107. doi: 10.1371/journal.pone.0102107
  55. Guyon I, Elisseeff A. An Introduction to Variable and Feature Selection. *J Mach Learn Res* (2003) 3:1157–82. doi: 10.1162/153244303322753616
  56. Amin MB, Greene FL, Edge SB, Compton CC, Gershenwald JE, Brookland RK, et al. The Eighth Edition AJCC Cancer Staging Manual: Continuing to Build a Bridge From a Population-Based to a More “Personalized” Approach to Cancer Staging. *CA: Cancer J Clin* (2017) 67(2):93–9. doi: 10.3322/caac.21388
  57. In H, Solsky I, Palis B, Langdon-Embry M, Ajani J, Sano T. Validation of the 8th Edition of the AJCC TNM Staging System for Gastric Cancer Using the National Cancer Database. *Ann Surg Oncol* (2017) 24(12):3683–91. doi: 10.1245/s10434-017-6078-x
  58. Cocolini F, Nardi M, Montori G, Ceresoli M, Celotti A, Cascinu S, et al. Neoadjuvant Chemotherapy in Advanced Gastric and Esophago-Gastric Cancer. Meta-Analysis of Randomized Trials. *Int J Surg* (2018) 51:120–7. doi: 10.1016/j.ijsu.2018.01.008
  59. Koda Y. Neoadjuvant Chemotherapy for Gastric Adenocarcinoma in Japan. *Surg Today* (2017) 47(8):899–907. doi: 10.1007/s00595-017-1473-2
  60. Wang X, Sun J, Zhang W, Yang X, Zhu C, Pan B, et al. Use of Radiomics to Extract Splenic Features to Predict Prognosis of Patients With Gastric Cancer. *Eur J Surg Oncol* (2020) 46(10 Pt A):1932–40. doi: 10.1016/j.ejso.2020.06.021
  61. Park JE, Kim D, Kim HS, Park SY, Kim JY, Cho SJ, et al. Quality of Science and Reporting of Radiomics in Oncologic Studies: Room for Improvement

- According to Radiomics Quality Score and TRIPOD Statement. *Eur Radiol* (2020) 30(1):523–36. doi: 10.1007/s00330-019-06360-z
62. Lambin P, Leijenaar RTH, Deist TM, Peerlings J, de Jong EEC, van Timmeren J, et al. Radiomics: The Bridge Between Medical Imaging and Personalized Medicine. *Nat Rev Clin Oncol* (2017) 14(12):749–62. doi: 10.1038/nrclinonc.2017.141
  63. Moons KG, Altman DG, Reitsma JB, Ioannidis JP, Macaskill P, Steyerberg EW, et al. Transparent Reporting of a Multivariable Prediction Model for Individual Prognosis or Diagnosis (TRIPOD): Explanation and Elaboration. *Ann Intern Med* (2015) 162(1):W1–73. doi: 10.7326/M14-0698
  64. Shu Y, Zhang W, Hou Q, Zhao L, Zhang S, Zhou J, et al. Prognostic Significance of Frequent CLDN18-ARHGAP26/6 Fusion in Gastric Signet-Ring Cell Cancer. *Nat Commun* (2018) 9(1):1–11. doi: 10.1038/s41467-018-04907-0
  65. Network CGAR. Comprehensive Molecular Characterization of Gastric Adenocarcinoma. *Nature* (2014) 513(7517):202. doi: 10.1038/nature13480
  66. Zhang W-H, Zhang S-Y, Hou Q-Q, Qin Y, Chen X-Z, Zhou Z-G, et al. The Significance of the CLDN18-ARHGAP Fusion Gene in Gastric Cancer: A Systematic Review and Meta-Analysis. *Front Oncol* (2020) 10:1214. doi: 10.3389/fonc.2020.01214

**Conflict of Interest:** The authors declare that the research was conducted in the absence of any commercial or financial relationships that could be construed as a potential conflict of interest.

Copyright © 2021 Qin, Deng, Jiang, Hu and Song. This is an open-access article distributed under the terms of the Creative Commons Attribution License (CC BY). The use, distribution or reproduction in other forums is permitted, provided the original author(s) and the copyright owner(s) are credited and that the original publication in this journal is cited, in accordance with accepted academic practice. No use, distribution or reproduction is permitted which does not comply with these terms.



# Role of MRI-Based Functional Imaging in Improving the Therapeutic Index of Radiotherapy in Cancer Treatment

Mei Li<sup>1,2†</sup>, Qin Zhang<sup>2†</sup> and Kaixuan Yang<sup>1\*</sup>

<sup>1</sup> Department of Gynecology and Obstetrics, Key Laboratory of Birth Defects and Related Diseases of Women and Children, Ministry of Education, West China Second University Hospital, Sichuan University, Chengdu, China, <sup>2</sup> West China School of Medicine, West China Hospital, Sichuan University, Chengdu, China

## OPEN ACCESS

### Edited by:

Changqiang Wu,  
North Sichuan Medical College, China

### Reviewed by:

Roshankumar Patil,  
HealthCare Global Enterprises Ltd  
(HCG), India  
Gaurav Sharma,  
University of Texas Southwestern  
Medical Center, United States

### \*Correspondence:

Kaixuan Yang  
kaixuanyangmd@hotmail.com

<sup>†</sup>These authors have contributed  
equally to this work and share  
first authorship

### Specialty section:

This article was submitted to  
Cancer Imaging and  
Image-directed Interventions,  
a section of the journal  
Frontiers in Oncology

**Received:** 22 December 2020

**Accepted:** 30 July 2021

**Published:** 27 August 2021

### Citation:

Li M, Zhang Q and Yang K (2021) Role  
of MRI-Based Functional Imaging in  
Improving the Therapeutic Index of  
Radiotherapy in Cancer Treatment.  
Front. Oncol. 11:645177.  
doi: 10.3389/fonc.2021.645177

Advances in radiation technology, such as intensity-modulated radiation therapy (IMRT), have largely enabled a biological dose escalation of the target volume (TV) and reduce the dose to adjacent tissues or organs at risk (OARs). However, the risk of radiation-induced injury increases as more radiation dose utilized during radiation therapy (RT), which predominantly limits further increases in TV dose distribution and reduces the local control rate. Thus, the accurate target delineation is crucial. Recently, technological improvements for precise target delineation have obtained more attention in the field of RT. The addition of functional imaging to RT can provide a more accurate anatomy of the tumor and normal tissues (such as location and size), along with biological information that aids to optimize the therapeutic index (TI) of RT. In this review, we discuss the application of some common MRI-based functional imaging techniques in clinical practice. In addition, we summarize the main challenges and prospects of these imaging technologies, expecting more inspiring developments and more productive research paths in the near future.

**Keywords:** functional imaging, organs at risk, target volume, radiation therapy, therapeutic index

## INTRODUCTION

Radiation therapy (RT) is the cornerstone of curative cancer care (1). Ideally, the optimal RT strategy is supposed to deliver the highest potential radiation dose to the tumor target volume (TV) without affecting nearby structures or organs at risk (OARs). To meet the requirement, radiation oncology has undergone a huge transition in the last decades from 2D therapy to 3D conformal RT (3DCRT) and intensity-modulated RT (IMRT), and even to intensity-modulated proton therapy (IMPT), which allows for better performance in terms of dose escalation in the TV and dose reduction in the OARs. Theoretically, therapeutic index (TI) is optimized by maximizing the dose in the TV while minimizing the dose in the OARs in the treatment plan (**Figure 1D**).

With regard to IMPT, it has been widely studied due to its unique depth-dose characteristics of protons, which can increase the dose to the TV while reducing the dose exposure to normal tissue,



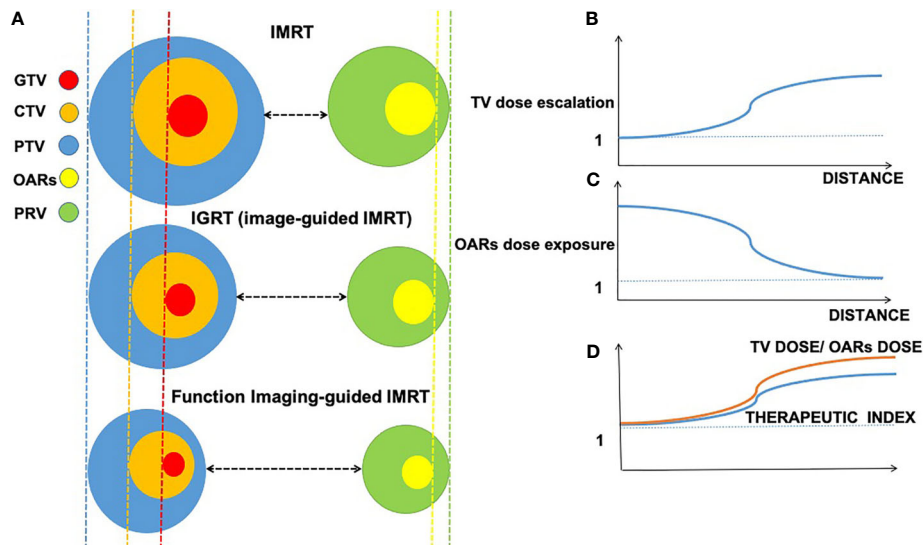


**FIGURE 1 |** Interaction among imaging-guided techniques, treatment margins of tumor target, and organs at risk (OARs) based on the accuracy of imaging approaches. Decreasing volume around gross tumor volume (GTV, in red), clinical target volume (CTV, in orange), planning target volume (PTV, in blue), planning organ at risk volume (PRV, in green), and organs at risk (OARs, in yellow); distance changes between treatment margins and OARs in intensity-modulated radiation therapy (IMRT), image-guided radiation therapy (IGRT), and function imaging-guided IMRT. **(A)** Relations between distance (x-axis) of gross target and organ at risk. **(B)** Relations between the distance (x-axis) and TV dose escalation (y-axis). **(C)** Relations between the distance (x-axis) and OARs dose exposure (y-axis). **(D)** Relations between TV dose/OARs dose and therapeutic index.

however, the majority of studies on the application of IMPT is based on small-scale studies and is poorly cost-effective (2). Therefore, herein, we focus on photon-based RT techniques such as 3DCRT and IMRT, which are currently the main RT strategies in large-scale clinical practice, despite the lack of TI optimization during RT. Fortunately, a growing body of evidence suggests that the integration of functional imaging techniques into RT brings hope for improving TI based on photon-based RT. In RT, imaging plays a critical role in tumor location, staging, target delineation, and outcome monitoring (3). In contrast to conventional IMRT and imaging-guided RT (IGRT), functional imaging-guided IMRT tends to provide a more accurate delineation of TV and OARs, resulting in diminishing treatment margin of the gross tumor volume (GTV), clinical target volume (CTV), and planning target volume (PTV) in tumor target and a smaller volume of OARs and planning OAR volume (PRV) in OARs (**Figure 1A**). In addition to anatomical information (such as location and size), functional imaging provides the physiological and functional status of the tumor and its surroundings compared with conventional magnetic resonance imaging (MRI) (3). Currently, functional imaging plays various roles in radiation oncology, such as tumor localization, staging, target delineation, assessment of early response to therapy, prognosis, and monitoring recurrence (4).

In general, functional imaging has widely enabled clinicians to improve TI ratios by reducing the risk of geographic miss and selectively increasing radiotherapy (RT) dose to the TV, and minimizing unnecessary dose exposure to the OARs simultaneously. In this review, we outline several common

MRI-based functional imaging techniques that used in the field of RT to explore improvement in TI ratios. Furthermore, we summarize current challenges and prospects.

## FUNCTIONAL IMAGING

At present, many functional imaging techniques have been gradually integrated into oncologic RT planning. Herein, we review some common imaging techniques in clinical practice, including diffusion-weighted (DW) imaging (DWI), intravoxel incoherent motion DWI (IVIM-DWI), MR-spectroscopic imaging (MRSI), dynamic susceptibility contrast (DSC), dynamic contrast-enhanced (DCE), diffusion tensor imaging (DTI)-MRI, and blood oxygenation level-dependent functional MRI (BOLD-fMRI) (**Table 1**).

### Diffusion-Weighted MRI

DWI is a simple and readily available functional imaging technique with capability to visualize the motion of the water molecules (also called Brownian motion) in biological tissues (5). DWI can evaluate the differences in tissue cellular density and offer visibility of cellular construction (102, 103). Sensitized b-value, known as, the real diffusion weighting (measured in  $s/mm^2$ ), is used to measure the levels of diffusion weighting applied. Motion-sensitizing gradients are used for parameter acquisition. Thus, there is no need for contrast injection on DW-MRI due to its tissue contrast. The amount of diffusion (of water molecules) in different tissues can be quantitatively evaluated using the apparent diffusion

coefficient (ADC) value (6) and then presented as a map, which holds better diffusion than traditional DWI. ADC value can be calculated by changing gradient amplitude using different b-values (104–106) and at least two b-values (107). In clinical practice, to achieve the lower mobility of water molecules and shorter diffusion distances in these tissues, using a larger b-value (e.g.,  $b = 500 \text{ s/mm}^2$ ) on DWI is suggested.

Generally, the spread of water molecules on DW-MRI is restricted on malignant lesions with hypercellular areas or complex structures, presenting a high signal on DWI and accompanying low ADC value (108, 109). Clinical practice shows (110) that the standard ADC value obtained by the traditional single-index DWI model is affected by the water molecule diffusion and microcirculation perfusion in the tissue and cannot well reflect the movement of water molecules in the tumor tissue. IVIM-DWI introduced by Le Bihan (5, 27) can more accurately assess diffusion movement and microcirculation perfusion in tumor tissues due to its ability to separate diffusion and perfusion. IVIM-based parameters involve pure diffusion coefficient (D), pseudodiffusion coefficient ( $D^*$ ), and perfusion fraction (f).

Based on the fact that the ADC value and signal intensity between tumor and normal tissue are significantly different, recently, DWI has been gradually explored to accurately delineate TV and OARs in radiation treatment planning. For example, it has been indicated that the addition of DWI to MRI can better distinguish lung cancer from atelectasis (7). DWI also takes advantage of nodal staging (8–10); thus, DWI provides smaller nodal TV delineation than conventional imaging (8). Similarly, DWI provides smaller rectal tumor volume (GTV) delineation than does T2-weighted (T2W) MRI (11–13), and probably because DWI provides a better edge contrast than T2W images (111). These findings indicate that a better RT boost to TV is possible. The quantitative data provided by DW-MRI could reflect intratumoral heterogeneity, highlighting more radioresistant areas (14, 15). Subsequently, elective dose escalation can be individually delivered to these areas. Moreover, DWI may be a potential tool to evaluate the salivary gland function in head and neck cancer (HNC) patients (16), resulting in the accurate protection for normal tissue, also with the ability to predict RT-induced xerostomia incident in RT. Several studies conclude that ADC histogram has a promising value of predicting overall survival (OS) and progression-free survival (PFS) and risk stratification in recurrent glioblastoma patients treated with bevacizumab (19–22).

Regarding clinical applications, IVIM-DWI can be used to detect positive resection margins in breast cancers (30, 31), lung tumors (26), and hepatic lesions in liver cancer (32, 33); and the diagnostic efficacy of D values is the highest (28, 29). A meta-analysis showed that the IVIM-DWI parameter (D value) showed better diagnostic performance than mono-exponential ADC (26). In addition, IVIM plays a pivotal role in benign and malignant identification (33, 34), especially for the D value (33). The D value is superior to ADC in distinguishing benign and malignant lesions (35). Moreover, IVIM-DWI-derived parameters can be used to grade malignant lesions (28, 34, 36)

and have the potential to differentiate true progression from pseudoprogression after early chemoradiotherapy in glioblastoma multiforme (GBM) (23, 24). Besides, IVIM can predict treatment response, such as parotid changes and vertebral bone marrow changes (17, 18). Taken together, the ability of IVIM-DWI to detect and identify benign and malignant would be helpful in target delineation and OAR avoidance in RT. Regarding tumor grading, IVIM-DWI may aid in predicting tumor aggressiveness and prognosis. In terms of pseudo/true progression identification and prediction of treatment response, IVIM may help to determine early therapeutic intervention and improve prognosis.

Overall, DWI may be a promising tool to obtain a better TI when being incorporated into RT planning assistance. However, some limitations of DWI, such as geometric distortions, which are closely related to TV delineation, and uncertainty of diffusion parameters, where low reproducibility means high variations, impede its widespread use within clinical practice. To solve this issue, conjunction with other MR images is suggested such as higher-resolution anatomic images, high-quality data with different b-values, and, if possible, contrast material-enhanced images (25).

## MR-Spectroscopic Imaging

MRSI allows non-invasive measurement of biochemical information in tissues, especially in the brain with the existence of tumors. MRSI is also an analytical and non-injected contrast agent (CA) technique without ionizing radiation, related to MRI *in vivo* (37, 38). However, unlike MRI, which can only identify the anatomic structure and location of a tumor or normal tissue, MRSI can be used to determine the concentration and presence of various biochemical substances, often referred to as “metabolites” because of their role in metabolism. Therefore, MRSI can effectively supplement the characterization of tissue beyond MRI function. In recent years, proton MRSI has gained a great popularity due to its higher sensitivity and greater convenience, since proton MRSI does not need hardware modification while being performed on most MRI machines. Therefore, the remainder of this article in brain tumor studies focuses on protocols for  $^1\text{H}$ -MRSI. The common metabolites of  $^1\text{H}$ -MRSI include choline (Cho), *N*-acetyl aspartate (NAA), lactate (Lac), and creatine (Cr) in clinical routine (37).

In normal conditions, NAA exists in the intact neuronal and axonal structures, and its reduction demonstrates loss or damage of neuronal tissue (40). Cho is associated with phospholipid membrane turnover, and an increase in Cho indicates a process of leading to elevated glial proliferation and membrane synthesis (41). Lactate is implicated in various cancer mechanisms such as facilitating cancer cell proliferation and angiogenesis (112). Creatine is related to cellular energy metabolism. It is considered a useful reference metabolite due to its relative stability in different pathological processes involved in the central nervous system. In malignant tumors, NAA is reduced or lost since neurons are replaced by neoplastic tissue; Cho is increased directly; lactate may implicate a high level of

malignancy (41). Based on the above, the NAA/Cho ratio is a sensitive marker for brain tumors, with the potential to distinguish active tumors from normal tissue and other non-cancerous lesions, such as necrosis (42). Cho/NAA ratio is widely utilized to describe tumor volume and invasion, because these metabolites change inversely in the tumor, increasing contrast (47). At present, the application of MRSI in clinical practice is involved in differential diagnosis (43–46), classification (45, 46), staging (46), treatment planning (49, 50), and posttreatment monitoring (54). Moreover, Lac/Cr, NAA/Cho, and Lac/NAA can predict overall survival (OS) and progression free survival (PFS) (41).

Herein, we mainly focus on the use of MRSI in radiation planning. In glioma, compared with conventional RT alone, adding of MRSI could provide metabolism information of tumor cells and OARs, resulting in more accurate target delineation (50). Croteau et al. conducted a study in 31 low- and high-grade-glioma patients. Their findings showed that MRSI can more accurately define the tumor boundary and normal tissues and can quantify the extent of the disease compared with conventional MRI *via* histopathological validation (54). Pirzkall et al. studied 34 patients with high-grade gliomas (52). When using T2 to define high-risk regions, the volume is extended by as much as 28 mm as compared with tumor definition from MRSI. Thus, the MRSI technique may have the potential to accurately optimize dose distribution of tumor TV and reduce the exposure to normal tissue (52). Moreover, Narayana et al. showed that Cho/Cr greater or equal to 3 defined by MRSI reduced 40% GTV volumes (GTVs) compared with GTVs defined by T1-weighted MRI (49). A study by Deviers et al. showed that tumor areas with lactate-to-*N*-acetyl aspartate ratio (LNR) 0.4 voxels before RT are likely to relapse, suggesting additional biological TVs for dose painting in GBM (53). In addition, a small study demonstrates that MRSI can aid in the delineation of hypoxic regions in solid tumors by exploring the metabolic outcome of tumor hypoxia, presenting increased total choline-containing metabolites (tCho) and lipid CH3 in breast tumors (51). Previous studies demonstrated that MRSI possesses great potential for the differentiation of tumor recurrence from radiation necrosis (37, 55, 56). This technology would be helpful for reirradiation settings in brain tumors due to its accurate delineation of recurrent lesions and successful avoidance of normal structures or radiation-induced reactions.

Overall, it seems that MRSI has been gradually and widely used to improve treatment planning for RT, with the ability to deliver dose escalation at particular tumor targets and reduce dose exposure to OARs. Even for recurrent disease, MRSI may perform well in improving TI, such as identifying and predicting tumor lesion recurrence. However, we should also be aware of the limitations of MRSI, such as the presence of spectral artifacts, which can result in false information, and lower specificity, although spectral artifacts may be solved by the automatic testing system (57) and by obtaining a higher field strength, like using 3T (113). A combination between MRSI and DW-MRI may improve the specificity of MRSI (114). However, other obstacles in MRSI, concerning low spatial resolution, long-time

**TABLE 1 |** Different components of fMRI-based functional imaging.

Modality	Principle	Related parameters	Treatment preparation	Clinical utility in radiation therapy	Treatment follow-up	Defects
DWI	Brownian motion of water molecule in biologic tissues (5)	DWI: ADC (6) IVIM-DWI: ADC, pure diffusion coefficient (D), pseudodiffusion coefficient (D*), perfusion fraction (f) (26–29).	DWI: tumor detection (7); staging (8–10); hypoxia (14, 15) IVIM-DWI: tumor detection (26, 30–33); benign and malignant identification (33–35); grading (28, 34, 36)	Delineation (8, 11–13); boost volumes (14, 15)	Treatment response (16–18); recurrent disease (19–24)	Poor geometric distortions; uncertainty of DWI-derived parameters (25)
MRSI	Biochemical and metabolic status of tissues (37, 38)	Cho, NAA, Lac, Cr (39–41)	Tumor identification (37, 42); diagnosis (41, 43–46); classification (39, 45, 47, 48); treatment planning (49, 50)	Delineation (49–51); boost volumes (49, 51–53)	Treatment response (37, 41, 54); recurrent disease (37, 55, 56)	Poor geometric distortions; uncertainty of diffusion parameters (57)
Perfusion MRI (DCE, DSC)	Tumor blood flow; Vascular permeability and vascularity (60–62)	DCE: v e, K trans (58–60) DSC: BV and BF (73)	Tumor detection (61–64); treatment planning (17, 65); hypoxia (67, 68)	Tumor hypoxia (66–69); delineation (63, 64); dose painting (63)	Treatment response (17, 59, 61, 62, 65); recurrent disease (70)	Unstable CB V and CBF (71, 72)
DTI-MRI	anisotropic diffusion of water molecular in tissues (74)	ADC FA (74)	Tumor detection (75, 76)	Delineation (75–81); dose painting (75, 77, 79)	Treatment response (82, 83); recurrent disease (80, 81)	Image distortion (84)
BOLD fMRI	Cerebral oxygen utilization (85)	onset-time, time-to-peak, full-width-at-halfmaximum (FWHM) and amplitude (86)	positioning of the functional cortical center, including vision, movement, hearing, etc (87–93); hypoxia (94)	Trajectory delineation in surgery; delineation (95, 96)	Reduced surgical time (97)	Poor spatial resolution (98, 99); NVU (100, 101)

fMRI, functional magnetic resonance imaging; DWI, diffusion-weighted imaging; ADC, apparent diffusion coefficient; IVM, intravoxel incoherent motion; MRSI, MR-Spectroscopic Imaging; Cho, choline; NAA, *N*-acetyl aspartate; Cr, creatine; DCE, dynamic contrast-enhanced; DSC, dynamic susceptibility contrast; BV, blood volume; BF, blood flow; CBF, cerebral blood flow; DTI, diffusion tensor imaging; FA, fractional anisotropy; BOLD, blood oxygenation level dependent; NVU, neurovascular uncoupling.

\*signal means false diffusion coefficient compared with true diffusion coefficient (D), mostly called pseudodiffusion coefficient (D\*).



acquisition, and unstable acquisition of high-quality spectral images, have impeded the widespread translation of MRSI in clinical practice.

## Perfusion MRI

Perfusion MRI is a well-established perfusion imaging technique, mainly including three techniques: DSC, DCE, and arterial spin labeling (ASL) MRI. Based on perfusion MRI modality, different parameters could be calculated, such as blood volume (BV) and blood flow (BF) in DSC, also the transfer rate constant ( $K^{\text{trans}}$ ) and the extravascular extracellular volume fraction (Ve) value in DCE. In perfusion MRI, individuals under inspection need a gadolinium-based agent *via* a peripheral vein during the continuous imaging process.

DSC refers to the BF through a certain tissue in a unit of time, which is an important physiological characteristic of the tissue and can specifically reflect the characteristics of vascular lesions. In DSC, the post-processed acquired time series can be used to acquire perfusion maps with the above parameters. DCE can measure the hemodynamic properties of tissues, such as density, integrity, leakiness, and permeability of tissue vasculature, by obtaining continuous MRI from the pre- and post-intravenous injection of a CA (58, 61). To acquire quantitative DCE-MRI data, three main components of measurements are needed: 1) an original T1 map before contrast administration; 2) acquiring T1-weighted images after CA injection at a proper temporal resolution; and 3) a method to evaluate the arterial input function (59). Compared with DSC-MRI, T1 DCE-MRI has a lower temporal resolution and is mainly used to reflect the density of microvessels.

Based on all aforementioned data, perfusion MRI plays an essential role in tumor treatment within clinical practice. The formation of increasing new blood vessels is essential to the growth of malignancy (73); as a result, BV and BF will rise correspondingly. In brain tumors, previous studies have shown that cerebral BV (CBV) and cerebral BF (CBF) are associated with predicting clinical outcomes, such as OS and PFS (62). A study in high-grade-glioma and low-grade-glioma patients indicated that CBV (the mean relative CBV = 1.75) correlates positively with disease progression (62). However, in clinical practice, the use of median CBV and CBF is limited because of highly heterogeneous gliomas, resulting in low sensitivity and specificity of assessing efficacy. Additionally, it should be noticed that a tumor may display low-rise CBV. An increasing number of studies indicate that DCE-MRI may improve differential diagnosis, localization, tissue features, staging, and monitoring treatment response in neoplastic diseases (60, 70, 115, 116). In prostate cancer, previous studies demonstrate that DCE-MRI may be useful for delineating both tumors and surrounding normal tissues in the prostate gland with sensitivity of 59%–87% and specificity of 74%–84% (63, 64, 117). DCE could predict the volume change of radiation-induced parotid by evaluating individual microvascular perfusion and tissue diffusion rates in HNC patients, suggesting an adjustment of the treatment plan before RT (17, 65). In advanced cervical carcinoma, evidence illustrates that DCE is likely to provide a clinically useful biomarker for the prognosis based on pharmacokinetic analysis

of DCE-MRI data (118, 119). Additionally, different levels of tumor hypoxia are common during RT but are not easily assessable in patients. In clinical practice, parameter  $K^{\text{trans}}$  is a potentially useful biomarker for tumor hypoxia, RT resistance, and metastasis in cancers (66–69) as well as Ve (66, 69).

Although DSC and DCE have been relatively mature, there are still some limitations of parameter calculation in clinical practice. First, CBV and CBF are always changeable in any region of gliomas owing to circuitous vasculature and immature vascular structures, especially in high-grade gliomas (71, 72). Second, many factors may influence the leakiness of blood vessels, such as vascular permeability, BF, vascular lumen area, and even temperature (120–122). Therefore,  $K^{\text{trans}}$  and Ve value can be influenced easily by the above factors and not only reflect vessel permeability. A study conducted by Law et al. probably provides us with some insights into which a combination between DSC and DCE can significantly improve diagnostic accuracy and sensitivity (62).

## Blood Oxygenation Level-Dependent Functional MRI

BOLD-fMRI signals provide real-time cerebral oxygen distribution under normal physiological conditions, based on local magnetic field properties resulting from a mismatch between local oxygen consumption caused by neuronal activity and increased CBF reactivity (85). BOLD signal has four parameters: onset time, time to peak, full width at half maximum (FWHM), and amplitude (86). The increase of local CBF causes a reduction in the local amount of deoxygenated hemoglobin generated by metabolism in response to neuronal activity, presenting signal enhancement (T2 and T2\*) in related brain regions (100). Among these regions, transparent contrast relies on repeatedly averaging subtle differences of signal enhancement. Brain activation mapping using BOLD-fMRI is based on the prerequisite that there is a tight coupling between neuronal activity and hemodynamic changes (101). Deoxyhemoglobin in the blood vessels is regarded as an endogenous CA during the production of functional activation maps. Oxyhemoglobin contains an unpaired electron and is therefore diamagnetic. Deoxyhemoglobin contains four unpaired electrons and is a paramagnetic substance. The different concentrations of oxyhemoglobin and deoxyhemoglobin will cause local magnetic field inhomogeneity, leading to the difference in the signal on the image and then production of imaging.

Current clinical application is mainly used for the positioning of the functional cortical center, including vision, movement, and hearing. BOLD-fMRI has become a valuable tool for presurgical functional brain mapping. In surgery, BOLD-fMRI can guide the safest surgical trajectory between functionally viable brain tissue and the lesion. In particular, in brain tumor patients, who are often neurologically impaired, we should take patient preparation and neurobehavioral evaluation into special consideration when performing fMRI. BOLD-fMRI for preoperative planning allows for accurate risk assessment of surgery-related brain damage, such as postoperative motion,



visual and somatosensory deficits, and intraoperative cortical stimulation (ICS) mapping, reducing surgical time (97) and need for further preoperative diagnostic studies (123). Moreover, BOLD-fMRI demonstrates an excellent concordance with ICS for motor mapping (87–90) and language mapping (91–93). Wang et al. and Pantelis et al. have demonstrated that the combination of BOLD-fMRI and DTI could be beneficial of marking and sparing OARs in radiation treatment planning, resulting in less radiation toxicity (95, 96). In addition, a study showed that BOLD-fMRI is a non-invasive technique that could explore hypoxia information by analyzing the correlations of the  $\ast R$  value and HIF-1 $\alpha$  (94).

Spatial resolution is one of the limitations of BOLD-fMRI, as flow increases in some of the larger arteries or veins feeding or draining large neuronal areas. The solution is to insert a “diffused” gradient pulse (corresponding to low b-values) into the MRI sequence; the largest vascular contribution in the BOLD signal (high  $D^\ast$  values are associated with fast flow) can be squeezed to improve the spatial resolution of the activation map (98, 99). In addition, neurovascular uncoupling is another key limitation that could affect the accuracy of BOLD-fMRI surrounding brain tumors, but combining an observed vaso-task dependency with the BOLD signal analysis may partially overcome this shortcoming (101).

## Diffusion Tensor Imaging–MRI

DTI-MRI is an MRI technique that can be used *in vivo* non-invasively to measure anisotropic diffusion of water molecules in various tissues, leading to producing neural tract images (74). Abnormalities in the fiber structure of the axonal (white matter) can be detected by DTI-MRI, which can model brain connectivity. Thus, it has been rapidly developed to implement RT of white matter disorders (77). At present, DTI-MRI had been extensively utilized for glioma researches. DTI parameters include ADC and fractional anisotropy (FA) values (74).

Price et al. showed that glioma cells are prone to invade tissue along the direction of white matter tracks (WMTs) (75). Another study by Krishnan et al. calculated routes of water diffusion from the primary tumor location to tumor progression location by using DTI-MRI in glioma patients. Meanwhile, this study also showed that the direction of elevated water diffusion may be a reliable indicator of routes of tumor progression (78), which is consistent with Price’s study. Thus, DTI MRI would help localize and identify the possible microscopic disease and will help to delineate CTV more accurately. Also, some previous studies have proved that it may aid in the optimal delineation of biological CTV by incorporating DTI-MRI into RT planning while reducing the dose exposure to nearby function regions (76, 78–81). A study by Conti et al. demonstrated that radiation dose exposure to OARs was decreased by up to 16.86% after the integration of functional neuroimaging as compared with their initial values (124). In addition, DTI-MRI can evaluate response to neoadjuvant chemotherapy in patients with breast cancer (82, 83).

In DTI, there are still some other technique defects, such as the distortion of the image because of an uneven magnetic field and poor display for smaller fiber bundles (84). However, DTI

has been rapidly developed in nervous system diseases, with an extensive clinical prospect to optimize TV, predict prognosis, and better protect functional regions of the brain.

## THERAPEUTIC INDEX IN RADIATION THERAPY

Conventional MRI already anatomically offers better soft tissue imaging in contrast to CT (125). However, it is not enough to provide high sensitivity and specificity delineation of TV due to a lack of functional indications. At the anatomic level, previous studies have demonstrated that functional imaging can provide a more accurate delineation of tumor TV base on better background contrast between tumor and normal tissue (12, 63, 64, 113, 117). Accurately defining the boundaries between tumor and normal tissue gives rise to the increased distance between tumor and OARs in function imaging-guided IMRT (**Figure 1A**). Moreover, the increased distance is beneficial for imaging-guided dose escalation in TV and decreased dose exposure in OARs (**Figures 1B, C**). In addition to the clear anatomical display, we note that there are several concepts and advanced radiation techniques related to fMRI-based RT that have great potential to improve TI, including tumor hypoxia, dose painting, adaptive RT (ART), local recurrence, and MR-guided linear accelerator (MR-LINAC). Among them, the integration of fMRI can provide TI benefits.

### Tumor Hypoxia

Despite improvement in the accuracy of target delineation and radiation delivery due to advances in RT and imaging techniques, in-field recurrence remains the predominant local failure model (126), which may be explained by the fact that the PTV of the entire primary tumor and the involved lymph nodes is delivered with a homogenous radiation dose without considering the intratumoral heterogeneity. Heterogeneity is one of the inherent characteristics of tumors, which is mainly manifested in the heterogeneity of intracellular and molecular biological features (including glucose metabolism, cell proliferation, hypoxia, epithelial growth factor receptor (EGFR) expression, and choline metabolism, etc.) (127). Tumor hypoxia is fairly common in RT due to abnormal vessel structures. Hypoxia is highly associated with poor prognosis because oxygen-deprived cells are strongly resistant to chemoradiotherapy, which leads to failure. Therefore, identifying and quantifying tumor hypoxia are important and necessary for improving TI in RT treatment. Numerous studies have shown that fMRI is an attractive option to identify, quantify, and spatially map hypoxic areas prior to therapy, as well as to track hypoxia changes during radiation (51, 66–69, 94), resulting in guiding increased radiation doses to hypoxic RT-resistant areas.

### Dose Painting

The concept of dose painting has been proposed to improve local control through increasing the dose to a segment of intra-tumor radiation-resistant while decreasing the dose to a radiosensitive segment based on fMRI (126). IMRT can deliver non-uniform

dose distribution, but how to follow the region of interest (ROI) remains unknown. Therefore, biological/molecular information derived from fMRI may be a help to identify and track tumor hypoxia, proliferation, and other ROIs. The fMRI-based dose painting opens a new era called “biological conformality.” Previous studies showed that fMRI-guided imaging could help radiation dose boost in certain areas by means of dose painting in tumor target (128–131) while sparing OARs (128–132). According to the quantitative parameter maps from functional imaging (126, 133), the radiation dose can be spatially redistributed in the target area and OARs. The dose mapping seems to be more reasonable than surgery, a way of all-or-nothing therapy, as intratumoral heterogeneity is a natural feature. DCE-MRI can also be used for dose painting based on its ability to display microvasculature permeability and BF, which is associated with the tumor’s oxygenation (134–137). DWI can reflect areas with a higher tumor burden (138, 139) and with radiation resistance (14, 15). MRSI possesses the ability to monitor tumor metabolism (140, 141) and is also useful for dose painting.

## Adaptive Radiation Therapy

In clinical practice, the target for RT is dynamic. It changes over a time frame, including position, size, shape, and biology. ART strategies systematically track variations in targets and adjacent structures to timely inform treatment-plan modification during RT. Monitoring variations is necessary because a single pre-treatment plan is inadequate to reflect the actual dose distribution on the tumor and its surroundings during RT (142). This technology allows for increasing doses delivered to tumors while simultaneously limiting dose exposure to the normal structures. MRI-guided ART provided both personalized geometric and biological adaption (143). Bladder cancer is well suitable for ART since the bladder has large inter-fractional changes and intra-fractional motion (144, 145). MRI-guided adaptive brachytherapy in cervical cancer (146, 147) and primary vaginal cancer (148) results in effective and stable long-term local control at all stages of cervical cancer, while decreasing severe radiation-induced morbidity. Similarly, promising results are also observed in liver tumors (149), prostate cancer (150), and unresectable primary malignancies of the abdomen. It seems like MRI-guided ART is more suitable for highly radiosensitive tumors with large motion changes and volume changes over the course of RT.

## Local Recurrence

Despite advances in RT and imaging techniques, in-field recurrence remains a common failure model. Recurrent lesions are a treatment challenge because of RT resistance and radiation dose limitation to surrounding normal tissues. The ability of fMRI to differentiate tumor recurrence to post-radiation treatment effects, including pseudoprogression and radiation necrosis, provides assistance in reirradiation settings in patients treated after primary chemoradiotherapy (23, 24). ADC values for radiation necrosis were found to be higher than for recurrence in some studies; however, the reported values are inconsistent and may be explained by technical factors (151).

A study by Xu et al. (152) using DTI showed that the mean ADC ratios for radiation necrosis in recurrent tumors were 1.62 and 1.34. An alternative to DTI is that it favors tumor recurrence over radiation necrosis when diffusion restriction is present on the ADC image, which does not show diffusion restriction. DCE-MRI perfusion measures CBV and CBF, which can be accurately measured in the presence of a blood–brain barrier breakdown (151). A study by Larsen et al. (153) measured CBV in patients with MRI contrast-enhanced. They found that lesion regression shows low CBV (less than 1.7 ml/100 g), while lesion progression shows high CBV (>2.2 ml/100 g). Therefore, Larsen et al. concluded that an absolute CBV threshold of 2.0 ml/100 g can detect lesion degeneration or progression, with a reported sensitivity and specificity of 100%. Several studies have shown that patients with tumor recurrence have higher Cho/Cr and Cho/NAA values than patients with radiation necrosis (151, 154). In addition, fMRI can predict tumor aggressiveness and early treatment response, with the assistance of deciding early therapy intervention and improving the prognosis (17, 23, 24).

## MR-Guided Linear Accelerator

In recent years, with the advancement of MR-guided RT, accurate radiation is facing new challenges and prospects. MR-LINAC is a new technology and the first machine in the world to combine radiation equipment (such as a linear accelerator or  $^{60}\text{Co}$  sources) and high-resolution MRI (155). The key benefits of MR-LINAC are that it can record MR images for every fraction and use these for daily plan adaptation. During the radiation treatment of the tumor, the radiation beams are accurately located in and destroy tumors, while avoid radiating and harming the nearby healthy tissues. Currently, MR-LINAC has been applied in various tumors, including pancreatic cancer, prostate cancer, and liver cancer (156–159). To date, MR-LINAC seems to be the most efficient method to optimize the TI of RT in cancer treatment. Combining MRI with the most accurate RT techniques, such as proton therapy, will be our ultimate goal (160). However, prolonged treatment times, patient tolerance, and high cost are the major obstacles. At present, related studies on MR-LINAC are still at an early stage with sparse clinical evidence, despite interesting potential.

## CHALLENGES AND PROSPECTS

Although the use of quantitative imaging was studied since the early 1990s in RT (125), there are still significant barriers to its widespread use in clinical practice. Excitingly, with the development of fMRI techniques, some prospects are inspiring.

### Challenges of Functional MRI for Radiation Therapy

From the object technology perspective, inconsistent imaging is commonly produced by different vendors, machines, and imaging protocols. However, quantitative imaging in RT is not a simple substitute for quantitative imaging in radiology. For example, in an RT scan, the patient’s position needs to be as

similar as possible to the treatment setting. However, it is not easy to accomplish this in many institutions because of various policies and management. In addition, robust calibration for biomarkers is still a big challenge, as the current quantitative imaging technique needs one or multiple measurable parameters to produce a voxel, leading to in worse signal-to-noise ratio (SNR) and greater voxels than traditional imaging (107). Last but not least, when applying different imaging techniques together, it is difficult for clinicians to interpret multiparametric functional images with transparently conflicting information; for example, the overlap is largely restricted in the area identified by DWI and DCE-MRI simultaneously.

On the artificial perspective, currently, delineation of most tumors and OARs are still through manual procedures, in which the TV is determined by a radiation oncologist and a radiologist together on the basis of clinical information and images. Therefore, differences in which different spectators have various definitions in anatomic features of OAR boundary may cause inconsistency in the OAR definition. Moreover, errors caused by mistakenly missing or adding parts can give rise to inaccurate delineation in OARs. Finally, a small part of oncologists, particularly those in rural areas, do not receive sufficient training and clear instructions which leads to discrepancies in the anatomic definition of OARs.

From the economic perspective, compared with conventional MRI, fMRI is more expensive. This is because the application of fMRI requires higher machine costs. Some studies speculate that models combined with multiparametric MRI (mpMRI) have advantages of cost-effectiveness, but their findings are based on several *a priori* assumptions for every model (161–165). Therefore, any change in the selected criteria might result in a major change in the cost and, consequently, in the conclusions. Notably, to date, the evidence for the use of mpMRI to consider further biopsy is at best based on minimal clinical data (166, 167). Furthermore, such a policy is still under observation, as almost all publications are related only to systematic biopsy. There are several limitations associated with the widespread utilization of mpMRI in clinical practice. First, low-quality mpMRI is still a major issue. Surprisingly, the initial cost of repeat low-quality mpMRI is very common but not mentioned. Most importantly, there are no standardized principles to evaluate mpMRI progression in patients on AS. For example, how should we assess the lesion status in Prostate Imaging-Reporting? Is it an increase in tumor size, if so, how about the threshold? Finally, above all, evidence is mainly from small studies and extrapolation of various strategies such as enlarging the merit of initial mpMRI for biopsy.

## Prospects of Functional MRI for Radiation Therapy

According to the above challenges, there are some relative solutions. To acquire consistent and continuous images, we suggest that it would be better if patients are willing to receive a complete examination under same conditions. To analyze the conflicting information, some researchers suggest defining the area identified by two imaging approaches as gross tumor volume (GTV); the areas indicated by only one of the imaging techniques can be defined as CTV with high risk. To reduce

inter-observer variability of OAR delineation, an automatically delineated system might be recommended in the future. Also, standardized training should be publicized widely.

Concerning cost-effectiveness improvement, the growing body of evidence demonstrates that fMRI may bring cost-effectiveness in prostate cancer. In contrast to transrectal ultrasound-guided biopsy (TRUS) alone, the use of mpMRI to select patients for repeat biopsy holds fewer biopsies and lower cost, despite that a few cancers are being missed, but further research is needed to determine whether missed cancers represent clinically significant tumors (168). Another study showed that an mpMRI-first strategy and then TRUS are cost-effective to diagnose clinically significant prostate cancer (169). In patients with low-risk cancer, overtreatment will lead to adverse effects and unnecessary costs (170). Active surveillance (AS) program, which contains digital rectal examination (DRE), prostate-specific antigen (PSA), and standard repeated 12-core TRUS, is currently recommended for avoiding overtreatment (170). However, the standard AS has some limitations, including missing high-risk tumors and performing unnecessary biopsies. The strategy of using mpMRI combined with limited MR-guided TRUS can improve quality of life and greatly reduce cost in low-risk prostate cancer patients during follow-up (170). Adequate data are further needed from large randomized prospective cohorts in the future.

In terms of some new insights or techniques, based on the above, the application of fMRI to guide dose painting and ART to detect tumor hypoxia area and postoperative local recurrence, in combination with MR-LINAC, has led to some promising findings. Despite the lack of a uniform measurement standard, we expect to further explore the function of fMRI in improving TI through large-scale randomized clinical studies.

## CONCLUSION

Incorporating functional imaging techniques into RT planning has big potential to improve TI in RT *via* different mechanisms. Functional imaging possesses potential advantages, as follows. First, quantitative imaging may provide superior contour and visibility between tumors and normal tissues, with the benefit of dose escalation in TV and dose reduction in OARs, with the promising potential for guiding de-escalation in oropharyngeal carcinoma patients (171, 172). Second, quantitative imaging may be a potent toxicity prediction tool during RT. These can give us a clinical indication for precaution. Third, the combination of different functional imaging techniques may make up for shortcomings that exist in single imaging. We believe that it is worthwhile to overcome the above challenges and explore larger, multicenter, randomized clinical studies on quantitative imaging in RT.

## AUTHOR CONTRIBUTIONS

KY and ML: study design. KY, ML, and QZ: data collection. KY and ML: data interpretation and writing. All authors contributed to the article and approved the submitted version.



## REFERENCES

- Wilson J, Hammond E, Higgins G, Petersson K. Corrigendum: Ultra-High Dose Rate (FLASH) Radiotherapy: Silver Bullet or Fool's Gold? *Front Oncol* (2010) 10: 00210. doi: 10.3389/fonc.2020.00210
- Lin SH, Hobbs BP, Verma V, Tidwell RS, Smith GL, Lei X, et al. Randomized Phase IIB Trial of Proton Beam Therapy Versus Intensity-Modulated Radiation Therapy for Locally Advanced Esophageal Cancer. *J Clin Oncol* (2020) 38(14):1569–79. doi: 10.1200/JCO.19.02503
- Lecchi M, Piero F, Federica E, Roberto O, Giovanni L, et al. Current Concepts on Imaging in Radiotherapy. *Eur J Nucl Med Mol Imaging* (2008) 35(4):821–37. doi: 10.1007/s00259-007-0631-y
- Press RH, Shu HG, Shim H, Mountz JM, Kurland BF, Wahl RL, et al. The Use of Quantitative Imaging in Radiation Oncology: A Quantitative Imaging Network (QIN) Perspective. *Int J Radiat Oncol Biol Phys* (2018) 102(4):1219–35. doi: 10.1016/j.ijrobp.2018.06.023
- Le BD, Breton E, Lallemand D, Aubin ML, Vignaud J, Laval-Jeantet M. Separation of Diffusion and Perfusion in Intravoxel Incoherent Motion MR Imaging. *Radiology* (1988) 168(2):497–505. doi: 10.1148/radiology.168.2.3393671
- Bammer R. Basic Principles of Diffusion-Weighted Imaging. *Eur J Radiol* (2003) 45(3):169–84. doi: 10.1016/s0720-048x(02)00303-0
- Zhang X, Fu Z, Gong G, Wei H, Duan J, Chen Z, et al. Implementation of Diffusion-Weighted Magnetic Resonance Imaging in Target Delineation of Central Lung Cancer Accompanied With Atelectasis in Precision Radiotherapy. *Oncol Lett* (2017) 14(3):2677–82. doi: 10.3892/ol.2017.6479
- Dirix P, Vandecaveye V, Keyzer DF, Beek DOK, Poorten VV, Delaere P, et al. Diffusion-Weighted MRI for Nodal Staging of Head and Neck Squamous Cell Carcinoma Impact on Radiotherapy Planning. *Int J Radiat Oncol Biol Phys* (2010) 76(3):761–6. doi: 10.1016/j.ijrobp.2009.02.068
- Vandecaveye V, De KF, Vander PV, Dirix P, Verbeken E, Nuyts P, et al. Head and Neck Squamous Cell Carcinoma: Value of Diffusion-Weighted MR Imaging for Nodal Staging. *Radiology* (2009) 251(1):134–46. doi: 10.1148/radiol.2511080128
- Wu LM, Xu JR, Liu MJ, Zhang XF, Hua J, Zheng J, et al. Value of Magnetic Resonance Imaging for Nodal Staging in Patients With Head and Neck Squamous Cell Carcinoma: A Meta-Analysis. *Acad Radiol* (2012) 19(3):331–40. doi: 10.1016/j.acra.2011.10.027
- Regini F, Gourtsoyianni S, Cardoso De Melo R, Charles-Edwards GD, Griffin N, Parikh J, et al. Rectal Tumour Volume (GTV) Delineation Using T2-Weighted and Diffusion-Weighted MRI: Implications for Radiotherapy Planning. *Eur J Radiol* (2014) 83(5):768–72. doi: 10.1016/j.ejrad.2014.02.007
- Rosa C, Caravatta L, Delli Pizzi A, Di Tommaso M, Cianci R, Gasparini L, et al. Reproducibility of Rectal Tumor Volume Delineation Using Diffusion-Weighted MRI: Agreement on Volumes Between Observers. *Cancer Radiother* (2019) 23(3):216–21. doi: 10.1016/j.canrad.2018.10.004
- Burbach JP, Kleijnen JP, Reerink O, Seravalli E, Philippens ME, Schakel T, et al. Inter-Observer Agreement of MRI-Based Tumor Delineation for Preoperative Radiotherapy Boost in Locally Advanced Rectal Cancer. *Radiation Oncol* (2016) 118(2):399–407. doi: 10.1016/j.radonc.2015.10.030
- Vandecasteele K, Tummers P, Van BM, De VP, Vercauteren T, De GW, et al. EXclusion of non-Involved Uterus From the Target Volume (EXIT-Trial): An Individualized Treatment for Locally Advanced Cervical Cancer Using Modern Radiotherapy and Imaging Techniques. *BMC Cancer* (2018) 18(1):898. doi: 10.1186/s12885-018-4800-0
- Atwell D, Elks J, Cahill K, Hearn N, Vignarajah D, Lagopoulos J, et al. A Review of Modern Radiation Therapy Dose Escalation in Locally Advanced Head and Neck Cancer. *Clin Oncol (R Coll Radiol)* (2020) 32(5):330–41. doi: 10.1016/j.clon.2019.12.004
- Loimu V, Seppälä T, Kapanen M, Tuomikoski L, Nurmi H, Mäkitie A, et al. Diffusion-Weighted Magnetic Resonance Imaging for Evaluation of Salivary Gland Function in Head and Neck Cancer Patients Treated With Intensity-Modulated Radiotherapy. *Radiation Oncol* (2017) 122(2):178–84. doi: 10.1016/j.radonc.2016.07.008
- Marzi S, Farneti A, Vidiri A, Di Giuliano F, Marucci L, Spasiano F, et al. Radiation-Induced Parotid Changes in Oropharyngeal Cancer Patients: The Role of Early Functional Imaging and Patient-/Treatment-Related Factors. *Radiat Oncol* (2018) 13(1):189. doi: 10.1186/s13014-018-1137-4
- Yoon MA, Hong SJ, Lee CH, Kang CH, Ahn KS, Kim BH. Intravoxel Incoherent Motion (IVIM) Analysis of Vertebral Bone Marrow Changes After Radiation Exposure From Diagnostic Imaging and Interventional Procedures. *Acta Radiol* (2017) 58(10):1260–8. doi: 10.1177/0284185116688380
- Ellingson BM, Sahebjam S, Kim HJ, Pope WB, Harris RJ, Woodworth DC, et al. Cloughesy, Pretreatment ADC Histogram Analysis is a Predictive Imaging Biomarker for Bevacizumab Treatment But Not Chemotherapy in Recurrent Glioblastoma. *AJNR Am J Neuroradiol* (2014) 35(4):673–9. doi: 10.3174/ajnr.A3748
- Pope W, Kim H, Huo J, Alger J, Brown M, Gjertson D, et al. Recurrent Glioblastoma Multiforme: ADC Histogram Analysis Predicts Response to Bevacizumab Treatment. *Radiology* (2009) 252(1):182–9. doi: 10.1148/radiol.2521081534
- Pope W, Qiao X, Kim H, Lai A, Nghiemphu P, Xue X, et al. Cloughesy, Apparent Diffusion Coefficient Histogram Analysis Stratifies Progression-Free and Overall Survival in Patients With Recurrent GBM Treated With Bevacizumab: A Multi-Center Study. *J Neurooncol* (2012) 108(3):491–8. doi: 10.1007/s11060-012-0847-y
- Rahman R, Hamdan A, Zweifler R, Jiang H, Norden A, Reardon D, Reardon D, et al. Histogram Analysis of Apparent Diffusion Coefficient Within Enhancing and Nonenhancing Tumor Volumes in Recurrent Glioblastoma Patients Treated With Bevacizumab. *J Neurooncol* (2014) 119(1):149–58. doi: 10.1007/s11060-014-1464-8
- Liu ZC, Yan LF, Hu YC, Sun YZ, Tian Q, Nan HY, et al. Combination of IVIM-DWI and 3D-ASL for Differentiating True Progression From Pseudoprogression of Glioblastoma Multiforme After Concurrent Chemoradiotherapy: Study Protocol of a Prospective Diagnostic Trial. *BMC Med Imaging* (2017) 17(1):10. doi: 10.1186/s12880-017-0183-y
- Suh CH, Kim HS, Jung SC, Choi CG, Kim SJ. Multiparametric MRI as a Potential Surrogate Endpoint for Decision-Making in Early Treatment Response Following Concurrent Chemoradiotherapy in Patients With Newly Diagnosed Glioblastoma: A Systematic Review and Meta-Analysis. *Eur Radiol* (2018) 28(6):2628–38. doi: 10.1007/s00330-017-5262-5
- Koh DM, Collins DJ, Orton MR. Intravoxel Incoherent Motion in Body Diffusion-Weighted MRI: Reality and Challenges. *AJR Am J Roentgenol* (2011) 196(6):1351–61. doi: 10.2214/AJR.10.5515
- Liang J, Li J, Li Z, Meng T, Chen J, Ma W, et al. Differentiating the Lung Lesions Using Intravoxel Incoherent Motion Diffusion-Weighted Imaging: A Meta-Analysis. *BMC Cancer* (2020) 20(1):799. doi: 10.1186/s12885-020-07308-z
- Le Bihan D, Breton E, Lallemand D, Grenier P, Cabanis E, Laval-Jeantet M. MR Imaging of Intravoxel Incoherent Motions: Application to Diffusion and Perfusion in Neurologic Disorders. *Radiology* (1986) 161(2):401–7. doi: 10.1148/radiology.161.2.3763909
- Wang CC, Dong HB, Ding F, Li YD, Wang GY, Ding HX. Quantitative Evaluation of Intravoxel Incoherent Motion Diffusion-Weighted Imaging and Three-Dimensional Arterial Spin Labeling in Ki-67 Labeling Index and Grading of Brain Gliomas. *Zhonghua Yi Xue Za Zhi* (2019) 99(5):338–42. doi: 10.3760/cma.j.issn.0376-2491
- Wang C, Dong H. Ki-67 Labeling Index and the Grading of Cerebral Gliomas by Using Intravoxel Incoherent Motion Diffusion-Weighted Imaging and Three-Dimensional Arterial Spin Labeling Magnetic Resonance Imaging. *Acta Radiol* (2020) 61(8):1057–63. doi: 10.1177/0284185119891694
- Cen D, Hu W, Wang X, Wu X. Re: Identification of Preoperative Magnetic Resonance Imaging Features Associated With Positive Resection Margins in Breast Cancer? . *Korean J Radiol* (2019) 20(6):999–1000. doi: 10.3348/kjr.2019.0044
- Youn I, Choi S, Choi YJ, Moon JH, Park HJ, Ham SY, et al. Contrast Enhanced Digital Mammography Versus Magnetic Resonance Imaging for Accurate Measurement of the Size of Breast Cancer. *Br J Radiol* (2019) 92(1098):20180929. doi: 10.1259/bjr.20180929
- Ai Z, Han Q, Huang Z, Wu J, Xiang Z. The Value of Multiparametric Histogram Features Based on Intravoxel Incoherent Motion Diffusion-Weighted Imaging (IVIM-DWI) for the Differential Diagnosis of Liver Lesions. *Ann Transl Med* (2020) 8(18):1128. doi: 10.21037/atm-20-5109
- Wang M, Li X, Zou J, Chen X, Chen S, Xiang W. Evaluation of Hepatic Tumors Using Intravoxel Incoherent Motion Diffusion-Weighted MRI. *Med Sci Monit* (2016) 22:702–9. doi: 10.12659/msm.895909
- Mao X, Zou X, Yu N, Jiang X, Du J. Quantitative Evaluation of Intravoxel Incoherent Motion Diffusion-Weighted Imaging (IVIM) for Differential Diagnosis and Grading Prediction of Benign and Malignant Breast



- Lesions. *Med (Baltimore)* (2018) 97(26):e11109. doi: 10.1097/MD.00000000000011109
35. Yoon JH, Lee JM, Yu MH, Kiefer B, Han JK, Choi BI. Evaluation of Hepatic Focal Lesions Using Diffusion-Weighted MR Imaging: Comparison of Apparent Diffusion Coefficient and Intravoxel Incoherent Motion-Derived Parameters. *J Magn Reson Imaging* (2014) 39(2):276–85. doi: 10.1002/jmri.24158
  36. Sun H, Xu Y, Song A, Shi K, Wang W. Intravoxel Incoherent Motion MRI of Rectal Cancer: Correlation of Diffusion and Perfusion Characteristics With Prognostic Tumor Markers. *AJR Am J Roentgenol* (2018) 210(4):W139–w147. doi: 10.2214/AJR.17.18342
  37. Cao Y, Sundgren PC, Tsien CI, Chenevert TT, Junck L. Physiologic and Metabolic Magnetic Resonance Imaging in Gliomas. *J Clin Oncol* (2006) 24(8):1228–35. doi: 10.1200/JCO.2005.04.7233
  38. Jansen JFA, Backes WH, Nicolay K, Kooi ME. 1h MR Spectroscopy of the Brain: Absolute Quantification of Metabolites. *Radiology* (2006) 240(2):318–32. doi: 10.1148/radiol.2402050314
  39. Zhu H, Barker PB. MR Spectroscopy and Spectroscopic Imaging of the Brain. *Methods Mol Biol* (2011) 711:203–26. doi: 10.1007/978-1-61737-992-5\_9
  40. Moffett JR, Ross B, Arun P, Madhavarao CN, Namboodiri AM. N-Acetylaspartate in the CNS: From Neurodiagnostics to Neurobiology. *Prog Neurobiol* (2007) 81(2):89–131. doi: 10.1016/j.pneurobio.2006.12.003
  41. Ratai EM, Zhang Z, Fink J, Muzi M, Hanna L, Greco E, et al. ACRIN 6684: Multicenter, Phase II Assessment of Tumor Hypoxia in Newly Diagnosed Glioblastoma Using Magnetic Resonance Spectroscopy. *PLoS One* (2018) 13(6):e0198548. doi: 10.1371/journal.pone.0198548
  42. Amstalden van Hove E, Blackwell T, Klinkert I, Eijkel G, Heeren R, Glunde K. Multimodal Mass Spectrometric Imaging of Small Molecules Reveals Distinct Spatio-Molecular Signatures in Differentially Metastatic Breast Tumor Models. *Cancer Res* (2010) 70(22):9012–21. doi: 10.1158/0008-5472.CAN-10-0360
  43. Chen WS, Li JJ, Hong L, Xing ZB, Wang F, Li CQ. Diagnostic Value of Magnetic Resonance Spectroscopy in Radiation Encephalopathy Induced by Radiotherapy for Patients With Nasopharyngeal Carcinoma: A Meta-Analysis. *BioMed Res Int* (2016) 2016:5126074. doi: 10.1155/2016/5126074
  44. Ramazan A, Demircioglu O, Ugurlu U, Kaya H, Aribal E. Efficacy of Single Voxel 1H MR Spectroscopic Imaging at 3T for the Differentiation of Benign and Malign Breast Lesions. *Clin Imaging* (2016) 40(5):831–6. doi: 10.1016/j.clinimag.2016.03.007
  45. Casciani E, Poletini E, Bertini L, Emiliozzi P, Amini M, Pansadoro V, et al. Prostate Cancer: Evaluation With Endorectal MR Imaging and Three-Dimensional Proton MR Spectroscopic Imaging. *Radiol Med* (2004) 108(5-6):530–41.
  46. Benzakoun J, Robert C, Legrand L, Pallud J, Meder JF, Oppenheim C, et al. Anatomical and Functional MR Imaging to Define Tumoral Boundaries and Characterize Lesions in Neuro-Oncology. *Cancer Radiother* (2020) 24(5):453–62. doi: 10.1016/j.canrad.2020.03.005
  47. Cordova JS, Shu HK, Liang Z, Gurbani SS, Cooper LA, Holder CA, et al. Whole-Brain Spectroscopic MRI Biomarkers Identify Infiltrating Margins in Glioblastoma Patients. *Neuro Oncol* (2016) 18(8):1180–9. doi: 10.1093/neuonc/now036
  48. Diamandis E, Gabriel CPS, Wurtemberger U, Guggenberger K, Urbach H, Staszewski O, et al. MR-Spectroscopic Imaging of Glial Tumors in the Spotlight of the 2016 WHO Classification. *J Neurooncol* (2018) 139(2):431–40. doi: 10.1007/s11060-018-2881-x
  49. Narayana A, Chang J, Thakur S, Huang W, Kowalski A, Perera G, et al. Use of MR Spectroscopy and Functional Imaging in the Treatment Planning of Gliomas. *Br J Radiol* (2007) 80(953):347–54. doi: 10.1259/bjr/65349468
  50. Chang J, Thakur SB, Huang W, Narayana A. Magnetic Resonance Spectroscopy Imaging (MRSI) and Brain Functional Magnetic Resonance Imaging (fMRI) for Radiotherapy Treatment Planning of Glioma. *Techol Cander Res Treat* (2008) 7(5):349–62.
  51. Jiang L, Greenwood TR, Artemov D, Raman V, Winnard PT Jr., Heeren RM, et al. Localized Hypoxia Results in Spatially Heterogeneous Metabolic Signatures in Breast Tumor Models. *Neoplasia* (2012) 14(8):732–41. doi: 10.1593/neo.12858
  52. Pirzkall A, McKnight TR, Graves EE, Carol MP, Sneed PK, Wara WW, et al. MR-Spectroscopy Guided Target Delineation for High-Grade Gliomas. *Int J Radiat Oncol Biol Phys* (2001) 50(4):915–28. doi: 10.1016/S0360-3016(01)01548-6
  53. Deviers A, Ken S, Filleron T, Rowland B, Laruelo A, Catalaa I, et al. Evaluation of the Lactate-to-N-Acetyl-Aspartate Ratio Defined With Magnetic Resonance Spectroscopic Imaging Before Radiation Therapy as a New Predictive Marker of the Site of Relapse in Patients With Glioblastoma Multiforme. *Int J Radiat Oncol Biol Phys* (2014) 90(2):385–93. doi: 10.1016/j.ijrobp.2014.06.009
  54. Croteau D, Scarpace L, Hearshen D, Gutierrez J, Fisher JL, Rock JP, et al. Correlation Between Magnetic Resonance Spectroscopy Imaging and Image-Guided Biopsies: Semiquantitative and Qualitative Histopathological Analyses of Patients With Untreated Glioma. *Neurosurgery* (2001) 49(2):823–9. doi: 10.1097/00006123-200110000-00008
  55. Rock J, Hearshen D, Scarpace L, Croteau D, Gutierrez J, Fisher J, et al. Correlations Between Magnetic Resonance Spectroscopy and Image-Guided Histopathology, With Special Attention to Radiation Necrosis. *Neurosurgery* (2002) 51(4):912–9. doi: 10.1097/00006123-200210000-00010
  56. Verma N, Cowperthwaite MC, Burnett MG, Markey MK. Differentiating Tumor Recurrence From Treatment Necrosis: A Review of Neuro-Oncologic Imaging Strategies. *Neuro Oncol* (2013) 15(5):515–34. doi: 10.1093/neuonc/nos307
  57. Gurbani SS, Schreibmann E, Maudsley AA, Cordova JS, Soher BJ, Poptani H, et al. A Convolutional Neural Network to Filter Artifacts in Spectroscopic Magnetic Resonance Imaging. *Magn Reson Med* (2018) 80(5):1765–75. doi: 10.1002/mrm.27166
  58. Tofts PS, Brix G, Buckley DL, Evelhoch JL, Henderson E, Knopp MV, et al. Estimating Kinetic Parameters From Dynamic Contrast-Enhanced T(1)-Weighted MRI of a Diffusible Tracer: Standardized Quantities and Symbols. *J Magn Reson Med* (1999) 10(3):223–32. doi: 10.1002/(sici)1522-2586(199909)10:3<223::aid-jmri2>3.0.co;2-s
  59. Teo QQ, Thng CH, Koh TS, Ng QS. Dynamic Contrast-Enhanced Magnetic Resonance Imaging: Applications in Oncology. *Clin Oncol (R Coll Radiol)* (2014) 26(10):e9–20. doi: 10.1016/j.clon.2014.05.014
  60. Kargar S, Borisch EA, Froemming AT, Kawashima A, Mynderse LA, Stinson EG, et al. Robust and Efficient Pharmacokinetic Parameter non-Linear Least Squares Estimation for Dynamic Contrast Enhanced MRI of the Prostate. *Magn Reson Imaging* (2018) 48:50–61. doi: 10.1016/j.mri.2017.12.021
  61. Cao Y. The Promise of Dynamic Contrast-Enhanced Imaging in Radiation Therapy. *Semin Radiat Oncol* (2011) 21(1):147–56. doi: 10.1016/j.semradi.2010.11.001
  62. Law M, Young RJ, Babb JS, Pecorelli N, Chheang S, Gruber ML, et al. Gliomas: Predicting Time to Progression or Survival With Cerebral Blood Volume Measurements at Dynamic Susceptibility-Weighted Contrast-Enhanced Perfusion MR Imaging. *Radiology* (2008) 247(2):490–8. doi: 10.1148/radiol.2472070898
  63. Li C, Chen M, Li S, Zhao X, Zhang C, Liu M, et al. Diffusion Imaging of the Prostate at 3.0 Tesla. *Acta Radiol* (2011) 52(7):813–7. doi: 10.1258/ar.2011.100487
  64. Futterer JJ, Heijmink SW, Scheenen TW, Veltman J, Huisman HJ, Vos P, et al. Prostate Cancer Localization With Dynamic Contrast-Enhanced MR Imaging and Proton MR Spectroscopic Imaging. *Radiology* (2006) 241(2):449–58. doi: 10.1148/radiol.2412051866
  65. Zhou N, Chu C, Dou X, Li M, Liu S, Zhu L, et al. Early Evaluation of Irradiated Parotid Glands With Intravoxel Incoherent Motion MR Imaging: Correlation With Dynamic Contrast-Enhanced MR Imaging. *BMC Cancer* (2016) 16(1):865. doi: 10.1186/s12885-016-2900-2
  66. Klaassen R, Gurney-Champion OJ, Wilmink JW, Besselink MG, Engelbrecht MRW, Stoker J, et al. Repeatability and Correlations of Dynamic Contrast Enhanced and T2\* MRI in Patients With Advanced Pancreatic Ductal Adenocarcinoma. *Magn Reson Imaging* (2018) 50:1–9. doi: 10.1016/j.mri.2018.02.005
  67. Ellingsen C, Hompland T, Galappathi K, Mathiesen B, Rofstad EK. DCE-MRI of the Hypoxic Fraction, Radioresponsiveness, and Metastatic Propensity of Cervical Carcinoma Xenografts. *Radiat Oncol* (2014) 110(2):335–41. doi: 10.1016/j.radonc.2013.10.018
  68. Hauge A, Gaustad JV, Huang R, Simonsen TG, Wegner CS, Andersen LMK, et al. DCE-MRI and Quantitative Histology Reveal Enhanced Vessel Maturation But Impaired Perfusion and Increased Hypoxia in Bevacizumab-Treated Cervical Carcinoma. *Int J Radiat Oncol Biol Phys* (2019) 104(3):666–76. doi: 10.1016/j.ijrobp.2019.03.002

69. Ovrebo KM, Ellingsen C, Galappathi K, Rofstad EK. Dynamic Contrast-Enhanced Magnetic Resonance Imaging of the Metastatic Potential of Melanoma Xenografts. *Int J Radiat Oncol Biol Phys* (2012) 83(1):e121–7. doi: 10.1016/j.ijrobp.2011.12.019
70. Bonekamp D, Macura KJ. Dynamic Contrast-Enhanced Magnetic Resonance Imaging in the Evaluation of the Prostate. *Top Magn Reson Imaging* (2008) 19(6):273–84. doi: 10.1097/RMR.0b013e3181aacdc2
71. Zaca D, Hua J, Pillai JJ. Cerebrovascular Reactivity Mapping for Brain Tumor Presurgical Planning. *World J Clin Oncol* (2011) 2(7):289–98. doi: 10.5306/wjco.v2.i7.289
72. Jain RK, Carmeliet P. SnapShot: Tumor Angiogenesis. *Cell* (2012) 149(6):1408–8.e.1. doi: 10.1016/j.cell.2012.05.025
73. Thomas MA, Nagarajan R, Huda A, Margolis D, Sarma MK, Sheng K, et al. Multidimensional MR Spectroscopic Imaging of Prostate Cancer *In Vivo*. *NMR BioMed* (2014) 27(1):53–66. doi: 10.1002/nbm.2991
74. Shaikh S, Kumar A, Bansal A. Diffusion Tensor Imaging: An Overview. *Neurol India* (2018) 66(6):1603–11. doi: 10.4103/0028-3886.246233
75. Price SJ, Jena R, Burnet NG, Hutchinson PJ, Dean AF, Pena A, et al. Improved Delineation of Glioma Margins and Regions of Infiltration With the Use of Diffusion Tensor Imaging: An Image-Guided Biopsy Study. *AJNR Am J Neuroradiol* (2006) 27(9):1969–74.
76. Berberat J, McNamara J, Remonda L, Bodis S, Rogers S. Diffusion Tensor Imaging for Target Volume Definition in Glioblastoma Multiforme. *Strahlenther Onkol* (2014) 190(10):939–43. doi: 10.1007/s00066-014-0676-3
77. Hagmann P, Jonasson L, Maeder P, Thiran JP, Wedeen VJ, Meuli R. Understanding Diffusion MR Imaging Techniques: From Scalar Diffusion-Weighted Imaging to Diffusion Tensor Imaging and Beyond. *Radiographics* (2006) 26 Suppl 1:S205–23. doi: 10.1148/rg.26si065510
78. Krishnan AP, Asher IM, Davis D, Okunieff P, O'Dell WG. Evidence That MR Diffusion Tensor Imaging (Tractography) Predicts the Natural History of Regional Progression in Patients Irradiated Conformally for Primary Brain Tumors. *Int J Radiat Oncol Biol Phys* (2008) 71(5):1553–62. doi: 10.1016/j.ijrobp.2008.04.017
79. Jensen MB, Guldberg TL, Harboll A, Lukacova S, Kallehauge JF. Diffusion Tensor Magnetic Resonance Imaging Driven Growth Modeling for Radiotherapy Target Definition in Glioblastoma. *Acta Oncol* (2017) 56(11):1639–43. doi: 10.1080/0284186X.2017.1374559
80. Trip AK, Jensen MB, Kallehauge JF, Lukacova S. Individualizing the Radiotherapy Target Volume for Glioblastoma Using DTI-MRI: A Phase 0 Study on Coverage of Recurrences. *Acta Oncol* (2019) 58(10):1–4. doi: 10.1080/0284186X.2019.1637018
81. Price SJ, Jena R, Burnet NG, Carpenter TA, Pickard JD, Gillard JH. Predicting Patterns of Glioma Recurrence Using Diffusion Tensor Imaging. *Eur Radiol* (2007) 17(7):1675–84. doi: 10.1007/s00330-006-0561-2
82. Wilmes LJ, Li W, Shin HJ, Newitt DC, Proctor E, Harnish R, Hylton NM. Diffusion Tensor Imaging for Assessment of Response to Neoadjuvant Chemotherapy in Patients With Breast Cancer. *Tomography* (2016) 2(4):438–47. doi: 10.18383/j.tom.2016.00271
83. Furman-Haran E, Nissan N, Ricart-Selma V, Martinez-Rubio C, Degani H, Camps-Herrero J. Quantitative Evaluation of Breast Cancer Response to Neoadjuvant Chemotherapy by Diffusion Tensor Imaging: Initial Results. *J Magn Reson Imaging* (2018) 47(4):1080–90. doi: 10.1002/jmri.25855
84. Gerhardt J, Sollmann N, Hiepe P, Kirschke JS, Meyer B, Krieg SM, et al. Retrospective Ddistortion Correction of Diffusion Tensor Imaging Data by Semi-Elastic Image Fusion - Evaluation by Means of Anatomical Landmarks. *Clin Neurol Neurosurg* (2019) 183:105387. doi: 10.1016/j.clineuro.2019.105387
85. Rodan LH, Poulblanc J, Fisher JA, Sobczyk O, Mikulis DJ, Tein I. L-Arginine Effects on Cerebrovascular Reactivity, Perfusion and Neurovascular Coupling in MELAS (Mitochondrial Encephalomyopathy With Lactic Acidosis and Stroke-Like Episodes) Syndrome. *PloS One* (2020) 15(9):e0238224. doi: 10.1371/journal.pone.0238224
86. Mazzetto-Betti KC, Leoni RF, Pontes-Neto OM, Sturzbecher MJ, Santos AC, Leite JP, et al. Quantification of BOLD fMRI Parameters to Infer Cerebrovascular Reactivity of the Middle Cerebral Artery. *J Magn Reson Imaging* (2013) 38(5):1203–9. doi: 10.1002/jmri.23943
87. Roux FE, Boulouaou K, Ranjeva JP, Tremoulet M, Henry P, Manelfe C, et al. Usefulness of Motor Functional MRI Correlated to Cortical Mapping in Rolandic Low-Grade Astrocytomas. *Acta Neurochir (Wien)* (1999) 141(1):71–9. doi: 10.1007/s007010050268
88. Hirsch J, Ruge MI, Kim KH, Correa DD, Victor JD, Relkin NR, et al. An Integrated Functional Magnetic Resonance Imaging Procedure for Preoperative Mapping of Cortical Areas Associated With Tactile, Motor, Language, and Visual Functions. *Neurosurgery* (2000) 47(3):711–21. doi: 10.1097/00006123-200009000-00037
89. Roux FE, Ibarrola D, Tremoulet M, Lazorthes Y, Henry P, Sol JC, et al. Methodological and Technical Issues for Integrating Functional Magnetic Resonance Imaging Data in a Neuronavigational System. *Neurosurgery* (2001) 49(5):1145–56. doi: 10.1097/00006123-200111000-00025
90. Krings T, Schreckenberger M, Rohde V, Spetzger U, Sabri O, Reinges MH, et al. Functional MRI and 18F FDG-Positron Emission Tomography for Presurgical Planning: Comparison With Electrical Cortical Stimulation. *Acta Neurochir (Wien)* (2002) 144(9):889–99. doi: 10.1007/s00701-002-0992-8
91. Hertz-Pannier L, Gaillard WD, Mott SH, Cuenod CA, Bookheimer SY, Weinstein S, et al. Noninvasive Assessment of Language Dominance in Children and Adolescents With Functional MRI: A Preliminary Study. *Neurology* (1997) 48(4):1003–12. doi: 10.1212/wnl.48.4.1003
92. Brannen JH, Badie B, Moritz CH, Quigley M, Meyerand ME, Houghton VM. Reliability of Functional MR Imaging With Word-Generation Tasks for Mapping Broca's Area. *AJNR Am J Neuroradiol* (2001) 22(9):1711–8.
93. Benson RR, FitzGerald DB, LeSueur LL, Kennedy DN, Kwong KK, Buchbinder BR, et al. Language Dominance Determined by Whole Brain Functional MRI in Patients With Brain Lesions. *Neurology* (1999) 52(4):798–809. doi: 10.1212/wnl.52.4.798
94. Liu M, Guo X, Wang S, Jin M, Wang Y, Li J, et al. BOLD-MRI of Breast Invasive Ductal Carcinoma: Correlation of R2\* Value and the Expression of HIF-1 $\alpha$ . *Eur Radiol* (2013) 23(12):3221–7. doi: 10.1007/s00330-013-2937-4
95. Wang M, Ma H, Wang X, Guo Y, Xia X, Xia H, et al. Integration of BOLD-fMRI and DTI Into Radiation Treatment Planning for High-Grade Gliomas Located Near the Primary Motor Cortexes and Corticospinal Tracts. *Radiat Oncol* (2015) 10:64. doi: 10.1186/s13014-015-0364-1
96. Pantelis E, Papadakis N, Verigos K, Stathochristopoulou I, Antypas C, Lekas L, et al. Integration of Functional MRI and White Matter Tractography in Stereotactic Radiosurgery Clinical Practice. *Int J Radiat Oncol Biol Phys* (2010) 78(1):257–67. doi: 10.1016/j.ijrobp.2009.10.064
97. Petrella JR, Shah LM, Harris KM, Friedman AH, George TM, Sampson JH, et al. Preoperative Functional MR Imaging Localization of Language and Motor Areas: Effect on Therapeutic Decision Making in Patients With Potentially Resectable Brain Tumors. *Radiology* (2006) 240(3):793–802. doi: 10.1148/radiol.2403051153
98. Michelich CR, Song AW, Macfall JR. Dependence of Gradient-Echo and Spin-Echo BOLD fMRI at 4 T on Diffusion Weighting. *NMR BioMed* (2006) 19(5):566–72. doi: 10.1002/nbm.1035
99. Song AW, Li T. Improved Spatial Localization Based on Flow-Moment-Nulling and Intra-Voxel Incoherent Motion-Weighted fMRI. *NMR BioMed* (2003) 16(3):137–43. doi: 10.1002/nbm.819
100. Agarwal S, Sair HI, Gujar S, Hua J, Lu H, Pillai JJ. Functional Magnetic Resonance Imaging Activation Optimization in the Setting of Brain Tumor-Induced Neurovascular Uncoupling Using Resting-State Blood Oxygen Level-Dependent Amplitude of Low Frequency Fluctuations. *Brain Connect* (2019) 9(3):241–50. doi: 10.1089/brain.2017.0562
101. Voss HU, Peck KK, Petrovich Brennan NM, Pogosebekyan EL, Zakharova NE, Batalov AI, et al. A Vascular-Task Response Dependency and its Application in Functional Imaging of Brain Tumors. *J Neurosci Methods* (2019) 322:10–22. doi: 10.1016/j.jneumeth.2019.04.004
102. Yeom KW, Lober RM, Mobley BC, Harsh G, Vogel H, Allaggio R, et al. Diffusion-Weighted MRI: Distinction of Skull Base Chordoma From Chondrosarcoma. *AJNR Am J Neuroradiol* (2013) 34(5):1056–61. doi: 10.3174/ajnr.A3333
103. Taouli B, Beer AJ, Chenevert T, Collins D, Lehman C, Matos C, et al. Diffusion-Weighted Imaging Outside the Brain: Consensus Statement From an ISMRM-Sponsored Workshop. *J Magn Reson Imaging* (2016) 44(3):521–40. doi: 10.1002/jmri.25196

104. Rana S, Albayram S, Lin DDM, Yousem David M. Diffusion-Weighted Imaging and Apparent Diffusion Coefficient Maps in a Case of Intracerebral Abscess With Ventricular Extension. *AJNR Am J Neuroradiol* (2002) 23 (1):109–12.
105. El KRM, Choudhary AK, Tappouni R. Accuracy of Apparent Diffusion Coefficient Value Measurement on PACS Workstation: A Comparative Analysis. *AJR Am J Roentgenol* (2011) 196(3):W280–4. doi: 10.2214/AJR.10.4706
106. Mascialchi M, Filippi M, Floris R, Fonda C, Gasparotti R, Villari N. Diffusion-Weighted MR of the Brain: Methodology and Clinical Application. *Radiol Med* (2005) 109(3):155–97.
107. Gurney-Champion OJ, Mahmood F, van SM, Julian R, George B, Philippens MEP, et al. Quantitative Imaging for Radiotherapy Purposes. *Radiother Oncol* (2020) 146:66–75. doi: 10.1016/j.radonc.2020.01.026
108. Allarakha A, Gao Y, Wang PJ. Progresses of MRI Diagnosis in Breast Cancer. *Chin J Med Imaging Technol* (2018) 34(2):306–9. doi: 10.4103/2347-5625.158017
109. Chandarana H, Wang H, Tijssen RHN, Das JJ. Emerging Role of MRI in Radiation Therapy. *J Magn Reson Imaging* (2018) 48(6):1468–78. doi: 10.1002/jmri.26271
110. Xie M, Ren Z, Bian D, Li D, Yu L, Zhu F, et al. High Resolution Diffusion-Weighted Imaging With Readout Segmentation of Long Variable Echo-Trains for Determining Myometrial Invasion in Endometrial Carcinoma. *Cancer Imaging* (2020) 20(1):66. doi: 10.1186/s40644-020-00346-7
111. Esthappan J, Ma DJ, Narra VR, Raptis CA, Grigsby PW. Comparison of Apparent Diffusion Coefficient Maps to T2-Weighted Images for Target Delineation in Cervix Cancer Brachytherapy. *J Contemp Brachyther* (2011) 3 (4):193–8. doi: 10.5114/jcb.2011.26470
112. Marchiq I, Pouyssegur J. Hypoxia, Cancer Metabolism and the Therapeutic Benefit of Targeting Lactate/H(+) Symporters. *J Mol Med (Berl)* (2016) 94 (2):155–71. doi: 10.1007/s00109-015-1307-x
113. Suppiah S, Rahmat K, Mohd-Shah MN, Azlan CA, Tan LK, Aziz YFA, et al. Improved Diagnostic Accuracy in Differentiating Malignant and Benign Lesions Using Single-Voxel Proton MRS of the Breast at 3 T MRI. *Clin Radiol* (2013) 68(9):e502–10. doi: 10.1016/j.crad.2013.04.002
114. Zeng QS, Li CF, Liu H, Zhen JH, Feng DC. Distinction Between Recurrent Glioma and Radiation Injury Using Magnetic Resonance Spectroscopy in Combination With Diffusion-Weighted Imaging. *Int J Radiat Oncol Biol Phys* (2007) 68(1):151–8. doi: 10.1016/j.ijrobp.2006.12.001
115. Li X, Zhu Y, Kang H, Zhang Y, Liang H, Wang S, et al. Glioma Grading by Microvascular Permeability Parameters Derived From Dynamic Contrast-Enhanced MRI and Intratumoral Susceptibility Signal on Susceptibility Weighted Imaging. *Cancer Imaging* (2015) 15(1):4. doi: 10.1186/s40644-015-0039-z
116. Torheim T, Groendahl AR, Andersen EK, Lyng H, Malinen E, Kvaal K, et al. Cluster Analysis of Dynamic Contrast Enhanced MRI Reveals Tumor Subregions Related to Locoregional Relapse for Cervical Cancer Patients. *Acta Oncol* (2016) 55(11):1294–8. doi: 10.1080/0284186X.2016.1189091
117. van DFA, van DGM, Engelbrecht MR, van LGJ, Verhofstad A, Rijpkema M, et al. Combined Quantitative Dynamic Contrast-Enhanced MR Imaging and (1)H MR Spectroscopic Imaging of Human Prostate Cancer. *J Magn Reson Imaging* (2004) 20(2):279–87. doi: 10.1002/jmri.20113
118. Lund KV, Simonsen TG, Kristensen GB, Rofstad EK. Pharmacokinetic Analysis of DCE-MRI Data of Locally Advanced Cervical Carcinoma With the Brix Model. *Acta Oncol* (2019) 58(6):828–37. doi: 10.1080/0284186X.2019.1580386
119. Lund KV, Simonsen TG, Kristensen GB, Rofstad EK. DCE-MRI of Locally-Advanced Carcinoma of the Uterine Cervix: Tofts Analysis Versus non-Model-Based Analyses. *Radiat Oncol* (2020) 15(1):79. doi: 10.1186/s13014-020-01526-2
120. Filoti DI, Shire SJ, Yadav S, Laue TM. Comparative Study of Analytical Techniques for Determining Protein Charge. *J Pharm Sci* (2015) 104 (7):2123–31. doi: 10.1002/jps.24454
121. Hardee ME, Zagzag D. Mechanisms of Glioma-Associated Neovascularization. *Am J Pathol* (2012) 181(4):1126–41. doi: 10.1016/j.ajpath.2012.06.030
122. Li KL, Zhu XP, Checkley DR, Tessier JJ, Hillier VF, Waterton JC, et al. Simultaneous Mapping of Blood Volume and Endothelial Permeability Surface Area Product in Gliomas Using Iterative Analysis of First-Pass Dynamic Contrast Enhanced MRI Data. *Br J Radiol* (2003) 76(901):39–50. doi: 10.1259/bjr/31662734
123. Medina LS, Bernal B, Dunoyer C, Cervantes L, Rodriguez M, Pacheco E, et al. Seizure Disorders: Functional MR Imaging for Diagnostic Evaluation and Surgical Treatment—Prospective Study. *Radiology* (2005) 236(1):247–53. doi: 10.1148/radiol.2361040690
124. Sun L, Qu B, Wang J, Ju Z, Zhang Z, Cui Z, et al. Integration of Functional MRI and White Matter Tractography in CyberKnife Radiosurgery. *Technol Cancer Res Treat* (2017) 16(6):850–6. doi: 10.1177/1533034617705283
125. Schad LR, Blüml S, Zuna IIX. MR Tissue Characterization of Intracranial Tumors by Means of Texture Analysis. *Magn Reson Imaging* (1993) 11 (6):889–96. doi: 10.1016/0730-725x(93)90206-s
126. van der Heide UA, Houweling AC, Groenendaal G, Beets-Tan RG, Lambin P. Functional MRI for Radiotherapy Dose Painting. *Magn Reson Imaging* (2012) 30(9):1216–23. doi: 10.1016/j.mri.2012.04.010
127. Prasetyanti PR, Medema JP. Intra-Tumor Heterogeneity From a Cancer Stem Cell Perspective. *Mol Cancer* (2017) 16(1):41. doi: 10.1186/s12943-017-0600-4
128. Onjukka E, Uzan J, Baker C, Howard L, Nahum A, Syndikus I. Twenty Fraction Prostate Radiotherapy With Intra-Prostatic Boost: Results of a Pilot Study. *Clin Oncol (R Coll Radiol)* (2017) 29(1):6–14. doi: 10.1016/j.clon.2016.09.009
129. Pollack A, Chinae FM, Bossart E, Kwon D, Abramowitz MC, Lynne C, et al. Phase I Trial of MRI-Guided Prostate Cancer Lattice Extreme Ablative Dose (LEAD) Boost Radiation Therapy. *Int J Radiat Oncol Biol Phys* (2020) 107 (2):305–15. doi: 10.1016/j.ijrobp.2020.01.052
130. Uzan J, Nahum AE, Syndikus. Prostate Dose-painting Radiotherapy I. And Radiobiological Guided Optimisation Enhances the Therapeutic Ratio. *Clin Oncol (R Coll Radiol)* (2016) 28(3):165–70. doi: 10.1016/j.clon.2015.09.006
131. von Eyben FE, Kiljunen T, Kangasmaki A, Kairemo K, von Eyben R, Joensuu T. Radiotherapy Boost for the Dominant Intraprostatic Cancer Lesion-A Systematic Review and Meta-Analysis. *Clin Genitourin Cancer* (2016) 14 (3):189–97. doi: 10.1016/j.clgc.2015.12.005
132. Henke L, Kashani R, Robinson C, Curcuro A, DeWees T, Bradley J, et al. Phase I Trial of Stereotactic MR-Guided Online Adaptive Radiation Therapy (SMART) for the Treatment of Oligometastatic or Unresectable Primary Malignancies of the Abdomen. *Radiother Oncol* (2018) 126(3):519–26. doi: 10.1016/j.radonc.2017.11.032
133. Ling CC, Humm J, Larson S, Amols H, Fuks Z, Leibel S, et al. Towards Multidimensional Radiotherapy (MD-CRT): Biological Imaging and Biological Conformality. *Int J Radiat Oncol Biol Phys* (2000) 47(3):551–60. doi: 10.1016/s0360-3016(00)00467-3
134. van Der Wel A, Nijsten S, Hochstenbag M, Lamers R, Boersma L, Wanders R, et al. Increased Therapeutic Ratio by 18FDG-PET CT Planning in Patients With Clinical CT Stage N2-N3M0 non-Small-Cell Lung Cancer: A Modeling Study. *Int J Radiat Oncol Biol Phys* (2005) 61(3):649–55. doi: 10.1016/j.ijrobp.2004.06.205
135. Forastiere AA, Zhang Q, Weber RS, Maor MH, Goepfert H, Pajak TF, et al. Long-Term Results of RTOG 91-11: A Comparison of Three Nonsurgical Treatment Strategies to Preserve the Larynx in Patients With Locally Advanced Larynx Cancer. *J Clin Oncol* (2013) 31(7):845–52. doi: 10.1200/JCO.2012.43.6097
136. Nutting CM, Morden JP, Harrington KJ, Urbano TG, Bhide SA, Clark C, et al. Parotid-Sparing Intensity Modulated Versus Conventional Radiotherapy in Head and Neck Cancer (PARSPORT): A Phase 3 Multicentre Randomised Controlled Trial. *Lancet Oncol* (2011) 12(2):127–36. doi: 10.1016/S1470-2045(10)70290-4
137. Wang J, Zheng J, Tang T, Zhu F, Yao Y, Xu J, et al. A Randomized Pilot Trial Comparing Position Emission Tomography (PET)-Guided Dose Escalation Radiotherapy to Conventional Radiotherapy in Chemoradiotherapy Treatment of Locally Advanced Nasopharyngeal Carcinoma. *PLoS One* (2015) 10(4):e0124018. doi: 10.1371/journal.pone.0124018
138. Houweling AC, Wolf AL, Vogel WV, Hamming-Vrieze O, van Vliet-Vroegindewij C, van de Kamer JB, et al. FDG-PET and Diffusion-Weighted MRI in Head-and-Neck Cancer Patients: Implications for Dose Painting. *Radiother Oncol* (2013) 106(2):250–4. doi: 10.1016/j.radonc.2013.01.003
139. Grönlund E, Johansson S, Nyholm T, Thellenberg C, Ahnesjö A. Dose Painting of Prostate Cancer Based on Gleason Score Correlations With



- Apparent Diffusion Coefficients. *Acta Oncol* (2018) 57(5):574–81. doi: 10.1080/0284186X.2017.1415457
140. Abedi I, Tavakkoli MB, Jabbari K, Amouheidari A, Yadegarfar. Dosimetric G. And Radiobiological Evaluation of Multiparametric MRI-Guided Dose Painting in Radiotherapy of Prostate Cancer. *J Med Signals Sens* (2017) 7 (2):114–21.
  141. Laprie A, Ken S, Filleron T, Lubrano V, Vieillelveigne L, Tensaouti F, et al. Dose-Painting Multicenter Phase III Trial in Newly Diagnosed Glioblastoma: The SPECTRO-GLIO Trial Comparing Arm A Standard Radiochemotherapy to Arm B Radiochemotherapy With Simultaneous Integrated Boost Guided by MR Spectroscopic Imaging. *BMC Cancer* (2019) 19(1):167. doi: 10.1186/s12885-019-5317-x
  142. Hunt A, Hansen VN, Oelfke U, Nill S, Hafeez S. Adaptive Radiotherapy Enabled by MRI Guidance. *Clin Oncol (R Coll Radiol)* (2018) 30(11):711–9. doi: 10.1016/j.clon.2018.08.001
  143. Kupelian P, Sonke JJ. Magnetic Resonance-Guided Adaptive Radiotherapy: A Solution to the Future. *Semin Radiat Oncol* (2014) 24(3):227–32. doi: 10.1016/j.semradonc.2014.02.013
  144. Grönborg C, Vestergaard A, Hoyer M, Söhn M, Pedersen EM, Petersen. Intra-fractional bladder motion JB. And Margins in Adaptive Radiotherapy for Urinary Bladder Cancer. *Acta Oncol* (2015) 54(9):1461–6. doi: 10.3109/0284186X.2015.1062138
  145. Vestergaard A, Hafeez S, Muren LP, Nill S, Hoyer M, Hansen VN, et al. The Potential of MRI-Guided Online Adaptive Re-Optimisation in Radiotherapy of Urinary Bladder Cancer. *Radiother Oncol* (2016) 118(1):154–9. doi: 10.1016/j.radonc.2015.11.003
  146. Pötter R, Tanderup K, Schmid MP, Jürgenliemk-Schulz I, Haie-Meder C, Fokdal LU, et al. MRI-Guided Adaptive Brachytherapy in Locally Advanced Cervical Cancer (EMBRACE-I): A Multicentre Prospective Cohort Study. *Lancet Oncol* (2021) 22(4):538–47. doi: 10.1016/S1470-2045(20)30753-1
  147. Tan Mbbs Mrcp Frcr LT, Tanderup DK, Kirisits DC, de Leeuw DA, Nout Md DR, Duke Mbbs Frcr S, et al. Image-Guided Adaptive Radiotherapy in Cervical Cancer. *Semin Radiat Oncol* (2019) 29(3):284–98. doi: 10.1016/j.semradonc.2019.02.010
  148. Westerveld H, Nesvacil N, Fokdal L, Chagari C, Schmid MP, Milosevic M, et al. Definitive Radiotherapy With Image-Guided Adaptive Brachytherapy for Primary Vaginal Cancer. *Lancet Oncol* (2020) 21(3):e157–67. doi: 10.1016/S1470-2045(19)30855-1
  149. Witt JS, Rosenberg SA, Bassetti MF. MRI-Guided Adaptive Radiotherapy for Liver Tumours: Visualising the Future. *Lancet Oncol* (2020) 21(2):e74–82. doi: 10.1016/S1470-2045(20)30034-6
  150. Bruynzeel AME, Tetar SU, Oei SS, Senan S, Haasbeek CJA, Spoelstra FOB, et al. A Prospective Single-Arm Phase 2 Study of Stereotactic Magnetic Resonance Guided Adaptive Radiation Therapy for Prostate Cancer: Early Toxicity Results. *Int J Radiat Oncol Biol Phys* (2019) 105(5):1086–94. doi: 10.1016/j.ijrobp.2019.08.007
  151. Parvez K, Parvez A, Zadeh. The diagnosis G. And Treatment of Pseudoprogression, Radiation Necrosis and Brain Tumor Recurrence. *Int J Mol Sci* (2014) 15(7):11832–46. doi: 10.3390/ijms150711832
  152. Xu JL, Li YL, Lian JM, Dou SW, Yan FS, Wu H, et al. Distinction Between Postoperative Recurrent Glioma and Radiation Injury Using MR Diffusion Tensor Imaging. *Neuroradiology* (2010) 52(12):1193–9. doi: 10.1007/s00234-010-0731-4
  153. Larsen VA, Simonsen HJ, Law I, Larsson HB, Hansen AE. Evaluation of Dynamic Contrast-Enhanced T1-Weighted Perfusion MRI in the Differentiation of Tumor Recurrence From Radiation Necrosis. *Neuroradiology* (2013) 55(3):361–9. doi: 10.1007/s00234-012-1127-4
  154. Verma N, Cowperthwaite MC, Burnett MG, Markey MK. Differentiating Tumor Recurrence from Treatment Necrosis: A Review of Neuro-Oncologic Imaging Strategies. *Neuro Oncol* (2013) 15(5):515–34. doi: 10.1093/neuonc/nos307
  155. Groot Koerkamp ML, Vasmel JE, Russell NS, Shaitelman SF, Anandadas CN, Currey A, et al. Optimizing MR-Guided Radiotherapy for Breast Cancer Patients. *Front Oncol* (2020) 10:1107. doi: 10.3389/fonc.2020.01107
  156. Podder TK, Fredman ET, Ellis RJ. Advances in Radiotherapy for Prostate Cancer Treatment. *Adv Exp Med Biol* (2018) 1096:31–47. doi: 10.1007/978-3-319-99286-0\_2
  157. Cusumano D, Boldrini L, Menna S, Teodoli S, Placidi E, Chiloiro G, et al. Evaluation of a Simplified Optimizer for MR-Guided Adaptive RT in Case of Pancreatic Cancer. *J Appl Clin Med Phys* (2019) 20(9):20–30. doi: 10.1002/acm2.12697
  158. Hall W, Straza M, Chen X, Mickevicius N, Erickson B, Schultz C, et al. Initial Clinical Experience of Stereotactic Body Radiation Therapy (SBRT) for Liver Metastases, Primary Liver Malignancy, and Pancreatic Cancer With 4D-MRI Based Online Adaptation and Real-Time MRI Monitoring Using a 1.5 Tesla MR-Linac. *PLoS One* (2020) 15(8):e0236570. doi: 10.1371/journal
  159. Tocco BR, Kishan AU, Ma TM, Kerkmeijer LGW, Tree. MR-Guided Radiotherapy for Prostate Cancer. *Front Oncol AC*. (2020) 10:616291. doi: 10.3389/fonc.2020.616291
  160. Raaymakers BW, Raaijmakers AJ, Lagendijk JJ. Feasibility of MRI Guided Proton Therapy: Magnetic Field Dose Effects. *Phys Med Biol* (2008) 53 (20):5615–22. doi: 10.1088/0031-9155/53/20/003
  161. Mowatt G, Scotland G, Boachie C, Cruickshank M, Ford JA, Fraser C, et al. The Diagnostic Accuracy and Cost-Effectiveness of Magnetic Resonance Spectroscopy and Enhanced Magnetic Resonance Imaging Techniques in Aiding the Localisation of Prostate Abnormalities for Biopsy: A Systematic Review and Economic Evaluation. *Health Technol Assess* (2013) 17(20):vii–xix, 1–281. doi: 10.3310/hta17200
  162. Cerantola Y, Dragomir A, Tanguay S, Bladou F, Aprikian A, Kassouf W. Cost-Effectiveness of Multiparametric Magnetic Resonance Imaging and Targeted Biopsy in Diagnosing Prostate Cancer. *Urol Oncol* (2016) 34 (3):119.e1–9. doi: 10.1016/j.urolonc.2015.09.010
  163. Gordon LG, James R, Tuffaha HW, Lowe A, Yaxley J. Cost-Effectiveness Analysis of Multiparametric MRI With Increased Active Surveillance for Low-Risk Prostate Cancer in Australia. *J Magn Reson Imaging* (2017) 45 (5):1304–15. doi: 10.1002/jmri.25504
  164. Barnett CL, Davenport MS, Montgomery JS, Kunju LP, Denton BT, Pierr M. (18)F-Choline PET/mpMRI for Detection of Clinically Significant Prostate Cancer: Part 2. Cost-Effectiveness Analysis. *J Nucl Med* (2019) 60(12):1705–12. doi: 10.2967/jnumed.119.225771
  165. Macleod LC, Yabes JG, Fam MM, Bandari J, Yu M, Maganty A, et al. Multiparametric Magnetic Resonance Imaging Is Associated With Increased Medicare Spending in Prostate Cancer Active Surveillance. *Eur Urol Focus* (2020) 6(2):242–8. doi: 10.1016/j.euf.2019.04.008
  166. Walton Diaz A, Shakir NA, George AK, Rais-Bahrami S, Turkbey B, Rothwax JT, et al. Use of Serial Multiparametric Magnetic Resonance Imaging in the Management of Patients With Prostate Cancer on Active Surveillance. *Urol Oncol* (2015) 33(5):202.e1–7. doi: 10.1016/j.urolonc.2015.01.023
  167. Nassiri N, Margolis DJ, Natarajan S, Sharma DS, Huang J, Dorey FJ, et al. Targeted Biopsy to Detect Gleason Score Upgrading During Active Surveillance for Men With Low Versus Intermediate Risk Prostate Cancer. *J Urol* (2017) 197(3 Pt 1):632–9. doi: 10.1016/j.juro.2016.09.070
  168. Lotan Y, Haddad AQ, Costa DN, Pedrosa I, Rofsky NM, Roehrborn CG. Decision Analysis Model Comparing Cost of Multiparametric Magnetic Resonance Imaging vs. Repeat Biopsy for Detection of Prostate Cancer in Men With Prior Negative Findings on Biopsy. *Urol Oncol* (2015) 33 (6):266.e9–16. doi: 10.1016/j.urolonc.2015.03.007
  169. Faria R, Soares MO, Spackman E, Ahmed HU, Brown LC, Kaplan R, et al. Optimising the Diagnosis of Prostate Cancer in the Era of Multiparametric Magnetic Resonance Imaging: A Cost-Effectiveness Analysis Based on the Prostate MR Imaging Study (PROMIS). *Eur Urol* (2018) 73(1):23–30. doi: 10.1016/j.eururo.2017.08.018
  170. Patel S, Rongen JJ, Fütterer JJ, Boltyenkov A, Rovers MM. The Role of Multiparametric Magnetic Resonance Imaging in Active Surveillance for Men With Low-Risk Prostate Cancer: A Cost-Effectiveness Modeling Study. *Eur Urol Oncol* (2018) 1(6):476–83. doi: 10.1016/j.euo.2018.05.007
  171. Lee N, Schoder H, Beattie B, Lanning R, Riaz N, McBride S, et al. Strategy of Using Intratreatment Hypoxia Imaging to Selectively and Safely Guide Radiation Dose De-Escalation Concurrent With Chemotherapy for Locoregionally Advanced Human Papillomavirus-Related Oropharyngeal Carcinoma. *Int J Radiat Oncol Biol Phys* (2016) 96(1):9–17. doi: 10.1016/j.ijrobp.2016.04.027



172. Riaz N, Sherman E, Pei X, Schöder H, Grkovski M, Paudyal R, et al. Precision Radiotherapy: Reduction in Radiation for Oropharyngeal Cancer in the 30 ROC Trial. *J Natl Cancer Inst* (2021) 113(6):742–51. doi: 10.1093/jnci/djaa184

**Conflict of Interest:** The authors declare that the research was conducted in the absence of any commercial or financial relationships that could be construed as a potential conflict of interest.

**Publisher's Note:** All claims expressed in this article are solely those of the authors and do not necessarily represent those of their affiliated organizations, or those of

the publisher, the editors and the reviewers. Any product that may be evaluated in this article, or claim that may be made by its manufacturer, is not guaranteed or endorsed by the publisher.

Copyright © 2021 Li, Zhang and Yang. This is an open-access article distributed under the terms of the Creative Commons Attribution License (CC BY). The use, distribution or reproduction in other forums is permitted, provided the original author(s) and the copyright owner(s) are credited and that the original publication in this journal is cited, in accordance with accepted academic practice. No use, distribution or reproduction is permitted which does not comply with these terms.

# Advantages of publishing in Frontiers



## OPEN ACCESS

Articles are free to read  
for greatest visibility  
and readership



## FAST PUBLICATION

Around 90 days  
from submission  
to decision



## HIGH QUALITY PEER-REVIEW

Rigorous, collaborative,  
and constructive  
peer-review



## TRANSPARENT PEER-REVIEW

Editors and reviewers  
acknowledged by name  
on published articles

## Frontiers

Avenue du Tribunal-Fédéral 34  
1005 Lausanne | Switzerland

**Visit us:** [www.frontiersin.org](http://www.frontiersin.org)

**Contact us:** [frontiersin.org/about/contact](http://frontiersin.org/about/contact)



## REPRODUCIBILITY OF RESEARCH

Support open data  
and methods to enhance  
research reproducibility



## DIGITAL PUBLISHING

Articles designed  
for optimal readership  
across devices



## FOLLOW US

@frontiersin



## IMPACT METRICS

Advanced article metrics  
track visibility across  
digital media



## EXTENSIVE PROMOTION

Marketing  
and promotion  
of impactful research



## LOOP RESEARCH NETWORK

Our network  
increases your  
article's readership